UNIVERSITÉ DE STRASBOURG

ÉCOLE DOCTORALE ED182_Physique et Chimie Physique

UMR7504

THÈSE présentée par :

Anna BONFIGLIO

Soutenue le : **9 decémbre 2021**

pour obtenir le grade de : **Docteur de l'Université de Strasbourg**

Discipline / Spécialité : Chimie et Chimie Physique

Novel phosphorescent N-heterocyclic carbene-based complexes: from photocatalysis and biomedical applications to optoelectronic devices

THÈSE dirigée par :

M. Matteo MAURO	Maître de Conférences-HDR, Université de Strasbourg

RAPPORTEURS :

M^me^ Paola CERONI	Professeure, Università degli Studi di Bologna
M. Gilles LEMERCIER	Professeur, Université de Reims Champagne-Ardenne

AUTRES MEMBRES DU JURY :

M^me^ Chantal DANIEL	Directrice de Recherche, CNRS & Université de Strasbourg

A Francesco

What is research but a blind date with knowledge?

Will Harvey

Abbreviations

ACN acetonitrile

ATP adenosine triphosphate

BMIM[PF_6] 1-butyl-3-methylimidazolium hexafluorophosphate

CAACs cyclic (alkyl)aminocarbenes

CFT crystal field theory

COD 1,5-cyclooctadiene

CT charge transfer

CV cyclic voltammetry

DFT density functional theory

DNA deoxyribonucleic acid

EC electron transfer for electron chemical reaction

EDB ethyl-4-(dimethylamino) benzoate

EGL energy gap law

EL electroluminescence

EL electroluminescence

ENT electronic energy transfer

EQE external quantum efficiency

ER endoplasmic reticulum

ET electron transfer

ETL electron transport layer

FRP free radical polymerization

FT-ATR-IR Fourier-transformed attenuated total reflection infrared spectroscopy

HBL hole blocking layer

HCT116 human colon carcinoma cell line

HE high energy

HIL hole injecting layer

HOMO highest occupied molecular orbital

HR-ESI-MS High resolution electrospray ionization mass spectrometry

HTL hole transport layer

IL intra-ligand

ILCT intra-ligand charge transfer

IQE internal quantum efficiency

IR infrared

ISC intersystem crossing

KS Kohn-Sham

LC ligand center

LE low energy

LEC light emitting electrochemical cell

LED light emitting diode

LF ligand field

LFT ligand field theory

LLCT ligand to ligand charge transfer

LMCT ligand to metal charge transfer

LMOA localized molecular orbital approximation

LUMO lowest unoccupied molecular orbital

MC metal-center

MDA-MB-231 human breast cancer cell line

MDEA N-Methyldiethanolamine

MLCT metal to ligand charge transfer

MLLCT metal ligand to ligand charge transfer

MOs molecular orbitals

MTS (3-(4,5-dimethylthiazol-2-yl)-5-(3-carboxymethoxyphenyl)-2-(4-sulfophenyl)-2H-tetrazolium)

MW microwave

NADH hydrogen- nicotinamide adenine dinucleotide

NADPH hydrogen- nicotinamide adenine dinucleotide phosphate

NHC N-heterocyclic carbene

NIR near infrared

OLED organic light emitting device

ORTEP Oak Ridge thermal ellipsoid plot

PCs photocatalytic systems

PEG polyethylene glycol

PI photo initiator

PISs photo initiating systems

PL photoluminescence

PLQY photoluminescence quantum yield

PMMA poly-(methyl methacrylate)

RISC revers-intersystem crossing

ROS reactive oxygen species

SCE saturated calomel electrode

SEM scanning electron microscope

SET single electron transfer

SOC spin–orbit coupling

TADF thermally-activated delayed fluorescence

TBACl tert-butyl ammonium chloride

TBAP tetra-*n*-butylammonium perchlorate

$TBAPF_6$ tetrabutylammonium hexafluorophosphate

TD-DFT time dependent density functional theory

TGA thermogravimetric analysis

TMCs transition metal complexes

TPA triplet polaron annihilation

TTA triplet triplet annihilation

Contents

Summary

S.1 Version française

1. *Introduction*

La chimie des complexes de métaux de transition est un domaine fascinant qui a attiré une attention remarquable des scientifiques afin de moduler et de comprendre leurs propriétés électroniques. Au cours des dernières décennies, des milliers de composés ont été étudiés afin de les rendre aptes à différentes applications, telles que la photocatalyse[1], la biomédecine[2] et les dispositifs optoélectroniques[3].

Selon une configuration électronique d^6, le métal lourd est entouré de ligands formant un complexe à géométrie octaédrique idéalisée. En conséquence, les cinq orbitales d du métal se divisent en deux ensembles, c'est-à-dire "t_{2g}" et "e_g". L'écart d'énergie entre eux est désigné par Δ_0 et dépend de la coquille de valence de l'ion métallique et de la force du champ de ligands impliqué. Comme les transitions électroniques dans un complexe métallique peuvent se produire entre différentes parties des molécules, on peut les distinguer sur la base des orbitales moléculaires impliquées : *i)* métal-centré (MC) ; *ii)* ligand-centré (LC) ; *iii)* transfert de charge ligand-métal (LMCT) et *iv)* transfert de charge métal-ligand (MLCT).

Dans les complexes luminescents de Ir(III) et Re(I), l'état excité le plus faible est un mélange de ^{3}MLCT/^{3}LC qui dépend de la contribution de l'orbitale d du métal et de la conjugaison π des ligands coordonnés. Étant donné que le ^{3}MLCT/^{3}LC, indiqué comme T_1, peut être considéré comme un mélange des contributions de ^{1}MLCT/^{3}LC, le mélange des états excités est lié à la constante SOC, qui varie avec la charge nucléaire des atomes lourds, le long du tableau périodique (Ru= 1042, Os= 3381, Ir= 3909 cm^{-1}). Le degré de mélange influence le processus de la constante de vitesse radiative et la durée de vie corrélée, conduisant à des émetteurs luminescents[4]. Puisque le but de mon projet de recherche est de maximiser la constante de vitesse radiative afin d'améliorer le rendement quantique de la photoluminescence, il est nécessaire de minimiser tous les processus non

radiatifs tels que : *i)* l'annihilation triplet-triplet (TTA), *ii)* le couplage vibronique sans radiation entre l'état excité le plus bas et l'état fondamental (loi d'écart d'énergie)[5] et iii) la population thermique des états ^{3}MC, qui sont proches en énergie des états émissifs[6]. Afin d'atteindre mon objectif, l'utilisation de carbènes NHC comme ligands σ-donneurs puissants est cruciale pour pousser les états ^{3}MC vers une énergie plus élevée. Les carbènes N-hétérocycliques sont des espèces contenant un carbéne en position C2 qui est stabilisé par au moins un atome d'azote adjacent présent dans la structure du cycle.[7] La stabilisation est donnée par deux facteurs : *i)* l'effet mésomère par le don d'électron π du N par sa paire solitaire et *ii)* l'effet inductif par le retrait d'électron σ de l'atome N plus électronégatif qui abaisse l'énergie des orbitales sp^2 remplies. Par conséquent, les NHC sont des ligands fortement σ-donneurs et faiblement π-accepteurs, réalisant une forte interaction avec le métal. De plus, la grande stabilité du complexe résultant et la grande versatilité structurelle des carbènes sont utiles pour régler les propriétés électroniques finales du complexe de métal de transition, atteignant les caractéristiques souhaitées.[8]

2. *Complexes de Re(I) émettant dans le rouge et portant un carbène N-hétérocyclique pyridyl- annulé*

Les dérivés du rhénium portant des ligands donneurs de σ plus puissants avec des atomes de carbone coordinateurs, tels que les ligands de type N-heterocyclic carbene (NHC), ont été étonnamment beaucoup moins explorés que les complexes diimine du rhénium(I) $[Re(N\hat{}N)(CO)_3L]^{n+}$ à ce jour. En raison de leurs caractéristiques électroniques et chimiques attrayantes, les NHC ont attiré une attention considérable en tant que ligands dans le domaine des émetteurs phosphorescents également.[9]

Une nouvelle famille de complexes de rhénium tris-carbonyle neutres et cationiques photoactifs est décrite ici. Les premiers ont la formule générale fac-$[Re(N\hat{}C:)(CO)3X]^0$ (**Re1-Re2**), tandis que les seconds sont fac-$[Re(N\hat{}C :)(CO)_3L]PF_6$, (**Re3-Re4**) où N^C: est le carbène N-hétérocyclique pyrido-annulé (NHC) provenant du proligand hexafluorophosphate de 2-(2-pyridinyl) imidazo[1,5-a]pyridinium, à savoir $[pyipy]PF_6$, et X est Cl^- (**Re1**) et Br^- (**Re2**), tandis que L est la pyridine (**Re3**) et la phosphine (**Re4**). La voie de synthèse est une réaction à un seul pot pour les composés neutres, en commençant par le sel d'azolium comme source de NHC et $[Re(CO)_5X]$ pour donner les complexes fac-$[Re(pyipy)(CO)_3X/L]$ neutres de charge souhaités (**Re1-Re4**). L'abstraction ultérieure

d'halogène et l'addiction du ligand auxiliaire neutre pyridine ou phosphine donne les complexes cationiques analogues sous forme de sel hexafluorophosphate (**Re3-Re4**). Les composés sont présentés dans la *Figure 1* et la voie de synthèse dans le *Schéma 1*.

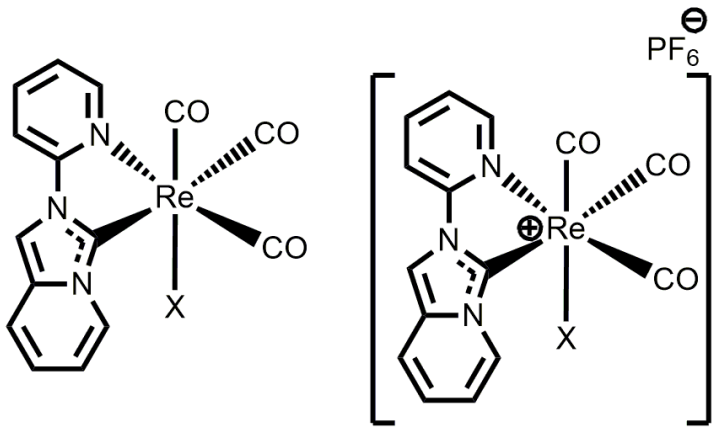

Figure 1. Structure chimique des complexes de rhénium étudiés **Re1-Re4.**

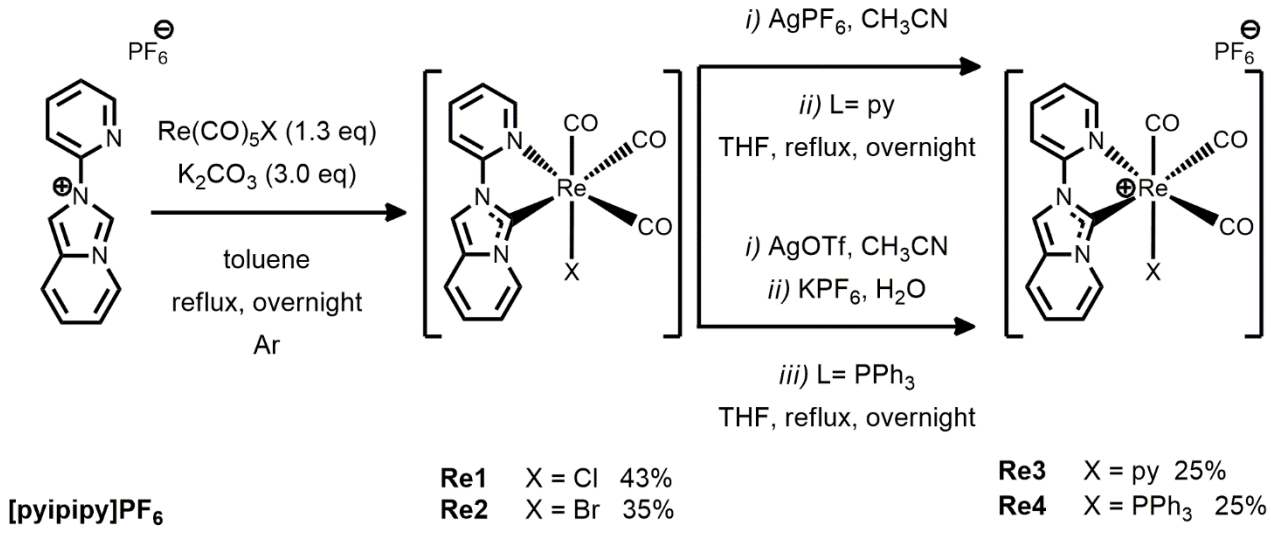

Schéma 1. Voie de synthèse schématique employée pour la synthèse des complexes **Re1-Re2** et **Re3-Re4.**

Les propriétés photophysiques des complexes ont été étudiées à une concentration de $2{,}0\times10^{-5}$ M dans une solution de dichlorométhane équilibrée à l'air et dégazée pour **Re1-Re2** et une solution d'acétonitrile pour **Re3-Re4** à température ambiante et dans une matrice vitreuse de 2-méthyltétrahydrofurane à 77 K. Les composés neutres et cationiques

présentent un spectre d'absorption électronique assez similaire dans les deux solutions diluées.

Dans le domaine UV (*Figure 2*), une bande d'absorption intense présente un λabs,max = 270 nm avec ε = 13,5 × 10^3 M^{-1} cm^{-1} pour **Re1** correspond au profil d'absorption du ligand [pyipy]PF_6. La première transition est décrite comme étant centrée sur le ligand (^{1}LC). La deuxième transition implique un transfert de charge à la fois de la fraction Re(CO)3Cl vers le ligand et du carbène vers le cycle pyridyle. D'autre part, la transition de plus basse énergie qui apparaît comme un épaulement à $\lambda_{abs,max}$ = 430 nm montre également un caractère ^{1}ILCT partiel avec un transfert de charge net de l'anneau carbène hétérocyclique vers la fraction pyridyle et est donc attribuée comme une transition électronique avec un transfert de charge mixte métal vers ligand et un transfert de charge intraligand (^{1}MLCT/^{1}ILCT) [dπ(Re)p(X)π(NHC) → π*(N^C)].

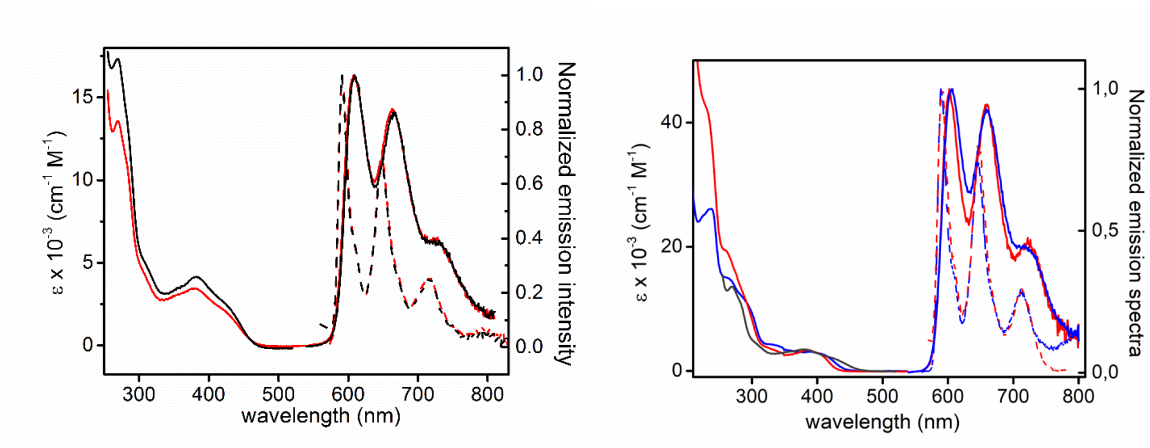

Figure 2. Spectres d'absorption électronique et d'émission normalisés des complexes **Re1** (traces noires) et **Re2** (traces rouges) dans une solution dégazée de CH_2Cl_2 (à gauche) et **Re3** (traces bleues) et **Re4** (traces rouges) dans du CH_3CN dégazé (à droite) à une concentration de 2X10^{-5} M à température ambiante (ligne continue) et à 77 K (ligne pointillée).

Les propriétés de photoluminescence (PL) des complexes ont également été étudiées, et les spectres correspondants dans du CH_2Cl_2 dilué dégazé et équilibré à l'air sont présentés dans la *Figure 2*.

Après irradiation à λ_{exc} = 370-420 nm, les complexes **Re1-Re2** montrent des propriétés photophysiques similaires. Les échantillons en solution présentent une photoluminescence rouge modérée avec un profil structuré avec des maxima à λ_{em} = 608, 664 et 728 nm

indépendamment de la présence de molécules de dioxygène à température ambiante. Le dégazage des échantillons produit une augmentation importante de l'intensité d'émission et une prolongation de la durée de vie de l'état excité, soit le PLQY de 0.08% vs. 1.5% et τ = 345 ns vs. 12.8 µs pour le complexe **Re1**, respectivement. Contrairement à ce qui a été observé pour d'autres classes de complexes luminescents de [Re(N^N)$(CO)_3$X] caractérisés par une émission ^{3}MLCT,[10] l'absence de tout décalage spectral lors de la variation de l'halogène ainsi que les valeurs plus faibles de la constante de vitesse radiative (k_r = 1,2 × 10^3 s^{-1} pour le complexe **Re1**) et la progression vibronique similaire observée pour les deux complexes et le ligand [pyipy]PF_6 suggèrent sans aucun doute une nature ^{3}LC de l'état excité responsable du processus d'émission dans les complexes **Re1-Re2**.

Les composés **Re3** et **Re4** présentent une bande d'absorption intense dans le domaine UV avec $\lambda_{abs,max}$ = 237 nm (ε = 2,61×10^4 M^{-1} cm^{-1}) et $\lambda_{abs,max}$ = 231 nm (ε = 4,22×10^4 M^{-1} cm^{-1}), respectivement. La contribution supplémentaire des transitions π-π* impliquant les cycles phényles du ligand PPh_3 dans les composés **Re4** explique l'augmentation du coefficient d'extinction molaire observé pour ce complexe. À plus basse énergie, la bande d'absorption observée dans la région à λ_{abs} environ 400 nm est attribuée à une transition électronique de caractère ^{1}MLCT, à savoir d(Re)π(NHC) π*(py), mélangée à un transfert de charge intraligand (^{1}ILCT) impliquant le ligand cyclométallisant de nature π(NHC) π*(py), où NHC est le fragment NHC benzannulé et py est le cycle pyridyle. Lors de l'irradiation à la bande ^{1}MLCT, les complexes **Re3** et **Re4** présentent des propriétés photophysiques similaires. Le spectre de photoluminescence des deux échantillons dans du CH_3CN dégazé montre une émission structurée avec des maxima à λ_{em} = 602 et 606, 660 et 725 nm à température ambiante qui sont décalés de Stokes d'environ 6500 et 6650 cm^{-1} pour **Re3** et **Re4**, respectivement. Lors de l'élimination du dioxygène, une augmentation des valeurs du rendement quantique de la photoluminescence (PLQY) (de 0,14 % à 0,72 %) ainsi qu'une prolongation de la durée de vie de l'état excité (de τ = 204 ns à 19,3 µs) sont observées pour le composé **Re3**. De même, le PLQY et la durée de vie augmentent de 0,04% à 1,60% et de τ= 209 ns à 30,0 µs, respectivement, pour le dérivé **Re4**.

Grâce à l'absorption relativement intense de la lumière visible, aux états excités à longue durée de vie et aux potentiels redox appropriés, ces composés semblent être de bons candidats pour un nouveau type de systèmes photocatalytiques (PCs), en particulier pour les expériences de photopolymérisation.[11]

Le comportement photocatalytique des composés **Re1** et **Re2** a été étudié dans le cadre d'une collaboration avec le groupe du Prof. Jacques Lalevée de l'Université de Haute Alsace (Mulhouse, France).

L'efficacité de l'initiation de la polymérisation radicalaire (PRF) à la fois dans les films minces [i] et épais [ii] pour les monomères PEG-diacrylate sous air lors de l'irradiation avec la LED@405 nm est meilleure pour les systèmes photoinitiateurs (PISs) complexe de rhénium/Iod/amine que le blanc (iod/amine) (**Re1**= 64% [i] / 94% [ii] **Re2**= 61% [i] / 94% [ii] vs 49% [i] / 89% [ii]). Par conséquent, la vitesse de polymérisation est plus rapide en utilisant les complexes de rhénium (≈ 50 s vs 200 s), ce qui démontre que les complexes de rhénium ont un effet significatif sur l'amélioration de l'efficacité de la photopolymérisation.

3. Complexes cationiques d'Ir(III) comportant un carbène N-hétérocyclique pyridyl-annulé comme agents théranostiques puissants

En 1965, Rosenberg a découvert la cytotoxicité du cisplatine et, à partir de là, son utilisation comme agent chimiothérapeutique s'est généralisée.[12] Cependant, la présence de multiples effets secondaires a poussé les scientifiques à chercher une alternative aux complexes de platine. Parmi les autres métaux, les composés d'iridium(III) constituent une option prometteuse. Il a déjà été démontré que les complexes iridium(III)-NHC possèdent des propriétés de cytotoxicité élevées contre les cellules cancéreuses,[13] étant donné la perméabilisation anormalement élevée de la membrane mitochondriale. Dans ce chapitre, une nouvelle série de métamédicaments Ir(III)-NHC est rapportée et leur cytotoxicité est étudiée, tout en conservant les propriétés d'émission pour leur localisation cellulaire. Les nouveaux composés ont la formule générale $[Ir(C\hat{}N)_2(pyipy)]PF_6$ où C^N est un dérivé de la phénylpyridine utilisé comme ligand cyclométallique et pyipi est le ligand procarbénique 2-(2-pyridyl)imidazo[1,5-a]pyridinium hexafluorophosphate. Ils sont présentés dans la *Figure 3*.

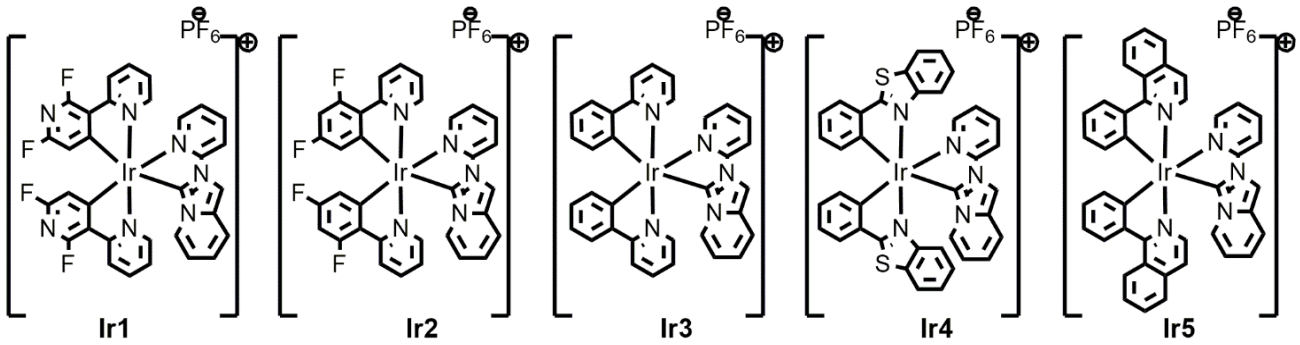

Figure 3. Structure chimique des complexes d'iridium étudiés **Ir1-Ir5**

La synthèse (*Schéma 2*) commence par la déprotonation en position C(3) du ligand procarbénique 2-(2-pyridyl)imidazo[1,5-a]pyridinium hexafluorophosphate, à savoir [pyipy]PF_6, via l'activation de la liaison C-H supportée par Ag_2O, donnant lieu à la formation du ligand NHC annelé selon la procédure originale rapportée par Lassaletta.[14] Par la suite, la réaction de transmétallation a été réalisée in situ en ajoutant le dimère d'iridium à pont chloré correspondant. Ces derniers ont été préparés en utilisant la procédure classique rapportée précédemment par Nonoyama.[15] Cinq complexes cibles **Ir1-Ir5** portant différents ligands C^N cyclométallants ont été obtenus en rendements modérés après purification.

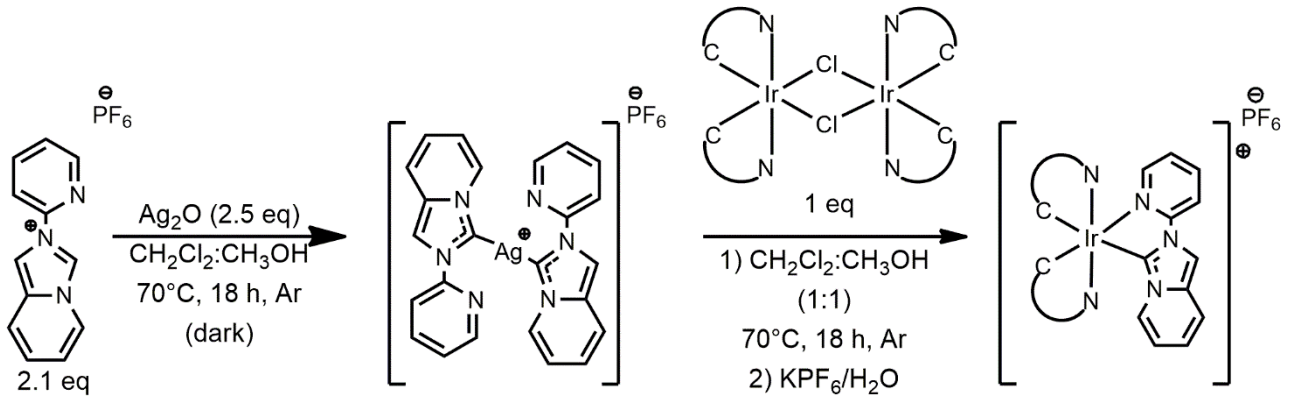

Schéma 2. Voie de synthèse schématique utilisée pour la synthèse des complexes **Ir1-Ir5.**

Dans la région de plus haute énergie (λ_{abs} <350 nm), le spectre d'absorption électronique est caractérisé par des bandes intenses (ε = environ 1-4X10^4 M^{-1} cm^{-1}) qui peuvent être attribuées à la transition intraligand du caractère π-π* localisée sur le ligand C^N, à savoir

$^1IL_{C\wedge N}$. À plus basse énergie, les bandes moins intenses (ε = environ 0,3-1X10^4 M^{-1} cm^{-1}) et plus larges peuvent être attribuées de manière confidentielle à des processus d'absorption électronique qui se chevauchent et qui résultent de différentes combinaisons de transfert de charge intraligand de caractère singlet-manifold autorisé par le spin (^{1}ILCT) et de transfert de charge métal-ligand (^{1}MLCT). En ce qui concerne les complexes **Ir1-Ir2**, un pic supplémentaire est clairement visible dans le profil d'absorption à λ_{max} = 400 (ε = 2.4X10^3 M^{-1} cm^{-1}) et 410 nm (ε = 2. 6X10^3 M^{-1} cm^{-1}) pour les composés **Ir1** et **Ir2**, respectivement, attribuable à l'absorption intraligand impliquant le caractère ligand NHC auxiliaire (IL_{NHC}), où NHC est la fraction pyipy carbène benzannulée, en raison de l'importante conjugaison π-étendue de cette dernière.

Lors de la photo-excitation dans la bande d'énergie basse, les échantillons dilués des complexes **Ir1-Ir5** présentent une photoluminescence faible à modérée, mais avec une double émission surprenante.

Le spectre d'émission du composé **Ir1** présente une bande structurée avec des maxima λ_{em} à 444 et 473 nm, à savoir la bande d'émission à haute énergie (HE). En outre, une deuxième bande structurée est visible du côté de la basse énergie (LE) avec λ_{em} à 590 et 648 nm, mais avec une très faible intensité. En passant au complexe **Ir2**, la bande HE affiche un décalage bathochrome à λ_{em} = 467 nm et 494 nm ; tandis que la bande LE augmente son intensité sans décalage spectral apparent.

La bande LE apparaît encore plus clairement pour le composé **Ir3** et la bande HE est faible, large et sans caractéristiques. Dans les complexes **Ir4-Ir5**, la stabilisation des orbitales π* conférée par la conjugaison plus étendue du ligand C^N provoque un décalage bathochrome attendu du profil d'émission et la structure de la bande est moins marquée. L'origine différente des deux bandes d'émission est soutenue par le comportement indépendant observé pour les spectres d'excitation enregistrés à la longueur d'onde HE et LE qui suggère un faible couplage électronique entre les deux états excités responsables de la double émission.

En ce qui concerne les complexes **Ir1-Ir3,** la bande HE peut être attribuée avec confiance à un processus radiatif provenant d'un état excité triplet avec un caractère principalement $^3IL_{C\wedge N}$, bien qu'avec un degré partiel de mélange avec l'état $^1MLCT_{C\wedge N}$ selon la nature du ligand C^N, comme cela est typique de cette classe d'émetteurs.[16]

En ce qui concerne le complexe **Ir3**, les durées de vie mesurées pour les échantillons dégazés dans les bandes HE et LE présentent une décroissance mono-exponentielle avec τ_{HE} = 555 ns et τ_{LE} = 6,0 µs, respectivement. Pour les complexes **Ir4-Ir5**, l'analyse des traces de décroissance a nécessité un ajustement bi-exponentiel dans la région des longueurs d'onde plus courtes et plus longues avec des composantes de durée de vie similaires (par exemple, τ_1 = 6,1 µs et τ_2 = 1,8 µs pour le complexe **Ir4**), mais avec des poids différents, ce qui indique que le profil PL enregistré est composé de deux bandes d'émission qui se chevauchent presque. Des résultats similaires ont été obtenus pour le complexe **Ir2**. La bande HE a surpassé la bande LE pour le complexe **Ir1**. Dans l'ensemble, ces résultats confirment la nature principalement triplet des deux états excités impliqués dans le processus d'émission double et indiquent un caractère $^3MLCT_{C\wedge N}/^3IL_{C\wedge N}$ et $^3IL_{NHC}$ pour les bandes HE et LE, respectivement ; ce dernier état, qui possède de moins bonnes propriétés d'émission, étant responsable de l'extinction du collecteur $^3MLCT_{C\wedge N}/^3IL_{C\wedge N}$ supérieur.

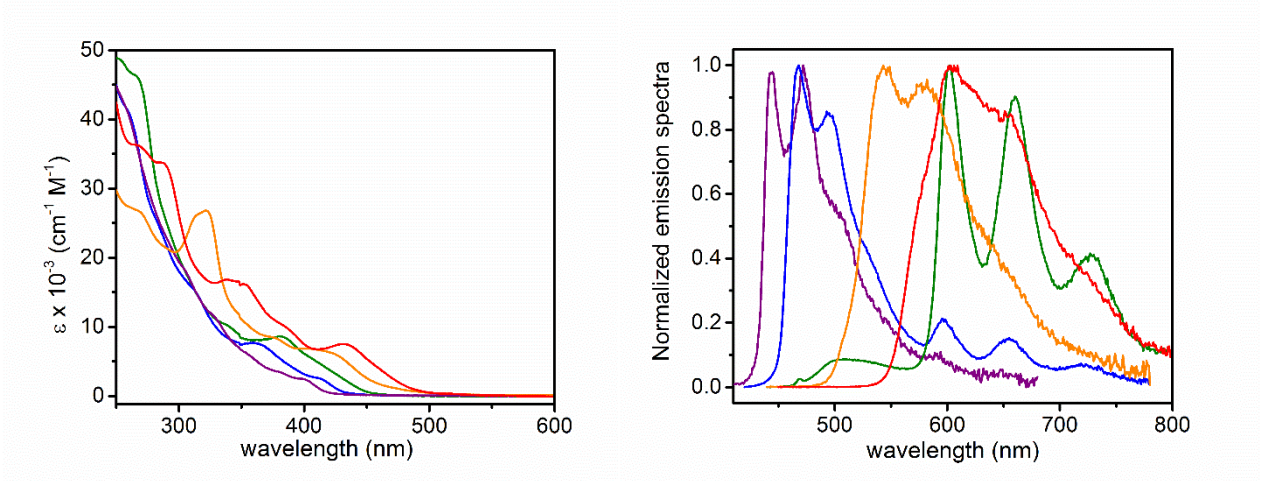

Figure 4. Spectres d'absorption électronique (case de gauche) et de photoluminescence (case de droite) des composés **Ir1** (traces violettes), **Ir2** (traces bleues), **Ir3** (traces vertes), **Ir4** (traces orange) et **Ir5** (traces rouges) dans une solution de CH_2Cl_2 à une concentration de $3X10^{-5}$ M à température ambiante. Les spectres d'émission ont été enregistrés après excitation à λ_{exc} = 350 nm pour **Ir1**, λ_{exc} = 400 nm pour **Ir2,** λ_{exc} = 410 nm pour **Ir3,** λ_{exc} = 420 nm pour **Ir4** et λ_{exc} = 430 nm pour **Ir5**. Les spectres des composés **Ir1-Ir5** se rapportent à des échantillons dégazés.

La cytotoxicité in vitro des composés a été étudiée dans le cadre d'une collaboration avec le groupe du Pr. Sylvie Fournel, Dr. Antoine Kichler et Conor McCartin à la faculté de

pharmacie de l'Université de Strasbourg. En particulier, les complexes ont été testés contre deux lignées cellulaires cancéreuses humaines, HCT116 (carcinome du côlon humain) et MDA-MB-231 (cancer du sein humain), en mesurant la diminution de l'activité déshydrogénase dépendante du NADH et du NADPH, reflétant une diminution de l'activité métabolique, en utilisant le test MTS après 24 et 48 heures de traitement.

Tous les composés présentent un niveau de cytotoxicité similaire - bien supérieur à celui de l'oxaliplatine - à l'exception du composé **Ir1**. Notamment, les composés ont montré une diminution d'environ deux à dix fois de la CI_{50} après 48 heures - atteignant des valeurs de CI_{50} d'environ 1 µM - à l'exception du composé **Ir1**. D'autres résultats obtenus après 72 heures de traitement de cellules HeLa avec les composés **Ir2** et **Ir4** ont montré des valeurs de CI_{50} de 3,6 µM et 1,6 µM, respectivement, affichant une puissance comparable à celle des composés Ir bis-N-hétérocycliques rapportés par Che *et al.*[17] Comme le composé **Ir4** a montré un niveau d'activité plus élevé, le mécanisme de mort cellulaire a été étudié en profondeur. Il a été constaté que la voie de l'induction apoptotique par le composé **Ir4** est dépendante des caspases, ce qui est probablement dû à l'activation directe de la voie apoptotique intrinsèque par la perturbation mitochondriale.

4. *Complexes phosphorescents mononucléaires d'iridium(III) et hétérodinucléaires d'Ir(III)/M(I) (M = Cu(I), Au(I)) avec un pont carbène N-hétérocyclique de type Janus*

Les complexes Ir(III) cyclométallisés constituent une classe exceptionnelle d'émetteurs dans les dispositifs optoélectroniques efficaces, tels que les diodes électroluminescentes organiques (OLED) et les cellules électrochimiques émettrices de lumière (LEC).[18] La forte SOC induite par le métal lourd et l'effet structurel jouent un rôle important dans l'origine des propriétés luminescentes.[19]

Jusqu'à présent, la modulation fine des propriétés redox et photophysiques a été principalement réalisée par une conception moléculaire judicieuse et le contrôle de la géométrie et des liaisons d'isomérisation des ligands coordonnés autour du centre Ir(III) qui opèrent sélectivement sur la topologie des surfaces d'énergie potentielle et la réorganisation

de la densité électronique. Ainsi, une palette colorée de complexes cyclométalliques homo- et hétéro-épicés de Ir(III) a été obtenue lorsque ce centre métallique est combiné avec des échafaudages mono-, bi- et tri-dentés. De manière surprenante, des efforts importants ont été consacrés à l'étude des espèces monométalliques.

Bien que les deux requièrent une recombinaison des porteurs de charge, qui a lieu avec une statistique de spin du rapport exciton simple/triplet de 1:3, les dispositifs LEC affichent toujours une efficacité inférieure et une durée de vie réduite par rapport aux OLED dans une région spectrale comparable, malgré les efforts de recherche actuels.[20] En particulier, les LEC nécessitent la présence d'ions mobiles qui migrent lors de l'application d'une polarisation électrique appropriée, assurant une injection, une migration et une recombinaison efficaces des charges au sein de la couche électroactive.[21] Dans ce cadre, les complexes d'iridium cationiques mononucléaires portant des ligands cyclométalliques se sont révélés être des matériaux émetteurs de premier plan.[22]

L'un des problèmes à résoudre en ce qui concerne les composés luminescents est la chute sévère de la PLQY lorsqu'on passe à des longueurs d'onde plus grandes, ce qui rend la conception dans le proche infrarouge (NIR) particulièrement difficile.[23] Par conséquent, l'exploration de nouvelles stratégies de conception pour les émetteurs du rouge au NIR est d'une importance capitale pour réaliser des dispositifs électroluminescents très performants dans cette région spectrale difficile. Seul un nombre très limité de travaux décrit l'application de complexes dinucléaires et/ou multinucléaires dans des dispositifs LEC et des efficacités quantiques externes (EQE) encore inférieures à 2% ont été rapportées à ce jour.[24]

Nous présentons ici une nouvelle famille de complexes phosphorescents Ir(III)/M(I) où les deux métaux sont reliés par le pont hétéroditopique 1,3-dimesityl-5-acétyllimidazol-2-ylidène-4-olate (IMesAcac) (voir *Schéma 3*). La capacité de liaison du site "acac" est utilisée sélectivement pour chélater la partie luminescente [$(C\hat{}N)_2Ir^{III}$], ce qui donne une nouvelle famille de complexes Ir(III) émettant dans le rouge avec des propriétés optiques améliorées.

Trois complexes mononucléaires différents de formule générale [$Ir(1C:1N\text{-}C\hat{}N)_2(2O,O\text{-}$IMesAcacH)]$PF_6$ (**1-3**) ont été préparés, où IMesAcacH est le précurseur d'imidazolium protoné et C^N est le pro-ligand cyclométallisant 2-phényl-pyridine (ppy), 2-phényl-benzotiazole (2-pbt) et 1-phénylisoquinoline (1-piq), respectivement. Les complexes dinucléaires chloro-pontés de Ir(III) [$Ir(C\hat{}N)_2(\mu\text{-}Cl)]_2$ ont été utilisés comme composés

d'iridium de départ pour les étapes de réaction suivantes. La synthèse a commencé par l'abstraction d'un halogène en utilisant $AgPF_6$ comme source d'argent (I) dans un solvant légèrement coordinateur, tel que le méthanol, ce qui a permis d'obtenir le complexe bis-solvato correspondant de formule générale $[Ir(C^N)_2(MeOH)_2]_2$. Après élimination de l'AgCl par filtration, l'IMesAcacH zwitterionique a ensuite été ajouté directement au mélange réactionnel qui a été porté à reflux pendant 12 heures. Les complexes mononucléaires cibles **1-3** ont été obtenus (*Figure 5*) avec une pureté adaptée à l'étude photophysique, avec un rendement modéré à bon (44-87%) après recristallisation.

La synthèse des complexes hétérodinucléaires a utilisé une procédure de métallisation sélective par étapes qui a permis d'obtenir directement les espèces Ir(III)/M(I) cibles (*Schéma 3*). Après abstraction du chlorure en utilisant $AgPF_6$ sur le dimère dichloro iridium, le métalloligand zwitterionique qui présente un motif de coordination de type acac, à savoir MI(1C-IPr)(1C-IMesAcac), est ensuite ajouté, donnant les complexes cibles **4-5** et **6-7** avec M = Cu(I) et Au(I), respectivement, après recristallisation avec une solution aqueuse de KPF_6 (*Figure 5*).

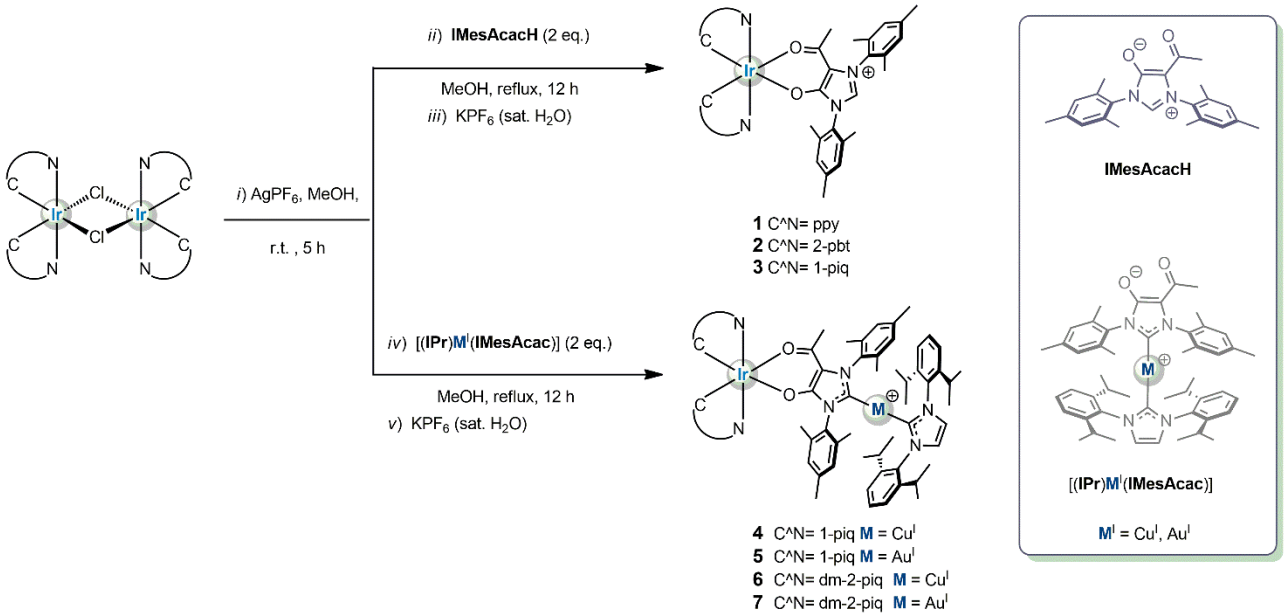

Schéma 3. Voie de synthèse schématique utilisée pour la synthèse des complexes **1-7** Tous les complexes ont été préparés sous forme de sel de PF_6^-.

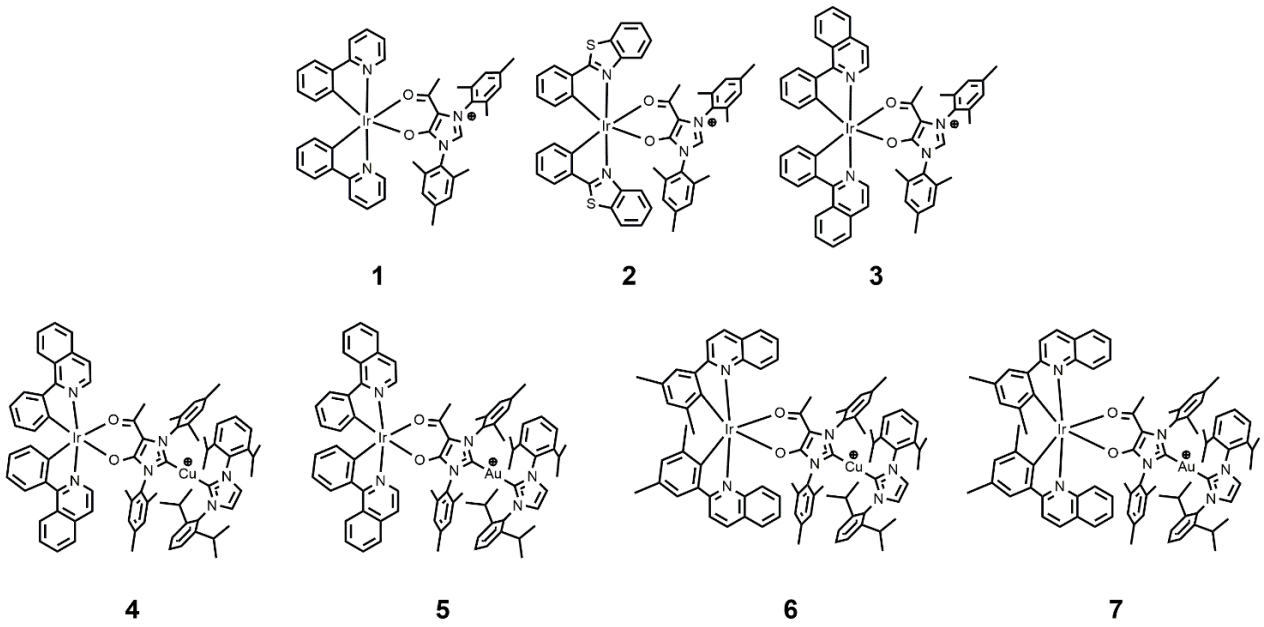

Figure 5. Structure chimique des complexes d'iridium étudiés **1-7**

Les propriétés photophysiques des complexes **1-7** ont été étudiées dans différentes conditions d'échantillonnage (*Figure 6,7, 8* et *9*). Les complexes monométalliques **1-3** ont été analysés dans l'acétone, car ils sont stables uniquement dans les solvants de coordination faibles et dans les solvants non chlorés, ce qui permet un choix sélectif des conditions. À titre de comparaison, les complexes **4** et **5** ont également été étudiés dans l'acétone, bien qu'ils soient stables même dans le dichlorométhane. Par la suite, les propriétés photophysiques des complexes **4** à **7** ont été étudiées dans le dichlorométhane, afin d'être directement comparables aux complexes de référence [Ir(1-piq)$_2$(acac)] et [Ir(dm-2-piq)$_2$(acac)][4] et d'obtenir des informations sur leur aptitude à servir d'émetteurs dans les dispositifs LEC.

recouvrent partiellement. Cette bande est attribuée aux processus électroniques autorisés par le spin avec un caractère principalement de transfert de charge métal-ligand (^{1}MLCT) comme par comparaison avec les complexes [Ir(C^N)$_2$(acac)] apparentés rapportés précédemment.[25]

Une modulation claire du début de l'absorption est observée dans la série avec un décalage bathochrome dans l'ordre **1** à **2** à **3**, qui est parallèle à l'augmentation de la capacité d'acceptation de π de l'anneau hétéroaromatique contenant N coordonné sur l'atome d'iridium.

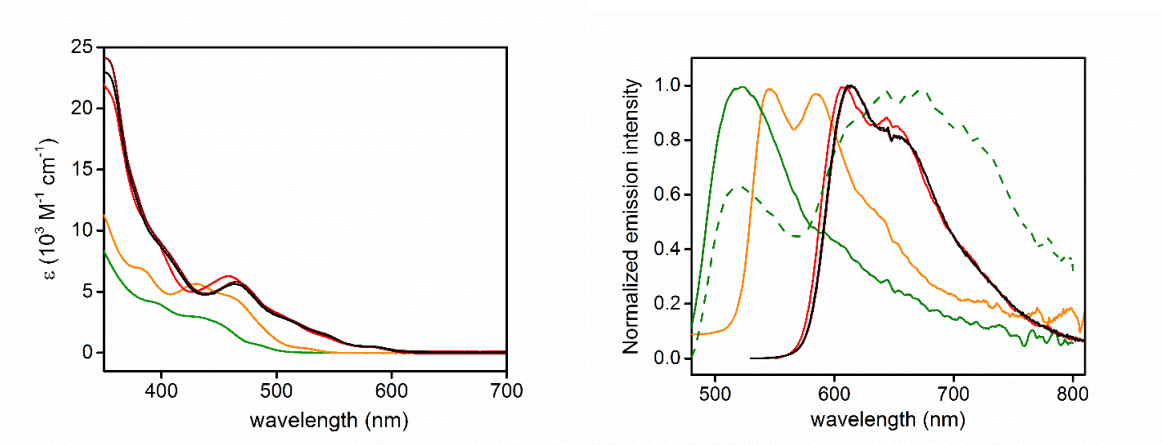

Figure 6. Spectres d'absorption électronique (gauche) et d'émission (droite) pour **1** (vert), **2** (orange), **3** (rouge), **4** (rouge foncé) et **5** (noir) dans l'acétone à des concentrations de 3,0X10^{-5} cm en condition dégazée. Pour **1**, le spectre d'émission de l'échantillon équilibré à l'air est représenté en pointillés. Les échantillons ont été excités à λ_{exc} = 410, 450, 460, 470 et 460 nm pour les composés **1**, **2**, **3**, **4** et **5**, respectivement.

Lors de l'excitation dans la bande ^{1}MLCT, les échantillons d'acétone des composés **1-5** montrent une photoluminescence à la fois dans des conditions équilibrées à l'air et dégazées (*Figure 6*). Les spectres d'émission montrent un décalage bathochrome allant de **1** à **2** et **3** qui est parallèle à la tendance observée dans les spectres d'absorption. De manière surprenante, les échantillons équilibrés à l'air du complexe **1** montrent clairement deux bandes d'émission larges et sans caractéristiques centrées à 520 et 655 nm et un PLQY global aussi bas que 0,05%. En condition dégazée, la bande à 520 nm domine le profil d'émission avec une durée de vie de 1,2 µs. Cette bande est attribuée à T_3 par un calcul informatique impliquant la contribution de l'état IL_{C^N}. Ce résultat confirme la nature

phosphorescente de la bande de haute énergie (à savoir P1), attribuée à un état émissif de caractère $^3MLCT_{ppy}/^3IL_{ppy}$. L'incorporation d'un système π plus étendu, tel que le cycle benzothiazole ou la fraction isoquinoléine, sur le ligand C^N cyclométallisant provoque un déplacement de l'émission vers des énergies plus basses, soit λ_{em} = 546 et 583 nm (**2**), et 607 et 650 nm (**3**), dont le profil semble être pratiquement indépendant de la présence de dioxygène. Néanmoins, une augmentation du PLQY de 1,9 à 3,5% (composé **2**) et de 2,5 à 18% (composé **3**) est observée, pointant à nouveau vers la nature triplet de l'état excité émissif. Les deux spectres d'excitation présentent un profil légèrement différent, également lorsqu'on les compare au spectre d'absorption, ce qui corrobore l'idée que les deux bandes d'émission proviennent d'états excités électroniquement non couplés. L'analyse résolue en temps de la photoluminescence des composés **1-3** a révélé des informations intéressantes. En effet, les données cinétiques de l'état excité enregistrées en condition dégazée ont nécessité un ajustement avec un modèle bi-exponentiel pour les trois composés **1-3**. Un tel état P2 semble être présent dans les trois complexes de la série **1-3** et il est très probablement à l'origine de la bande clairement observée à λ_{em} = 655 nm pour le complexe **1**. Pour approfondir les propriétés émissives et l'origine de la bande d'énergie inférieure, des expériences de photoluminescence à basse température (77 K) ont été réalisées pour des échantillons de **1-3** dans une matrice vitreuse de 2-MeTHF (*Figure 7*).

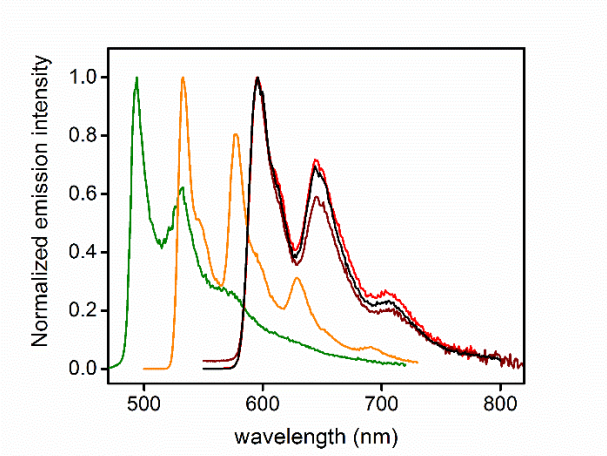

Figure 7. Spectres d'émission enregistrés pour **1** (vert), **2** (orange), **3** (rouge), **4** (rouge foncé) et **5** (noir) dans une matrice vitreuse de 2Me-THF à 77 K. Les échantillons ont été excités à λ_{exc} = 400 nm pour **1** et **2**, 420 nm pour **3**, 450 nm pour **4** et 460 nm pour **5**.

Dans ces conditions, les complexes **1-3** montrent une émission intense avec un profil hautement vibronique et une décroissance mono-exponentielle sur l'ensemble de la bande d'émission ressemblant à ceux des complexes parentaux [Ir(C^N)$_2$(acac)], indiquant que la population de la bande P2 pourrait se produire par un processus thermiquement activé à température ambiante. Dans l'ensemble, la bande P2 est provisoirement attribuée à un caractère de transfert de charge triplet de ligand à ligand, à savoir ^{3}LLCT$_{IMesAcacH}$, avec un caractère C^N$_{IMesAcacH}$ perturbé par le métal, proche du caractère émissif ^{3}IL$_{C^N}$/^{3}MLCT$_{C^N}$. En effet, en passant du composé **1** au composé **2** puis au composé **3**, le niveau de ^{3}LLCT$_{IMesAcacH}$ devrait être affecté de façon mineure. La stabilisation du ^{3}MLCT$_{C^N}$/^{3}IL$_{C^N}$ fournie par la π-conjugaison plus étendue pour les complexes **2** et **3** du système augmente la barrière énergétique pour le processus P1→P2, rendant plus difficile la population thermique du P2 peu émissif. En passant de **3** à **4** et **5**, un petit décalage bathochrome est observé pour la bande attribuable au mélange des transitions ^{1}MLCT et ^{3}MLCT qui implique la partie C^N et acac cyclométallisante ($\lambda_{abs,max}$ = 458 nm pour **3** et 465 nm pour **4** et **5**). Les états MLCT$_{C^N}$ sont plus stabilisés, augmentant leur participation dans les états mixtes IL$_{C^N}$/MLCT$_{C^N}$ de basse altitude du complexe **4** par rapport au complexe **3**.

Les spectres de photoluminescence de **4** et **5** sont décalés bathochromiquement de 8 nm (215 cm^{-1}) par rapport au composé parental **3**. En revanche, les espèces bimétalliques présentent une cinétique mono-exponentielle de décroissance de l'état excité et une PLQY multipliée par deux (τ = 1,6 µs et PLQY = 36% dans l'acétone dégazée). Il faut noter que cette valeur de PLQY est beaucoup plus élevée que celle du complexe de référence [Ir(1-piq)$_2$(acac)] et qu'elle est parmi les plus élevées pour les complexes Ir(III) cationiques émettant dans le rouge.

Dans un deuxième temps, les propriétés photophysiques des quatre complexes **4-7** ont été étudiées dans une solution de CH_2Cl_2 à une concentration de 3X10^{-5} M, à la fois dans des conditions équilibrées à l'air et dégazées à température ambiante (*Figure 8*). Dans la région de plus haute énergie à λ_{abs} = 340-350 nm, les quatre complexes présentent des bandes intenses (ε = 2,06-2,28X10^4 M^{-1} cm^{-1}) qui peuvent être attribuées à des processus électroniques avec principalement un singlet-manifold centré sur le ligand (^{1}LC) à un certain degré de mélange avec un transfert de charge métal-ligand autorisé par le spin (1MLCT). A plus basse énergie (λ_{abs} ca. 400 nm), les transitions moins intenses avec ε = 6.8-8.3 X 10^3 M^{-1} cm^{-1} sont attribuables aux processus électroniques avec principalement le caractère ^{1}MLCT mixte avec transfert de charge intraligand (^{1}ILCT). Lors de l'excitation sur les bandes

inférieures, les échantillons de CH_2Cl_2 dilués des composés **4-7** présentent une émission rouge intense et vibrante. En particulier, les composés **4** et **5** montrent une large bande d'émission centrée à λ_{em} = 610 nm avec une caractéristique vibrationnelle à 645 nm qui peut être attribuée à une émission provenant d'un état excité avec un caractère ^{3}MLCT/^{3}LC admixé impliquant l'atome lourd et les ligands C^N. D'autre part, le profil spectral d'émission des composés **6** et **7** est large, sans caractéristique et plus étroit que celui des composés **4** et **5**, indiquant un caractère ^{3}MLCT plus élevé et une distorsion géométrique moindre de l'état excité émissif pour les composés **4-5**. Les dérivés portant le ligand dm-2-pic ont montré un PLQY plus élevé parmi la série, avec des valeurs aussi élevées que 0,77 et 0,73 pour les composés **6** et **7**, respectivement, dans du CH_2Cl_2 dégazé. Il est intéressant de noter que ces valeurs PLQY sont remarquablement élevées et parmi les plus élevées pour les complexes cationiques émetteurs de rouge.

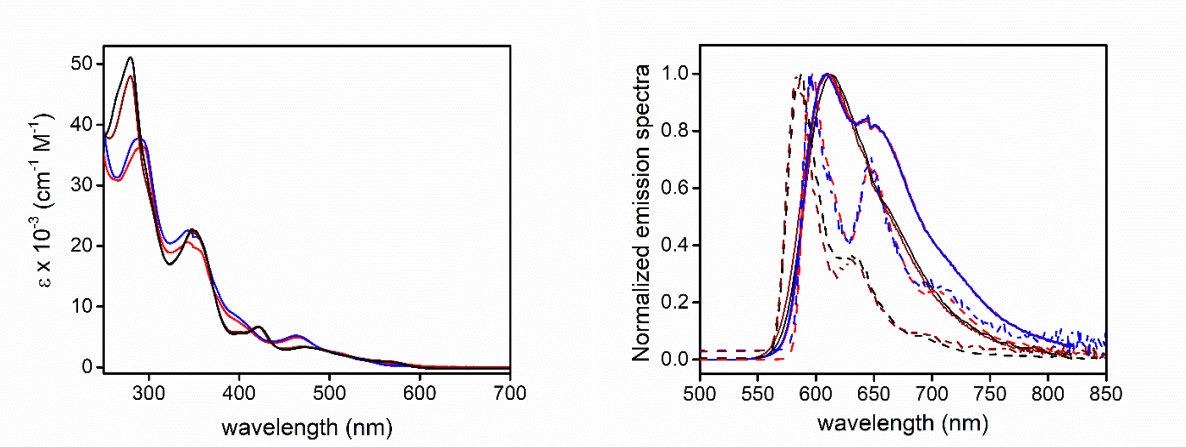

Figure 8. Spectres d'absorption électronique (à gauche) et d'émission (à droite) pour **4** (trace rouge), **5** (trace bleue), **6** (trace rouge foncé) et **7** (trace noire) dans le dichlorométhane à une concentration de 3,0×10^{-5} M en condition dégazée (traces solides) et dans la matrice vitreuse 2-MeTHF à 77 K (traces pointillées). Les échantillons ont été excités à λ_{exc} = 420, 460 et 480 nm pour le composé **4**,**5**,**6** et **7**, respectivement.

Dans la couche mince (*Figure 9*), les spectres d'émission de tous les échantillons montrent un décalage bathochrome par rapport à l'échantillon de solution diluée, ce qui est accompagné d'une chute du PLQY dans la phase condensée, comme prévu. Il est important de noter que la diminution de l'efficacité d'émission, ainsi que le décalage bathochrome, était moins spectaculaire pour les composés **6** et **7**, ce qui soutient l'idée que la présence de groupes méthyles supplémentaires dans la structure chimique des complexes aide à maintenir les émetteurs de triplets plus éloignés et donc à atténuer les effets d'extinction causés par l'agrégation et les phénomènes d'annihilation triplet-triplet en phase condensée. C'est un point important à aborder en vue de leur application potentielle dans les dispositifs émetteurs de lumière à l'état solide.

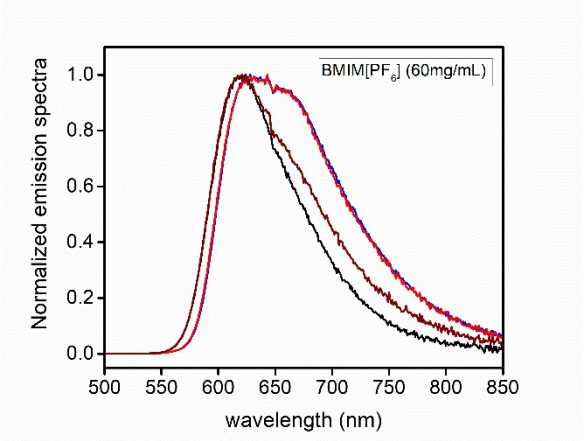

Figure 9. Spectres d'émission du complexe (80 % en poids) de BMIM[PF_6] (20 % en poids) enduit par centrifugation à une concentration totale de 60 mg mL-1 dans l'acétonitrile pour les échantillons de **4** (trace rouge), **5** (trace bleue), **6** (trace noire) et **7** (trace rouge foncé) sur λ_{exc} = 450 nm.

une solution d'acétonitrile à différentes concentrations. Les LEC hôte-guest optimisés basés sur le complexe hôte **B** (voir *figure ES4.25*, *chapitre 4*) dopé avec 5% en poids de complexes invités **6** et **7** présentent un EQE maximal d'environ 4,5 et 6%, respectivement. Ces efficacités sont les plus élevées jamais rapportées pour des émetteurs bi et/ou multimétalliques et parmi les plus élevées pour les phosphores rouges, confirmant que les complexes hétérobimétalliques proposés sont des candidats potentiels pour une utilisation dans des LEC efficaces.

Parmi les quatre complexes testés en tant que matériaux électroactifs dans des dispositifs LEC monocouches, les composés **6** et **7** ont démontré qu'ils atteignaient un temps d'allumage rapide, une luminosité allant jusqu'à 1100 cd m^{-2} et une efficacité quantique externe allant jusqu'à 6%, se révélant être les meilleurs émetteurs rouges bimétalliques rapportés jusqu'à présent.

5. Complexes hétéroleptiques bis-tridentés de Ir(III) émettant dans le bleu vif et portant un ligand de structure 1,2,4-triazolate

Malgré l'énorme succès des complexes d'iridium homoleptiques pour les OLED, l'instabilité structurelle, due à l'isomérisation méridionale à faciale lors de l'excitation thermique et de la photo-excitation[26], et les possibles voies de dégradation par perte de ligand[27], encourage la recherche d'une structure alternative aux composés tris-bidentés.

Les ligands bidentés se lient par l'intermédiaire de deux sites donneurs, provoquant un effet chélateur autour du métal. Cet effet est l'affinité accrue d'un ligand chélateur pour un ion métallique par rapport à son ou ses homologues ligands monodentés. Le résultat est une liaison ligand-métal plus stable et plus robuste.[28]

Dans ce travail, une nouvelle série de complexes bis-tridentés d'iridium(III) comme émetteurs potentiels de dopants dans les diodes électroluminescentes organiques (OLED) est rapportée. Une OLED est un dispositif qui convertit une entrée électrique en énergie lumineuse par électroluminescence (EL). Afin d'obtenir une bonne efficacité dans le dispositif, le composé émissif doit avoir une stabilité thermique et photoélectrique, une photoluminescence élevée, une longue durée de vie et la possibilité d'accorder les couleurs

d'émission.[29] L'utilisation de ligands chélateurs est cruciale pour obtenir des complexes d'iridium(III) émetteurs bleus hétéroleptiques stables et efficaces pour l'application de dispositifs. L'effet chélateur permet d'améliorer la force du champ du ligand autour du métal, augmentant ainsi l'efficacité du dopant dans le dispositif.[30] L'utilisation d'un ligand dérivé de la triazolyl-pyridine rend accessible la modulation des propriétés électroniques. Si d'une part le ligand dicarbène améliore l'intensité du champ du ligand, augmentant l'énergie des états ^{3}MC et conduisant à un knr plus petit, d'autre part un dérivé phényl triazolyl pyridine permet de régler la longueur d'onde d'émission.[31,32]

Dans le but d'obtenir des complexes d'iridium(III) efficaces et robustes émettant dans le bleu en tant que dopants potentiels pour les OLEDs, nous décrirons ci-après une nouvelle série de dérivés bis-tridentate d'iridium(III) neutres et hétéroleptiques **TR1-TR5** portant soit un 2-(2, 4-difluorophényl)-6-(5-(trifluorométhyl)-4H-1,2,4-triazol-3-yl)pyridine, soit une 2-(5-(trifluorométhyl)-4H-1,2,4-triazol-3-yl)-6-(4-(trifluorométhyl)phényl)pyridine, comme ligand chromophore et un ligand bis-N-hétérocyclique carbène (*Figure 10*).

Malheureusement, deux des cinq complexes prévus, **TR4** et **TR5**, n'ont pas été isolés avec succès, mais ils n'ont été détectés que par spectroscopie de masse.

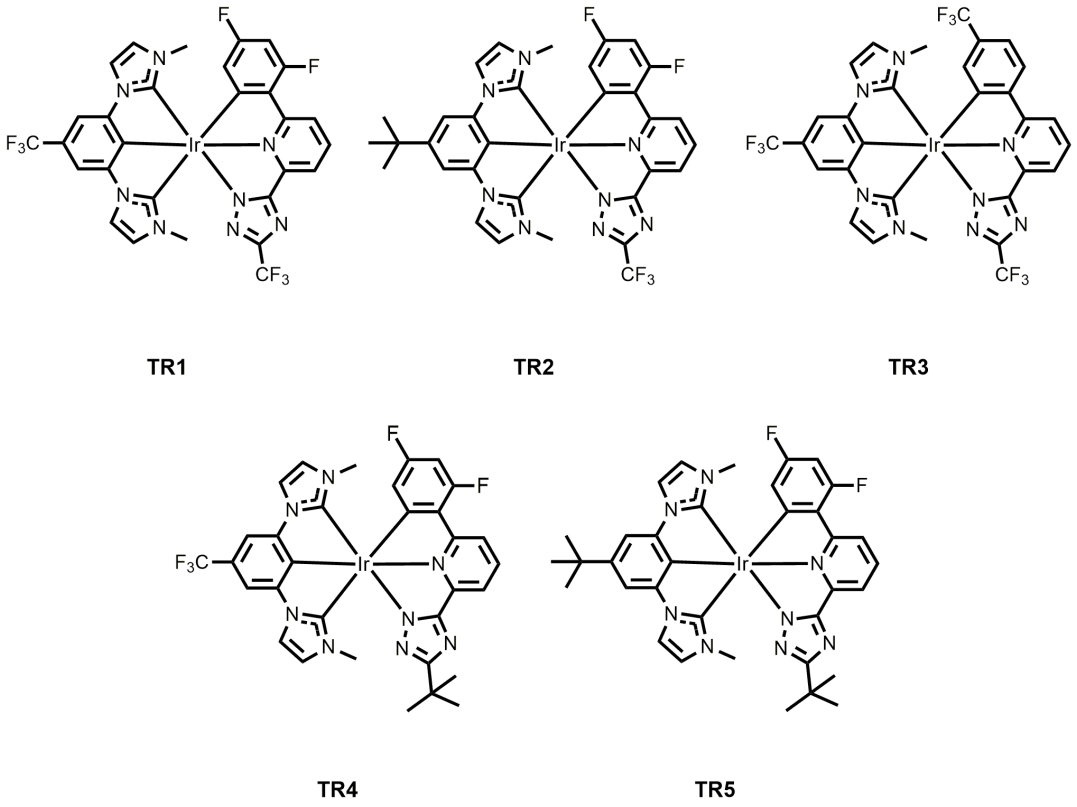

Figure 10. Structure chimique des complexes d'iridium **TR1-TR5** étudiés.

Afin de moduler les propriétés optiques des complexes finaux, deux proligands tridentés basés sur les échafaudages phényl-bis-imidazolium ont d'abord été ciblés, à savoir [fpbmiH2][PF_6]$_2$ et [bpbmiH2][PF_6]$_2$ portant respectivement un groupe CF_3 attracteur d'électrons et un groupe tert-butyle modérément donneur d'électrons en position 5 du groupe phényle. Pour la synthèse des deux pinces bis-carbènes, le produit de départ 2,6-dibromophényle a été converti en 1,3-di(1H-imidazol-1-yl)benzène correspondant, suivi d'une méthylation en position 3 de l'imidazole pour donner l'hexafluorophosphate de bis-3-méthyl-imidazolium final, conformément aux rapports précédents.[33]

La voie de synthèse utilisée pour la synthèse de [fpbmiH2][PF_6]$_2$ et [tpbmiH2][PF_6]$_2$ est une réaction de couplage de type Ullmann catalysée par Cu(I) entre le 1,3-dibromo-benzène et le 1H-imidazole. Les cations diimidazolium ont été obtenus en utilisant l'iodure de méthyle par méthylation en position N(3). Les sels de bis(hexafluorophosphate) cibles ont été obtenus directement par métathèse anionique à partir des sels d'iode (*Schéma 4*).

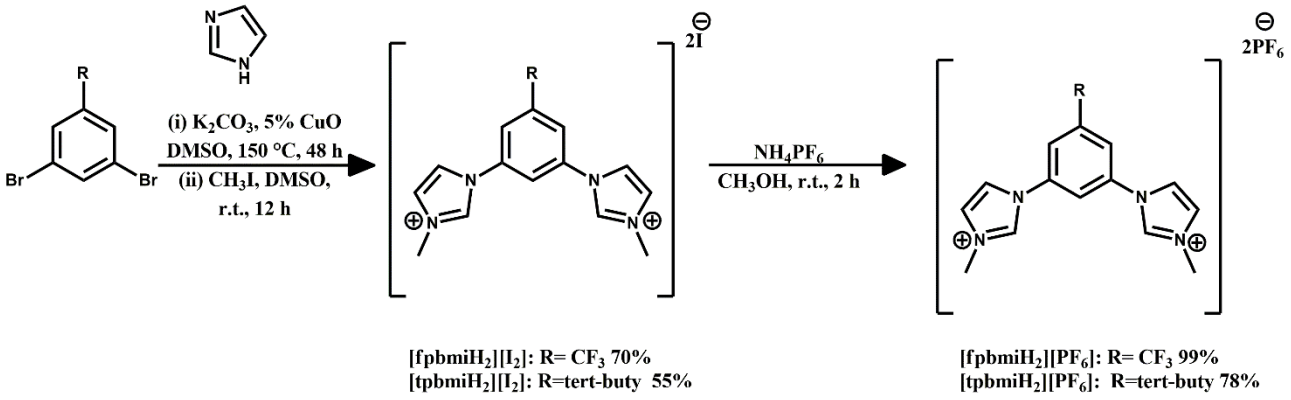

Schéma 4. Procédure générale de synthèse pour le bis-carbène pinçant.

Les dérivés 1,2,4-triazolyle cibles ont été préparés par une réaction par étapes. Le couplage de Suzuki entre l'acide difluoro-phényl-boronique et la 6-bromo-2-cyano-pyridine est suivi de l'introduction du cycle triazole par traitement avec de l'hydrazine monohydratée et de l'anhydride trifluoroacétique (pour L1H2 et L2H2), ou par acylation avec du chlorure de triméthylacétyle (pour L3H2) en accord avec les procédures modifiées déjà rapportées (*Schéma 5*).[34]

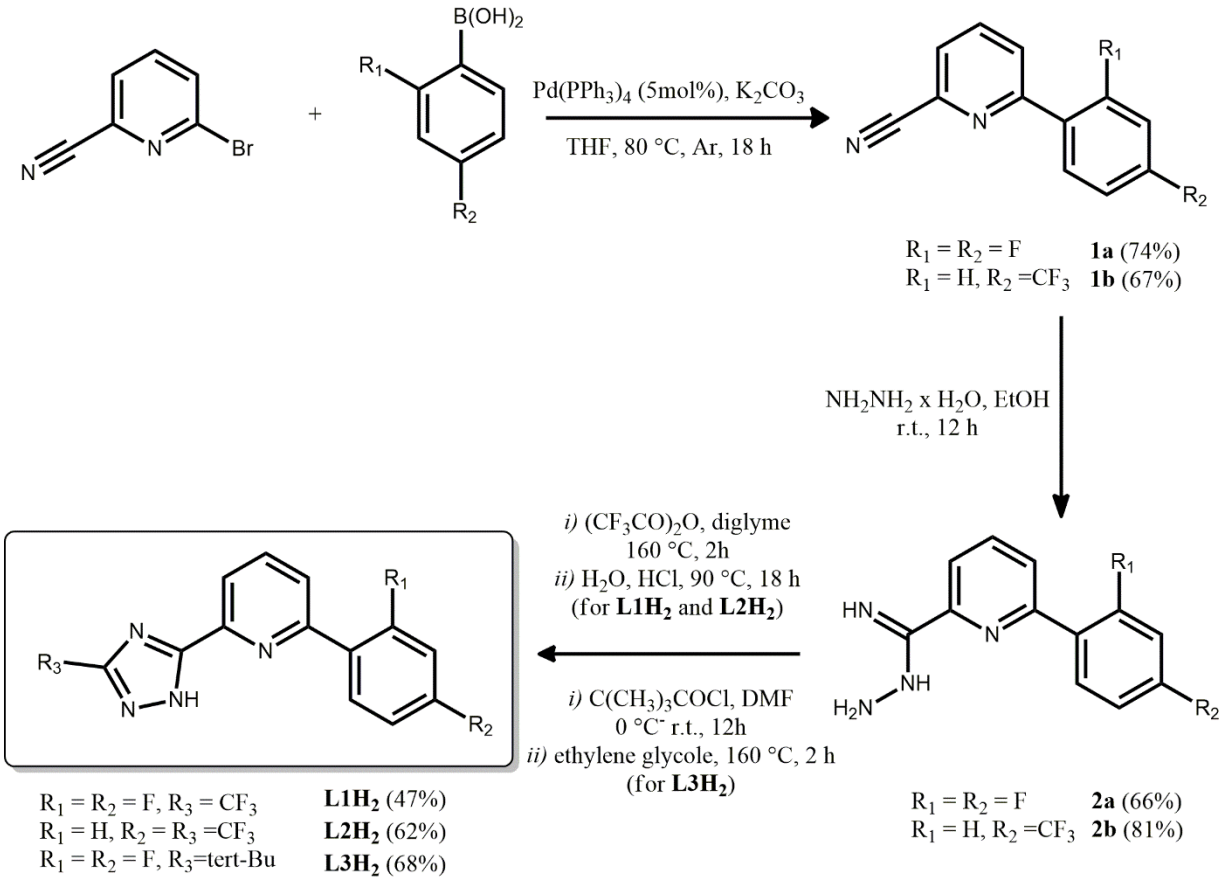

Schéma 5. Procédure de synthèse des ligands dérivés du triazolyle **L1H2, L2H2** et **L3H2.**

Les complexes métalliques cibles de Ir(III) ont été synthétisés en suivant la même méthode rapportée ailleurs (*Schéma 6*). Tout d'abord, le proligand bis(imidazolium) a réagi avec $[Ir(1,5\text{-cod})Cl]_2$ dans un rapport de 2:1 équiv. et un excès (10 équiv.) de NaOAc dans de l'acétonitrile sec à reflux. Comme indiqué précédemment,35,36 les molécules de solvant coordonnent deux sites du métal, laissant le dernier site au ligand hydrure. Les mêmes réactions ont été réalisées sous irradiation micro-ondes (MW). Bien que la première étape soit la même dans les deux procédures, la cyclisation de la deuxième étape a été tentée en chauffant à 230°C pendant 2 h sous MW (100). Les composés **TR1** et **TR3** ont été synthétisés selon cette procédure. Tous les complexes ont été testés par les deux voies de synthèse mais, dans les deux cas, les réactions n'étaient pas bien reproductibles, il n'a donc pas été possible de les comparer en termes de rendement et de pureté.

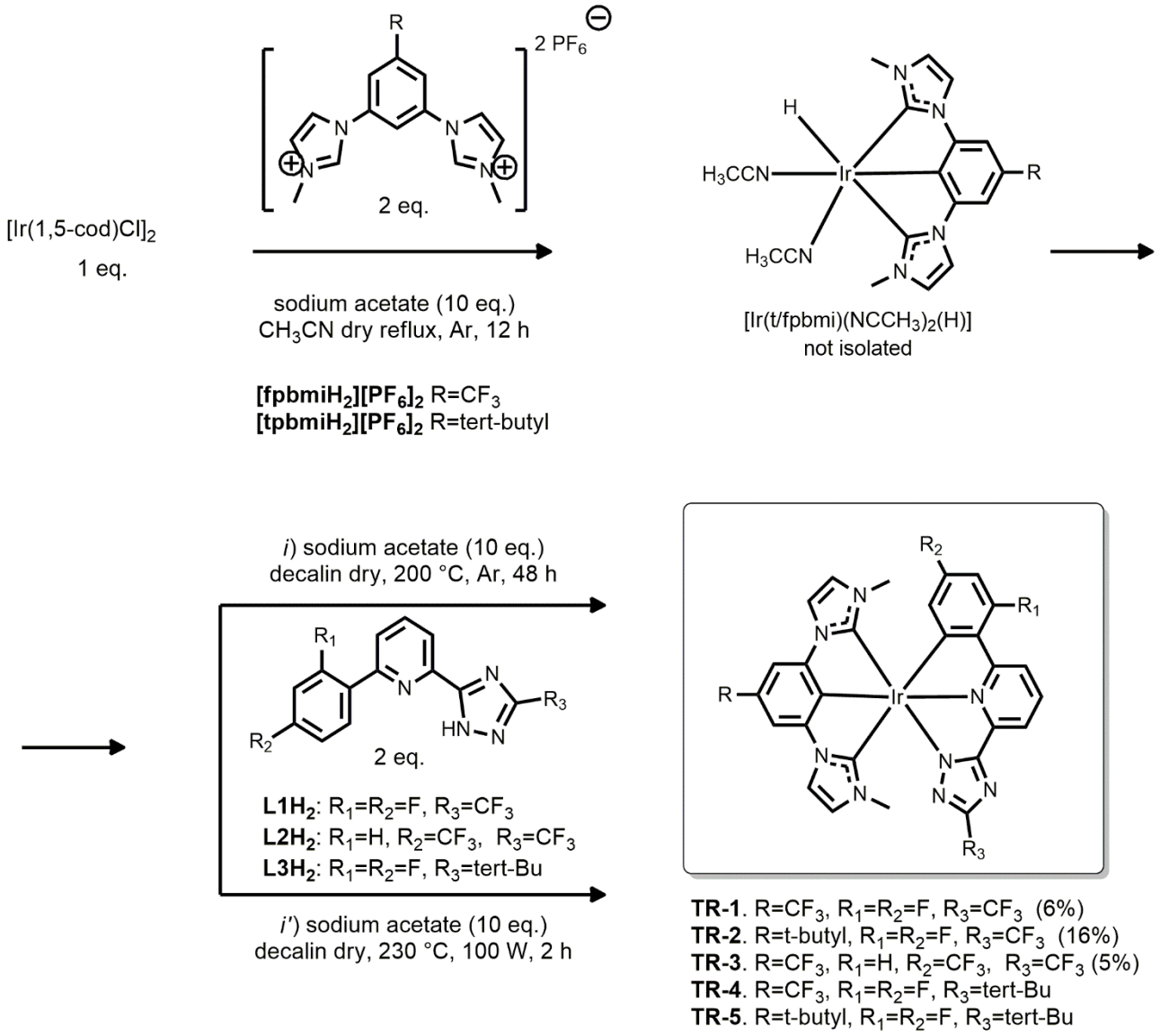

Schéma 6. Procédure de synthèse des complexes métalliques **TR1-TR5** de Ir(III).

Tout d'abord, les propriétés photophysiques des complexes de Ir(III) **TR1-TR3** ont été étudiées dans une solution diluée de CH_2Cl_2 à la fois équilibrée à l'air et dégazée à température ambiante à une concentration de 3 X 10^{-5} M et dans une matrice vitreuse de 2Me-THF.

Dans les spectres UV-vis (*Figure 11*), la bande d'absorption intense à λ_{abs} = ca. 325 nm avec ε = 12,8, 19,6 et 12,3 X 10^3 M pour **TR1**, **TR2** et **TR3**, est attribuée au ligand ^{1}LC (1π-π*) centré impliquant le ligand terdentate à base de triazolyle L1H2 et L2H2. À des longueurs d'onde plus grandes, dans la région λ_{abs} = 370-400 nm, la bande peut être attribuée de manière confidentielle à une transition électronique unique de transfert de

charge métal-ligand (^{1}MLCT) du métal et de la fraction bis-NHC métallisée vers la portion phénylpyridine du ligand terdendate à base de triazolyle. Les propriétés de photoluminescence (PL) révèlent un comportement similaire pour tous les composés après irradiation à λ_{exc} = 355-400 nm. Les échantillons présentent des spectres d'émission dans la région bleu ciel avec un profil vibronique avec les maxima de plus haute énergie à λ_{em} = 463, 468 et 485 nm, pour **TR1**, **TR2** et **TR3**, respectivement. De manière attendue, les échantillons dégazés subissent une augmentation importante de l'intensité d'émission avec un PLQY de 51.7-81.8% accompagné d'une prolongation de la durée de vie de l'état excité (τ= 3.1-6.2 µs) confirmant la nature triplet de l'état excité émissif. Par conséquent, il est proposé que l'état excité émissif soit un mélange de caractère ^{3}MLCT et ^{3}LC, avec une plus grande contribution du ^{3}LC pour les complexes **TR1** et **TR3**. Au contraire, le complexe **TR2** révèle un caractère ^{3}MLCT légèrement plus important.

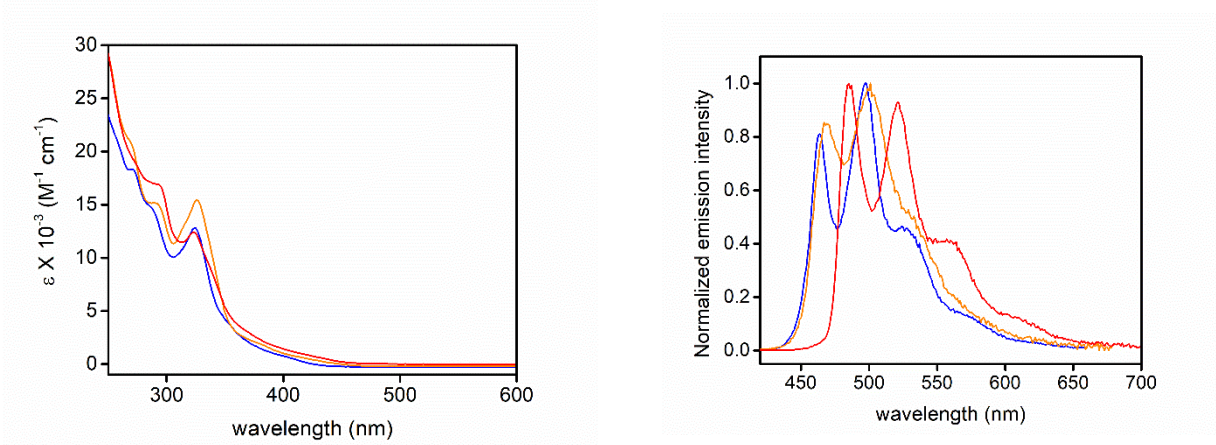

Figure 11. Spectres d'absorption électronique (gauche) et d'émission (droite) pour les complexes **TR1-TR3** dans le dichlorométhane à la concentration de 3,0×10^{-5} M en condition dégazée. Les échantillons ont été excités à λexc = 355 nm pour **TR1** (trace bleue), 400 nm pour **TR2** (trace orange), et 380 nm pour **TR3** (trace rouge).

Des expériences à basse température dans une matrice vitreuse 2Me-THF congelée à 77 K ont été réalisées pour mieux comprendre la nature de l'état excité émissif (*Figure 12*). Lors de l'excitation à λ_{exc} = 380 nm, pour les trois échantillons, les spectres d'émission montrent seulement un décalage hypsochrome mineur par rapport à la photoluminescence à température ambiante (décalage de 141 cm^{-1}). En outre, l'analyse de la décroissance en fonction du temps révèle que **TR1** et **TR3** ont une durée de vie plus longue (τ = 7,1 et 5,9

μs, respectivement), tandis que l'échantillon du complexe **TR2** présente la plus courte (τ = 3,7 μs) parmi les séries étudiées, conformément aux données de photoluminescence enregistrées à température ambiante.

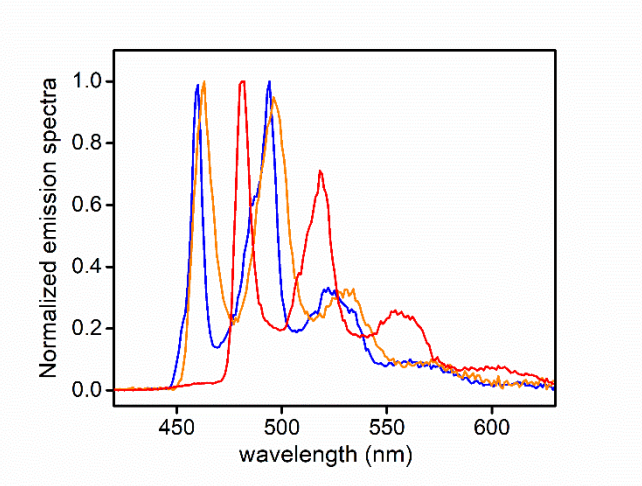

Figure 12. Spectres d'émission pour les complexes **TR1-TR3** dans le 2-MeTHF à 77 K. Les échantillons ont été excités à λ_{exc} = 380 nm. (**TR1**, trace bleue ; **TR2**, trace orange ; **TR3**, trace rouge).

Les spectres d'émission de **TR1-TR3** dans les films minces de PMMA à un niveau de dopage de 5% en poids sont présentés dans la *Figure 13*. En ce qui concerne le complexe **TR1**, son profil d'émission conserve une forme similaire à celle enregistrée en solution (*Figure 11*), sans également aucun décalage des maxima (λ_{em} = 463, 497 et 524 nm). De plus, le PLQY est également similaire avec une valeur de 63,0% dans le film mince contre 61,6% dans des conditions dégazées. Globalement, ces résultats indiquent qu'à une concentration de dopage aussi faible, l'échantillon **TR1** ne présente pas d'interactions intermoléculaires entre les complexes émissifs et que les phénomènes d'annihilation triplet-triplet sont négligeables. Les complexes **TR2** présentent un profil d'émission différent dans le PMMA dopé par rapport à l'échantillon dans la solution de CH_2Cl_2. En particulier, le profil d'émission dans la couche mince apparaît plus large et sans caractéristique avec un maximum centré à λ_{em} = 470 nm.

Cette émission est caractérisée par une cinétique de décroissance de l'état excité (mesurée à λ_{em} = 470) qui peut être ajustée avec un modèle bi-exponentiel, étant τ_1 = 487 ns (84%) et τ_2 = 1.6 μs (16%), ainsi qu'une émission fortement éteinte (PLQY = 7.3%). Dans l'ensemble, ces résultats soutiennent l'idée que le composé **TR2** dans la couche mince de

PMMA présente une tendance beaucoup plus prononcée à l'agrégation intermoléculaire et aux processus d'extinction triplet-triplet.

Comme pour le complexe **TR3**, le spectre de photoluminescence dans le PMMA montre une progression vibronique avec des maxima de longueur d'onde similaires à ceux observés en solution mais avec un rapport d'intensité différent. La durée de vie bi-exponentielle est également codée, avec τ_1 = 498 ns (80 %) et τ_2 = 1,6 µs (20 %) ainsi qu'un PLQY de 9,0 %, ce qui indique que le processus d'extinction se produit dans une plus grande mesure si on le compare à l'échantillon de solution de CH_2Cl_2.

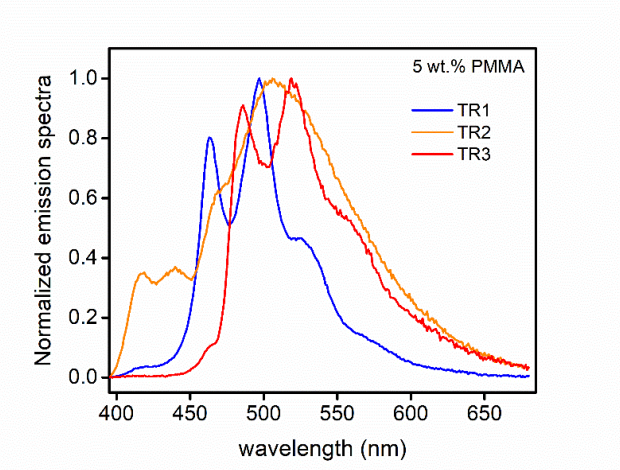

Figure 13. Emission spectra for **TR1-TR3** 5 wt.% in PMMA thin films. λ_{exc} = 380 nm

Les composés **TR1-TR3** présentent un spectre d'émission comparable à celui des dérivés apparentés rapportés par Chi *et al.*[32,38] D'autre part, la légère diminution du PLQY dans **TR1-TR3** peut être attribuée à l'angle d'attaque non optimal des ligands coordonnés [fpbmi] et [tpbmi]. L'introduction d'un atome d'azote entre les deux fluorines sur le cycle phényle du ligand chromophore peut mieux stabiliser le niveau HOMO, en élargissant l'écart HOMO-LUMO et peut fournir des spectres d'émission plus décalés en hypochromie.[31] Des recherches à cet égard sont actuellement en cours dans le groupe de recherche où j'ai effectué ma thèse. En conclusion, des recherches plus approfondies sur les dopants émetteurs pour les dispositifs OLED devraient être menées sur **TR1**, qui révèle le meilleur comportement photophysique dans les films minces de PMMA.

S.2 English version

1. Introduction

The chemistry of transition-metal complexes is a fascinating field that has attracted remarkable attention by scientists in order to modulate and understand their electronic properties. In the last few decades, thousands compounds have been investigated to make them suitable for different applications, such as photocatalysis,[1] biomedicine[2] and optoelectronic devices.[3]

According to a d^6-electronic configuration, the heavy metal is surrounded by ligands forming a complex with idealized octahedral geometry. As a result, the five metal d-orbitals split in two sets namely "t_{2g}" and "e_g". The energy gap between them is denoted as Δ_0 and it depends on valence shell of the metal ion and the strength of the ligand field involved. Since electronic transitions in a metal complex can occur among different moieties of the molecules, they can be distinguished on the basis of molecular orbitals involved: *i)* metal-centered (MC); *ii)* ligand-centered (LC); *iii)* ligand-to-metal-charge transfer (LMCT) and *iv)* metal-to-ligand charge transfer (MLCT).

In luminescent Ir(III) and Re(I) complexes, the lowest emitting excited state is a mix of ^{3}MLCT/^{3}LC which depends on metal d-orbital contribution and π-coniugation of the coordinated ligands. Given that the ^{3}MLCT/^{3}LC, indicated as T_1, can be considered as a mix of the contributions of ^{1}MLCT/^{3}LC, the excited states mixing is related to the SOC constant, which varies with the nuclear charge of the heavy atoms, along the periodic table (Ru= 1042, Os= 3381, Ir= 3909 cm^{-1}). The degree of mixing influences the radiative rate constant process and the correlated lifetime, leading to luminescent emitters.[4] Since, the aim of my research project is to maximize the radiative rate constant to improve the photoluminescence quantum yield, it's necessary to minimize all non radiative processes as: *i)* triplet-triplet annihilation (TTA), *ii)* radiationless vibronic coupling between the lowest excited state and the ground state (energy gap law)[5] and *iii)* thermal population of the ^{3}MC states, which are close in energy to the emissive ones.[6] In order to achieve my aim, the use of NHC carbene as strong σ-donor ligands is crucial to push ^{3}MC states up to higher energy. N-heterocyclic carbenes are species containing a carbine at C2 position which is stabilized

by at least one adjacent nitrogen atom present in the ring structure.[7] The stabilization is given by two factors: *i)* the mesomeric effect by the π-electron donation of the N through its lone pair and *ii)* the inductive effect by the σ-electron withdrawing of the more electronegative N atom which lowers the energy of the filled sp^2-orbitals. As a result, NHCs are strong σ-donor and weak π-accepting ligands, making a strong interaction with the metal. Moreover, the high stability of the resulting complex and high structural versatility of the carbenes are useful to tune the final electronic properties of the transition metal complex, reaching the desiderate features.[8]

2. *Red-emitting rhenium(I) complexes bearing a pyridyl pyridoannelated N-heterocyclic carbene*

Rhenium derivatives bearing stronger σ-donating ligands with coordinating C atoms, such as N-heterocyclic carbene (NHC) type of ligands, have been surprisingly much less explored than rhenium(I) diimine complexes $[Re(N\hat{}N)(CO)_3L]^{n+}$ to date. Owing to their appealing electronic and chemical features, NHCs attracted a considerable attention as ligands in the field of phosphorescent emitters as well.[9]

A novel family of photoactive neutral and cationic tris-carbonyl rhenium complexes are herein described. The former have general formula *fac*-$[Re(N\hat{}C:)(CO)_3X]^0$ (**Re1–Re2**), while the latter are *fac*-$[Re(N\hat{}C:)(CO)_3L]PF_6$, (**Re3**–**Re4**) where N^C: is the pyridoannelated N-heterocyclic carbene (NHC) arising from 2-(2-pyridinyl) imidazo[1,5-a]pyridinium hexafluorophosphate proligand, namely [pyipy]PF_6, and X is Cl^- (**Re1**) and Br^- (**Re2**), while L is pyridine (**Re3**) and phosphine (**Re4**). The synthetic pathway is a one-pot reaction for neutral compounds, starting from the azolium salt as the NHC source and $[Re(CO)_5X]$ to yield the desired charge-neutral *fac*-$[Re(pyipy)(CO)_3X/L]$ complexes (**Re1**–**Re4**). Subsequent halogen abstraction and addiction of the pyridine or phosphine neutral ancillary ligand yields the analogue cationic complexes as hexafluorophosphate salt (**Re3**–**Re4**). The compounds are shown in *Figure 1* and the synthetic pathway in *Scheme 1*.

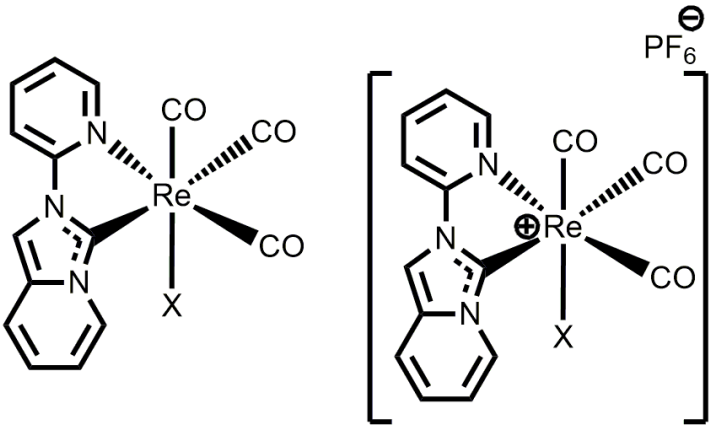

Figure 1. Chemical structure of the investigated rhenium complexes **Re1–Re4**.

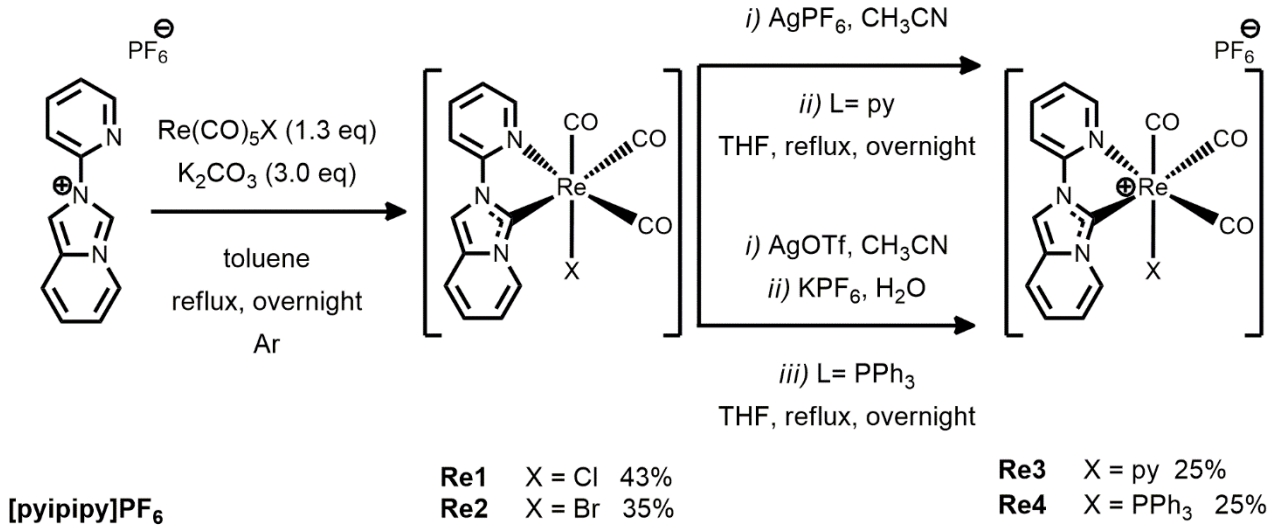

Scheme 1. Schematic synthetic pathway employed for the synthesis of complexes **Re1–Re2** and **Re3–Re4**.

In the UV range (*Figure 2*), an intense absorption band shows a $\lambda_{abs,max}$ = 270 nm with ε = 13.5 × 10^3 M^{-1} cm^{-1} for **Re1** corresponds to the absorption profile of the ligand [pyipy]PF_6. The first transition is described as ligand centered (^{1}LC). The second transition involves charge transfer both from the $Re(CO)_3Cl$ moiety to the ligand and from the carbene to the pyridyl ring. On the other hand, the lowest energy transition that appears as a shoulder at $\lambda_{abs,max}$ = 430 nm shows also a partial ^{1}ILCT character with a net charge transfer from the heterocyclic carbene ring to the pyridyl moiety and so is ascribed as an electronic transition with admixed metal-to-ligand charge transfer and intraligand charge transfer (^{1}MLCT/^{1}ILCT) character [d_π(Re)p(X)π(NHC) → π*(N^C)].

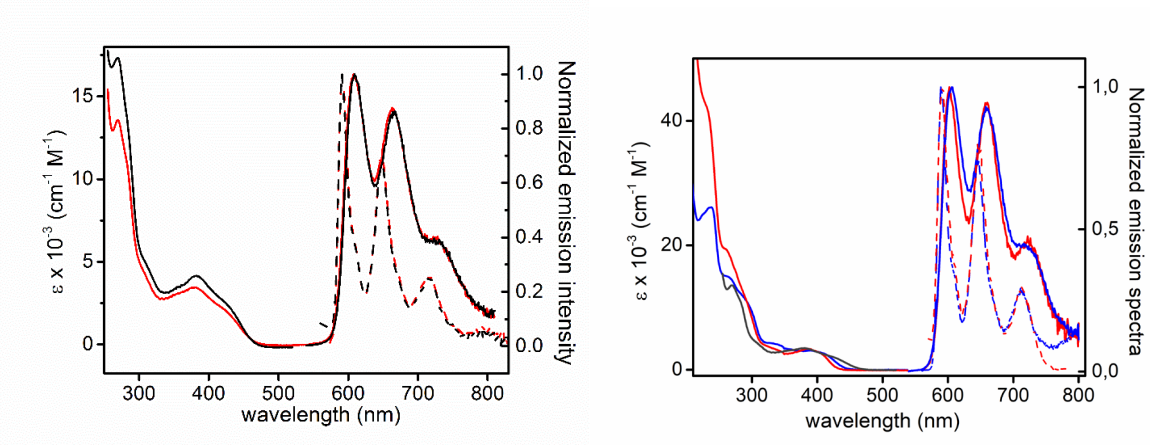

Figure 2. Electronic absorption and normalized emission spectra of complex **Re1** (black traces) and **Re2** (red traces) in degassed CH_2Cl_2 solution (*left*) and **Re3** (blue traces) and **Re4** (red traces) in degassed CH_3CN (*right*) at a concentration of 2×10^{-5} M at room temperature (solid line) and 77 K (dashed line).

The photoluminescence (PL) properties of the complexes were investigated as well, and the corresponding spectra in both degassed and air-equilibrated dilute CH_2Cl_2 are displayed in *Figure 2.*

Upon irradiation at λ_{exc} = 370–420 nm, complexes **Re1–2** show similar photophysical properties. Solution samples display a moderate red photoluminescence with a structured profile with maxima at λ_{em} = 608, 664 and 728 nm independently of the presence of dioxygen molecules at room temperature. Degassing the samples yields a sizeable increase of the emission intensity and a prolongation of the excited-state lifetime, being the PLQY of 0.08% vs. 1.5% and τ = 345 ns *vs.* 12.8 μs for complex **Re1**, respectively. In sharp contrast to what observed for other classes of luminescent [Re(N^N)$(CO)_3$X] complexes characterized by a

^{3}MLCT emission,[10] the absence of any spectral shift upon halogen variation along with the smaller radiative rate constant values (k_r = 1.2 × 10^3 s^{-1} for complex **Re1**) and similar vibronic progression observed for both complexes and the [pyipy]PF_6 ligand undoubtedly suggest a ^{3}LC nature of the excited state responsible for the emission process in complexes **Re1**–**Re2**.

Compound **Re3** and **Re4** show an intense absorption band in the UV range with $\lambda_{abs,max}$ = 237 nm (ε = 2.61×10^4 M^{-1} cm^{-1}) and $\lambda_{abs,max}$ = 231 nm (ε = 4.22×10^4 M^{-1} cm^{-1}), respectively. The additional contribution of the π-π* transitions involving the phenyl rings of the PPh_3 ligand in compounds **Re4** accounts for the increased molar extinction coefficient observed for this complex. At lower energy, the absorption band observed in the region at λ_{abs} *ca.* 400 nm is ascribed to an electronic transition with ^{1}MLCT character, namely d(Re)π(NHC) → π*(py), admixed with intraligand charge-transfer (^{1}ILCT) involving the cyclometalating ligand with π(NHC) → π*(py) nature, where NHC is the benzannulated NHC moiety and py is the pyridyl ring. Upon irradiation at the ^{1}MLCT band, complexes **Re3** and **Re4** show similar photophysical properties. The photoluminescence spectrum of both samples in degassed CH_3CN show a structured emission with maxima at λ_{em} = 602 and 606, 660 and 725 nm at room temperature that are Stokes shifted by *ca.* 6500 and 6650 cm^{-1} for **Re3** and **Re4**, respectively. Upon removing dioxygen, increase of the photoluminescence quantum yield (PLQY) values (from 0.14% to 0.72%) as well as prolongation of the excited-state lifetime (from τ = 204 ns to 19.3 µs) is observed for compound **Re3**. Likewise, PLQY and lifetime increase from 0.04% to 1.60% and τ = 209 ns to 30.0 µs, respectively, for derivative **Re4**.

Thanks to the relatively intense visible light absorption, long-lived excited states, and suitable redox potentials, these compounds appear to be good candidates for a new type of photocatalytic systems (PCs), in particular for photopolymerization experiments.[11]

The photocatalytic behaviour of the compounds **Re1** and **Re2** were investigated in the frame of a collaboration with Prof. Jacques Lalevée's group from University of Haute Alsace (Mulhouse, France).

The efficiency in initiating free radical polymerization (FRP) both in thin[i] and thick[ii] films for PEG-diacrylate monomers under air upon irradiation with the LED@405 nm is better for rhenium complex/Iod/amine photoinitiating systems (PISs) than blank (iod/amine) (**Re1**= 64% [i] / 94% [ii] **Re2**= 61% [i] / 94% [ii] *vs* 49% [i] / 89% [ii]). Consequently, the polymerization rate is faster using rhenium complexes (≈ 50 s *vs* 200 s), demonstrating that the rhenium complexes have a significant effect on improving the photopolymerization efficiency.

Photopolymerization based 3D printing technology such as stereolithography and digital light processing require innovations related to polymer chemistry. In this regard, 3D laser writing experiments in air by a combination of rhenium complex/Iod/amine (0.1%/ 1.5%/1.5%, w/w/w)-based PIS and the PEG-DA monomer were carried out to confirm the high efficiency of the novel PIS based on **Re1** or **Re2/**Iod/amine for FRP process in 3D.

The space control experiments carried out on the 3D printed hydrogels by photopolymerization reveal a two-way reversible shape-memory effect through thermal response and water response using as Re/Iod/amine-based PIS-induced polymers. On the contrary, any shape memory effect was observed using the blank control, where Iod and EDB were used only.

3. Cationic Ir(III) complexes featuring a pyridyl pyridoannelated N-heterocyclic carbene as potent theragnostic agents

In 1965, Rosenberg discovered the cytotoxicity of the cisplatin and from there on the use of it as a chemotherapeutic agent became widespread overtime.[12] However, the presence of multiple side-effects pushed scientists to search an alternative to platinum complexes. Among other metals, iridium(III) compounds are a promising option. Iridium(III)-NHC complexes have already shown to possess high cytotoxicity properties against cancer cells[13], given the abnormally high mitochondrial membrane permeabilization. In this chapter, a novel series of Ir(III)-NHC metallodrugs is reported and investigated their cytotoxicity, while maintaining the emission properties for their cellular localization. The new compounds have general formula $[Ir(C\hat{}N)_2(pyipy)]PF_6$ where C^N is a phenyl pyridine derivative used as cyclometalatind ligand and pyipi is 2-(2-pyridyl)imidazo[1,5-a]pyridinium hexafluorophosphate procarbenic ligand. They are displayed in *Figure 3*.

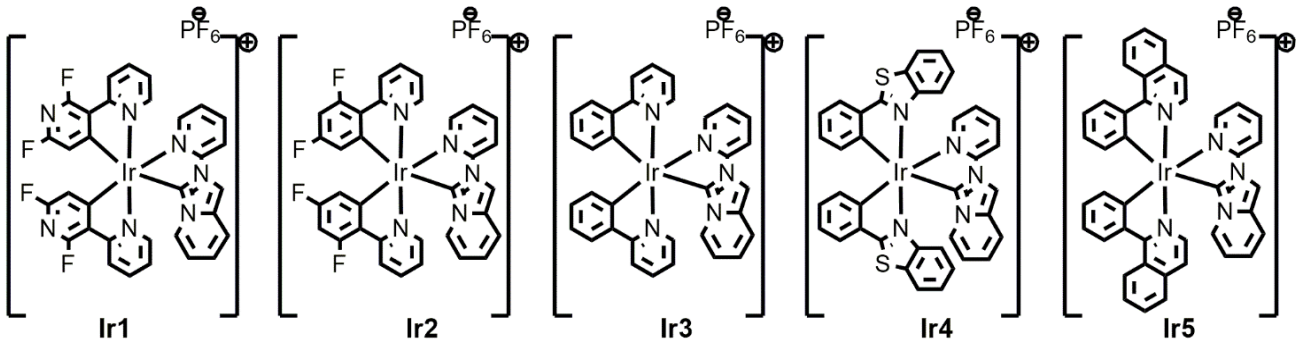

Figure 3. Chemical structure of the investigated iridium complexes **Ir1-5**

The synthesis (*Scheme 2*) starts with deprotonation at C(3) position of the 2-(2-pyridyl)imidazo[1,5-a]pyridinium hexafluorophosphate procarbenic ligand, namely [pyipy]PF_6, via Ag_2O-supported C–H bond activation yielding the formation of the annelated NHC ligand following the original procedure reported by Lassaletta.[14] Subsequently, transmetallation reaction was carried out in situ by adding the corresponding chloro-bridged iridium dimer. These latter were prepared using the classical procedure reported previously by Nonoyama.[15] Five target complexes **Ir1–5** bearing different cyclometalating C^N ligands were obtained in moderate yields after purification.

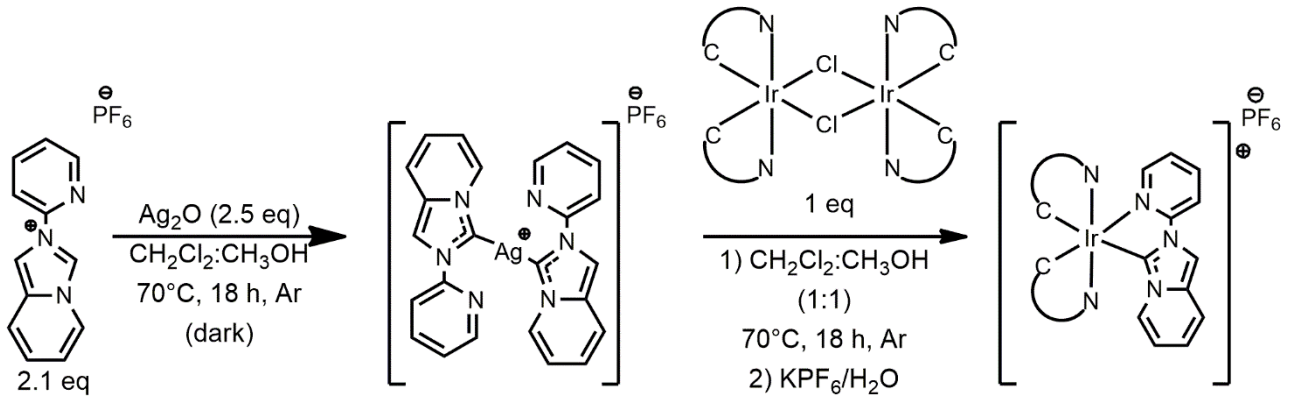

Scheme 2. Schematic synthetic pathway used for the synthesis of complexes **Ir1**–**5**.

In the higher energy region (λ_{abs} <350 nm) the electronic absorption spectrum is characterized by intense (ε = ca. 1–4X10^4 M^{-1} cm^{-1}) bands that can be ascribed to the

intraligand transition of π-π* character localized onto the C^N ligand, namely $^1IL_{C^N}$. At lower energy, the less intense (ε = ca. 0.3–1X10^4 M^{-1} cm^{-1}) and broader bands can be confidentially attributed to overlapping electronic absorption processes arising from different combination of spin-allowed singlet-manifold intraligand charge transfer (^{1}ILCT) and metal-to-ligand charge transfer character (^{1}MLCT). As far as complexes **Ir1–Ir2** are concerned, an additional peak is clearly visible in the absorption profile at λ_{max} = 400 (ε = 2.4X10^3 M^{-1} cm^{-1}) and 410 nm (ε = 2.6X10^3 M^{-1} cm^{-1}) for compound **Ir1** and **Ir2**, respectively, attributable to the intraligand absorption involving the ancillary NHC ligand (IL_{NHC}) character, where NHC is the benzannulated pyipy carbene moiety, owing to the sizeable π-extended conjugation of this latter.

Upon photo-excitation into the low-lying energy band, dilute samples of complexes **Ir1**–**Ir5** exhibit low to moderate photoluminescence, yet with a dual emission surprisingly. Emission spectrum of compound **Ir1** features one structured band with λ_{em} maxima at 444 and 473 nm, namely high-energy (HE) emission band. In addition, a second structured band is visible on the lower energy (LE) side with λ_{em} at 590 and 648 nm, yet with very low intensity. Moving to complex **Ir2**, the HE band display a bathochromic shift to λ_{em} = 467 nm and 494 nm; whereas, the LE band increases its intensity with no spectral shift apparently.

The LE appears even more clearly for compound **Ir3** and the HE band is weak, broad and featureless instead. In complexes **Ir4**–Ir**5**, the stabilization of the π* orbitals imparted by the more extended conjugation of the C^N ligand causes an expected bathochromic shift of the emission profile and band structure is less marked. The different origin of the two emission bands is supported by the independent behaviour observed for the excitation spectra recorded at the HE and LE wavelength that suggests poor electronic coupling between the two excited states responsible of the dual emission.
As far as complexes **Ir1**–**Ir3** are concerned, the HE band can be ascribed with confidence to a radiative process arising from a triplet excited state with mainly $^3IL_{C^N}$ character, although with a partial degree of mixing with the $^1MLCT_{C^N}$ state depending on the nature of the C^N ligand, as typical of this class of emitters.[16]

As far as complex **Ir3** is concerned, lifetimes measured for degassed samples at the HE and LE bands display mono-exponential decay with τ_{HE} = 555 ns and τ_{LE} = 6.0 μs, respectively. For complexes **Ir4**–**Ir5**, analysis of the decay traces required a bi-exponential fitting at both shorter and longer wavelength region with similar lifetime components (for examples, τ_1 = 6.1 μs and τ_2 = 1.8 μs for complex **Ir4**), yet with different weights, indicating

that the recorded PL profile is composed of two almost overlapping emission bands. Similar results were obtained for complex **Ir2**. The HE band overwhelmed the LE one for complex **Ir1**. Overall, these findings confirm the mainly triplet nature for both excited states involved in the dual emission process and point towards a $^3MLCT_{C\wedge N}/^3IL_{C\wedge N}$ and $^3IL_{NHC}$ character for the HE and LE bands, respectively; the latter state, which possesses poorer emission properties, being responsible of the quenching of the higher-lying $^3MLCT_{C\wedge N}/^3IL_{C\wedge N}$ manifold.

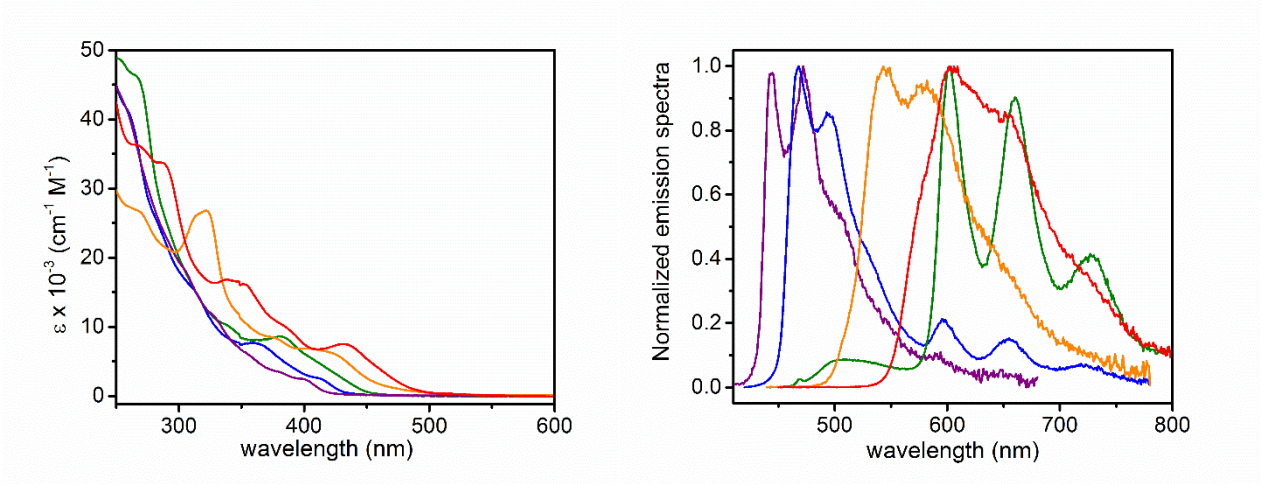

Figure 4. Electronic absorption (*left box*) and photoluminescence spectra (*right box*) of compound **Ir1** (purple traces), **Ir2** (blue traces), **Ir3** (green traces), **Ir4** (orange traces) and **Ir5** (red traces) in CH_2Cl_2 solution at a concentration of 3×10^{-5} M at room temperature. Emission spectra were recorded upon excitation at λ_{exc} = 350 nm for **Ir1**, λ_{exc} = 400 nm for **Ir2**, λ_{exc} = 410 nm for **Ir3**, λ_{exc} = 420 nm for **Ir4** and λ_{exc} = 430 nm for **Ir5**. Spectra of compound **Ir1**–**5** refer to degassed samples.

The *in vitro* cytotoxicity of the compounds was investigated in the frame of a collaboration with the group of Pr. Sylvie Fournel, Dr. Antoine Kichler and Conor McCartin at the faculty of Pharmacy, University of Strasbourg. In particular, the complexes were tested against two Human cancer cell lines, HCT116 (human colon carcinoma) and MDA-MB-231 (human breast cancer), by measuring the decrease of NADH and $NADPH^-$ dependant dehydrogenase activity, reflecting a decrease of metabolic activity, using the MTS assay after 24- and 48-hours treatment.

All the compounds show a similar level of cytotoxicity - much higher than oxaliplatin - except for compound **Ir1**. Notably, the compounds showed a roughly two- to ten-fold decrease in IC_{50} after 48 hours - reaching IC_{50} values of around 1 μM - except for compound **Ir1**. Additional results following 72 h treatment of HeLa cells with compounds **Ir2** and **Ir4** showed IC_{50} values of 3.6 μM and 1.6 μM, respectively, displaying comparable potency to the *bis*-N-heterocyclic Ir compounds reported by Che *et al.*[17] As compound **Ir4** showed a higher level of activity, the mechanism of cell death was deeply investigated. It was found that the pathway of apoptotic induction by compound **Ir4** is caspase dependant, which likely occurs due to direct activation of the intrinsic apoptotic pathway through mitochondrial disruption.

4. Phosphorescent mononuclear iridium(III) and heterodinuclear Ir(III)/M(I) complexes (M = Cu(I), Au(I)) with a Janus-type N heterocyclic carbene bridge

Cyclometalated Ir(III) complexes are an outstanding class of emitters in efficient optoelectronic devices, such as organic light-emitting diodes (OLEDs) and light emitting electrochemical cells (LECs).[18] Strong SOC induced by heavy metal and structural effect play an important role in the origin of luminescent properties.[19]

To date, fine modulation of both redox and photophysical properties have been mainly achieved by judicious molecular design and control of the geometry and isomerization linkage of the coordinated ligands around the Ir^{III} center that selectively operate onto both the topology of the potential energy surfaces and electron density reorganization. Hence, a colorful palette of homo- and heteroleptic cyclometalated Ir^{III} complexes has been obtained when this metal center is combined with mono-, bi-, and tri-dentate scaffolds. Surprisingly, major efforts have been devoted to studying monometallic species.

Although both of them require recombination of charge carriers, which take place with a spin statistic of singlet-to-triplet exciton ratio of 1:3, LEC devices still display lower efficiency and reduced lifetime compared to OLEDs at comparable spectral region, in spite of the research efforts that have been currently made.[20] In particular, LEC requires the presence of mobile ions that migrate upon application to a suitable electrical bias, ensuring efficient charge

injection, migration and recombination within the electroactive layer.[21] In this framework, mononuclear cationic iridium complexes bearing cyclometalated ligands have demonstrated being leading emitting materials.[22]

One of the issues to address concerning luminescent compound is the severe drop of PLQY when moving towards longer wavelengths, making the near-infrared (NIR) design particularly challenging.[23] Therefore, the exploration of novel design strategies for red to NIR emitters is of paramount importance to achieve highly performing electroluminescent devices in this challenging spectral region. Only a very limited number of works describes the application of dinuclear and/or multinuclear complexes in LEC devices and External Quantum Efficiency (EQE) still below 2% have been reported to date.[24]

Herein, it is reported on a novel family of phosphorescent Ir(III)/M(I) complexes where the two metals are connected by the 1,3-dimesityl-5-acetylimidazol-2-ylidene-4-olate (IMesAcac) heteroditopic bridge (see *Scheme 3.*). The binding ability of the "acac" site is selectively employed to chelate the luminescent [$(C^N)_2Ir^{III}$] moiety yielding a novel family of red-emitting Ir^{III} complexes with enhanced optical properties.

It has been prepared three different mononuclear complexes of general formula [$Ir(\kappa^1C{:}\kappa^1N\text{-}C^N)_2(\kappa^2O,O\text{-}IMesAcacH)]PF_6$ (**1**–**3**), where IMesAcacH is the protonated imidazolium precursor and C^N is the cyclometalating pro-ligand 2-phenyl-pyridine (ppy), 2-phenyl-benzotiazole (2-pbt), and 1-phenylisoquinoline (1-piq), respectively. The dinuclear chloro-bridged Ir^{III} complexes $[Ir(C^N)_2(\mu\text{-}Cl)]_2$ were used as the starting iridium compounds for the following reaction steps. The synthesis started with a halogen abstraction by using $AgPF_6$ as the silver(I) source in a slightly coordinating solvent, such as methanol, affording the corresponding *bis*-solvato complex of general formula $[Ir(C^N)_2(MeOH)_2]_2$. Upon removal of AgCl by filtration, the zwitterionic IMesAcacH was then added directly to the reaction mixture that was refluxed for 12 hours. Target mononuclear complexes **1**–**3** were obtained (*Figure 5*) in purity suitable for photophysical investigation in moderate to good yield (44–87%) upon recrystallization.

The synthesis of the heterodinuclear complexes employed a stepwise site-selective metalation procedure that straightforwardly afforded the target Ir^{III}/M^{I} species (*Scheme 3.*). Upon chloride abstraction by using $AgPF_6$ onto the dichloro iridium dimer, the zwitterionic metalloligand that features an acac type of coordination motif, namely $M^{I}(\kappa^1C\text{-}IPr)(\kappa^1C\text{-}$

IMesAcac), is then added, yielding the target complexes **4-5** and **6-7** with M = Cu(I) and Au(I), respectively, upon re-crystallization with an aqueous solution of KPF_6 (*Figure 5*).

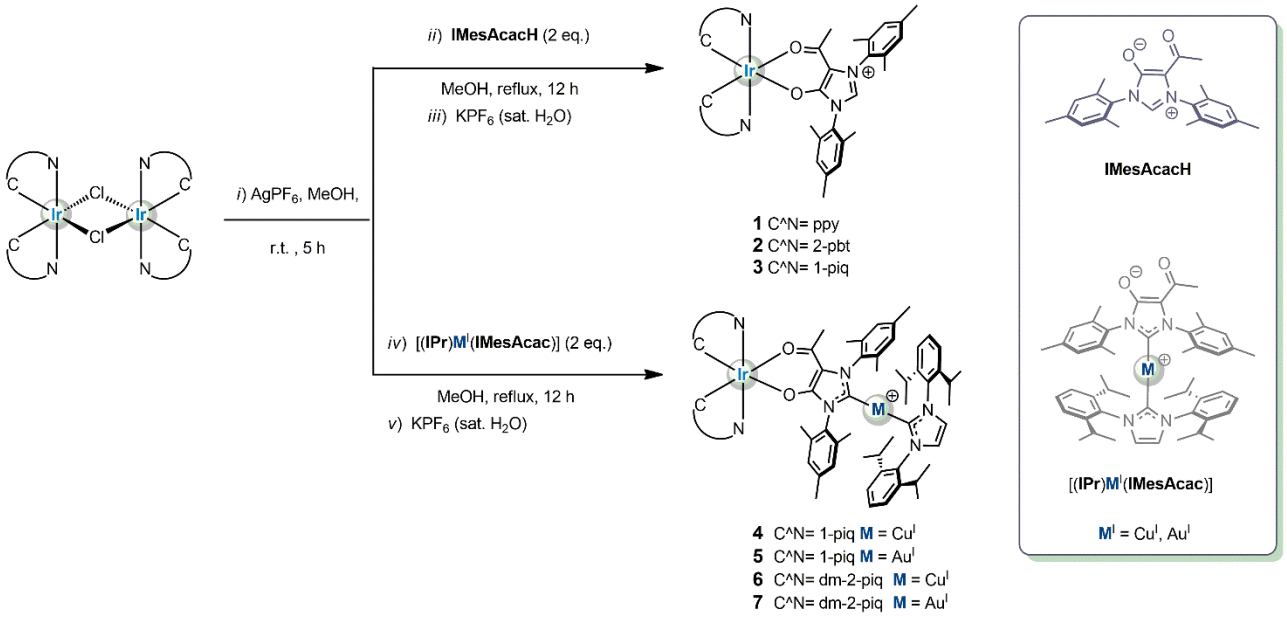

Scheme 3. Schematic synthetic pathway used for the synthesis of complexes **1–7** All complexes were prepared as PF_6^- salt.

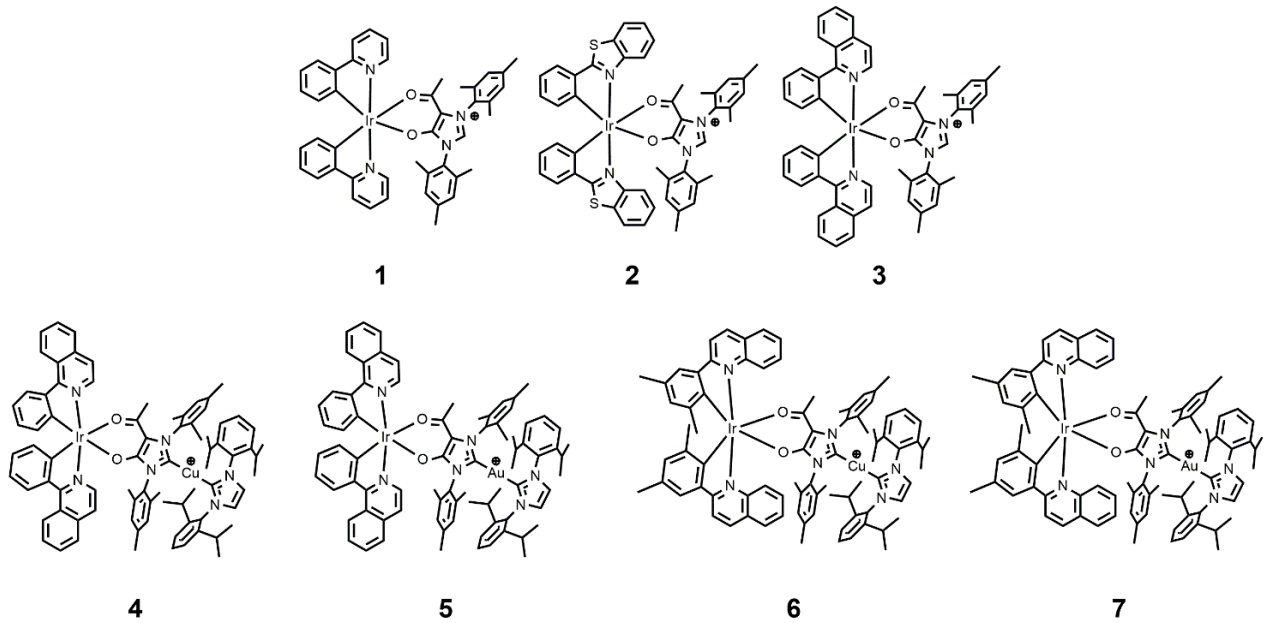

Figure 5. Chemical structure of the investigated iridium complexes **1-7**

The photophysical properties of complexes **1-7** were investigated in different sample conditions (*Figure 6,7, 8* and *9*). The monometallic complexes **1-3** were analyzed in acetone, since they are stable just in weak coordinating solvents and in non-chlorinated solvents, providing a selective choice of conditions. For sake of comparison, complexes **4** and **5** were also investigated in acetone, although they are stable even in dichloromethane. Subsequently, the photophysical properties of complexes **4–7** was further carried out in dichloromethane, to be directly comparable with benchmark complexes $[Ir(1\text{-}piq)_2(acac)]$ and $[Ir(dm\text{-}2\text{-}piq)_2(acac)]$[4] and to obtain information about their suitability as emitters in LEC devices.

Firstly, the photophysical properties of complexes **1**–**3** were investigated at concentration of $3.0X10^{-5}$ M in both air-equilibrated and degassed acetone solution at room temperature (*Figure 6*). The most intense transition present in the region λ_{abs} = 350–400 nm is attributed with confidence to spin-allowed ligand-centered (^{1}IL) processes, localized on the cyclometalating ligands, although the complete profile of the band could not be recorded due to the limitation of the spectral window of the solvent employed. At lower energy, in the region λ_{abs} = 400–500 nm, the spectra feature broad and featureless transitions with moderate intensity ($\varepsilon \approx 2–6X10^3$ $M^{-1}cm^{-1}$) that are partially overlapped. This band is ascribed to spin-allowed electronic processes with mainly metal-to-ligand charge transfer (^{1}MLCT) character as by comparison with related $[Ir(C\text{^}N)_2(acac)]$ complexes reported previously.[25]

A clear modulation of the absorption onset is observed in the series featuring a bathochromic shift in the order **1** to **2** to **3**, which parallels the increasing π-accepting ability of the N-containing heteroaromatic ring coordinated onto the iridium atom.

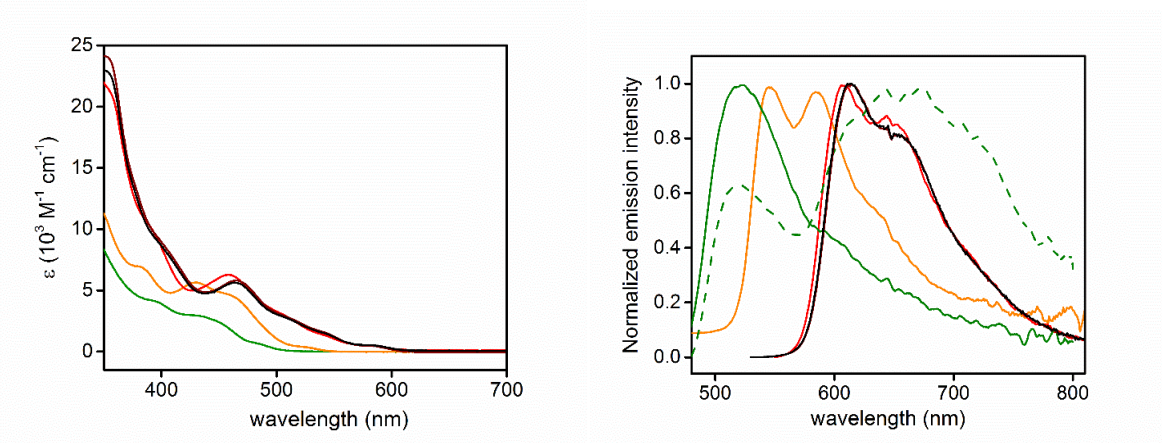

Figure 6. Electronic absorption (*left*) and emission spectra (*right*) for **1** (green), **2** (orange), **3** (red), **4** (dark red), and **5** (black) in acetone at concentrations of $3.0X10^{-5}$ cm in degassed condition. For **1**, the emission spectrum of the air-equilibrated sample is shown as dashed line. Samples were excited at λ_{exc} = 410, 450, 460, 470, and 460 nm for compounds **1**, **2**, **3**, **4** and **5**, respectively.

Upon excitation in the ^{1}MLCT band, acetone samples of compounds **1**–**5** display photoluminescence in both air-equilibrated and degassed condition (*Figure 6*). The emission spectra display a bathochromic shift going from **1** to **2** to **3** that parallels the trend observed in the absorption spectra. Surprisingly, air-equilibrated samples of complex **1** clearly show two broad and featureless emission bands centred at 520 and 655 nm and an overall PLQY as low as 0.05%. In degassed condition, the band at 520 nm dominates the emission profile along with a lifetime of 1.2 μs. This band is assigned to T_3 by computational calculation involving the contribution of the IL_{C^N} state. This result confirms the phosphorescence nature of the high energy band (namely P1), attributed to an emissive state with $^3MLCT_{ppy}/^3IL_{ppy}$ character. Incorporation of a more extended π-system, such as either the benzothiazole ring or the isoquinoline moiety, onto the cyclometalating C^N ligand causes a shift of the emission to lower energies, being λ_{em} = 546 and 583 nm (**2**), and 607 and 650 nm (**3**), whose profile appear to be virtually independent of the presence of dioxygen. Nonetheless, increase of the PLQY from 1.9 to 3.5% (compound **2**) and from 2.5 to 18% (compound **3**) is observed, again pointing toward the triplet nature of the emissive excited state. The two excitation spectra show slightly different profile, also when compared to the absorption spectrum, corroborating the idea that the two emission bands originate from electronically

uncoupled excited states. Time-resolved analysis of the photoluminescence of compounds **1**–**3** revealed interesting information. Indeed, the excited state kinetic data recorded in degassed condition required a fitting with bi-exponential model for the three compounds **1**–**3**. Such P2 state appears to be present in the three complexes of the series **1**–**3** and it is most likely at the origin of the band clearly observed at λ_{em} = 655 nm for complex **1**. To further investigate the emissive properties and the origin of the lower energy band, low temperature (77 K) photoluminescence experiments were carried out for samples of **1**–**3** in 2-MeTHF glassy matrix (*Figure 7*).

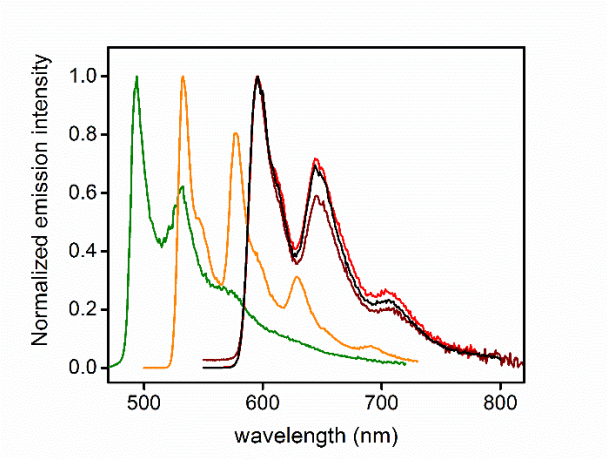

Figure 7. Emission spectra recorded for **1** (green), **2** (orange), **3** (red), **4** (dark red), and **5** (black) in 2Me-THF glassy matrix at 77 K. Samples were excited at λ_{exc} = 400 nm for **1** and **2**, 420 nm for **3**, 450 nm for **4**, and 460 nm for **5**.

Under this condition complexes **1**–**3** display intense emission with highly vibronic profile and mono-exponential decay over the whole emission band resembling those of parental [Ir(C^N)$_2$(acac)] complexes, indicating that population of the P2 band might occur through a thermally-activated process at room temperature. Overall, the P2 band is tentatively attributed to a triplet ligand-to-ligand charge transfer character, namely ^{3}LLCT$_{IMesAcacH}$, with a metal-perturbed C^N→IMesAcacH character, close-lying to the emissive ^{3}IL$_{C^N}$/^{3}MLCT$_{C^N}$. Indeed, going from compound **1** to **2** to **3**, the ^{3}LLCT$_{IMesAcacH}$ level is expected to be affected to a minor extent. The stabilization of the ^{3}MLCT$_{C^N}$/^{3}IL$_{C^N}$ provided by the more extended π-conjugation for complexes **2** and **3** of the system increases the energetic barrier for the P1→P2 process, rendering the thermal population of the poorly emissive P2 more difficult. going from **3** to **4** and **5** a small bathochromic shift is observed

for the band attributable to the admixture of ^{1}MLCT and ^{3}MLCT transitions that involves the cyclometalating C^N and acac moiety ($\lambda_{abs,max}$ = 458 nm for **3** and 465 nm for **4** and **5**). The $MLCT_{C^N}$ states are more stabilized, increasing their participation in the low-lying mixed $IL_{C^N}/MLCT_{C^N}$ states of complex **4** as compared to complex **3**.

The photoluminescence spectra of **4** and **5** are bathochromically shifted by 8 nm (215 cm^{-1}) in comparison with the parental compound **3**. In sharp contrast, the bimetallic species display mono-exponential excited-state decay kinetics and a twofold increase of PLQY (τ = 1.6 μs and PLQY = 36% in degassed acetone). One should notice that this value of PLQY is much higher than the benchmark complex $[Ir(1\text{-}piq)_2(acac)]$[47] and amongst the highest for red-emitting cationic Ir^{III} complexes.

At a second stage, the photophysical properties of the four complexes **4-7** were investigated in CH_2Cl_2 solution at concentration of $3\cdot10^{-5}$ M in both air-equilibrated and degassed condition at room temperature (*Figure 8*). In the higher energy region at λ_{abs} = 340–350 nm, all four complexes display intense (ε = 2.06–2.28X10^4 M^{-1} cm^{-1}) bands that can be ascribed to electronic processes with mainly singlet-manifold ligand centered (^{1}LC) to a certain degree of admixing with spin-allowed metal-to-ligand charge transfer (^{1}MLCT). At lower energy (λ_{abs} *ca.* 400 nm), the less intense transitions with ε = 6.8–8.3 X 10^3 M^{-1} cm^{-1} are attributable to electronic processes with mainly ^{1}MLCT character admixed intraligand charge transfer (^{1}ILCT). Upon excitation on the lower-lying bands, dilute CH_2Cl_2 samples of compounds **4**–7 display intense vibrant red emission. In particular, compounds **4** and **5** show a broad emission band centered at λ_{em} = 610 nm with a vibrational feature at 645 nm that can be ascribed to an emission originating from an excited state with admixed ^{3}MLCT/^{3}LC character involving the heavy atom and the C^N ligands. On the other hand, emission spectral profile of compounds **6** and **7** are broad, featureless and narrower than those of **4** and **5**, indicating higher ^{3}MLCT character and lesser geometrical distortion of the emissive excited state for compounds **4-5**. Derivatives bearing the dm-2-pic ligand displayed higher PLQY amongst the series, with values as high as 0.77 and 0.73 for the **6** and **7**, respectively, in degassed CH_2Cl_2. It is worth to notice that these PLQY values are remarkably high and amongst the highest for cationic red-emitting complexes.

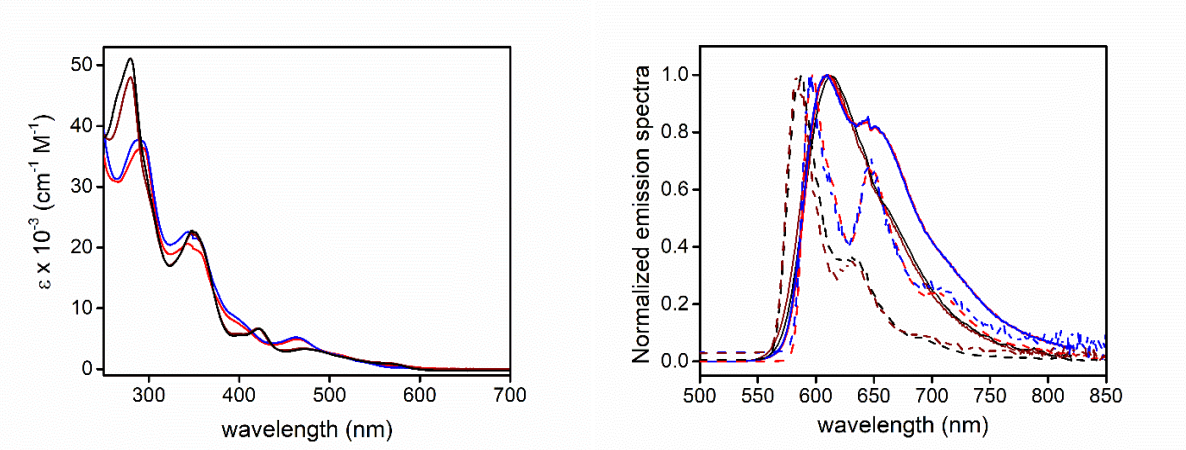

Figure 8. Electronic absorption (*left*) and emission spectra (*right*) for **4** (red trace), **5** (blue trace), **6** (dark red trace) and **7** (black trace) in dichloromethane at concentration of 3.0×10^{-5} M in degassed condition (solid traces) and in 2-MeTHF glassy matrix at 77 K (dashed traces). Samples were excited at λ_{exc} = 420, 460 and 480 nm for compound **4**,**5**,**6** and **7**, respectively.

Whereas the lowest triplet state of **6** and **7** possess an ILCT/MLCT character, which corresponds to the HOMO-LUMO transition; the T_1 states of **4** and **5** features a LC character involving the phenyl-isoquinoline ligand mixed with MLCT. Overall, the investigated bimetallic species possess smaller k_{nr} values when compared to the monometallic counterparts, indicating that non-radiative channels are suppressed to a larger extent and, therefore, bimetallic structures help providing a more rigid scaffold. Even more interestingly, k_r values are higher for bimetallic species.

In thin-film (*Figure 9*), emission spectra of all the samples display bathochromic shift compared to dilute solution sample, which is accompanied by a drop of the PLQY in condensed phase, expectantly. It is important to notice that the decrease of the emission efficiency, as well as the bathochromic shift, was less dramatic for compounds **6** and **7**, thus supporting the idea that the presence of additional methyl groups in the chemical structure of the complexes helps to keep the triplet emitters further apart and therefore mitigating aggregation-caused quenching effects and triplet-triplet annihilation phenomena in condensed phase. This is an important point to address in view of their potential application in solid-state light emitting devices.

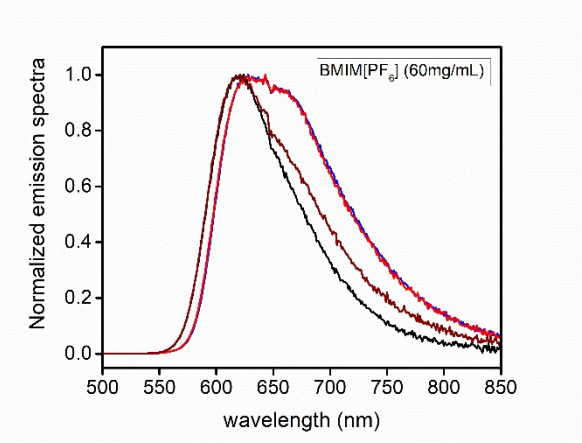

Figure 9. Emission spectra of spin-coated BMIM[PF_6] (20 wt.%) **complex** (80 wt.%) at total concentration of 60 mg mL^{-1} in acetonitrile for samples of **4** (red trace), **5** (blue trace), **6** (black trace) and **7** (dark red trace) upon λ_{exc} = 450 nm.

To evaluate the EL performance of the proposed heterodinuclear iTMCs, the LECs based on complexes **4**, **5**, **6**, and **7** were fabricated and their EL characteristics were measured. All emissive layers of these iTMC were spin-coated from the mixture of the complex (80 wt.%) and [$BMIM^+(PF_6)^-$] (20 wt.%) in acetonitrile solution with various concentrations. The optimized host-guest LECs based on the host complex **B** (see *Figure ES4.25*, *Chapter 4*) doped with 5 wt.% guest complexes **6** and **7** show the peak EQE of *ca.* 4.5 and 6%, respectively. Such device efficiencies are the highest ever reported for bi and/or multimetallic emitters and amongst the highest for red phosphors, confirming that the proposed heterobimetallic complexes are potential candidates for use in efficient LECs.

5. *Bright blue-emitting heteroleptic bis-tridentate Ir(III) complexes bearing a 1,2,4-triazolate scaffold*

Although the huge success of the homoleptic iridium complexes for OLED, the structural instability, owing to the meridional to facial isomerization upon thermal and photo-excitation[26], and possible ligand-loss degradation pathways[27], encourages the research to find an alternative structure to *tris*-bidentate compounds.

Bidentate ligands bind through two donor sites, causing the chelating effect around the metal. This effect is the enhanced affinity of a chelating ligand for a metal ion compared to its monodentate ligand counterpart(s). The result is a more stable and robust ligand-metal bond.[28]

In this work a novel series of *bis*-tridentate iridium(III) complexes as potential dopant emitters in organic light-emitting diodes (OLEDs) is reported. An OLED is a device that converts an electrical input into light energy via electroluminescence (EL). In order to achieve a good efficiency in the device, the emissive compound must have thermal- and photo-stability, high photoluminescence, long lifetime and tunability of the emission colors.[29] Aiming at obtaining stable and efficient heteroleptic blue emitters iridium(III) complexes for devices application, the use of the chelating ligands is crucial. The chelating effect allows to improve the ligand field strength around the metal, increasing the efficiency of the dopant in the device.[30] The use of a triazolyl-pyridine derivative ligand makes accessible the modulation of the electronic properties. If on one hand the dicarbene ligand improves the ligand field strength, enhancing the ^{3}MC states in energy and leading to a smaller k_{nr}, on the other hand a phenyl triazolyl pyridine derivative allows to tune the emission wavelength.[31,32]

Aiming at efficient and robust blue-emitting iridium(III) complexes as potential dopants for OLEDs, hereafter it will be described a novel series of neutral heteroleptic *bis*-tridentate iridium(III) derivatives **TR1-TR5** bearing either a 2-(2,4-difluorophenyl)-6-(5-(trifluoromethyl)-4H-1,2,4-triazol-3-yl)pyridine, or a 2-(5-(trifluoromethyl)-4H-1,2,4-triazol-3-yl)-6-(4-(trifluoromethyl)phenyl)pyridine, as chromophoric ligand and a *bis*-N-heterocyclic carbene ligand (*Figure 10*).

Unfortunately, two out of five planned complexes, **TR4** and **TR5** were not successful isolated but they were only detected by mass spectroscopy.

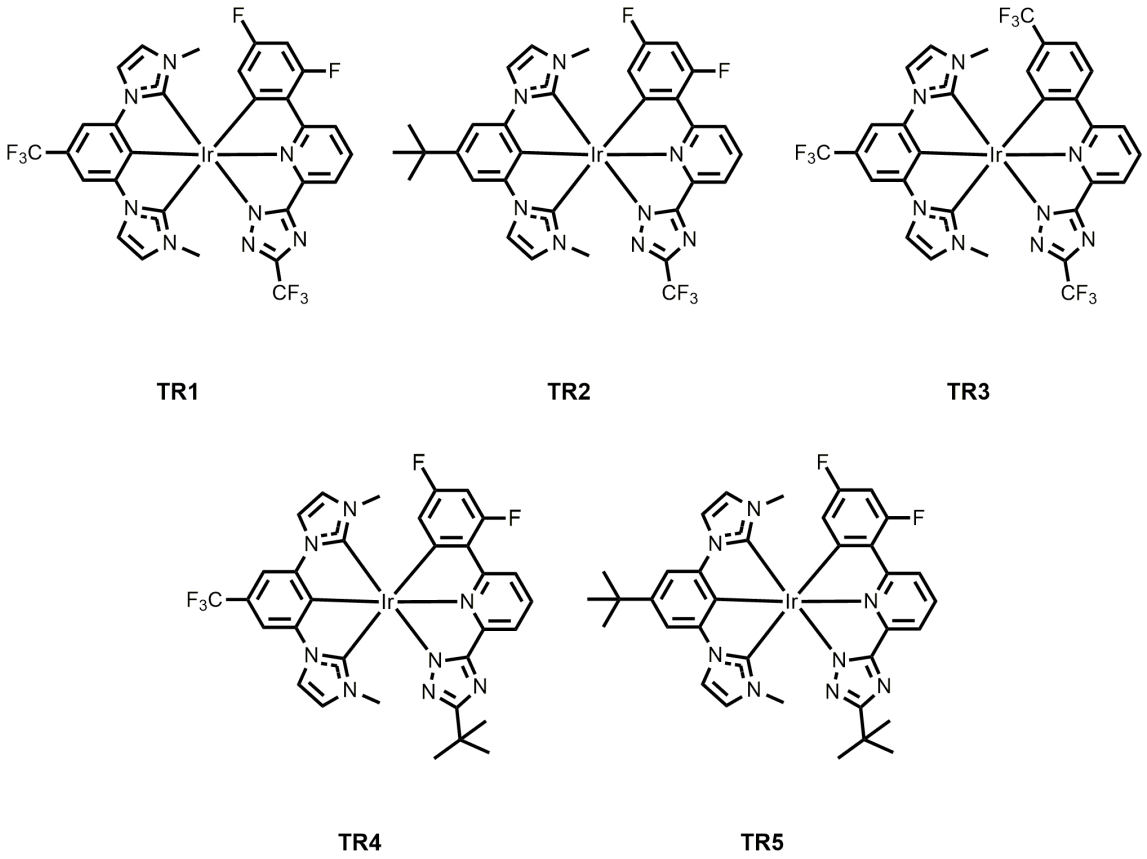

Figure 10. Chemical structure of the investigated iridium complexes **TR1-5.**

In order to modulate the optical properties of the final complexes, two tridentate proligands based on the phenyl-bis-imidazolium scaffolds were firstly targeted, namely [fpbmiH_2][PF_6]$_2$ and [bpbmiH_2][PF_6]$_2$ bearing an electron-withdrawing CF_3 and a moderate electron-donating tert-butyl group, respectively, in position 5 of the phenyl group. For the synthesis of the both *bis*-carbene pincers, the starting material 2,6-dibromophenyl was converted to the corresponding 1,3-di(1H-imidazol-1-yl)benzene, followed by methylation at the 3-position of the imidazole to give the final *bis*-3-methyl-imidazolium hexafluorophosphate, accordingly to previous reports. [33]

The synthetic pathway employed for the synthesis of [**fpbmiH_2**][**PF_6**]$_2$ and [**tpbmiH_2**][**PF_6**]$_2$ is a Cu(I) catalyzed Ullmann-type coupling reaction between the 1,3-dibromo-benzene and 1H-imidazole. The diimidazolium cations were obtained using methyl iodide by methylation at N(3) position. The target *bis*(hexafluorophosphate) salts were obtained straightforwardly by anion metathesis from the iodine salts (*Scheme 4*).

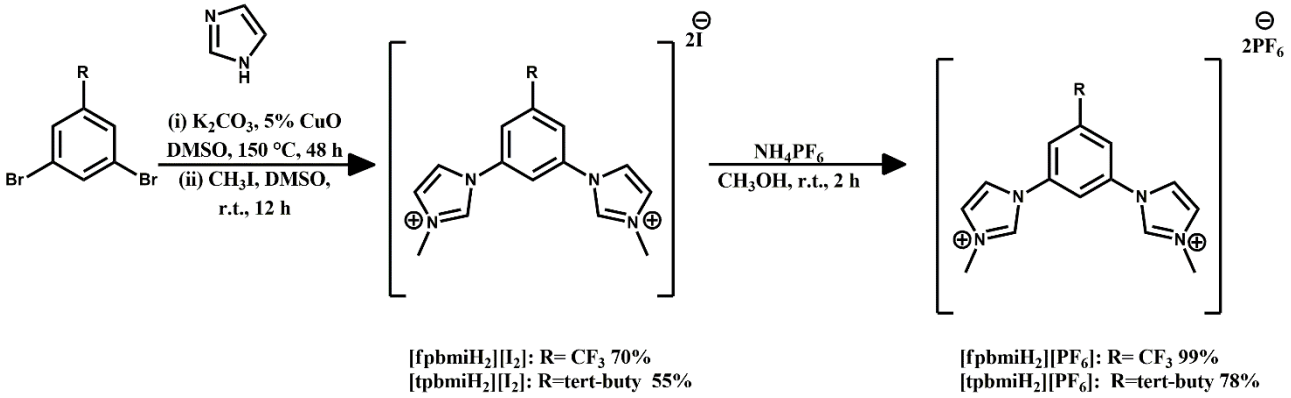

Scheme 4. Synthetic general procedure for pincer bis-carbene.

The target 1,2,4-triazolyl derivatives were prepared by a stepwise reaction. The Suzuki coupling between the difluoro-phenyl boronic acid and the 6-bromo-2-cyano pyridine is followed by the introduction of the triazole ring by treatment with hydrazine monohydrate and trifluoroacetic anhydride (for $L1H_2$ and $L2H_2$), or acylation with trimethylacetyl chloride (for $L3H_2$) in agreement with modified procedures already reported (*Scheme 5*).[34]

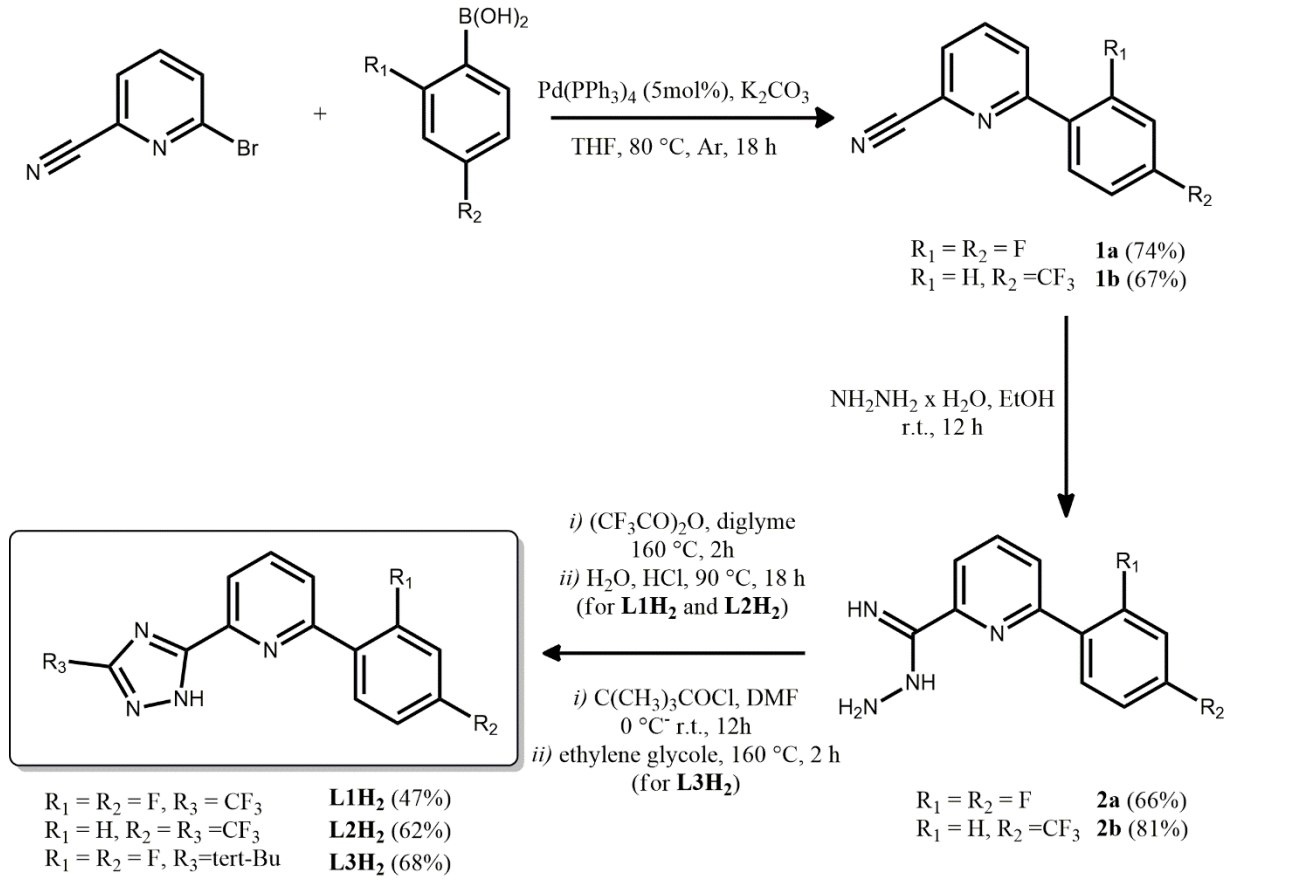

Scheme 5. Synthetic procedure for the triazolyl derivative ligands **$L1H_2$**, **$L2H_2$** and **$L3H_2$**.

The target Ir(III) metal complexes were synthesized following the same method reported elsewhere (*Scheme 6*). First, the bis(imidazolium) proligand reacted with [Ir(1,5-cod)Cl]$_2$ in a ratio of 2:1 equiv., and an excess (10 equiv.) of NaOAc in refluxing dry acetonitrile. As reported previously,[35,36] solvent molecules coordinates two sites of the metal, leaving the last site to hydride ligand. The same reactions were performed under microwave (MW) irradiation. Although the first step was the same in both of the procedures, the cyclization from the second step was tried by heating at 230°C for 2 h under MW (100). The compounds **TR1** and **TR3** were synthesized according to this procedure. All complexes were tested by the two synthetic paths but, in both cases, the reactions were not well reproducible, so it was not possible to compare them in terms of yield and purity.

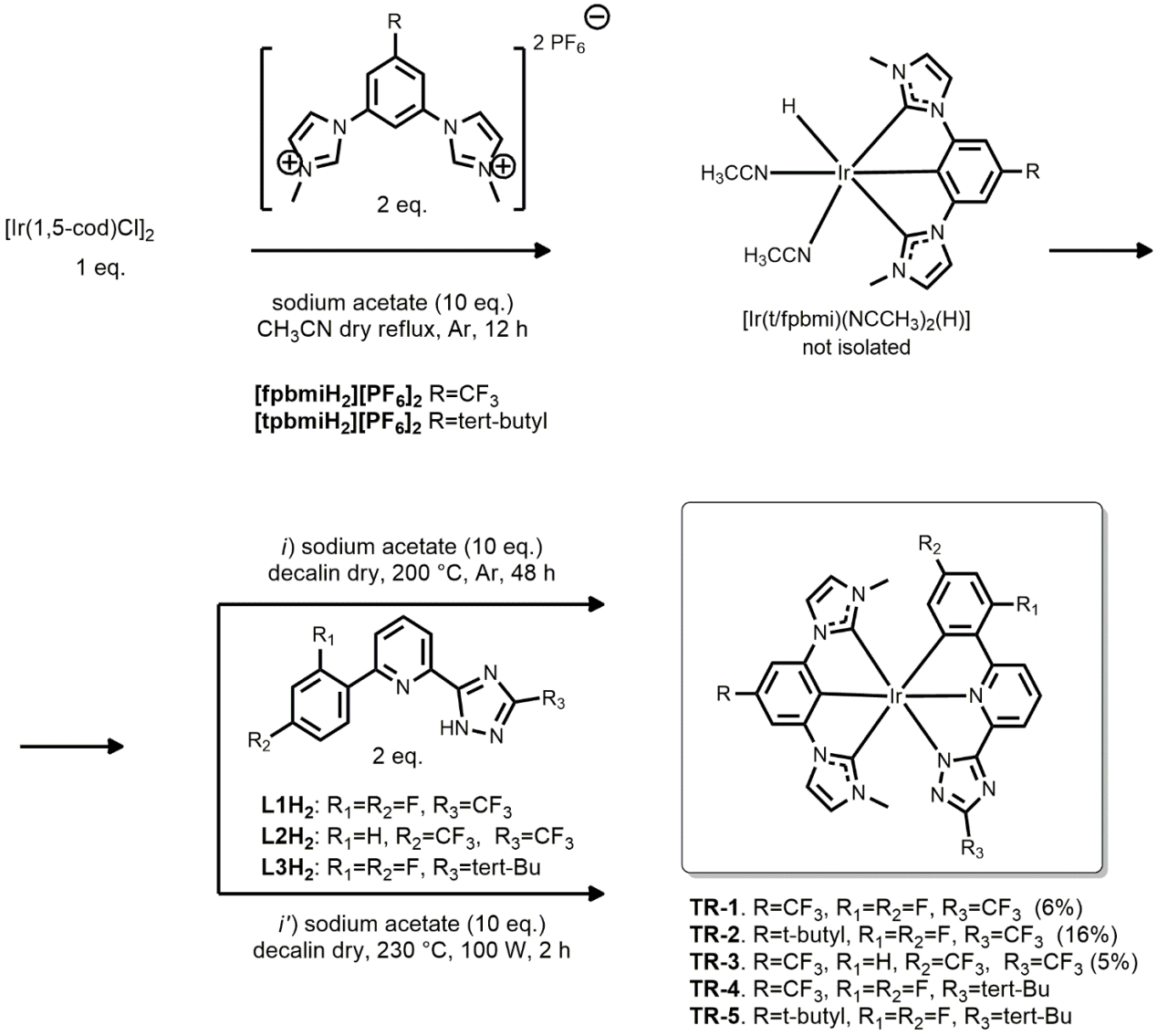

Scheme 6. Synthetic procedure for the Ir(III) metal complexes **TR1-5**.

Firstly, the photophysical properties of the investigated Ir(III)-complexes **TR1-TR3** were studied in dilute CH_2Cl_2 solution in both air-equilibrated and degassed condition at room temperature at concentration 3 X 10^{-5} M and in a glassy matrix of 2Me-THF.

In the UV-vis spectra (*Figure 11*), the intense absorption band at λ_{abs} = ca. 325 nm with ε = 12.8, 19.6 and 12.3 X 10^3 M for **TR1**, **TR2** and **TR3**, is ascribed to the ^{1}LC (1π-π*) ligand centered involving triazolyl-based terdentate ligand L1H2 and L2H2. At longer wavelengths, in the region λ_{abs} = 370–400 nm the band can be confidentially ascribed to a single metal-to-ligand charge-transfer (^{1}MLCT) electronic transition from metal and metalated bis-NHC moiety towards the phenylpyridine portion of the terdendate triazolyl-containing ligand. The photoluminescence (PL) properties reveal similar behavior for all compounds upon irradiation at λ_{exc} = 355–400 nm. The samples display emission spectra within the sky-blue region with vibronic profile with the highest-energy maxima at λ_{em} = 463, 468 and 485 nm, for **TR1**, **TR2** and **TR3**, respectively. Expectantly, degassed samples undergo a sizeable increase of the emission intensity with PLQY of 51.7-81.8% accompanied by prolongation of the excited-state lifetime (τ = 3.1–6.2 μs) confirming the triplet nature of the emissive excited state. Therefore, it is proposed that the emissive excited state is a mixing of ^{3}MLCT and ^{3}LC character, with a larger contribution of the ^{3}LC for complexes **TR1** and **TR3**. On the contrary, complex **TR2** reveals a slightly more ^{3}MLCT character.

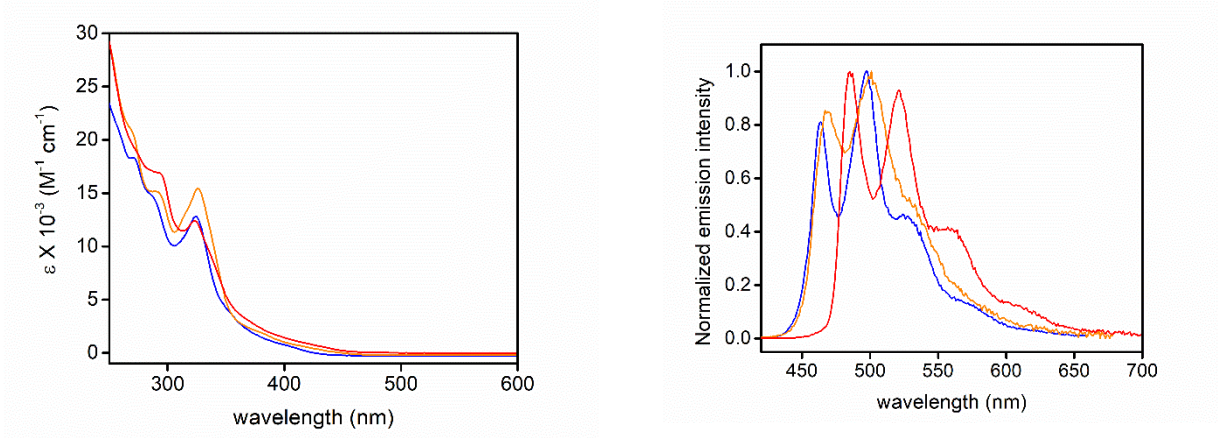

Figure 11. Electronic absorption (*left*) and emission (*right*) spectra for **TR1-3** complexes in dichloromethane at concentration of 3.0×10^{-5} M in degassed condition. Samples were excited at λ_{exc} = 355 nm for **TR1** (blue trace), 400 nm for **TR2** (orange trace), and 380 nm for **TR3** (red trace)**.**

Low temperature experiments in frozen 2Me-THF glassy matrix at 77 K were carried out to gain deeper insights onto the nature of the emissive excited state (*Figure 12*). Upon excitation at λ_{exc} = 380 nm, for all three samples emission spectra display only a minor hypsochromic shift compared to the room temperature photoluminescence (shift 141 cm^{-1}). In addition, time-resolved decay analysis reveals that **TR1** and **TR3** maintain a longer lifetime (τ = 7.1 and 5.9 µs, respectively), while sample of complex **TR2** displays the shortest one (τ = 3.7 µs) among the investigated series, in accordance with photoluminescence data recorded at room temperature.

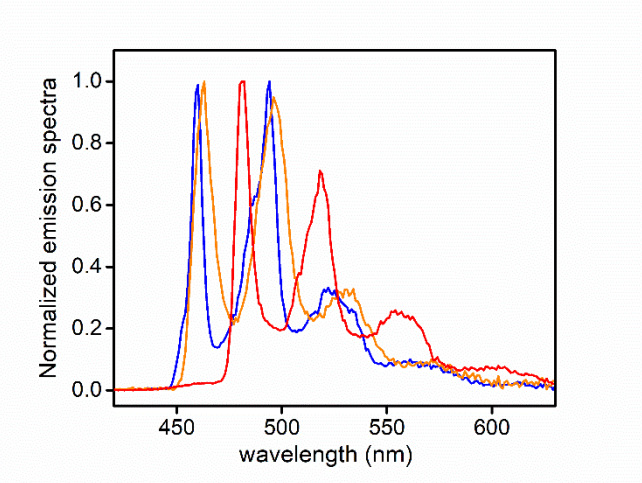

Figure 12. Emission spectra for **TR1-3** complexes in in 2-MeTHF at 77 K. Samples were excited at λexc = 380 nm. (**TR1**, blue trace; **TR2**, orange trace; **TR3** red trace).

The emission spectra of **TR1-TR3** in PMMA thin films at 5 wt.% doping level are showed in *Figure 13*. As far as complex **TR1** is concerned, its emission profile maintains similar shape to that recorded in solution (*Figure 11*), with also no shift of the maxima (λ_{em} = 463, 497 and 524 nm). Moreover, the PLQY is similar as well with value of 63.0% in thin film vs 61.6% in degassed conditions. Overall, these finding indicate that at such low doping concentration **TR1** sample display a no intermolecular interactions amongst emissive complexes and negligible triplet-triplet annihilation phenomena. Complexes **TR2** displays a different emission profile in doped PMMA when compared to the sample in CH_2Cl_2 solution. In particular, emission profile in thin-film appears broader and featureless with a maximum centered at λ_{em} = 470 nm.

This emission is characterized by an excited state decay kinetics (when measured at λ_{em} = 470) that can be fitted with a bi-exponential model, being τ_1 = 487 ns (84%) and τ_2 = 1.6 µs (16%), along with highly quenched emission (PLQY = 7.3%). Overall, these finding support the idea that compound **TR2** in PMMA thin-film display a much more pronounced tendency towards intermolecular aggregation and triplet-triplet quenching processes.

As for complex **TR3**, photoluminescence spectrum in PMMA display a vibronic progression with similar wavelength maxima than those observed in solution but with different intensity ratio. Bi-exponential lifetime is recoded as well, with τ_1 = 498 ns (80%) and τ_2 = 1.6 µs (20%) along with a PLQY of 9.0%, indicative of quenching process occurring to a larger extent if compared to the CH_2Cl_2 solution sample.

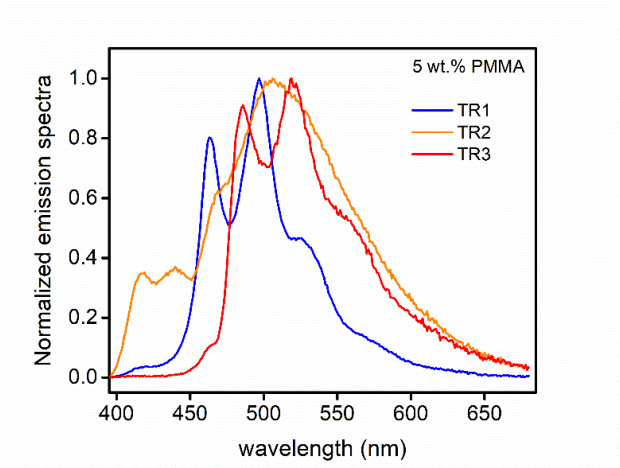

Figure 13. Emission spectra for **TR1-TR3** 5 wt.% in PMMA thin films. λ_{exc} = 380 nm

Compounds **TR1-TR3** display an emission spectrum that are comparable to related derivatives reported by Chi *et al.*.[32,37] On the other hand, the slightly decrease of the PLQY in **TR1-TR3** may be attributed to the non-optimal bite angle of the coordinated [fpbmi] and [tpbmi] ligands. The introduction of a nitrogen atom between the two fluorine on the phenyl ring of the chromophoric ligand can stabilize better the HOMO level, enlarging the HOMO-LUMO gap and may provide more hyspochromically shifted emisison spectra.[31] Investigation in this respect are currently ongoing in the research group where I have carried out my thesis. To conclude, further investigation about dopants emitters for OLED devices should be carried out on **TR1**, which reveals the better photophysical behavior in PMMA thin films.

References

1. J. Twilton, C. Le, P. Zhang, M. H. Shaw, R. W. Evans, D. W. C. MacMillan, *Nat. Rev. Chem.* **2017**, *1*, 52.
2. [a] C. Caporale, M. Massi, *Coord. Chem. Rev.* **2018**, *363*, 71; [b] Q. Zhao, C. Huang, F. Li, *Coord. Chem. Rev.* **2011**, *40*, 2508.
3. H. Yersin (Ed.) in *Highly Efficient OLEDs with Phosphorescent Materials*, Wiley-VCH, Weinheim, **2008**.
4. [a] H. Yersin, A. F. Rausch,R. Czerwieniec, T. Hofbeck, T. Fischer, *Coord. Chem. Rev.* **2011**, *255*, 2622; [b] Y. Komada, S. Yamauchi, N. Hirota, *J. Phys. Chem.* **1986**, *90*, 6425.
5. [a] R. Englman, J. Jortner, *Mol. Phys.* **1970**, *18*, 145; [b] J. V. Caspar, T. J. Meyer, *Inorg. Chem.* **1983**, *22*, 2444; [c] J.V. Caspar, T. J. Meyer, *J. Phys. Chem.* **1983**, *87*, 952; [d] E. M. Kober, J. V. Caspar, R. S. Lumpkin, T. J. Meyer, *J. Phys. Chem*. **1986**, *90*, 3722.
6. [a] T. Sajoto, P. I. Djurovich, A. B. Tamayo, J. Oxgaard, W. A. Goddard, M. E. Thompson, *J. Am. Chem. Soc*. **2009**, *131*, 9813; [b] F.Barigelletti, A. Juris, V. Balzani, P. Belser, A. Von Zelewsky, *J. Phys. Chem*. **1987**, *91*, 1095; [c] B. Durham, J. V. Caspar, J. K. Nagle, T. J. Meyer; *J. Am. Chem. Soc*. **1982**, *104*, 4803; [d] L.S. Forster *Coord. Chem. Rev.* **2002**, *227*, 59.
7. [a] D. Bourissou, O. Guerret, F. P. Gabbaï, G. Bertrand, *Chem. Rev.* **2000**, *100*, 39; [b] M. N. Hopkinson, C. Richter, M. Schedler, F.Glorius; *Nature* **2014**, *510*, 485.
8. R. Tonner, G. Heydenrych, G. Frenking, *Chem. Asian. J*. **2007**, *2*, 1555.
9. [a] T. Sajoto, P. I. Djurovich, A. Tamayo, M. Yousufuddin, R. Bau, M. E. Thompson, R. J. Holmes,S. R. Forrest, *Inorg. Chem.,* **2005**, *44*, 7992; [b] C.-F. Chang, Y.-M. Cheng, Y. Chi, Y.-C. Chiu, C.-C. Lin, G.-H. Lee, P.-T. Chou, C.-C. Chen, C.-H. Chang, C.-C. Wu, *Angew. Chem.,* **2008**, *47*, 4542; [c] N. Darmawan, C.-H. Yang, M. Mauro, M. Taynal, S. Heun, J. Pan, H. Buchholz, P. Braunstein and L. De Cola, *Inorg. Chem.,* **2013**, *52*, 10756; [d] C. Yang, F. Mehmood, T. L. Lam, S. L.-F. Chan, Y. Wu, C.-S. Yeung, X. Guan, K. Li, C. Y.-S. Chung, C.-Y. Zhou, T. Zoua, C.-M. Che, *Chem. Sci.,* **2013**, *4*, 2630.
10. D. J. Stukfens, A. Vlcek Jr., *Coord. Chem. Rev.,* **1998**, *177*, 127.
11. [a] A.-H. Bonardi, F. Bonardi, G. Noirbent, F. Dumur, D. Gigmes, C. Dietlin, J. Lalevée, *J. Polym. Sci*. **2020**, *58*, 300. [b] D.-A. Nicewicz, D.-W.-C. MacMillan, *Science* **2008**, *322*, 77.
12. B. Rosenberg, L. Vancamp, T. Krigas, *Nature* **1965**, *205*, 698
13. Y. Li, K-N. Wang, L. He, L-N. Ji, Z-W. Mao, *J. Inorg. Biochem.* **2020**, *205*, 110976.
14. M. Alcarazo, S. J. Roseblade, A. R. Cowley, R. Fernández, J. M. Brown, J. M. Lassaletta, *J. Am. Chem. Soc.* **2005**, *127*, 3290.

15. M. Nonoyama, *Bull. Chem. Soc. Jpn.* **1974**, *47*, 767.
16. [a] S. Lamansky, P. Djurovich, D. Murphy, F. Abdel-Razzaq, H.-E. Lee, C. Adachi, P. E. Burrows, S. R. Forrest, M. E. Thompson, *J. Am. Chem. Soc.* **2001**, *123*, 4304
17. C. Yang, F. Mehmood, T. L. Lam, S. L.-F. Chan, Y. Wu, C.-S. Teung, Z. Guan, K. Li, C. Y.-S. Chung, C.-Y. Zhou, T. Zou, C.-M. Che, *Chem. Sci.* **2016**, *7*, 3123.
18. [a] *Iridium (III) in optoelectronic and photonics applications (Ed.: E. Zysman-Colman),* **2017**, Wiley, New York; [b] N. Armaroli, H. J. Bolink, *Photoluminescent materials and electroluminescent devices in Topics in Current Chemistry*, Springer, Heidelberg, **2016**; [c] H. Yersin, *Highly Efficient OLEDs with Phosphorescent Materials*, **2008** Wiley-VCH, Weinheim.
19. [a] A. J. Howarth, R. Patia, D. L. Davies, F. Lelj, M. O. Wolf, K. Singh, Eur. J. *Inorg. Chem.* **2014**, 3657; [b] C. Latouche, D. Skouteris, F. Palazzetti, V. Barone, *J. Chem. Theory Comput.* **2015**, *11*, 3281; [c] D. Han, L. Zhao, X. Han, *Photochem. Photobiol. Sci.* **2019**, *18*, 2766; [d] B. J. Powell, *Coord. Chem. Rev.* **2015**, *295*, 46; [e] H. Brahim, C. Daniel, *Comput. Theor. Chem.* **2014**, *219*, 1040; [f] H. Brahim, B. Haddad, M. Boukabene, S. Brahim, B. Ariche, *Comput. Theor. Chem.* **2017**, *8*, 1101; [g] H. Brahim, B. Haddad, S. Brahim, A. Guendouzi, *J. Mol. Model.* **2017**, *23*, 344; [h] D. Hadji, H. Brahim, *Theor. Chem. Acc*. **2018**, 137.
20. [a] R. D. Costa (Ed.), in *Light-emitting Electrochemical Cells: Concepts, Advances and Challenges*, Springer, **2017**; [b] E. Fresta, R. D. Costa, *J. Mater. Chem. C*, **2017**, *5*, 5643.
21. [a] Q. Pei, G. Yu, C. Zhang, Y. Yang, A. J. Heeger, *Science*, **1995**, *269*, 1086; [c]Q. Pei, A. J. Heeger, *Nature Mater.*, **2008**, *7*, 167; [d] J. D. Slinker, J. A. DeFranco, M. J. Jaquith, W. R. Silveira, Y.-W. Zhong, J. M. Moran-Mirabal, H. G. Craighead, H. D. Abruña, J. A. Marohn, G. G. Malliaras, *Nature Mater.*, **2007**, *6*, 894
22. R. D. Costa, E. Ort., H. J. Bolink, F. Monti, G. Accorsi, N. Armaroli, *Angew. Chem. Int. Ed.* **2012**, *51*, 8178.
23. [a] Y. Zheng, A. S. Batsanov, M. A. Fox, H. A. Al-Attar, K. Abdullah, V. Jankus, M. R.Bryce and A. P. Monkman, *Angew. Chem., Int. Ed.*, **2014**, *53*, 11616; [b] A. M'hamedi, M. A. Fox, A. S. Batsanov, H. A. Al-Attar, A. P. Monkman and M. R. Bryce, *J. Mater. Chem. C*, **2017**, *5*, 6777.
24. M. Z. Shafikov, S. Tang, C. Larsen, M. Bodensteiner, V. N. Kozhevnikov and L. Edman, J. Mater. Chem. C, 2019, 7, 10672;. R. D. Costa, G. Fernandez, L. Sanchez, N. Martin, E. Ortí, H. J. Bolink, *Chem. Eur. J*., **2010**, *16*, 9855; M.-G. La-Placa, A. M. Igual-Munõz, J. Romero, R. E. Daniels, V. N. Kozhevnikov, M. Sessolo, H. J. Bolink, *ECS Solid State Sci. Tech*., **2019**, *8*, R84.
25. [a] S. Lamansky, P. Djurovich, D. Murphy, F. Abdel-Razzaq, H.-E. Lee, C. Adachi, P. E. Burrows, S. R. Forrest, M. E. Thompson, *J. Am. Chem. Soc.* **2001**, *123*, 4304; [b] S. Lamansky, P. Djurovich, D. Murphy, F. Abdel-Razzaq, R. Kwong, I. Tsyba, M. Bortz, B. Mui, R. Bau, M. E. Thompson, *Inorg. Chem.* **2001**, *40*, 1704.

26. A.B. Tamayo, B. D. Alleyne, P. I. Djurovich, S. Lamansky, I. Tsyba, N. N. Ho, R.Bau, M. E. Thompson, *J.Am.Chem.Soc*., **2003**, *125*, 7796.
27. M. J. Jurow, A. Bossi, P. I. Djurovich, M. E. Thompson, *Chem. Mater.* **2014**, *26*, 22, 6578.
28. F.P. Dwyer, D.P. Mellor, *Chelating agents and metal chelates. Elsevier,* **2012***.*
29. L-Y. Hsu, Q. Liang, Z. Wang, H-H. Kuo, W-S. Tai, S-J. Su, X. Zhou, Y. Yuan, Y. Chi, *Chem. Eur. J.* **2019**, *25*, 15375.
30. J. Lin, N-Y. Chau, J-L. Liao, W-Y. Wong, C-Yu Lu, Z-T Sie, C-H. Chang, Mark A. Fox, Paul J. Low, G-H. Lee, Y. Chi, *Organometallics.* **2016**, *35*, 1813.
31. Z-L. Zhu, W-C- Chen, S-F. Ni, J. Yan, S. F. Wang, L-W. Fu, H-Y. Tsai, Y. Chi, C-S. Lee *J. Mater. Chem. C*, **2021**, *9*, 1318.
32. Z.-L. Zhu, L.-Y. Hsu, W.-S. Tai, S.-F. Ni, C.-S. Lee, Y. Chi, *Mater. Today Energy* **2021**, *20*, 100636.
33. [a] V. C. Vargas, R. J. Rubio, T. K. Hollis, M.E. Salcido, *Org. Lett.* **2003**, *5*, 4847; [b] V. Charra, P. De Fremont, P-A. R. Breuil, H. Olivier-Bourbigou, P. Braunstein, *J. Organometallics. Chem.,* **2015**, *795*, 25.
34. J. Sanning, L. Stegemann, P. R. Ewen, C. Schwermann, C. G. Daniliuc, D. Zhang, N. Lin, L. Duan, D. Wegner, N. L. Doltsinis, C. A. Strassert, *J. Mater. Chem. C*, **2016**,*4*, 2560.
35. A. R. Chianese, A. Mo, N. L. Lampland, R. L. Swartz, P. T. Bremer, *Organometallics*, **2010**, *29*, 13.
36. C.-Y. Kuei, W.-L. Tsai, B. Tong, M. Jiao, W.-K Lee, Y. Chi, C.-C. Wu, S.-H. Liu, G.-H. Lee, P.-T. Chou, *Adv. Mater.* **2016**, *28*, 2795.
37. J. Lin, N-Y. Chau, J-L. Liao, W-Y. Wong, C-Yu Lu, Z-T Sie, C-H. Chang, Mark A. Fox, Paul J. Low, G-H. Lee, Y. Chi, *Organometallics.* **2016**, *35*, 1813.

1.Introduction

ABSTRACT

Herein, some basics concepts in photophysics along with the corresponding features peculiar of the transition metal complexes are recalled that will allow the reader to better follow the discussion in the forthcoming chapters. A particular interest is devoted to Ir(III), with a brief comparison with other common metals, and Re(I) complexes. A short overview about N-heterocyclic carbenes (NHC)s, their synthetic pathways, the structural variety, and their application in coordination chemistry is also given. Finally, general insights about the use of photoactive metal complexes in photocatalysis, bioimaging and light-emitting devices, such as organic-light emitting devices (OLEDs) and light-emitting electrochemical cells (LECs) are presented.

1.1 Light–matter interaction

The study of light-matter interaction began as early as the seventeenth century, when two theories were proposed about the nature of light, the corpuscular and the undulatory. Although Maxwell proposed in 1860 that light was only an electromagnetic wave, we had to wait until the early years of the twentieth century to define light as a "quantum of energy", called *photon* in 1926 by Lewis. Light and matter interact with each other based on the energy of the photons involved.[1]

Emission of a photon arising from an electronic excited state can be classified depending on the way how this latter has been generated. The excitation can be chemically, optically or electrically induced, giving rise to chemiluminescence, photoluminescence and electroluminescence, respectively. The excited states formed by different means may or may not have similar emission properties.[2]

If the excited state of the molecule has been optically generated, the absorbed photon must have an energy (*hv*) equal to the energy gap between the ground and the excited states involved in the electronic process. Once this excited state is generated, it can undergo several deactivation pathways, being either radiative or radiationless. Depending on which pathway is favored different processes may occur, and the fate of the excited state is strictly related to the chemical design of the compound. A simplified scheme depicting all possible photophysical processes that can take place upon formation of an electronic excited state is represented by the Perrin-Jablonski diagram,[3] as depicted in *Figure 1.1.*

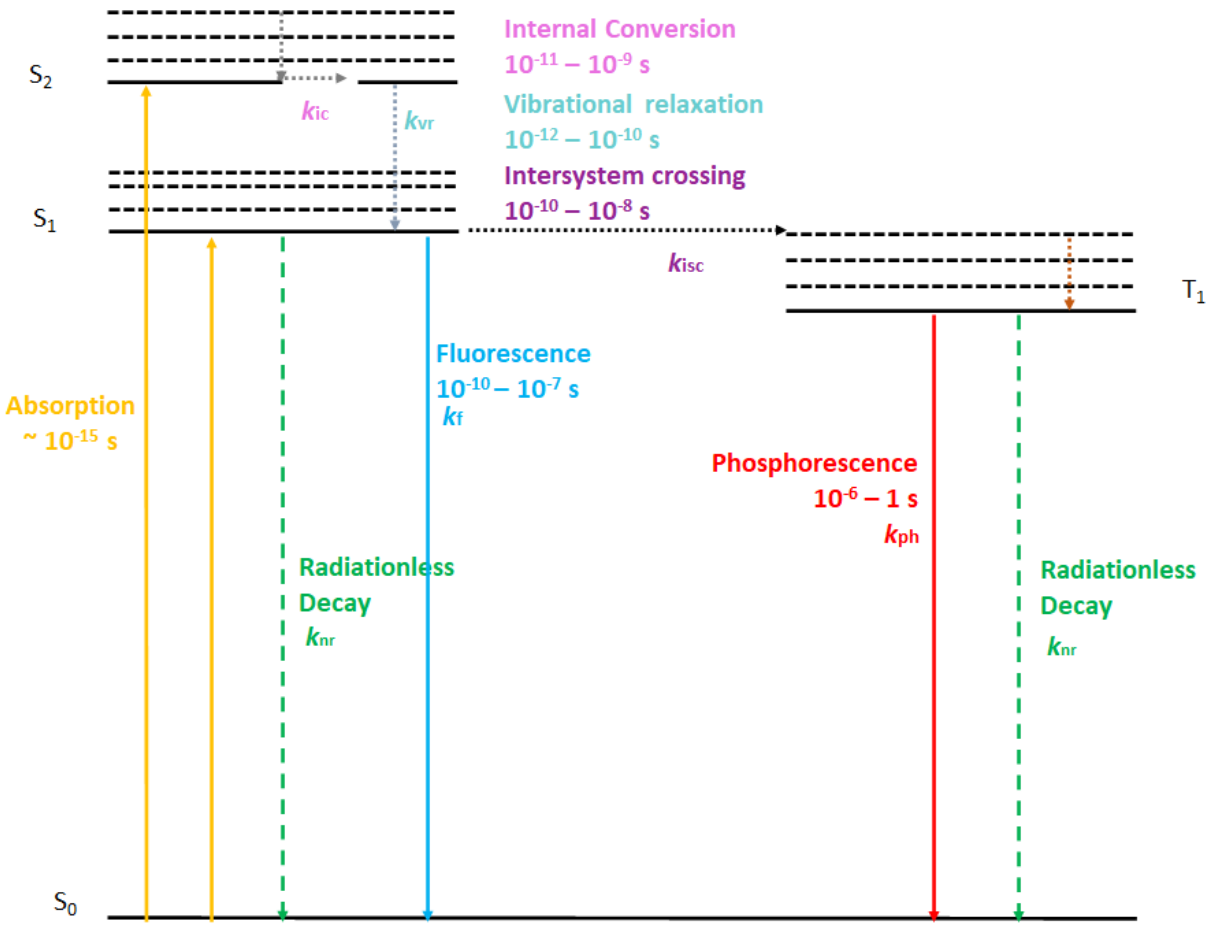

Figure 1.1 Simplified Perrin-Jablonski diagram showing the different radiative and non-radiative processes along with their corresponding rate constants and typical time scale.

It is also important to notice that absorption and emission processes are vertical transitions (Franck-Condon principle) and occur from the electronic ground and an excited state – typically the lowest lying one –, respectively. During such processes, nuclear positions remains unchanged due to the fact that the photon absorption is a much faster process (~10^{-15} s)[4] than nuclear motion (Born-Oppenheimer approximation). Therefore, the electronic transitions are represented with vertical lines in the Perrin-Jablonski diagram. It is also worth to recall that optical electronic excitation processes occur between states with the same multiplicity of spin (spin selection rule); whereas, processes involving a change of the spin multiplicity are formally spin forbidden, within a zeroth-order approximation.

As the molecule is in an excited electronic state is not in equilibrium with its environment, it will spontaneously relax back to the ground state either radiatively or non-radiatively. Radiative decay to lower lying excited state (typical the ground state) is referred

to as *luminescence*. If the radiative process occurs between two different states with same spin-multiplicity, the process is called *fluorescence* (typically, $S_1 \rightarrow S_0$). On the other hand, if the emission process takes place between states having different spin-multiplicity, it will be denoted as *phosphorescence* (typically, $T_1 \rightarrow S_0$). The spin-multiplicity depends on the spin of the unpair electrons in the state. If the electrons have anti-parallel orientation, the resulting state is called *singlet* (S_0, S_1, S_2…) and if they are parallel, they are in a triplet state (T_1,T_2,T_3..). The triplet state lies typically at lower energy than the corresponding singlet state. Moreover, transitions between two states with different multiplicity are forbidden by the *spin-selection rule*.[5]

The probability of radiative deexcitation from an excited state depends on several intramolecular and intermolecular (or environmental) parameters and the efficiency of such process over nonradiative ones is expressed by the *photoluminescence quantum yield (PLQY).* The PLQY is defined as the number of emitted photons relative to the number of absorbed photons, and it can be referred to the kinetics of all possible radiative and non-radiative processes, such as *internal conversion*, *intersystem crossing*, *vibrational relaxation* and, of course, the *radiative pathways*. Briefly, the emission quantum yield describes the probability of having radiative relaxation from the excited state to the ground state according to its radiative and non-radiative decay rates, following the equation (1.1):

$$\Phi = \frac{k_r}{k_r + k_{nr}} \qquad Eqn.\ 1.1$$

with k_r and k_{nr} is the rate constant for radiative and overall non-radiative processes, respectively.

The following excited state lifetime describes the time required by the excited state of the molecule to decay to *1/e* of its initial value. So, the lifetime is the reverse of the sum of all the rate constants (Equation 1.2.)

$$\tau = \frac{1}{k_r + k_{nr}} \qquad Eqn.\ 1.2$$

Among different factors that can influence k_{nr}, the vibronic coupling between the lowest-lying excited state (ES) and the ground state (GS), called *energy gap law*, (EGL) must be consider. As shown in equation 1.3, k_{nr} increases with the decrease of the energy gap between ES and GS, and this effect becomes predominant moving to the red region of the spectrum.[6]

$$\ln(k_{nr}) \propto -\Delta E_{ES-GS} \qquad Eqn.\,1.3$$

It worth to notice that improving the quantum yield requires maximization of k_r as well as minimization of k_{nr}. It derives that the quantum yield and the lifetime are correlated according to the following equation (1.4):

$$\phi = \tau \cdot k_r \qquad Eqn.\,1.4$$

1.2 Photophysics of Transition Metal Complexes (TMCs): a general overview

The photochemistry and photophysics of transition metal complexes is a fascinating field that has attracted remarkable attention by scientists across different chemical disciplines from both fundamental and application points of view.[7]

In the last few decades, an impressive number of photoactive transition metal-based compounds have been investigated: a pursuit that has been also driven by their potential and real marked application in light-emitting devices,[8] biomedicine,[9] and photocatalysis,[10] just to cite a few.

In the frame of *crystal field theory* (CFT), the ligands surrounding the metal ion are considered as negative point charges that generate an electrostatic field interacting with the d orbitals of transition metal ion. The interaction between the d orbitals and ligands would provide a fivefold d-orbital degeneracy if the ligand field would be spherically symmetric. Since the *ligand field* is never symmetric and d electronic orbitals are directional, ligand field interactions yield a d-orbitals split following a specific symmetry according to that of the coordination environment.[11]

As far as d^6 electronic configuration is concerned, having ligands in an octahedral geometry around the ion, the five d orbitals split in two sets: the t_{2g} (d_{xy}, d_{xz}, and d_{yz} orbitals) and the e_g (d_{z^2} and $d_{x^2-y^2}$). Considering that the ligands lie at each corner of the octahedron, the orbitals that point directly toward the ligands lie at higher energy (e_g) than those which

point between two ligands (t_{2g}). This splitting is quantified by Δ_o or 10 *Dq* and it is the difference in energy between the two d-orbitals sets. The magnitude of Δ_o changes accordingly to the central ion and ligands involved. Moving from first to third row of transition metals withing the same group, the splitting between t_{2g} and e_g increases.

Several experiments have proved that the metal-ligand interaction can not be treated as a purely electrostatic in nature, instead a certain degree of covalency has to be taken into account for a more suitable description. The *ligand field theory* (LFT) preserves the conceptual advantages of the simple CFT, considering, however, an appreciable degree of covalent bond between the metal and the ligands.[12] This takes into account a possible metal-ligand orbital overlap. The relative energy of the molecular orbitals (Mos) as well as the Δ_o varies largely depending on the position on the periodic table of the metal atom, its degree of oxidation, and the strength of the coordinated ligands. This latter follows the so-called spectrochemical serie.[13] Moreover, according to LFT, inter-electronic repulsion and spin–orbit coupling parameters are noticeably reduced in the transition metal-ligand complex, explaining better the photophysics of these latter.

The complexity of electronic structure of coordination compounds has been discussed in the frame of Mos theory. First of all, the metal orbitals have a specific symmetry, such as e_g and t_{2g} for d-orbitals and a_{1g} and t_{1u} for the s and p orbitals, which interacts with σ and π bonding/anti-bonding ligand orbitals having suitable symmetry.[14] The outcome of Mos diagram of the complex can be, in first approximation, described as a linear combination of metal and ligand orbitals, leading to a d^6 closed-shell metal-ligand complex as, for example, Ru(II), Fe(II), Re(I) and Ir(III).[15] In agreement with a criterion called *localized molecular orbital approximation* (LMOA), the electronic transitions of coordination compounds can be described according to the main localization on the molecule of the Mos involved.

Although the electronic structure of transition metal complexes has to be better treated as a whole entity, also given the high covalency degree of the metal‑ligand (M‑L) interactions in these species, it is convenient to localize electrons into sets mainly onto either the metal ion or the ligands. Therefore, the electronic transitions that occur can be classified following such localized MO approximation as *metal-center* (MC), *intra-ligand* (IL), also called *ligand center* (LC), and *charge-transfer* (CT). Among these latter, there are *metal-to-*

ligand charge transfer (MLCT), *ligand-to-metal* charge transfer (LMCT), *ligand-to-ligand charge transfer* (LLCT) and *intra-ligand charge transfer* (ILCT).[16]

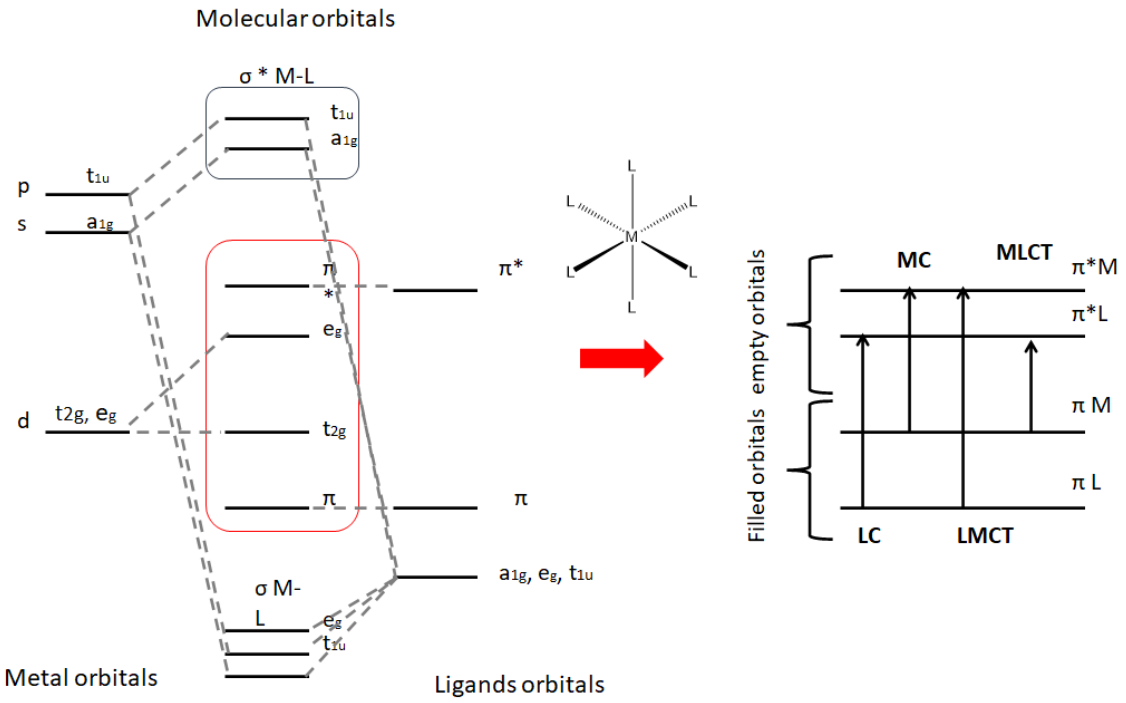

Figure 1.2 Schematic Mos diagram for an idealized octahedral complex $[ML_6]^{n+}$ and the main corresponding electronic absorption transitions.

***Metal-center* (MC)** transition occur within the d-metal orbitals, namely between the filled t_{2g} and empty virtual e_g^* orbitals for a metal complex with d^6 electronic configuration and an idealized octahedral geometry. The reorganization of the electron density does not yield to a charge redistribution between metal and ligand. In complexes with an inversion center, d-d transitions are forbidden due to *Laporte's rule*. Nevertheless, they become partially allowed in complexes of lower symmetry, as for a tetrahedral (T_d) or octahedral (O_h), than square planar geometry. When the metal is in high oxidation state and the ligands relatively weak, the lowest excited state of the complex is MC type. These states are usually not emissive due to the high frequency vibrations from the coordination sphere and it is rare to observe luminescence at room temperature. Instead, it is possible to observe a broad and structureless spectrum at 77 K with a very low quantum yield, as for instance what observed for $[RhCl_2(phen)_2]^+$ (phen = 1,10-phenanthroline). In order to obtain strong metal-ligand

bonds, it is necessary a good overlap between their orbitals in a large space to avoid the electronic repulsion between core electrons of the metal and the shell electrons of the ligand. For the first row of the transition-metals, this overlap is small due to the more contracted d orbitals, resulting in a weak metal-ligand bonds. In conclusion, MC states lie at the lowest energy with a large distortion respect to the ground state, becoming non emissive states.[17]

Ligand-centered **(LC)** transitions involve the ligands orbitals, occurring from π-bonding to π* anti-bonding orbitals ($\pi_L \rightarrow \pi_L^*$). As for MC transitions, LC states does not cause large electron density redistribution in the complex. However, they may modify the coordination properties of the ligands, thus influencing the strength of the metal-ligand bond. The ligand becomes sensitive toward its dissociation from the metal, leading to an instability of the complex. [18]

Ultimately, the *charge-transfer* (CT) transitions occur among different moieties of the molecule and they are the most present in transition-metal complexes. In this case, the transitions can take place from the metal to ligands orbitals (MLCT) or *vice-versa* (LMCT), between two different ligands of the complex (LLCT) or within the same ligand (ILCT). This time, the charge redistribution between diverse moieties of the molecule occurs to a larger extent, modifying the reactivity of the complex towards redox and substitution reactions and the environmental conditions (*e.g.*, solvent, coordination sphere, molecular geometry).[19]

Intra-ligand-charge transfer *(ILCT)* is a transition that takes place within the same ligand of the complex. In order that the charge transfer occurs, the ligand must include a "push-pull" system which allowed the charge reorganization just on the ligand and not between the ligand and a second moiety of the complex.

Ligand-to-ligand charge transfer *(LLCT)* takes place between two different coordinated ligand with largely different electronic properties, namely an easily oxidized an easily reduced ligand.

Ligand-to-metal charge transfer *(LMCT)* is from π-bonding ligand to σ*-anti-bonding metal orbital ($\pi_L \rightarrow \sigma_{M\text{-}L}^*$). The electron density redistribution occurs from a ligand to the metal, and it be formally described as a metal-centered reduction and ligand-centered oxidation. LMCT typically occurs in metal complexes characterized by electron rich ligands

and metal with a high oxidation state. The wavenumber of LMCT bands decreases as the increasing the oxidation number of the metal and the reduction of the ligands. In a homoleptic complex bearing all equal ligands, the charge distribution doesn't change among them, but in a heteroleptic complex having different ligands, the electron transfer occurs on the most reductive ligand. As an example, zirconium (IV), which possess a d^0 electronic configuration show LMCT state at the lowest energy position for the absence of MC states.[20]

Metal-to-ligand charge transfer *(MLCT)* occurs from an occupied (either bonding or non-bonding) d orbitals to a π*-anti-bonding ligand orbital ($d_M \rightarrow \pi_L^*$). An MLCT transition can be formally described as a one-electron metal oxidation and a ligand reduction. Obviously, these states are correlated to the redox potential of the complex, where the easier oxidation should indicate the lowest energy of the MLCT state.[19,20]

The nature of the metal atom and its oxidation state has profound impact onto the photophysical properties of the metal complex. In d^6 electronic configuration, the value of Δ_O increases with increasing oxidation state of the central metal ion and also increases down a group (Co< Rh< Ir). The variation with oxidation state reflects the smaller size of more highly charged ions and the consequently shorter metal-ligand distances and stronger interaction energies. The increase down a group reflects the larger size of the 4d and 5d orbitals compared with the compact 3d orbitals and the consequent stronger interactions with the ligands. If all parameters herein described cause a large d-d splitting, the resulting quenching MC states will be higher in energy, far away from the low-lying emissive states.[21] Indeed, while $[Fe(II)(bpy)_3]^{2+}$ (bpy = 2,2'-bipyridine) is virtually not emissive at room temperature due to the presence of low-lying ^{3,5}MC state that efficiently and rapidly (ultrafast process) quench the corresponding ^{1,3}MLCT state; the Ru(II) analogue, namely $[Ru(bpy)_3]^{2+}$ displays a moderate orange-red photoluminescence.[16b]

In a zeroth-order description, the ground state of a molecule is a pure singlet while the higher-lying excited states can possess either singlet or triplet multiplicity. However, the effect of the heavy atom leads a perturbation of this descriptions meaning that an electronic state can possess a mix of singlet and triplet character. The presence of the heavy atom induces a mix of electronic states and provokes a change of molecular orbital type with conservation of total angular momentum *J* (*El Sayed's rule*), that in turns allows *intersystem*

crossing (ISC) between two states with different multiplicity.[22] Hence, compounds comprising a heavy transition-metal have fast and efficient intersystem crossing processes between excited singlet and triplet states, and decays from triplet-excited states become competitive over other radiative and non-radiative processes.[23] The $\widehat{H}_{SOC}$ operator that influences the magnitude of SOC perturbation is related to the extent of the singlet and triplet mixing by the SOC constant, ξ, the electron's spin angular (S) and orbital angular (L) momenta, as described by: [24]

$$\widehat{H}_{SOC} = \xi SL \qquad Eqn.\,1.5$$

This constant scales with the fourth power of the nuclear charge *Z* and thus changes a largely along the periodic table. An example is given by ξ_{Fe} = 431, ξ_{Ru} = 1042, ξ_{Os} = 3381 and ξ_{Ir} = 3909 cm^{-1}.

The abovementioned description of the nature of the electronic transitions as LC, MC, MCLT, LMCT, LLCT and ILCT can be also applied for emission processes involving transition metal complexes, and typically states with admixed triplet MLCT and LC character are of interest for the most efficient photoluminescent complexes.

However, it should be pointed out that the energy level of the quenching states plays an important role in the photoluminescence efficiency. In fact, MC and/or LC states must be far away in energy to the potentially emissive T_1 state. Importantly, the coordination environment of the metal center can control the energetic positioning of both quenching ^{3}MC and emissive ^{3}LC/^{1}MLCT.

Two limiting cases can be drawn in the frame of a de-excitation model that was found to be valid for d^6 metal complexes such as Ru(II) and Ir(III). The first case represents the strong electronic coupling between the ^{3}MC and the S_0 where $k_2 >> k_1$ and the second case is given by the thermal equilibration between the T_1 and ^{3}MC states that is kinetically competitive with the deactivation pathway from ^{3}MC, $k_1 >> k_2$.

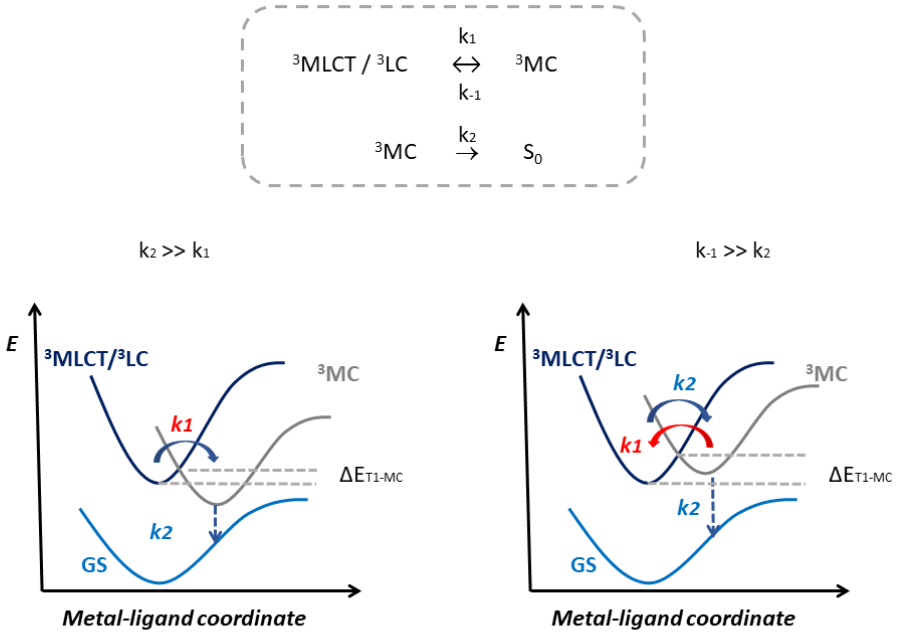

Figure 1.3 Kinetic model for the deactivation of the T_1 state with ^{3}MLCT/^{3}LC character via MC states.

1.3 Photophysics of Ir(III) complexes

The nature of the lowest excited state in Ir(III) complexes can span from mainly ^{3}LC to ^{3}MLCT with often intermediate level of mixing ^{3}MLCT/^{3}LC. Hence, it can be generally described as ^{3}LC with some degree of admixing with the higher-lying ^{1}MLCT manifold through SOC. The luminescence of this complexes depends on the triplet excited state, better described as a mixture of both ^{1}MLCT and ^{3}LC wavefunctions.[25] In agreement with this statement, the T_1 state can be written as follows equation 1.6:

$$\Psi_{T1} = \alpha \left[{}^3LC \right\rangle + \beta \left[{}^1MLCT \right\rangle \qquad Eqn.\ 1.6$$

Where α and $\beta = \sqrt{1 - a^2}$ are normalized coefficients referred to the contributions to the wavefunction of the mixing ^{3}LC and ^{1}MLCT excited state, respectively. The mixing coefficient, α can be expressed as by the following equation (1.7):

$$\alpha = \frac{\left\langle {}^3LC\middle|\hat{H}_{SOC}\middle|{}^1MLCT\right\rangle}{\Delta E_{S1-T1}} \qquad Eqn.\ 1.7$$

Where $\left\langle {}^3LC\middle|\hat{H}_{SOC}\middle|{}^1MLCT\right\rangle$ is the SOC matrix element and ΔE_{S1-T1} is the energy gap between the two mixing states.

The extent of the ^{3}LC/^{1}MLCT influences the resulting emission properties. For efficient Ir(III) emitters, typical values for k_r and lifetime are in the order of a few 10^5 s^{-1} and 0.5-5 μs, respectively.

A large variety of iridium(III) complexes with good optical and redox properties belongs to the family *fac*-Ir(C^N)$_3$, where C^N can be either 2-(2,4-difluorophenyl)pyridine or the 2-phenylpyridine as archetypal ligand. In this compound, HOMO is localized between metal and phenyl ring and LUMO is basically on the pyridine moiety. Introducing electron-donating or electron-withdrawing groups on the phenyl ring or increasing the conjugation on the pyridine moiety can modify the HOMO-LUMO gap.[26] Hence, great modulation of the excited state properties in terms of emission wavelength, excited-state lifetime and PLQY was achieved in this class of compounds, that typically display excellent emission properties in the green-to-orange region of the electromagnetic spectrum. As the first studied example, Ir(ppy)$_3$ (ppy=2-phenylpyridine) showed fast ISC from the excited singlet to the emitting triplet MLCT and high PLQY of about 40% at room temperature. The emission color at 514 nm matches well to the Commission Internationale d'Eclairage (CIE) coordinates for green color.[27]

However, such C^N scaffolds have demonstrated being much suitable for achieving comparable optical properties in the blue to to deep-blue region of the emission spectrum due to the population of the close-lying quenching ^{3}MC state as well as the increase of the ^{3}LC nature of the emissive T_1. A valuable alternative is represented by the use of strong σ-donor N-heterocyclic carbene (NHC) ligands in order to rise the energy of the ^{3}MC states to a larger extent compared to emitting ^{3}MLCT/^{3}LC state.

The first report on iridium(III)-NHC complex was reported by Lappert in 1980 who synthesized a new type of scaffold using NHC carbene ligands, to make Ir(C^C)$_3$ where C^C

is N,N-diarylcarbene ligand.[28] The compound were further investigated by Thompson and co-workers in 2005, along with iridium tris(1-phenyl-3-methylimidazolin-2-ylidene-C,$C^{2'}$), abbreviated as $Ir(pmi)_3$, and iridium tris(1-phenyl-3-methylbenzimidazolin-2-ylidene-C,$C^{2'}$), abbreviated as $Ir(pmb)_3$. They found a lifetime and a PLQY at room temperature equal to 0.2-0.6 μs, and 0.02-0.04. [26c] From there on, different groups[29] demonstrated the importance to employ NHC-based ligands to improve the photophysical and photostability properties of the Ir(III) complexes, in particular in the higher energy side of the visible spectrum.[30]

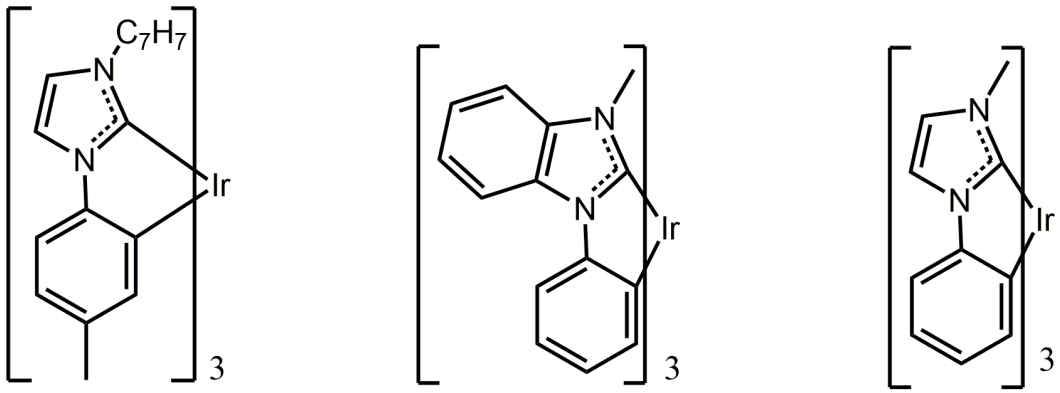

Ir-Lappert $Ir(pmb)_3$ $Ir(pmi)_3$

Figure 1.4 Examples of Ir(C^C) bearing NHC-carbenes as ligands.

1.4 Photophysics of Re(I) tris-carbonyl complexes

Organometallic rhenium complexes have played an important role in contributing to an understanding of the photophysical and light-induced electron-transfer (ET) and electronic energy-transfer (ENT) processes.[31]

In the 1970s, tricarbonyl rhenium(I) complexes of general formula *fac*-$[Re(N^N)(CO)_3X]^{n+}$, where N^N is a chelating diimine chromophoric ligand as the archetypical 2,2′-bipyridine or 1,10-phenanthroline, and X is either a neutral (n = 1) or an anionic monodentate ancillary ligand (n = 0), were studied for the first time by Wrighton and coworkers.[32] These compounds revealed interesting features such as strong absorption, intense emission, long lifetime and catalytic activities from where several possible applications as photocatalysts, especially for CO_2 reduction; building blocks of emissive multinuclear complexes, and as target molecules for time-resolved IR measurements have been possible.[33]

The lower oxidation state of Re(I) ion compared to Ir(III) and Os(II) results into a smaller Δ_o. As a consequence, quenching MC states lies lower in energy and closer to the emissive T_1 state. The use of a strong ligand field moiety with both σ-donor and strong π-accepting properties, such as C≡O, allow increase of the Δo to such an extent that re(I) tricarbonyl complexes often display emission properties.[31,34]

The interaction of the π-π* ancillary ligand orbitals play an important role in the excited states behavior, tuning the HOMO-LUMO gap. Most of Re(I) diimine complexes are emissive from ^{3}MLCT states in solution at room temperature with a moderate quantum yield (PLQY < 5%) and a long lifetime (~ several hundred nanoseconds to microseconds), easily quenched by bimolecular electron- and/or energy transfer processes in solution. [32,35]

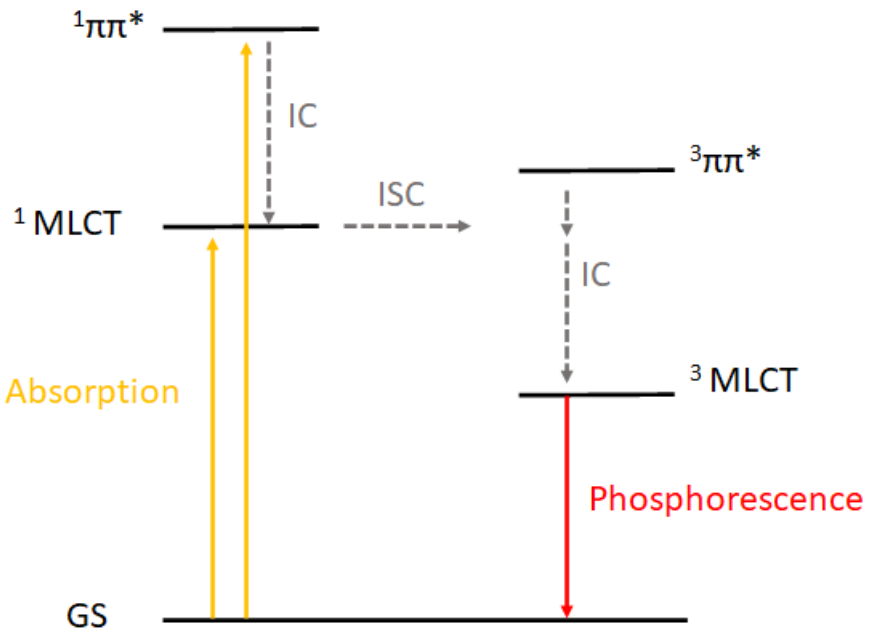

Figure 1.5. Energy diagram of electronic states of rhenium(I) diimine complexes.

The lowest lying excited state of rhenium(I) diimine complexes is tipically the triplet MLCT state due to the fact that the ligand π* orbital energy is lower than the empty d orbital. In conclusion, the allowed transitions do not involve any antibonding orbital regard to the M-L bonds, making Re(I) complexes highly photostable, in contrast to the forbidden transitions to the LF excited states. [33]

Upon irradiation, the ^{1}MLCT and ^{1}LC bands are often populated simultaneously. After the ISC from these bands to the ^{3}MLCT and ^{3}LC states, these latter can be varied in energy relative to each other. The consequence is that rhenium(I) complexes can show emission spectra either with strong vibronic character if the ^{3}LC is lower in energy than ^{3}MLCT (in a range of 500 nm) or with a structureless profile if the ^{3}MLCT is the lowest lying emitting state (near 600 nm).

However, a combination of ^{3}LC and ^{3}MLCT states is often employed to account for the emission behavior. [36] The variation of charge density on the metal, given by ancillary ligands, can manipulate the energetic separation between the two emissive states.

The first example of intraligand emission was reported by Wrighton in 1978 for *fac*-$XRe(CO)_3$(3-benzoylpyridine)$_2$ (X = Cl, Br, I) , revealing a dual emission at 77 K. A deep study showed that two n-π* intraligand triplet excited and Re→3-benzoylpyridine charge transfer states were in equilibrium. [35e]

A second example was reported by cationic *fac*- $[Re(CO)_3L(S)]$ where L is L = 2,2'-biquinoline, 1,10-phenanthroline and S is the solvent as CH_3CN, PhCN, pyridine or piperidine. For L = 1,10-phenanthroline complexes, variation in the ligand S controls the energy of the ReLCT state; for the higher energy ReLCT the relative importance of the ^{3}(π-π*) emission becomes greater. The internal conversion between the two states is apparently slow, making the two emissive simultaneously.[37] In conclusion, a dual emission from Re(I) diamine complexes is also possible as well as the emission from the intraligand triplet excited state, as we will discuss in the *chapter 2*.

1.5 Carbene ligand: general properties and synthetic pathways

Carbenes are extremely reactive species containing a bivalent carbon atom with a six-electron valence shell, therefore these molecules are typically not stable in the free state. A generic carbene has two spin isomers, singlet (↑↓) and triplet (↑↑), leading to different reactivity and structure.[38] Depending on the spin of the electrons in the ground state, they can be classified into two main classes, namely Fischer-[39] and Schrock-type of carbenes.[40]

In the triplet electronic configuration state of Schrock carbenes, two unpaired electrons are in sp^2 and p orbitals, respectively. Instead, in the singlet configuration of Fischer carbenes, two paired electrons are in sp^2 orbital while p orbital is empty.[38] A σ-donor character by the lone pair in sp^2 makes a strong and stable metal-ligand bond with a π-acceptor character given by the empty p-orbital in Fischer carbene. Among Fischer carbene types, there are N-Heterocyclic Carbenes (NHC), that play an important role in coordination chemistry.[41]

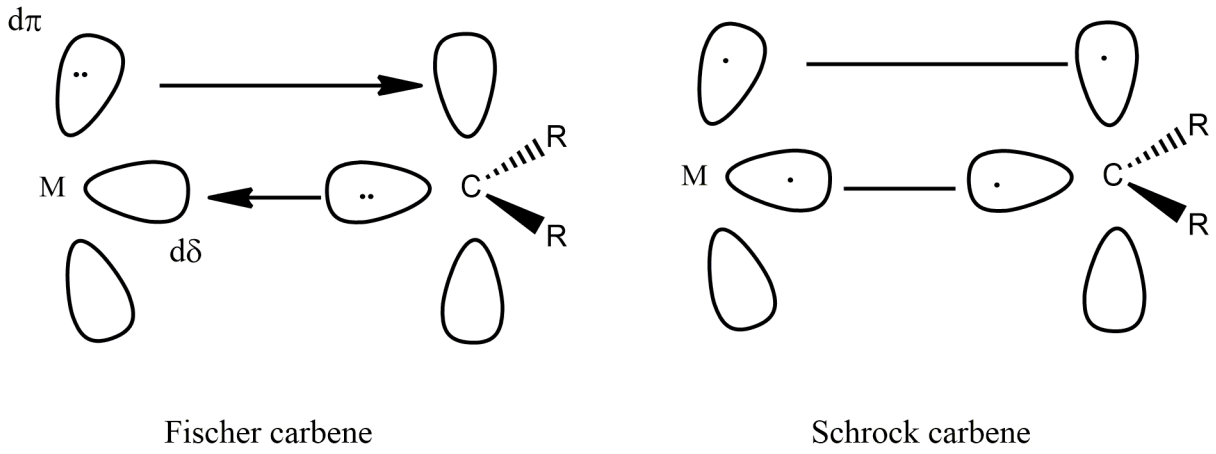

Figure 1.6 Schematic bonding representation of Fischer- and Schrock-type of carbenes.

NHC carbenes are heterocyclic species containing a carbonic carbon stabilized by at least one nitrogen atom in the ring structure.[38] The stabilization occurs inductively, lowering the energy of the σ orbital, and mesomerically, giving electron density to the empty p-orbital of the carbenic carbon.[42]

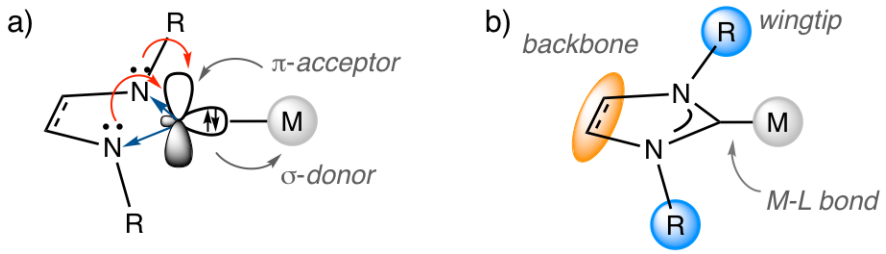

Figure 1.7 a) Schematic representation of the electronic properties of NHCs. An imidazole-2-ylidene is depicted as an example, and the σ-withdrawing and π-donating character of the

nitrogen atom adjacent to the C^2 atom favor the stabilization of the carbene structure via inductive (blue arrows) and mesomeric (red arrows) effects, respectively; b) structural and electronic variation of the NHC ligands at the backbone (substituent effect and aromaticity), wingtip (electronic and steric effect) that influence the M–L interaction via σ -donation and π -bonding.

In the early 1960s, Wanzlick was the first who proposed the NHC concept predicting the stabilization of the carbene by amino substituents.[43] Nevertheless, he did not manage to isolate it,[44] and few years later, he reported an imidazol-2-ylidene by the deprotonation of an imidazolium salt using a strong base. However, the carbene was trapped but not isolated.[45] In 1968, Wanzlick and Ofele synthesized the first metal-carbene complexes based on chromium and mercury.[46]

From 1975, Lappert extended the literature about the coordination chemistry of bivalent group (IV) donors and in 1982,[47] he published the first article about iridium(III) complexes bearing a N,N'-diarylcarbene.[28]

In 1991, Arduengo was the first who managed to characterize a free carbene based on 1,3-imidazolyl structure, bearing adamantly groups on the nitrogen atoms. The deprotonation of 1,3-di-1-adamantylimidazolium chloride took place in THF at room temperature with catalytic dimsyl anion $(CH_2S(O)CH_3)^-$ in the presence of sodium hydride to give the final carbene, which was stable just in absence of oxygen and moisture.[48] The first consideration was that the steric hindrance and aromaticity in the scaffold were fundamental to the isolation of the compound, but it was partially true. In fact, one year later, Arduengo isolated a carbene having only methyl substituents on the heterocycle, avoiding bulky groups, using sodium hydride and potassium *tert*-butoxide in THF. On this way, new synthetic routes to obtain alkyl substituted NHC carbene were developed. Soon, these types of carbenes were recognized as excellent donors for metal in high oxidation state, becoming a milestone of the coordination chemistry.

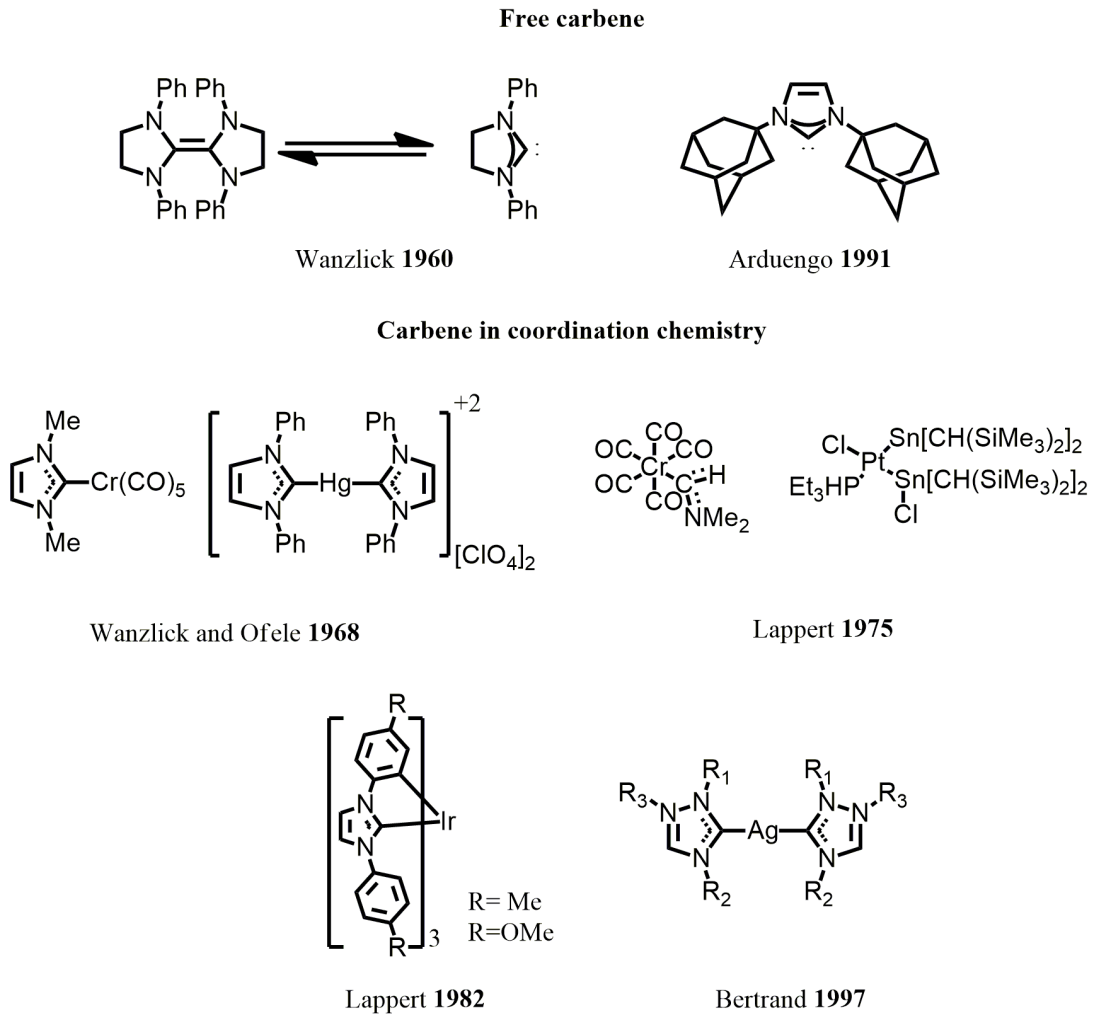

Figure 1.8 Representation of some pioneering works about carbenes from their isolation to coordination chemistry applications.

From there on, silver(I)-NHC carbene received great attention as transfer agents from silver to a second metal, useful for the synthesis of new metal-carbene complexes. The two main synthetic pathways to obtain Ag(I)-NHC complex can be summarize in the synthesis based on silver base, as silver acetate reported by Bertrand for the synthesis of bis(carbene)-silver(I) polymer with 1,2,4-triazole-3,5-diylidene as ligand[49] or Ag_2O reported by Lin[50], and the synthesis based on free carbene in presence of a silver source.

Regarding the first synthetic pathway, Ag_2O is the most used for its stability and accessibility. The reactions can carry out under air atmosphere at room temperature, any solvent pretreatment is necessary, and the chirality is preserved. The efficiency of this route is related to the acidity of the proton-carbene at C^2. This property is influenced by substituent

groups in $^{4/5}$C position, and, if the carbene is an imidazolium salt, by the correlated anions (the acidity is higher for halides than non-coordinating anions like BF_4 or PF_6).[51] Some of the first examples that describe the importance of silver(I)-NHC complexes as transfer agents have been seen by Crabtree, who reported the preparation of $[Ir(COD)(NHC)(NHC)']^+$ type complexes via two sequential transfers using Ag_2O,[52] and Herrmann,[53] who synthesized two chiral Rh(I)-NHC complexes showing the retention of chirality. Nowadays, it is the most common method to prepare transition-metal complexes bearing carbene ligands.

Regarding the second synthetic pathway, the first example was reported in 1993 by Arduengo. He made the reaction between a free carbene and AgOTf in THF at room temperature.[54] However, the free carbenes reactants are air–, moisture–, and temperature–sensitive, disadvantaging this method due to the tedious precautions required to synthesize free carbenes. In addition, when an imidazolium salt is deprotonated by a strong base, the carbene could undergo decomposition.

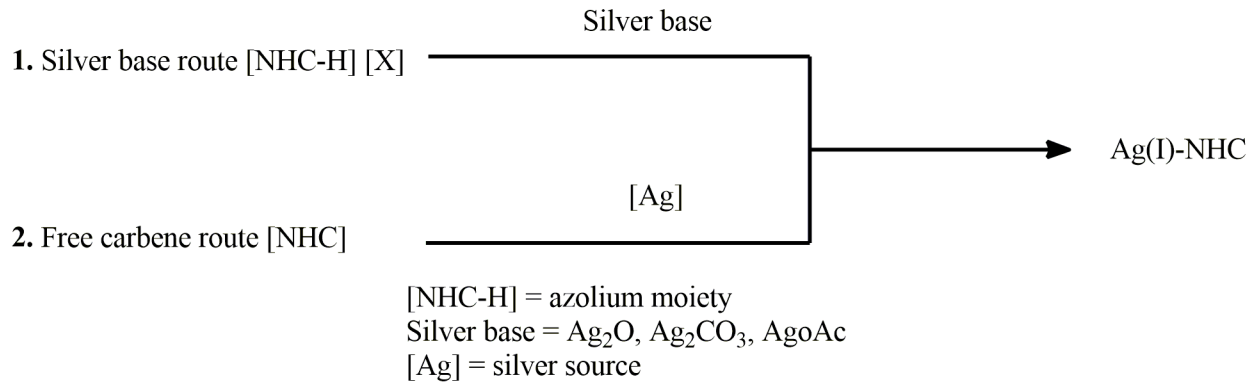

Scheme 1.1 Summary of the most common synthetic pathway for metal-carbene complexes[51]

According to this view, carbenes reported so far can be classified as *monodentate*. The popularity of NHCs is the result of their unique features, summarized in versatile synthetic procedures, ease of the metalation step, high stability of the resulting complexes and high structural modularity owing to the modulation of its electronic and steric properties. These properties can be finely tuned by modification on the number of heteroatoms in the

ring, backbone and wingtip positions with either saturated or unsaturated groups as well as electron-donating or electron-withdrawing substituents.[55]

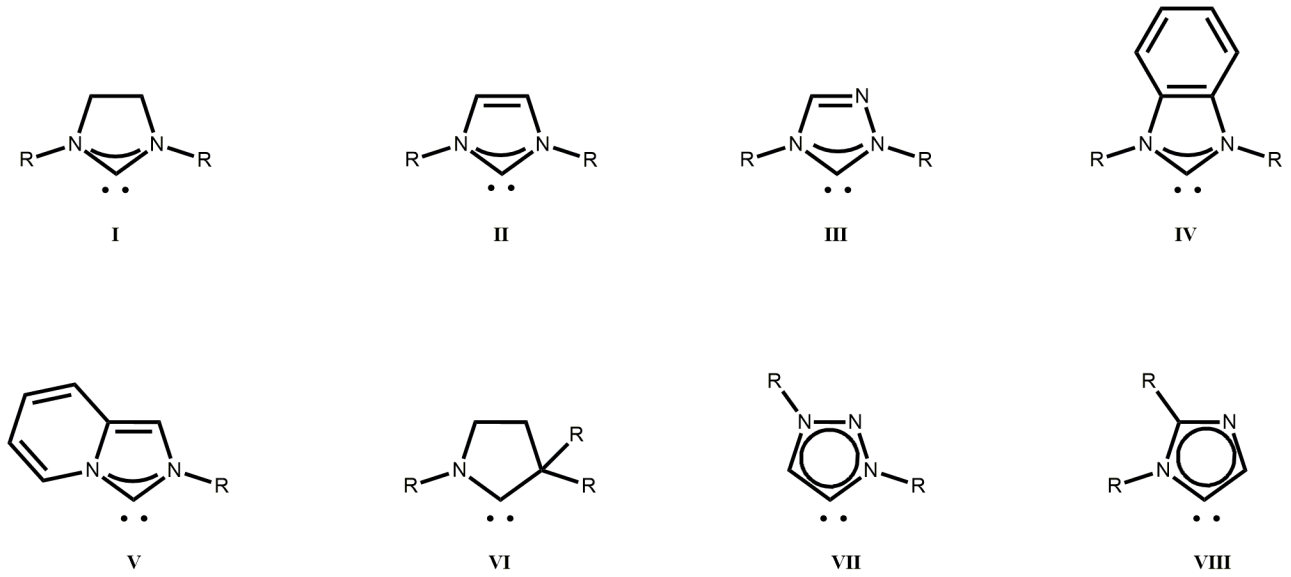

Figure 1.9 Schematic representation of the most important normal C^2 (**I-VI**) and abnormal C^4/C^5 (**VII-VIII**) carbene binding motifs.

The main structure is based on a five-membered heteroaromatic ring such as imidazolidinylidenes (**I**), imidazolylidenes (**II**), triazolylidenes (**III**) and their benzannulated derivatives (**IV-V**). Recently Bertrand introduced a new class called cyclic (alkyl)aminocarbenes (*CAACs*) (**VI**) for the presence of a stronger σ- donor alkyl group in α position of the carbenic atom, respect to the classic nitrogen atom.[56] Such substitution renders the carbene C^2 position more electron rich and more sterically demanding, giving rise to the development of a new generation of complexes of interest in various fields.

Besides the "normal" coordination motif, a new type of carbene, able to bind the metal atom at the C^4/C^5 position, is called *abnormal* or *mesoionic* carbene. (**VII**–**VIII**). [57]

The difference between "*normal*" and "*abnormal*" is that the normal carbene is represented by Lewis structures containing positive and negative charges; the abnormal carbene wants additional charges in the resonance form. These latter emphasize the resulting betaine structure for the presence of additional charges.[58] As a consequence, aNHCs display an even higher σ-donating and weaker π-accepting ability when compared

to the corresponding nNHC, due to the formally carbanionic configuration of the carbenic atom in the former one.

In the last two decades, NHC carbenes have reached a good success for their application in coordination chemistry, so that the attention of the scientific community moved to think about new carbene-ligands able to connect different metals between them and able to achieve greater robustness in the final complex. On this way, it began the development of a great number of polytopic ligands bearing more than one NHC moiety. The interest for this new class of ligands found its origin in the ability to increase the stability of the resulting complex by the *chelating effect* and the possibility to use a carbene like a bridge between two different metal-centers, from this statement they can be named *polydentate* and/or *bridged*. In fact, poly-NHCs provide an excellent scaffold for the preparation of polynuclear homo- and heterometallic complexes.[59] Since the field of application is very extended, polytopic NHC carbenes have been analyzed by their steric and electronics properties, being classified in different categories, such as *pincer*- and "*Janus type*" NHCs ligands. The importance of polytopic NHCs is to lead a "cooperative effect" between the metal centers through the spatial separation induced by the ligand.

1.5.1 Pincer class carbenes

The *pincer class*, or *pseudopincer*, regards a ligand able to attach the metal from two different NHC units by a central coordination moiety which serves to balance the charge on the metal, obtaining a more stable complex. Several pincer ligands with a central amido moiety have been developed coordinating a metal center such as palladium(II), platinum(II), rhodium(I) and iridium(III). These robust undergo easily oxidative addition at the metal center, useful for catalysis or, in the case of iridium, to make photostable complexes for better performances in OLED devices.[60]

Poethig and Strassner proposed a new scaffold based on an anion triazidone which is a very weak electron donor. This ligand was adopted to synthesize binuclear complexes of silver(I) and gold(I).[61] A further alternative was a thioether group as central coordinating moiety reported by Huynh and coworkers where the thioeter group can be easily oxidized to sulfoxide, making this ligand labile.[62]

Another example was reported by Biffis by the synthesis of a macrocyclic pincer-type ligands. This ligand is able to strongly coordinate d^8 metal centers as palladium(II) and platinum(II) given the *trans* configuration of the two NHC moieties.[63]

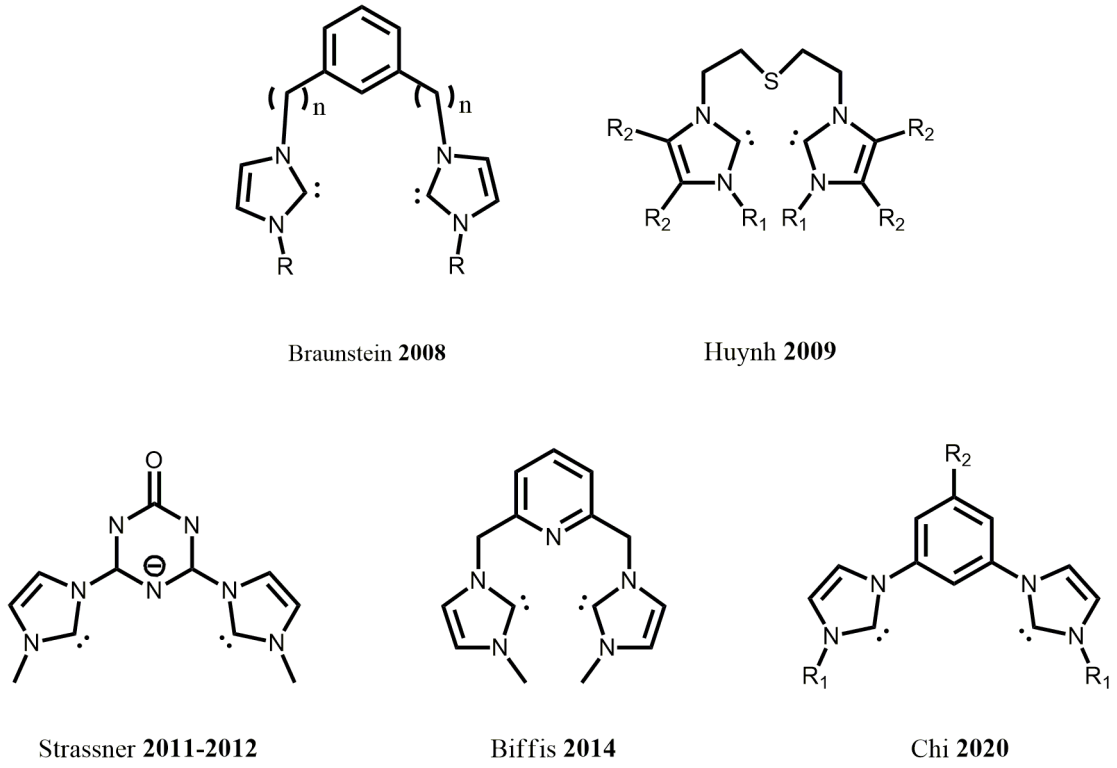

Figure 1.10 Chemical structure of some pincer-carbenes for organometallic applications.

1.5.2 Janus type carbenes

A Janus type carbene takes its name from the Roman god Janus who is depicted in art with two fused faces. The same way, a Janus-carbene has two fused and linearly opposed NHC carbenes or an NHC and second coordination motif. The interest on these kind of ligands lies in their structure which favorites the bridging coordination between two metal centers. This scaffold paves the way for preparing homo- or hetero-bimetallic complexes.[64] This ditopic ligand was introduced for the first time in 1997 by Bertrand, based on 1,2,4-triazol-3,5-diylidene structure (*ditz*).[49] Most of *ditz*-based dinuclear complexes were synthesized by Huynh *et al.* as catalysts in C5-arylation of 1-methylimidazole. The enhanced catalytic activity was owned to the shorter distance (6 Å) between the two metal centers,

suggesting an electronic communication between them.[65] It was supposed that the π-delocalized aromatic linker between the two carbenes promotes the communication between the two carbenes moiety, and as consequence between the metal centers. In other case, the π-stacking between the carbene was responsible for the catalytic performance.[66]

Peris reported that the interaction between the two metal centers depends only on the σ-delocalized electron density, while the π contribution is negligible. The strength of the communication between the two metals depends therefore only on the spatial separation between them and becomes negligible for distances exceeding 10 Å.[67] Further examples of these carbene and their applications in dinuclear complexes will be reported in the *state of art* of *chapter 4*.

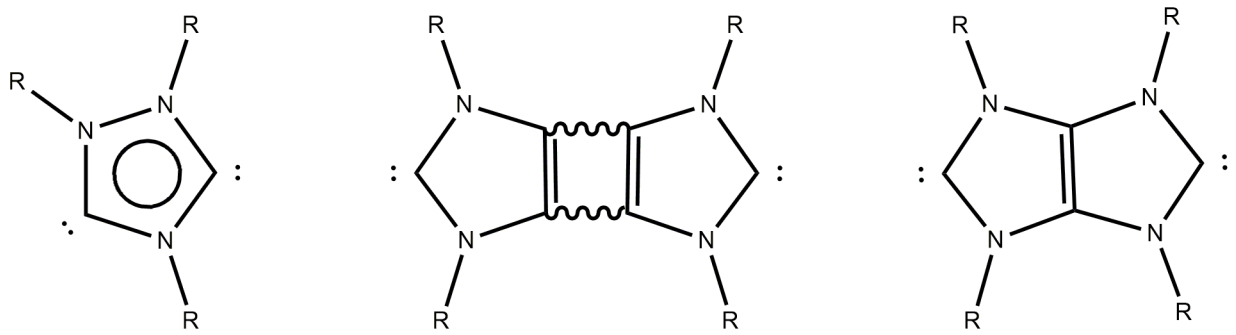

Figure 1.11 Chemical structure of some Janus-carbenes for organometallic applications.

1.6 Photocatalysis

Light as either energy source or reagents has stimulated the interest of chemists since 1912, when Giacomo Ciamican reproduced the natural photosynthesis by photochemical reactions.[68] The electronic configuration in the system changes along with the reactivity of the chemical compounds.[69] These reactions are often useful to activate substrates adopted in organic synthesis.[70] Since photons are employed as reagents to trigger the reaction, even they are used in large excess, they are traceless; in contrast to conventional chemical substances. Being a catalyst means decreasing the activation

barriers between starting materials and final product. Decreasing E factor means also decreasing the waste/desired products ratio,[71] which is related to the atom efficiency.[72] As I will describe in detail in *chapter 2*, "sensitizer" and "photocatalyst" have similar photochemical meaning.[73] Both are promoted to the excited state, which reacts with the substrates following redox processes, and then is regenerated after each cycle.[74]

Among different organometallic photocatalysts, the first report was on $[Ru(bpy)_3]^{2+}$ in 1978, to induce the reduction of phenacyl onium salts by 1,4.dihydropyridines.[75] In 2008 two groups, MacMillan[76] and Yoon[77] published its application for asymmetric alkylation of aldehydes and [2+2] enone cycloadditions, respectively, making photoredox catalysis an interesting field for synthetic organic chemistry. From there on, other compounds[78] were studied as photocatalyst for various organic reactions, previously inaccessible. In fact, the importance of metal-complexes consists in their suitability for different substrates and chemical reactions, leading to a new bond-formation or bond-breakage not accessible by pure organic molecules. Moreover, most of inorganic compounds absorb at low energy-visible light, in contrast with general high energy absorption from organic molecules, avoiding the excitation of both photocatalyst and substrate at the same time.
To design new inorganic photocatalysts, the following aspects have to be taken into account:

1. Photocatalytic reactions exploit the enhanced reactivity of a catalyst in its electronic excited states. The absorption of the photocatalyst should be in a range of wavelength where the other species in solution do not absorb.
2. The yield of the formed excited states needs to be as high as possible. This is related to the absorption cross-section and molar absorptivity.
3. The excited states have to live as long as possible to provide the desired reaction with the substrate. This is connected with time of the reagents diffusion.
4. The photophysics and the electrochemistry of the photocatalyst has to be reversible (no photodegradation when the quencher is absent, no secondary reactions).
5. If electron transfer is involved in the catalytic cycle, the redox potentials of the ground and excited states need to provide exergonic reactions.
6. All these properties must be tuned by the synthetic design of the ligands around the metal.[79]

The common mechanism promoted by transition-metal complexes is the absorption at high wavelength, corresponding to singlet metal-to-ligand charge transfer followed by intersystem crossing to long-lived triplet excited states. In this configuration, a photocatalyst has an electron in a high energy state, localized onto ligand and a vacancy localized predominantly on the metal center. As a result, the catalyst is simultaneously a better reductant and oxidation respect to the molecule on the ground state, retaining a strong thermodynamic driving force to return to the original oxidation state.[79] Higher oxidation state will lead to a better thermodynamic driving force for reductive elimination, vice-versa, low oxidation state promotes oxidative addition.[80] In this perspective, a photocatalyst upon excitation can remove or donate an electron from or to an organic or organometallic substrate. The most common proposed mechanisms for a photocatalytic reaction are either energy transfer or electron transfer.

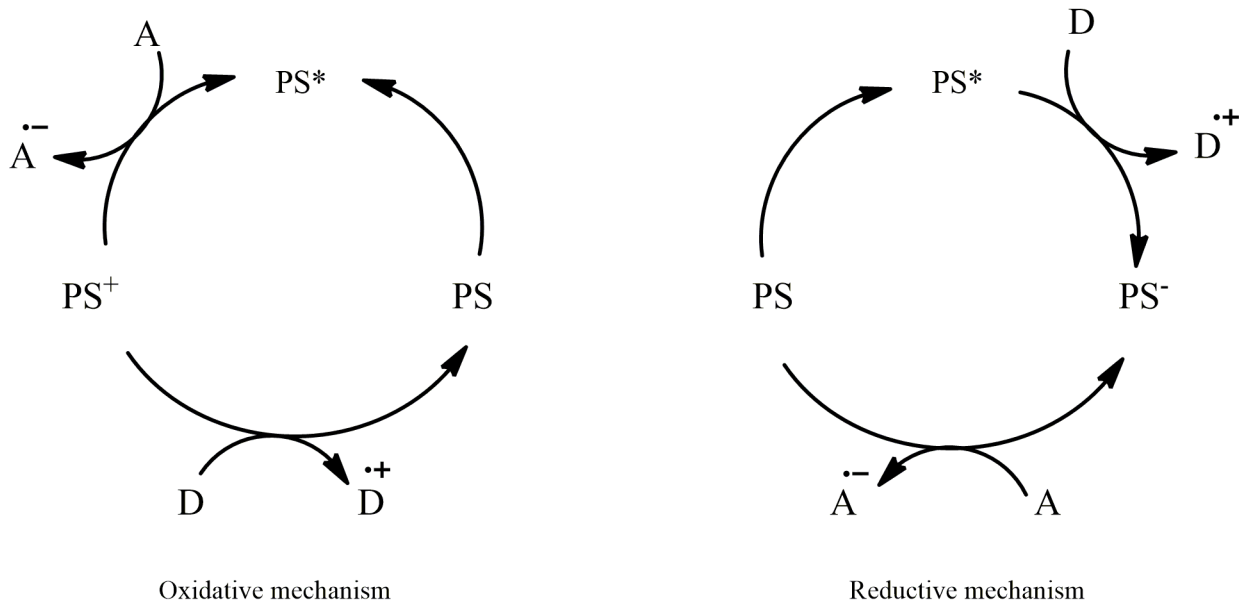

Figure 1.12 Schematic mechanism of photoredox catalytic cycle following either an oxidative or a reductive mechanism.

Single electron transfer (SET) is a mechanism that occurs at the excited state of the molecule. The electron is promoted from the lower to the higher orbital, where it can be easily removed due to the smaller ionization potential. At the same time, the vacancy left from the electron at the lower orbital can be filled accepting a new electron from a different specie. According to the following reaction equation 1.8

$$A + B \rightarrow A^{+} + B^{-} \qquad Eqn.\,1.8$$

The free energy is calculated as equation 1.9

$$\Delta G^{0} = E^{0}(A^{+} / A) - E^{0}(B / B^{-}) \qquad Eqn.\,1.9$$

When the excited state is involved, the same reaction becomes:

$$^{*}A + B \rightarrow A^{+} + B^{-}$$

And the free energy is now equation 1.10

$$\Delta G^{0}(^{*}A / A) = \Delta H(^{*}A / A) - T\Delta S(^{*}A / A) \qquad Eqn.\,1.10$$

ΔH (*A / A) is the difference between the zero-zero vibrational levels of the excited and ground state at 0 K, thus E_{00} (*A / A).

Since the change of shape, size, solvation (etc..) between ground and excited state is experimentally visible by the Stokes-shift between absorption and emission, E_{00} (*A / A) corresponds to the zero-zero spectroscopic energy of the excited state, so the first experimental point of the emission spectra. This value is really important to approximately calculate the redox potentials of the excited state, following the approximated Rehm-Weller equations (1.11):

$$E^{0}(A^{+} / {}^{*}A) = E^{0}(A^{+} / A) - E_{00}({}^{*}A / A)$$

$$E^{0}({}^{*}A / A^{-}) = E^{0}(A / A^{-}) - E_{00}({}^{*}A / A) \qquad Eqn.\,1.11$$

The possibility of the excited state being involved in electron transfer process increases along with its lifetime. [81]

Among different transition metal complexes, those based on rhenium(I) are the most studied as CO_2 reductant.[82] However, in the last two decades, rhenium(I) complexes have been employed in synthetic reactions as well.[83] The advantages of photocatalyst rhenium complexes are diverse oxidation states, ranging from -1 to +7, and especially, the stability under air- and moisture-condition, easily findable in several organic reaction. The most common [$Re(CO)_3$(N^N)(X)] complexes are usually stable again photo-substitution reactions and against irradiation with light over than 340 nm, due to the lowest lying ^{3}MLCT excited state.[33] A detailed description will be reported in the *chapter 2* where classic rhenium(I)-diimine complexes will be compared to our rhenium(I)-NHC carbene. At last, a new photocatalytic system based on rhenium(I)-NHC complex will be investigated for photopolymerization processes.

1.7 Theranostic agents

The combination of the two words, “therapeutics” and “diagnostics” gives rise to a new word, “theragnostic”. Consequently, the definition of theragnostic agent is a material that has simultaneously imaging and therapeutic properties.[84] The improvement of cellular imaging techniques has become more and more powerful in the last decades according to the direct visualization of cells and their micro-organelles, such as nucleus and mitochondria.[85] Improving optical imaging as technique for medical diagnostics has been becoming even more important due to it is a harmless technique compared to radioactive labels. The detection ability of biological structure is in the picomolar range, which is comparable to conventional nuclear imaging.[86] Optical imaging techniques can be either label-free, exploiting the autofluorescence of the single compartments of the cell, or by the incubation of luminescent markers into the cell.[87] These luminescent compounds can be either organics or organometallics. If the diagnostic agent is a fluorescent emitter, so an organic molecule, and its emission profile overlap with the fluorescence given by endogenous species like flavins, nicotinamides or aminoacids, it is not possible to distinguish between the two signals. Moreover, organic molecules can undergo photobleaching, which occurs once the compound is excited to higher energy states. At that step, several processes can destroy the emissive properties.[88]

All these drawbacks have leaded to find an alternative with organometallics compounds and then, the research moved in a new direction. Following the discovery of the *cis*platinum, transition metal complexes have been longer used as efficient therapeutics agents and, some of them, as cellular markers as well. Platinum(II)[89] ruthenium(II),[90] rhenium(I)[91] and iridium(III) are the most investigated so far. The spread of these kind of complexes is due to several structural and electronic advantages. The thermodynamic and kinetic properties of the metal-complex can be adapted to the biological environments using a different combination of ligands. Lastly, the stepwise synthesis for organometallics allows to achieve a great modularity and flexibility of each synthetic step.[92]

As mentioned before, the cisplatin was the first organometallic compound investigated as anticancer agents. Its mechanism of action is the following. When the compound enters the cell forms active species by aqueous hydrolysis that interact with DNA, RNA and protein. The formation of crosslinks with these species causes apoptosis.[93] Following these steps, new inorganic cytostatic drugs have been developed. A first example was ruthenium(III) bis(imidazole) tetrachloride complex, namely $[Ru(Im)_2Cl_4]_2$ where Im is imidazole, and its mono-dimethylsulfoxide counterpart, $[Ru(Im)(DMSO)Cl_4]_2$ that showed very promising anticancer due to the hydrolysis of the chloride ligands.[94] On the contrary, the Ir(III) analogues did not show biological activity and for this reason, iridium complexes were less explored.[95] Combining the tunable reactivity and the high-water solubility, along with long-lived excited state, iridium complexes have gained attention just recently. The long lifetime is exploited in imaging techniques, ensuring that the luminescent signal comes from the probe, and not from the cellular organelles. In a range of hundred nanoseconds-microseconds, light-emission arising from autofluorescence is nearly zero, therefore phosphorescence of the transition-metal complex can be selectively detected.

Luminescent cyclometalated iridium(III) complexes are a versatile class of compounds with great potential in theranostics that enables easy modification of ligands coordination sphere around the metal. In turns, this is expected to influence properties like solubility, lipophilicity and photophysics, opening up for chemical structure-properties relationships. In these thesis, five novel Iridium compounds targeting mitochondria will be described in *Chapter 3*. Mitochondria are dynamic rod-shaped organelles localized in the cytoplasm of eukaryotic cells, responsible for the energy production and apoptosis.[96]

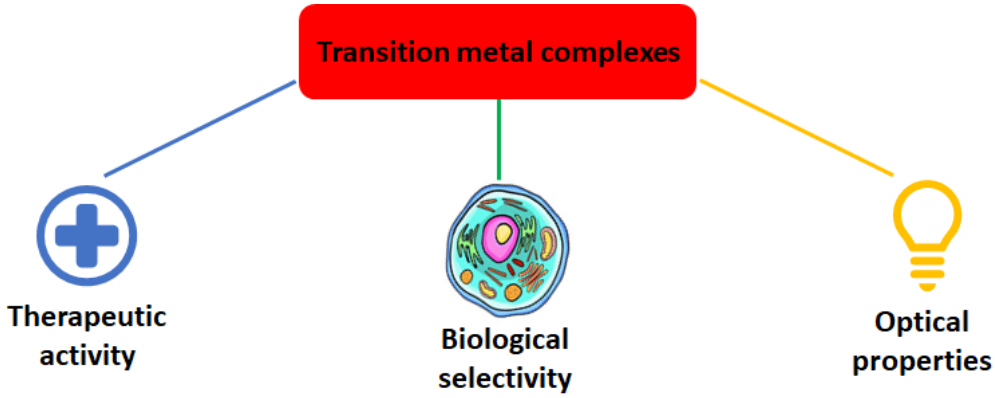

Figure 1.13 Key features of transition metal complexes and their properties as theragnostic agents.

Most of the compounds specific for mitochondria are charges because it is possible to have a better localization thanks to mitochondrial membrane electrical potential. Nevertheless, the tough mitochondrial membrane permeabilization makes challenging the molecular targeting owing to the metal-ligand bond cleavage.[97] To circumvent this drawback, NHC carbenes have gained remarkable popularity in the design of robust metal-ligand bond suitable for different biological targets.[98] Previous studies on imidazolium salt revealed antimicrobial and antifungal properties related to the substituents onto N atoms. Those influence the hydrophobicity of the molecules.[51]

The NHC-derivatives, when bind to the metal, provide anticancer activity and a specific selectivity toward mitochondrial membrane, thanks to the strong chemical stability of the resulting metal-carbene bond.[99] However, chemical structure-biological interaction have elucidated a lipophilicity-citotoxcity relationship well explored with different Ir(III)-NHC complexes.[100]Thus, increasing the lipophilicity of the structure, the absorption from the cell is improved, leading to a better activity of the molecule, so the cytotoxicity. Iridium(III) complexes are already well known for their amazing photophysical properties that combining with the biological activity make a new interesting class of theragnostic compounds.

1.8 Light-emitting Electrochemical Cells (LECs)

The acronym LEC means *light emitting electrochemical cells*, which indicates a single layer device that converts an electrical input into light energy via *electroluminescence* (EL),

discovered in 1990 by Pei and co-workers.[101] The fabrication method is low-cost, such as spin-coating or printing, generally named *solution-based technologies*.[102] The emissive layer is sandwiched between an anode composed by a transparent oxide film, normally indium tin oxide (ITO) and a cathode, typically an air-stable metal such as Al or Ag. The *emissive layer* (EML) can contain either a polymer or a transition-metal complex. When a polymer is used, a salt needs to be added to provide ions; while a charged metal complex perform the dual role of both emitter and charge transporter. The presence of ions is paramount importance for the working principle of the device.

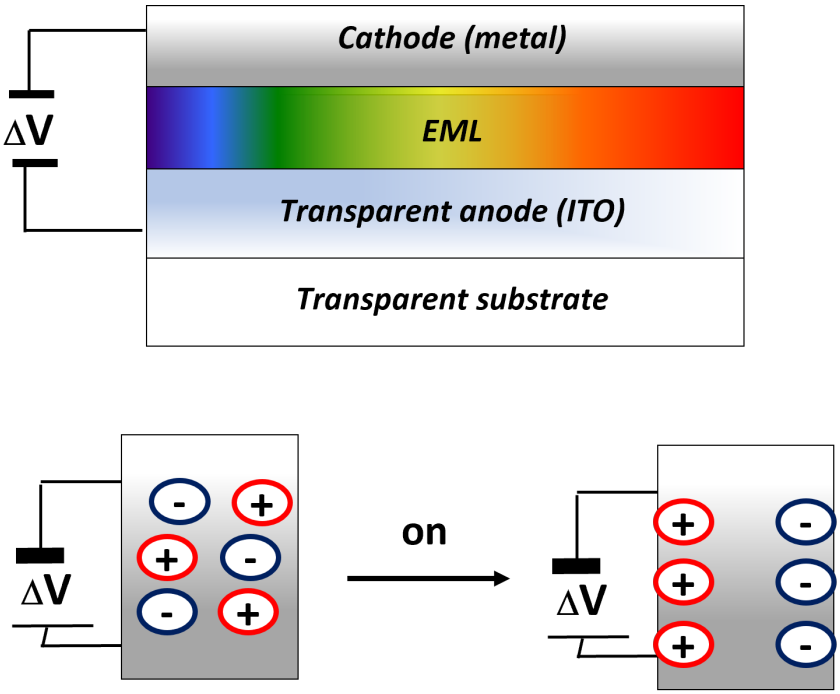

Figure 1.14 LEC single layer structure and charges migration toward the two electrodes upon application of an electrical bias.

The low-cost fabrication method as well as the cheap materials used for that make LECs are very attractive for market application and large-scale devices. Since the light depends on the migration of ions in the EML, the time required to emit light, called *turn-on time*, ranges from milliseconds to hours, and it is related to the time ion require to across approximately half of the electrode spacing.[103]

Two models about the operating mechanism have been subject of an intense debate: the electrochemical dynamic model (ECD) and electrodynamic (ED).

When suitable electric bias is applied, anions and cations move towards the relative electrode, forming a thin layer of uncompensated ions, named electric double layers (EDLs). According to the ECD model, on the anode there are anions, forming the p-doped layer; on the cathode there are cations, forming n-doped layer, so a p-i-n structure is formed. Since the molecules forming the semiconductor material of the anode and of the cathode, are oxidized and reduced as well, they are electrostatically compensated by anions and cations already present in the emissive layer. The region between these two layers is the region when the injected electronic charges recombine.

According to the ED model, two electric double layers are formed by mobile ions at the interfaces. When the voltage is applied, they migrate towards the electrode interfaces, creating the interfacial electric fields. This electric field promotes the injection of electronic charge carriers which move by diffusion and recombine when electrons and holes meet. [104]

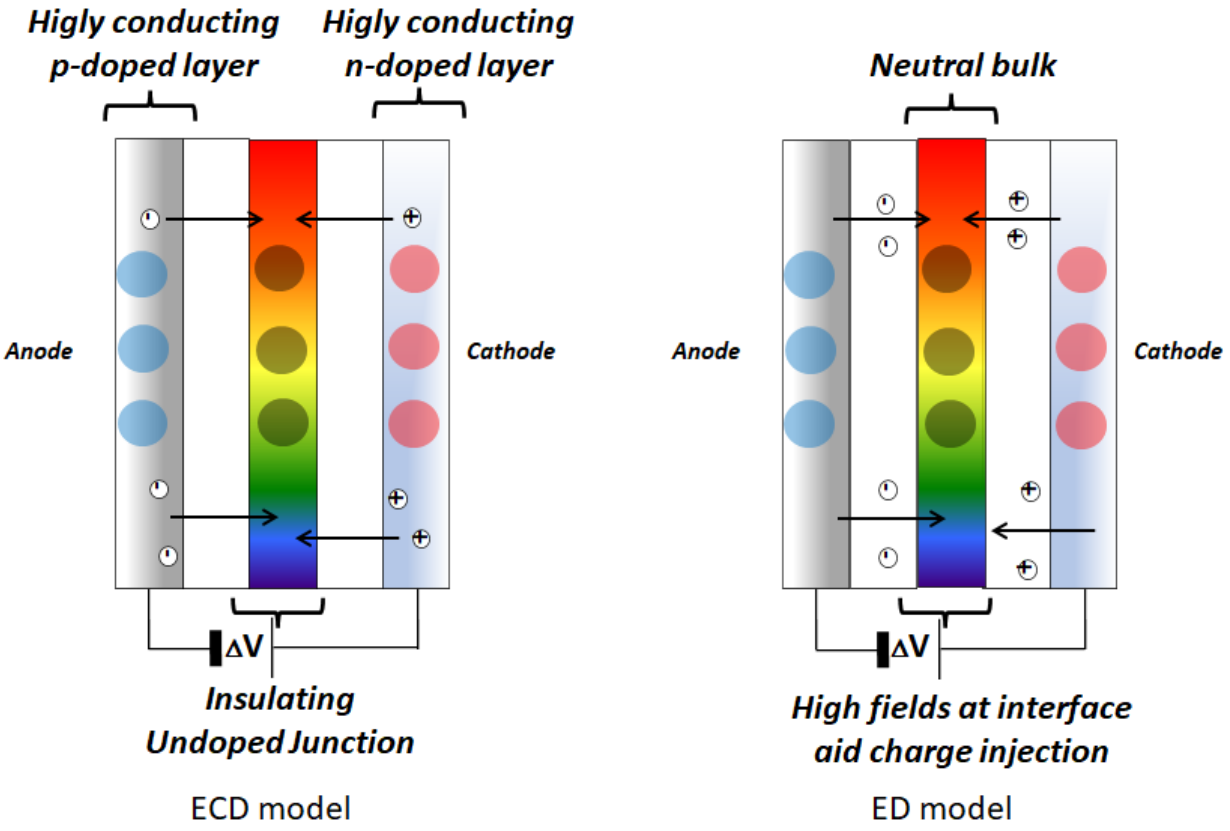

Figure 1.15 Schematic diagram for the ECD (left) and ED (right) model of working principle of a LEC device.

The p-type and n-type doped zones respectively at the anode and at the cathode, form a high conductive region which quenches excitons leading to a photoluminescence decreasing.[105] These zones can grow up until when they make contact, decreasing the exciton-photon conversion. The luminance is decreased as consequence. The doped zones are related to both electronic and ionic mobility, applied bias voltage and thickness of the active layer.[106]

Performances of a LEC device are characterized by means of several parameters, including the thickness of the emitting layer, the voltage employed to measure the luminescence and the external quantum efficiency (EQE). This latter is defined as by equation 1.12, where b is the fraction of electrons and holes that recombine to form excitons; φ is the exciton-to-photon generation efficiency and the number of photons that can escape the device or outcoupling efficiency estimated by 1/2n.[107]

$$EQE = \frac{b\varphi}{2n^2} \qquad Eqn.1.12$$

The outcoupling efficiency depends mainly on the device architecture and on the light generation zone in the device.[108] In LECs, after the injection barriers have been overcome, all electrons and holes recombine (b = 1)[109] to form excitons. These excitons can have either singlet or triplet spin-multiplicity. According to the spin statistic, 25% are singlet and 75% are triplet. Organic molecules, as fluorescent emitters, can harvest just the 25% of excitons by excited singlet states; whereas the employment of transition-metal complexes respect to organic molecules is owing to the ability to efficiently collect both of them. The φ factor depends on the photoluminescence quantum yield, which is quenched by the grow of the doped layers. Since those are related to the current intensity, increasing the current intensity, the efficiency of the device decreases.

1.9 Organic Light-Emitting Diodes (OLEDs)

OLED is the acronym of *organic light emitting diode* and the fabrication method may be more expensive than that one of LEC. Two main processes can take place to make this device: i) thermal evaporation in high vacuum (*vacuum process*) and ii) solution-processed deposition of organic materials (*wet process*).[110]

Efficent OLEDs require a *multi*-layers architecture where all the layers are sandwiched between an anode (ITO) and a cathode, typically an air-sensitive metal, such as Ca and Ba. Upon application of an electrical bias, holes and electrons cross multiple semiconductor layers before to recombine in the emissive one where they form the excitons, responsible for the excitation of the molecule. The emissive layer consists in a matrix as "host-material" doped with a suitable triplet emitter complex at low concentration, "guest material"[119] The most common type of emissive layer materials are CBP (4,4′-bis(carbazole-9-yl)biphenyl) for vacuum deposition processes,[111] and OXD-7 mixed into the PVK for solution processes[112] and TSPO1 (Diphenyl[4-(triphenylsilyl)phenyl]phosphine oxide), also used as ETL.[113] The choice of the host material depends on the type of the dopant is used because it is necessary that the triplet state of the matrix must be higher in energy than that one of the emitting materials, as to avoid back energy transfer onto the triplet (dark) state of the host materials. Furthermore, doping concentration should be carefully optimized and maintained at low level to avoid bimolecular quenching processes such as the *triplet-triplet annihilation* (TTA) and the *triplet-polaron annihilation* (TPA).

These phenomena are described as following, where $A^{+/-}$ denotes the corresponding charge carrier (equation 1.13) [114]

TTA: $$ {}^*T_1 + {}^*T_1 \xrightarrow{k_{TTA}} {}^*S_1 + S_0 \qquad Eqn.\,1.13 $$

TPA (*hole*): $$ {}^*T_1 + A^+ \xrightarrow{k_{TPA,h}} S_0 + {}^*A^+ \qquad Eqn.\,1.14 $$

TPA (*electron*): $$ {}^*T_1 + A^- \xrightarrow{k_{TPA,e}} S_0 + {}^*A^- \qquad Eqn.\,1.15 $$

These quenching processes can occur for long-lived T_1 excited state of the molecule which collides with the excitons.

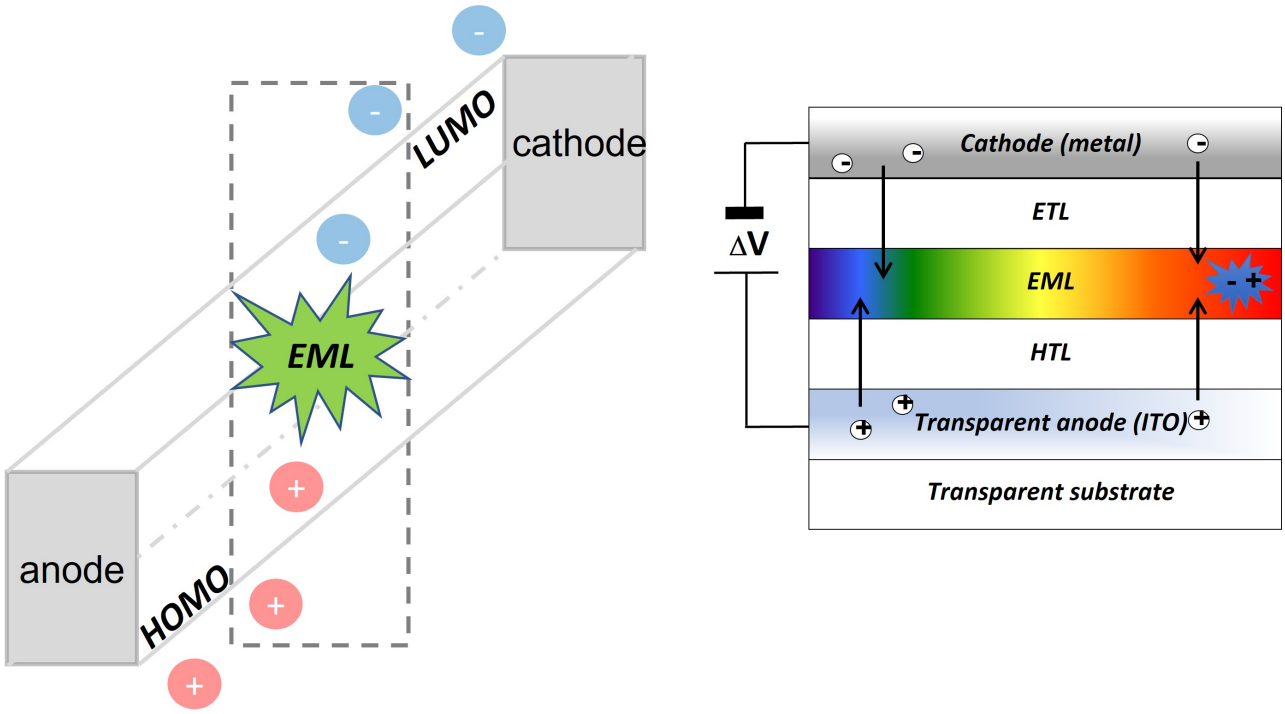

Figure 1.16 OLED multi layers structure and excitons recombination in the emissive layer.

Overall, TTA and TPA processes reduce the efficiency (EQE) of the device when higher current densities are applied. This phenomenon is named *efficiency roll-off*. [115] As for LEC, an OLED must have the highest brightness with the lowest possible driving current density, to achieve a good performance. However, on one hand, the higher number of layers leads to a higher applied voltage, and, on the other hand, the lifetime of the device decreases with the current increasing. To figure out the problem about the device efficiency a multi layers system takes place. The hole-injecting layer (HIL) and the hole-transport layer (HTL) promote the hole migration as well as the electron-transport layer (ETL) for the electrons, while the hole-blocking layer (HBL) avoid the stockpile of the charges. HTL and ETL refer to p-type and n-type doped layer and this structure allows to obtain high luminance and efficiency despite of the low voltage.

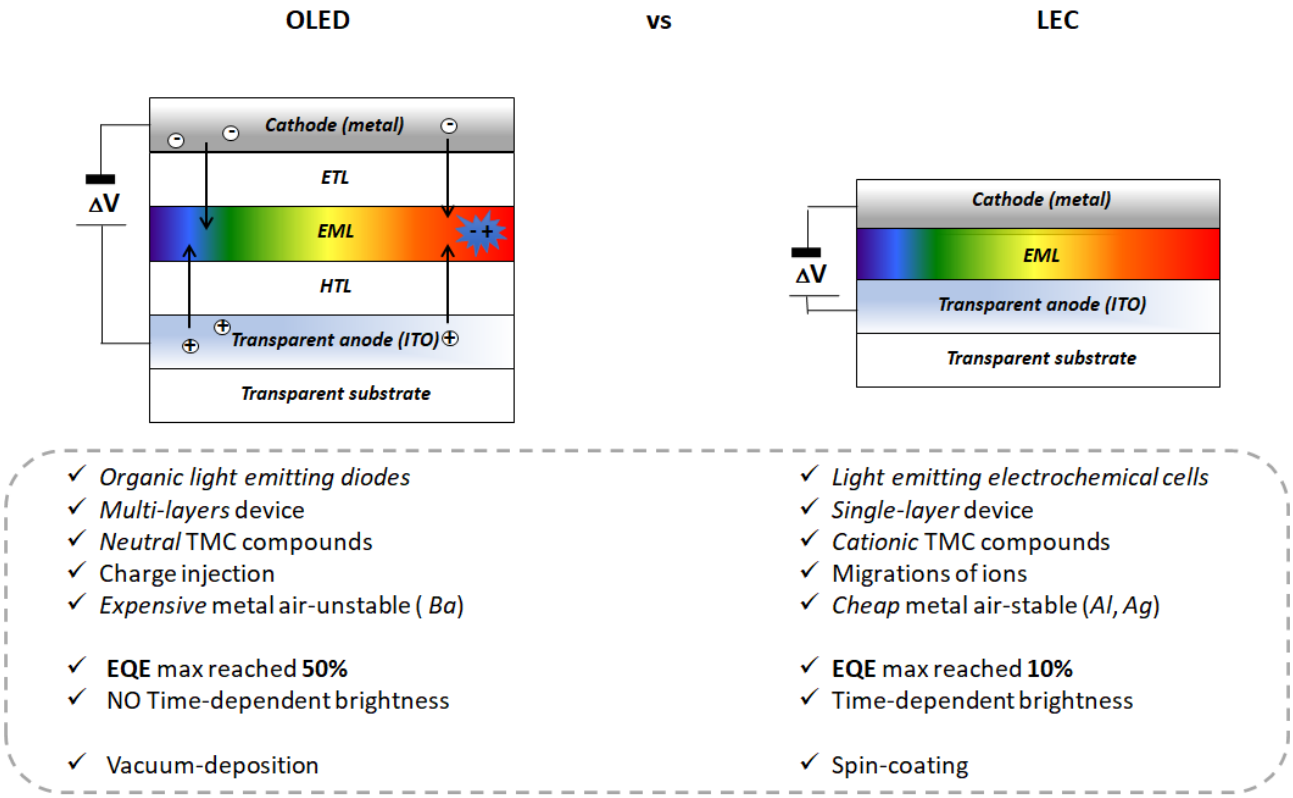

Figure 1.17 Layers structures and comparison between OLED and LEC performances.

Likewise to LEC, an indicative factor about the performance of the device is the *External Quantum Efficiency*, EQE. EQE is given by the ratio between the number of photons emitted from the device and the number of injected charges. This can also be expressed as the product between the *Internal Quantum Efficiency*, IQE and the *outcoupling efficiency* (η_{out}).

$$EQE = IQE . \eta_{out} \qquad Eqn. 1.16$$

While η_{out} depends on the direction and propagation via external modes, IQE varies with the device architecture and the molecule chosen as emitter. Since the IQE is equal to the following equation:

$$IQE = \gamma . \eta_{ST} . \phi_{PL} \qquad Eqn. 1.17$$

Where γ is the fraction of injected carriers that form excitons, η_{ST} is the fraction of excitons referred to spin statistic and ϕ_{PL} (or PLQY) is the fraction of excitons deactivated radiatively; the key to optimizing the I.Q.E is to achieve an efficiency close to unity.[116]

However, η_{ST} can vary depending on the type of emitter used in the device, fluorescent or phosphorescent, which is related to the spin-statistic rule of the excitons.[117]

As said for LEC, when holes and electrons recombine to form excitons, 25% of them are in S_1 and 75% in T_1 owing to the *spin-multiplicity rule* (2S+1). In order to achieve the maximum luminescence efficiency, it's necessary to modulate the fraction of the excitons in the singlet state (η_s). In this regard, three different generations of OLED devices have been fabricated.[118]

The *first OLED generation* is based on fluorescent materials, where only singlet excitons are used for the light emission. In fact, these materials, like organic molecules, can emit just from an excited state having the same spin of the ground state, making an internal quantum efficiency equal to 25%.[119] An intelligent strategy to increase the IQE is to save the 75% of light emission from triplet states. Studying how S_1 and T_1 inter-conversion works, it is possible to grow the electroluminescence efficiency (η_{EL}) of the device.

The *second generation* of OLED is based on transition-metal complexes which emit from T_1 for the second generation and from S_1 for the third generation. In the first case, phosphorescent materials present intersystem crossing between S_1 and T_1 because of the strong SOC effect given by the heavy atom. The 25% of the singlet excitons is saved and the desired 100% of internal quantum efficiency is reached.

In the *third generation*, a less common radiative decay takes place from S_1 for those compounds (either organic or organometallic emitters) display TADF process. TADF is an acronym for *thermally activated delayed fluorescence* and occurs when the *reverse-intersystem crossing* (RISC) is possible. On the contrary of the second generation of OLED devices, the 75% of the triplet excitons is saved by the transfer from T_1 to S_1, achieving the 100% of internal quantum efficiency by fluorescence.[118]

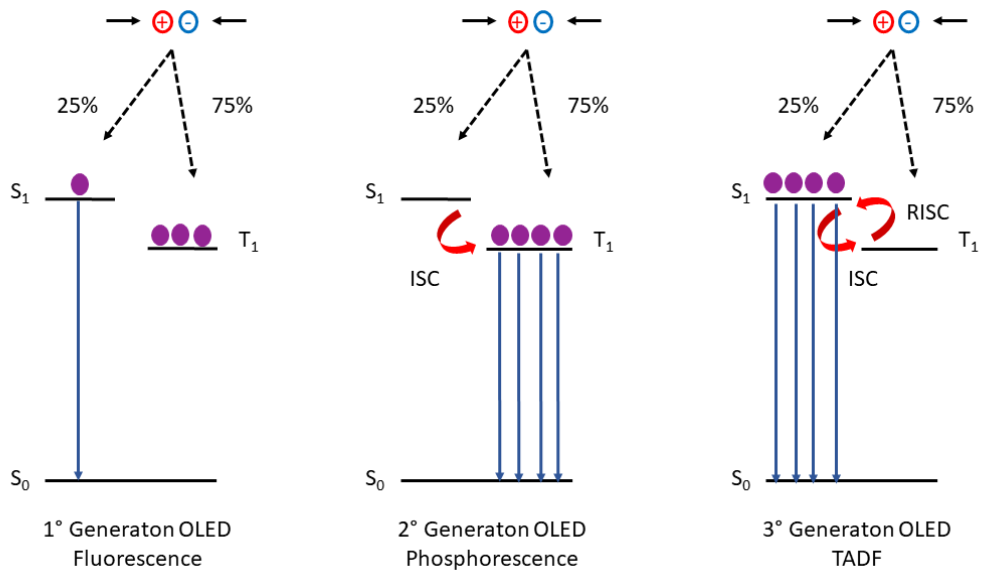

Figure 1.18 Schematic representation of different OLED generations.

1.10 Aim of the thesis

In this doctoral work, we aim to explore different classes of NHC-based ligands as privileged scaffolds for the preparation and investigation of novel families of emitters, based on Ir(III) and Re(I) metal complexes for application in organic electronics, photocatalysis and as theragnostic agents. In particular, in *chapter 2*, two new Re(I) based on a pyridyl pyridoannelated N-heterocyclic carbene show an enhancement of luminescence and vibronic emission profile, due to the lowest lying ^{3}LC states, compared to the numerous examples of ^{3}MLCT and low emissive compounds, reported in literature. Two out of four compounds showed good efficiency in photopolymerization for 3D laser writing applications. The same ligand was also used for new five Ir(III) complexes as potential theragnostic agents via mitochondria targeting. By a photophysical point of view, this class displays two deactivated channels based one on the cyclometallating ligand (C^N = phenylpyridine derivatives) and one on the ancillary ligand, so the pyridyl pyridoannelated N-heterocyclic carbene. The dual-emission properties, combined with therapeutic those, reveal a new family of iridium compounds as theragnostic agents for mitochondria targeting (*chapter 3*). A new class of heterobimetallic iridium complexes bearing a hybrid Janus type carbene was fully characterized and investigated for light emitting electrochemical cells application, resulting among the highest luminescent polynuclear compounds and the highest bimetallics

for light emitting electrochemical cells (*chapter 4*). Finally, a bis-carbene pincer chelate ligand was used to make robust blue iridium complexes for future OLEDs applications (*chapter 5*).

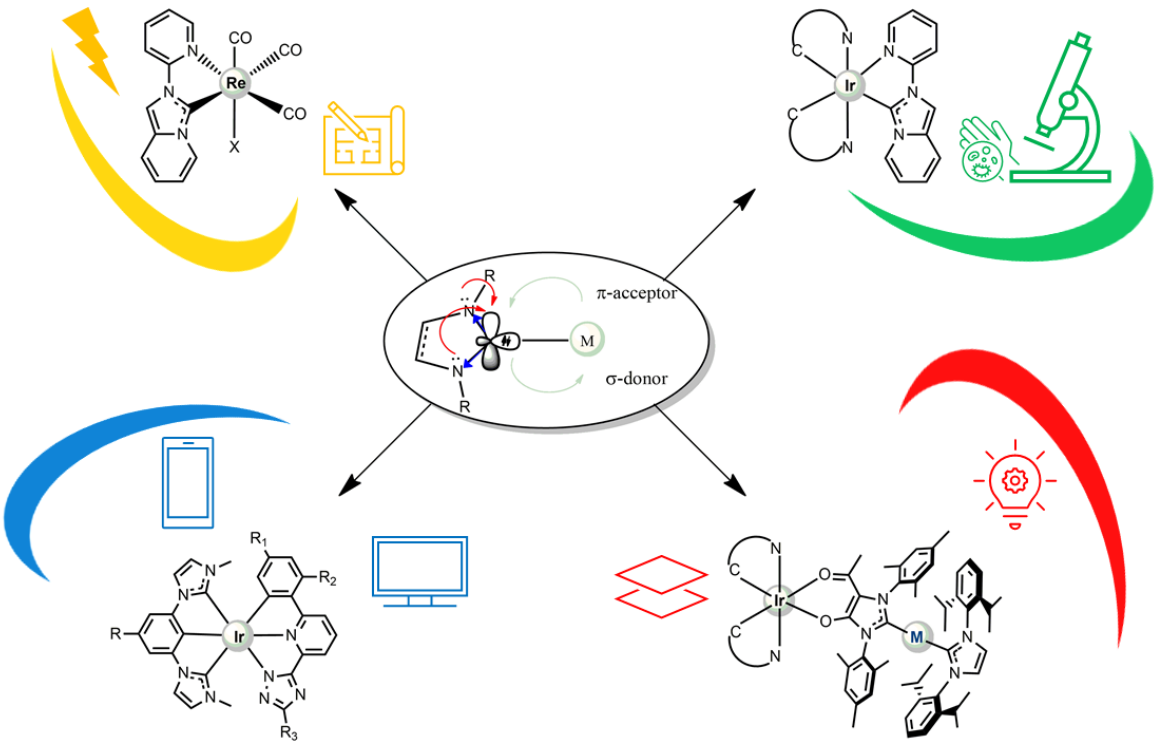

Figure 1.19 All NHC-carbenes used for this doctoral work.

1.11 References

1. L. Moggi, A. Juris, M.T. Gandolfi, *Manuale del Fotochimico*, Bonomia Press University, **2006.**
2. [a] B. Valeur, *Molecular Fluorescence: Principles and Applications*, Wiley-VCH, Weinheim **2001**; [b] J. R. Lakowicz, *Principles of Fluorescence Spectroscopy*, Springer, **2006**.
3. A. Jabłoński, *Nature,* **1933**, *131*, 839.
4. [a] J. Franck, *Trans. Faraday Soc*. **1926**, *21*, 536; [b] E. Condon, *Phys.Rev*. **1926**, *27*, 640; [c] E. Condon, *Phys. Rev*. **1926**, *28*, 1182; [d] E. Condon, *Phys.Rev*. **1928**, *32*, 858.
5. M. Montalti, A. Credi, L. Prodi, M.T. Gandolfi, *Handbook of photochemistry,* **2006.**
6. [a] R. Englman, J. Jortner, *Mol. Phys.* **1970**, *18*, 145; [b] J. V. Caspar, T. J. Meyer, *Inorg. Chem.* **1983**, *22*, 2444; [c] J. V. Caspar, T. J. Meyer, *J. Phys. Chem.* **1983**, *87*, 952; [d] E. M. Kober, J. V. Caspar, R. S. Lumpkin, T. J. Meyer, *J. Phys. Chem*. **1986**, *90*, 3722.

7. [a] C. K. Jørgensen, *Absorption Spectra and Chemical Bonding in Complexes,* Pergamon Press, London, **1962**; [b] V. Balzani, V. Carassiti, *Photochemistry of Coordination Compounds*, Academic Press, New York, **1970**; [c] A. W. Adamson, P. D. Fleischauer, *Concepts of Inorganic Photochemistry*, Wiley-Interscience, New York, **1975.**
8. [a] H. Yersin, *Highly Efficient OLEDs with Phosphorescent Materials*, Wiley-VCH, Weinheim, **2008**; [b] C. E. Housecroft, E. C. Constable, *Coord. Chem. Rev.* **2017**, *350*, 155; [c] A. F. Henwood, E. Zysman-Colman, *Chem. Commun.* **2017**, *53*, 807; [d] Y. Chi, T.-K. Chang, P. Ganesan, P. Rajakannu, *Coord. Chem. Rev.* **2017**, *346*, 91.
9. [a] C. Caporale, M. Massi, *Coord. Chem. Rev.* **2018**, *363*, 71; [b] Q. Zhao, C. Huang, F. Li, *Coord. Chem. Rev.* **2011**, *40*, 2508.
10. J. Twilton, C. Le, P. Zhang, M. H. Shaw, R. W. Evans, D. W. C. MacMillan, *Nat. Rev. Chem.* **2017**, *1*, 52.
11. [a] J. S. Griffith, *The Theory of Transition-Metal Ions.* Cambridge University Press: Cambridge, UK, **1961**; [b] F. A. Cotton, G. Wilkinson, P. L. Gauss, *Basic Inorganic Chemistry*. Wiley Interscience: USA, **1995**
12. L. E. Orgel, *An Introduction to Transition-Metal Chemistry: Ligand-Field Theory*, Methuen, London, UK, **1966**
13. L. Flamigni, A. Barbieri, C. Sabatini, B. Ventura, F. Barigelletti, *Top. Curr. Chem.*, **2007**, *281*, 43.
14. [a] F. A. Cotton, G. Wilkinson, C. A. Murillo, M. Bochmann, *Adv. Inorg. Chem.*, Wiley-Interscience: New York, **1999**; [b] J. McCleverty, T. J. Meyer, *In Comprehensive Coordination Chemistry II*; Elsevier Pergamon: New York, **2003**; [c] C. J. Ballhausen, H. B. Gray, *Molecular Orbital Theory*. Benjamin: New York, **1964**; [d] H. B. *J* Gray, *Chem. Educ.* **1964**, 41, 2.
15. M. Mauro, C. Cebriàn, *Isr. J. Chem.* **2018**, *58*, 901.
16. [a] R.C. Evans, P. Douglas, H. D. Burrows, *Appl. Photochem.*, Springer, **2013**; [b] C. Förster, K. Heinze, *Chem. Soc. Rev.,* **2020**, *49*, 1057.
17. [a] McCusker, *Science* **2019**, *363*, 484, [b] G. A. Crosby, *Acc. Chem. Res.* **1975***, 8, 7,* 231.
18. G. A. Crosby, R. J. Watts, S. J. Westlake, *J. Chem. Phys.* **1971,** *55*, 4663.
19. F. Puntoriero, F. Nastasi, M. Galletta, S. Campagna. *Comprehensive Inorganic Chemistry II*, Oxford, Elsevier, **2013**, *8*, 255.
20. [a] Y. Zhang, T. S. Lee, J. M. Favale, D. C. Leary, J. L. Petersen, G. D. Scholes, F. N. Castellano, C. Milsmann, *Nat. Chem.*, **2020**, *12*, 345; [b] Y. Zhang, T. S. Lee, J. L. Petersen, C. Milsmann, *J. Am. Chem. Soc.* **2018**, *140*, 5934.
21. P. Atkins*, Shriver and Atkins' Inorganic Chemistry*, Oxford University Press, **2010.**
22. [a] M. A. El-Sayed. *J. Chem. Phys.* **1963**, *38*, 2834; [b] M. A. El-Sayed. *Accounts Chem. Res.* **1968**, *1*, 8.
23. [a] I. Baraldi, *Quaderni di fotochimica, La luminescenza,*Bonomia University Press, **2007** [b] M. Chergui *Acc. Chem. Res.* **2015**, *48*, 801; [c] J. V. Caspar, E. M. Kober, B. P. Sullivan, T. J. Meyer, *J. Am. Chem. Soc.* **1982**, *104*, 630; [d] P. Chen, T. J. Meyer, *Chem. Rev.***1998**, *98*, 1439.

24. N. J. Turro, V. Ramamurthy, J. C. Scaiano, *Principles of Molecular Spectroscopy*, University Science Books, **2009**.
25. [a] H. Yersin, A. F. Rausch, R. Czerwieniec, T. Hofbeck, T. Fischer, *Coord. Chem. Rev.* **2011**, *255*, 2622; [b] Y. Komada, S. Yamauchi, N. Hirota, *J. Phys. Chem.* **1986**, *90*, 6425.
26. [a] B. D. Stringer, L. M. Quan, P. J. Barnard, D. J. D. Wilson, C. F. Hogan, *Organometallics* **2014**, *33*, 4860; [b] R. Visbala, M. Concepción Gimeno, *Chem. Soc. Rev.,* **2014**, *43*, 3551; [c] T. Sajoto, P. I. Djurovich, A. Tamayo, M. Yousufuddin, R. Bau, M. E. Thompson, R. J. Holmes, S.R. Forrest, *Inorg. Chem*. **2005**, *44*, 7992
27. W.J. Finkenzeller, H. Yersin, *Chem. Phys. Lett.,* **2003**, *377*, 299
28. P. B. Hitchcock; M. F. Lappert; P. J. Terreros, *Organomet. Chem.***1982**, *239*, C26
29. [a] A. K. Pal, S. Krotkus, M. Fontani, C.F. R. Mackenzie, D. B. Cordes, A. M. Z. Slawin, D. W. Samuel, E. Zysman-Colman, *Adv. Mater.* **2018***, 30,* 1804231; [b] M. Idris, S. C. Kapper, A. C. Tadle, T. Batagoda, D. S. M. Ravinson, O. Abimbola, P. I. Djurovich, J. Kim, C. Coburn, S. R. Forrest, M. E. Thompson, *Adv. Opt. Mater.* **2021**, 2001994; [c] G. J. Barbante, E. H. Doeven, P. S. Francis, B. D. Stringer, C.F. Hogan, P. R. Kheradmand, D. J. D. Wilsonb, P. J. Barnard, *Dalton Trans.,* **2015**, *44*, 8564.
30. [a] O. S. Wenger, *Chem. Eur. J.,* **2019**, *25*, 6043; [b] O. S. Wenger, *J. Am. Chem. Soc.,* **2018**, *140*, 13522; [c] A. K. C. Mengel, C. Förster, A. Breivogel, K. Mack, J. R. Ochsmann, F. Laquai, V. Ksenofontov, K. Heinze, *Chem. Eur. J.,* **2015**, *21*, 704
31. [a] R.A. Kirgan, B.P. Sullivan, D.P. Rillema, *Top. Curr. Chem.* **2007**, *281*, 45; [b] A.J. Lees, *Comm. Inorg. Chem.* **1995**, *17*, 319.
32. M. Wrighton, D. L. Morse, *J. Am. Chem. Soc.* **1974**, *96*, 998.
33. H.Takeda, K. Koike, T. Morimoto, H. Inumaru, O. Ishitani, *Adv. Inorg. Chem.,* **2011**, *63*, 137.
34. [a] A. J. Lees, *Comm. Inorg. Chem.* **1995**, *17*, 319 [b] J. G. Vos, M. T. Pryce, *Coord. Chem. Rev*. **2010**, *254*, 2519.
35. [a] A. G. Crosby, *Coord. Chem. Rev.,* **2011**, *211*, 163; [b] M. Panigati, M. Mauro, D. Donghi, P. Mercandelli, P. Mussini, L. De Cola, G. D'Alfonso, *Coord. Chem. Rev.,* **2012**, *256*, 1621; [c] P. V. Simpson, M. Falasca, M. Massi, *Chem. Commun.,* **2018**, *54*, 12429; [d]. J. Giordano, S. M. Fredericks, M. Wrighton, D. L. Morse, *J. Am. Chem. Soc.,* **1978**, *100*, 2257; [e] P. J. Giordano, M. Wrighton, *J. Am. Chem. Soc.,* **1979**, *101*, 2888. [f] L. Wallace, D. P. Rillema, *Inorg. Chem*., **1993**, *32*, 3836; [g] L. Wallace, D. C. Jackman, D. P. Rillema, J. W. Merkert, *Inorg. Chem*., **1995**, 34, 5210; [h] L. Sackteder, A. P. Zipp, E. A. Brown, J. Streich, J. N. Demas, B. A. DeGraff, *Inorg. Chem*., **1990**, *29*, 4335.
36. A. Kumar, SS. Sun, A.J. Lees, *Photophysics and Photochemistry of Organometallic Rhenium Diimine Complexes*, Springer, Berlin, Heidelberg **2009**.
37. S. M. Fredericks, J. C. Luong, M. S. Wrighton *J. Am. Chem. Soc.* **1979**, *101*, 24, 7415.
38. R. H. Crabtree, *The organometallic chemistry of the transition metals*, Wiley, **2014.**
39. [a] G. Bertrand, *Carbene Chemistry: From Fleeting Intermediates to Powerful Reagents*, Marcel Dekker, New York, **2002**; [b] P. de Fremont, N. Marion, S. P. Nolan, *Coord. Chem. Rev.,* **2009**, *253*, 862.
40. R. R. Schrock, *Chem. Rev.,* **2002**, *102*, 145.

41. [a] L Arrico, L Di Bari, F Zinna, *Chem. Eur. J.* **2020**, *26*, 1; [b] J. C. Y. Lin, Roy T. W. Huang, C. S. Lee, Amitabha Bhattacharyya, W. S. Hwang, I. J. B. Lin, *Chem. Rev.* **2009**, *109*, 3561.
42. M. N. Hopkinson, C. Richter, M. Schedler, F. Glorius, *Nature* **2014**, *510,* 485.
43. [a] H. W. Wanzlick, E. Schikora, *Angew. Chem.,* **1960**, *72*, 494; [b] H. W. Wanzlick, H. J. Kleiner, *Angew. Chem.,* **1961,** *73*, 493; [c] H. W. Wanzlick, B. Lachmann, E. Schikora, *Chem. Ber.,* **1965**, *98*, 3170.
44. I. J. B. Lin, C. S. Vasam, *Comm. Inorg. Chem.,* **2004**, 25, 75.
45. [a] F. E. Hahn, L. Wittenbecher, D. Le Van, R. Fröhlich, *Angew. Chem.,* **2000,** *112*, 551; [b] F. E. Hahn, L. Wittenbecher, D. Le Van, R. Fröhlich, *Angew. Chem. Int. Ed.,* **2000**, *112*, 541; [c] Y. Liu, P. E. Lindner, D. M. Lemal, *J. Am. Chem. Soc.,* **1999**, *121*, 10626; [d] V. P. W. Böhm, W. A. Herrmann, *Angew. Chem. Int. Ed.* **2000**, *39*, 4036; [c] I.J. B. Lin, C. S. Vasam, *Comm. Inorg. Chem.,* **2004**, *25*, 3-4, 75.
46. [a] K. Ofele, *J. Organomet. Chem.,* **1968**, *12*, 42; [b] H. W. Wanzlick, H.J. Schönherr, *Angew. Chem.* **1968**, *80*, 154; [c] H. W. Wanzlick, H. J.Schönherr, *Angew. Chem. Int. Ed.* **1968**, *7*, 141.
47. M.F. Lappert, *J. Organomet. Chem.*, **1975**, *100*, 139.
48. A. J. Arduengo, R. L. Harlow, M. Kline, *J. Am. Chem. Soc.* **1991**, *113*, 361.
49. O. Guerret, S. Sole´, H. Gornitzka, M. Teichert, G. Trinquier, G. Bertrand, *J. Am. Chem. Soc*., **1997,** *119*, 6668.
50. H. M. J. Wang, I. J. B. Lin, *Organomet.* **1998**, *17*, 972.
51. A. J. Arduengo, G. Bertrand*, Chem. Rev.*, **2009**, *109*, 8.
52. L. N. Appelhans, C. D. Incarvito, R. H. J. Crabtree, *Organometallics. Chem.* **2008**, *693*, 2761.
53. [a] S. C. Zinner, W. A. Herrmann, F. E. J. Kühn, *Organometallic. Chem.* **2008**, 693, 1543; [b] S. C. Zinner, W. A. Herrmann, F. E. Kühn, *Tetrahedron: Asymmetry* **2008**, *19*, 1532.
54. A.J. Arduengo, H. V. Rasika Dias, J. C. Calabrese, F. Davidson, *Organometallics* **1993**, *12*, 3405
55. [a] A. Danopoulos, T. Simler, P. Braunstein, *Chem. Rev.* **2019**, *119*,3730 ; [b] D. G. Gusev, *Organometallics* **2009**, *28*, 6458; [c] D. J. Nelson, S. P. Nolan, *Chem. Soc. Rev.* **2013**, *42*, 6723; [d] S. Diez-Gonzalez, S.P. Nolan, *Coord. Chem. Rev.* **2007**, *251*, 874; [e] H. V. Huynh, *Chem. Rev*. **2018**, *118*, 9457.
56. V. Lavallo, Y. Canac, C. Präsang, B. Donnadieu, G. Bertrand, *Angew. Chem. Int*. **2005**, *44*, 5705.
57. [a] R. H. Crabtree, *Coord. Chem. Rev*. **2013**, *257*, 755; [b] O. Schuster, L. Yang, H. G. Raubenheimer, M. Albrecht, *Chem. Rev.* **2009**, *109*, 3445; [c] E. Aldeco-Perez, A. J. Rosenthal, B. Donnadieu, P. Parameswaran, G. Frenking, G. Bertrand, *Science,* **2009**, *326*, 556; [d] P. L. Arnold, S. Pearson, *Coord. Chem. Rev.* **2007**, *251*, 596.
58. D. Martin, M. Melaimi, M. Soleilhavoup, G. Bertrand, *Organomet.***2011**, *30*, 5304.
59. J.M. Aizpurua, M. Sagartzazu-Aizpurua, Z. Monasterio, *Top. Heterocycl. Chem.*, **2015**, *40*, 211

60. [a] M. Raynal, C.S.J. Cazin, C. Vallée, H. Olivier-Bourbigou, P. Braustein, *Chem Commun*. **2008**, 3983; [b] N. Darmawan, C-H. Yang, M. Mauro, M. Raynal, S. Heun, J. Pan, H. Buchholz, P. Braµstein, L. De Cola, *Inorg. Chem.* **2013**, *52*, 10756 ;
61. [a] A. Poethig, T. Strassner *Organomet*. **2011**, *30*, 6674; [b] A. Poethig, T. Strassner *Organomet.* **2012**, *31*, 3431.
62. HV. Huynh, D. Yuan, Y. Han *Dalton Trans.* **2009**, *35*, 7262.
63. A. Biffis, M. Cipani, E. Bressan, C. Tubaro, C. Graiff, A. Venzo *Organomet*. **2014**, *33*, 2182.
64. A.Biffis, M. Baron, C. Tubaro, *Adv. Organomet. Chem.* **2015**, 63, 203.
65. [a] S. Guo, HV. Huynh *Organomet.*. **2014**, *33*, 2004; [b] S. Guo, HV. Huynh *Organometallics*. **2012**, *31*, 4565
66. [a] A. Prades, E. Peris, *Organometallics*. **2012**, *31*, 4623; [b] G. Guisado-Barrios, J. Hiller, E. Peris *Chem. Eur. J.* **2013**, *19*, 10405; [c] S. Gonell, M. Poyatos, E.Peris *Chem Eur J.* **2014**, *20*, 9716; [d] S. Gonell, E.Peris *ACS Catal*. **2014**, *4*, 2811.
67. [a] A. Prades, M. Poyatos, J.A. Mata, E. Peris *Angew Chem Int Ed Engl.* **2011**, *50*, 7666; [b] H. Valde´s, M. Poyatos, E. Peris *Organometallics*. **2013**, *32*, 6445.
68. G. Ciamician, *Science* **1912**, *36*, 385.
69. P. Kln, J. Wirz, *Photochemistry of Organic Compounds*, Wiley, Chichester, **2009**.
70. [a] N. Hoffmann, *Chem. Rev.* **2008**, *108*, 1052; [b] T. Bach, J. P. Hehn, *Angew. Chem.* **2011**, *123*, 1032; [c] T. Bach, J. P. Hehn,*Angew. Chem. Int. Ed*. **2011**, *50*, 1000; [d] C.L. Ciana, C. G. Bochet, *Chimia* **2007**, *61*, 650; [e] A. Albini, M. Fagnoni, *Handbook of Synthetic Photochemistry* Wiley-VCH, Weinheim, **2010**
71. R. A. Sheldon, I. Arends, U. Hanefeld, *Green Chemistry and Catalysis,* Wiley-VCH, Weinheim, **2007.**
72. [a] B. M. Trost, *Angew. Chem.* **1995**, *107*, 285; [b] B. M. Trost, *Angew. Chem. Int. Ed. Engl.* **1995**, *34*, 259
73. A. Heumann, M. Chanon, *Applied Homogeneous Catalysis with Organometallic Compounds*, Wiley-VCH, Weinheim, **2002**.
74. [a] E. Gómez Alvarez, H. Wortham, R. Strekowski, C. Zetzsch, S. Gligorovski *Environmental Science & Technology*. **2012**, *46*, 1955. [b] Y. Zhang, TS. Lee, JL. Petersen, C. Milsmann *J. Am. Chem. Soc.* **2018**, *140*, 5934.
75. D. M. Hedstrand, W. H. Kruizinga, R. M. Kellogg, *Tetrahedron Lett*., **1978**, *19*, 1255
76. D. A. Nicewicz, D. W. C. MacMillan, *Science*, **2008**, *322*, 77.
77. M. A. Ischay, M. E. Anzovino, J. Du, T. P. Yoon, *J. Am. Chem. Soc.,* **2008**, *130*, 12886.
78. C. K. Prier, D. A. Rankic, D. W. C. MacMillan, *Chem. Rev.,* **2013**, *113*, 5322.
79. D. M. Arias-Rotondo, J. K. McCusker, *Chem. Soc. Rev.* **2016**, *45*, 5803.
80. J. Twilton, C. Le, P. Zhang, M. H. Shaw, R. W. Evans, D. W. C. Macmillan, *Nat. Rev. Chem*, **2017**, 1, 0052.
81. V.Balzani, P. Ceroni, A. Juris, *Photochemistry and Photophysics*, Wiley, **2014.**
82. H.Takeda, K. Koike, H. Inoue, O. Ishitani, *J. Am. Chem. Soc.*. **2008**, *130*, 2023-2031
83. R. Hua, J-L. Jiang, *Curr. Org. Synt.* **2007**,*4*,151.
84. S. Rajendrakumar Kalash, V. K. Lakshmanan, C-S. Cho, I. K. Park, *Biomater. Nanoarchitectonics*, **2016**,197.

85. [a] R.A. Benson, I.B. McInnes, J.M. Brewer, P. Garside, *Nat. Rev. Rheumatol.* **2015**, *11*, 1; [b] P. Lang, K. Yeow, A. Nichols, A. Scheer, *Nat. Rev. Drug Discov.* **2006**, *5*, 343; [c] T. Hirayama, K. Okuda, H. Nagasawa, *Chem. Sci.* **2013**, *4*, 1250; [d] S.C. Dodani, S.C. Leary, P.A. Cobine, D.R. Winge, C.J. Chang, *J. Am. Chem. Soc*. **2011**, *133*, 8606.
86. [a] H. G. Eckert, *Angew. Chem.*, **1976**, *88*, 565-574; [b] R. Weissleder, U. Mahmood, *Radiology*, **2001**, *219*, 316; [c] V. Ntziachristos, C. Bremer, R. Weissleder, *Eur. Radiol.*, **2003**, *13*, 195.
87. [a] A. Sorvina, C.A. Bader, M.C. Lock, D.A. Brooks, J.L. Morrison, S.E. Plush, *J. Biophotonics*, **2017**, 1; [b] C. Stringari, R. Sierra, P.J. Donovan, E. Gratton, *J. Biomed. Opt.* **2012,** *17*, 1; [c] D. Aigner, S.M. Borisov, F.J. Orriach Fernández, J.F. Fernández Sánchez, R. Saf, I. Klimant, *Talanta* **2012,** *99*, 194; [d] L. Long, X. Li, D. Zhang, S. Meng, J. Zhang, X. Sun, C. Zhang, L. Zhou, L. Wang, *RSC Adv.* **2013,** *3*, 12204.
88. [a] L.D. Lavis, R.T. Raines, *ACS Chem. Biol.* **2008,** *3*, 142; [b] N. Tayeh, T. Rungassamy, J.R. Albani, *J. Pharm. Biomed. Anal.* **2009,** *50*, 107; [c] E.P. Ippen, C.V. Shank, A. Dienes, IEEE *J. Quantum Electron.***1971**, 178.
89. [a] D. Wang, S. J. Lippard, *Nat. Rev. Drug Discovery*, **2005**, *4*, 307; [b] A. S. Abu-Surrah, M. Kettunen, *Curr. Med. Chem.,* **2006**, *13*, 1337; [c] R. Gust, W. Beck, G. Jaouen, H. Schönenberger, *Coord. Chem. Rev*., **2009**, *253*, 2742.
90. [a] A. Bergamo, G. Sava, *Dalton Trans.* **2007**, 1267; [b] F. Lentz, A. Drescher, A. Lindauer, M. Henke, R.A. Hilger, C.G. Hartinger, M.E. Scheulen, C. Dittrich, B.K. Keppler, U. Jaehde, *Anti-Cancer Drugs* **2009**, *20*, 97.
91. [a] V. Fernandez-Moreira, F.L. Thorp-Greenwood, M.P. Coogan, *Chem. Commun.* **2010**, *46,* 186; [b] F.L. Thorp-Greenwood, R.G. Balasingham, M.P. Coogan, *J. Organomet. Chem.* **2012**, *714*, 12.
92. A.L. Noffke, A. Habtemariam, A.M. Pizarro, P.J. Sadler, *Chem. Commun.* **2012**, *48*, 5219.
93. R. Agarwal, S. B. Kaye, *Nature*, **2003**, *3*, 502.
94. [a] B. K. Keppler, *Metal Complexes in Cancer Chemotherapy*, Wiley-VCH, Weinheim, **1993**; [b] G. Sava, A. Enzo, A. Bergamo, G. Mestroni, *Metallopharmaceuticals I*, **1999**, *6*, 143.
95. [a] G. Marcon, A. Casini, P. Mura, L. Messori, A. Bergamo, P. Orioli, *Met.-Based Drugs*, **2000**, *7*, 195; [b] L. Messori, G. Marcon, P. Orioli, M. Fontani, P. Zanello, A. Bergamo, P. Mura, *J. Inorg. Biochem*., **2003**, *95*, 37.
96. J.R. Friedman, J. Nunnari, *Nature* **2014**, *505*, 335.
97. C. Alvarez-Breckenridge, B. Kaur, E. A. Chiocca, *Chem. Rev.*, **2009**, *109*, 3125
98. [a] A. Gautier, F. Cisnetti, *Metallomics* **2012**, *4*, 23; [b] L. Oehninger, R. Rubbiani, I. Ott, *Dalton Trans.* **2013**, *42*, 3269
99. Y. Li, B. Liu, XR. Lu, MF. Li, LN. Ji, ZW. Mao, *Dalton Trans.,* **2017**, *46*, 11363
100. [a] PK Lee, HW Liu, SM Yiu, MW Louie, KKW Lo*, Dalton Trans.,* **2011**, *40*, 2180; [b] K.K.-W. Lo, B.T.-N. Chan, H.-W. Liu, K.Y. Zhang, S.P.-Y. Li, T.S.-M. Tang, *Chem. Commun.* **2013,** *49*, 4271; [c] A. Nakagawa, Y. Hisamatsu, S. Moromizato, M. Kohno, S. Aoki, *Inorg. Chem.* **2014,** *53*, 409; [d] C. Jin, J. Liu, Y. Chen, R. Guan, C. Ouyang, Y. Zhu, L. Ji, H. Chao, *Sci. Rep*. **2016**, 1.

101. Q.B. Pei, G. Yu, C. Zhang, Y. Yang, A.J. Heeger, *Science* **1995,** *269*, 1086.
102. [a] G. Mauthnera, K. Landfester, A.Köck, H. Brückl, M. Kast, C.Stepperd, E.J.W.List, Org. Electron. **2008,** *9*, 164. [b] A. Sandström, H.F. Dam, F. C. Krebs, L. Edman, *Nat. Commun*. **2012,** *3,* 1002.
103. S.B. Meier, D.Tordera, A. Pertegas, C. Roldan-Carmona, E. Ortì, H.J.Bolink, *Mater. Today*, **2014**, *17*, 5, 217.
104. R. D. Costa, *Light-Emitting Electrochemical Cells*, Springer **2017.**
105. S. B. Meier, D. Hartmann, D. Tordera, H. J. Bolink, A. Winnacker, W. Sarfert, *Phys. Chem. Chem. Phys.* **2012,** *14*, 10886.
106. S. van Reenen, R.A.J. Janssen, M. Kemerink, *Org. Electron.* **2011,** *12*, 1746.
107. H. J. Bolink, E. Coronado, R. D. Costa, N. Lardiés, E. Ortí, *Inorg. Chem.* **2008,** *47*, 9149.
108. M. Melchionna, P. Fornasiero, *Materials Today*, **2014**, 17, 349
109. G.G. Malliaras, J.C. Scott, *J. Appl. Phys.* **1998**, *83*, 5399.
110. E. Zysman Colman (Ed) in *Iridium(III) in Optoelectronic and Photonic Applications* Wiley-VCH, Weinheim, **2017.**
111. S. Izumi, H. F. Higginbotham, A. Nyga, P. Stachelek, N. Tohnai, P. de Silva, P. Data, Y. Takeda, S. Minakata, *J. Am. Chem. Soc.* **2020**, *142*, 1482.
112. F. Zhang, L. Duan, J. Qiao, G. Dong, L. Wang, Y. Qiu *Organic Electronics* **2012**, *13*, 1277.
113. J. Lee, H-F. Chen, T.Batagoda, C. Coburn, P. I. Djurovich,M. E. Thompson, S. R. Forrest, *Nature Materials*, **2016**, *15*, 92.
114. C. Murawski, K. Leo and M. C. Gather, *Adv. Mater.,* **2013**, *25*, 6801.
115. [a] C. Murawski, K. Leo and M. C. Gather, *Adv. Mater.*, 2013, **25**, 6801; [b] M. A. Baldo, C. Adachi, S. R. Forrest, *Phys. Rev. B*., 2000, **62**, 10967; [c] S. Reineke, K. Walzer, K. Leo, *Phys. Rev. B*, 2007, **75**, 125328.
116. S. Reineke, M. Thomschke, B. Lüssem, and K. Leo, *Rev. Mod. Phys.*, **2013**, *85*, 1245,
117. A. P. Monkman, C. Rothe, S. M. King, *Singlet generation yields in organic lightemitting diodes*, *Proc. IEEE*, **2009,** *97*, 1597.
118. D. S. M. Ravinson, M.E. Thompson *Mater. Horiz.***, 2020**,*7*, 1210
119. T-T Bui, F. Goubard, M.Ibrahim-Ouali , D. Gigmes, F. Dumur *J. Org. Chem*. **2018**, *14*, 282.

2. Red-emitting rhenium(I) complexes bearing a pyridyl pyridoannelated N-heterocyclic carbene[a]

ABSTRACT

A novel family of photoactive neutral and cationic tris-carbonyl rhenium complexes are herein described. The former have general formula *fac*-[Re(N^C:)$(CO)_3$X]^0 (**Re1–Re2**), while the latter are *fac*-[Re(N^C:)$(CO)_3$L]PF_6, where N^C: is the pyridoannelated N-heterocyclic carbene (NHC) arising from 2-(2-pyridinyl) imidazo[1,5-a]pyridinium hexafluorophosphate proligand, namely [pyipy]PF_6, and X is Cl^- (**Re1**) and Br^- (**Re2**), while L is pyridine (**Re3**) and phosphine (**Re4**). The synthetic pathway is a one-pot reaction for neutral compounds, starting from the azolium salt as the NHC source and [Re$(CO)_5$X] to yield the desired charge-neutral *fac*-[Re(pyipy)$(CO)_3$X] complexes (**Re1**–**Re2**). Subsequent halogen abstraction and addiction of the pyridine or phosphine neutral ancillary ligand yields the analogue cationic complexes as hexafluorophosphate salt (**Re3**–**Re4**). The neutral and cationic compounds display a rather similar electronic absorption spectrum in dilute CH_2Cl_2 and CH_3CN solution, respectively. Degassed samples of the **Re1** and **Re2** display moderate (Φ ≈ 1.5%) and long-lived (τ = 12.8–13.4 μs) red photoluminescence with highly structured profile independent of the nature of the ancillary halogen ligand. A similar structured profile is observed for **Re3** and **Re4**, with a long-lived excited state (τ = 19.3–30.0 μs in degassed condition). All compounds display luminescence arising from mainly triplet ligand center states (^{3}LC). Furthermore, **Re1** and **Re2** were investigated as efficient photo-initiating systems to initiate free radical polymerization. Remarkably, excellent radical polymerization profiles and final conversions are obtained under soft irradiations (LED lamp, λ_{exc} = 405 nm) by using the proposed complexes with iodonium salt and amine as photoinitiating systems (PISs) for polyethyleneglycol (PEG)-acrylate monomers.

[a] The results reported in this chapter have been published in
A. Bonfiglio, K. Magra, C. Cebrián, F. Polo, P. C. Gros, P. Mercandelli, M. Mauro, *Dalton Trans.*, **2020**, *49*, 3102; H. Chen, Y. Zhang, A. Bonfiglio, F. Morlet-Savary, M. Mauro, J. Lalevée, *ACS Appl. Polym. Mater.*, **2021**, *3*, 1,464; Z. Asbai, A. Bonfiglio, P. Mercandelli, F. Polo, M. Mauro, *Polyhedron*, **2021**, *197*, 115025.

2.1 State-of-art and introduction

Since the pioneering works of Wrighton[1] and following investigations carried out by other groups,[2] rhenium(I) diimine complexes have attracted much interest by the inorganic photochemistry community for several applications, such as photo-catalysis[3], solar energy conversion[4], bio-imaging[5] and medicine.[6]

In this framework, derivatives of general formula $[Re(N^N)(CO)_3L]^{n+}$, where N^N is a bidentate N-heterocyclic ligand such as 2,2'-bipyridine, 1,10-phenanthroline and related scaffolds, and L is either an anionic monodentate ancillary ligand (L = halogen, cyanide, alkoxy, alkynyl, etc.; n = 0) or a neutral ligand such as pyridines, phosphines, isonitriles (with n = 1), are the most investigated ones by far. Several studies have shown that these compounds display broad and featureless photoluminescence in the green-to-red portion of the electromagnetic spectrum with excited state lifetime ranging from hundreds of nanoseconds to a few microseconds time scale. The nature of the emissive excited state may vary from purely triplet metal-to-ligand charge transfer (^{3}MLCT) to ligand-to-ligand charge transfer (^{3}LLCT) and up to (sizable) triplet ligand-centered (^{3}LC) character depending on the nature and electronic properties of both the N^N and the ancillary ligand, with often a certain degree of mixing between the two states.[1,7] Hence, a metal-ligand-to-ligand character is more often associated to the emissive triplet manifold (^{3}MLLCT). Photoluminescence quantum yield (PLQY) values largely varies as well, being cationic rhenium(I) complexes typically more efficient than neutral counterparts with values almost one order of magnitude higher for the former.[8] Furthermore, neutral dinuclear species of general formula $[Re_2(\mu\text{-}X)_2(CO)_6(\mu\text{-diaz})]$, where X = halogen and diaz = 1,2-diazine type of ligands, have shown superior properties and efficient electroluminescence.[9]

However, rhenium derivatives bearing stronger σ-donating ligands with coordinating C atoms, such as N-heterocyclic carbene (NHC) type of ligands, have been surprisingly much less explored to date. Owing to their appealing electronic and chemical features, NHCs attracted a considerable attention as ligands in the field of phosphorescent emitters as well.[10] The first report describing the synthesis and photophysical investigation of Re(I)-NHC derivatives in which the NHC acted as the emissive ligand was reported by Massi and co-workers in 2011.[11] The compounds possess the general formula *fac*-$[Re(N^C:)(CO)_3X]$, where N^C: is [3-butyl-1-(2-pyridyl)benzimidazol-2-ylidene] and X is either Cl or Br, and display a moderate and relatively short-lived photoluminescence (PLQY <0.01%, τ <0.05

μs) attributed to an excited state with triplet metal–ligand-to-ligand charge transfer (^{3}MLLCT) character. This last was explained by the relative low conjugation of the NHC ligand.

A few other reports by the groups of Massi[12] and Barnard[13] described other photoactive Re(I)-NHC complexes bearing either imidazol-2-ylidene or benzimidazol-2-ylidene types of NHC and their potential use as photo-catalysts and radiopharmaceutical agents. Furthermore, a series of rhenium(I) tricarbonyl complexes bearing a pyridyl-NHC ligand was reported by Zheng and co-workers, in which the two coordinating rings were spaced by a methylene bridge.[14] In this latter case, the authors found that the interruption of the conjugation was detrimental, and the complexes resulted to be poorly emissive in both solution and solid state.

More recently, new articles by Massi group[15] showed the photolability of many Re(I)-NHC complexes in acetonitrile, limitating the estimation of their excited state redox potential. Despite the comparable lifetime in deaerated solutions (1065 ns) with the classic $[Ru(bpy)_3]Cl_2$ (1100 ns) already adopted as photocatalyst, these new complexes revealed promising applications in photoredox reactions (*Figure 2.1*).

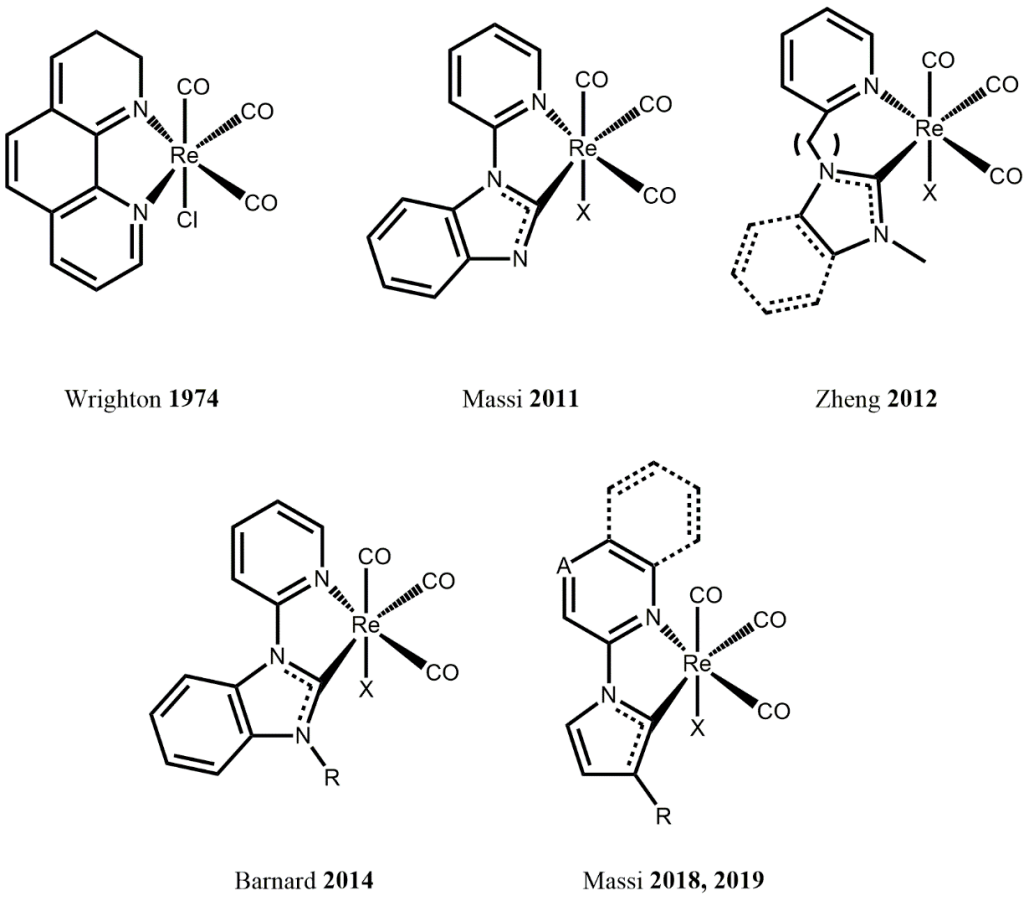

Figure 2.1 Overview of the different Re(I)-NHC complexes described in the literature.

In spite of their popularity as triplet emitters for OLED devices,[16] the use of rhenium complexes in PISs is quite scarce and mentioned in only a few works.[17] Also, the use of $Re(CO)_3(NHC)$ complexes in the field of photoredox catalysis was explored only very recently.[18]

In this chapter, the effect of employing a [1,5-a] benzannulated NHC ligand instead of a more classical benzo[d]imidazole is investigated (see *Figure 2.2*) and its influence on the electronic and excited states of the resulting rhenium(I) *tris*-carbonyl complexes. These latter have general formula *fac*-$[Re(N^C:)(CO)_3X]$ for **Re1–Re2**, and *fac*-$[Re(N^C:)(CO)_3L]PF_6$ for **Re3–Re4,** where N^C: is the pyridoannelated N-heterocyclic carbene (NHC) arising from 2-(2-pyridinyl) imidazo[1,5-a]pyridinium hexafluorophosphate proligand, namely $[pyipy]PF_6$, and X is Cl^- (**Re1**) and Br^- (**Re2**), while L is pyridine (**Re3**) and phosphine (**Re4**).

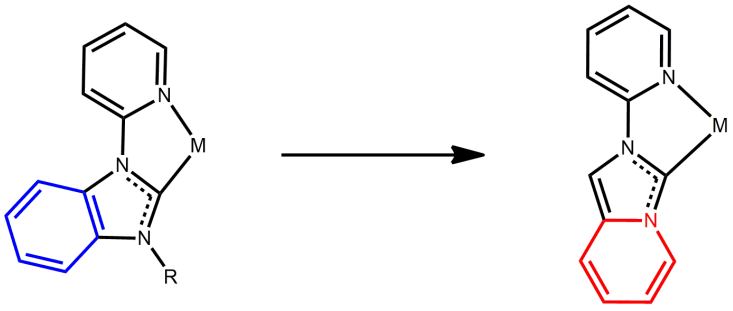

pyridin-benzo[d]imidazolylidene pyridin- imidazo[1,5-a]pyridin-3-ylidene

Figure 2.2 Comparison between pyridine-benzo[d]imidazolylidene and [1,5-a] pyridoannelated NHC ligand.

In addition, the effect of neutral *vs.* cationic nature of the complexes onto both optical and redox properties is investigated. Differently to the results previously reported on related Re-NHC complexes,[11] complexes **Re1**–**Re4** display red ligand-centred (LC) phosphorescence, which does not depend on the nature of the ancillary ligand X or L. Moreover, complexes **Re1** and **Re2** were investigated as novel photo-initiating systems in photopolymerization experiments towards 3D and 4D printed materials.

2.2 Results and discussion

2.2.1 Synthesis[b]

The two neutral rhenium(I) tricarbonyl complexes of general formula *fac*-[Re(pyipy)$(CO)_3$X], where X = Cl (**Re1**) and Br (**Re2**), were synthesized from 2-(2-pyridinyl)imidazo[1,5-a]pyridinium hexafluorophosphate, [$Re(CO)_5$X] and K_2CO_3 as the base in refluxing dry toluene under argon atmosphere. The one-pot synthesis is similar to the procedure reported in literature for related complexes.[11] Upon purification by column chromatography, the desired complexes **Re1**–**2** have been obtained as yellow powders in moderate yield. The two cationic rhenium(I) tricarbonyl complexes [Re(N^C:)$(CO)_3$L]PF_6 with L = pyridine (**Re3**) and phosphine (**Re4**) followed a stepwise reaction. De-halogenation procedure is carried out by treatment with an Ag(I) source and metathesis with a PF_6^- salt in a coordinating solvent, such as CH_3CN, yielding the intermediate solvo-complex [$Re(CO)_3$(pyipy)(CH_3CN)]PF_6. This latter is readily reacted with a monodentate ligand in THF to give the desired cationic complex as pale-yellow air-stable solids (*Scheme 2.1*).

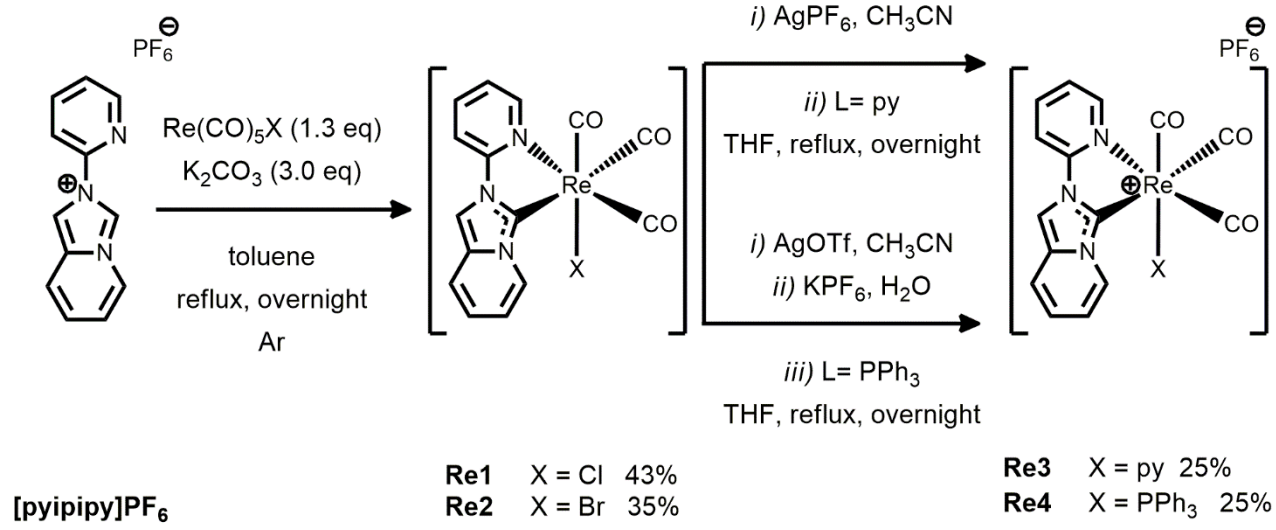

Scheme 2.1 Schematic synthetic pathway employed for the synthesis of complexes **Re1–Re2** and **Re3–Re4**.

[b] Kevin Magra, Cristina Cebrián Ávila and Philippe Gros (University of Lorraine) are kindly acknowledged for the synthesis of the pyridyl pyridoannelated carbene proligand.

The NMR spectra showed the predicted number of signals expected for the target complexes. Successful coordination of the pyipy ligand was assessed by the downfield shift of the proton resonances observed in the ^{1}H NMR of the pyridine and pyridoannelated moieties when compared to the free ligand precursor. In addition, the clear indication of the Re–NHC bond formation is provided by the complete disappearance of the pro-carbenic proton at δ = 10.17 ppm (*Figure 2.3*) as well as by the presence of four downfield resonances in the region δ = 185–198 ppm of the ^{13}C NMR spectrum (see *ES2.1-2.4 bottom*) These latter are attributable to the three C≡O and the carbenic C atoms.

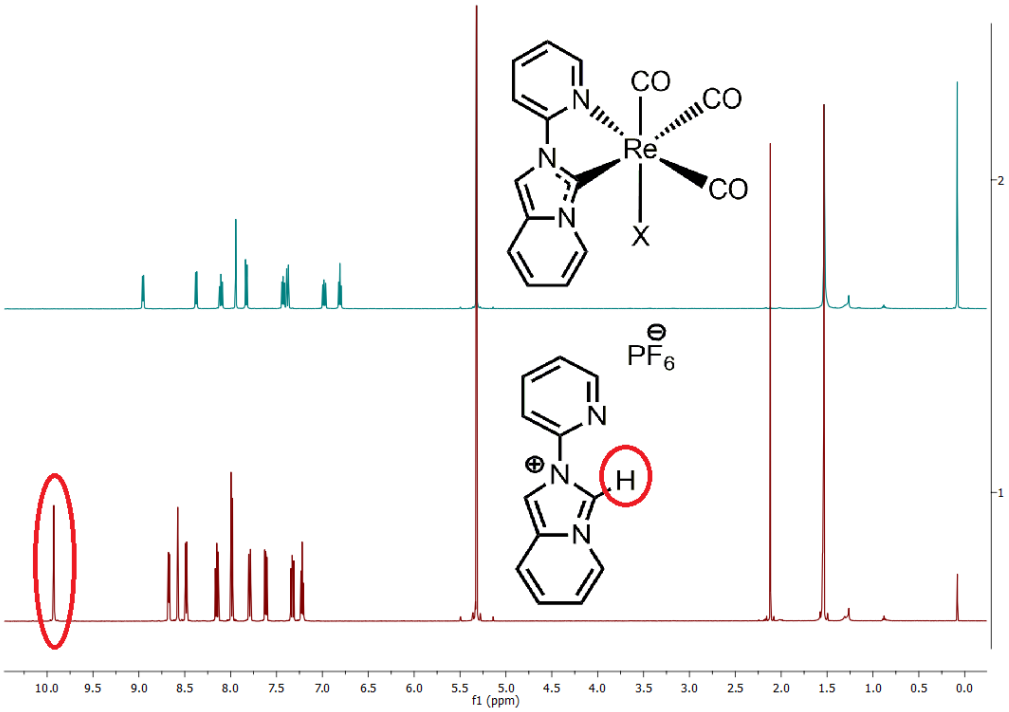

Figure 2.3 Overlap ^{1}H NMR (500 MHz, CD_2Cl_2) for **Re1** complexes and NHC pro-ligand.

Moreover, the formation of the complex with facial arrangement of the three carbonyl ligands was supported by FT-IR spectroscopy.[19] For complexes as neat powder, the vibrational spectra display three intense bands attributable to the C≡O stretching frequencies at $\tilde{\nu}$ = 2006,1905 and 1874 and 2012, 1914 and 1889 cm^{-1} for compound **Re1** and **Re2**, respectively, in agreement with previously reported investigations. For complexes **Re3** and **Re4** the C≡O stretching frequencies are reported at $\tilde{\nu}$ = 2024, 1935 and 1884 and 2039, 1960 and 1917 cm^{-1} respectively (see *Figure ES2.9-2.12*).

The position of the carbonyl IR bands is sensitive to the electron density on the metal centre (M). When the σ-bond is formed between the metal and the carbonyl carbon, the lone-pair electrons of the carbon are transferred to the empty d orbital of the metal. To

compensate the excess of electron density, a full d orbital of the metal interacts with empty π* orbital of the carbonyl bond through a process called backdonation. The larger the σ-donation of the carbonyl is, the stronger the π-backdonation will be.

However, if the metal is also bonded to a second ligand besides the carbonyl, such as a halide or neutral molecule, the metal-carbonyl bond will also be affected by the electronic density given by the second ligand to the metal. The more electronegative the second ligand is, the more electron poor the metal will be, and the π-backdonation of the metal to the CO will be less intense. This will cause a stretching and a weakening of the metal-carbonyl bond, and as consequence the IR bands will shift to lower frequencies.

In the cases described here, the frequencies of **Re1** (X = Cl) and **Re3** (L = py) are lower than **Re2** (X = Br) and **Re4** (L = PPh_3). Overall, cationic rhenium complexes have CO-infrared bands at higher energy than neutral ones as expected, because the M-L bond is weaker than M-X bond.

Single crystals of compounds grown from slow diffusion of *n*-hexane in acetone for **Re1**–**Re2**, and *n*-hexane in THF for **Re3** were found suitable for X-ray diffractometric analysis that unambiguously confirmed the atoms connectivity (see *Figure 2.4* and *ES2.19* for compound **Re1** and **Re2**, respectively and *Figure 2.5* for **Re3**). All X-ray structures display a slightly distorted octahedral geometry around the metal center with the three carbonyl ligands organized in a facial arrangement.

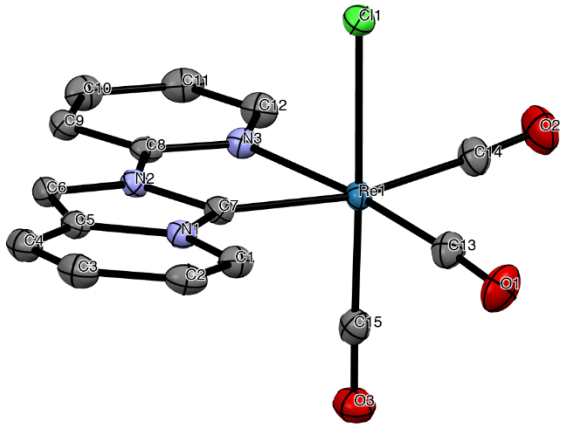

Figure 2.4 ORTEP diagram of compound **Re1** with thermal ellipsoids shown at 50% probability level obtained by single-crystal X-ray diffractometric analysis. Hydrogen atoms are omitted for clarity. Selected bond lengths (Å): Re–C(7) = 2.126(2) Å; Re–C(13) =

1.913(2) Å; Re–C(14) = 1.957(2) Å, Re–C(15) = 1.914(2) Å, Re–N(3) = 2.2085(17) Å; Re–Cl(1) = 2.5049(5) Å.

As expected, among the three carbonyl ligands, the Re–C bond in trans to the carbene possesses the longest distance due to the strong *trans* influence exerted by this latter ligand. Overall, geometrical parameters are in agreement with those Re-NHC structures previously reported.[11,20]

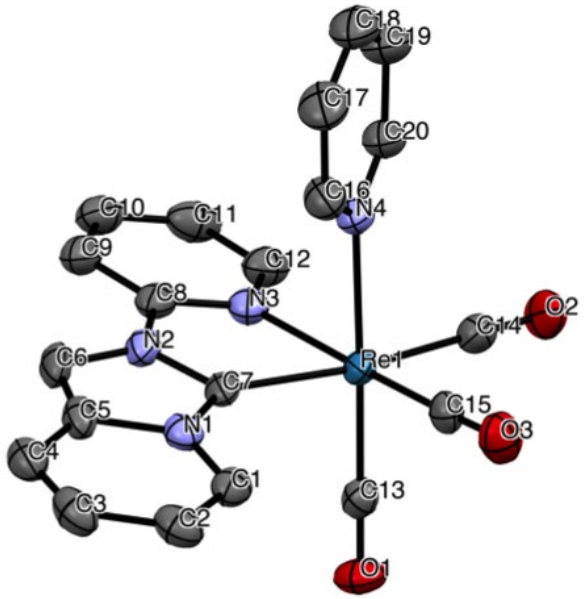

Figure 2.5 ORTEP diagram of compound **Re3** with thermal ellipsoids shown at 50% probability level obtained by single-crystal X-ray diffractometric analysis. Hydrogen atoms, PF_6^- anion and THF solvent molecule are omitted for clarity. Selected bond lengths (Å): Re–C(7) = 2.137(5) Å; Re–C(13) = 1.920(5) Å; Re–C(14) = 1.967(6) Å, Re–C(15) = 1.917(5) Å, Re–N(3) = 2.221(4) Å; Re–N(4) = 2.216(4) Å.

2.2.2 Photophysics and theoretical investigation[c]

*2.2.2.1 Neutral tricarbonyl Re(I) complexes **Re1** and **Re2***

The photophysical properties of complexes **Re1** and **Re2** were firstly investigated in dilute CH_2Cl_2 solution in both air-equilibrated and degassed condition at room temperature at concentration of 2×10^{-5} M. *Figure 2.6* displays the electronic absorption and emission spectra and *Table 2.1* summarizes the photophysical data. For both derivatives **Re1** and **Re2**, the absorption spectra show nearly identical features, thus only complex **Re1** will be described in detail hereafter.

In the UV range, an intense absorption band shows a $\lambda_{abs,max}$ = 270 nm with ε = 13.5 × 10^3 M^{-1} cm^{-1} for **Re1** corresponds to the absorption profile of the ligand [pyipy]PF_6. Computed analysis reveals that two intense electronic transitions, mainly HOMO−4 → LUMO and HOMO−2 → LUMO+2, generate the π–π* transition localized onto the annelated NHC ligand (*Figure 2.7*). The first transition is described as ligand centered (^{1}LC) because the redistribution of the electron density remains within the pyipy moiety. The second transition involves charge transfer both from the $Re(CO)_3Cl$ moiety to the ligand and from the carbene to the pyridyl ring. In the region at λ_{abs} *ca.* 400 nm, two less intense bands are present, yet partially overlapping. The band at $\lambda_{abs,max}$ = 378 nm with ε = 3.4 × 10^3 M^{-1} cm^{-1} for complex **Re1** can be attributed to the singlet manifold spin-allowed metal-halogen-to-ligand charge transfer (^{1}MXLCT) with d_π(Re)p(X) → π*(py) nature and is described as a single determinant HOMO−1 → LUMO.

[c] Dr. Pierluigi Mercandelli is kindly acknowledged for performing the theoretical investigation.

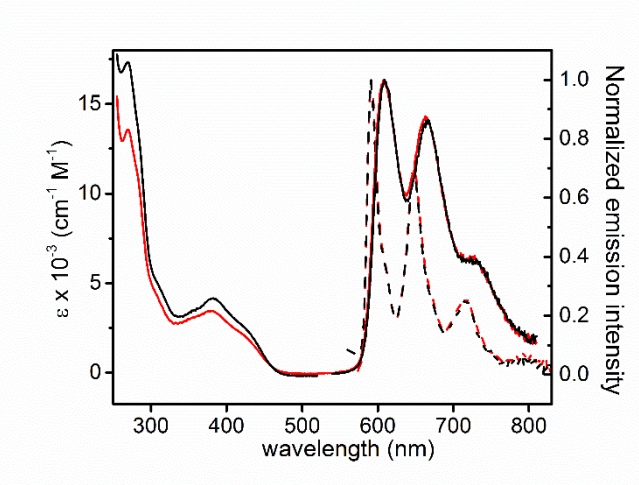

Figure 2.6 Electronic absorption and normalized emission spectra of complex **Re1** (black traces) and **Re2** (red traces) in degassed CH_2Cl_2 solution at a concentration of 2×10^{-5} M at room temperature (solid line) and 77 K (dashed line). Emission spectra were recorded upon excitation at λ_{exc} = 420 nm.

In agreement with these results, the oxidation process (O_1) is related to the oxidation of the metal-NHC moiety. A partial contribution of the M–X bond onto the oxidation process is demonstrated by the poor modulation (*ca*. 26 mV) exerted by the halogen ligand. Computed energetic levels, performed by Dr. Pierluigi Mercandelli from University of Milan, display a similar trend with a 15 meV shallower HOMO computed for **Re1** when compared to **Re2**, given the higher contribution of the bromine π orbitals in the HOMOs respect to the chlorine.

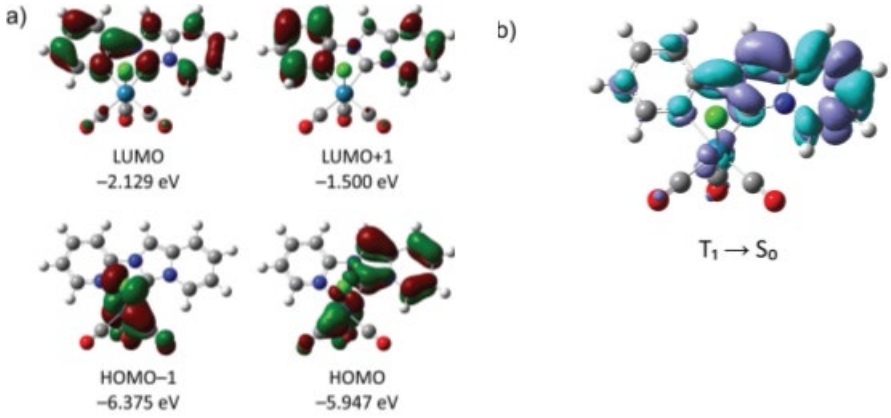

Figure 2.7 Selected DFT calculation results for compound **Re1**. (a) Isodensity surface plots and energies computed for the HOMO−1 to LUMO+1 orbitals; (b) electronic density difference maps for the vertical transition $T_1 \rightarrow S_0$, computed at the T_1 at the optimized geometry. Cyan and violet indicates a decrease and increase in electron density, respectively.

On the other hand, the lowest energy transition that appears as a shoulder at $\lambda_{abs,max}$ = 430 nm shows also a partial ^{1}ILCT character with a net charge transfer from the heterocyclic carbene ring to the pyridyl moiety and so is ascribed as an electronic transition with admixed metal-to-ligand charge transfer and intraligand charge transfer (^{1}MLCT/^{1}ILCT) character [d_π(Re)p(X)π(NHC) → π*(N^C)]. The one-electron reduction (R_1), indeed, occurs on the cyclometalating ligand. However, the more electron-rich nature of the free ligand, compared to the cyclometalating one, makes this transition less favored (35-80 mV).

The photoluminescence (PL) properties of the complexes were investigated as well, and the corresponding spectra in both degassed and air-equilibrated dilute CH_2Cl_2 are displayed in *Figure 2.6*.

Upon irradiation at λ_{exc} = 370–420 nm, complexes **Re1–2** show similar photophysical properties. The photoluminescence spectra proved to be independent of the excitation wavelength, with no evidence of photodegradation for both complexes under the employed experimental condition. Solution samples display a moderate red photoluminescence with a structured profile with maxima at λ_{em} = 608, 664 and 728 nm independently of the presence of dioxygen molecules at room temperature. The pronounced vibronic progression observed in the emission profile features a fundamental spacing in the range of *ca.* 1350 cm^{-1} and it is attributable to intraligand modes, such as ring–ring scissoring, ring–ring stretching, ring

breathing and in-plane ring deformations, as confirmed by the computed vertical transitions. This is further corroborated by the similar spacing observed in the emission spectrum of the ligand [pyipy]PF_6 that displays a structured emission at λ_{em} = 345, 362, 381 and 403 nm (see *Figure ES2.14*).

Degassing the samples yields a sizeable increase of the emission intensity and a prolongation of the excited-state lifetime, being the PLQY of 0.08% vs. 1.5% and τ = 345 ns *vs.* 12.8 μs for complex **Re1**, respectively. Similar results were obtained for complex **Re2** and the PL data are summarized in *Table 2.1*. This finding clearly supports the triplet nature of the emissive excited state. Furthermore, the two complexes display a large Stokes shift of 4080 and 3800 cm^{-1} for **Re1** and **Re2**, respectively. In sharp contrast to what observed for other classes of luminescent [Re(N^N)$(CO)_3$X] complexes characterized by a ^{3}MLCT emission,[21] the absence of any spectral shift upon halogen variation along with the smaller radiative rate constant values (k_r = 1.2 × 10^3 s^{-1} for complex **Re1**) and similar vibronic progression observed for both complexes and the [pyipy]PF_6 ligand undoubtedly suggest a ^{3}LC nature of the excited state responsible for the emission process in complexes **Re1**–**2**. To further verify the LC character, both vertical and adiabatic energies have been calculated for the $T_1 \rightarrow S_0$ and $T_2 \rightarrow S_0$ transitions displayed in *Figure 2.8*. As expected, vertical and adiabatic values are quite different, denoting the geometry difference between the triplet and ground state, (0.384 and 0.487 eV for T_1 and T_2, respectively). The adiabatic transition underestimates the experimental value raging from −0.057 eV to −460 cm^{-1}. The vertical transition is really close to the photophysical results (670 and 718 nm vs. 664 and 728 nm). These values validate heavily that the intraligand modes contribute to the vibronic emission profile.

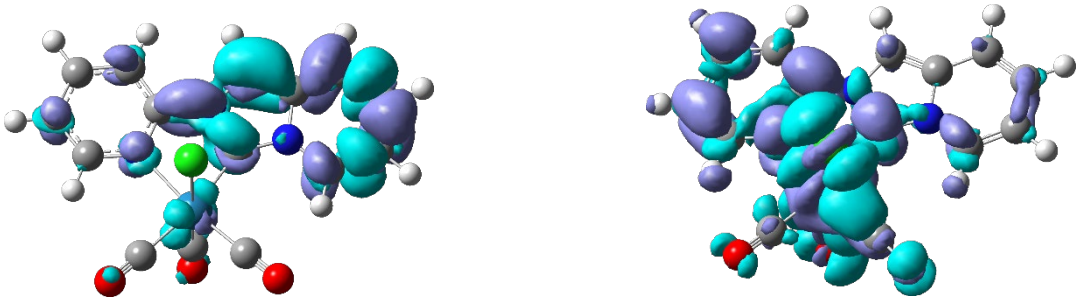

$T_1 \rightarrow S_0$

vertical transition: 1.598 eV; 776 nm

adiabatic transition: 1.982 eV; 626 nm

$T_2 \rightarrow S_0$

vertical transition: 2.344 eV; 529 nm

adiabatic transition: 2.831 eV; 438 nm

Figure 2.8 Electronic density difference maps computed (at the optimized geometry of the corresponding triplet) for the vertical transition $T_1 \rightarrow S_0$ and $T_2 \rightarrow S_0$ of *fac*-[Re(pyipy)$(CO)_3$Cl] (**Re1**). Energy computed for the corresponding adiabatic transition is also reported. The difference in energy between the T_1 and T_2 minima is 31.210 mE_h (0.849 eV; 6850 cm^{-1}).

Table 2.1 Photophysical properties of complexes **Re1**–**2** in air-equilibrated and degassed CH_2Cl_2 solution at a concentration of 2×10^{-5} M at room temperature and at 77 K in 2-MeTHF glassy matrix.

Cmpd	$\lambda_{max,abs}$ (ε) [nm, (10^3 M^{-1} cm^{-1})]	λ_{em} [nm]	PLQY (%)		λ_{obs}		k_r [a] [10^3 s^{-1}]	k_{nr} [b] [10^4 s^{-1}]	λ_{em} (77 K) [nm]
			air-equilibrated	*degassed*	*air-equilibrated*	*degassed*			
Re1	270 (13.5), 378 (3.4), 427*sh* (1.9)	608, 664, 728	0.08	1.5	345 ns	12.8 µs	1.2	7.70	590, 647, 715, 795
Re2	269 (17.3), 381 (4.1), 429*sh* (2.2)	608, 664, 728	0.06	1.4	297 ns	13.4 µs	1.0	7.36	590, 647, 715, 795

sh denotes a shoulder; [a] k_r = PLQY/ τ; [b] k_{nr} = (1 – PLQY)/τ. The $Ru(bpy)_3Cl_2$ complex in air-equilibrated water solution at room temperature was used as reference (PLQY = 0.04).[22]

Solvent effect experiments were carried out to gain deeper insights onto the nature of the low-lying absorption processes and emitting excited state. The spectra recorded in toluene, THF, CH_2Cl_2 and DMF are displayed in *Figure 2.9* and the corresponding data listed

in *Table 2.2*. Upon increasing solvent polarity, absorption spectra show a negative solvatochromism of the lower-lying band as typical of Re(I) tris-carbonyl complexes.[1] On the other hand, the highest energy emission maximum shows a minor shift from 604 to 614 nm on decreasing solvent polarity, pointing towards a small decrease of the dipole moment when going from the ground to the excited state, and indicating a negligible CT nature of the emissive excited state. Overall, these findings suggest that for both complexes upon excitation into the ^{1}MLCT band excited state relaxation induces a large electronic reorganization, funneling the energy into the lowest-lying emissive state with metal-perturbed ^{3}LC character that is localized onto the annelated NHC ligand.

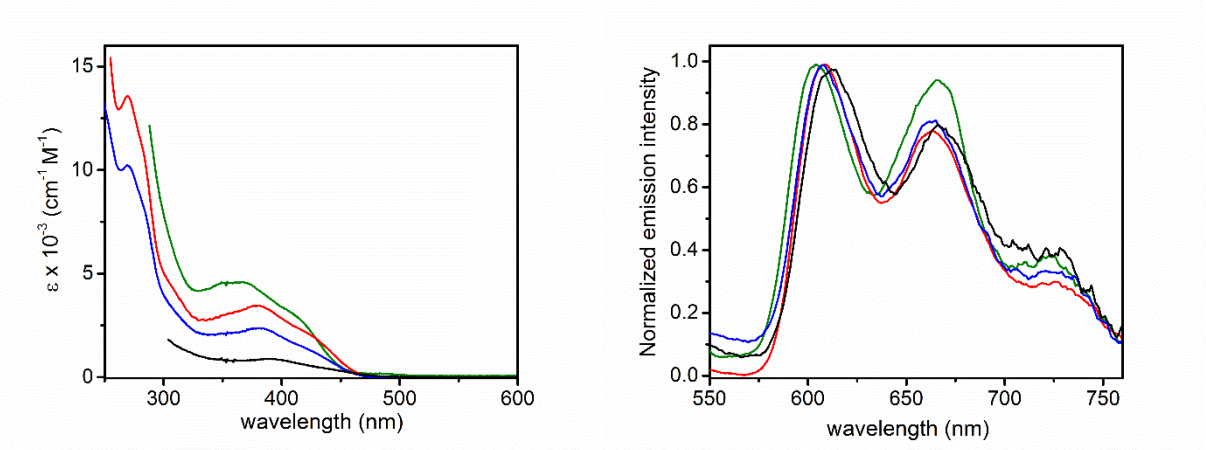

Figure 2.9 Absorption (*right*) and emission (*left*) spectra of diluted samples of complex **Re1** recorded in solvents with different polarities. DMF (green trace), CH_2Cl_2 (red trace), THF (cyan trace) and toluene (black trace).

Table 2.2 Solvent effect recorded for complex **Re1** in solvents of different polarity at a concentration of 2×10^{-5} M at room temperature.

Solvent	$\lambda_{max,abs}$ (ε) [nm, 10^3 M^{-1} cm^{-1}]	λ_{em} [nm]
Toluene	389[a]	614, 671, 732
CH_2Cl_2	270 (13.5), 378 (3.4), 427 (1.9)	608, 664, 728
THF	269 (10.1), 380 (2.3), 425 (1.2)	607, 663, 728
DMF	367 (4.5), 418 (2.6)	604, 665, 724

[a] sample not fully solubilized

*2.2.2.2 Cationic tricarbonyl Re(I) complexes **Re3** and **Re4***

The photophysical properties of complexes **Re3** and **Re4** were investigated at concentration of 2×10^{-5} M in both air-equilibrated and degassed acetonitrile solution at room temperature as well as at 77 K in 2-MeTHF glassy matrix. The electronic absorption and the normalized emission spectra are displayed in *Figure 2.10* and the corresponding photophysical data are listed in *Table 2.3*. In the UV range, an intense absorption band in observed with $\lambda_{abs,max}$ = 237 nm ($\varepsilon = 2.61\times10^4$ M^{-1} cm^{-1}) and $\lambda_{abs,max}$ = 231 nm ($\varepsilon = 4.22\times10^4$ M^{-1} cm^{-1}) for compound **Re3** and **Re4**, respectively. This band can be mainly ascribed to ligand-centered transitions localized onto the coordinated NHC-ligand in agreement with computational investigation as well as reported investigation on the neutral congeners. The additional contribution of the π-π* transitions involving the phenyl rings of the PPh_3 ligand in compounds **Re4** accounts for the increased molar extinction coefficient observed for this complex. At lower energy, the absorption band observed in the region at λ_{abs} *ca.* 400 nm is ascribed to an electronic transition with ^{1}MLCT character, namely d(Re)π(NHC) → π*(py), admixed with intraligand charge-transfer (^{1}ILCT) involving the cyclometalating ligand with π(NHC) → π*(py) nature, where NHC is the benzannulated NHC moiety and py is the pyridyl ring.

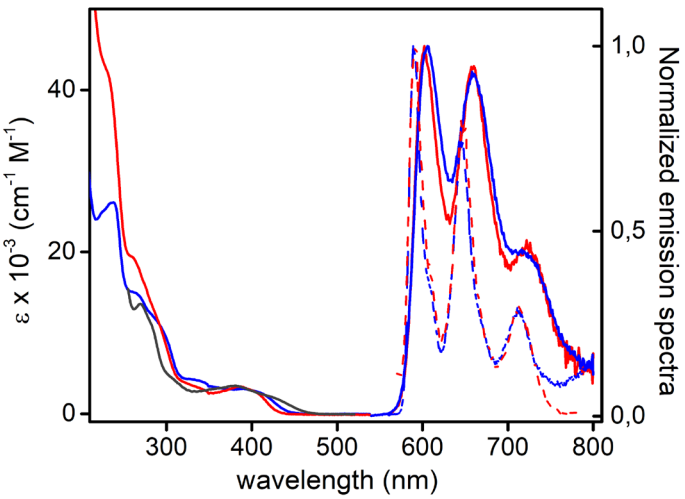

Figure 2.10 Electronic absorption and photoluminescence spectra of compound **Re3** (blue traces) and **Re4** (red traces) and in degassed CH_3CN solution at a concentration of 2×10^{-5} M at room temperature (solid line) and 77 K (dashed line). The UV-visible spectrum of the parental complex **Re1** in CH_2Cl_2 (black trace) is displayed as well for comparison. Emission spectra at 298 K were recorded upon excitation at λ_{exc} = 420 and 440 nm for compound **Re3**

and **Re4**, respectively. Emission spectra at 77 K were recorded upon excitation at λ_{exc} = 400 and 420 nm for compound **Re3** and **Re4**, respectively.

The DFT calculation confirmed these findings. In **Re3** the rhenium d orbitals mainly contribute to the four highest occupied molecular orbitals, close-lying in energy. The HOMO and HOMO–3 are the two combinations (anti-phase and in-phase, respectively) of one of the d orbitals and the highest lying π orbital of the heterocyclic carbene moiety. On the contrary, the HOMO–1 and HOMO–2 do not show contributions from the organic ligand. In these four orbitals no contribution from the pyridine ancillary ligand is present. Lying at lower energy, HOMO–4 is a ligand π orbital extended over both the pyridyl and the heterocyclic carbene rings. The lowest unoccupied molecular orbital is a π* orbital delocalized all over the pyridylcarbene ligand. In addition, the LUMO+1 shows a substantial contribution from the lowest π* orbital of the pyridine ancillary ligand (*Figure 2.11*).

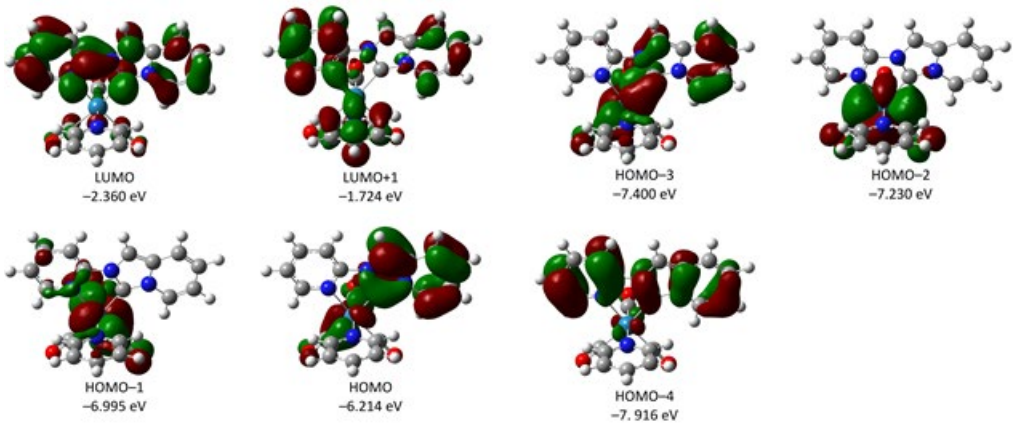

Figure 2.11 Isodensity surface plots and energies computed for some relevant molecular orbitals of **Re3**.

Upon irradiation at the ^{1}MLCT band, complexes **Re3** and **Re4** show similar photophysical properties. The photoluminescence spectrum of both samples in degassed CH_3CN show a structured emission with maxima at λ_{em} = 602 and 606, 660 and 725 nm at room temperature that are Stokes shifted by *ca.* 6500 and 6650 cm^{-1} for **Re3** and **Re4**, respectively. The photoluminescence profile is independent of the presence of dioxygen molecules and excitation wavelength. Furthermore, similar vibronic progression is observed with fundamental spacing of *ca.*1350 cm^{-1} that is attributable to intraligand modes of the

cyclometalatated pyipy scaffold. Upon removing dioxygen, increase of the photoluminescence quantum yield (PLQY) values (from 0.14% to 0.72%) as well as prolongation of the excited-state lifetime (from τ = 204 ns to 19.3 µs) is observed for compound **Re3**. Likewise, PLQY and lifetime increase from 0.04% to 1.60% and τ = 209 ns to 30.0 µs, respectively, for derivative **Re4**. Going from room temperature to 77 K glassy matrix, the photoluminescence spectra display a minor hypsochromic shift and band profile becomes even more structured. Overall, these findings along with the small k_r values, being in the range 3.8–5.3×10^3 s^{-1}, are indicative for an excited state with largely triplet ligand-centered (^{3}LC) character, in agreement with related complexes **Re1**–**2**.

The electron density difference map computed for the cationic species **Re3** shows an enhanced LC character of the emission with respect to the neutral species **Re1**, in agreement with an increased contribution of the π orbital of the carbene ligand to the HOMO (69% and 52% in **Re3** and **Re1**, respectively).

The adiabatic energy computed for the $T_1 \rightarrow S_0$ transition slightly underestimate the experimental value (624 vs 606 nm, corresponding to a difference of –0.058 eV or –464 cm^{-1}). The vibrationally resolved emission spectra computed within the framework of the Franck-Condon principle reproduces reasonably well the observed additional maxima (673 and 752 nm vs 660 and 725 nm). As expected for a LC transition, the normal mode primarily contributing to the vibronic structure of the band is an IL one, and, in particular, an in-plane ring deformation (*Figure 2.12*).

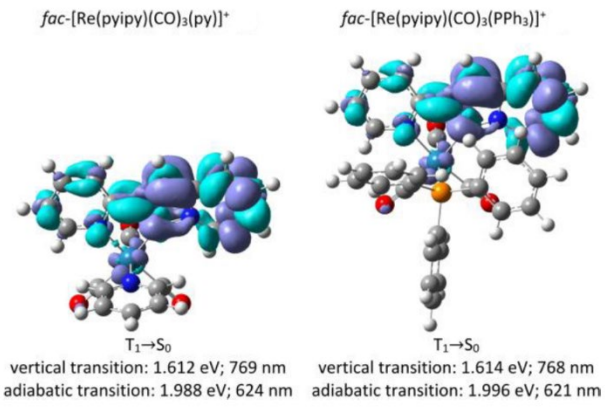

Figure 2.12 Electronic density difference maps computed (at the optimized geometry of the corresponding triplet) for the vertical transition $T_1 \rightarrow S_0$ of **Re3** and **Re4**. Energy computed for the corresponding adiabatic transition is also reported. Cyan and violet indicates a decrease and increase in electron density, respectively.

Table 2.3 Photophysical data for complexes **Re3** and **Re4** recorded in air-equilibrated and degassed CH_3CN solution at room temperature and 77 K 2-MeTHF glassy matrix.

Cmpd	$\lambda_{max,abs}$ (ε) [nm, (10^3 M^{-1} cm^{-1})]	λ_{em} [nm]	PLQY (%)		λ_{obs}		k_r [a] [10^3 s^{-1}]	k_{nr} [b] [10^4 s^{-1}]	λ_{em} (77 K) [nm]
			air-equilibrated	*degassed*	*air-equilibrated*	*degassed*			
Re3	405 (2.77), 339 (4.07), 265 (14.88), 237 (26.09)	606, 660, 725	0.14	0.72	204 ns	19.3	3.79	5.23	592, 647, 710
Re4	394 (3.00), 329 (3.53), 261 (19.29), 231 (42.15)	602, 660, 725	0.04	1.60	209 ns	30.0 μs	5.33	3.28	592,647, 710

The $Ru(bpy)_3Cl_2$ complex in air-equilibrated water solution at room temperature was used as reference (PLQY = 0.04).[22]

2.2.3 Electrochemistry[d]

The electrochemical behaviour of **Re1–Re4** was assessed by cyclic voltammetry (CV) in N,N-dimethylformamide (DMF)/0.1 M tetra-n-butylammonium perchlorate (TBAP), performed by Dr. Federico Polo from University of Venice. The data are listed in *Table 2.4*.

*2.2.3.1 Neutral tricarbonyl Re(I) complexes **Re1** and **Re2***

Complexes **Re1** and **Re2** showed very similar features (see *Figure 2.13*) as both compounds underwent an irreversible oxidation process (O_1) at E_{ox1} = +1.151 and +1.177 V vs. SCE, respectively, and one main irreversible reduction process (R_1) at E_{R1} = −1.586 and −1.543 V vs. SCE, respectively. Owing to the lower π-acidity of the NHC ligand when compared to the pyridine,[23] O_1 occurs at less positive potentials than that of benchmark complex [Re(bpy)$(CO)_3$Cl], while R_1 was observed at more negative values due to the decreased π-accepting strength of the chelating ligand in compounds **Re1**–**Re2**.[24] R_1 can be ascribed to the one-electron reduction of the cyclometalating ligand, which was less favored (35–80 mV) than that of the free ligand owing to the more electron-rich nature of this latter upon carbene formation.

[d] Dr. Federico Polo is kindly acknowledged for performing the electrochemical analysis.

Since more reduction processes are present, R_2 (at about E_{R2} = −1.900 V) and R_3 (at about E_{R3} = −2.050 V), the other peaks can be related to the dissociation of the halide ligand or secondary chemical reaction. The effect of the scan rate was investigated over the range 50–500 mV s^{-1}, and the peak current was found to depend linearly on the square root of scan rate for both **Re1** and **Re2**. These data are in agreement with the occurrence of a diffusion-controlled heterogeneous electron transfer reaction, followed by a very fast chemical reaction (EC process).[25]

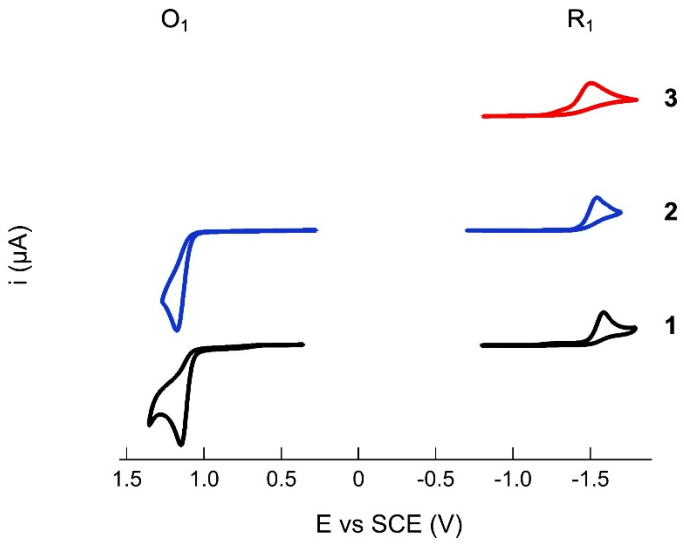

Figure 2.13 Blank-subtracted CVs recorded for 1 mM of compounds **Re1** (trace1), compound **Re2** (trace 2) and ligand [pyipy]PF_6 (trace 3) in DMF/0.1 M TBAP. Scan rate: 0.1 V s^{-1}.

*2.2.3.2 Cationic tricarbonyl Re(I) complexes **Re3** and **Re4***

Complexes **Re3** and **Re4** showed the same pattern previously observed for neutral parental complexes **Re1** and **Re2**. In fact, as displayed in *Figure 2.14*, compound **Re3** and **Re4** showed an irreversible oxidation process (O_1) at E_{O1} = +1.340 V and +1.391 V, and one main irreversible reduction process (R_1) at E_{R1} = –1.285 V and –1.479 V for **Re3** and **Re4**, respectively. The redox potential values for both O_1 and R_1 processes of **Re3** and **Re4** are shifted anodically, compared to **Re1** and **Re2**, due to the overall cationic character of rhenium(I) complex upon substitution of chloride with the neutral pyridine or triphenylphosphine ancillary ligand. In fact, O_1 and R_1 are related to the oxidation of the metal-NHC moiety and to the reduction of the chelating NHC ligand, respectively. With respect to **Re3**, O_1 occurs at more positive potentials (*ca.* 200 mV) than that of **Re1** and

Re2. Instead, with respect to **Re4**, O_1 occurs at even more positive potential compared to **Re3** (*ca.* 50 mV), whereas R_1 is sizeably shifted cathodically (*ca.* 200 mV), owing to the triphenylphosphine ligand.

The electrochemical bandgap (2.63 eV for **Re3** and 2.87 eV for **Re4**) is in qualitative agreement with the optical bandgap observed in the UV-visible spectrum going from the neutral complex **Re2** to the cationic derivatives **Re3** and **Re4**, as demonstrated by the hypsochromic shift of the onset of the ^{1}MLCT band recorded for these latter.

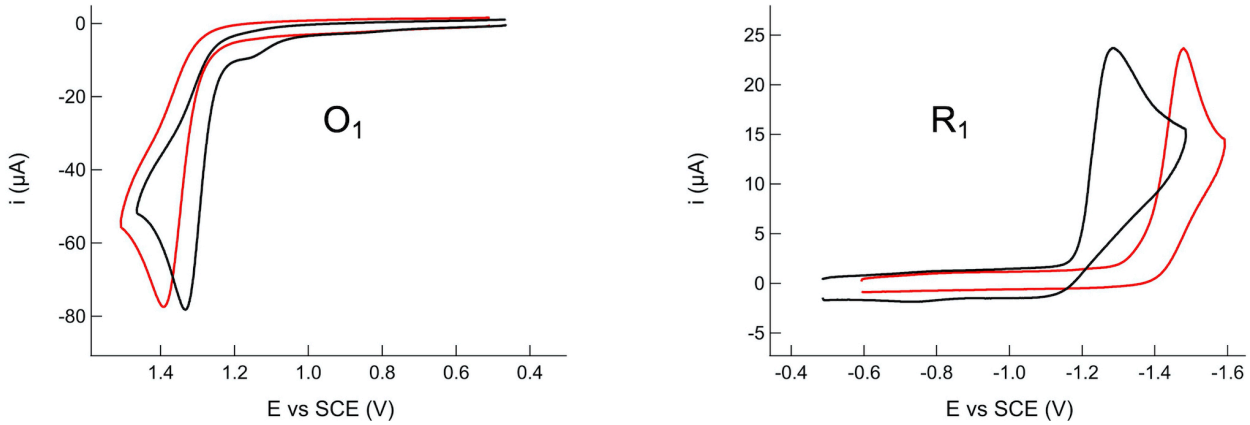

Figure 2.14 CVs recorded showing O_1 and R_1 redox processes for 1 mM of compounds **Re3** (black) and **Re4** (red) in DMF/0.1 M TBAP. Scan rate: 0.2 V s^{-1}.

Table 2.4 Electrochemical data for compound **Re3** and **Re4** obtained by cyclic voltammetry (CV) carried out in DMF and 0.1 M TBAP as the supporting electrolyte. Data for compound **Re1**–**Re2** and the chelating ligand [pyipy]PF_6 are also reported for comparison.

Cmpd	$E_{p\|O1}$ [V] [a]	$\Delta E_{p/2\|O1}$ [mV] [b]	$E_{p\|R1}$ [V] [a]	$\Delta E_{p2\|R1}$ [mV] [b]	*Gap* [eV]
Re1	+1.151	46	-1.586	54	2.737
Re2	+1.177	55	-1.543	60	2.720
Re3	+1.340	51	-1.285	54	2.625
Re4	+1.391	54	-1.479	54	2.870
[pyipy]PF_6			-1.507	88	

[a] Potential values are referred to SCE at the scan rate of 0.1 Vs^{-1}. [b] $\Delta E_{p/2}$ is defined as E_p-$E_{p/2}$, where $E_{p/2}$ is the potential value when the current i is at half its peak value, i_p, for the processes under investigation (O_1 or R_1, respectively).

2.3 Application in photopolymerization[e]

Thanks to the relatively intense visible light absorption, long-lived excited states, and suitable redox potentials, these compounds appear to be good candidates for a new type of photocatalytic systems (PCs), in particular for photopolymerization experiments.[26] In this framework, several ruthenium(II)[27], iridium(III)[28], platinum(II)[29] and copper(I)[30] complexes have been used as photo initiating system (PISs), working in the presence of other additives under visible light irradiation in the polymer photochemistry field (*Figure 2.15*).

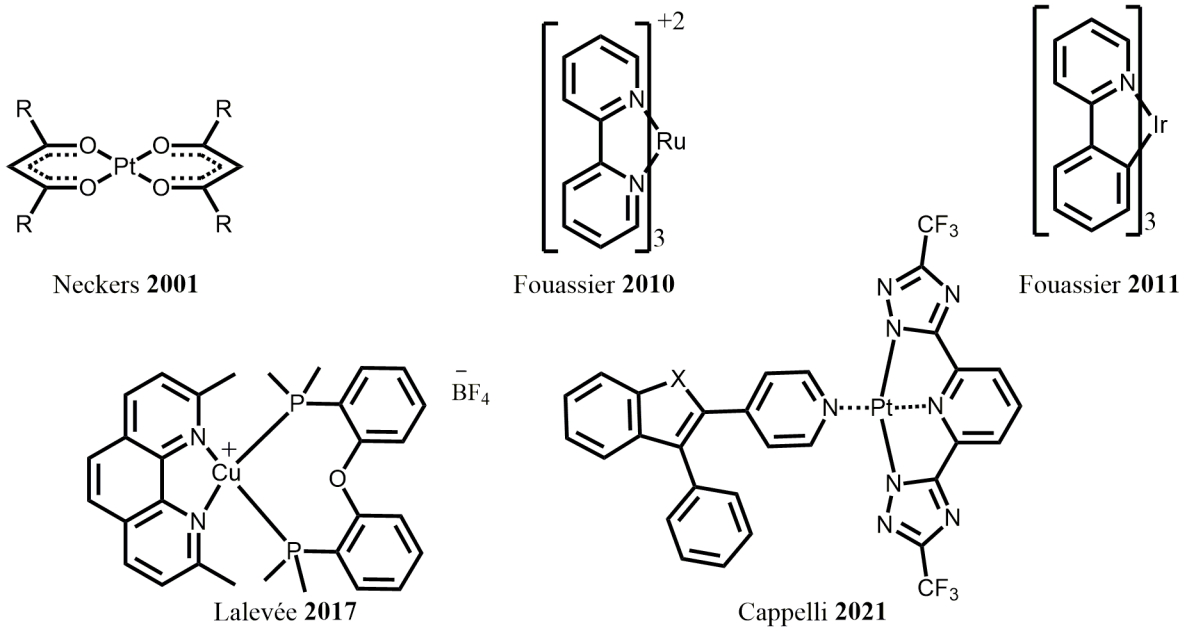

Figure 2.15 Selected examples of metal complexes used in photocatalytic systems for photopolymerization.

The photocatalytic behaviour of the compounds **Re1** and **Re2** were investigated in the frame of a collaboration with Prof. Jacques Lalevée's group from University of Haute Alsace (Mulhouse, France).

A photocatalyst is a species which is optically excited to its higher electronic energy level and provides energy to a reacting substance, participating and making chemical reactions occur. The photocatalyst is regenerated after each cycle of such interaction.[31]

[e] Jacques Lalevée's group is acknowledged for performing photopolymerization experiments.

A polymerization is a reaction where many monomer units are added to each other to form a macromolecule. The first step is usually obtained by the decomposition of an initiator via thermal or optical processes producing ions or free radicals, named generally initiating species. These latter attack the first monomer unit to start a chain reaction. Monomers or oligomers are usually not sensitive to light and thus the addition of a photoinitiator (PI) is at least necessary. The mechanism for free-radical polymerization is the following (*Scheme 2.2*):

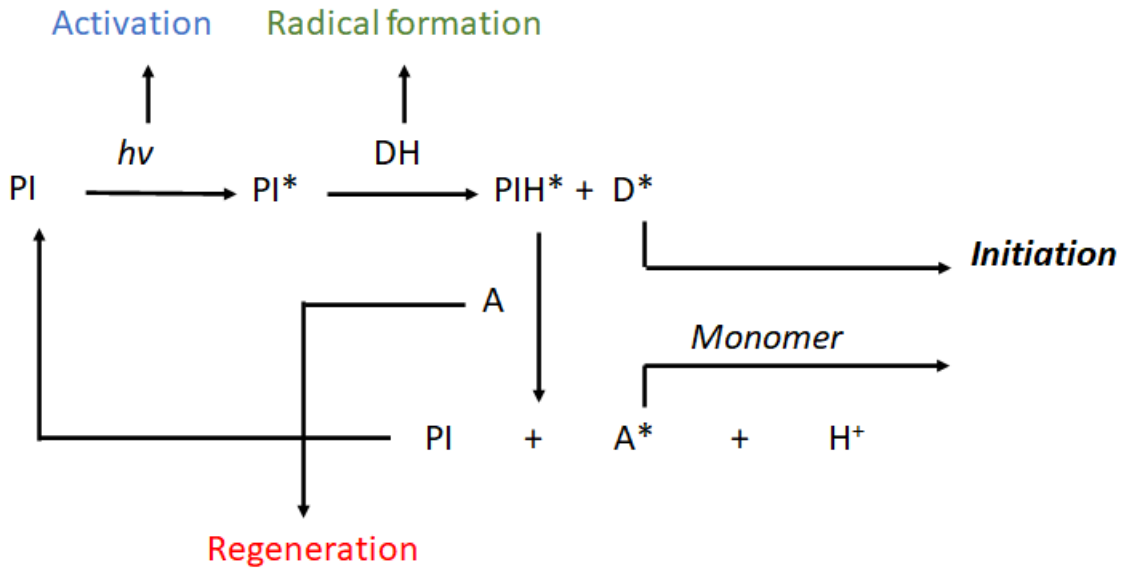

Scheme 2.2 General mechanism for free radical polymerization.

The photoinitiator (PIs) or photoinitiating systems ((PISs) play a pivotal role in the photopolymerization process for its ability to generates reactive species by absorption of selective wavelengths of light, which finally induces the liquid monomer to solid polymer transformation.[32] The main challenge to design high-performance organometallic PIs is to create a molecule able to work under air and low intensity of light sources, including visible light exposures. A promising PIs must have high molar extinction coefficients in the visible light region, displaying outstanding absorption properties and a good capacity to incorporated additives (*e.g.*, Iod or methyldiethanolamine, MDEA); the absorption spectra has to match the emission spectra of the irradiation sources and lastly, the excited states should leave sufficiently long to efficiently interact with substrates and/or additives.[33] This also means that a long lifetime is recommended to facilitate the photocatalytic reaction.

As already mentioned, several other metals have been employed as photocatalyst in most of redox reactions and, specifically in photopolymerization. Beside the stability to air

and moisture from rhenium complexes, they are little exploited so far for reactions different from catalytic CO_2 reduction. Although it is well known that iridium and ruthenium complexes are more stable than rhenium ones, given the longer lifetime of **Re1** – **Re4** complexes compared to Ir^{III} and Ru^{II}, $\tau \approx 12–30$ µs *vs.* 1-5 µs, respectively, we decided to preliminarily investigate the two new neutral compounds as components in PISs for photopolymerization experiments. Both rhenium(I) complexes, **Re1** and **Re2** acted as photoredox catalytic systems in light-promoted polymerization reactions for polyethyleneglycol (PEG)-acrylate monomers.[34]

An efficient radical polymerization profiles and final conversions are obtained under soft irradiation by using the proposed complexes with iodonium salt and amine (EDB, ethyl-4-(dimethylamino) benzoate) as PISs, following the proposed mechanism herein described (*Scheme 2.3*).

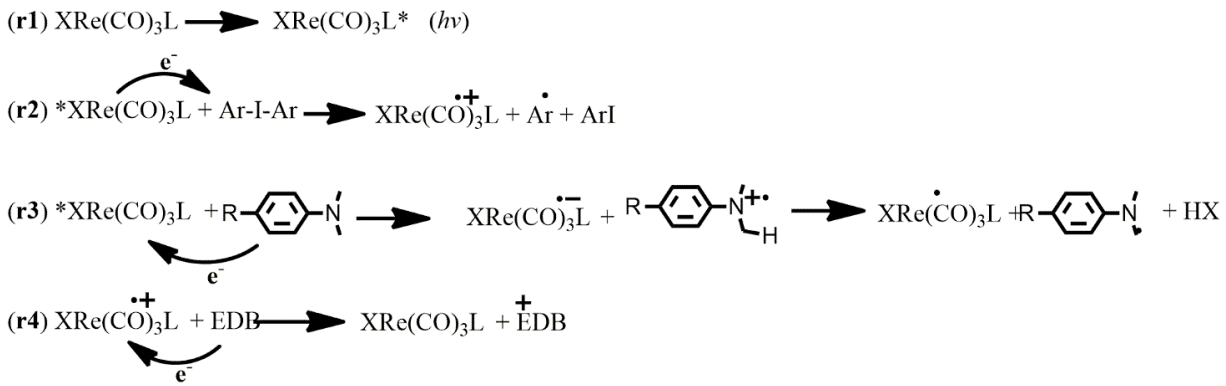

Scheme 2.3 Proposed mechanisms for the rhenium complexes/Iod/Amine redox PIS.

As displayed in *Figure 2.16* exciting at 405 nm by LED lamp, only the absorption Re characteristic peak near 380 nm is reduced with 1 min, while other two absorption peaks at 350 and 450 nm referred to Re/Iod-based systems gradually increase. The absorption peaks for Re/amine system at 380 and 430 nm significantly decrease with light irradiation, suggesting that EDB, as N-aromatic electron donor, transfers electrons to Re to form $EDB^{\bullet+}$ radicals. The reaction yield between the complex and additives (Iod and amine) determines the reactivity, thus the rate of free radical formation.[35]

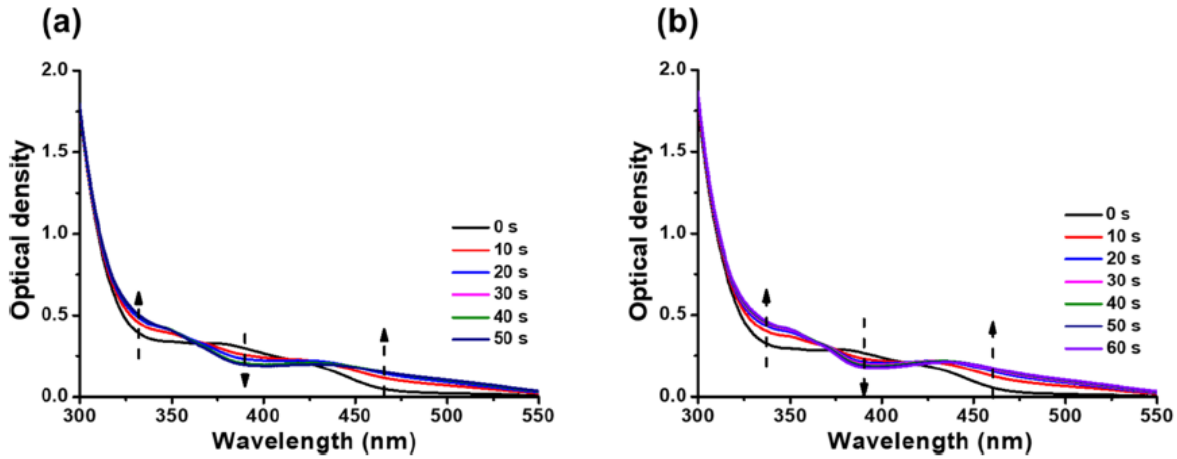

Figure 2.16 Photolysis of complexes **Re1** (a) or **Re2** (b) (1 × 10^{-5}% w/w) / iodonium salt (1.5×10^{-4}%, w/w)-based two-component PIS exposure to LED (λ_{exc} = 405 nm) in air in dichloromethane.

The efficiency in initiating free radical polymerization (FRP) both in thin[i] and thick[ii] films for PEG-diacrylate monomers under air upon irradiation with the LED@405 nm is better for rhenium complex/Iod/amine photoinitiating systems (PISs) than blank (iod/amine) (**Re1**= 64% [i] / 94% [ii] **Re2**= 61% [i] / 94% [ii] *vs* 49% [i] / 89% [ii]). Consequently, the polymerization rate is faster using rhenium complexes (≈ 50 s *vs* 200 s), demonstrating that the rhenium complexes have a significant effect on improving the photopolymerization efficiency.

Photopolymerization based 3D printing technology such as stereolithography and digital light processing require innovations related to polymer chemistry. In this regard, 3D laser writing experiments in air by a combination of rhenium complex/Iod/amine (0.1%/ 1.5%/1.5%, w/w/w)-based PIS and the PEG-DA monomer were carried out to confirm the high efficiency of the novel PIS based on **Re1** or **Re2**/Iod/amine for FRP process in 3D.

The space control experiments carried out on the 3D printed hydrogels by photopolymerization reveal a two-way reversible shape-memory effect through thermal response and water response using as Re/Iod/amine-based PIS-induced polymers. On the contrary, any shape memory effect was observed using the blank control, where Iod and EDB were used only (*Figure 2.17*).

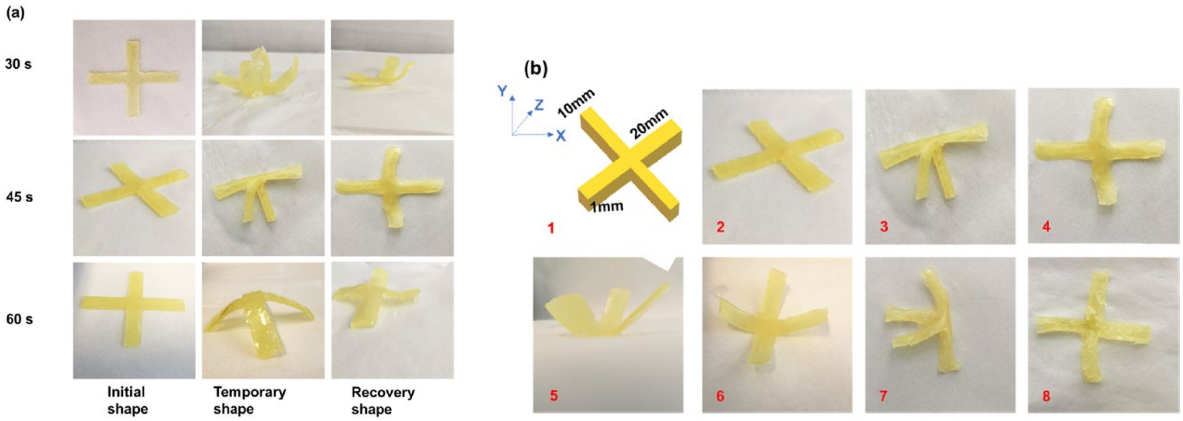

Figure 2.17 Swelling- and dehydration-induced actuation of the PEG polymer initiated by **Re1**/Iod/EDB irradiation at 405 nm. (a) Shape memory effect of the cross for the different light exposure times; (b) reversible deformation process of the cross at 405 nm:
(1) the designed geometry of the cross; (2) cross of the PEG polymer after 45 s light irradiation; (3) cross after soaking in water for 120 s; (4) cross after dehydration for 100 s (heating at 80°C); (5) cross after dehydration for 300 s (heating at 80°C); (6) cross after cooling at room temperature for 600 s; (7) cross after soaking again in water for 120 s; and (8) cross after dehydration again for 100 s (heating at 80 °C).

2.4 Conclusion

In this chapter, it is described the synthesis and characterization of a novel class of four tricarbonyl rhenium(I) complexes bearing a pyridyl pyridoannelated N-heterocyclic carbene as the chromophoric ligand. A comparison between the neutral **Re1** and **Re2** with the cationic **Re3** and **Re4** was made in terms of optical and electronic properties. For three derivatives the coordination of the NHC chelate was unambiguously confirmed by determining the single-crystal X-ray structure. Differently to what observed for other Re(I)-NHC counterparts reported previously, the complexes investigated herein display a stable and long-lived, ligand-centered, red phosphorescence. Assignments of the nature of the electronic transitions involved in both absorption and emission processes were corroborated by TD-DFT calculations and computed results agreed nicely with experimental findings. The electrochemical properties were investigated as well and cyclic voltammograms feature ligand centered reduction and metal-NHC centered oxidation processes for the four

complexes. Finally, our results demonstrate that the combination of strongly σ-donor and weakly π-acceptor NHC ligands with the tricarbonyl Re(I) core provide photoactive complexes with interesting photophysical and redox properties that might be exploitable in photopolymerization. Indeed, the two neutral complexes **Re1** and **Re2** were further investigated as new efficient photocatalyst for the PEG-diacrylate photopolymerization. The results revealed better polymerization rate and two-way reversible shape-memory (thermal and water response) for the new Re/Iod/amine based PIS-induced polymers compared to the blank, Iod/amine, where any shape memory was observed.

2.5 Experimental section

2.5.1 General considerations

Rhenium pentacarbonyl chloride was purchased from Acros, rhenium pentacarbonyl bromide[36] and the ligand [pyipy]PF_6[37] were prepared accordingly to a procedure published elsewhere. All procedures involving rhenium complexes were carried out under an argon atmosphere using standard Schlenk techniques. Silica gel for column chromatography was purchased from Sigma-Aldrich.

*2.5.2 Synthesis of neutral **Re1** and **Re2***

A solution of dry toluene was bubbled with argon for a few minutes prior addition of 3 eq. of K_2CO_3, 1.3 eq. of $Re(CO)_5X$ and 1 eq. of the ligand [pyipy]PF_6. The reaction was refluxed overnight under argon. After cooling, the mixture was extracted with CH_2Cl_2 and distilled H_2O. The organic phase was then dried over Na_2SO_4 and the solvent evaporated. The crude was purified by column chromatography using a mixture of CH_2Cl_2:CH_3CN (10:1) for X = Cl (R_f = 0.5) and pure CH_2Cl_2 for X = Br (R_f = 0.8). The desired products were obtained as yellow powders.

***fac*-[Re(pyipy)(CO)$_3$Cl] (Re1).** (65 mg, 0.13 mmol) 43% yield. ^{1}H NMR (500 MHz, 298 K, CD_2Cl_2) δ: 8.96 (dd, J = 5.5, 0.9 Hz, 1H), 8.38 (dd, J = 7.3, 0.8 Hz, 1H), 8.11 (td, J = 8.2, 1.6 Hz, 1H), 7.94 (s, 1H), 7.83 (d, J = 8.3 Hz, 1H), 7.43 (ddd, J = 7.4, 5.6, 0.9 Hz, 1H), 7.39 (d, J = 9.4 Hz, 1H), 6.99 (dd, J = 9.2, 6.5 Hz, 1H), 6.83–6.79 (m, 1H).^{13}C{^{1}H} NMR (125.77 MHz, 298 K, CD_2Cl_2) δ: 199.1, 198.2, 188.3, 185.8, 154.3, 153.4, 141.7, 132.9, 128.8, 125.1, 124.8, 118.2, 116.0, 113.5, 106.5. ESI-MS calcd for $C_{15}H_9ClN_3NaO_3Re$: 523.9773. Found

for ([M + Na]$^+$): 523.9769. Anal. calcd for $C_{15}H_9ClN_3O_3Re$: C 35.97 H 1.81 N 8.39. Found C 34.88 H 1.89 N 7.99. FT-ATR-IR (neat powder): 2006(s), 1905 (br), 1874(br) (*v* CO) cm^{-1}.

***fac*-[Re(pyipy)(CO)$_3$Br] (Re2).** (55 mg, 0.10 mmol) 35% yield. ^{1}H NMR (500 MHz, 298 K, CD_2Cl_2) δ: 8.97 (dd, J = 5.5, 0.9 Hz, 1H), 8.36 (dd, J = 7.3, 0.9 Hz, 1H), 8.16–8.12 (m, 1H), 7.94 (s, 1H), 7.84 (d, J = 8.3 Hz, 1H), 7.44–7.40 (m, 2H), 7.01 (dd, J = 9.3, 6.5 Hz, 1H), 6.83–6.80 (m, 1H).^{13}C{^{1}H} NMR (125.77 MHz, 298 K, CD_2Cl_2) δ: 198.6, 197.6, 187.8, 184.9, 154.5, 153.4, 141.6, 133.0, 128.8, 125.2, 124.7, 118.2, 160.0, 113.5, 106.4. ES-MS calcd for $C_{15}H_9BrN_3KO_3Re$: 583.8998. Found for ([M + K]$^+$): 583.8981. Anal. calcd for $C_{15}H_9BrN_3O_3Re$: C 33.04 H 1.66 N 7.71. Found C 32.46 H 1.71 N 7.48. FT-ATR-IR (neat powder): 2012(s), 1914 (br), 1889(br) (*v* CO) cm^{-1}.

*2.5.3 Synthesis of cationic complex **Re3***

Complex **Re1** (100 mg, 0.20 mmol) and $AgPF_6$ (65 mg, 0.26 mmol) were dissolved in 10 mL of CH_3CN and refluxed in the dark for 18 h. The yellow solution was filtered on Celite to remove AgCl and then the solvent was evaporated. The crude was dissolved in 5 mL of dry THF and pyridine (16 mg, 0.20 mmol) was added under an argon atmosphere. The mixture refluxed for 2 hours. After cooling down the solution, THF was evaporated, and the crude was purified on chromatographic column on SiO_2 using CH_2Cl_2 as eluent mixture. An air-stable yellow solid was obtained. Yield 25% (38 mg, 0.05 mmol).

***fac*-[Re(pyipy)(CO)$_3$Py]PF$_6$ (Re3).** ^{1}H NMR (500 MHz, 298 K, CD_2Cl_2) δ: 9.07 (ddd, J = 5.6, 1.5, 0.6 Hz, 1H), 8.49 (dd, J = 7.3, 1.0 Hz, 1H), 8.39–8.34 (m, 2H), 8.24 (m, 2H), 8.19 (d, J = 8.3 Hz, 1H), 7.83 (tt, J = 7.7, 1.5 Hz, 1H), 7.69 (ddd, J = 7.6, 5.6, 1.1 Hz, 1H), 7.64 (dt, J = 9.4, 1.0 Hz, 1H), 7.33–7.29 (m, 2H), 7.14 (dd, J = 9.4, 6.5 Hz, 1H), 7.05–7.01 (m, 1H). ^{13}C{^{1}H} NMR (126 MHz, 298 K, CD_2Cl_2) δ: 206.5, 196.9, 189.4, 180.5, 153.5, 143.7, 139.2, 133.2, 126.9, 126.2, 124.9, 119.1, 117.5, 114.8, 108.6, 53.5, 30.6. ES-MS calcd for $C_{20}H_{14}F_6N_4O_3PRe$: 545.06 Found for ([M+K]$^+$): 545.06 Anal. calcd for $C_{20}H_{14}F_6N_4O_3PRe$: C 34.84 H 2.05 N 8.13. Found C 34.12 H 2.08 N 7.87. FT-ATR-IR (neat powder): 1884(s), 1935 (br), 2024(br) (*v* CO) cm^{-1}.

*2.5.4 Synthesis of cationic complex **Re4***

For complex **Re4**, a modified version of that previously reported for the synthesis of related $[Re(CO)_3(N^N)(PPh_3)]PF_6$ derivatives was employed.[38] Complex **Re1** (100 mg, 0.2 mmol) and AgOTf (66 mg, 0.26 mmol) were dissolved in 10 mL of CH_3CN and heated at 85 °C under the dark for 12 h. The yellow solution was filtered over Celite, then concentrated until 2 mL. A volume of 5 mL of saturated aqueous KPF_6 was added dropwise to the solution. The suspension was kept stirring for 1 hour, then dried on the rotary evaporator to eliminate CH_3CN. The precipitate was filtered, washed with ethanol and diethyl ether and air-dried. The obtained solid was dissolved in 10 mL of dry THF and PPh_3 (1.0 g, 4 mmol) was added. The resulting mixture heated at 77°C for 12 h under argon. The solvent was evaporated, and the crude was purified by chromatographic column on Al_2O_3 using hexane/DCM (20:80) as eluent mixture to obtain a green oil. The oil was dissolved in 1 mL of DCM and diethyl ether was added dropwise under stirring until a solid precipitate. The solution was carefully removed with a syringe and the solid dried. An air-stable pale-green solid was collected. Yield 25% (50 mg, 0.05 mmol).

***fac*-[Re(pyipy)(CO)$_3$PPh$_3$]PF$_6$ (Re4).** ^{1}H NMR (500 MHz, CD_2Cl_2) δ: 8.46–8.43 (m, 1H), 8.29 (s, 1H), 8.18–8.13 (m, 1H), 8.00 (d, J = 8.3 Hz, 1H), 7.86 (dd, J = 7.4, 1.0 Hz, 1H), 7.52 (d, J = 9.4 Hz, 1H), 7.38 (td, J = 7.4, 1.8 Hz, 3H), 7.28 (td, J = 7.7, 2.5 Hz, 6H), 7.22–7.18 (m, 1H), 7.16–7.10 (m, 6H), 7.01 (dd, J = 9.4, 6.5 Hz, 1H), 6.76 – 6.72 (m, 1H). $^{13}C\{^1H\}$ NMR (126 MHz, CD_2Cl_2) δ: 206.9, 206.4, 195.95, 195.9, 195.6, 195.5, 185.7, 185.2, 175.4, 175.3, 153.7, 152.5, 142.5, 133.4, 132.5, 132.4, 131.0, 130.3, 130.0, 129.0, 129.0, 126.6, 125.1, 124.5, 119.0, 116.5, 114.4, 108.6. ES-MS calcd for $C_{33}H_{24}F_6N_3O_3P_2Re$: 728.11. Found for ($[M + K]^+$): 728.11. Anal. calcd for $C_{33}H_{24}F_6N_3O_3P_2Re$: Calcd C 45.42 H 2.77 N 4.81. Found C 44.44 H 3.05 N 4.33. FT-ATR-IR (neat powder): 1917(s), 1960 (br), 2039(br) (*v* CO) cm^{-1}.

Supplementary data

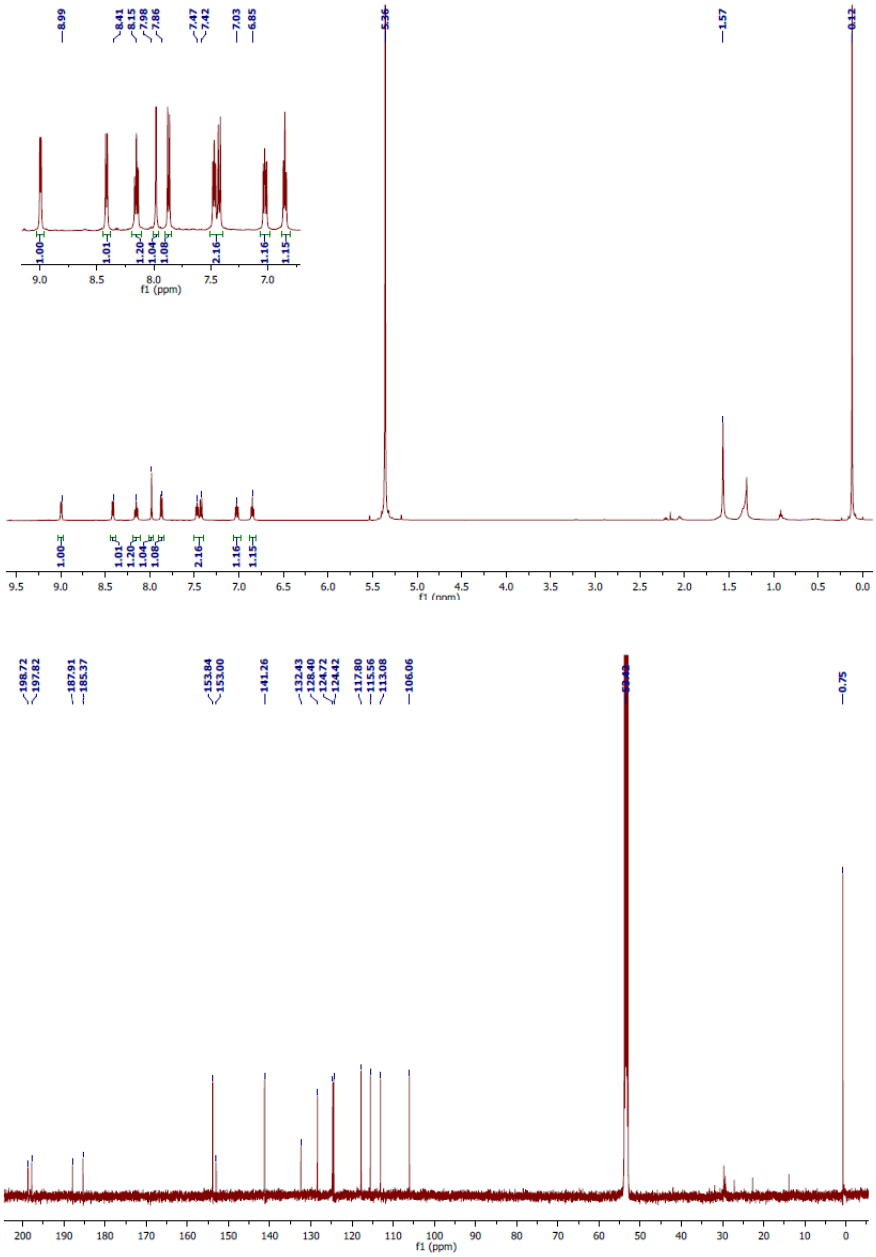

Figure ES2.1 ^{1}H (500 MHz, *top*) and ^{13}C NMR (125 MHz, *bottom*) spectra recorded for complex **Re1** in CD_2Cl_2 at 298 K.

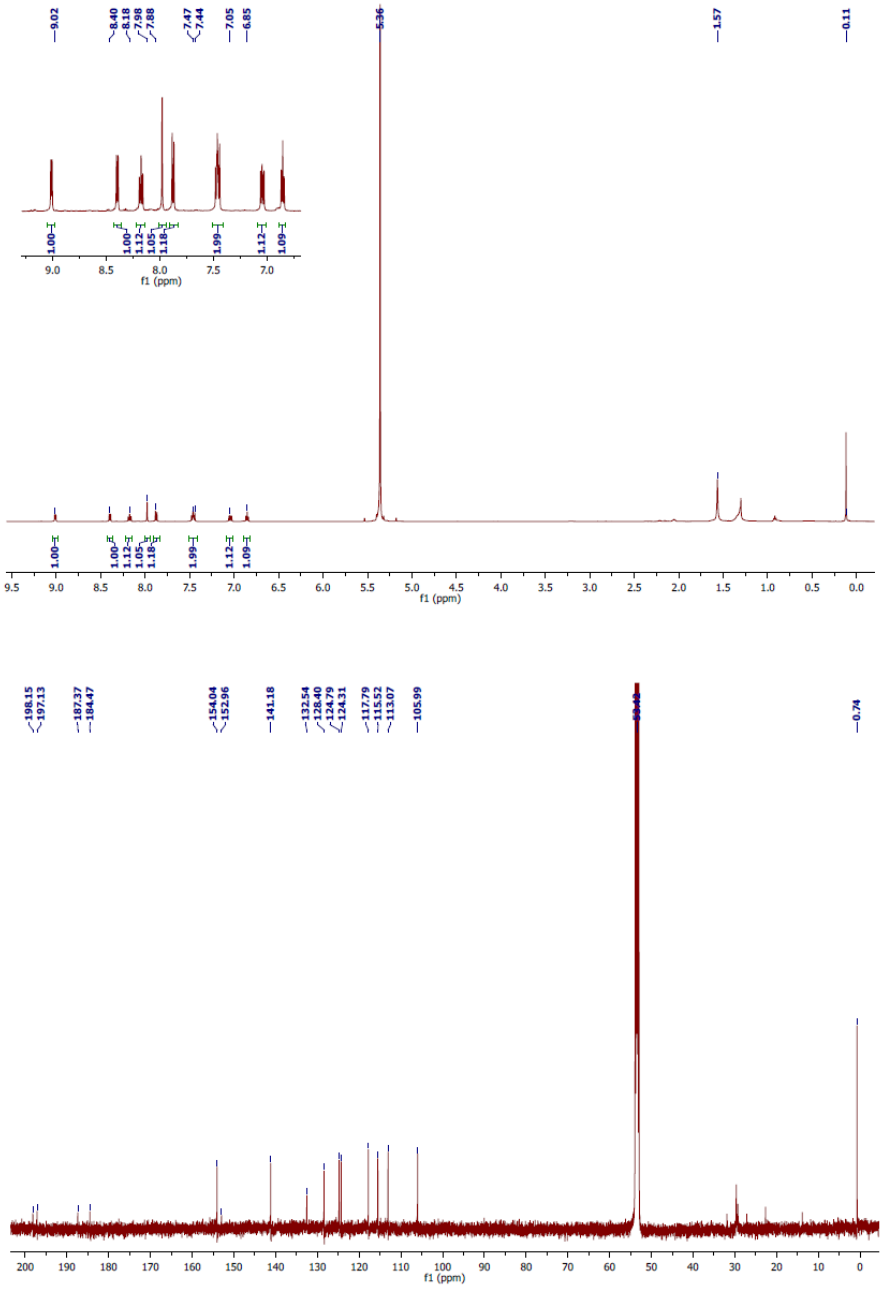

Figure ES2.2 ^{1}H (500 MHz, *top*) and ^{13}C NMR (125 MHz, *bottom*) spectra recorded for complex **Re2** in CD_2Cl_2 at 298 K.

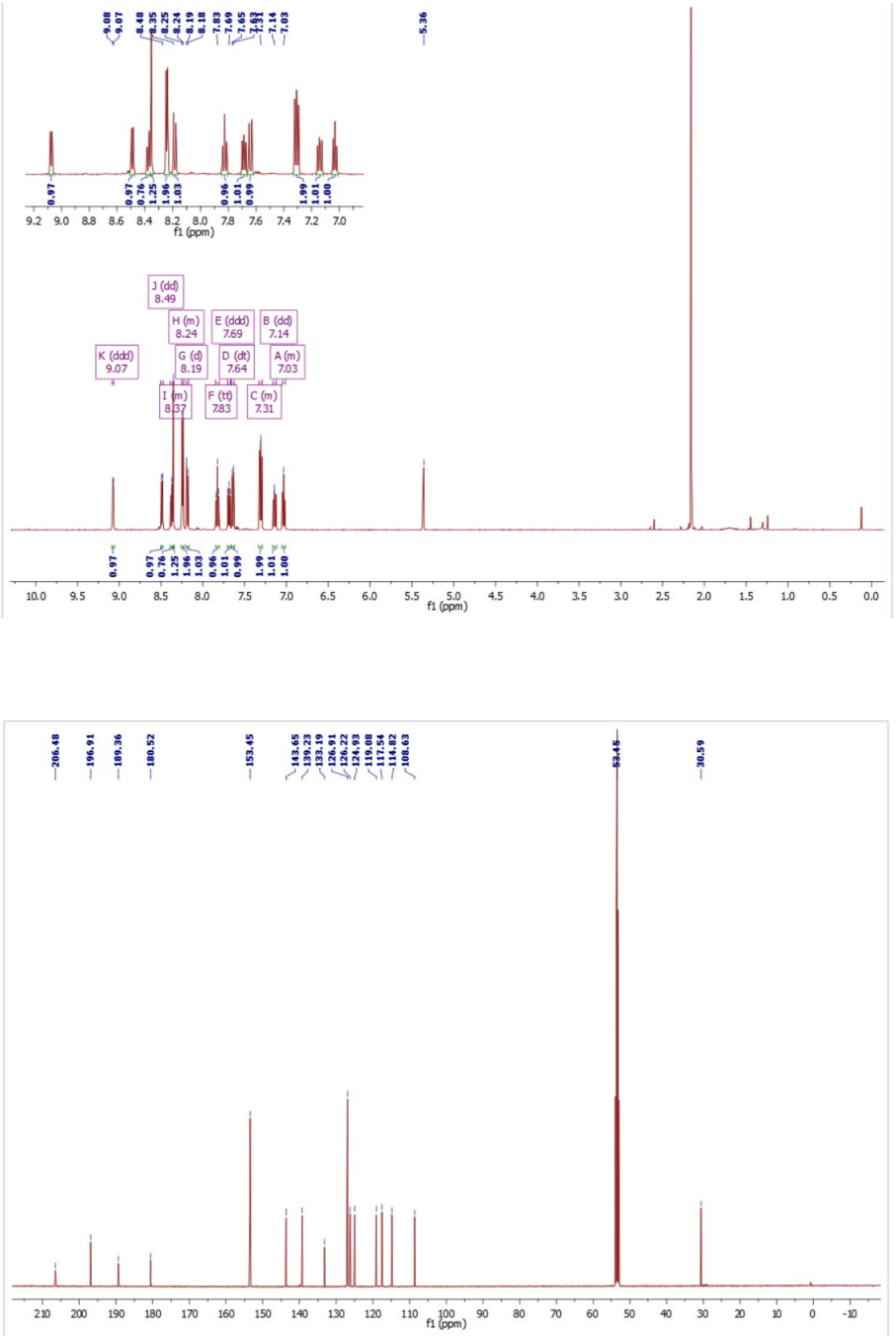

Figure ES2.3 ^{1}H (500 MHz, *top*) and $^{13}C\{^{1}H\}$ NMR (125 MHz, *bottom*) spectra recorded for complex **Re3** in CD_2Cl_2 at 298 K.

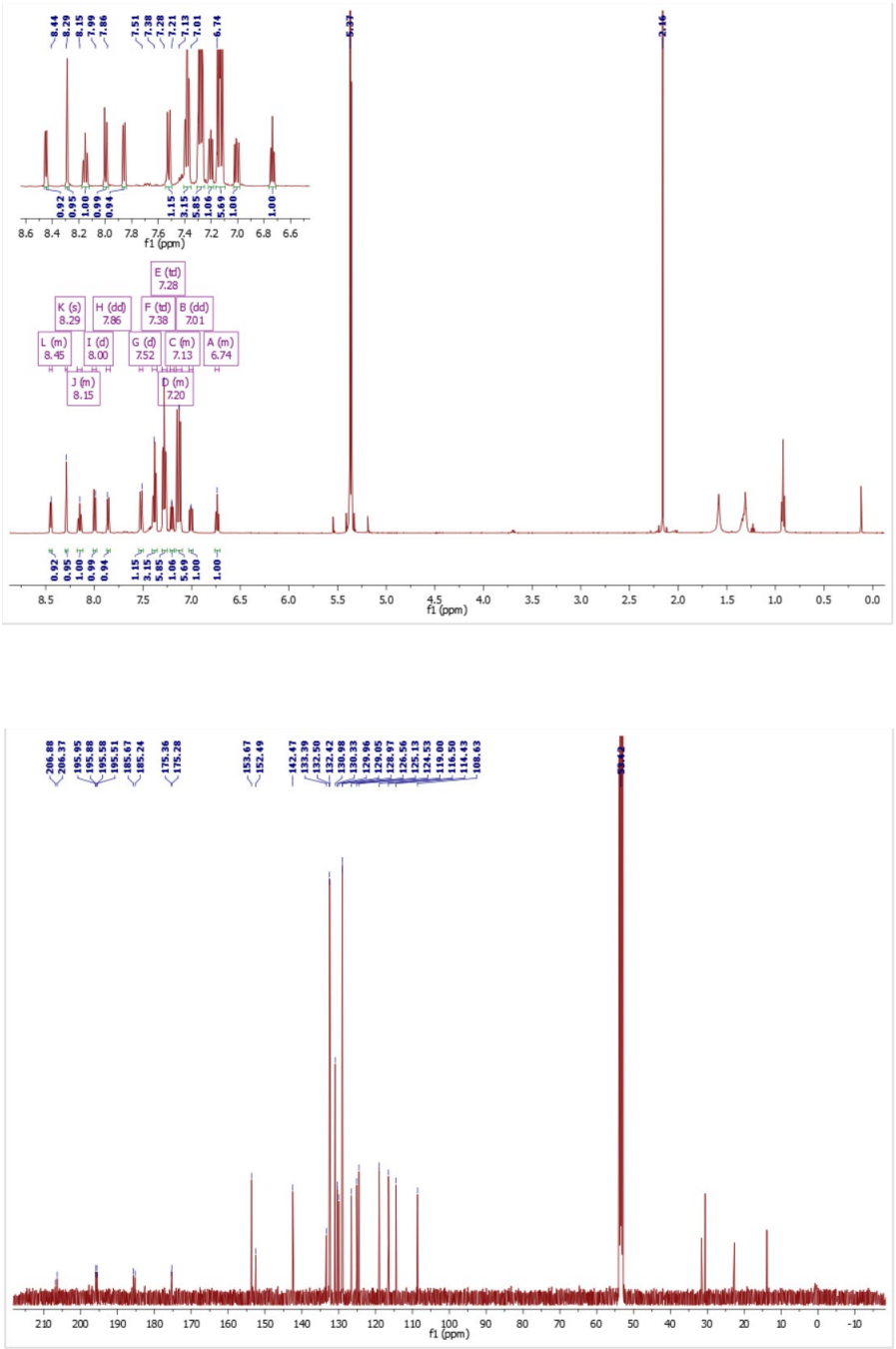

Figure ES2.4 ^{1}H (500 MHz, *top*) and $^{13}C\{^{1}H\}$ NMR (125 MHz, *bottom*) spectra recorded for complex **Re4** in CD_2Cl_2 at 298 K.

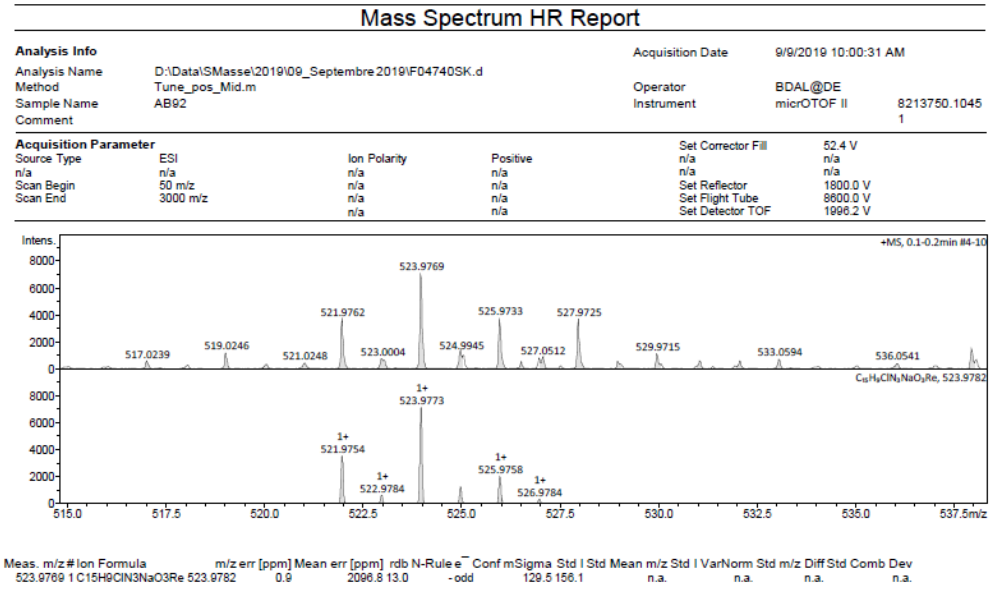

Figure ES2.5 High-resolution ESI-MS spectrum of compound **Re1**.

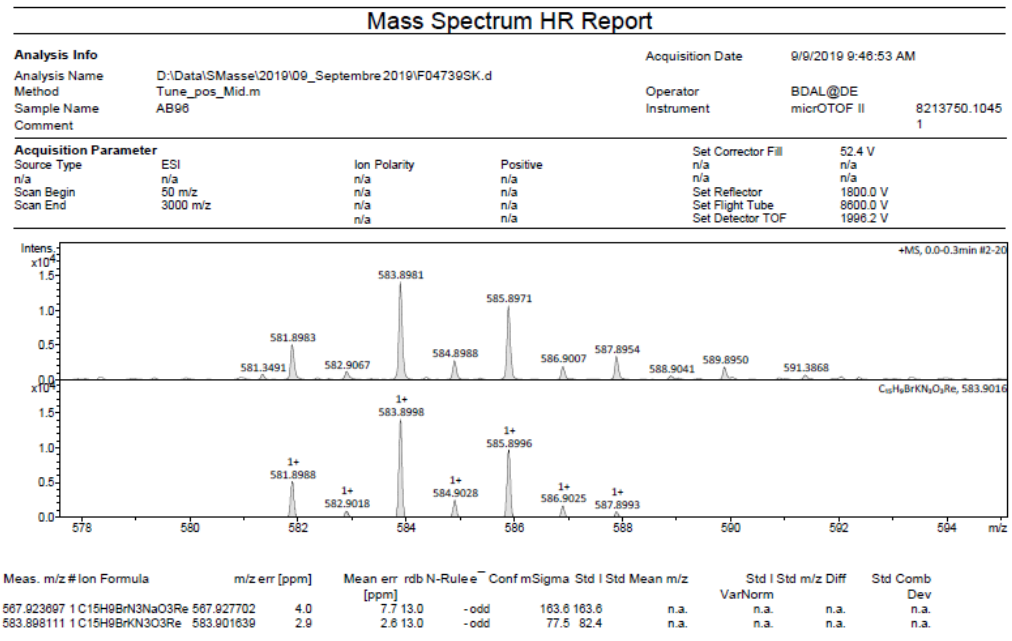

Figure ES2.6 High-resolution ESI-MS spectrum of compound **Re2**.

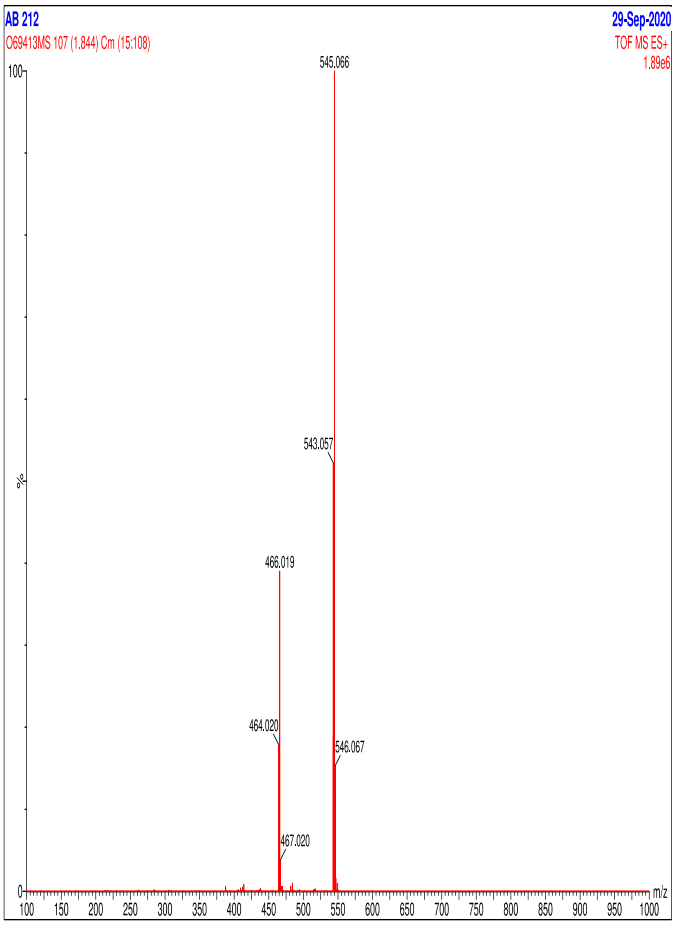

Figure ES2.7 HR- ESI-MS spectrum of compound **Re3**.

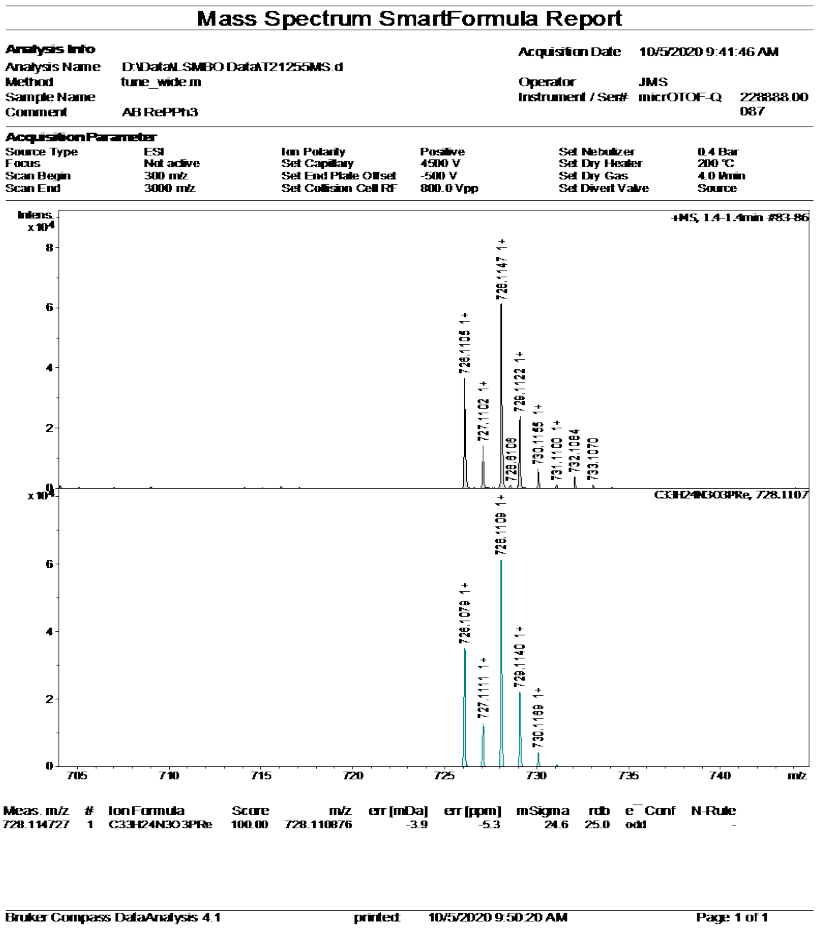

Figure ES2.8 HR- ESI-MS spectrum of compound **Re4**.

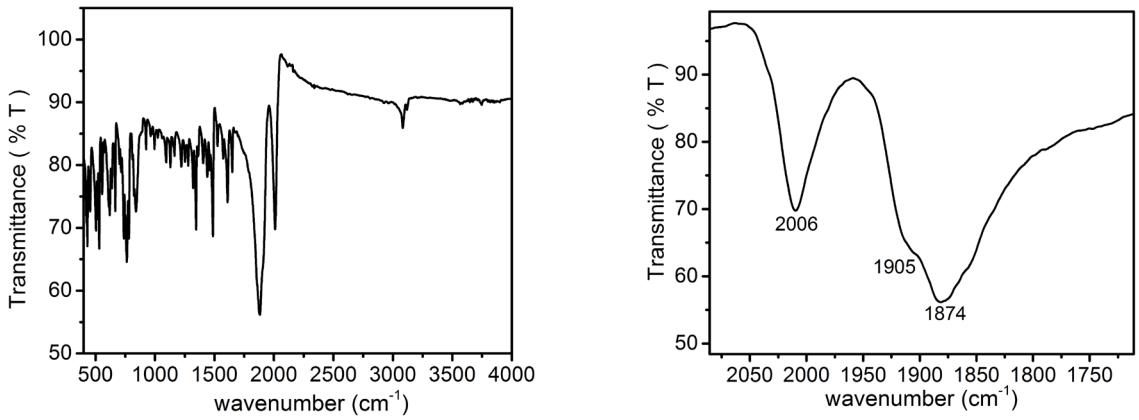

Figure ES2.9 FT-ATR-IR spectra obtained for complex **Re1** in solid state as neat powder in the region 4000 – 400 cm^{-1} (*left box*) and enlarged spectrum in the ν_{co} =C≡O region 2085 – 1711 cm^{-1} (*right box*).

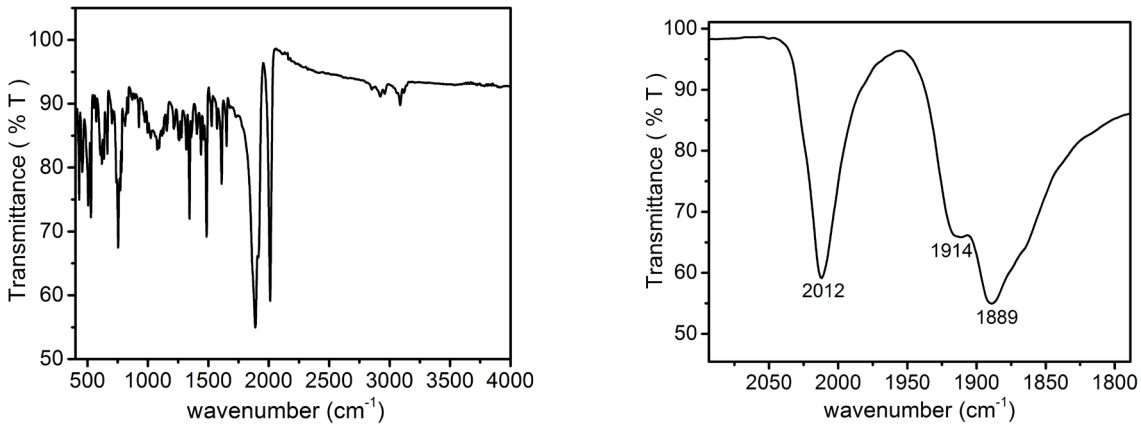

Figure ES2.10 FT-ATR-IR spectra obtained for complex **Re2** in solid state as neat powder in the region 4000 – 400 cm^{-1} (*top*) and enlarged spectrum in the ν_{co} =C≡O region 2093 – 1788 cm^{-1} (*bottom*).

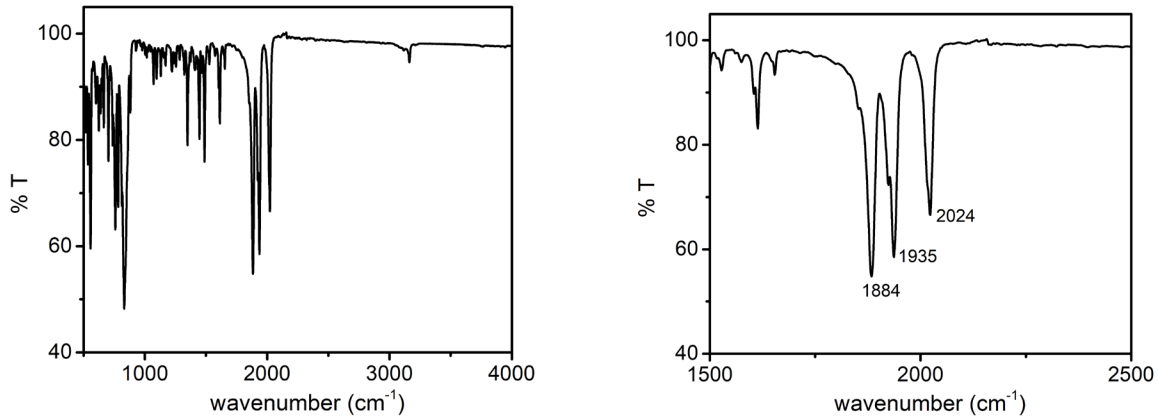

Figure ES2.11 FT-ATR-IR spectra obtained for complex **Re3**. in solid state as neat powder in the region 4000–400 cm^{-1} (*left*) and enlarged spectrum in the ν_{co} =C≡O region 2100–1500 cm^{-1} (*right*).

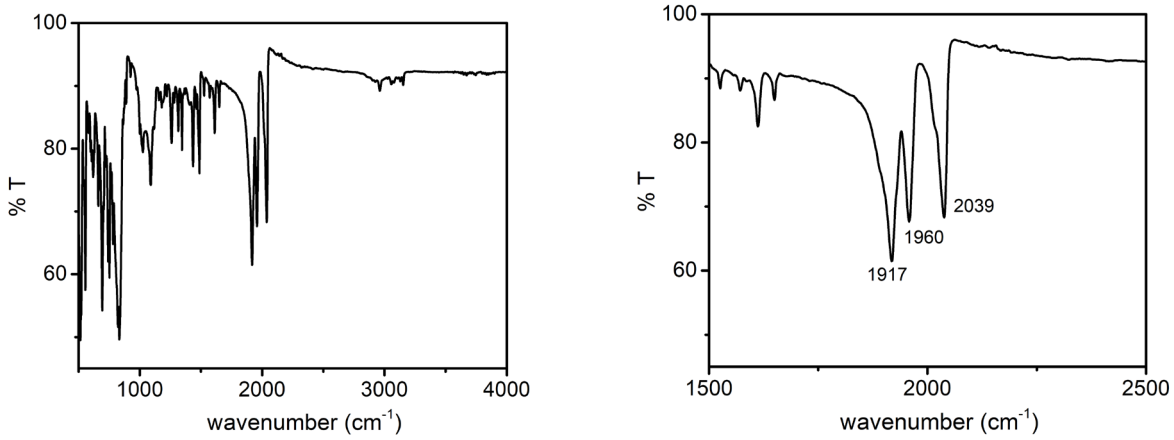

Figure S2.12 FT-ATR-IR spectra obtained for complex **Re4**. in solid state as neat powder in the region 4000–400 cm^{-1} (*left*) and enlarged spectrum in the ν_{co} =C≡O region 2100–1500 cm^{-1} (*right*).

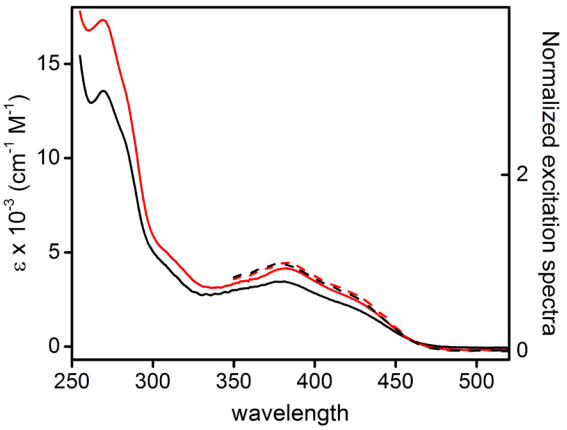

Figure ES2.13 Electronic absorption (solid line) and normalized excitation spectra (dashed line) of complex **Re1** (black traces) and **Re2** (red traces) in degassed CH_2Cl_2 solution at a concentration of 2×10^{-5} M at room temperature. Excitation spectra were recorded setting emission at λ_{em} = 660 nm.

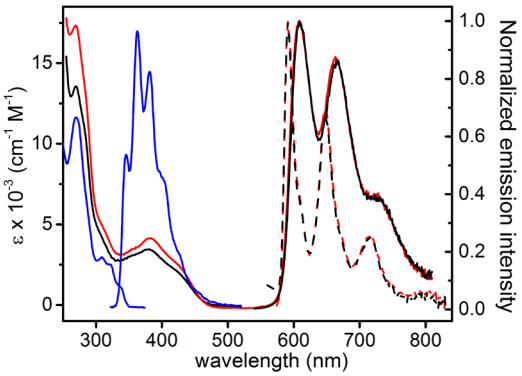

Figure ES2.14 UV-Vis and normalized emission spectra for **Re1** (**black**) and **Re2** (**red**) and ligand NHC (**blue**) in CH_2Cl_2 at $2.0 \cdot 10^{-5}$ M in degassed condition (solid line) and 77 K (dashed line).

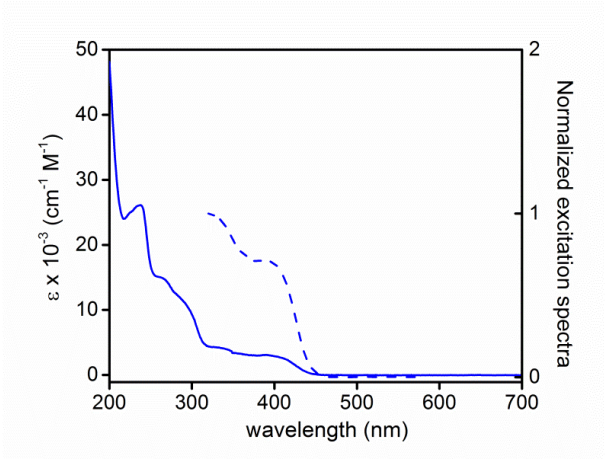

Figure ES2.15 Electronic absorption (solid line) and normalized excitation spectra (dashed line) of complex **Re3**. (blue traces) in degassed CH_3CN solution at a concentration of 2×10^{-5} M at room temperature. Excitation spectra were recorded setting emission at λ_{em} = 600 nm.

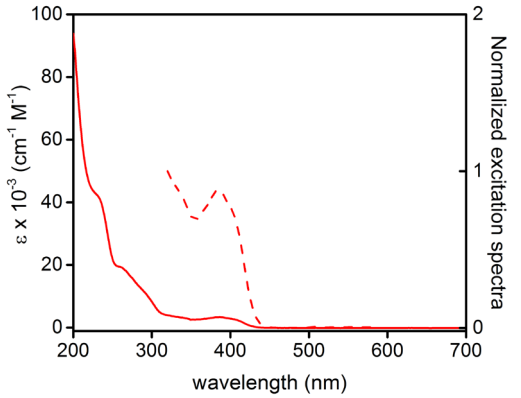

Figure ES2.16 Electronic absorption (solid line) and normalized excitation spectra (dashed line) of complex **Re4** (red traces) in degassed CH_3CN solution at a concentration of 2×10^{-5} M at room temperature. Excitation spectra were recorded setting emission at λ_{em} = 600 nm.

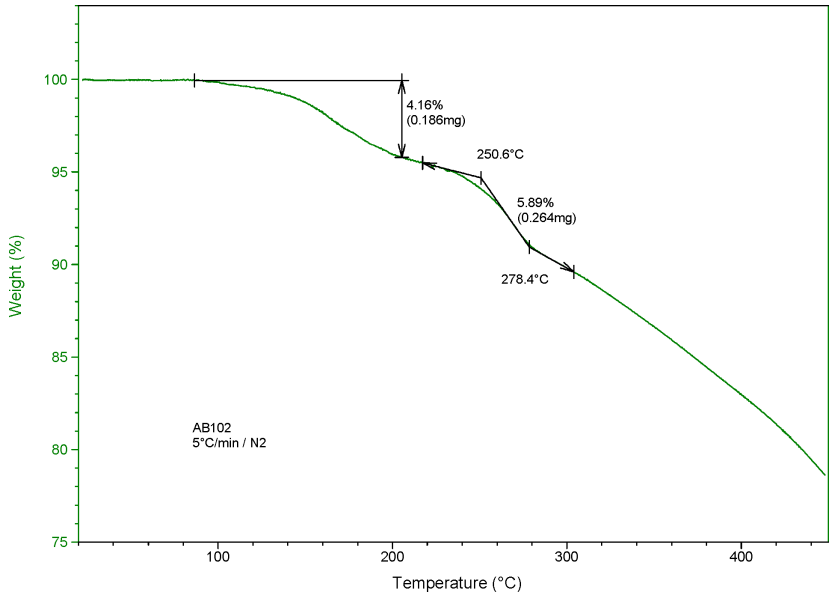

Figure ES2.17 Thermogravimetric analysis recorded for complex **Re1**.

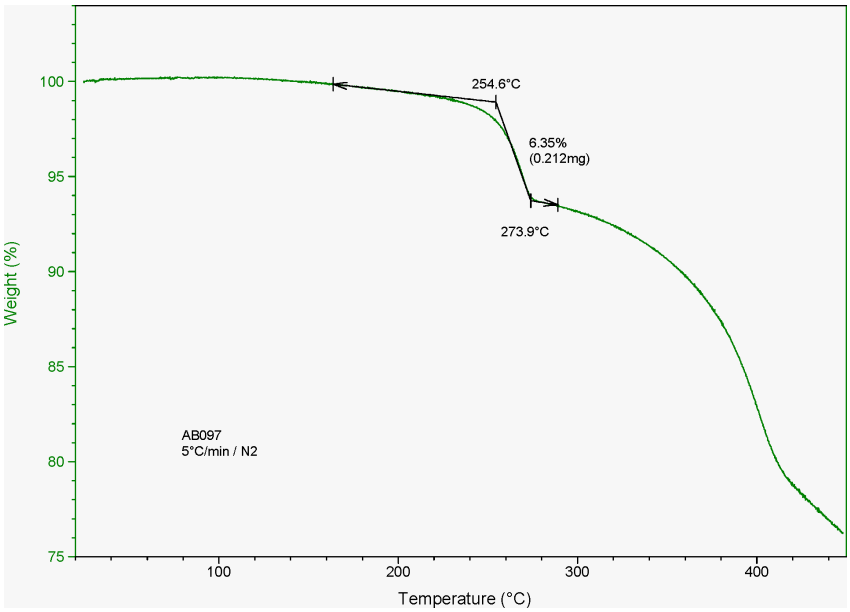

Figure ES2.18 Thermogravimetric analysis recorded for complex **Re2**.

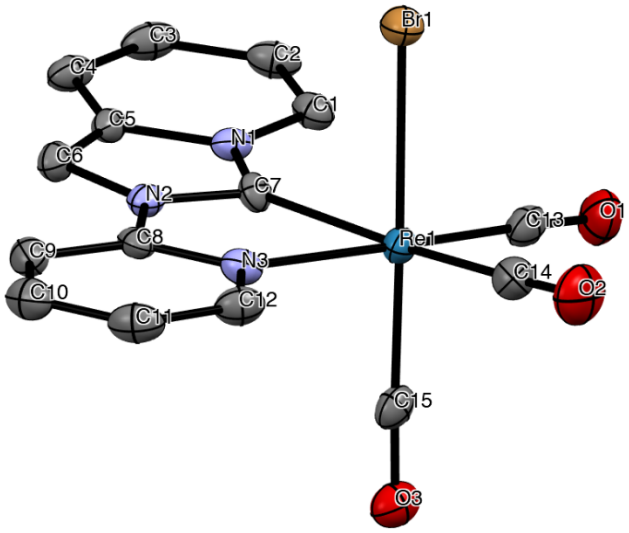

Figure ES2.19 ORTEP diagram of compound **Re2** with thermal ellipsoids shown at 50% probability level obtained by single-crystal X-ray diffractometric analysis. Hydrogen atoms are omitted for clarity. Selected bond lengths (Å): Re–C(7) = 2.129(4) Å; Re–C(13) = 1.915(5) Å, Re–C(14) = 1.951(5) Å, Re–C(15) = 1.910(5) Å, Re–N(3) = 2.208(4) Å; Re–Br(1) = 2.6199(5) Å.

Table ES2.1 Crystal data and structure refinement for compound **Re1**.

Identification code CCDC 1973530

Empirical formula C15 H9 Cl N3 O3 Re

Formula weight 500.90

Temperature 120(2) K

Wavelength 0.71073 Å

Crystal system, space group Triclinic, P -1

Unit cell dimensions a = 6.6594(2) Å α = 89.3060(10)°

b = 10.8376(4) Å β = 77.6610(10)°

c = 11.1557(4) Å γ = 72.2660(10)°

Volume 747.94(4) Å3

Z, Calculated density 2, 2.224 Mg/m^3

Absorption coefficient 8.319 mm^{-1}

F(000) 472

Crystal size 0.200 x 0.150 x 0.120 mm

Theta range for data collection 1.976 to 30.076 deg.

Limiting indices -9<=h<=9, -15<=k<=13, -15<=l<=15

Reflections collected / unique 54563 / 4399 [R(int) = 0.0367]

Completeness to theta = 25.242 99.9%

Absorption correction Semi-empirical from equivalents

Max. and min. transmission 0.7460 and 0.6059

Refinement method Full-matrix least-squares on F^2

Data / restraints / parameters 4399 / 0 / 208

Goodness-of-fit on F2 1.106

Final R indices [I>2σ(I)] R1 = 0.0152, wR2 = 0.0302

R indices (all data) R1 = 0.0163, wR2 = 0.0305

Extinction coefficient n/a

Largest diff. peak and hole 1.616 and -0.985 e $Å^{-3}$

Table ES2.2 Crystal data and structure refinement for compound **Re2**.

Identification code CCDC 1980932

Empirical formula C15 H9 Br N3 O3 Re

Formula weight 545.36

Temperature 120(2) K

Wavelength 0.71073 Å

Crystal system, space group Triclinic, P -1

Unit cell dimensions a = 6.7338(3) Å α = 88.7910(10)°

b = 10.8986(4) Å β = 76.4800(10)°

c = 11.3120(5) Å γ = 72.1440(10)°

Volume 767.14(6) Å3

Z, Calculated density 2, 2.361 Mg/m^3

Absorption coefficient 10.542 mm^{-1}

F(000) 508

Crystal size 0.180 x 0.150 x 0.120 mm

Theta range for data collection 1.966 to 29.168 deg.

Limiting indices -9<=h<=9, -14<=k<=14, -15<=l<=15

Reflections collected / unique 54752 / 4137 [R(int) = 0.0597]

Completeness to theta = 25.242 100.0 %

Absorption correction Semi-empirical from equivalents

Max. and min. transmission 0.7458 and 0.5741

Refinement method Full-matrix least-squares on F^2

Data / restraints / parameters 4137 / 0 / 208

Goodness-of-fit on F2 1.109

Final R indices [I>2σ(I)] R1 = 0.0295, wR2 = 0.0621

R indices (all data) R1 = 0.0342, wR2 = 0.0649

Extinction coefficient n/a

Largest diff. peak and hole 3.362 and -1.941 e $Å^{-3}$

Table ES2.3 Crystal data and structure refinement for **Re3.**

Identification code CCDC 2036080

Empirical formula C24 H22 F6 N4 O4 P Re

Formula weight 761.62

Temperature 120(2) K

Wavelength 0.71073 Å

Crystal system, space group Monoclinic, P 21/n

Unit cell dimensions a = 14.1531(8) Å α = 90°

b = 9.6637(6) Å β = 107.724(2)°

c = 20.0753(10) Å γ = 90°

Volume 2615.4(3) $Å^3$

Z, Calculated density 4, 1.934 Mg/m^3

Absorption coefficient 4.790 mm^{-1}

F(000) 1480

Crystal size 0.180 × 0.150 × 0.120 mm

Theta range for data collection 2.097 to 28.033 deg.

Limiting indices -18<=h<=18, -12<=k<=12, -26<=l<=26

Reflections collected / unique 74370 / 6335 [R(int) = 0.0771]

Completeness to theta = 25.242 100.0%

Absorption correction Semi-empirical from equivalents

Max. and min. transmission 0.7456 and 0.7016

Refinement method Full-matrix least-squares on F^2

Data / restraints / parameters 6335 / 0 / 361

Goodness-of-fit on F^2 1.057

Final R indices [I>2sigma(I)] R1 = 0.0386, wR2 = 0.0782

R indices (all data) R1 = 0.0505, wR2 = 0.0851

Extinction coefficient n/a

Largest diff. peak and hole 2.326 and -1.504 e $Å^{-3}$

2.5.5 Computational details

Ground state and low-lying triplet geometries were optimized by means of density functional calculations. The parameter free hybrid functional PBE0[39] was employed along with the standard valence double-ζ polarized basis set 6-31G(d,p) for C, H, Cl, N, and O. For Re and Br the Stuttgart–Dresden effective core potentials were employed along with the

corresponding valence triple-ζ basis set and a set of polarization functions on Br (αd,Br = 0.389).[40] All the calculations were done in the presence of solvent (dichloromethane, used in the photophysical characterizations) described by a polarizable continuum model (PCM).[41] The nature of all the stationary points was checked by computing vibrational frequencies and all the geometries were found to be true minima. In order to simulate the absorption electronic spectrum down to 230 nm the lowest 25 singlet excitation energies were computed by means of time-dependent density functional calculations. The vibrationally- resolved emission spectra were simulated in the framework of the Franck–Condon principle,[42] shifting the 0–0 energy to its observed value. All the calculations were done with Gaussian 09.[43] For cationic tricarbonyl rhenium complexes, all the calculations were done in the presence of acetonitrile, used in the photophysical characterizations, described by a polarizable continuum model (PCM).[44] Optimization of the ground state geometry in dimethylformamide, used in the electrochemical characterization, gives almost indistinguishable results (difference in bond distances lower than 0.0001 Å and differences in orbital energies lower than 0.003 eV). Only data computed in acetonitrile are described.

2.6 Authors contributions

Zakaria Asbai (M2 student) contributed equally to the work. Kevin Magra, Cristina Cebrián Ávila and Philippe Gros (University of Lorraine) contributed to the synthesis of the pyridyl pyridoannelated N-heterocyclic carbine. Federico Polo (University of Venice) and Pierluigi Mercandelli (University of Milan) provided the electrochemical analysis and the computational investigation. Dr. Benoit Heinrich is kindly acknowledged for performing TGA analyses. Corinne Bailly is acknowledged for X-ray analysis. The group of Pr. J. Lalevée (IS2M, UHA) studied the applications of my Re(I) complexes as PI systems and the development of photosensitive resins for 3D and 4D applications. All the collaborators are kindly acknowledged for their fundamental contribution to the work.

2.7 References

1. [a] M. Wrighton, D. L. Morse, *J. Am. Chem. Soc.,* **1974**, *96*, 998; [b] P. J. Giordano, S. M. Fredericks, M. Wrighton, D. L. Morse, *J. Am. Chem. Soc*., **1978**, *100*, 2257; [c] P. J. Giordano, M. Wrighton, *J. Am. Chem. Soc.,* **1979**, *101*, 2888.
2. [a] J. V. Caspar, T. J. Meyer, *J. Phys. Chem.,* **1983**, *87*, 952; [b] J. V. Caspar, T. D. Westmoreland, G. H. Allen, P. G. Bradley, T. J. Meyer and W. H. Woodruff, *J. Am. Chem. Soc.*, **1984**, *106*, 3492. [c] L. Wallace,D. P. Rillema, *Inorg. Chem.,* **1993**, *32*, 3836; [d] L. Wallace, D. C. Jackman, D. P. Rillema, J. W. Merkert, *Inorg. Chem*., **1995**, *34*, 5210; [e] L. Sackteder, A. P. Zipp, E. A. Brown, J. Streich, J. N. Demas, B. A. DeGraff, *Inorg. Chem.,* **1990**, *29*, 4335.
3. J. Twilton, C. Le, P. Zhang, M. H. Shaw, R. W. Evans, D. W. C. MacMillan, *Nat. Rev. Chem.,* **2017**, *1*, 52.
4. A. Hagfeldt, G. Boschloo, L. Sun, L. Kloo,H. Petterson, *Chem. Rev*., **2010**, *110*, 6595.
5. [a] C. Caporale,M. Massi, *Coord. Chem. Rev.,* **2018**, *363*, 71; [b] Q. Zhao, C. Huang,F. Li, *Chem. Soc. Rev.,* **2011**, *40*, 2508.
6. [a] A. Zamora, G. Vigueras, V. Rodríguez, M. D. Santana,J. R. Ruiz, *Coord. Chem. Rev.,* **2018**, *360*, 34; [b] G. Gasser, I. Ott,N. Metzler-Nolte, *J. Med. Chem.*, **2010**, *54*, 3; [c] A. Leonidova,G. Gasser, *ACS Chem. Biol.,* **2014**, *9*, 2180.
7. [a] S. M. Fredericks, J. C. Luong, M. S. Wrighton, *J. Am. Chem. Soc.,* **1979**, *101*, 7415; [b] L. Wallace, D. P. Rillema, *Inorg. Chem.,* **1993**, *32*, 3836; [c] L. Wallace, D. C. Jackman, D. P. Rillema, J. W. Merkert, *Inorg. Chem.,* **1995**, *34*, 5210.
8. [a] L. Sacksteder, M. Lee, J. N. Demas, B. A. DeGraaf, *J. Am. Chem. Soc.,* **1993**, *115*, 8230; [b] L. Sacksteder, A. P. Zipp, E. A. Brown, J. Streich, J. N. Demas, B. A. DeGraff, *Inorg. Chem.,* **1990**, *29*, 4335.
9. [a] D. Donghi, G. D'Alfonso, M. Mauro, M. Panigati, P. Mercandelli, A. Sironi, P. Mussini, L. D'Alfonso, *Inorg. Chem.,* **2008**, *47*, 4243; [b] M. Mauro, E. Quartapelle Procopio, C.-H. Chien, D. Donghi, M. Panigati, P. Mercandelli, P. Mussini, G. D'Alfonso, L. De Cola, *Adv. Funct. Mater.*, **2009**, *19*, 2607; [c] M. Mauro, C.-H. Yang, C.-Y. Shin, M. Panigati, C.-H. Chang, G. D'Alfonso, L. De Cola, *Adv. Mater.*, **2012**, *24*, 2054.
10. [a] T. Sajoto, P. I. Djurovich, A. Tamayo, M. Yousufuddin, R. Bau, M. E. Thompson, R. J. Holmes,S. R. Forrest, *Inorg. Chem.,* **2005**, *44*, 7992; [b] C.-F. Chang, Y.-M. Cheng, Y. Chi, Y.-C. Chiu, C.-C. Lin, G.-H. Lee, P.-T. Chou, C.-C. Chen, C.-H. Chang, C.-C. Wu, *Angew. Chem.,* **2008**, *47*, 4542; [c] N. Darmawan, C.-H. Yang, M. Mauro, M. Taynal, S. Heun, J. Pan, H. Buchholz, P. Braunstein and L. De Cola, *Inorg. Chem.,* **2013**, *52*, 10756; [d] C. Yang, F. Mehmood, T. L. Lam, S. L.-F. Chan, Y. Wu, C.-S. Yeung, X. Guan, K. Li, C. Y.-S. Chung, C.-Y. Zhou, T. Zoua, C.-M. Che, *Chem. Sci.,* **2013**, *4*, 2630.
11. L. A. Casson, S. Muzzioli, P. Raiteri, B. W. Skelton, S. Stagni, M. Massi, *Dalton Trans*., **2011**, *40*, 11960.
12. [a] J. G. Vaughan, B. L. Reid, S. Ramchandani, P. J. Wright, S. Muzzioli, B. W. Skelton, P. Raiteri, D. H. Brown, S. Stagni, M. Massi, *Dalton Trans*., **2013**, *42*, 14100; [b] P. V. Simpson, I. Casaro, S. Paternoster, B. W. Skelton, M. Falasca, M. Massi, *Chem.Eur.*

J., **2017**, *23*, 6518; [c] T. P. Nicholls, L. K. Burt, P. V. Simpson, M. Massi, A. C. Bissember, *Dalton Trans*., **2019**, *48*, 12749.
13. C. Y. Chan, P. A. Pellegrini, I. Greguric, P. J. Barnard, *Inorg. Chem.,* **2014**, *53*, 10862.
14. [a] X.-W. Li, H.-Y. Li, G.-F. Wang, F. Chen, Y.-Z. Li, X.-T. Chen, Y.-X. Zheng, Z.-L. Xue, *Organomet.*, **2012**, *31*, 3829; [b] G.-F. Wang, Y. Z. Liu, X.-T. Chen, Y.-X. Zheng, Z.-L. Xue, *Inorg. Chim. Acta*, **2013**, *394*, 488.
15. P.V. Simpson, M. Falasca, M. Massi, *Chem. Commun.* **2018**, *54*, 12429; T.P. Nicholis, L.K. Burt, P.V. Simpson, M. Massi, A.C. Bissembler, *Dalton Trans.* **2019**, *48*, 12749.
16. [a] E. Zysman-Colman, *Iridium(III) in Optoelectronic and Photonics Applications*, John Wiley & Sons Ltd, **2017**; [b] R. D. Costa, E. Ortí, J. J. Bolink, F. Monti, G. Accorsi, N. Armaroli, *Angew. Chem., Int. Ed.,* **2012**, *51*, 8178. [c] S. Campagna, F. Puntoriero, F. Nastasi, G. Bergamini, V. Balzani, *Top. Curr. Chem.,* **2007**, *280*, 117. [d] D. Kumaresan, K. Shankar, S. Vaidya, R. H. Schmehl, *Top. Curr. Chem*., **2007**, *281*, 101. [e] A. G. Crosby, *Coord. Chem. Rev*., **2011**, *211*, 163; [f] M. Panigati, M. Mauro, D. Donghi, P. Mercandelli, P. Mussini, L. De Cola, G. D'Alfonso, *Coord. Chem. Rev*., **2012**, *256*, 1621; [g] P. V. Simpson, M. Falasca, M. Massi, *Chem. Commun*., **2018**, *54*, 12429. [h] M. A. Baldo, D. F. O'Brien, Y. You, A. Shoustikov, S. Sibley, M. E. Thompson, S. R. Forrest, *Nature*, **1998**, *395*, 151; [i] M. A. Baldo, M. E. Thomspon, S. R. Forrest, *Nature*, **2000**, *403*, 750.
17. [a] H. Uegaki, Y. Kotani, M. Kamigaito, M. Sawamoto, *ACS Symp. Ser.* **2000**, *760*, 196. [b] C.-P. Tsonis, M.-F. Farona, *J. Polym. Sci. Polym. Chem. Ed.* **1979**, *17*, 1779. [c] M. Kamachi, H. Miyama, *J. Polym. Sci. A*. **1965**, *3*, 1337.
18. T.-P. Nicholls, L.-K. Burt, P.-V. Simpson, M. Massi, A.-C. Bissember, *Dalton Trans*. **2019**, *48*, 12749.
19. K. Nakamoto*, Infrared and Raman spectra of inorganic and coordination compounds: part B: applications in coordination, organometallic, and bioinorganic chemistry*, John Wiley & Sons, Inc., 6th edn, **2008**.
20. C. Y. Chan, P. A. Pellegrini, I. Greguric, P. J. Barnard, *Inorg. Chem*., **2014**, *53*, 10862.
21. D. J. Stukfens, A. Vlcek Jr., *Coord. Chem. Rev.,* **1998**, *177*, 127.
22. I. Ishida, S. Tobita, Y. Hasegawa, R. Katoh, K. Nozaki, *Coord. Chem. Rev*., **2010**, *254*, 2449.
23. F. Paolucci, M. Marcaccio, C. Paradisi, S. Roffia, C. A. Bignozzi, C. Amatore, *J. Phys. Chem. B*, **1998**, *102*, 4759.
24. L. Suntrup, S. Klenk, J. Klein, S. Sobottka, B. Sarkar, *Inorg. Chem.,* **2017**, *56*, 5771.
25. A. J. Bard, L. R. Faulkner., *Electrochemical Methods: Fundamentals and Applications*, Wiley, 2nd edn, **2000**.
26. [a] A.-H. Bonardi, F. Bonardi, G. Noirbent, F. Dumur, D. Gigmes, C. Dietlin, J. Lalevée, *J. Polym. Sci*. **2020**, *58*, 300. [b] D.-A. Nicewicz, D.-W.-C. MacMillan, *Science* **2008**, *322*, 77.
27. [a] J. Lalevée, N. Blanchard, M.-A. Tehfe, F. Morlet-Savary, J.-P. Fouassier, *Macromolecules* **2010**, *43*, 10191. [b] P. Xiao, J. Zhang, F. Dumur, M.-A. Tehfe, F. Morlet-Savary, B. Graff, D. Gigmes, J.-P. Fouassier, J. Lalevée, *Prog. Polym. Sci*. **2015**, *41*, 32.

28. J. Lalevée, N. Blanchard, M.-A. Tehfe, M. Peter, F. Morlet-Savary, J.-P. Fouassier, *Macromol. Rapid Commun.* **2011**, *32*, 917.
29. M. Paolino, A. Reale, G. Magrini, V. Razzano, M. Saletti, G. Giuliani, A. Donati, F. Samperi, A. Scamporrino, M. Canetti, M. Mauro, F. Villafiorita-Monteleone, E.Fois, C. Botta, A. Cappelli, *Eur. Polym. J.*, **2021**, *156*, 110597; F. Wang, D. C. Neckers, *Macromol.* **2001**, *34*, 6202.
30. P. Garra, F. Dumur, D. Gigmes, A.Al Mousawi, F. Morlet-Savary, C. Dietlin, J.P. Fouassier, J. Lalevée, *Macromol.* **2017**, *50*, 3761.
31. [a] Y. Oshida, *Bioscience and Bioengineering of Titanium Materials*, **2013**, 2nd edition, pp 87-115. [b] M. Sillanpää, M. Shestakova, *Electrochemical Water Treatment Methods*, **2017**, pp 131-225
32. [a] F. Marquardt, M. Bruns, H. Keul, Y. Yagci, M. Müller, *Chem. Commun.* **2018**, *54*, 1647. [b] J.P. Fouassier, J. Lalevée, *Photoinitiators for Polymer Synthesis-Scope, Reactivity, and Efficiency*; Wiley-VCH Verlag GmbH & Co. KGaA: Weinheim, Germany, **2012**.
33. P. Xiao, J. Zhang, F. Dumur, M.A. Tehfe, F. Morlet-Savary, B. Graff, D. Gigmes, J.P. Fouassier, J. Lalevée, *Prog. Polym. Sci.*, **2015**, *41*, 32.
34. H. Chen, Y. Zhang, A. Bonfiglio, F. Morlet-Savary, M. Mauro, J. Lalevee, *ACS Appl. Polym. Mater.*, **2021**, *3*, 1, 464.
35. M.-A Tehfe, J. Lalevée, D. Gigmes, J.-P. Fouassier, *J. Polym. Sci. A Polym. Chem.* **2010**, *48*, 1830.
36. S. Schmidt, W. C. Trogler, F. Basolo, *Inorg. Synth.,* **1985**, *23*, 41.
37. J. T. Hutt, Z. D. Aron, *Org. Lett.,* **2011**, *13*, 5256.
38. [a] N. J. Lundin, A. G. Blackman, K. C. Gordon, D. L. Officer, *Angew. Chem. Int. Ed.*, **2006**, *45*, 2582; [b] H. Hori, K. Koike, M. Ishizuka, K. Takeuchi, T. Ibusuki, O. Ishitani, *J. Organomet. Chem.*, **1997**, *530*, 169.
39. Called PBE1PBE in Gaussian. [a] C. Adamo, V. Barone, *J. Chem. Phys.,* **1999**, *111*, 6158; [b] J. P. Perdew, K. Burke, M. Ernzerhof, *Phys. Rev. Lett.,* **1996**, *77*, 3865; [c] J. P. Perdew, K. Burke, M. Ernzerhof, *Phys. Rev. Lett.,* **1997**, *78*, 1396.
40. S. Huzinaga, J. Andzelm, M. Kłobukowski, E. Radzio- Andzelm, Y. Sakai, H. Tatewaki, *Gaussian Basis Sets for Molecular Calculations, Elsevier, Amsterdam*, **1984**, p. 23.
41. [a] G. Scalmani, M. J. Frisch, B. Mennucci, J. Tomasi, R. Cammi, V. Barone, *J. 43 Chem. Phys*., **2006**, *124*, 094107; [b] G. Scalmani, M. J. Frisch, *J. Chem. Phys*., **2010**, *132*, 114110.
42. V. Barone, J. Bloino, M. Biczysko, F. Santoro, *J. Chem. Theory Comput.,* **2009**, *5*, 540.
43. Gaussian09 (revision D.01), Gaussian Inc., Wallingford, CT, **2013**.
44. [a] G. Scalmani, M. J. Frisch, B. Mennucci, J. Tomasi, R. Cammi, V. Barone, *J. Chem. Phys.*, **2006**, *124*, 094107; [b] G. Scalmani, M. J. Frisch, *J. Chem. Phys.*, **2010**, *132*, 114110.

3. Ir^{III}-pyridoannelated N-heterocyclic carbene complexes: potent theranostic agents *via* mitochondria targeting[a]

ABSTRACT

A novel family of Ir^{III} complexes bearing a pyridoannelated N-heterocyclic carbene is herein described. The target compounds **Ir1**–**5** are straightforwardly prepared and fully characterized. Comprehensive investigation of their optical properties reveals a rare case of dual emission ascribed to two excited states localized onto different portions of the molecule, as confirmed by both optical spectroscopy and time-dependent density functional calculations including spin-orbit coupling. The cytotoxicity against cancer cell lines is investigated as well. Remarkably, **Ir2**–**5** show up to 50-fold higher anticancer activity *in vitro* compared to oxaliplatin market drug with concentration values required to reduce by 50% the cell viability (IC_{50}) in the low μM range. Finally, in-depth biological investigation on the most cytotoxic compound **Ir4** reveals its powerful mitochondrial dysfunctioning activity and efficient reactive oxygen species production, associated with apoptosis as the mechanism of cell death

[a] The results reported in this chapter have been published in
A. Bonfiglio**,** C. McCartin, U. A. Carrillo-Arco, C. Cebrián, P. C. Gros, C. A. Kichler, S. Fournel, C. Daniel, M. Mauro, *European Journal of Inorganic Chemistry,* **2021**, 1551.

3.1 State-of-art and introduction

Since the discovery of cisplatin in 1965, platinum compounds have remained a mainstay of cancer chemotherapy.[1] However, despite the development of second and third generation platinum compounds, namely carboplatin and oxaliplatin, severe side effects and drug resistance remain problematic in their usage.[2]

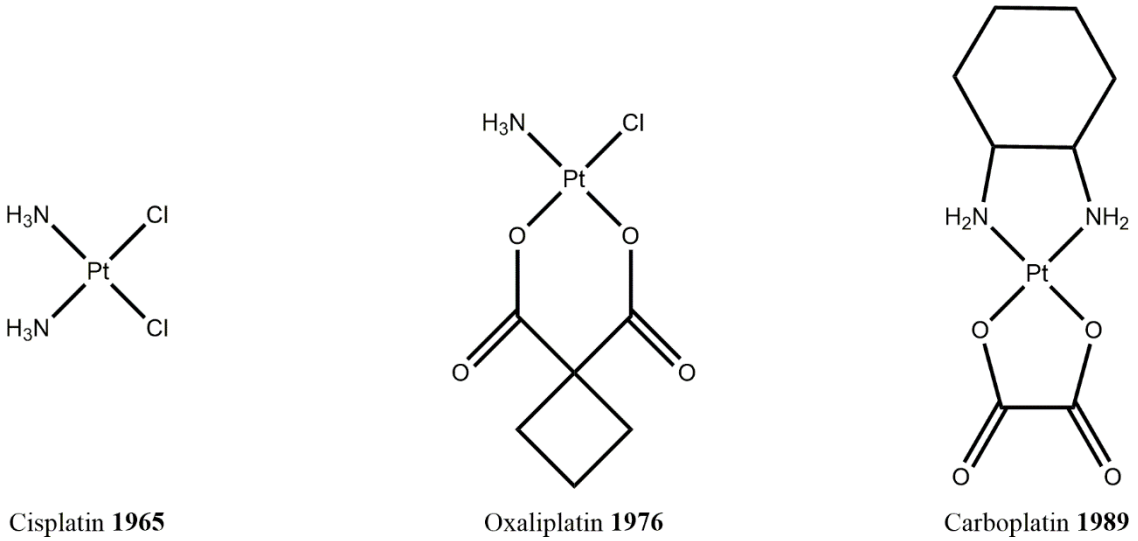

Figure 3.1 First, second and third generation of platinum compounds drugs.

In particular, their mechanism of action - which consists in the induction of cell death by the generation of genomic adducts *via* crosslink with DNA (*i.e.* DNA platinization) - is susceptible to interference at several points, due to mechanisms of resistance (platinum or glutathione uptake, DNA repair capability, reduction of the apoptodic response -*survival pathways*).[3] Thus, the continued development of metal-based anti-cancer complexes, which may overcome these adverse effects and chemo-resistance, is currently of great clinical interest.

In this respect, major attention is devoted to compounds capable of interfering with mitochondrial function due to their ability to by-pass apoptotic resistance mechanisms through direct induction of the intrinsic (*i.e.* mitochondrial mediated) apoptosis pathway.[4] Promising anti-cancer activity is to be found among compounds of several other metals including gold, silver, copper, palladium, ruthenium, rhodium, iron and rhenium.[5]

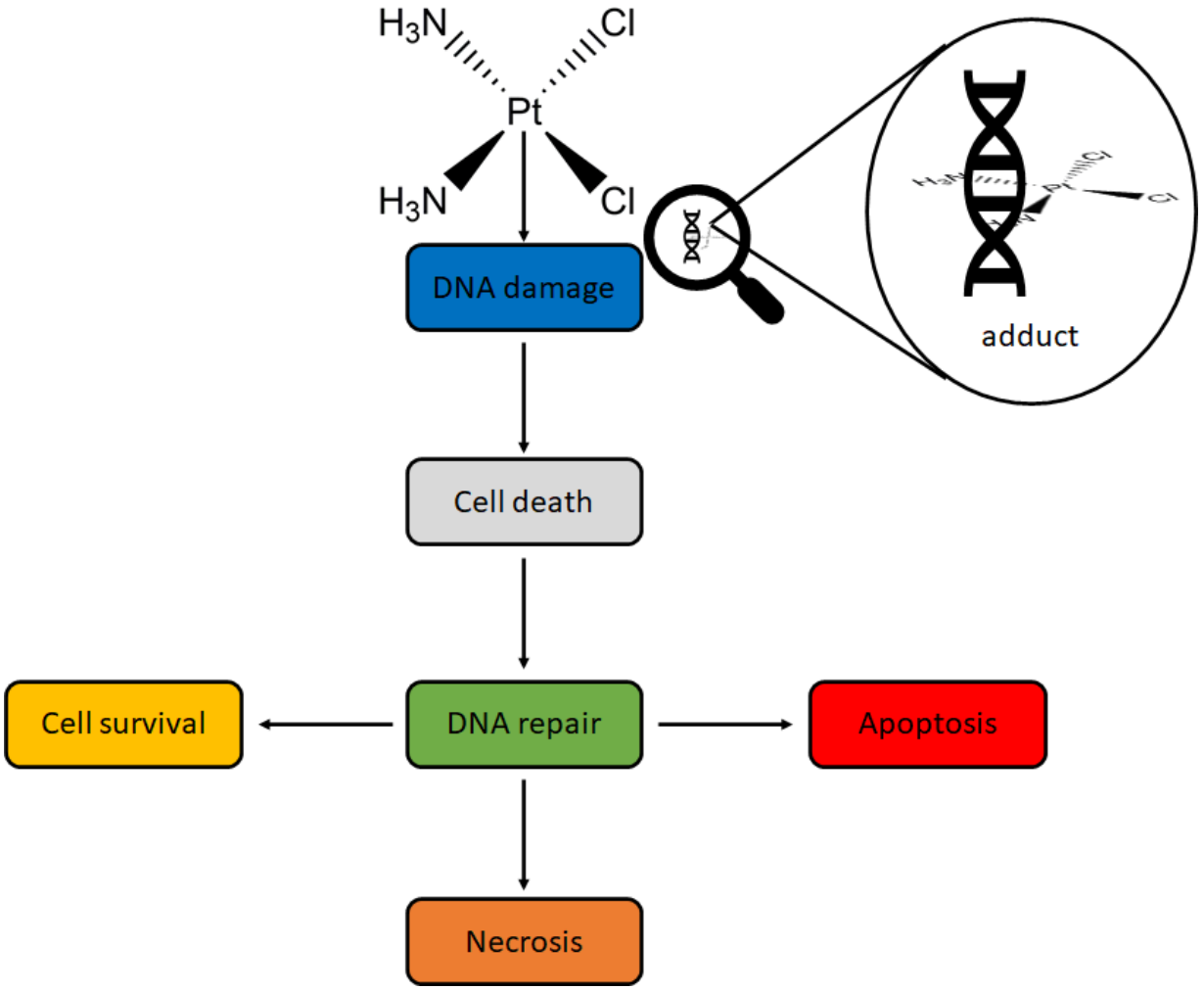

Figure 3.2 Cisplatin mechanism of action.

Cyclometalated Ir^{III} complexes are of particular interest since they can combine biological activity with excellent and highly tuneable photophysical properties.[6] This combination enables their application as theragnostic agents, *i.e.* simultaneous imaging and therapeutic properties. Monitoring cellular localization of exogenous metallodrugs upon internalization via optical techniques is of paramount importance for elucidating the mechanism of action and establishing structure-properties relationships without the need of chemical modification of the drug, which may perturb the activity of this latter. Furthermore, it is well established that both optical properties and biological activities are largely influenced by the nature of the coordinated ligands, also playing key role in the (photo-)chemical stability and cellular localization of the final metal complex. Hence, judicious choice of coordination sphere is of pivotal importance for the activity of this class of photo- and bio-active organometallic compounds.

N-heterocyclic carbenes (NHCs) are an outstanding class of ligands featuring peculiar characteristics, such as strong σ-donating and weak to moderate π-accepting properties. As such, they have come to prominence in the field of organometallics,[7] since their first attempts of isolation as stable species[8]. Currently, they find useful applications in several fields including molecular catalysis,[9] materials science,[10] and more recently in bio-medicine, for the development of biologically active compounds with potent anti-bacterial and anti-cancer effects[11,12]. Indeed, the presence of NHCs is advantageous for biological applications of metallodrugs due to the stability of the metal-carbene bond, and in the facile chemical modifications at both backbone and wingtip positions that enable straightforward tuning of both steric and electronic features.[13]

The first examples of luminescent Ir^{III}-NHC complexes with anticancer activity were reported by Mao and co-workers.[14] The first series of compounds belong to the family of phenylpyridine-based cyclometalated Ir^{III} with general formula $[Ir(ppy)_2(bis\text{-}NHC)]Cl$, where ppy is the 2-phenylpyridine.[14a] The *in vitro* toxicity tested after 48 hours of incubation of the complexes showed good to high activities against different human cancer and healthy cell lines *via* mitochondria targeting. More recently, the same group expanded upon the series describing two novel Ir^{III}-NHC displaying near infrared (NIR) emission achieved through extension of the π-aromatic system of the cyclometalating ligand.[14b] Similarly to their congeners, the compounds were found to specifically localize into mitochondria and able to efficiently induce cell death via the mitochondrial pathway. Independently, Che and co-workers investigated related Ir-NHC complexes of the family $[Ir(C\text{^}N)_2(bis\text{-}NHC)]^+$, where C^N is phenylpyridine-type of ligands. They found out that such complexes are highly cytotoxic against HeLa cell line, but compounds accumulated selectively into the endoplasmic reticulum (ER) instead.[15] Moreover, Liu and co-workers explored anti-cancer activity of Ir^{III}-ppz complexes, where ppz = 1-phenylpyrazole, bearing an imine-N-heterocyclic carbene ancillary ligand.[16] Nevertheless, these four series of Ir^{III}-NHC complexes share the same N-alkylated imidazol-2-ylidene scaffold, and effect of electronic and structural variation at the NHC site was not explored to date. All mentioned compounds are display in *Figure 3.3*.

In this chapter, a new series of luminescent Ir^{III} complexes bearing a pyridyl-pyridoannulated NHC ancillary ligand is investigated, combining enhanced cytotoxicity with suitable properties and gaining deeper understanding of structure-properties relationship in this class of metallodrugs. Their optical properties are presented and rationalized also with

the help of computational approaches. Finally, the biological activity of this novel class of Ir^{III}-NHC complexes is thoroughly evaluated showing potent anti-tumoral activity and demonstrating appealing application for these compounds as theragnostic agents.

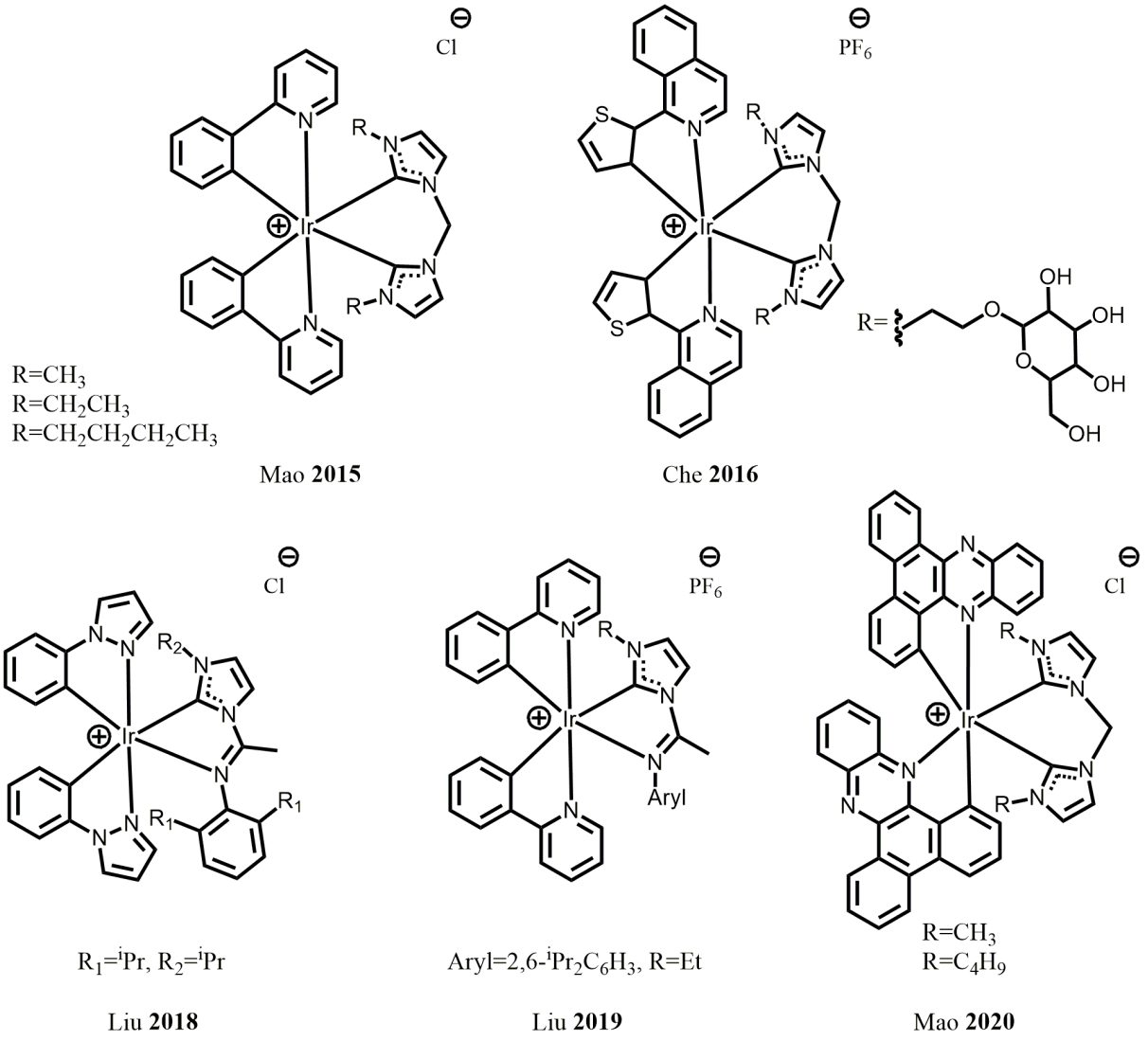

Figure 3.3 Schematic representation of the Ir(III)-NHC compounds reported so far as drugs.

3.2 Results and discussion

3.2.1 Synthesis[b]

The general synthetic pathway employed for the preparation of the cyclometalated $[Ir(C^N)_2(pyipy)]PF_6$ complexes and the chemical structure of the target complexes **Ir1–5** is depicted in *Scheme 3.1* and *Scheme 3.2*, respectively. The ^1H, ^{19}F and ^{13}C NMR as well as the HR-ESI-MS spectra of the target complexes are displayed in *Figure ES3.1–ES3.10*. The synthesis starts with deprotonation at C(3) position of the 2-(2-pyridyl)imidazo[1,5-a]pyridinium hexafluorophosphate procarbenic ligand, namely $[pyipy]PF_6$, via Ag_2O-supported C–H bond activation yielding the formation of the annelated NHC ligand following the original procedure reported by Lassaletta.[17] Subsequently, transmetallation reaction was carried out in situ by adding the corresponding chloro-bridged iridium dimer. These latter were prepared using the classical procedure reported previously by Nonoyama.[18] Five target complexes **Ir1–5** bearing different cyclometalating C^N ligands were obtained in moderate yields after purification.

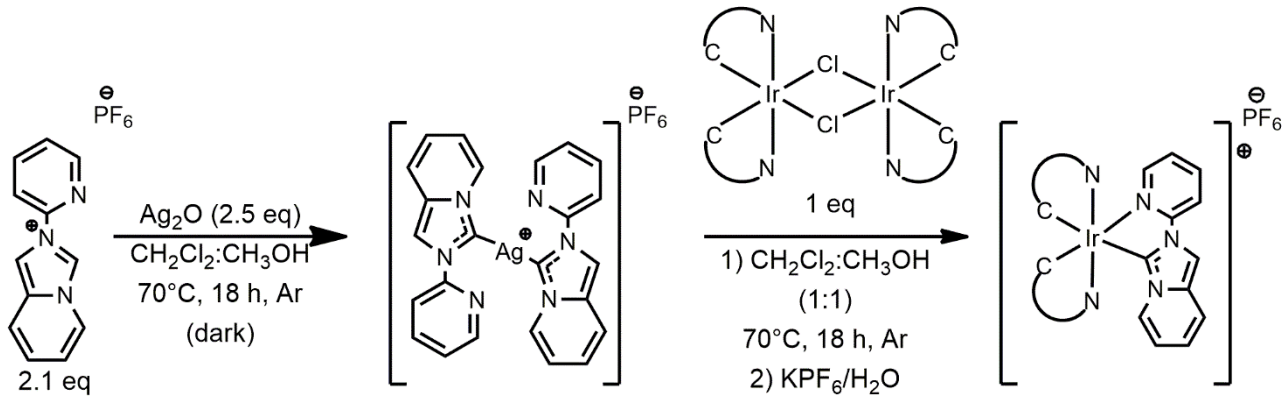

Scheme 3.1. Schematic synthetic pathway used for the synthesis of complexes **Ir1**–**5**.

[b] Ulises Carrillo, Cristina Cebrián Ávila and Philippe Gros (University of Lorraine) are kindly acknowledged for the synthesis of the pyridyl pyridoannelated carbene proligand

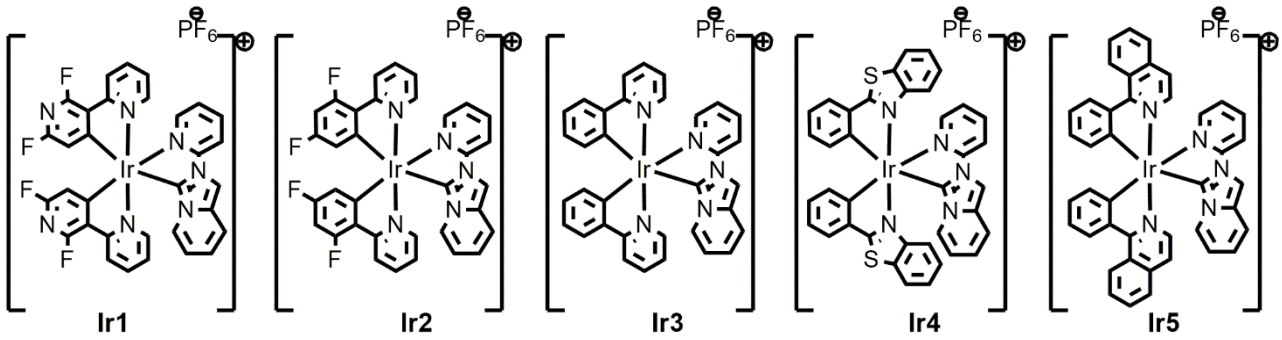

Scheme 3.2. Chemical structure of the Ir^{III} complexes **Ir1–5** investigated herein.

For derivative **Ir3** the chemical connectivity and the solid-state packing was unambiguously determined by solving the single crystal structure by means of X-ray diffractometric analysis (see *Figure 3.4*). Expectantly, the iridium atom is coordinated within a distorted octahedral geometry by two cyclometalating C^N ligand arranged in a *trans*-N,N fashion and a pyipy carbene ligand. As far as complex **Ir3** is concerned, Ir–N bonds are in the range 2.05–2.18 Å in agreement with related complexes.[19] Notably, while the Ir–C(34) bond located in *trans* to the pyridine of the pyipy is within the expected range of distances, Ir–C(7) and Ir–C(23) bond lengths display longer values due to the strong *trans* influence exerted by the cyclometalating phenyl and carbene ring, respectively, located in mutually *trans* position.

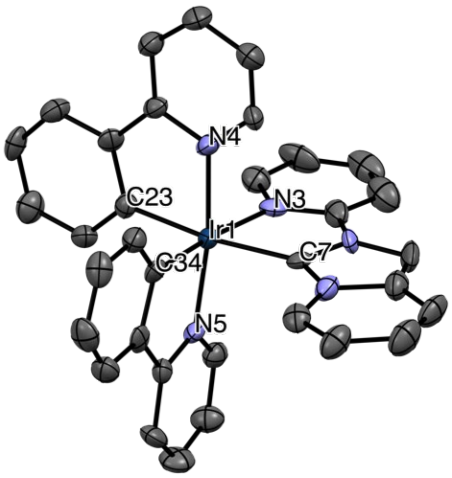

Figure 3.4 ORTEP diagram of compound **Ir3** with thermal ellipsoids shown at 50% probability level obtained by single-crystal X-ray diffractometric analysis. Hydrogen atoms and PF_6 anion are omitted for clarity. Selected bond lengths (Å): Ir–C(7) = 2.072(9) Å; Ir–

C(23) = 2.048(9) Å; Ir–C(34) = 1.995(9) Å; Ir–N(3) = 2.181(8) Å, Ir–N(4) = 2.053(7) Å, Ir–N(5) = 2.065(7) Å.

3.2.2 Photophysical characterization and theoretical calculations[c]

The electronic absorption and photoluminescence spectra recorded for samples of complexes **Ir1**–**5** in CH_2Cl_2 solution at a concentration of 3×10^{-5} M at room temperature are displayed in *Figure 3.5*. The corresponding steady state and time-resolved photophysical data are summarized in *Table 3.1.*

In the higher energy region (λ_{abs} <350 nm) the electronic absorption spectrum is characterized by intense (ε = *ca.* 1–4×10^4 M^{-1} cm^{-1}) bands that can be ascribed to the intraligand transition of π-π* character localized onto the C^N ligand, namely $^1IL_{C^N}$. At lower energy, the less intense (ε = *ca.* 0.3–1×10^4 M^{-1} cm^{-1}) and broader bands can be confidentially attributed to overlapping electronic absorption processes arising from different combination of spin-allowed singlet-manifold intraligand charge transfer (^{1}ILCT) and metal-to-ligand charge transfer character (^{1}MLCT). As far as complexes **Ir1**–**2** are concerned, an additional peak is clearly visible in the absorption profile at λ_{max} = 400 (ε = 2.4×10^3 M^{-1} cm^{-1}) and 410 nm (ε = 2.6×10^3 M^{-1} cm^{-1}) for compound **Ir1** and **Ir2**, respectively, attributable to the intraligand absorption involving the ancillary NHC ligand (IL_{NHC}) character, where NHC is the benzannulated pyipy carbene moiety, owing to the sizeable π-extended conjugation of this latter. Expectantly, the lower energy spectrum onset is monotonically shifted towards longer wavelength moving from compound **Ir1** to **Ir5** within the investigated series. This shift is due, on the one hand, to the destabilization of the highest-occupied molecular orbital (HOMO) going from **Ir1** to **Ir2** to **Ir3**; and, on the other hand, to the increased stabilisation of the lowest-occupied molecular orbital (LUMO) going from **Ir3** to **Ir4** to **Ir5** as consequence of the increased π-conjugation of the heteroaromatic ring.

[c] Dr. Chantal Daniel is kindly acknowledged for performing computational investigations.

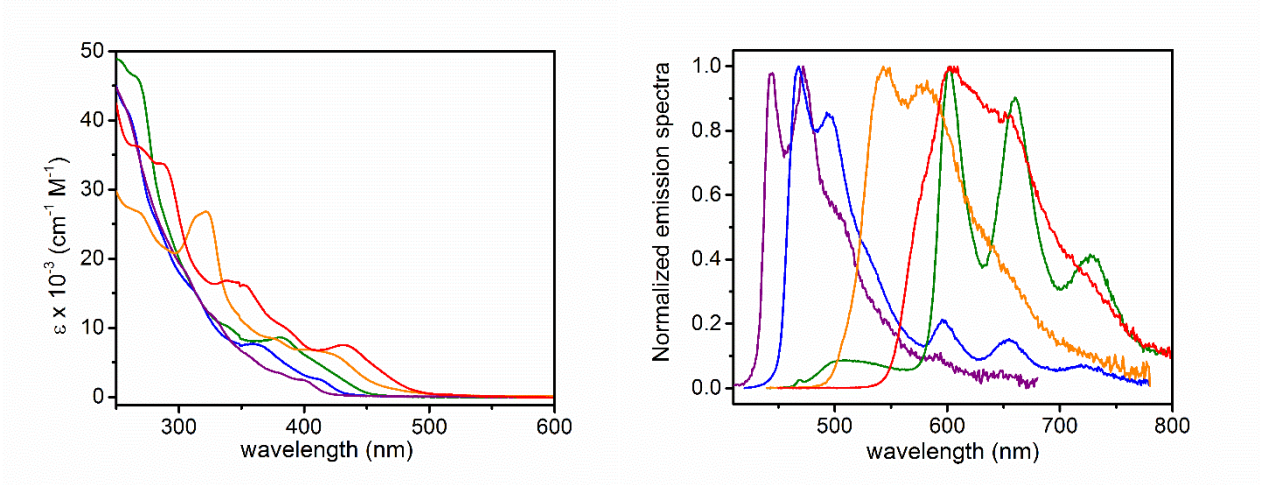

Figure 3.5 Electronic absorption (*left box*) and photoluminescence spectra (*right box*) of compound **Ir1** (purple traces), **Ir2** (blue traces), **Ir3** (green traces), **Ir4** (orange traces) and **Ir5** (red traces) in CH_2Cl_2 solution at a concentration of 3×10^{-5} M at room temperature. Emission spectra were recorded upon excitation at λ_{exc} = 350 nm for **Ir1**, λ_{exc} = 400 nm for **Ir2**, λ_{exc} = 410 nm for **Ir3**, λ_{exc} = 420 nm for **Ir4** and λ_{exc} = 430 nm for **Ir5**. Spectra of compound **Ir1**–**5** refer to degassed samples.

Computational findings carried out by Dr. Chantal Daniel of the Laboratoire de Chimie Quantique (LCQ, Unistra & CNRS) confirm these band assignments, which are also in agreement with related cyclometalated Ir^{III} complexes reported previously.[20] SOC effects induce an increasing bathochromic shift of the lowest band going from 5 nm (complex **Ir1**) to 73 nm (complex **Ir5**) that follows the character of the low-lying excited states from purely IL_{NHC} states in complexes **Ir1** and **Ir2** to mixed IL/MLCT and LLCT/MLCT in the other compounds. This bathochromic shift is governed by the important singlet/triplet mixing and increases with the $MLCT_{C^N}/LLCT_{C^N}$ contributions in the visible energy domain (500–400 nm; complexes **Ir4** and **Ir5**). The most intense peaks are attributed to IL_{C^N} transitions centred at 340–300 nm (complex **Ir4**) and 360–330 nm (complex **Ir5**). The IL_{NHC} excited states calculated at about 390–400 nm in the five complexes are characterized by modest intensities. The Kohn-Sham orbitals involved in the main electronic transitions are depicted in *Figure 3.6*.

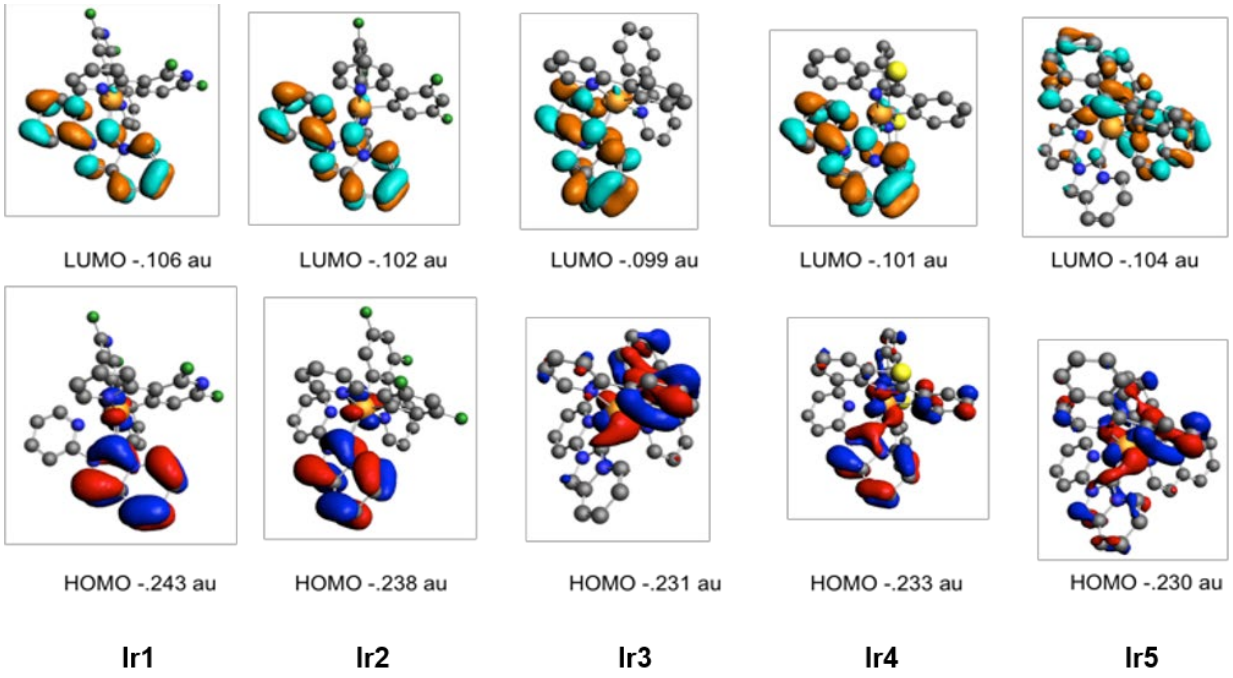

Figure 3.6 Kohn-Sham frontier orbitals of complexes **Ir1–5** after structure optimization at DFT level of theory in CH_2Cl_2 at their electronic ground state.

Upon photo-excitation into the low-lying energy band, dilute samples of complexes **Ir1**–**5** exhibit low to moderate photoluminescence (see *Table 3.1*), yet with a dual emission surprisingly.

The lowest triplet manifold (T_1) corresponds to an intraligand (IL_{NHC}) state that is localized onto the NHC moiety and it is calculated at *ca.* 700 nm in the five complexes. The low-lying IL_{C^N} emissive states are mixed with $LLCT_{C^N}$ and $MLCT_{C^N}$ states in T_2 and T_3 and significantly shifted to the red following the prevalence of IL_{C^N} contribution when going from complex **Ir1** to **Ir5**.

Emission spectrum of compound **Ir1** features one structured band with λ_{em} maxima at 444 and 473 nm, namely high-energy (HE) emission band. In addition, a second structured band is visible on the lower energy (LE) side with λ_{em} at 590 and 648 nm, yet with very low intensity. Moving to complex **Ir2**, the HE band display a bathochromic shift to λ_{em} = 467 nm and 494 nm; whereas, the LE band increases its intensity with no spectral shift apparently. The calculated emission wavelengths λ^{theo} reproduce the experimental trends with theoretical maxima at 426 and 508 nm (*vs.* 444 and 474 nm) in **Ir1**, 451 and 525 nm (*vs.* 467 and 484 nm) in **Ir2**, 490 and 532 nm (*vs.* 500 and 540 nm) in **Ir3**, 517 and 571 nm (*vs.* 545 and 580 nm) in **Ir4** and 582 and 605 nm (*vs.* 600 and 655 nm) in **Ir5**.

The LE appears even more clearly for compound **Ir3** and the HE band is weak, broad and featureless instead. In complexes **Ir4**–**5**, the stabilization of the π* orbitals imparted by the more extended conjugation of the C^N ligand causes an expected bathochromic shift of the emission profile and band structure is less marked. The different origin of the two emission bands is supported by the independent behaviour observed for the excitation spectra recorded at the HE and LE wavelength that suggests poor electronic coupling between the two excited states responsible of the dual emission.[21]

As far as complexes **Ir1**–**3** are concerned, the HE band can be ascribed with confidence to a radiative process arising from a triplet excited state with mainly $^3IL_{C^N}$ character, although with a partial degree of mixing with the $^1MLCT_{C^N}$ state depending on the nature of the C^N ligand, as typical of this class of emitters.[20] In particular, for complexes **Ir1**–**2** the sizeable contribution from a $^3IL_{C^N}$ state is supported by the vibronic profile of the emission spectra with spacing in the order 1100–1400 cm^{-1} attributed to the intraligand C=C and C=N vibrational modes. Furthermore, the formally triplet nature of the emitting state is corroborated by the observed increase of the photoluminescence quantum yield (PLQY) going from air-equilibrated to oxygen-free samples (see *Table 3.1*). The compound bearing the unsubstituted ppy ligand, namely complex **Ir3**, displays the lowest (PLQY = 1.3% in degassed CH_2Cl_2 sample) amongst the investigated series; whilst, orange-red emitter **Ir4** possesses the highest PLQY. These findings are in agreement with those reported by Baranoff and co-workers on a related series bearing the 3-methyl-1-(4-methyl-2-pyridyl)benzimidazol-2-ylidene NHC ligand.[20c]

It is worth to notice that examples of dual emission in cyclometalated Ir^{III} complexes are scarce, and this phenomenon is intriguing also in view of the potential application as broadband emitters.[22] Thus, this finding prompted us to carry out time-resolved emission decay analysis at different emission wavelengths to gain a better understanding of the nature the two emitting excited states. Observed lifetimes fall in the hundreds of nanoseconds to microseconds regime. Also, going from air-equilibrated to degassed samples a sizeable prolongation of the excited-state lifetimes is observed independently of the emission wavelength.

As far as complex **Ir3** is concerned, lifetimes measured for degassed samples at the HE and LE bands display mono-exponential decay with τ_{HE} = 555 ns and τ_{LE} = 6.0 μs, respectively. For complexes **Ir4**–**5**, analysis of the decay traces required a bi-exponential fitting at both shorter and longer wavelength region with similar lifetime components (for

examples, τ_1 = 6.1 μs and τ_2 = 1.8 μs for complex **Ir4**), yet with different weights, indicating that the recorded PL profile is composed of two almost overlapping emission bands. Similar results were obtained for complex **Ir2**. The HE band overwhelmed the LE one for complex **Ir1**. Overall, these findings confirm the mainly triplet nature for both excited states involved in the dual emission process and point towards a $^3MLCT_{C^N}/^3IL_{C^N}$ and $^3IL_{NHC}$ character for the HE and LE bands, respectively; the latter state, which possesses poorer emission properties, being responsible of the quenching of the higher-lying $^3MLCT_{C^N}/^3IL_{C^N}$ manifold.

Table 3.1. Photophysical data recorded for samples of compound **Ir1–Ir5** in air-equilibrated and degassed CH_2Cl_2 solution at concentration of 3×10^{-5} M at room temperature.

Cmpd	$\lambda_{max,abs}$ (ε) [nm, (10^3 M^{-1} cm^{-1})]	λ_{em} [nm]	PLQY (%)		τ_{obs}	
			air-equilibrated	*degassed*	*air-equilibrated* [a]	*degassed* [a]
Ir1	306 (17.62), 327 (11.50), 355 (6.03), 380 (3.47), 400 (2.40)	444, 473, 507, 590, 648	1.6	3.1	573 ns [443] 504 ns (56%) 65 ns (44%) [641]	1.1 μs [444] 344 ns (21%) 1.5 μs (79%) [641]
Ir2	262 (40.11), 283 (25.03), 313 (15.16), 359 (7.55), 410 (2.63)	467, 494, 596, 654, 720	0.6	6.2	139 ns [467] 628 ns (47%) 163 ns (53%) [652]	1.6 μs (35%) 1.3 μs (65%) [467] 7.0 μs (77%) 594 ns (23%) [652]
Ir3	266 (46.28), 309 (15.65), 340 (10.04), 383 (8.55), 420 (3.77)	510, 600, 660, 730	0.1	1.3	52 ns (66%) 139 ns (34%) [500] 478 ns [600]	555 ns [500] 6.0 μs [600]
Ir4	322 (26.80), 377(8.37), 420 (6.32), 450 (2.58)	545, 580	1.7	6.7	315 ns (65%) 839 ns (35%) [545] 851 ns (33%) 325 ns (67%) [580]	6.1 μs (12%) 1.8 μs (88%) [545] 6.1 μs (12%) 1.8 μs (88%) [680]
Ir5	267 (36.26), 287 (33.71), 344 (16.62), 387 (9.73), 432 (7.49), 460 (3.93)	600, 655	0.6	4.7	398 ns (42%) 661 ns (58%) [600] 349 ns (34%) 629 ns (66%) [650]	2.1 μs (20%) 5.9 μs (80%) [600] 2.0 μs (23%) 5.9 μs (77%) [650]

[a] emission wavelength (in nm) where the lifetime has been recorded at is reported in square brackets.

This picture agrees well with the experimental data obtained for related luminescent Re(I)-tricarbonyl species bearing the same pyipy NHC ligand that display a $^3LC_{NHC}$ emission with higher energy peak at λ_{em} = 608 nm.[23]

3.3 Biological activity as anticancer drugs[d]

The *in vitro* cytotoxicity of the compounds was investigated in the frame of a collaboration with the group of Pr. Sylvie Fournel, Dr. Antoine Kichler and Conor McCartin at the faculty of Pharmacy, University of Strasbourg. In particular, the complexes were tested against two Human cancer cell lines, HCT116 (human colon carcinoma) and MDA-MB-231 (human breast cancer), by measuring the decrease of NADH and $NADPH^-$ dependant dehydrogenase activity, reflecting a decrease of metabolic activity, using the MTS assay after 24- and 48-hours treatment. The resulting half maximal inhibitory concentration values (concentration required to reduce by 50% the cell viability; IC_{50}) are listed in *Table 3.2*.

Table 3.2. IC_{50} values (in µM) of the tested complexes **Ir1–Ir5**.

Compound	HCT116		MDA-MB-231	
	24 h	***48 h***	***24 h***	***48 h***
Ir1	>50	>50	>50	>50
Ir2	7.2 ± 1.2	2.3 ± 1.4	20.6 ± 2.9	9.2 ± 1.1
Ir3	21.2 ± 4.3	2.1 ± 1.2	16.4 ± 1.2	10.2 ± 1.1
Ir4	7.5 ± 1.1	1 ± 1.1	9.6 ± 1.1	4.8 ± 1.1
Ir5	8.3 ± 1.2	1.7 ± 1.1	13.2 ± 1.2	7.8 ± 1.2
Oxaliplatin	>50	46.57	>50	>50

All IC_{50} values are the mean of at least two independent experiments ± one standard error of the mean (SEM), with each experiment consisting of the mean of three technical replicates. IC_{50} and SEM were calculated by non-linear regression using Prism software.

All the compounds show a similar level of cytotoxicity - of a level much higher than that of the commonly used platinum based anti-cancer compound oxaliplatin - except for compound **Ir1**. Notably, the compounds showed a roughly two- to ten-fold decrease in IC_{50} after 48 hours - reaching IC_{50} values of around 1 µM - except for compound **Ir1**. Additional results following 72 h treatment of HeLa cells with compounds **Ir2** and **Ir4** showed IC_{50} values of 3.6 µM and 1.6 µM, respectively (*Figure ES3.12*), displaying comparable potency to the *bis*-N-heterocyclic Ir compounds reported by Che *et al.*[15] Taken together, we thus identified four new Ir^{III}-NHC complexes with high anti-tumoral activities. It should be pointed out that the p53 tumor suppressor is mutated in approx. 50% of cancers and it is a major

[d] Conor McCartin , Antoine Kichler and Sylvie Fournel are kindly acknowledged for the biological investigation.

cause of tumor resistance. While the efficiency of platinum derivatives such as cisplatin and oxaliplatin is often reduced against cells having a deficient p53,[24] we found that our Ir-NHC complexes were highly cytotoxic against MDA-MB-231 which have a mutated p53. This is consistent with the observed anti-mitochondrial effect of compounds **Ir1**–**5**, whose direct disruption of mitochondrial activity may cause p53 independent activation of apoptosis.[5]

3.3.1 Cellular uptake and localization

Cellular distribution was also investigated, showing that all compounds entered the cells with high visible photo-luminescence, expect compound **Ir1** which is poor cytotoxic as well (*Figure 3.7*). The co-localisation analysis were moderate to high Pearson correlation R values. This latter one is a factor that linearly correlates two variables between 0 and +1, representing absence and presence of co-localisation, respectively. The lower values was found for compound **Ir1** (0.48) and the highest for **Ir5** (0.90). As calculated by the partition coefficient $logP_{o/w}$ values (*Table 3.3*), as the hydrophobicity of the molecules increases, as the mitochondrial membrane permeabilization is higher. These results are in agreement with previous investigation as reported by Lo,[25] Mao,[14] and Che.[15]

Table 3.3. Partition coefficients $logP_{o/w}$ determined for complexes **Ir1–5**.

cmpd	log $P_{o/w}$	Pearson co-localisation value
Ir1	0.50	0.48
Ir2	1.26	0.63
Ir3	1.33	0.85
Ir4	1.58	0.84
Ir5	2.05	0.90

3.3.2 Mitochondrial dysfunction

Ir1-5 are able to disrupt mitochondrial function as well as Pt^{II}-NHC complexes. To evaluate if the cytotoxic activity of the Ir-NHC complexes is also correlated with mitochondrial dysfunctions, two experiments were carried out: mitochondrial ROS induction and mitochondrial respiratory activity.

3.3.2.1 Mitochondrial ROS induction

The first experiment measures mitochondrial reactive oxygen species (ROS) induction at sub-IC_{50} concentrations of the compounds, with staurosporine used as a positive control, as it is known to induce mitochondrial ROS.[26] Compounds **Ir1** and **Ir2** had no notable effect on ROS induction at low concentrations, while compound **Ir4** was capable of inducing levels of ROS comparable to staurosporine. This is consistent with the higher observed mitochondrial localisation of compound **Ir4** and indicates that it likely interferes with mitochondrial function upon entry. Such activity is in line with the anti-mitochondrial action of similar Ir^{III} complexes found in the literature.[14]

3.3.2.2 Mitochondrial respiratory activity

The second experiment measures anti-mitochondrial activity relied on the ability to distinguish populations of cells with inactive mitochondria. Only compound **Ir4** was capable of inducing notable loss of mitochondrial membrane potential at low micro-molar concentrations.

Loss of mitochondrial membrane potential prevents ATP production and will eventually lead to the energy starvation of the cell.[27] This confirms the activity of compound **Ir4** as a potent mitochondrial targeting compound, which may be explained by its higher lipophilicity and mitochondrial accumulation compared to compound **Ir2**, despite similar IC_{50} values.

3.3.3 Cell death and apoptosis

To investigate further the mechanism of cell death induced by the NHC-Ir complexes, and as damaging of mitochondria may lead to activation of intrinsic apoptosis, it was measured whether the cells entered apoptosis following 24 h treatment with sub-IC_{50} concentrations. While compound **Ir1** remained mostly inactive as expected, compound **Ir2** and **Ir4** showed induction of early apoptosis at low µM concentrations. The similar IC_{50} value and induction of early-apoptosis of compound **Ir2** and **Ir4** despite the much lower level of mitochondrial disruption of compound **Ir2** may be explained by its lower lipophilicity and mitochondrial

localisation. Suggesting a potentially different mechanism of action between the two derivatives. As compound **Ir4** showed a higher level of activity, its mechanism was further investigated. It was found that the pathway of apoptotic induction by compound **Ir4** is caspase dependant [28]- a family of cysteine proteases that serve as primary effectors during apoptosis[29]- which likely occurs due to direct activation of the intrinsic apoptotic pathway through mitochondrial disruption.

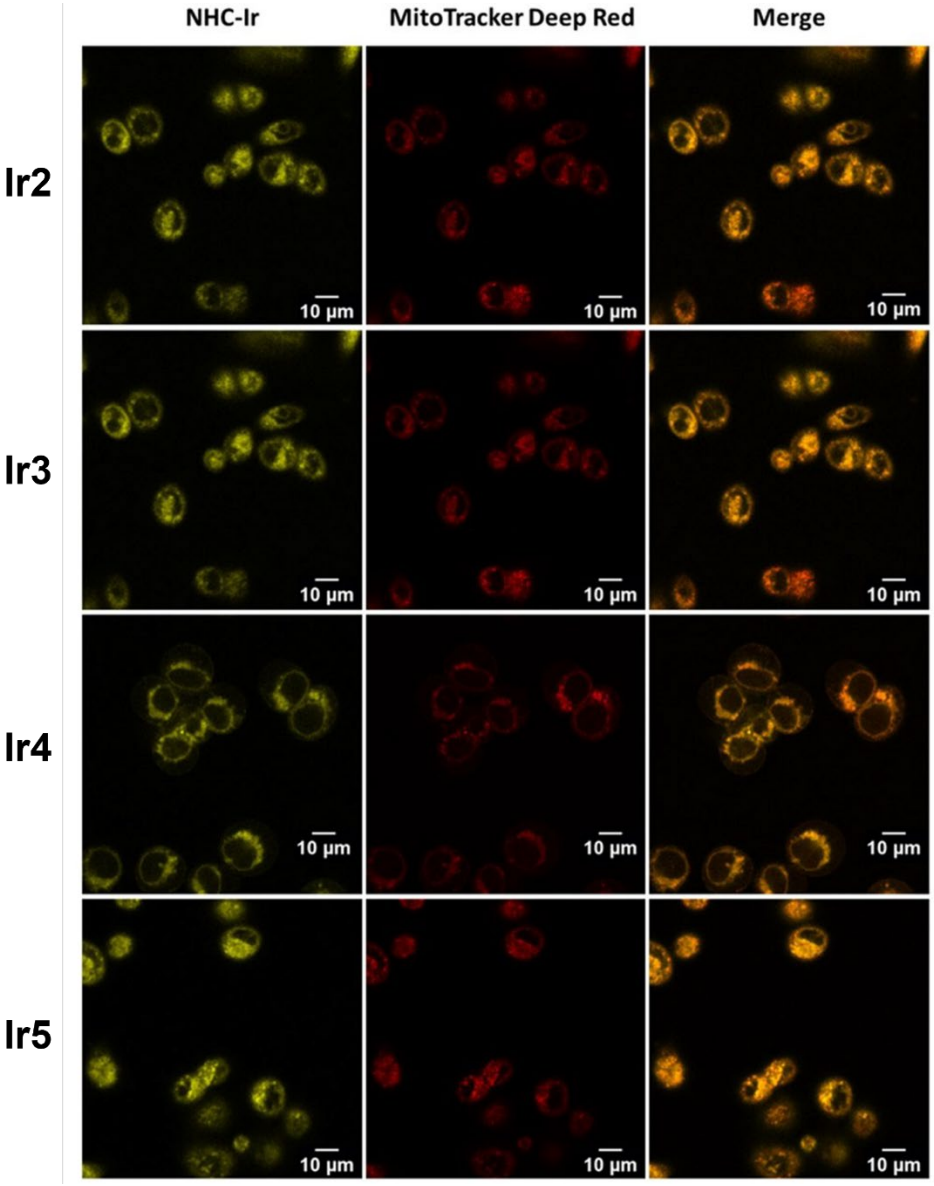

Figure 3.7 Confocal fluorescence microscopy of live HCT116 cells co-stained with 10 µM of each compound (90 min) and 500 nM MitoTracker Deep Red (30 min). Live cells were then maintained at 37°C and imaged immediately.

3.4 Conclusion

The synthesis and characterization of a novel class of cationic Ir^{III} complexes featuring a pyrido annulated NHC as the ancillary ligand is herein presented. The compounds display interesting photophysical properties with a rare case of dual-emission arising from two close-lying excited states with mixed $^3MLCT_{C^N}/^3IL_{C^N}$ and mainly $^3LC_{NHC}$ character. The optical properties are combined with high tumor cell killing activities, making the investigated compounds potent theragnostic agents with excellent cytotoxicity, as demonstrated by the IC_{50} values falling in the low μM regime. Remarkably, the investigated Ir-NHC complexes display high cytotoxicity independently of the nature, either wild type or mutated, of the p53 tumor suppressor. The presented results are consistent with previous reports of delocalised lipophilic cationic metallodrugs, which are capable of localising to, and disrupting mitochondria, resulting in activation of apoptosis. A characteristic that play potentially a key-role in overcoming resistance to current anti-cancer therapeutics. A potent candidate is thus revealed for further studies and potential theragnostic applications thanks to its combined optical and cytotoxicity properties.

3.5 Experimental section

3.5.1 General considerations

$IrCl_3 \times nH_2O$ was purchased from Precious Metals Online. 2-phenylpyridine (ppy), 2-(2,4 difluorophenyl)pyridine (dfppy) and 2-phenylbenzothiazole (2-pbt) were purchased from Fluorochem and used as received without further purification. All procedures involving iridium complexes were carried out under argon atmosphere using standard Schlenk techniques. Silica gel for column chromatography was purchased from Sigma-Aldrich. The pro-ligand [pyipy]PF_6,[30] 2',6'-difluoro-2,3'-bipyridine (dfpypy),[31] 1-phenyl isoquinoline (1-piq),[32] and the chloro-bridged iridium dimers[18] were synthetized accordingly to procedures reported previously.

3.5.2 Synthesis

A solution of CH_2Cl_2:CH_3OH 1:1 v/v was bubbled for 15 min before adding Ag_2O and 2-(2-pyridinyl)imidazo[1,5-a]pyridinium hexafluorophosphate. The mixture was kept in the dark

and refluxed for 18 hours under an argon atmosphere. Subsequently, the corresponding chloro-bridged iridium(III) dimer $[Ir(\mu\text{-}Cl)(C\text{^}N)_2]_2$, where C^N denotes one of the five phenylpyridine-type of ligands employed, was added and the solution was stirred in the same conditions for 18 hours, then reaction mixture was cooled to room temperature and filtered over Celite plug. The volume of the solution was reduced and the compound precipitated with the help of a saturated aqueous solution of KPF_6. The solid was filtered and washed with water and Et_2O repeatedly. Compounds **Ir4** and **Ir5** were purified by silica gel column chromatography using CH_2Cl_2as eluent. A mixture of CH_2Cl_2 with 0.2% of CH_3OH was used as TLC eluent mixture. R_f(**Ir4**) = 0.3; R_f(**Ir5**) = 0.5.

[Ir(dfpypy)$_2$(pyipy)]PF$_6$ (Ir1). ^{1}H NMR (500 MHz, 298 K, d_6-DMSO) δ: 9.04 (s, 1H), 8.67 (d, J = 8.2 Hz, 1H), 8.42 (t, J = 7.5 Hz, 1H), 8.30 (s, J = 3.5 Hz, 2H), 8.11 (dd, J = 13.8, 6.9 Hz, 2H), 8.02 (d, J = 5.4 Hz, 1H), 7.89 (d, J = 5.1 Hz, 1H), 7.77 (d, J = 5.4 Hz, 1H), 7.67 (d, J = 9.4 Hz, 1H), 7.61– 7.49 (m, 1H), 7.36–7.28 (m, 1H), 7.28–7.22 (m, 1H), 6.98 (dd, J = 18.4, 8.2 Hz, 2H), 6.69 (t, J = 6.7 Hz, 1H), 5.87 (s, 1H), 5.64 (s, 1H). ^{13}C NMR (126 MHz, DMSO) δ: 186.2, 171.4, 164.0, 161.8, 161.8, 160.7, 160.6, 155.4, 153.0, 151.0, 143.4, 140.8, 140.3, 132.3, 126.7, 126.5, 125.6, 125.2, 124.4, 124.3, 124.1, 123.9, 119.7, 117.2, 115.4, 110.3, 108.3. ^{19}F NMR (376 MHz, 298 K, CD_2Cl_2) δ: –67.22, –67.41, –68.83, –69.63. ES-MS calcd for $C_{32}H_{19}F_4IrN_7^+$ 770.12 ([M+H]$^+$); found 770.13. Anal for $C_{32}H_{19}F_4IrN_7\cdot H_2O$: found C 41.66 H 2.44 N 9.97, calcd C 41.21 H 2.27 N 10.51.

[Ir(dfppy)$_2$(pyipy)]PF$_6$ (Ir2). ^{1}H NMR (500 MHz, 298 K, CD_2Cl_2) δ: 8.41 (s, 1H), 8.39–8.34 (m, 2H), 8.29 (q, *J* = 8.0 Hz, 2H), 7.91 (d, *J* = 5.2 Hz, 1H), 7.86 (dd, *J* = 14.4, 7.0 Hz, 2H), 7.72 (d, *J* = 5.7 Hz, 1H), 7.53 (t, *J* = 7.8 Hz, 2H), 7.44 (t, *J* = 7.0 Hz, 1H), 7.09–7.04 (m, 2H), 7.00 (t, *J* = 6.7 Hz, 1H), 6.96–6.91 (m, 1H), 6.70–6.62 (m, 2H), 6.43 (t, *J* = 7.3 Hz, 1H), 5.96 (d, *J* = 2.3 Hz, 1H), 5.76 (dd, *J* = 7.8, 2.3 Hz, 1H). ^{13}C NMR (126 MHz, 298 K, CD_2Cl_2) δ: 167.6, 167.3, 165.1, 165.1, 163.9, 163.9, 153.2, 150.3, 148.7, 142.4, 138.9, 138.3, 132.5, 125.6, 125.5, 124.3, 124.1, 124.0, 123.8, 123.6, 123.4, 119.0, 116.1, 114.4, 113.3, 108.4, 99.8, 99.6, 99.4, 98.5, 98.3, 98.1. ^{19}F NMR (376 MHz, 298 K, CD_2Cl_2) δ: –106.36, –106.51, –108.42, – 108.84. ES-MS calcd for $C_{34}H_{21}F_4IrN_5^+$ 768.14 ([M+H]$^+$); found 768.13. Anal for $C_{34}H_{21}F_{10}IrN_5P\cdot 2H_2O$: found C 42.60 H 2.43 N 7.22, calcd C 43.04 H 2.66 N 7.38.

[Ir(ppy)$_2$(pyipy)]PF$_6$ (Ir3). ^{1}H NMR (500 MHz, 298 K, CD_2Cl_2) δ: 8.32 (s, 1H), 8.24–8.18 (m, 2H), 7.99 (d, J = 8.1 Hz, 2H), 7.92 (d, J = 5.2 Hz, 1H), 7.84– 7.78 (m, 4H), 7.74 (d, J = 6.4 Hz, 1H), 7.56 (d, J = 5.8 Hz, 1H), 7.48 (d, J = 9.5 Hz, 1H), 7.39–7.35 (m, 1H), 7.18–7.10

(m, 2H), 7.06 (td, J = 7.4, 1.2 Hz, 1H), 7.04–6.98 (m, 3H), 6.95 (ddd, J = 7.3, 5.9, 1.4 Hz, 1H), 6.87 (dd, J = 9.4, 6.4 Hz, 1H), 6.53 (d, J = 7.0 Hz, 1H), 6.34 (d, J = 6.7 Hz, 1H), 6.30–6.26 (m, 1H). ^{13}C NMR (126 MHz, 298 K, CD_2Cl_2) δ: 170.6, 168.7, 167.3, 163.1, 153.5, 153.2, 150.5, 148.7, 147.2, 144.5, 143.0, 141.7, 137.9, 137.2, 132.3, 131.1, 131.0, 130.8, 130.4, 126.2, 125.2, 124.9, 124.9, 123.9, 123.2, 123.0, 121.9, 120.0, 119.7, 118.7, 115.2, 113.8, 107.8. ES-MS calcd for $C_{34}H_{25}IrN_5^+$ 696.17 ([M+H]+); found 696.17. Anal for $C_{34}H_{25}F_6IrN_5P\cdot H_2O$: found C 47.08 H 2.97 N 8.01, calcd C 47.55 H 3.17 N 8.15.

[Ir(2-pbt)$_2$(pyipy)]PF$_6$ (Ir4). ^{1}H NMR (500 MHz, 298 K, CD_2Cl_2) δ: 8.33 (s, 1H), 8.22 (dt, *J* = 12.7, 8.4 Hz, 2H), 8.00 (d, *J* = 4.1 Hz, 1H), 7.97–7.88 (m, 4H), 7.50 (dd, *J* = 9.5, 1.1 Hz, 1H), 7.41 (td, *J* = 7.8, 4.1 Hz, 3H), 7.23– 7.13 (m, 4H), 7.03 (td, *J* = 7.4, 1.2 Hz, 1H), 6.97–6.87 (m, 3H), 6.56 (s, *J* = 157.6 Hz, 1H), 6.45 (s, 1H), 6.32 (ddd, *J* = 7.5, 6.6, 1.1 Hz, 1H), 6.16 (d, *J* = 8.4 Hz, 1H), 6.10 (d, *J* = 8.4 Hz, 1H). ^{13}C NMR (500 MHz, 298 K, CD_2Cl_2) δ: 182.8, 179.7, 167.0, 163.2, 153.9, 150.8, 149.6, 149.1, 147.3, 142.1, 140.7, 139.4, 132.8, 132.7, 132.3, 132.2, 131.8, 131.4, 131.3, 128.2, 127.9, 126.6, 126.5, 126.0, 125.8, 125.7, 125.2, 124.0, 123.9, 123.4, 122.5, 118.9, 118.0, 117.5, 115.8, 113.9, 108.0. ES-MS calcd for $C_{38}H_{25}IrN_5S_2^+$ 808.12 ([M+H]$^+$); found 808.11. Anal for $C_{38}H_{25}F_6IrN_5PS_2\cdot 2H_2O$: found C 46.47 H 2.77 N 7.02, calcd C 46.15 H 2.96 N 7.08.

[Ir(1-piq)$_2$(pyipy)]PF$_6$ (Ir5). ^{1}H NMR (500 MHz, 298 K, CD_2Cl_2) δ: 8.99 (t, *J* = 10.1 Hz, 2H), 8.42 (d, *J* = 8.1 Hz, 1H), 8.34 (dd, *J* = 11.3, 3.3 Hz, 2H), 8.21 (d, *J* = 10.2 Hz, 2H), 7.94 (d, *J* = 2.4 Hz, 2H), 7.84 (s, 2H), 7.74 (d, *J* = 6.3 Hz, 1H), 7.60 (d, *J* = 6.4 Hz, 1H), 7.47 (d, *J* = 8.5 Hz, 1H), 7.43 (d, *J* = 6.5 Hz, 1H), 7.35 (d, *J* = 7.0 Hz, 2H), 7.29 (d, *J* = 6.4 Hz, 1H), 7.22 (m, 2H), 7.04 (t, *J* = 7.4 Hz, 1H), 6.96 (t, *J* = 6.8 Hz, 1H), 6.84 (d, *J* = 9.5 Hz, 1H), 6.66 (d, *J* = 7.4 Hz, 1H), 6.53 (d, *J* = 7.7 Hz, 1H), 6.33 (d, *J* = 7.5 Hz, 1H), 6.22 (t, *J* = 7.5 Hz, 1H). ^{13}C NMR (126 MHz, CD_2Cl_2) δ: 151.2, 149.1, 141.7, 140.3, 139.5, 138.0, 132.0, 131.6, 131.5, 131.0, 130.8, 130.7, 130.4, 129.0, 128.9, 127.5, 126.9, 124.5, 122.9, 122.3, 122.3, 121.9, 119.1. ES-MS calcd for $C_{42}H_{29}IrN_5^+$ 796.20 ([M+H]$^+$); found 796.20. Anal for $C_{42}H_{29}F_6IrN_5P\cdot 4H_2O$: found C 49.00 H 3.13 N 6.41, calcd C 49.80 H 3.68 N 6.91.

Supplementary data

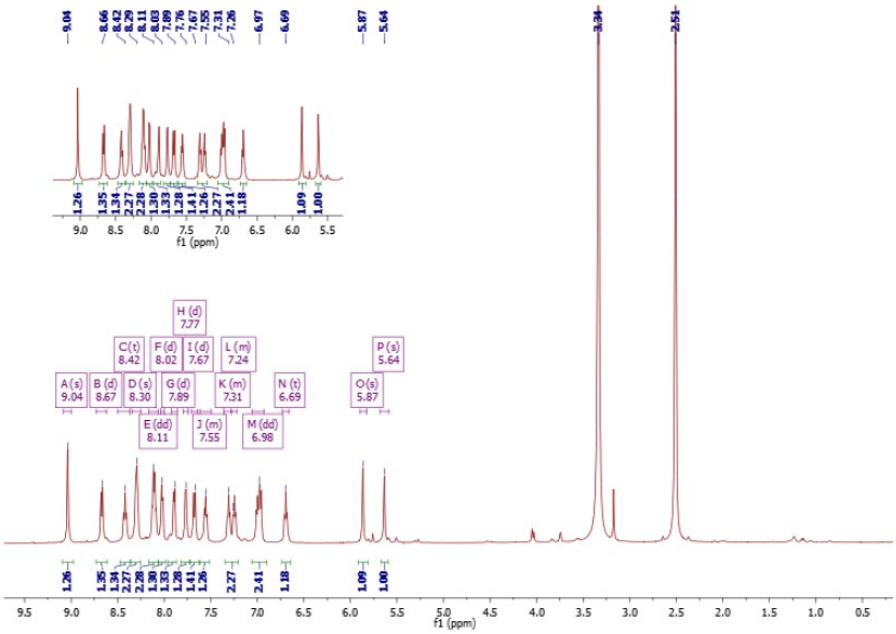

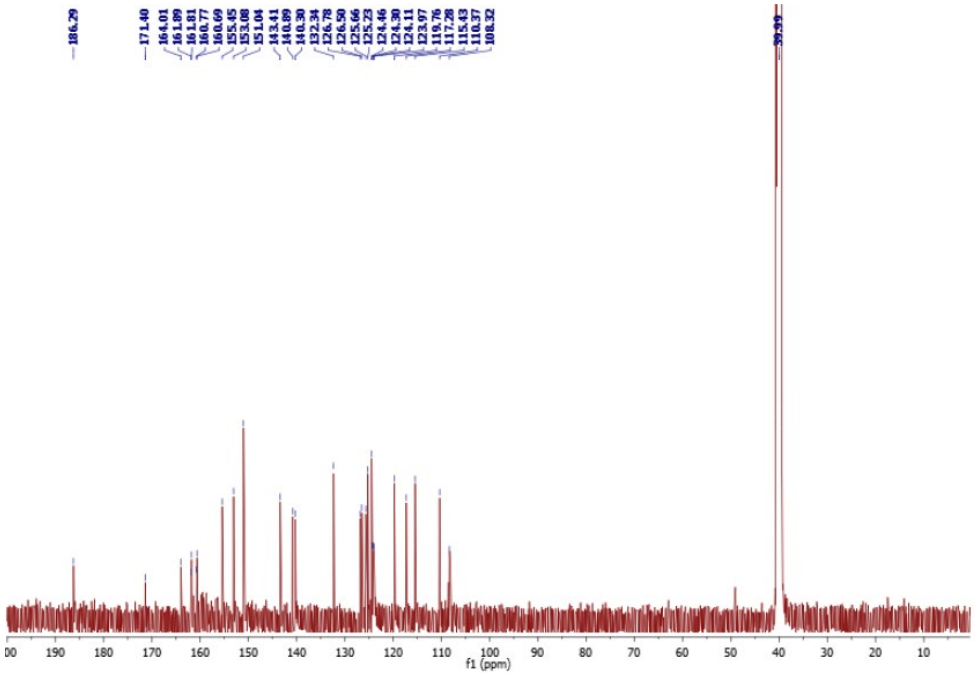

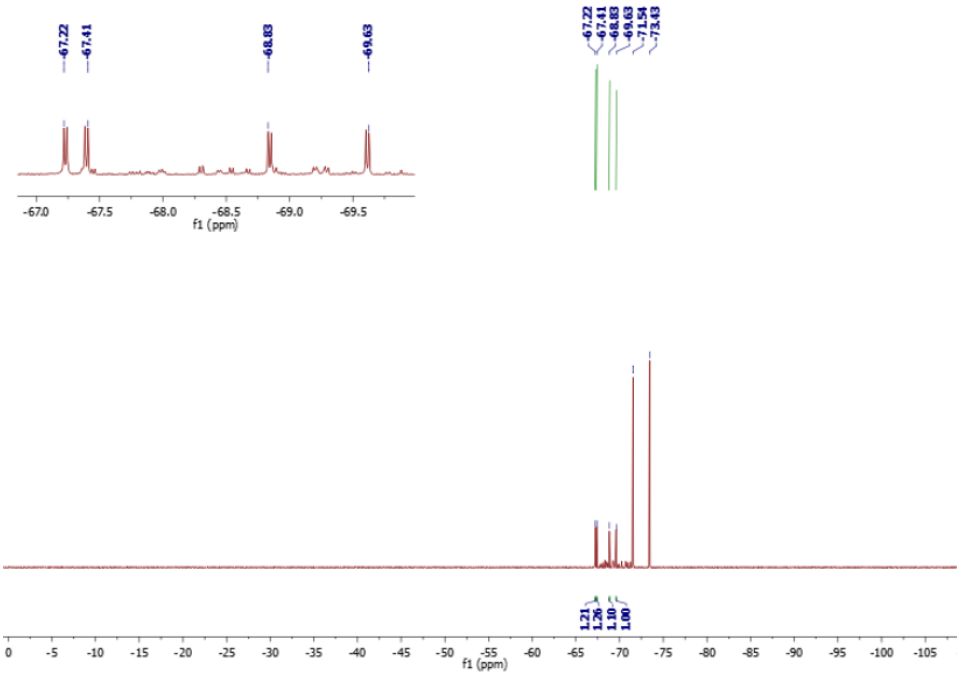

Figure ES3.1 ^{1}H (500 MHz, top), ^{13}C NMR (125 MHz, middle) and ^{19}F NMR (376 MHz, bottom) spectra recorded for complex **Ir1** in DMSO-d6 and CD_2Cl_2 at 298 K.

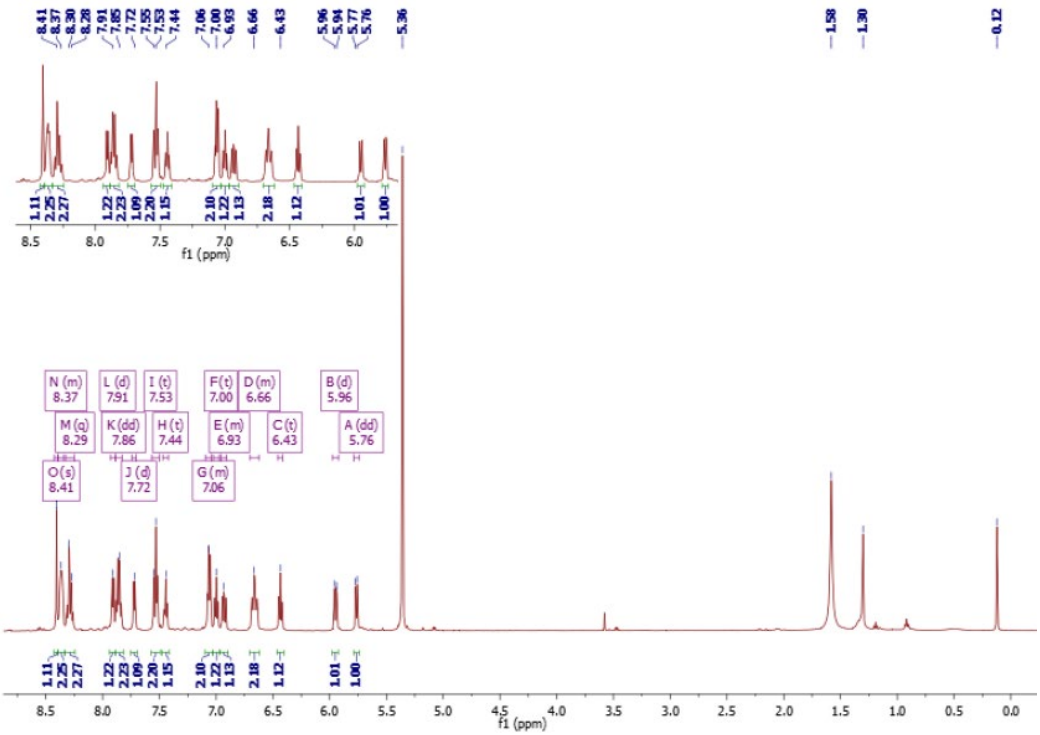
8.41
8.37
8.30
8.28
7.91
7.85
7.72
7.55
7.53
7.44
7.06
7.00
6.93
6.66
6.43
5.96
5.94
5.77
5.76
5.36
1.58
1.30
0.12
N (m) 8.37
L (d) 7.91
I (t) 7.53
F(t) 7.00
D(m) 6.66
B(d) 5.96
M(q) 8.29
K(dd) 7.86
H(t) 7.44
E(m) 6.93
C(t) 6.43
A(dd) 5.76
O(s) 8.41
J(d) 7.72
G(m) 7.06
f1 (ppm)

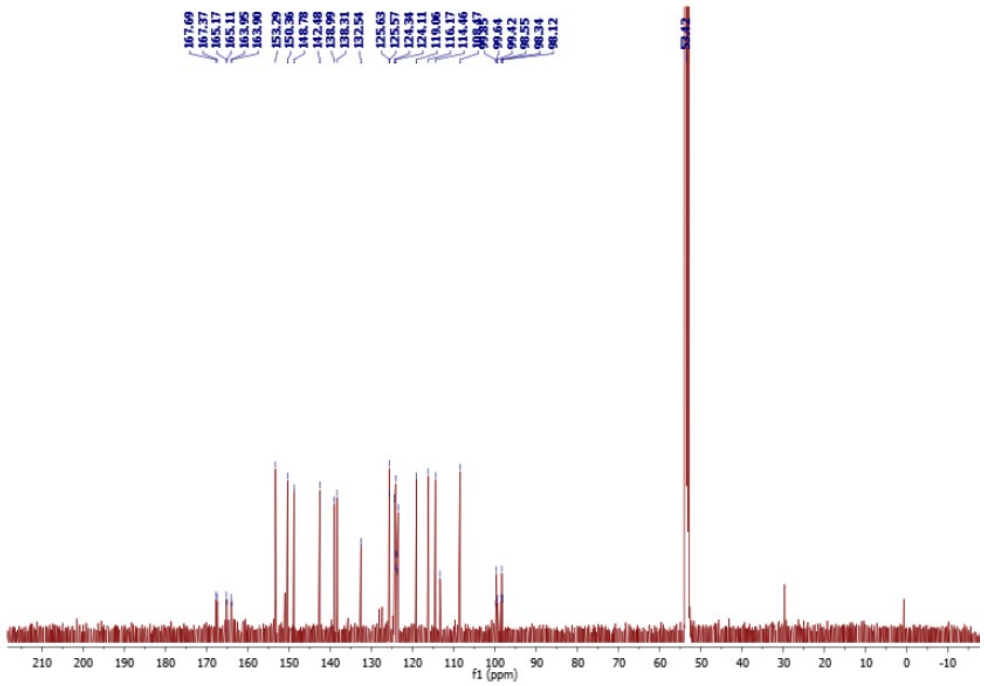
167.69
167.37
165.17
165.11
163.95
163.90
153.29
150.36
148.78
142.48
138.99
138.31
132.54
125.63
125.57
124.34
124.11
119.06
116.17
114.46
99.64
99.42
98.55
98.34
98.12
53.42
f1 (ppm)

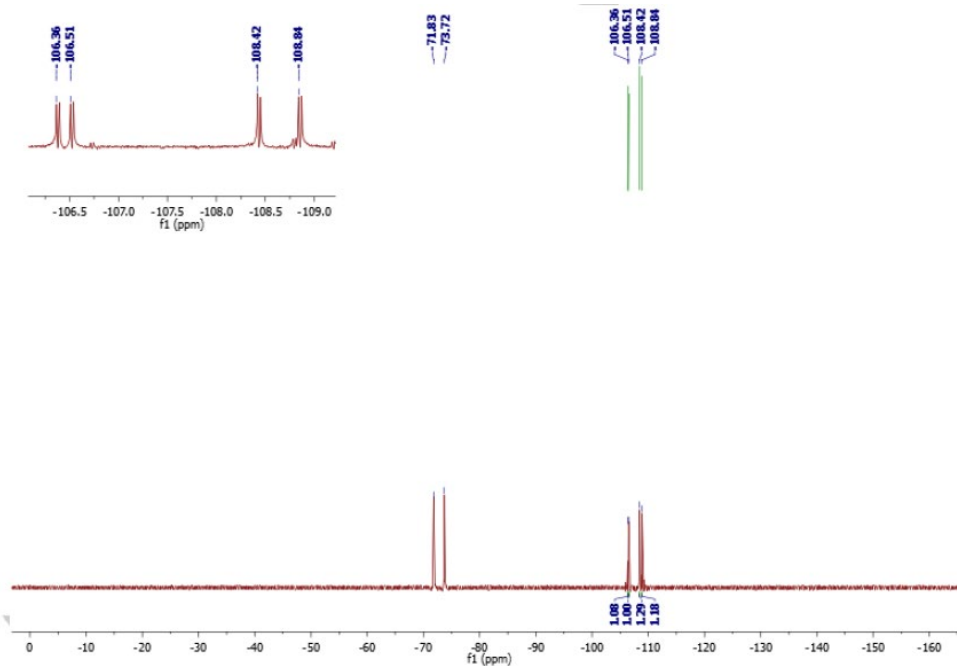

Figure ES3.2 ^{1}H (500 MHz, *top*), ^{13}C NMR (125 MHz, *middle*) and ^{19}F NMR (376 Mhz, *bottom*) spectra recorded for complex **Ir2** in CD_2Cl_2 at 298 K.

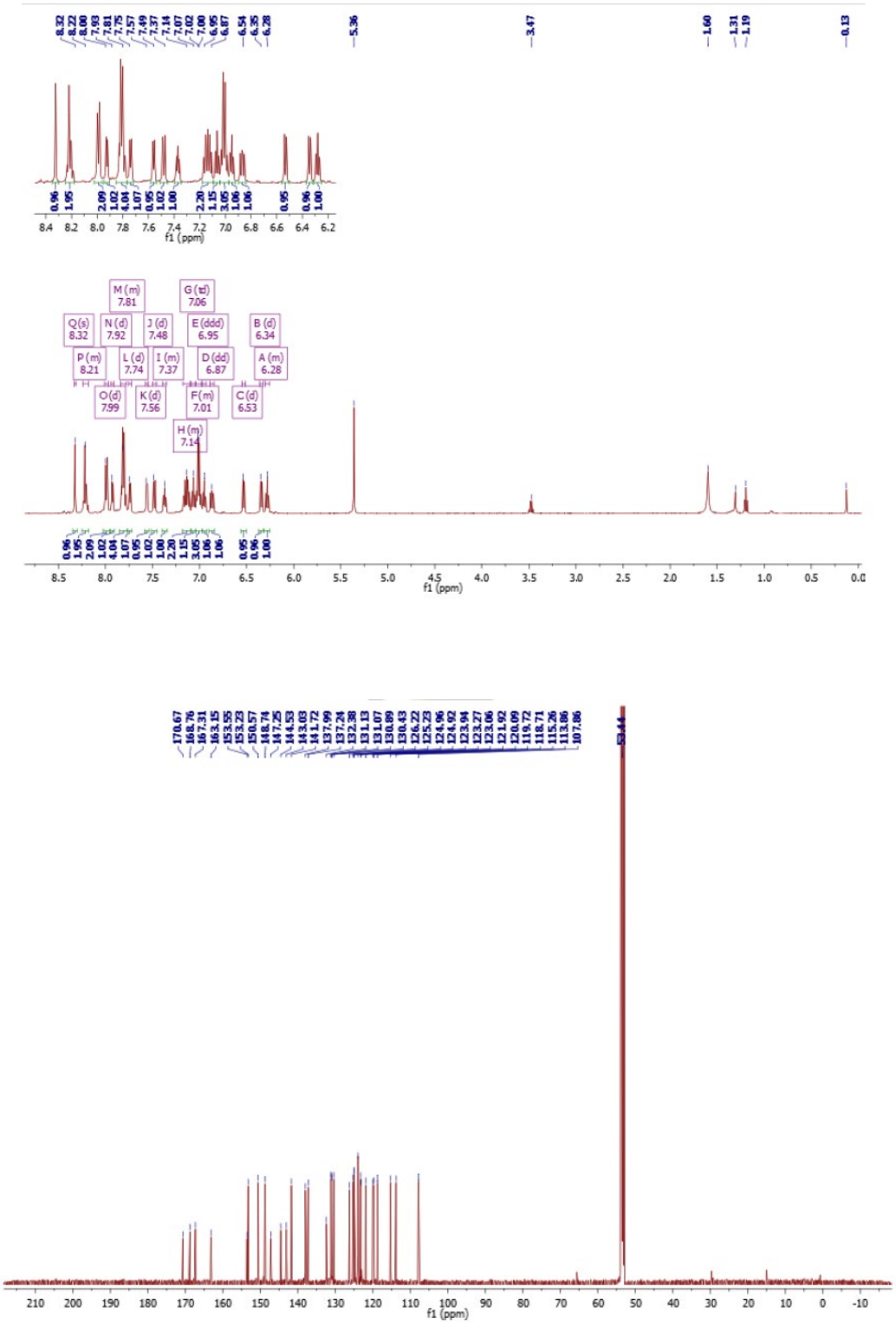

Figure ES3.3 ^{1}H (500 MHz, *top*) and ^{13}C NMR (125 MHz, *bottom*) spectra recorded for complex **Ir3** in CD_2Cl_2 at 298 K.

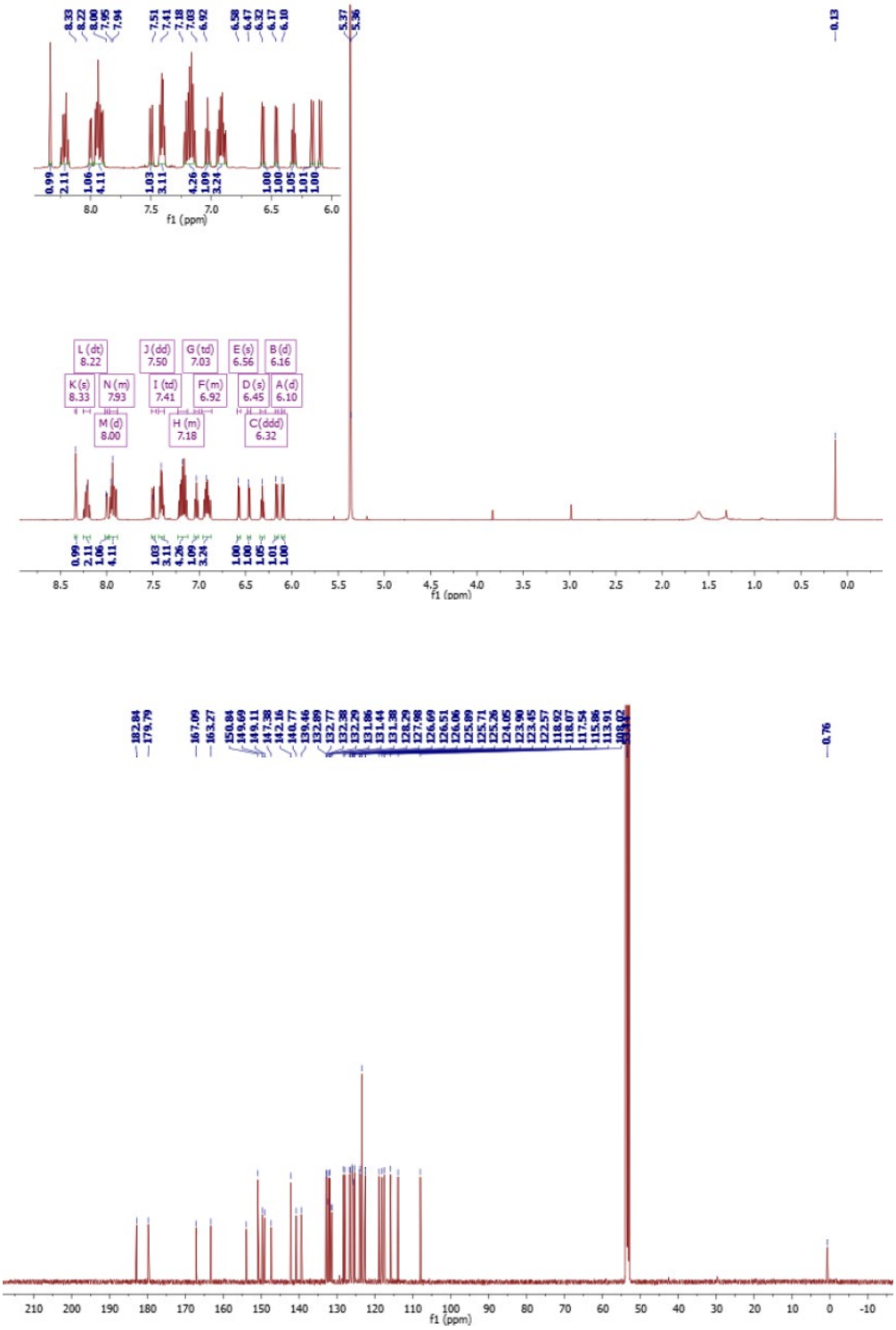

Figure ES3.4 ^{1}H (500 MHz, *top*) and ^{13}C NMR (125 MHz, *bottom*) spectra recorded for complex **Ir4** in CD_2Cl_2 at 298 K.

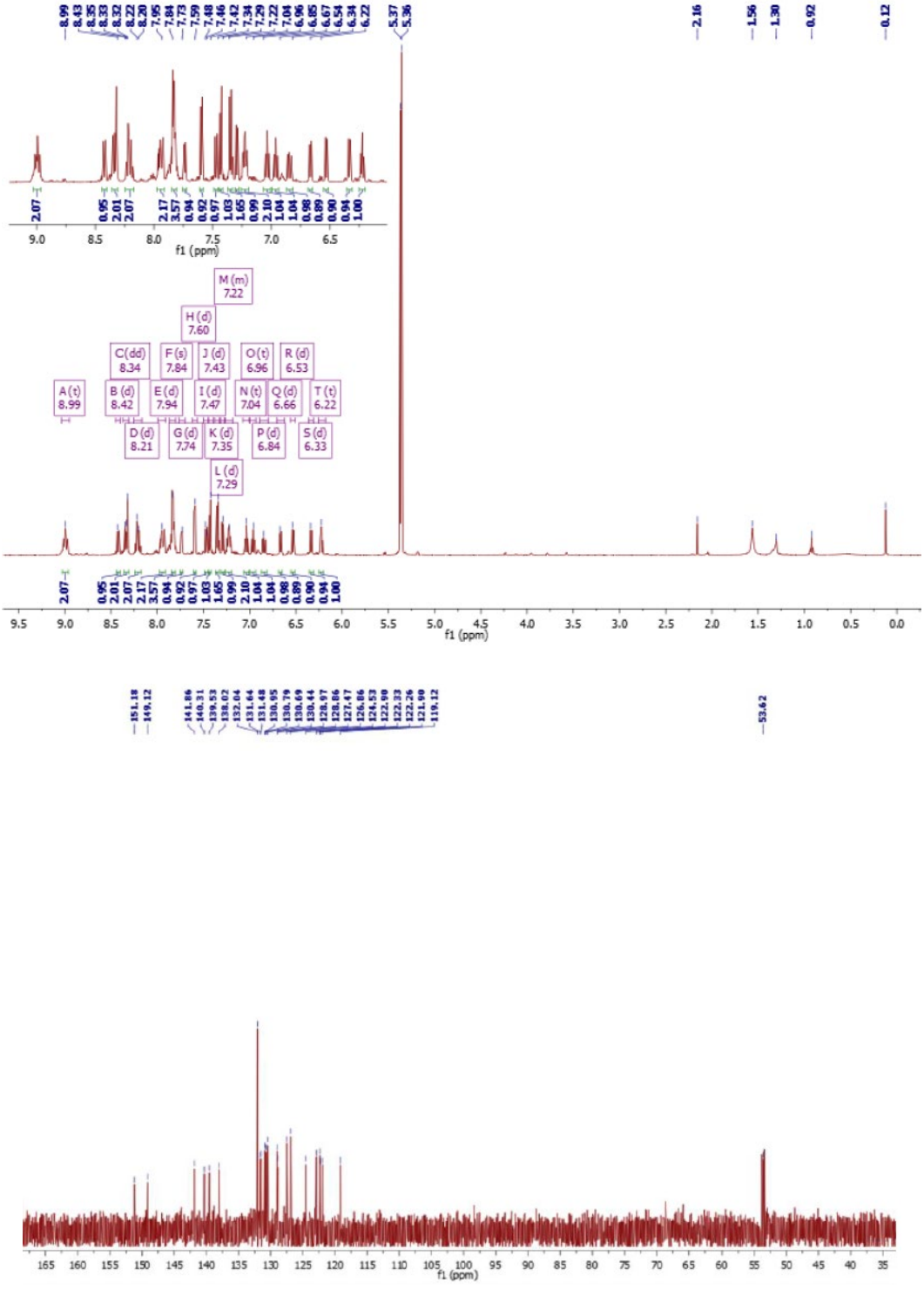

Figure ES3.5 ^{1}H (500 MHz, *top*) and ^{13}C NMR (125 MHz, *bottom*) spectra recorded for complex **Ir5** in CD_2Cl_2 at 298 K.

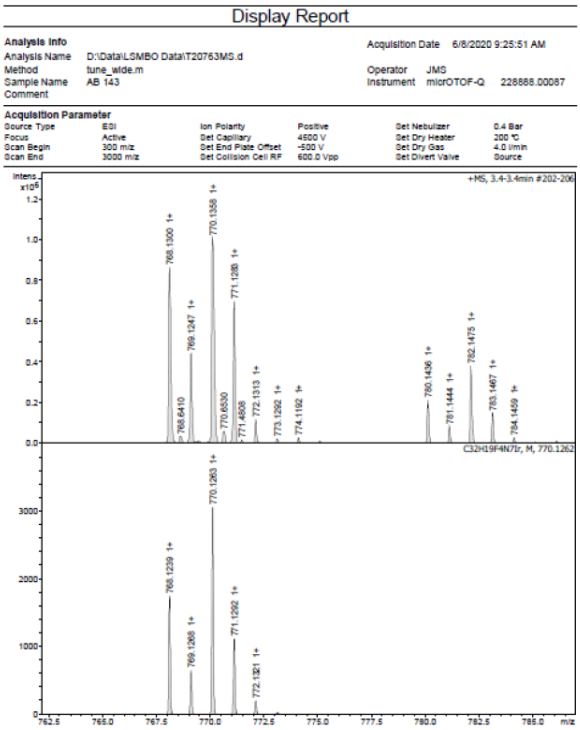

Figure ES3.6 High-resolution ESI-MS spectrum of compound **Ir1**.

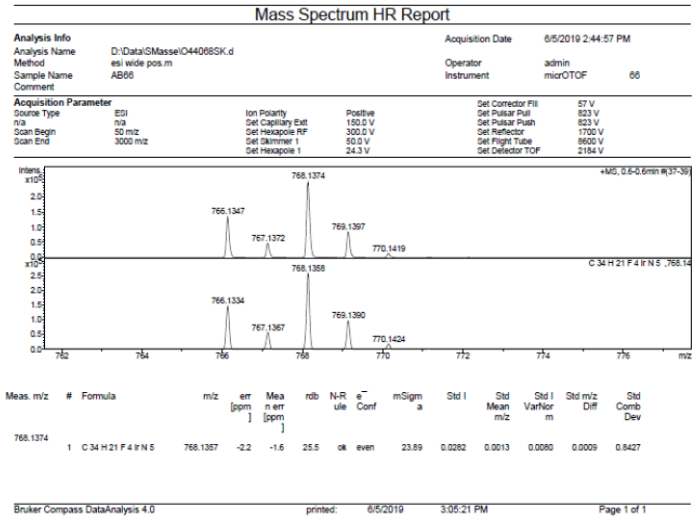

Figure ES3.7 High-resolution ESI-MS spectrum of compound **Ir2**.

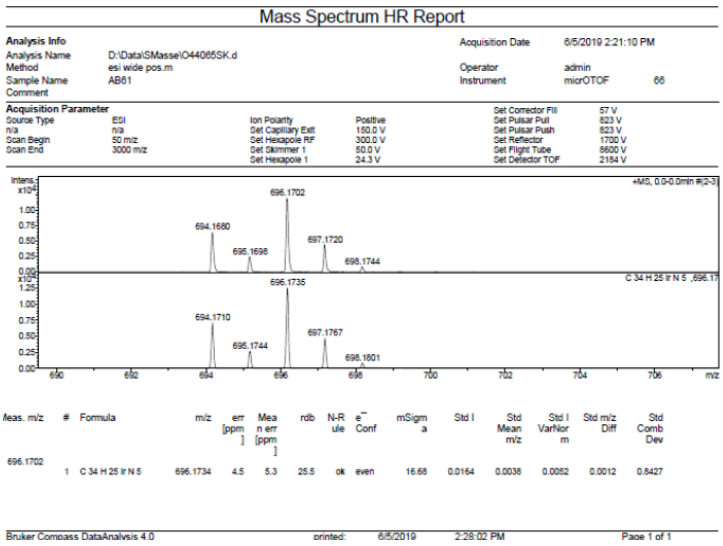

Figure ES3.8 High-resolution ESI-MS spectrum of compound **Ir3**.

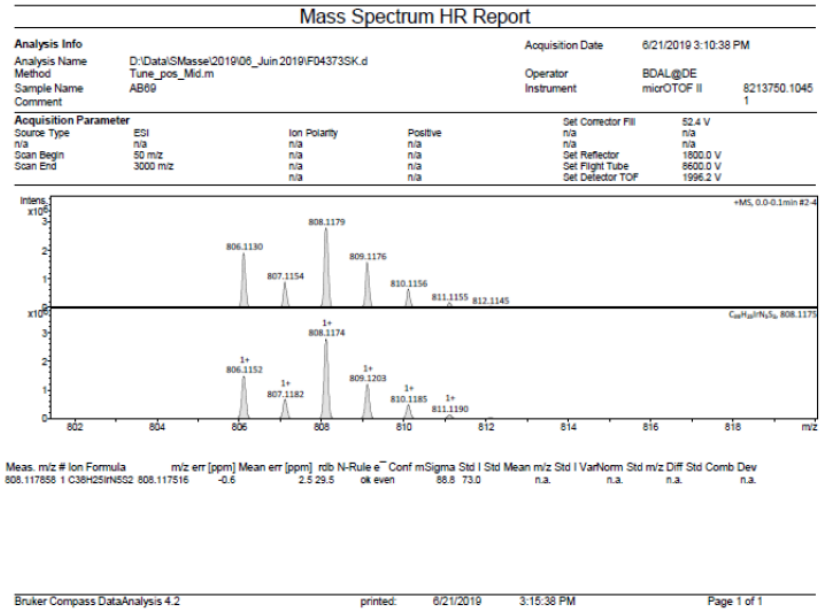

Figure ES3.9 High-resolution ESI-MS spectrum of compound **Ir4**.

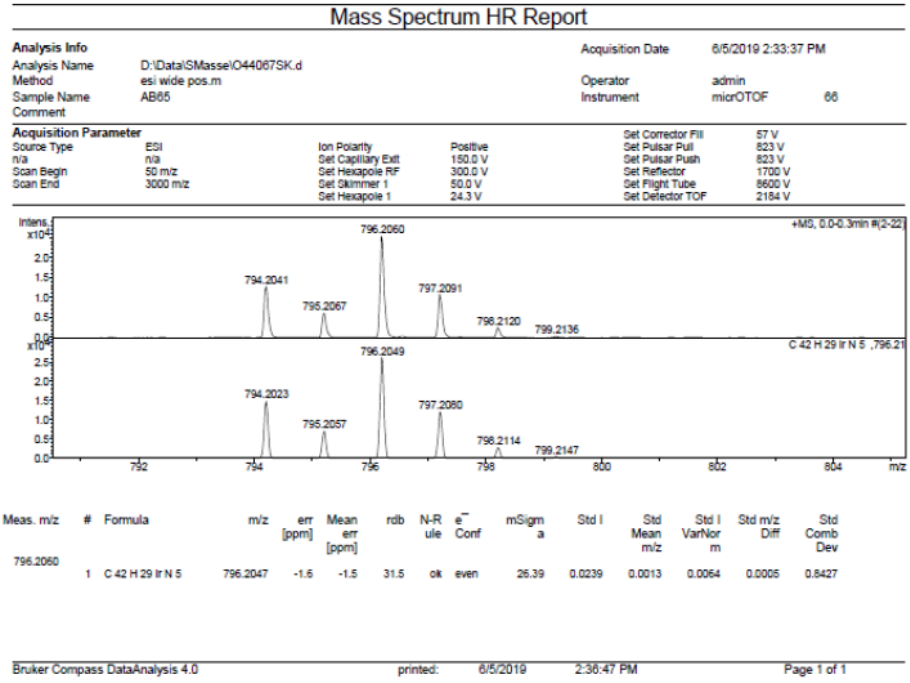

Figure ES3.10 High-resolution ESI-MS spectrum of compound **Ir5**.

Quinine sulphate in 0.5 M H_2SO_4 (PLQY = 0.55) and the $Ru(bpy)_3Cl_2$ complex in air-equilibrated water solution at room temperature (PLQY = 0.04) [43] were used as reference standard for complexes **Ir1** and **Ir2**–**5**, respectively.

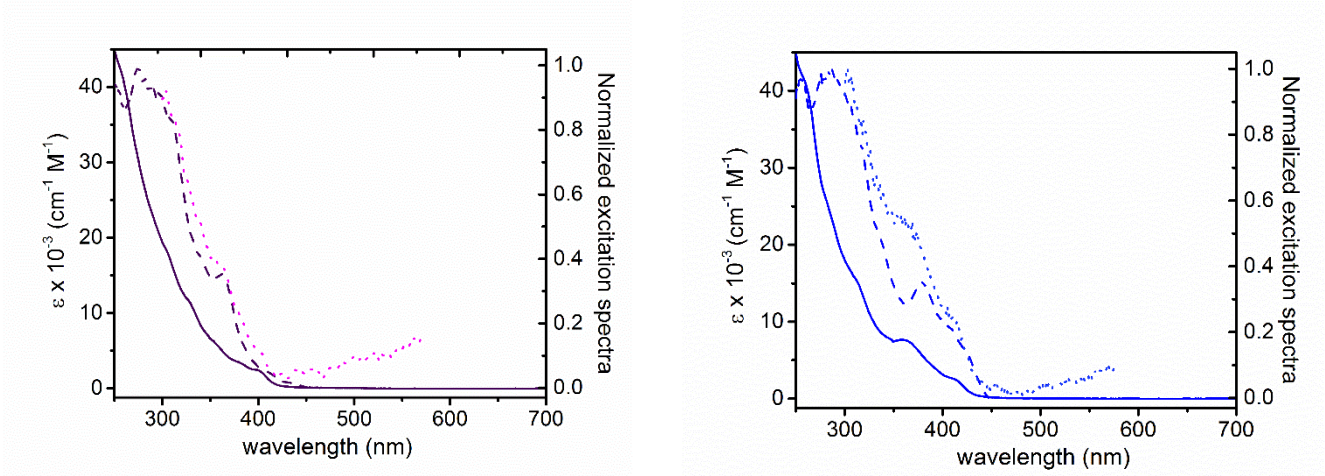

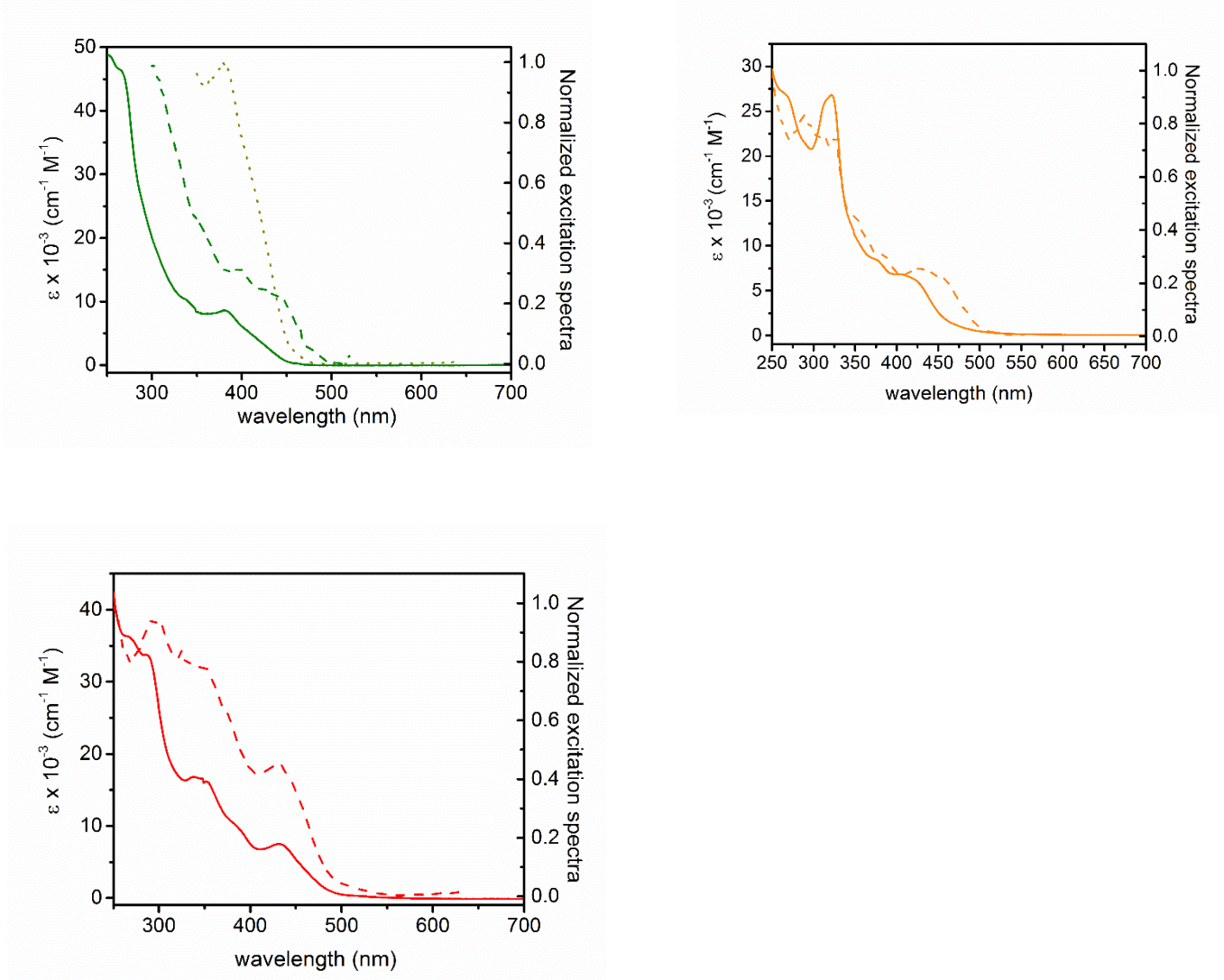

Figure ES3.11 Electronic absorption (solid line) and normalized excitation spectra of complex **Ir1** (purple trace), **Ir2** (blue trace), **Ir3** (green trace), **Ir4** (orange trace) and **Ir5** (red trace) in degassed CH_2Cl_2 solution at a concentration of 3 X 10^{-5} M at room temperature. Excitation spectra were recorded setting emission at λ_{em} = 473 nm for **Ir1**, λ_{em} = 467 nm for **Ir2**, λ_{em} = 540 nm for **Ir3**, λ_{em} = 580 nm for **Ir4** and λ_{em} = 650 nm for **Ir5** (dashed line) and at λ_{em} = 590 nm for **Ir1**, λ_{em} =596 nm for **Ir2** and λ_{em} = 660 nm for **Ir3** (dotted line).

3.5.3 Determination of log $P_{o/w}$

The octanol-water partition coefficient (Log$P_{o/w}$) for complexes **Ir1**–**5** were determined using the shake-flask method. Stock solutions of the compounds were prepared in a mixture of water and 1-octanol 50/50 $^{V}/_{V}$ (total complex concentration 3×10^{-5} M). The resultant solutions were shaken for 48 hours and then equilibrated for 24 hours. The partition coefficients were determined using UV absorbance spectroscopy. Log$P_{o/w}$ was defined as the logarithm of the ratio of the concentrations of the complex in the organic and aqueous phases as by the following equation (Eqn. 2):

$$\boldsymbol{logP_{o/w} = log\left\{\frac{[complex(octanol)]}{[complex(water)]}\right\}} \qquad \boldsymbol{Eqn.2}$$

where [complex(octanol)] and [complex[water] are the concentration of the complex under investigation in 1-octanol and water, respectively.

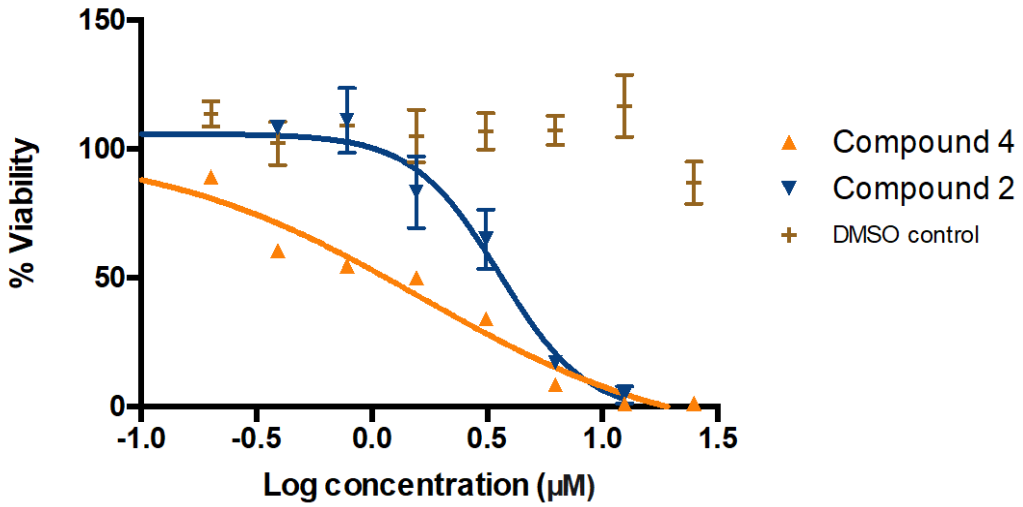

Figure ES3.12. MTS derived cell viability curves of HeLa cells after 72 h treatment with the tested compounds, with equivalent quantities of DMSO as vehicle control.

Table ES3.1 Crystal data and structure refinement for compound **Ir3**.

Identification code CCDC 1983105

Empirical formula C34 H25 F6 Ir N5 P

Formula weight 840.76

Temperature 173(2) K

Wavelength 0.71073 Å

Crystal system, space group Orthorhombic, P b c a

Unit cell dimensions a = 10.7554(6) Å α = 90°

b = 17.7006(11) Å β = 90°

c = 32.660(2) Å γ = 90°

Volume 7(6) Å^3

Z, Calculated density 8, 1.796 Mg/m^3

Absorption coefficient 4.416 mm^{-1}

F(000) 3280

Crystal size 0.120 x 0.100 x 0.080 mm

Theta range for data collection 2.267 to 25.270 deg.

Limiting indices -12<=h<=12, -21<=k<=21, -27<=l<=39

Reflections collected / unique 61788 / 5627 [R(int) = 0.1813]

Completeness to theta = 25.242 99.9%

Absorption correction Semi-empirical from equivalents

Max. and min. transmission 0.7452 and 0.6804

Refinement method Full-matrix least-squares on F^2

Data / restraints / parameters 5627 / 0 / 418

Goodness-of-fit on F^2 1.012

Final R indices [I>2□(I)] R1 = 0.0478, wR2 = 0.0862

R indices (all data) R1 = 0.0980, wR2 = 0.1036

Extinction coefficient n/a

Largest diff. peak and hole 2.868 and -1.326 *e* Å^{-3}

3.5.4 Computational analysis

The structures of the complexes **Ir1–5** in the electronic ground state have been fully optimized at the DFT/B3LYP[33] level of theory using essentially double-ζ basis sets including scalar relativistic effects for all atoms.[34] The use of triple-ζ basis sets does not modify drastically the results obtained for complex **Ir2** (systematic ~10 nm red-shift of the singlet transitions). This justifies the use of double-ζ basis sets for the large systems, which could not be handled otherwise. The calculations have been performed in CH_2Cl_2 within the COSMO (conductor-like-screening model) model.[35]The absorption spectra have been computed at the TD-DFT level (80 roots) including spin-orbit effects at the perturbation level of theory within the zero-order relativistic approximation (ZORA).[36] The structures of the low-lying triplet excited states Tn (n=1–4) have been optimized at the same level of theory using the Tamm-Dancoff approximation (TDA) in order to avoid triplet instability problems.[37] The calculations have been performed with the ADF 2019 package (ADF, SCM, Theoretical Chemistry, Vrije Universiteit, Amsterdam, The Netherlands https://www.scm.com/doc/ADF/index. html).

3.6 Authors contributions

Conor McCartin, Antoine Kichler and Sylvie Fournel (University of Strasbourg) are kindly acknowledged for the biological evaluation. Ulises Carrillo, Cristina Cebrián Ávila and Philippe Gros (University of Lorraine) contributed to the synthesis of the pyridyl pyridoannelated N-heterocyclic carbene. Chantal Daniel (University of Strasbourg) is kindly acknowledged for performing computational investigation. All the collaborators are kindly acknowledged for their fundamental contribution to the work.

3.7 References

1. C. Monneret, *Ann. Pharm. Fran.* **2011**, *69*, 3523.
2. E. Martinez-Balibrea, A. Martínez-Cardús, A. Ginés, V. Ruiz de Porras, C. Moutinho, L. Layos, J. L. Manzano, C. Bugés, S. Bystrup, M. Esteller, A. Abad, *Mol. Caner Ther.* **2015**, *14*, 1767.

3. W. Hu, J. J. Kavanagh, *Lancet Oncol.* **2003**, *4*, 721.
4. [a] A. Erxleben, *Curr. Med. Chem.* **2019**, *26*, 694; [b] V. Gogvadze, S. Orrenius, B. Zhivotovsky, *Apoptosis* **2009**, *14*, 624; [c] S. Fulda, L. Galluzzi, G. Kroemer, *Nat. Rev. Drug Discovery* **2010**, *9*, 447.
5. P. V. Simpson, N. M. Desai, I. Casari, M. Massi, M. Falasca, *Future Med. Chem.* **2019**, *11*, 119.
6. [a] K. K.-W. Lo, K. Y. Zhang, *RSC Adv.* **2012**, *2*, 12069; [b] C.-H. Leung, H.-J. Zhong, D. S.-H. Chan, D.-L. Ma, *Coord. Chem. Rev.* **2013**, *257*, 1764; [c] C. Caporale, M. Massi, *Coord. Chem. Rev.* **2018**, *363*, 71; [d] K. K.-W. Lo, *Luminescent and photoactive transition metal complexes as biomolecular probes and cellular reagents*, *Struct. Bonding.*, 165, Springer, **2015**.
7. [a] G. Bertrand, *J. Organomet. Chem.* **2005**, *690*, 5397; [b] R. H. Crabtree, *Coord. Chem. Rev.* **2007**, *251*, 595; [c] F. Glorius, *Top. Organomet. Chem.* **2007**, *21*, 47; [d] S. P. Nolan (Ed.), in *N-Heterocyclic Carbenes in Synthesis*; Wiley-VCH: Weinheim, Germany, **2006**; [e] W. A. Herrmann, C. Köcher, *Angew. Chem. Int. Ed. Engl.* **1997**, *36*, 2162; [f] V. César, S. Bellemin-Laponnaz, L. H. Gade, *Chem. Soc. Rev.* **2004**, *33*, 619; [g] W. A. Herrmann, L. J. Goossen, G. R. J. Artus, C. Köcher, *Chem. Rev.* **2014**, *114*, 8747; [h] M. N. Hopkinson, C. Richter, M. Schedler, F. Glorius, *Nature* **2014**, *510*, 485.
8. [a] A. Igau, H. Grutzmacher, A. Baceiredo, G. Bertrand, *J. Am. Chem. Soc.* **1988**, *110*, 6463; [b] A. J. Arduengo, R. L. Harlow, M. Kline, *J. Am. Chem. Soc.* **1991**, *113*, 361; [c] D. Bourissou, O. Guerret, F. P. Gabbaï, G. Bertrand, *Chem. Rev.* **2000**, *100*, 39.
9. [a] E. Peris, *Chem. Rev.* **2018**, *118*, 9988; [b] F. Glorius (Ed.) *in N-Heterocyclic Carbenes in Transition Metal Catalysis*; Springer-Verlag: Berlin, **2007**.
10. [a] A. Bonfiglio, M. Mauro, *Eur. J. Inorg. Chem.* **2020**, 3427; [b] C. A. Smith, M. R. Narouz, P. A. Lummis, I. Singh, A. Nazemi, C.-H. Li, C. M. Crudden, *Chem. Rev.* **2019**, *119*, 4986; [c] R. Visbal, M. C. Gimeno, *Chem. Soc. Rev.* **2014**, *43*, 3551; [d] L. Mercs, M. Albrecht, *Chem. Soc. Rev.* **2010**, *39*, 1903; [e] M. Albrecht, *Chimia* **2010**, *64*, 184; [f] B. M. Nelson, A. G. Tennyson, C. W. Biewlaski, *J. Phys. Org. Chem.* **2012**, *25*, 531.
11. For some selected examples of metallodrugs containing NHC ligands see: [a] Y. Gothe, T. Marzo, L. Lessori, N. Metzler-Nolte, *Chem. Eur. J.* **2016**, *22*, 12487; [b] F. Schmitt, K. Donnelly, J. K. Muenzner, T. Rehm, V. Novohradsky, V. Brabec, J. Kasparkova, M. Albrecht, R. Schobert, T. Mueller, *J. Inorg. Biochem.* **2016**, *163*, 221; [c] T.-L. Lam, K.-C. Tong, C. Yang, W.-L. Kwong, Z. Guan, M.-D. Li, V. K.-T. Lo, S. L-F. Chan, D. L. Phillips, C.-N. Lok, C.-M. Che, *Chem. Sci.* **2019**, *10*, 293; [d] Z. Xu, Y. Zhang, S. Zhang, X. Jia, G. Zhong, Y. Yang, Q. Du, J. Li, Z. Liu, *Cancer Lett*. **2019**, *447*, 75; [e] J. Zhang, J. Liu, Z. Liu, B. Liu, S. Song, X. He, C. Che, M. Si, G. Yang, Z. Liu, *J. Inorg. Biochem.* **2020**, *207*, 111063; [f] N. Chekkat, G. Dahm, E. Chardon, M. Wantz, J. Sitz, M. Decossas, O L. Lambert, B. Frisch, R. Rubbiani, G. Gasser, G. Guichard, S. Fournel, S. Bellemin-Laponnaz, *Bioconjug. Chem.* **2016**, *27*, 1942.
12. For some selected reviews see: [a] M. Skander, P. Retailleau, B. Bourrié, L. Schio, P. Mailliet, A. Marinetti, *J. Med. Chem.* **2010**, *53*, 2146; [b] S. Bellemin-Laponnaz, *Eur. J. Inorg. Chem.* **2020**, 10; [c] F. Cisnetti, A. Gautier, *Angew. Chem. Int. Ed.* **2013**, *52*, 11976; [d] W. Liu, R. Gust, *Chem. Soc. Rev.* **2013**, *42*, 755; [e] W. Liu, R. Gust, *Coord. Chem. Rev.* **2016**, *329*, 191.
13. [a] L. Benhamou, E. Chardon, G. Lavigne, S. Bellemin-Laponnaz, V. César, *Chem. Rev.* **2011**, *111*, 2705; [b] J. C. Y. Lin, R. T. W. Huang, C. S. Lee, A. Bhattacharyya,

W. S. Hwang, I. J. B. Lin, *Chem. Rev.* **2009**, *109*, 3561; [c] A. A. Danopoulos, T. Simler, P. Braunstein, *Chem. Rev.* **2019**, *119*, 3730; [d] D. G. Gusev, *Organometallics* **2009**, *28*, 6458; [e] D. J. Nelson, S. P. Nolan, *Chem. Soc. Rev.* **2013**, *42*, 6723; [f] S. Diez-Gonzalez, S. P. Nolan, *Coord. Chem. Rev.* **2007**, *251*, 874; [g] H. V. Huynh, *Chem. Rev.* **2018**, *118*, 9457.

14. [a] Y. Li, C.-P. Tan, W. Zhang, L. He, L.-N. Ji, Z.-W. Mao, *Biomater.* **2015**, *29*, 95; [b] Y. Li, K.-N. Wang, L. He, L.-N. Ji, Z.-W. Mao, *J. Inorg. Biochem.* **2020**, *205*, 110976.
15. C. Yang, F. Mehmood, T. L. Lam, S. L.-F. Chan, Y. Wu, C.-S. Teung, Z. Guan, K. Li, C. Y.-S. Chung, C.-Y. Zhou, T. Zou, C.-M. Che, *Chem. Sci.* **2016**, *7*, 3123.
16. [a] Z. Tian, Y. Yang, L. Guo, G. Zhong, J. Li, Z. Liu, *Inorg. Chem. Front.* **2018**, *5*, 3106; [b] Y. Yang, L. Guo, Z. Ge, Z. Tian, Y. Gong, H. Zheng, Q. Du, X. Zheng, Z. Liu, *Dyes Pigm.*, **2019**, *161*, 119.
17. M. Alcarazo, S. J. Roseblade, A. R. Cowley, R. Fernández, J. M. Brown, J. M. Lassaletta, *J. Am. Chem. Soc.* **2005**, *127*, 3290.
18. M. Nonoyama, *Bull. Chem. Soc. Jpn.* **1974**, *47*, 767.
19. [a] S. Lamansky, P. Djurovich, D. Murphy, F. Abdel-Razzaq, R. Kwong, I. Tsyba, M. Bortz, B. Mui, R. Bau, M. E. Thompson, *Inorg. Chem.* **2001**, *40*, 1704; [b] T. Yutaka, S. Obara, S. Ogawa, K. Nozaki, N. Ikeda, T. Ohno, Y. Ishii, K. Sakai, M. Haga, *Inorg. Chem.* ***2005***, *44*, 4737; [c] F. De Angelis, S. Fantacci, N. Evans, C. Klein, S. M. Zakeeruddin, J.-E. Moser, K. Kalyanasundaram, H. J. Bolink, M. Grätzel, M. K. Nazeeruddin, *Inorg. Chem.* **2007**, *46*, 5989.
20. [a] S. Lamansky, P. Djurovich, D. Murphy, F. Abdel-Razzaq, H.-E. Lee, C. Adachi, P. E. Burrows, S. R. Forrest, M. E. Thompson, *J. Am. Chem. Soc.* **2001**, *123*, 4304; [b] F. Monti, F. Kessler, M. Delgado, J. Frey, F. Bazzanini, G. Accorsi, N. Armaroli, H. J. Bolink, E. Ortí, R. Scopelliti, Md. K. Nazeeruddin, E. Baranoff, *Inorg. Chem.* **2013**, *52*, 10292; [c] F. Kessler, R. D. Costa, D. Di Censo, R. Scopelliti, E. Ortí, H. J. Bolink, S. Meier, W. Sarfert, M. Grätzel, Md. K. Nazeeruddina, E. Baranoff, *Dalton Trans.* **2012**, *41*, 180; [d] C.-H. Yang, J. Beltran, V. Lemaur, J. Cornil, D. Hartmann, W. Sarfert, R. Fröhlich, C. Bizzarri, L. De Cola, *Inorg. Chem.* **2010**, *49*, 9891.
21. Samples for photophysical investigation were prepared starting from crystalline materials thus to rule out the presence of impurities as the origin of the dual emission.
22. [a] A. K. Pal, S. Krotkus, M. Fontani, C. F. R. Mackenzie, D. B. Cordes, A. M. Z. Slawin, I. D. W. Samuel, E. Zysman-Colman, *Adv. Mater.* **2018**, 1804231; [b] S. Ladouceur, L. Donato, M. Romain, B. P. Mudraboyina, M. B. Johansen, J. A. Wisner, E. Zysman-Colman, *Dalton Trans.* **2013**, *42*, 8838; [c] Y.-S. Yeh, Y.-M. Cheng, P.-T. Chou, G.-H. Lee, C.-H. Yang, Y. Chi, C.-F. Shu, C.-H. Wang, *ChemPhysChem* **2006**, *7*, 2294; [d] D. N. Kozhevnikov, V. N. Kozhevnikov, M. Z. Shafikov, A. M. Prokhorov, D. W. Bruce, J. A. G. Williams, *Inorg. Chem.* **2011**, *50*, 3804; [e] Y. You, Y. Han, Y.-M. Lee, S. Y. Park, W. Nam, S. J. Lippard, *J. Am. Chem. Soc.* **2011**, *133*, 11488.
23. A.Bonfiglio, K. Magra, C. Cebrián, F. Polo, P. C. Gros, P. Mercandelli, M. Mauro, *Dalton Trans.* **2020**, *49*, 3102.
24. F. Toscano, B. Parmentier, Z. El Fajoui, Y. Estornes, J.-A. Chayvialle, J.-C. Saurin, J. Abello, *Biochem. Parmacol.* **2007**, *74*, 392.
25. P. K. Lee, H.-W. Liu, S.-M. Yiu, M.-W. Louie, K. K.-W. Lo, *Dalton Trans.***2011**, *40*, 2180.
26. I.Kruman, Q. Guo, M. P. Mattson, J. Neurosci. Res. 1998, 51, 293.

27. [a] D. Safiulina, V. Veksler, A. Zharkovsky, A. Kaasik, *J. Cell. Physiol.* **2006**, *206*, 347; [b] P. X. Petit, M. Goubern, P. Diolez, S. A. Susin, N. Zamzani, G. Kroemer, FEBS Lett. **1998**, *426*, 111.
28. J. Li, J. Yuan, *Oncogene* **2008**, *27*, 6194.
29. P.Y.P. Lie, C. Yan Cheng, D. D. Mruk*, Int. Rev. Cell. Mol. Biol.,* **2011**, *286*, 223
30. [a] J. T. Hutt, Z. D. Aron, *Org. Lett.* **2011**, *13*, 5256; [b] K. Magra, M. Darari, E. Domenichini, A. Francés-Monerris, C. Cebrián, M. Beley, M. Pastore, A. Monari, X. Assfeld, S. Haacke, P. C. Gros, *J. Phys. Chem. C* **2020**, *124*, 18379.
31. S. J. Lee, K.-M. Park, K. Yang, Y. Kang, *Inorg. Chem.* **2009**, *48*, 1030.
32. Y.-J. Su, H.-L. Huang, C.-L. Li, C.-H. Chien, Y.-T. Tao, P.-T. Chou, S. Datta, R.-S. Liu, *Adv. Mater.* **2003**, *15*, 884.
33. P. J. Stephens, F. J. Devlin, C. F. Chabalowski, M. J. Frisch, *J. Phys. Chem.* **1994**, *98*, 11623.
34. E. Van Lenthe, E. J. Baerends, *J. Comput. Chem.* **2002**, *23*, 1142.
35. A.Klamt, *J. Phys. Chem.* **1995**, *99*, 2224.
36. [a] E. van Lenthe, R. van Leeuwen, E. J. Baerends, J. G. Snijders, *Int. J. Quantum Chem.* **1996**, *57*, 281; [b] F. Wang, T. Ziegler, *J. Chem. Phys.* **2005**, *123*, 154102; [c] F. Wang, T. Ziegler, E. van Lenthe, S. van Gisbergen, E. J. Baerends, *J. Chem. Phys.* **2005**, *122*, 204103.
37. M. J. G. Peach, D. J. Tozer, *J. Phys. Chem. A* **2012**, *116*, 9783.

4. Heterodinuclear Ir^{III}/M^{I} (M^{I} = Cu^{I}, Au^{I}) complexes bearing a "Janus type" NHC bridge[a]

ABSTRACT

A novel class of phosphorescent cationic heterobimetallic Ir^{III}/M^{I} complexes, where M^{I} = Cu^{I} (**4,6**) and Au^{I} (**5,7**), is reported. The two metal centers are connected by the hybrid bridging 1,3-dimesityl-5-acetylimidazol-2-ylidene-4-olate (IMesAcac) ligand that combines both a chelating acetylacetonato-like and a monodentate N-heterocyclic carbene site coordinated onto an Ir^{III} and a M^{I} center, respectively. Complexes **4**–**7** have been prepared straightforwardly by a stepwise site-selective metalation with the zwitterionic [(IPr)M^{I}(IMesAcac)] metalloproligand (IPr = 1,3-(2,6-diisopropylphenyl)-2H-imidazol-2-ylidene) and they have been fully characterized by means of spectroscopical, electrochemical and computational investigation. The complexes **4-7** display vibrant red emission with an enhanced radiative rate constant and improved photoluminescence quantum yield when compared to their *mono*nuclear congeners **1**–**3**. Notably, complexes **6** and **7** are amongst the most efficient cationic *di*nuclear red-emitting Ir^{III} complexes with a ϕ_{PL} as high as 72-77% in degassed dichloromethane solution and lifetime in the range of 1.8 µs. Remarkably, their use as electroactive materials in single-layer LEC devices is demonstrated achieving fast turn-on time, brightness up to 1100 cd m^{-2} and EQE up to 6%.

[a] The results reported in this chapter have been published in
A. Bonfiglio**,** L. Pallova, V. César, C. Gourlaouen, S. Bellemin- Laponnaz, C. Daniel, F. Polo, M. Mauro, *Chemistry – A European Journal*, **2020**, 26,11751 –11766.
A. Bonfiglio, P-W. Hsiao, Y. Chen, C. Gourlaouen, Q. Marchand,V. César, S. Bellemin-Laponnaz, Y-X. Wang, C-W. Lu, C. Daniel, F. Polo, H.-C. Su, M. Mauro, *manuscript submitted.*

4.1 State-of-art and introduction

Cyclometalated Ir^{III} complexes are an outstanding class of emitters in efficient optoelectronic devices, such as organic light-emitting diodes (OLEDs) and light emitting electrochemical cells (LECs).[1] Strong SOC induced by heavy metal and structural effect play an important role in the origin of luminescent properties.[2]

To date, fine modulation of both redox and photophysical properties have been mainly achieved by judicious molecular design and control of the geometry and isomerization linkage of the coordinated ligands around the Ir^{III} center that selectively operate onto both the topology of the potential energy surfaces and electron density reorganization. Hence, a colorful palette of homo- and heteroleptic cyclometalated Ir^{III} complexes has been obtained when this metal center is combined with mono-, bi-, and tri-dentate scaffolds. Surprisingly, major efforts have been devoted to studying monometallic species. Photoactive *multi*metallic systems have been matter of intense studies as well, typically involving Ru^{II} donors and either Os^{II} or Re^{I} acceptors connected through (poly)-pyridyl ligands.[3] Briefly, in these systems the photophysical output depends on the nature of the connecting scaffold. When insulating bridges have been employed, electronic communication between the metal centers has been found to be weak. Thus, each photoactive metal center retained the excited-state properties of the parental, isolated, species and the multi-component system is typically characterized by photo-induced energy and/or electron transfer processes, which funnel the excitation energy onto the lowest-lying excited state. On the other hand, when the metal centers share the same heteroaromatic ligand, a certain degree of electronic coupling could be observed along with a sizeable perturbation of the excited-state properties. As far as Ir^{III} complexes are concerned, Balzani and co-workers authored the pioneering work describing homodinuclear Ir^{III} system connected through a 3,5-bis(pyridin-2-yl)-1,2,4-triazole.[4]

Other groups investigated the effect of the introduction of longer π-conjugated spacers into either homo- or heteronuclear structures as well, such as (oligo-)-p-phenylene bridges,[5] often acting as an insulating ligand as well as phenylene-bisethynylene,[6] arylesters,[7] and diynes[8] (*Figure 4.1*).

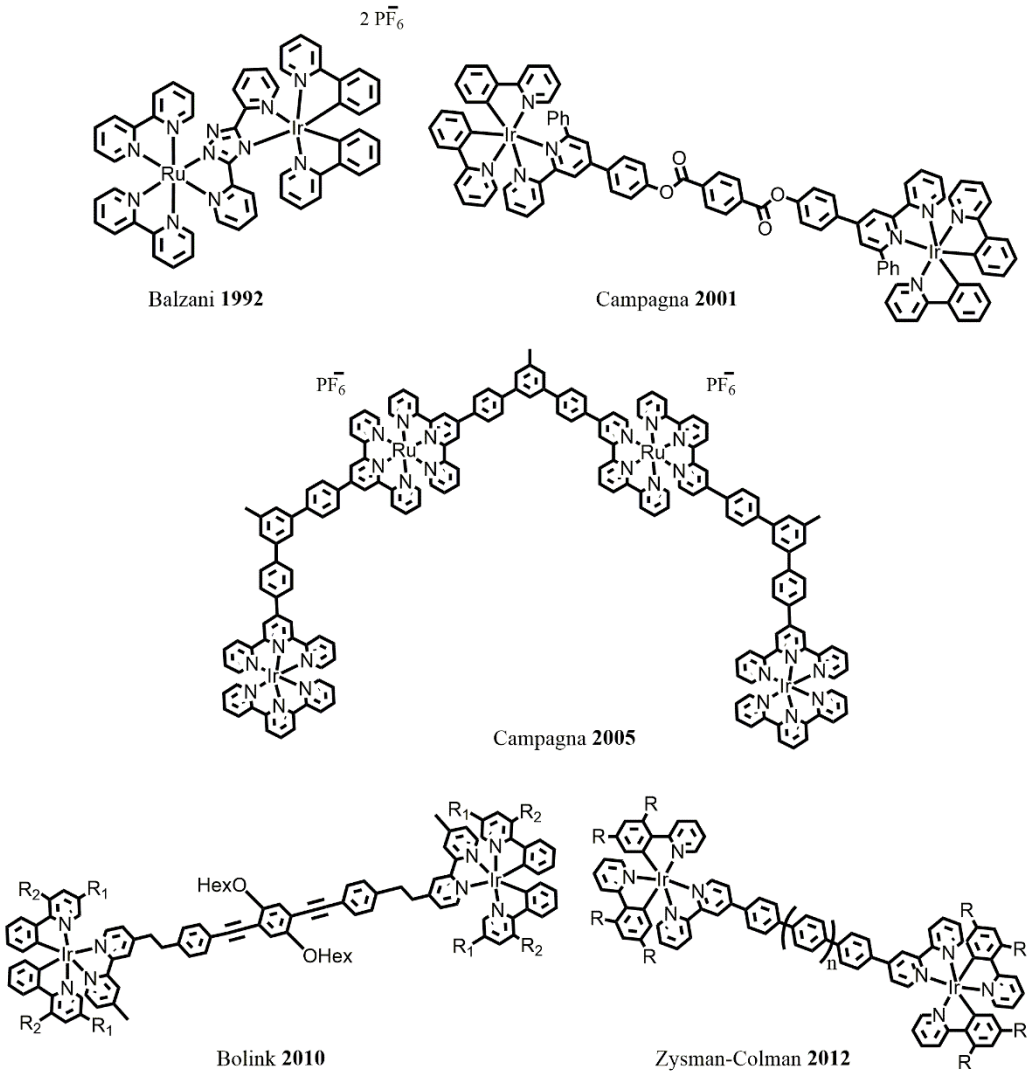

Figure 4.1 Selected examples of photoactive bimetallic systems longer π-conjugated spacers into either homo- or heteronuclear structures.

More recently, diiridium species connected through smaller ligands have gained increased attention sometimes featuring emissive properties that are comparable or even outperforming mononuclear counterparts.[9] This is because the presence of a second heavy metal center in close proximity may introduce manifold advantages, such as 1) additional degree of freedom in fine tuning the coordination environment and, thus, redox and optical properties; 2) increased structural rigidity and chemical stability, which render less accessible nonradiative channels, and 3) enhanced SOC that, in turn, enables larger values for the radiative rate constant, k_r. Therefore, a judicious design of poly-metallic species might afford compounds with enhanced optical properties. Chloro-bridged iridium dimers are ubiquitous precursors for the synthesis of highly emissive mononuclear complexes, but they typically display poorer emission compared to mononuclear counterparts. For this reason,

their investigation has often been overlooked. A few examples of dinuclear *bis*(μ-Cl) and *bis*(μ-NCO) dimers bearing fluorenylpyridine chromophoric ligand were described by Bryce et al.,[10] displaying photophysical properties also suitable for OLED device fabrication. The same group expanded upon the introduction of non-innocent hydrazide bridging ligands into diiridium complexes, yielding systems with remarkable PLQY, high OLED performances, and ground-state metal–metal electronic communication.[11] In addition, whereas fluorinated arylhydrazide bridging ligands promoted intramolecular π–π interaction leading to a sizeable decrease of the non-radiative rate constant, k_{nr}, as well as improvement of PLQY and device stability,[12] the concomitant introduction of 1,2-diarylimidazole as the chromophoric cyclometalating ligands allowed to further push the emission wavelength into the sky-blue region with high efficiency.[13] Moreover, oxamidato bridging ligands were found to favor electronic communication between the two iridium centers and yield highly efficient emitters with remarkably short excited-state lifetime attributed to the improved SOC effect exerted by the bimetallic system.[14] Chi and co-workers reported on sublimable diiridium systems containing bridging pyrazolate based tridentate ligands that displayed sky-blue to green emission, PLQY close to unity, and remarkable performances as emitters in OLED.[15] Taking advantage of the presence of two (potentially) coordinating N atoms, pyridazine- and pyridimidine-based bridging ligands have been employed as bis-bidentate,[16] and bis-terdentate[17] bridging scaffold by Kozhevnikov *et al.* yielding orange-red emitters with sometimes excellent emission properties attributable to the enhanced SOC effect. Zhou and co-workers also reported homodinuclear iridium complexes based on *bis*-bidentate phenylpyridazine bridges with good emission properties and electroluminescence efficiencies in the red region.[18] Luminescent heterometallic complexes containing an Ir^{III} center sharing the same bridging ligand are rare, also because their synthesis requires cumbersome multistep procedures. In particular, the structure of the ligand should be judiciously designed so that site-selective metalation is achieved while preserving the emission properties. Kozhevnikov *et al.* reported on a trimetallic Pt^{II}_2/Ir^{III} assembly consisting of two *bis*-terdentate pyrimidine-based ligands chelating onto the octahedral metal ion, showing improved photophysical properties.[19] At a second stage, the series was expanded upon yielding a bright tetrametallic Pt^{II}_3/Ir^{III} red emitter,[20] and a Pt^{II}_2/Ir^{III} system with good performances in light emitting electrochemical cells.[21] Notably, an example of starshaped $Au^{I}/Ir^{III}/Pt^{II}$ was reported, which featured a broadband emission arising from the partial energy transfer occurring between Ir^{III} and Pt^{II} centers.[22] As already mentioned, the importance of N-heterocyclic carbenes (NHCs) as ligands in organometallic chemistry grow

up in the last few decades for their unique electronic properties. [23] However, in the recent years, polytopic NHCs capable of coordinating two or more metal centers have emerged as a novel class of ligands that would enable "cooperative effects" induced by the spatial proximity of the metal ions through, for instance, intermetallic electronic coupling. In this way, polymetallic systems with enhanced chemical, redox and optical properties are expected. Nonetheless, most of the poly-metallic NHC-bridged systems investigated to date show no or weak electronic coupling between metal centers, due to the poor d_M–p_L orbital overlap in the metal–NHC scaffold. Yet, a few rare exceptions are known.[24] Although the subject of matter is still in its infancy, the main efforts in this field have been devoted to systems potentially suitable for tandem catalysis[25] and functional materials.[26] Instead, photoactive systems built upon metal centers that share a common N-heterocyclic carbene scaffold and investigation of the resulting effects onto their optical properties and electronic communication have been largely overlooked. The systems investigated to date are depicted in *Figure 4.2*.

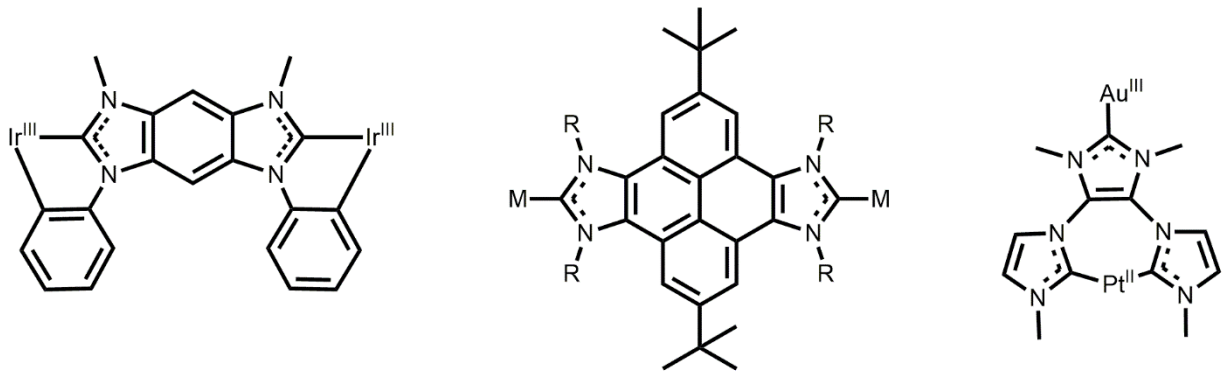

Bielawski **2009** Peris **2014, 2015, 2016** Peris **2016**

Figure 4.2 Previous examples of photoactive bimetallic systems supported by bridging NHC scaffolds.

Bielawski and co-workers reported on the first example of luminescent bimetallic system comprising two cyclometalated Ir^{III} fragments, namely $[Ir(ppy)_2]$ (ppy=2-phenylpyridyl), interconnected via the symmetric Janus-type di-NHC scaffold 1,7-dimethyl-3,5-diphenylbenzobis(imidazolylidene).[27] Comparison with the monometallic analogue

revealed lack of metal–metal electronic communication through the bridge in the bimetallic species. This latter displayed phosphorescence originated from the unperturbed $[Ir(ppy)_2]$ moiety, yet with slower k_r and faster k_{nr}, thus resulting in poorer emission efficiency. Peris and coworkers described a pyrene-decorated alkyl-N-substituted bis(imidazolylidene) scaffold employed as bridge in a series of homobimetallic systems comprising $[M^{I}(cod)Cl]$ (M = Ir^{I}, Rh^{I} and COD = 1,5-cyclooctadiene),[28] cyclometalated $[Pt^{II}(ppy)]$[29] and terdendate $[M^{II/III}(C^N^C)]$ (where $M^{II/III}$ = Pt^{II}, Au^{III} and C^N^C = 2,6-diphenylpyridine) fragments. Although the former example was not luminescent expectantly, the two latter ones displayed very weak luminescence attributable to the pyrene core that was largely quenched by the presence of the heavy metal. The same group described a heterobimetallic Pt^{II}-Au^{III} species bearing a Y-shaped *tris*-NHC scaffold that was weakly photoluminescent in polymer thin-film with emission attributable to the $[Au^{III}(C^N^C)]$ fragment. Aiming at phosphorescent compounds with improved photophysical properties we therefore turned our attention onto multimetallic species. To the best of our knowledge, no paper reports on the optical properties of cyclometalated bimetallic systems bridged by a hybrid ambidentate NHC scaffold to date. This is in spite of the potential advantages that such skeleton might provide towards the construction of multimetallic functional systems for optoelectronic devices, such as LECs and OLEDs.

Although both of them require recombination of charge carriers, which take place with a spin statistic of singlet-to-triplet exciton ratio of 1:3, LEC devices still display lower efficiency and reduced lifetime compared to OLEDs at comparable spectral region, in spite of the research efforts that have been currently made.[30] In particular, LEC requires the presence of mobile ions that migrate upon application to a suitable electrical bias, ensuring efficient charge injection, migration and recombination within the electroactive layer.[31] In this framework, mononuclear cationic iridium complexes bearing cyclometalated ligands have demonstrated being leading emitting materials.[32] Despite, it should be noticed that iTMCs typically display lower PLQY and less reversible redox properties in comparison with neutral counterpart, which represents a drawback for their efficient applications in light-emitting devices. One of the issues to address concerning luminescent compound is the severe drop of PLQY when moving towards longer wavelengths, making the near-infrared (NIR) design particularly challenging. The origin of this intrinsic limitation has two main causes. On one hand, increase of the vibronic coupling between the potentially-emitting excited state and electronic ground state takes place; a phenomenon described by the so-called energy gap law.[33] On the other hand, the radiative rate constant (k_r) scales with the third power of the

emission energy, as described by the Einstein quantum theory of radiation. Both effects cause detrimental consequences on the PLQY of red/NIR emitters. Nevertheless, bimetallic complexes are rapidly emerging as an attractive alternative to overcome the abovementioned drawbacks.[34] Indeed, suitable design strategies may provide *i*) enhanced spin-orbit coupling that induces faster radiative rate constants via increase of SOC constant and/or S–T mixing;[35] and *ii*) more rigid scaffold that helps suppressing radiationless deactivation channels.[36] Therefore, the exploration of novel design strategies for red to NIR emitters is of paramount importance to achieve highly performing electroluminescent devices in this challenging spectral region. Only a very limited number of works describes the application of dinuclear and/or multinuclear complexes in LEC devices and External Quantum Efficiency (EQE) still below 2% have been reported to date.[37]

Herein, it is reported on a novel family of phosphorescent Ir^{III}/M^{I} complexes where the two metals are connected by the 1,3-dimesityl-5-acetylimidazol-2-ylidene-4-olate (IMesAcac) heteroditopic bridge (see *Scheme 4.1*). The binding ability of the "acac" site is selectively employed to chelate the luminescent $[(C\hat{}N)_2Ir^{III}]$ moiety yielding a novel family of red-emitting Ir^{III} complexes with enhanced optical properties.

4.2 Results and discussion

4.2.1 Synthesis[b]

The IMesAcac ligand has been previously reported by César, Bellemin-Laponnaz *et al.*[38] and features both an acetylacetonate-type and a diaminocarbene coordination sites. Both motifs are known to be useful ligands largely employed for the construction of phosphorescent mononuclear complexes with remarkable optical properties based on Ir^{III}, Pt^{II}, Au^{I}, and Cu^{I}. Therefore, the merge of both coordination sites onto one hybrid ligand renders the IMesAcac an ideal candidate for the preparation of emissive heterodinuclear species. On one hand, the $[Ir^{III}(C\hat{}N)_2]$ fragment has been chosen for the coordination onto the acac site of IMesAcac, owing to their superior emission properties. On the other hand,

[b] Lenka Pallova, Quentin Marchand, Vincent César (Université de Toulouse) and Stéphane Bellemin-Laponnaz (Université de Strasbourg) are kindly acknowledged for the synthesis of the IMesAcacH] and $[(IPr)M^{I}(IMesAcac)]$ proligands.

the $[Cu(IPr)]^+$ scaffold has been selected for the coordination onto the diaminocarbene site of the IMesAcac, because of its chemical and photochemical stability, linear coordination geometry, and its suitable optical properties. It has been prepared three different mononuclear complexes of general formula $[Ir(\kappa^1C{:}\kappa^1N\text{-}C\text{^}N)_2(\kappa^2O,O\text{-}IMesAcacH)]PF_6$ (**1**–**3**), where IMesAcacH is the protonated imidazolium precursor and C^N is the cyclometalating pro-ligand 2-phenyl-pyridine (ppy), 2-phenyl-benzotiazole (2-pbt), and 1-phenylisoquinoline (1-piq), respectively. We then investigated their optical properties to better select the most suitable candidate to be subsequently incorporated into the heterobimetallic species. The general synthetic pathway employed for the target complexes **1**–**3** is depicted in *Scheme 4.1* and the chemical structures in *Scheme 4.2*.

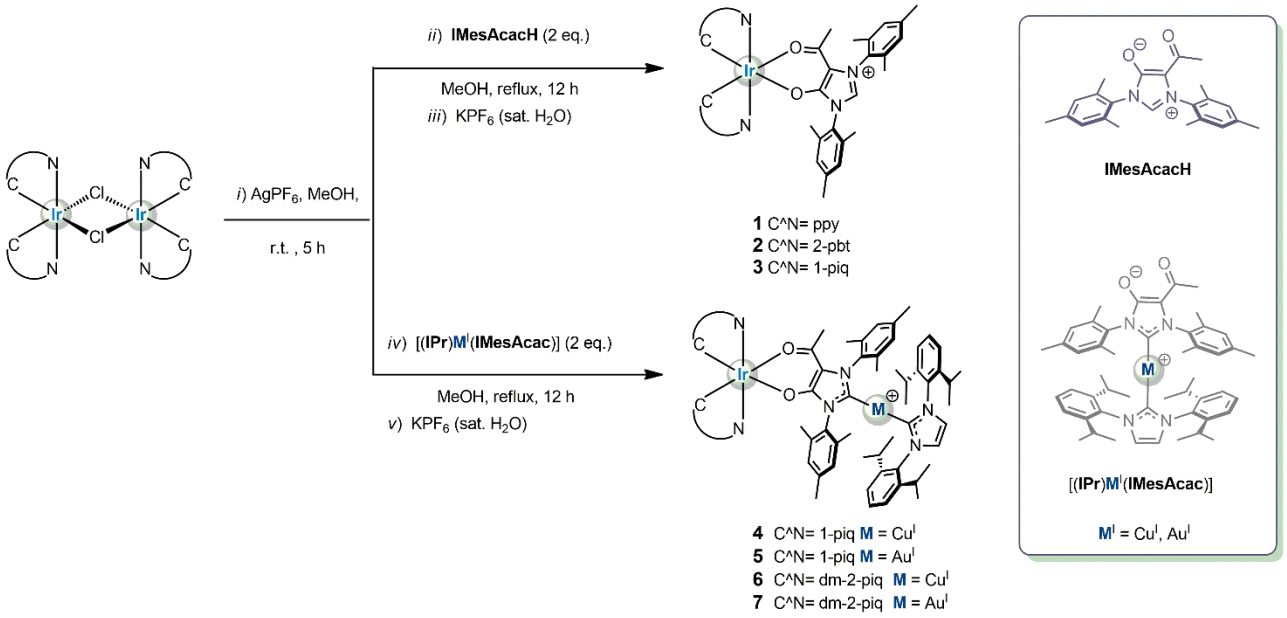

Scheme 4.1. Schematic synthetic pathway used for the synthesis of complexes **1–7** All complexes were prepared as PF_6^- salt.

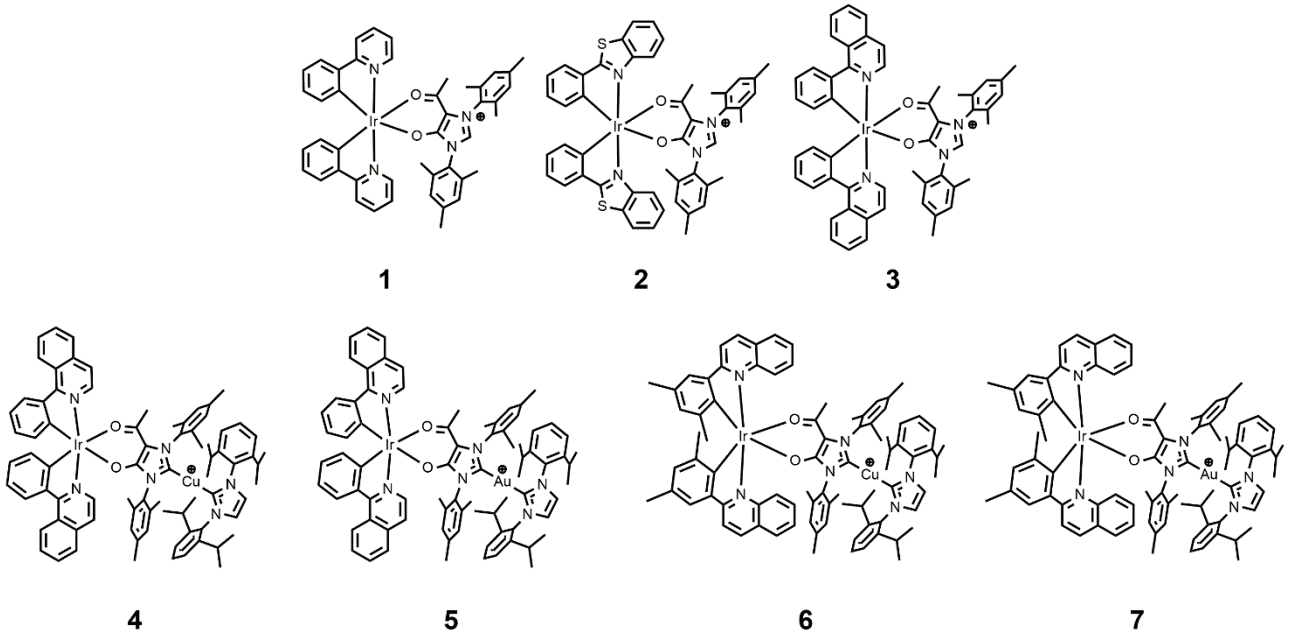

Scheme 4.2. Chemical structures of the investigated cationic complexes **1**–**7** prepared as PF_6^- salt.

The dinuclear chloro-bridged Ir^{III} complexes $[Ir(C\hat{}N)_2(\mu\text{-}Cl)]_2$ were used as the starting iridium compounds for the following reaction steps. They have been prepared by means of the classical Nonoyama reaction procedure.[39] The synthesis started with a halogen abstraction by using $AgPF_6$ as the silver(I) source in a slightly coordinating solvent, such as methanol, affording the corresponding *bis*-solvato complex of general formula $[Ir(C\hat{}N)_2(MeOH)_2]_2$. Upon removal of AgCl by filtration, the zwitterionic IMesAcacH was then added directly to the reaction mixture that was refluxed for 12 hours. Target mononuclear complexes **1**–**3** were obtained in purity suitable for photophysical investigation in moderate to good yield (44–87%) upon recrystallization. The formation of the desired complexes was supported by the lowering of the symmetry observed in the ^1H NMR spectra upon binding of the IMesAcacH ligand onto the $Ir(C\hat{}N)_2$ scaffold, which makes the protons onto the two cyclometalating ligand magnetically non-equivalent. Whereas, coordination through the pro-carbenic carbon can be ruled out due to the presence of the proton resonance at δ = 8.9 ppm with singlet multiplicity corresponding to the NC(*H*)N proton of the imidazolium ring. Furthermore, the connectivity and crystallographic metrics were undoubtedly established by X-ray diffraction analysis for derivative **2** (see below). It is worth to notice that the choice of both the solvent and reaction conditions are of crucial importance for the success of the synthesis. Indeed, any attempts to break the starting chloro-bridged dimer by direct addition of the IMesAcacH ligand in a solvent mixture more commonly used for similar reactions,

such as a 3:1 CH_2Cl_2/MeOH,[40] yielded the starting materials unreacted. This result agrees with previous findings reported by César, Bellemin-Laponnaz *et al.*[41] In fact, the poor chelating ability of the acac moiety in the mesoionic IMesAcacH ligand makes it unable to replace the chlorine ligand while reacted with the [(IPr)CuCl] motif. Abstraction of the bridging chlorine atoms with stoichiometric amount of $AgPF_6$ generated the solvato-complex $[Ir(C^N)_2(solvent)_2]_2$. Reaction of this latter with the IMesAcacH ligand in CH_2Cl_2 resulted in the formation of the starting chloro-bridged dimer. Most likely, residual chloride anions compete efficiently with the weakly coordinating acac motif of IMesAcacH, even when the former is present in rather low amount. Moreover, the use of a more coordinating solvent, such as CH_3CN, left the corresponding starting material $[Ir(C^N)_2(solvent)_2]_2$ unreacted.

To further prove the weak coordination ability of the acac binding motif (i.e., κ^2-O,O) when associated to the cationic formamidinium moiety within the mesoionic IMesAcacH compound **1** was mixed with TBACl and the resulting ^{1}H NMR was recorded at different time delay (*Figure 4.3*).

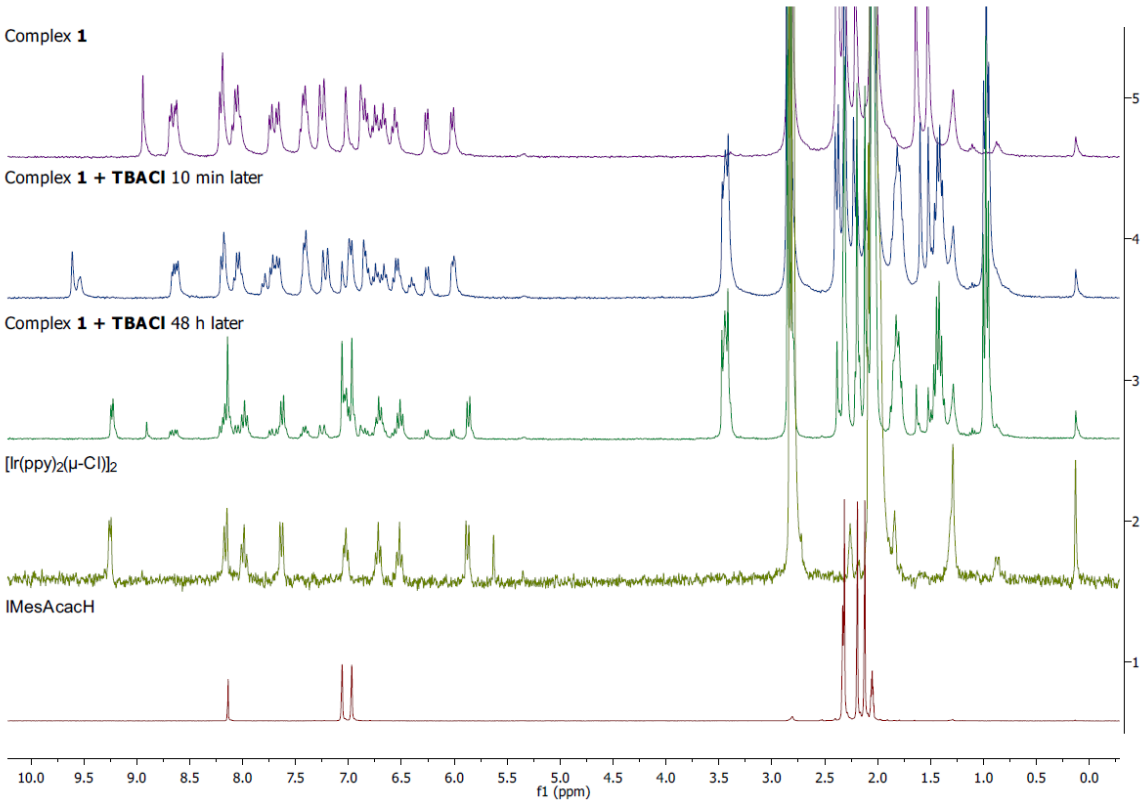

Figure 4.3. ^{1}H NMR (300 MHz, acetone-d_6) spectra recorded for compound **1** (violet), **1** upon addition of **TBACl** after 10 minutes (blue) and 48 hours later (green). The $[Ir(ppy)_2(\mu\text{-}Cl)_2]$ (yellow) and ImesAcacH (red) traces are reported for comparison.

The spectra show the decreasing of signals from compound **1** and the appearance of dinuclear chloro-bridged Ir^{III} complexes $[Ir(C^N)_2(\mu\text{-}Cl)]_2$ and the free IMesAcacH.

Single crystals suitable for X-ray diffractometric analysis were obtained by slow diffusion of *n*-hexane into acetone for complex **2** and into dichloromethane solution for complexes **4** and **7**. The corresponding ORTEP diagram is shown in *Figure 4.4* and *4.5*.

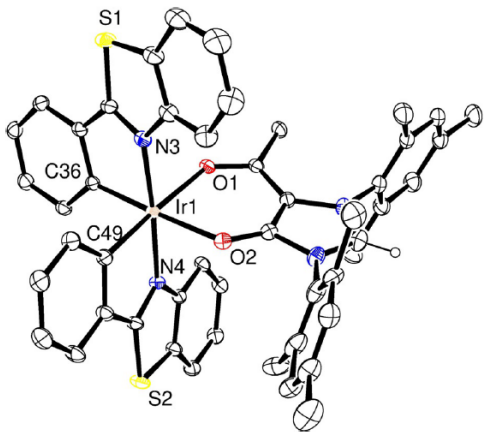

Figure 4.4. ORTEP diagram of compound **2** with thermal ellipsoids shown at 30% probability level obtained by single-crystal X-ray diffractometric analysis. All hydrogen atoms except the one on the pre-carbenic position, solvent and counter anion are omitted for clarity. Selected bond lengths (a): Ir-C(36) = 1.984(3), Ir-C(49) = 1.992(3), Ir-N(3) = 2.044(2), Ir-N(4) = 2.048(2), Ir-O(1) = 2.1703(19), Ir-O(2) = 2.162(2).

Complex **2** displays a slightly distorted octahedral geometry around the iridium center with the two cyclometalated ligands adopting a mutually eclipsed configuration. The X-ray structural characterization confirmed the *trans*-N,N coordination of the two phenyl-benzothiazole ligands with Ir–N distances lying at 2.044(2) and 2.048(2) Å for N(3) and N(4), respectively. The coordination sphere of the metal ion is completed by the IMesAcacH ligand that chelates through the acac-type coordination motif. As expected, slightly shorter bond distances are observed for the two Ir-C bonds with Ir-C(36) = 1.984(3) and Ir-C(49) = 1.992(3) Å, the latter residing to mutually *cis* positions. The slightly longer Ir-O distances in **2** (Ir-O(1) = 2.1703(19), Ir-O(2) = 2.162(2) a) relative to the ones observed within its benchmark analogue $[Ir(2\text{-}pbt)_2(acac)]$ (Ir-O = 2.158(4) and 2.145(5) Å[42] reflect the poorer coordinating ability of the neutral IMesAcacH ligand versus a classical anionic acac ligand.

For compounds **4** and **7**, the quality of their single crystals was not sufficient to achieve a complete crystallographic resolution, nevertheless, basic connectivity was verified. For both derivatives, the structure confirmed the N,N-*trans* arrangement of the two cyclometalating C^N around the iridium(III) atom with a pseudo-octahedral coordination geometry. The coordination sphere of the Ir center is completed by the coordination of the linear *bis*-carbenic [(IPr)MI(IMesAcac)] complex through the κ^2:O,O motif (acac moiety). The monovalent M^{I} atom is coordinated to the two different NHC ligand forming a linear heteroleptic complex, as expected (*Figure 4.5*).

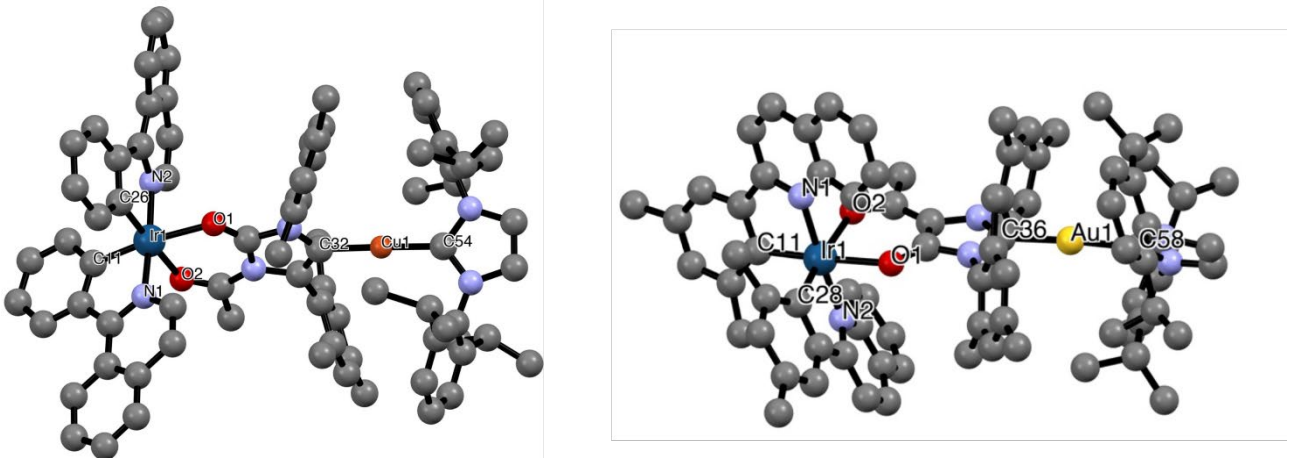

Figure 4.5 Single-crystal X-ray structure solved for compound **4** (*left*) and **7** (*right*). Hydrogen atoms and PF_6^- anion are omitted for clarity. Selected bond lengths (Å) 4: Ir(1)–C(11) = 2.005(9); Ir(1)–N(1) = 1.985(18); Ir(1)–C(26) = 2.015(8); Ir(1)–N(2) = 2.037(17); Ir(1)–O(2) = 2.167(11); Ir(1)–O(1) = 2.182(13); Cu(1)–C(32) = 1.92(2); Cu(1)–C(54) = 1.921(12). For **7**: Ir(1)–C(11) = 2.035(10); Ir(1)–C(28) = 1.995(11); Ir(1) –N(1) = 2.083(9); Ir(1)–N(2) = 2.058(8); Ir(1)–O(1) = 2.216(6); Ir(1)–O(2) = 2.198(7); Au(1)–C(36)= 2.023(11); Au(1)–C(58) = 2.026(12).

For the preparation of the heterodinuclear species, the "$[Ir(1\text{-}piq)_2]$" and "$[Ir(dm\text{-}2\text{-}piq)_2]$", where dm-2-piq is 2-(3,5-dimethylphenyl)quinoline, fragments were selected as the most suitable on the basis of the following grounds:

1) computational analysis shows less mixing between the low-lying triplet ligand-centered/metal-to-ligand charge transfer ($IL_{C^N}/MLCT_{C^N}$) states and those involving the IMesAcac moiety;

2) the parental complex **3** possesses the largest spectral separation with the [(IPr)-M^{I}(IMesAcac)] species along the series **1**–**3**, thus allowing selective excitation into the lowest-lying ^{1}MLCT band located onto the "[Ir(1-piq)$_2$]" (see *Figure 4.6*);

3) complexes emitting into the red/near-infrared portion of the electromagnetic spectrum typically display lower PLQY when compared to green and yellow emitters.

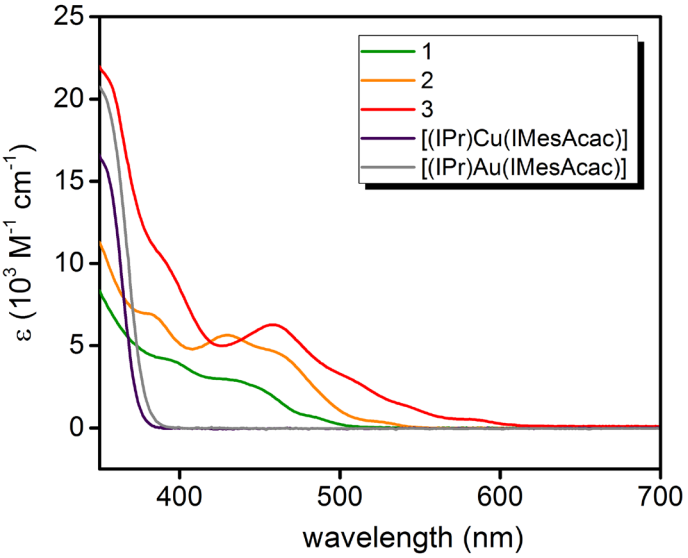

Figure 4.6 UV-Vis at r.t. in acetone at concentration of 3.0X10^{-5} M in air equilibrated condition for compounds **1**,**2**,**3** and pro-ligands **[(IPr)Cu(IMesAcac)]** and **[(IPr)Au(IMesAcac)]**. Note the large spectral separation between the ^{1}LC absorption band of the proligands and the ^{1}MLCT band of compound **3**.

This is because they possess typically slower k_r due to the ν^3 dependency of the Einstein spontaneous emission coefficient and faster k_{nr} due to energy gap law consideration.[43] Red emitters would then benefit the most from the favorable increase of the k_r. The synthesis of the heterodinuclear complexes employed a stepwise site-selective metalation procedure that straightforwardly afforded the target Ir^{III}/M^{I} species (*Scheme 4.1*). Upon chloride abstraction by using $AgPF_6$ onto the dichloro iridium dimer, the zwitterionic metalloligand that features an acac type of coordination motif, namely $M^{I}(\kappa^1C\text{-IPr})(\kappa^1C\text{-IMesAcac})$, is then added, yielding the target complexes **4-5** and **6-7** with M = Cu^{I} and Au^{I}, respectively, upon re-crystallization with an aqueous solution of KPF_6. The ^{1}H, ^{13}C and ESI MS spectra are displayed in the experimental section *Figure ES4.1-ES4.14*, respectively.

4.2.2 Photophysical characterization and theoretical calculations[c]

The photophysical properties of complexes **1-7** were investigated in different sample conditions. The monometallic complexes **1-3** were analysed in acetone, since they are stable just in weak coordinating solvents and in non-chlorinated solvents, providing a selective choice of conditions. For sake of comparison, complexes **4** and **5** were also investigated in acetone, although they are stable even in dichloromethane. Subsequently, the photophysical properties of complexes **4**–**7** were further carried out in dichloromethane, to be directly comparable with benchmark complexes [Ir(1-piq)$_2$(acac)] and [Ir(dm-2-piq)$_2$(acac)][44] and to obtain information about their suitability as emitters in LEC devices. Hereafter, three sections are reported for the photophysical investigation of the synthesized compounds. The computed investigation was performed by Dr. Chantal Daniel and Dr. Christophe Gourlaouen.

*4.2.2.1 Photophysical characterization of monometallics complexes **1-3***

Firstly, the photophysical properties of complexes **1**–**3** were investigated at concentration of $3.0X10^{-5}$ M in both air-equilibrated and degassed acetone solution at room temperature as well as in 2-methyltetrahydrofuran (2-MeTHF) glassy matrix at 77 K. The data are listed in *Table 4.1* and the electronic absorption and photoluminescence spectra are displayed in *Figure 4.7.* The most intense transition present in the region λ_{abs} = 350–400 nm is attributed with confidence to spin-allowed ligand-centered (^{1}IL) processes, localized on the cyclometalating ligands, although the complete profile of the band could not be recorded due to the limitation of the spectral window of the solvent employed. At lower energy, in the region λ_{abs} = 400–500 nm, the spectra feature broad and featureless transitions with moderate intensity ($\varepsilon \approx 2–6X10^3$ $M^{-1}cm^{-1}$) that are partially overlapped. This band is ascribed to spin-allowed electronic processes with mainly metal-to-ligand charge transfer (^{1}MLCT) character as by comparison with related [Ir(C^N)$_2$(acac)] complexes reported previously.[45] The weak band visible at an even longer wavelength (*e.g.* λ_{abs} = 578 nm, $\varepsilon \approx 0.5X10^3$ $M^{-1}cm^{-1}$ for compound **3**) is assigned to the formally spin-forbidden ^{3}MLCT transition owing to the improved zero-field splitting exerted by the octahedral coordination environment imposed by

[c] Dr. Chantal Daniel and Dr. Christophe Gourlaouen are kindly acknowledged for performing computational investigations.

the Ir^{III} atom.[46] A clear modulation of the absorption onset is observed in the series featuring a bathochromic shift in the order **1** to **2** to **3**, which parallels the increasing π-accepting ability of the N-containing heteroaromatic ring coordinated onto the iridium atom.

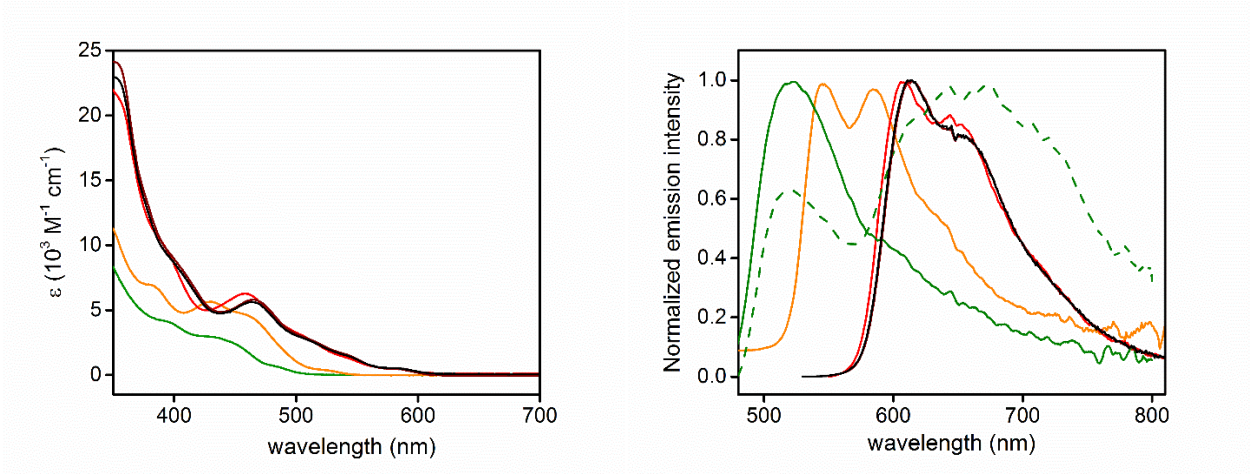

Figure 4.7 Electronic absorption (*left*) and emission spectra (*right*) for **1** (green), **2** (orange), **3** (red), **4** (dark red), and **5** (black) in acetone at concentrations of $3.0X10^{-5}$ cm in degassed condition. For **1**, the emission spectrum of the air-equilibrated sample is shown as dashed line. Samples were excited at λ_{exc} = 410, 450, 460, 470, and 460 nm for compounds **1**, **2**, **3**, **4** and **5**, respectively.

To confirm the band assignment, selected valence Kohn–Sham (KS) orbitals involved in the low-lying excited states (*Figure 4.8*) represent the HOMO mainly localized on the C^N ligand and the Ir^{III} center, and the LUMO localized onto the coordinated IMesAcacH ligand for complexes **1** and **2**. The presence of the fused phenyl rings onto the heteroaromatic part of the C^N ligand for complex **3** stabilizes the corresponding virtual orbitals. The LUMO and LUMO+1 form a couple of almost degenerate orbitals located onto each of the two isoquinoline moieties; whereas, the empty orbital localized on the IMesAcacH scaffold is now the LUMO+2. A similar picture can be drawn for the bimetallic complex **4** for LUMO and LUMO+1; whereas, its LUMO+2 is localized onto the IMesAcac fragment of the [(IPr)Cu(IMesAcac)] metalloligand.

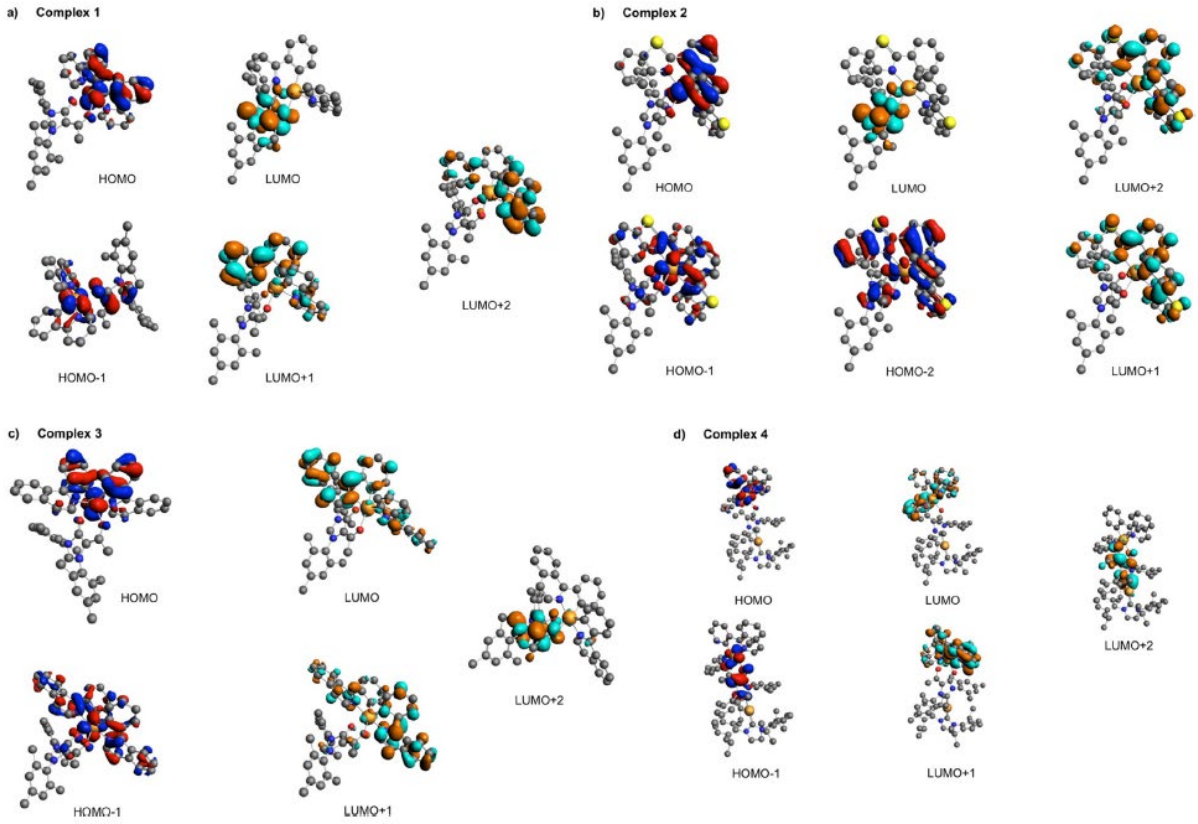

Figure 4.8 Selected valence KS orbitals involved in the low-lying excited states of a) complexes **1**, b) **2**, c) **3**, and d) **4**. Hydrogen atoms are omitted for clarity. The calculation were done considering acetone as solvent.

Upon excitation in the ^{1}MLCT band, acetone samples of compounds **1**–**5** display photoluminescence in both air-equilibrated and degassed condition. The corresponding normalized spectra are shown in *Figure 4.7* and the data listed in *Table 4.1*. The emission spectra display a bathochromic shift going from **1** to **2** to **3** that parallels the trend observed in the absorption spectra. Surprisingly, air-equilibrated samples of complex **1** clearly show two broad and featureless emission bands centered at 520 and 655 nm and an overall PLQY as low as 0.05%. In degassed condition, the band at 520 nm dominates the emission profile along with a lifetime of 1.2 μs. This band is assigned to T_3 by computational calculation involving the contribution of the $IL_{C\wedge N}$ state. This result confirms the phosphorescence nature of the high energy band (namely P1), attributed to an emissive state with $^{3}MLCT_{ppy}/^{3}IL_{ppy}$ character. The involved transition is d(Ir)π(-phenyl)←π*(pyridine), as by comparison with the parental $[Ir(ppy)_2(acac)]$ complex.[45]

Incorporation of a more extended π-system, such as either the benzothiazole ring or the isoquinoline moiety, onto the cyclometalating C^N ligand causes a shift of the emission to lower energies, being λ_{em} = 546 and 583 nm (**2**), and 607 and 650 nm (**3**), whose profile appear to be virtually independent of the presence of dioxygen. Nonetheless, increase of the PLQY from 1.9 to 3.5% (compound **2**) and from 2.5 to 18% (compound **3**) is observed, again pointing toward the triplet nature of the emissive excited state. Noteworthy, for compound **3** emission profile resembles closely that of the related complex [Ir(1-piq)$_2$(acac)] with PLQY value comparable within the experimental error.[47] The sizeable increase of the vibronic structure observed moving from compound **1** to **3** indicates that mixing between $^3MLCT_{C^N}$ and $^3IL_{C^N}$ occurs to a lower extent due to the more extended π-conjugation of the moiety involved in the radiative transition and agree well with the emission of the corresponding [Ir(C^N)$_2$(acac)] congeners.[45] Analysis of the excitation spectra recorded at both maxima for complexes **1** are displayed in *Figure ES4.15.* The two excitation spectra show slightly different profile, also when compared to the absorption spectrum, corroborating the idea that the two emission bands originate from electronically uncoupled excited states. On the other hand, for compounds **2** and **3** the excitation spectrum recorded at the emission band maximum resembles closely the absorption spectral profile (see *Figures ES4.16* and *ES4.17*). Time-resolved analysis of the photoluminescence of compounds **1**–**3** revealed interesting information. Indeed, the excited state kinetic data recorded in degassed condition required a fitting with bi-exponential model for the three compounds **1**–**3**. As an example, complex **3** displays two decays with τ_1 = 1.55 μs (62%) and τ_2 = 1.03 μs (38%) at λ_{em} = 610 nm, and τ_1 = 1.6 μs (51%) and τ_2 = 1.1 μs (49%) at λ_{em} = 660 nm, highlighting the presence of a triplet state (namely P2) that is close in energy to the emissive $^3IL_{C^N}/^3MLCT_{C^N}$ characteristic of the "[Ir(1-piq)$_2$(acac)]" scaffold (P1 state). Such P2 state appears to be present in the three complexes of the series **1**–**3** and it is most likely at the origin of the band clearly observed at λ_{em} = 655 nm for complex **1**. To further elucidate the origin of such poorly emissive state, the energy of the ^{3}IL state located onto the IMesAcacH ligand was evaluated by recording the photoluminescence spectrum of the corresponding Gd^{III} complexes at low temperature at 77 K glassy matrix in 2-MeTHF (see *Figure ES4.20* in the Experimental Section). The spectrum displays an onset at λ_{em} = 436 nm (2.84 eV) on the high-energy side, which allowed us to confidently rule out the π–π* nature localized onto the IMesAcacH ligand, namely $^3IL_{IMesAcacH}$, of the P2 band, being the former positioned to much higher in energy than the latter. Clearly, the broad and featureless profile of this latter points toward a ^{3}CT nature instead. To further investigate the emissive properties and the origin of the

lower energy band, low temperature (77 K) photoluminescence experiments were carried out for samples of **1**–**3** in 2-MeTHF glassy matrix (*Figure 4.9* and *Table 4.1*).

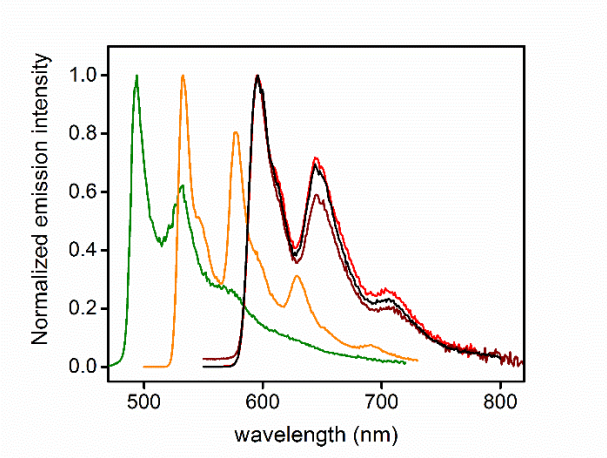

Figure 4.9. Emission spectra recorded for **1** (green), **2** (orange), **3** (red), **4** (dark red), and **5** (black) in 2Me-THF glassy matrix at 77 K. Samples were excited at λ_{exc} = 400 nm for **1** and **2**, 420 nm for **3**, 450 nm for **4**, and 460 nm for **5**.

Under this condition complexes **1**–**3** display intense emission with highly vibronic profile and mono-exponential decay over the whole emission band resembling those of parental [Ir(C^N)$_2$(acac)] complexes, indicating that population of the P2 band might occur through a thermally-activated process at room temperature. Overall, the P2 band is tentatively attributed to a triplet ligand-to-ligand charge transfer character, namely ^{3}LLCT$_{IMesAcacH}$, with a metal-perturbed C^N→IMesAcacH character, close-lying to the emissive ^{3}IL$_{C^N}$/^{3}MLCT$_{C^N}$ (*Figure 4.10*). Indeed, going from compound **1** to **2** to **3**, the ^{3}LLCT$_{IMesAcacH}$ level is expected to be affected to a minor extent. Theoretical calculations confirm that for complex **1** T_1 remains MLCT$_{IMesAcacH}$/LLCT$_{IMesAcacH}$ state and T_2 converges to a LLCT$_{IMesAcacH}$/MLCT$_{IMesAcacH}$ state.

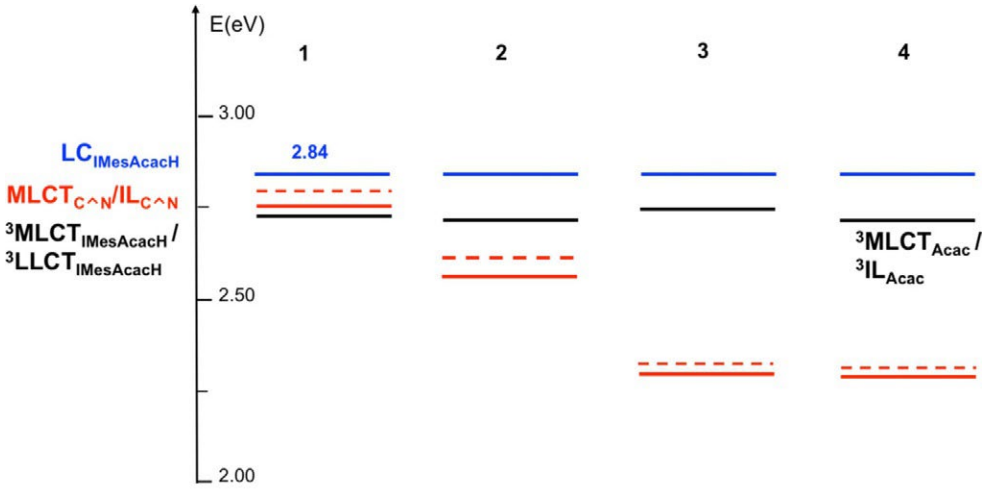

Figure 4.10. Schematic representation of the energy levels and nature of the low-lying excited states at Franck–Condon for compounds **1**–**4** based on theoretical results and experimental data for $^{3}IL_{IMesAcacH}$.

The stabilization of the $^{3}MLCT_{C^N}/^{3}IL_{C^N}$ provided by the more extended π-conjugation for complexes **2** and **3** of the system increases the energetic barrier for the P1→P2 process, rendering the thermal population of the poorly emissive P2 more difficult. This means that both T_1 and T_2 keep their $MLCT_{C^N}/IL_{C^N}$ character and the emissive behaviour of **2** and **3** is controlled essentially by a low-lying $MLCT_{C^N}/IL_{C^N}$.

*4.2.2.2 Photophysical characterization of bimetallic complexes **4**-**5** in acetone*

The absorption and emission spectra of the heterobimetallic complexes **4** and **5** are shown in *Figure 4.7* and the excitation spectra are displayed in *Figures ES18* and *ES19*. The data are listed in *Table 4.1*. They feature an absorption spectrum at room temperature that almost traces out the one of the monometallic counterpart **3**, thus confirming the negligible electronic coupling between the two metal centers at the electronic ground state. Remarkably, going from **3** to **4** and **5** a small bathochromic shift is observed for the band attributable to the admixture of $^{1}MLCT$ and $^{3}MLCT$ transitions that involves the cyclometalating C^N and acac moiety ($\lambda_{abs,max}$ = 458 nm for **3** and 465 nm for **4** and **5**). The $MLCT_{C^N}$ states are more stabilized, increasing their participation in the low-lying mixed $IL_{C^N}/MLCT_{C^N}$ states of complex **4** as compared to complex **3**.

This finding corroborates the energetic stabilization of the MLCT state in the bimetallic species. The photoluminescence spectra of **4** and **5** are bathochromically shifted by 8 nm (215 cm^{-1}) in comparison with the parental compound **3**. The spectra show comparable vibronic progression with fundamental spacing of 1290 cm^{-1} and similar Huang–Rhys factor; the latter indicates that compounds **3** and **4** possess comparable vibronic coupling between the emitting T_1 and the S_0 state. In sharp contrast, the bimetallic species display mono-exponential excited-state decay kinetics and a twofold increase of PLQY (τ = 1.6 μs and PLQY = 36% in degassed acetone). One should notice that this value of PLQY is much higher than the benchmark complex [Ir(1-piq)$_2$(acac)][47] and amongst the highest for red-emitting cationic Ir^{III} complexes.

For sake of comparison, the absorption and photoluminescence spectra of the parental complexes [(IPr)Cu(IMesAcac)] and [(IPr)Au(IMesAcac)] were recorded in acetone solution under identical condition (see *Figure ES4.21).* Expectantly, the electronic absorption spectrum displays intense and narrow emission band in the UV region with an onset at λ_{abs} = 380–385 nm for both complexes that can be attributed to a ^{1}IL transition. Upon photoexcitation at λ_{exc} = 340 nm, they both display a very weak, narrow and featureless emission with small Stokes shifts. In particular, for degassed samples of [(IPr)Cu(IMesAcac)] two bands are present, namely a higher and a lower energy bands with maximum centered at λ_{em} = 410 and 544 nm, respectively. Overall, these findings are in agreement with those reported previously for similar species.[48] As far as the heterobimetallic species **4** and **5** are concerned, the presence of a second metal atom coordinated through the bridging ancillary ligand onto the "[Ir(1-piq)$_2$]" scaffold is expected to modify the excited state properties by eliminating the poorly emissive close-lying ^{3}LLCT$_{IMesAcacH}$ state. Moreover, closer look at the excited state kinetic parameters indicates that the presence of the second metal center, such as the [(IPr)M^{I}(IMesAcac)] moiety, onto the emissive "[Ir(1-piq)$_2$]" scaffold largely improves the photophysical properties of this latter. The origin of this result stems from a two-fold effect. A decrease of the k_{nr} is observed due to the absence of the ^{3}LLCT$_{IMesAcacH}$ state in the bimetallic species, being k_{nr} = 4.0X10^5 and 6.1X10^5 s^{-1} for compounds **4**–**5** and **3**, respectively. Alongside, an almost two-fold enhancement of the radiative rate constant is determined, being k_r = 2.3X10^5 and 1.3X10^5 s^{-1} for **4**–**5** and **3**, respectively. The data obtained for compound **3** are in well agreement with those reported for "[Ir(1-piq)$_2$(acac)]" benchmark complex, k_r = 1.2X10^5 and k_{nr} = 4.8X10^5 s^{-1}.[47] In general, the radiative rate of the transition between the T_1 and S_0 can be expressed as follows for a transition metal complex (Eq. (4.1)):[44]

$$k_r \propto \bar{\nu}^3 \left| \sum_m \frac{\langle S_m | \hat{H}_{SO} | T_1 \rangle}{E_{T1} - E_{Sm}} \langle S_0 | e\boldsymbol{r} | S_m \rangle \right|^2 \qquad Eqn.\,4.1$$

Where $\bar{\nu}^3$ is the electronic transition energy expressed in cm^{-1}, $e\boldsymbol{r}$ is the electric dipole operator, the term $\sum_m \frac{\langle S_m | \hat{H}_{SO} | T_1 \rangle}{E_{T1} - E_{Sm}}$ in squared brackets relates with the SOC matrix elements between the singlet S_m and the T_1 state, and the matrix element of the second term, $\langle S_0 | e\boldsymbol{r} | S_m \rangle$, represents the transition dipole moment of the spin-allowed transition between singlet ground state S_0 and the higher-lying S_m state, E_{T1} and E_{Sm} is the energy of the T_1 and S_m state, respectively. A closer analysis of the parameters influencing the k_r indicates that the bathochromic shift observed for **4** and **5** when compared to the parental complex **3** might instead yield a smaller k_r. In addition, contribution from an increased transition dipole moment of the ^{1}MLCT state from where the emitting state stems from has to be ruled out. Indeed, the low-energy side of the profiles of the molar extinction coefficient spectra nicely overlap for complexes **3**–**5**. Likewise, in the frame of an indirect SOC mechanism, the energy level of the unperturbed ^{3}IL should be similar for **3**–**5**. Instead, the HOMO level is expected to be destabilized by the stronger donating nature of the “acac” moiety in the bimetallic species **4** and **5** compared to the monometallic counterpart **3**, yielding a decrease of the ^{1}MLCT and, thus, a smaller energetic separation between the first-order perturbation mixing of the ^{1}MLCT and ^{3}IL states.

Modulation of k_r via variation of the ancillary ligand has been previously reported,[49] but their enhancement in heterobimetallic systems connected via the ancillary ligand is unprecedented, to the best of our knowledge.

Table 4.1. Photophysical properties of complexes **1–5** recorded in air-equilibrated and degassed acetone solution at concentrations of $3X10^{-5}$ M at room temperature and 77 K.

cmpd	$\lambda_{max,abs}$ (ε) [nm, (10^3 M^{-1} cm^{-1})]	λ_{em} [nm]	PLQY (%)		τ μs		λ_{em} [nm]	τ μs
			air-equilibrated	*degassed*	*air-equilibrated*	*degassed*	*77 K*	
1	395 (4.13), 440 (2.78), 482 (0.63)	520, 655	0.05	0.2	0.021[a,b] 0.019[c]	1.24[a] 1.37[a,d]	493, 530, 570	1.3[a]
2	383 (7.02), 428 (5.71), 459 (4.65), 522 (0.40)	546, 583, 640	1.9	3.5	89 ns	152 ns	532, 578, 628	3.8
3	390 (10.1), 458 (6.24), 502 (3.14), 540 (1.43), 578 (0.51)	607, 650	2.5	18	199 ns	1.35[a]	596, 645, 704	2.8
4	410 (8.10), 465 (5.77), 511 (2.85), 582 (0.63)	615, 655	3.5	36	165 ns	1.6	596, 645, 704	2.8
5	410 (7.37), 465 (5.67), 511 (2.65), 582 (0.60)	612, 660	3.7	36	170 ns	1.6	596, 645, 704	2.9
[Ir(1-piq)$_2$(acac)][e]	–	622	–	20	–	1.7	–	–
[(IPr)Cu^{I}(IMes Acac)]	343 (17.6) 363 (9.69) 372 (2.00)	407, 539						
[(IPr)Au^{I}(IMes Acac)]	347 (21.2) 365 (11.5) 378 (2.00)	400, 534						

sh denotes a shoulder; a average lifetime (see experimental methods for details); b λ_{em} = 520 nm; c λ_{em} = 660 nm; d λ_{em} = 650 nm; [e] data from ref. [47]

*4.2.2.3 Photophysical characterization of bimetallic complexes **4**-**7** in dichloromethane*

At a second stage, the photophysical properties of the four complexes **4-7** were investigated in CH_2Cl_2 solution at concentration of $3{\cdot}10^{-5}$ M in both air-equilibrated and degassed condition at room temperature. A list of the most meaningful photophysical data is compiled in *Table 4.2* and the corresponding absorption and photoluminescence spectra are displayed in *Figure 4.11.* At first glance, UV-vis absorption of the four complexes evidenced

similarities in the overall profile of the transitions expectantly, owing to the rather similar electronic properties of the 1-phenyl-8-isoquinoline and 2-(dimethylphenyl)-isoquinoline ligands. Also, within homologous series of complexes bearing the same C^N ligands, a minor role is played by the nature of the M(I) center in the lower energy side of the spectra. In the higher energy region at λ_{abs} = 340–350 nm, all four complexes display intense (ε = 2.06–2.28·10^4 M^{-1} cm^{-1}) bands that can be ascribed to electronic processes with mainly singlet-manifold ligand centered (^{1}LC) to a certain degree of admixing with spin-allowed metal-to-ligand charge transfer (^{1}MLCT). At lower energy (λ_{abs} *ca.* 400 nm), the less intense transitions with ε = 6.8–8.3·10^3 M^{-1} cm^{-1} are attributable to electronic processes with mainly ^{1}MLCT character admixed intraligand charge transfer (^{1}ILCT). Broader, featureless and much less intense bands can be observed in the region at labs ca. 470 nm ascribed to a transition with mainly ^{1}MLCT character with partial ^{1}LC contribution. The much weaker spectral feature at ca. 565 nm is attributed to the ^{3}MLCT transition enabling population of the lowest-lying triplet state through the formally spin-forbidden S_0-T_1 process. This finding derives from the large SOC effect exerted by the heavy metal atom (Ir) that yields partial relaxation of spin selection rules and enables direct optical excitation of T_1 from the singlet ground state. All these assignments are based on previously investigations on related derivatives[44] and are further supported by TD-DFT analysis (*Figure 4.12*).

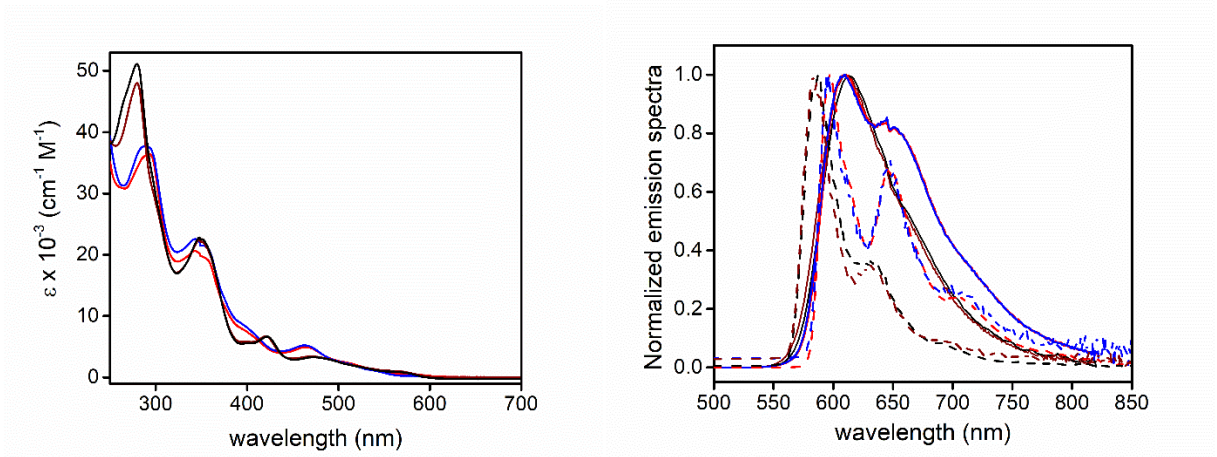

Figure 4.11 Electronic absorption (*left box*) and emission spectra (*right box*) for **4** (red trace), **5** (blue trace), **6** (dark red trace) and **7** (black trace) in dichloromethane at concentration of 3.0×10^{-5} M in degassed condition (solid traces) and in 2-MeTHF glassy matrix at 77 K (dashed traces). Samples were excited at λ_{exc} = 420, 460 and 480 nm for compound **4**,**5**,**6** and **7**, respectively.

In all complexes both LUMO and LUMO+1 orbitals are localized on the 1-phenyl-isoquinoline (for **4** and **5**) and 2-methylphenyl-isoquinoline (for **6** and **7**) ligands. The HOMO is located over both the cyclometalated C^N ligand and the Ir center, while the HOMO–1 is delocalized over the Ir metal center and the ancillary acac-substituted ligand. The addition of methyl groups on the phenyl-quinoline ligand modifies the percentage of iridium contribution in the HOMO, which is 41% in **4** and **5**, and 36% in **6** and **7**. Minor LLCT transitions involving charge transfer between the phenyl-quinoline and the acac ligands contribute to the absorption. As expected, Cu, Au and the NHC ligand do not significantly contribute to the charge transfer processes, whereas Ir, the phenyl isoquinoline ligand and to partially acac ligands exhibit important charge transfer character.

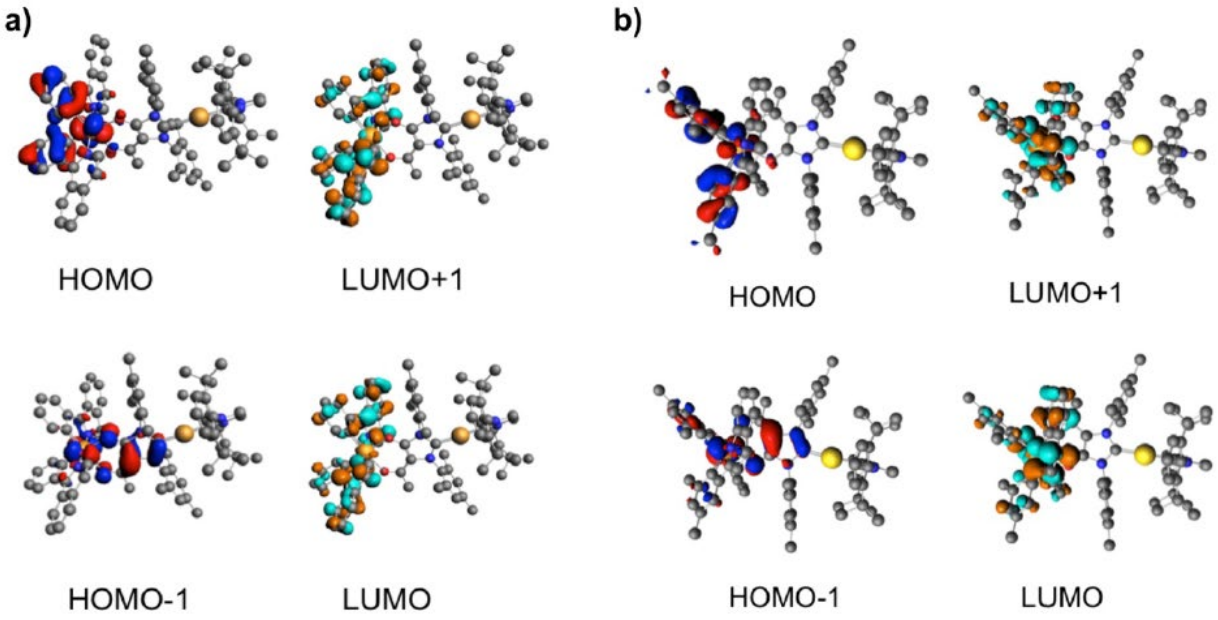

Figure 4.12 Kohn-Sham frontier orbitals of (a) **4** and (b) **7** optimized at DFT level in CH_2Cl_2. Hydrogen atoms are hidden for the sake of clarity.

Upon excitation on the lower-lying bands, dilute CH_2Cl_2 samples of compounds **4**–7 display intense vibrant red emission. In particular, compounds **4** and **5** show a broad emission band centered at λ_{em} = 610 nm with a vibrational feature at 645 nm that can be ascribed to an emission originating from an excited state with admixed ^{3}MLCT/^{3}LC character involving the heavy atom and the C^N ligands. On the other hand, emission spectral profile of compounds **6** and **7** are broad, featureless and narrower than those of **4** and **5**, indicating higher ^{3}MLCT character and lesser geometrical distortion of the emissive excited state for compounds **4-5**. Derivatives bearing the dm-2-pic ligand displayed higher PLQY amongst

the series, with values as high as 0.77 and 0.73 for the **6** and **7**, respectively, in degassed CH_2Cl_2. It is worth to notice that these PLQY values are remarkably high and amongst the highest for cationic red-emitting complexes.

The triplet nature of the radiative process was further corroborated by both the increase of the PLQY and prolongation of the excited state lifetime when going from air-equilibrated to degassed condition. Interestingly, degassed samples of **6** and **7** show an almost two-fold higher PLQY in comparison with **4** and **5** in spite of the rather similar excited state lifetime. Once again, this result corroborates more ^{3}MLCT character for the excited state in compounds belonging with the series bearing the dm-2-piq ligand. This is also in agreement with the higher extinction coefficient observed for the lowest energy side of the absorption spectrum, attributable to the ^{3}MLCT band,[44] for **6** and **7** when compared with **4** and **5** (see *Figure 4.11*) as well as low temperature measurements. Further comparison with the photophysical properties of the corresponding mononuclear parental complexes [Ir(1-piq)$_2$(acac)] and [Ir(dm-2-piq)$_2$(acac)], provides interesting insights concerning the origin of such remarkably high PLQY values (see *Table 4.2*).

Whereas the lowest triplet state of **6** and **7** possess an ILCT/MLCT character, which corresponds to the HOMO-LUMO transition; the T_1 states of **4** and **5** features a LC character involving the phenyl-isoquinoline ligand mixed with MLCT. These lowest computed T_1 states do not contribute to the experimental maximum measured at 610 nm due to the structure optimization of upper triplet states of these molecules is a rather challenging task.

Overall, the investigated bimetallic species possess smaller k_{nr} values when compared to the monometallic counterparts, indicating that non-radiative channels are suppressed to a larger extent and, therefore, bimetallic structures help providing a more rigid scaffold. Even more interestingly, k_r values are higher for bimetallic species. Going from room temperature to frozen in 2-MeTHF glassy matrix at 77 K, all the samples show an emission profile with enhanced vibronic progression and hypsochromically shifted spectra (see *Figure 4.11* and *Table 4.2*). In particular, **4** and **5** show a shift of 360–410 cm^{-1}, whereas a much larger shift is observed for compounds **6** and **7**, being as high as 720–810 cm^{-1}. Moreover, the photophysical properties of thin-film samples prepared by spin-coating techniques were investigated in poly-(methyl methacrylate) (PMMA) at 25 wt.% doping level, neat film prepared from CH_2Cl_2 solutions as well as in BMIM[PF_6] complex at 20:80 wt.% ratio in acetonitrile (*Figure 4.13*).

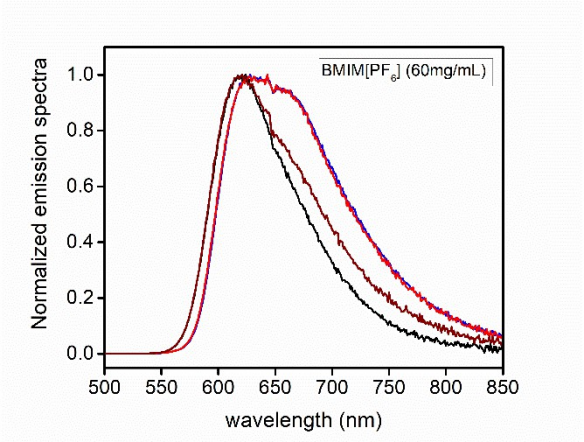

Figure 4.13 Emission spectra of spin-coated BMIM[PF_6] (20 wt.%) **complex** (80 wt.%) at total concentration of 60 mg mL^{-1} in acetonitrile for samples of **4** (red trace), **5** (blue trace), **6** (black trace) and **7** (dark red trace) upon λ_{exc} = 450 nm.

In thin-film, emission spectra of all the samples display bathochromic shift compared to dilute solution sample, which is accompanied by a drop of the PLQY in condensed phase, expectantly. It is important to notice that the decrease of the emission efficiency, as well as the bathochromic shift, was less dramatic for compounds **6** and **7**, thus supporting the idea that the presence of additional methyl groups in the chemical structure of the complexes helps to keep the triplet emitters further apart and therefore mitigating aggregation-caused quenching effects and triplet-triplet annihilation phenomena in condensed phase. This is an important point to address in view of their potential application in solid-state light emitting devices.

Table 4.2 Photophysical data recorded for compound **4-7** in degassed CH_2Cl_2 solution at concentration of $3 \cdot 10^{-5}$ M at room temperature as well as in frozen 2-MeTHF glassy matrix at 77 K. Literature data of the two benchmarks complexes [Ir(1-piq)$_2$(acac)] and [Ir(dm-2-piq)$_2$(acac)] are listed as well for sake of comparison.

cmpd	λ_{abs} (ε) [nm, (10^3 M^{-1} cm^{-1})]	λ_{em} [b] [nm]	PLQY [b,c] (%)	PLQY [b,d] (%)	τ [b,c] [ns]	τ [b,d] [µs]	k_r [$\times 10^5$ s^{-1}]	k_{nr} [$\times 10^5$ s^{-1}]	λ_{em} [e] [nm]	τ [e] [µs]
4	344 (20.57), 398 (7.57), 463 (4.76), 564 (0.58)	610, 645	8.7	40.5	361	1.6	2.5	3.7	597, 646, 709	2.8
5	341 (22.83), 399 (8.30), 464 (5.31), 564 (0.04)	610, 645	9.0	45.5	358	1.7	2.7	3.2	595, 646, 706	2.8
6	350 (22.65), 421 (6.76), 470 (3.40), 566 (1.21)	614	7.9	77.0	183	1.8	4.3	1.3	588, 633	7.6
7	350 (22.65), 421 (6.76), 470 (3.40), 566 (1.21)	611	8.2	72.8	179	1.8	4.0	1.5	582, 632	7.5
[Ir(1-piq)$_2$(acac)] [a]	-	622	-	0.20	-	1.1	1.8	7.3	–	–
[Ir(dm-2-piq)$_2$(acac)] [a]	-	623	-	0.50	-	1.7	2.9	2.9	–	–

a) data from Ref.44; b) CH_2Cl_2 solution at concentration of $3 \cdot 10^{-5}$ M at room temperature; c) air-equilibrated sample; d) degassed sample; e) frozen 2-MeTHF glassy matrix at 77 K.

Table 4.3 Photophysical data recorded for compound **4-7** in thin films samples under different condition upon excitation at λ_{exc} = 450 nm.

compound	λ_{em} [nm]			PLQY (%)		
	PMMA (25 wt.%)	neat	BMIM[PF_6]:complex 20:80 wt.%	PMMA (25 wt.%)	neat	BMIM[PF_6]:complex 20:80 wt.%
4	620, 647	622	631,658	1.5	0.5	3.3
5	620, 649	620	631, 658	6.0	0.5	4.1
6	622	623	620	2	0.9	6.5
7	610	623	620	7.5	1	6.6

4.2.3. Electrochemistry[d]

The electrochemical behavior of compounds was assessed by cyclic voltammetry (CV) in acetone/0.1m tetrabutylammonium hexafluorophosphate ($TBAPF_6$) for **1-4** and acetonitrile (ACN)/0.1 M tetra-*n*-butylammonium perchlorate (TBAP) for **4-7** by Dr. Federico Polo from University of Venice. All the electrochemical data are referenced against ferrocene/ferricenium couple as the internal standard.

*4.2.3.1 Electrochemistry of compounds **1**-**4** in acetone*

The electrochemical processes in the negative- and positive going scans are defined as $R_{i,n}$ and $O_{i,n}$, respectively, where i denotes the process number and n the compound number, namely **1**–**4.**

In the positive-going scan, all compounds **1**–**4** showed one main reversible oxidation process $O_{1,n}$, whose standard potential E° varied from +0.56 to +0.82 V. Instead, in the negative going scan, one or more irreversible and reversible reduction processes $R_{i,n}$ occurred in the potential range from -2.00 to -2.90 V (see *Figure 4.14* and *Table 4.4*). $O_{1,n}$ is related to the formally Ir^{III} to Ir^{IV} oxidation, involving the cyclometalated phenyl ring. The values for **1** and **3** are similar, demonstrating that the ppy and 1-piq have similar electron donating effect. Complex **2** shows an anodic shift about 120 mV, as previously reported in literature for similar compounds.[50]

[d] Dr. Federico Polo is kindly acknowledged for performing the electrochemical analysis.

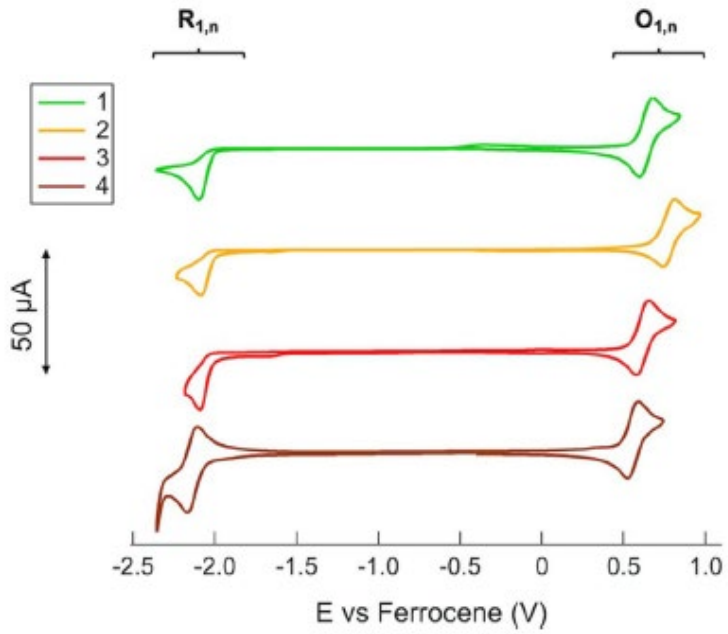

Figure 4.14. Background-subtracted cyclic voltammetry curves of 1 mm solutions of **1–4** in acetone/0.1 M $TBAPF_6$ at 0.2 Vs^{-1} for $O_{1,1–4}$ and $R_{1,1–4}$ processes.

Complex **4** displays 80 mV lower oxidative potential than **1-3**, up to +0.56 V, pointing out that the HOMO is affected by the presence of the second metal for complex **4**. $R_{i,n}$, in the range from -2.04 to -2.08 V, is related to the reduction of the IMesAcacH ancillary ligand for complexes **1-3.** Bearing in mind that the free IMesAcacH proligand shows two irreversible peaks at +0.85 and +1.20 V and one irreversible process at -2.82 V, it is understandable to say that the zwitterionic character of the free IMesAcacH ligand is lost when chelating the metal complex, making the reduction easier from -2.82 to -2.06. On the other hand, the residual positive charge from IMesAcacH makes the oxidation more difficult, assuring that oxidative processes occur just $Ir(C^N)_2$ moiety. In complex **4** the positive charge is localized on the copper center, leading to reversible reduction process at -2.14 V localized on the cyclometalating 1-piq ligand. CV of complexes **1-3** reveals that no reduction process occurs at potential lower than -2.50 V, confirming that the reduction can be only due to 1-piq. All compounds **1-4** show monoelectronic processes confirmed by the ratio close to unity between the anodic and cathodic peak current. Lastly, keeping the potential at -2.50 V for 20 s for complex **4**, an additional irreversible oxidation process appears at 0.35 V, which is attributed to the re-oxidation of IMesAcaH stripped away from the metal complex. Similar behavior is observed for **1-3**.

Table 4.4 Electrochemical data for compounds **1–4** obtained by cyclic voltammetry in acetone/0.1 M TBAP as the supporting electrolyte.

	$O_{i,n}$				$R_{i,n}$	
Cmpd *(n)*	**E^o (V) [a]**	**ΔE_p (mV) [b]**	**E_p-$E_{p/2}$ (mV) [b]**	**$I_{a,O1}/i_{c,R1}$ [c]**	**$E_{p,c}$ (V) [b]**	**E_p-$E_{p/2}$ (mV) [b]**
1	+0.640	70	64	0.93	-2.080 -2.68 -2.868	45
2	+0.816	74	72	1.00	-2.036 -2.394 [a] -2.763	40 72
3	+0.650 +0.368 [b,e]	69	60	1.05	-2.050 -2.567 [a] -2.771	42
4	+0.559 +0.345 [b,e] +1.443 [b]	72	62	0.78	-2.140 [a] -2.440 -2.640	57
IMesAcacH	0.852 1.204		109 51		-2.816	74
[(IPr)Cu(IMesAcac)]	+0.330					

[a] $E^o_{Oi,n}$ or $E^o_{Ri,n}$ = average value between the anodic and cathodic peaks, calculated over a scan rate range 0.05-0.5 Vs^{-1}. [b] Measured at 0.2 Vs^{-1}. [c] Calculated at 0.2 Vs^{-1}. [d] Measured by DPV. [e] It appears only when scanning in the positive bias, once the potential is kept for 20 s at -2.5 V. All the potential values are reported against the redox couple Ferrocene/Ferricinium, used as the internal standard

*4.2.3.2 Electrochemistry of compounds **4**-**7** in dichloromethane*

In the positive-going scan, all compounds showed a main reversible oxidation process, $O_{1,n}$ (with *n* denoting the investigated compound), whose standard potential E_{01}^0decreased progressively from 0.640 V to 0.453 V following the order **4**, **5**, **7** and **6**. Instead, in the negative-going scan, two or three reversible and irreversible reduction processes $R_{i,n}$ (where *i* denotes the process number and *n* the investigated compound) occurred in the potential range from –2.00 V to –2.67 V (see *Figure 4.15* and *Table 4.5*).

The oxidation is related to the iridium metal center, formally from Ir^{III} to Ir^{IV}, with involvement of the cyclometalated phenyl ring. The four compounds display similar value providing comparable electro-donating effect from **1-piq** and **dm-1-piq** to the metal**.** In the negative scan region, a full reversibility is showed for **4** and **5**, while a weak reversibility is present for **6** and **7**.

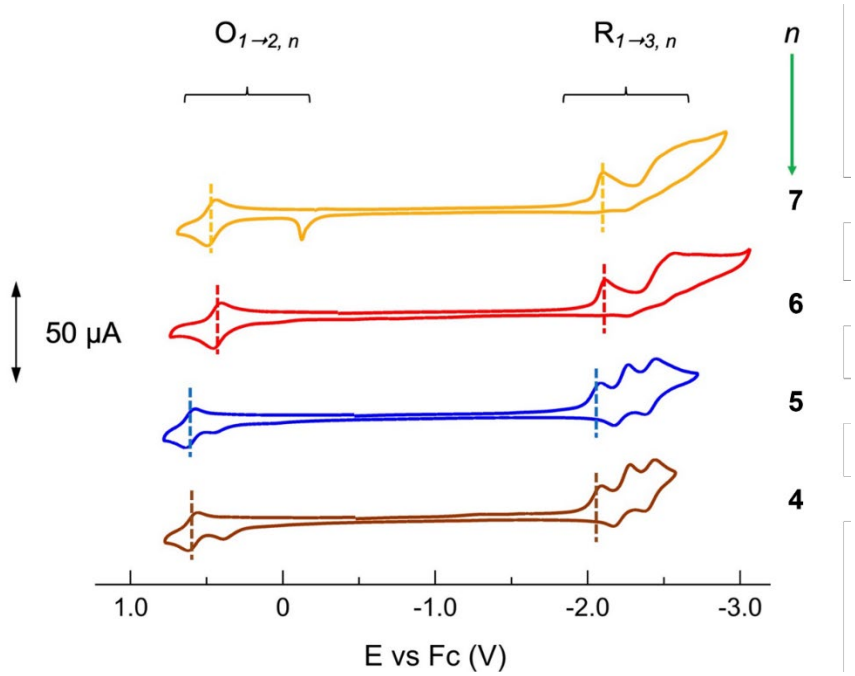

Figure 4.15 CVs of 1 mM of the investigated compounds in ACN/0.1 M TBAP showing $O_{1\text{-}2}$,n and $R_{1\text{-}3,n}$ redox processes. Scan rate: 0.1 V s^{-1}.

Compounds **4**, **5** and **7** also show a second oxidation process O_2 in the potential range from +0.5 to –0.15 V, whereas **6** seems to show a very weak current increase above the blank. The second oxidative process of **7** shows a very sharp anodic peak at about –0.14 V that, together with its cathodic counterpart (a weak peak at about –0.42 V), very much resembles the behavior of bare gold in solution. The hypothesis here is that the ligand capping Au^{+} is made labile and expose Au in solution, which is immediately re-oxidized when the scan is reverted. Lastly, since the ratio between the anodic and cathodic peak current is close to the unity, the processes are monoelectronics.[51]

Table 4.5 Electrochemical data for compounds **4–7** obtained by cyclic voltammetry in acetone/0.1 M TBAP as the supporting electrolyte.

Cmpd	E^0_{01}[V][a]	$\Delta E_{\frac{p}{2}O1}$[mV][b]	E_{pO2}[V][c]	E^0_{R1}[V][a]	$\Delta E_{\frac{p}{2}R1}$[mV][d]	E^0_{R2}[V][d]	E^0_{R3}[V][d]	eBand-Gap [eV][e]
4	+0.640	54	+0.453	-2.024	59	-2.729	-2.979	2.664
5	+0.616	63	+0.492	-2.031	63	-2.763	-3.011	2.647
6	+0.453	60	-	-2.073	43	-2.406	-2.699	2.526
7	+0.466	60	-0.144	-2.074	45	-2.380	-2.699	2.540

[a] The formal potential is defined as the average value between the cathodic and anodic peak potentials of the investigated redox process, *Ep,c* and *Ep,a*, respectively: $E^0 = \frac{E_{p,c}+E_{p,a}}{2}$. The values provided are the average values obtained when varying scan rate in the range 0.05-0.5 Vs^{-1}. [b] $\Delta Ep/2$ is defined as *Ep-Ep/2*, where *Ep/2* is the potential value when the current *i* is at half its peak value, *ip*, for the processes under investigation ($O_{1,n}$ or $R_{1,n}$, respectively). [c] O_2 are irreversible processes. d Both R_2 and R_3 processes for **4** and **5** are reversible, whereas R_2 and R_3 for **6** and **7** are irreversible, although R_2 for **6** showed some reversibility for scan rate higher than 0.2 V/s. Therefore, only the peak potential value, *Ep*, is reported for the latter ones. [e] The eBand-Gap is the electrochemical band-gap between O_1 and R_1 processes.

4.3 LEC devices[e]

The performance of compounds **4-7** in LEC devices were explored in the frame of a collaboration with Yun-Xin Wang and Dr.Chin-Wei Lu from Providence University and Pei-Wan Hsiao, Yin Chen, Prof. Hai-Ching Su from National Yang Ming Chiao Tung University.

To evaluate the EL performance of the proposed heterodinuclear iTMCs, the LECs based on complexes **4**, **5**, **6**, and **7** were fabricated and their EL characteristics are summarized in *Table 4.6*. All emissive layers of these iTMC were spin-coated from the mixture of the complex (80 wt.%) and [$BMIM^+(PF_6)^-$] (20 wt.%) in acetonitrile solution with various concentrations. Concentration of mixture solution can be tuned to modify the thickness of spin-coated emissive layer. Adjusting emissive layer thickness is an effective approach to optimize carrier balance and/or light outcoupling efficiency of LECs. The EL spectra of the LECs based on complexes **4**, **5**, **6**, and **7** with various emissive-layer thicknesses are depicted in *Figure 4.16*. All devices show thickness-dependent EL spectra since altered microcavity effect induced by distinct optical structure and shifted emission zone position modifies wavelength-dependent light in external mode and changes the output

[e] Yun-Xin Wang, Chin-Wei Lu (Providence University) and Pei-Wan Hsiao, Yin Chen, Hai-Ching Su (National Yang Ming Chiao Tung University) are kindly acknowledged for the device fabrication and electroluminescence characterization.

EL spectra.[52] In spite of thickness-dependent EL spectra affected by microcavity effect, the EL emissions from the proposed iTMCs are still similar to their PL emissions. Therefore, the proposed iTMCs are confirmed to be effective for LEC applications.

Table 4.6 Summary of the device EL characteristics of the neat-film LECs based on emissive layers of complexes **4**, **5**, **6**, and **7.**

Cmpd	Thickness (nm)	Voltage (V)	EL_{max} (nm)[a]	B_{max} (cd m^{-2})[b]	$\eta_{ext, max}$ (%)[c]	$\eta_{c, max}$ (cd A^{-1})[d]	$\eta_{P, max}$ (lm W^{-1})[e]
4	150	4	621	19.4	0.24	0.19	0.15
	240	4	624	11.8	0.36	0.27	0.21
5	150	3	641	23.1	0.43	0.40	0.42
	240	3	656	8.1	0.50	0.36	0.38
	340	3	632	7.4	0.75	0.62	0.65
	480	3	679	3.9	0.96	0.66	0.69
6	85	2.5	613	4.4	0.30	0.41	0.52
	150	2.5	620	2.5	0.55	0.60	0.76
	240	2.5	615	2.8	0.96	1.13	1.42
	305	2.5	614	3.2	1.31	1.92	2.41
	340	2.5	620	3.3	1.73	2.05	2.58
7	150	2.5	618	9.4	0.70	0.87	1.10
	240	2.5	633	7.4	1.03	1.03	1.30
	340	2.5	624	11.1	2.05	2.31	2.90

[a] EL peak wavelength of EL spectrum. [b] Maximal brightness. [c] Maximal external quantum efficiency. [d] Maximal current efficiency. [e] Maximal power efficiency.

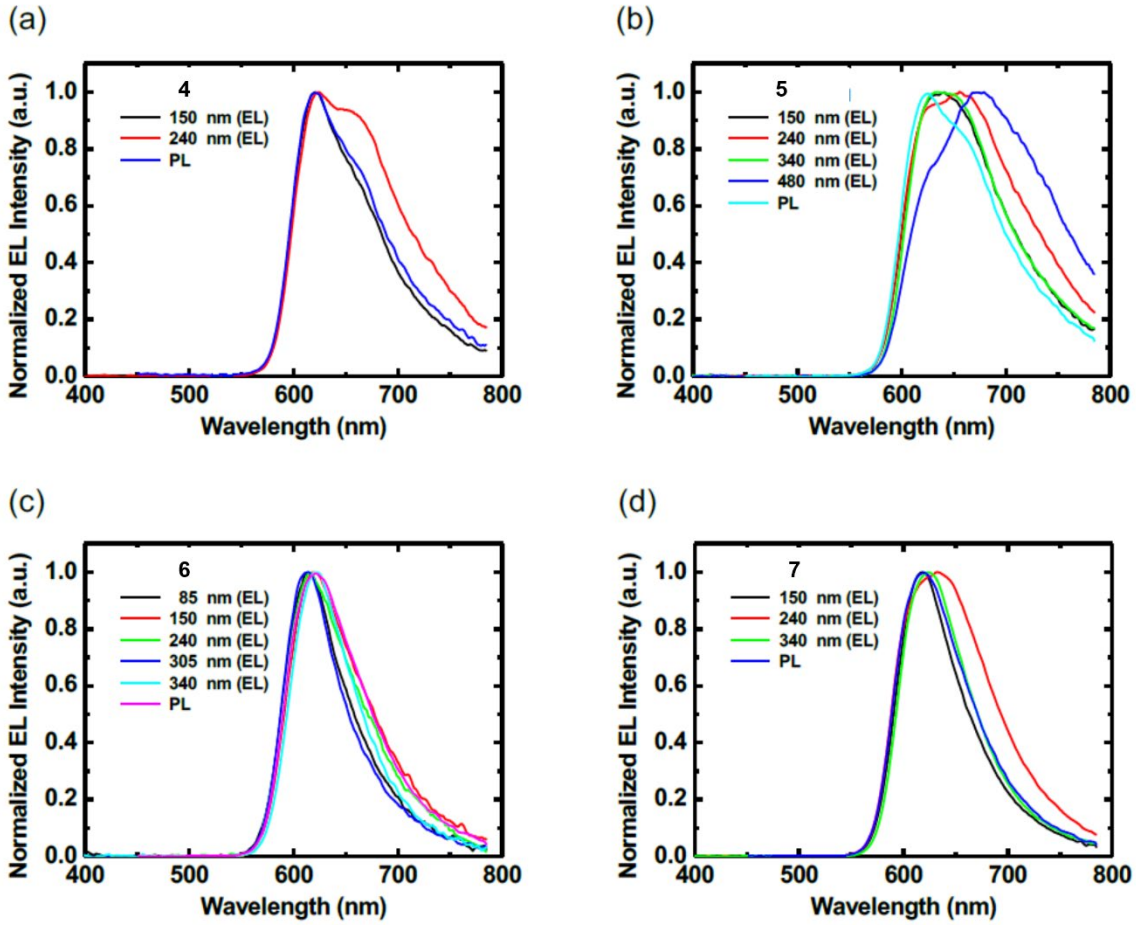

Figure 4.16 EL spectra of the neat-film LECs based on complexes (a) **4**, (b) **5**, (c) **6**, and (d) **7** under 4, 3, 2.5, and 2.5 V, respectively. Thin-film PL spectra of the emissive layers of LECs based on these complexes are also included for comparison.

The operating voltages employed in these LECs were optimized to achieve maximum device efficiencies. Under constant-voltage operation, the time-dependent currents of all LECs show a similar temporal evolution trend. The device current first increases with time after the bias is applied, reaching a maximum value before decreasing over time. After a bias is applied, the mobile ions in the emissive layer of the LEC are driven toward electrodes and the electrochemically *p*- and *n*-type doped layers are gradually growing. The *p*- and *n*-type doped layers facilitate carrier injection and thus the device current increases with time. When the doped layers are formed completely, the carrier injection rates approach the steady-state regime and the device current reaches a maximum value. Based on similar emissive-layer thicknesses, *e.g.*, 150 or 240 nm, the LECs based on **4**, **5** exhibit higher device currents than other LECs due to higher bias voltages. On the other hand, the LECs based on **7** (150, 240, or 340 nm) shows higher device currents than the LECs based on **6**

(150, 240, or 340 nm) under the same bias voltage. Since complexes **6** and **7** have similar bandgaps (see *Table 4.5*), higher device currents of the LECs based on **7** may be attributed to higher carrier mobilities of electroluminescent complex.

Brightness generally follows the temporal evolution of the device current initially. However, after reaching the maximum value, brightness decreases faster than device current, especially under lower bias voltages. It is related to the degradation of emissive material and exciton quenching near the ionic species in the continuously extended doped layers. Under a higher bias voltage, material degradation dominates due to a higher device current and thus decreasing brightness matches well with decreasing device current. When the bias voltage is reduced, material degradation is mitigated and exciton quenching near doped layers affects brightness reduction more significantly. It is the reason why brightness is decreasing while device current is relatively constant.

After a bias is applied, the rapid increase in EQE results from improved carrier balance due to the formation of the doped layers. After reaching the peak value, the EQE gradually decreases because of the same reasons responsible for the decrease in brightness with time. The peak EQEs of all LECs improves with increasing emissive-layer thickness (see *Table 4.6*). A thicker emissive layer ensures sufficient space between emission zone and doped layers, rendering reduced exciton quenching and improved device efficiency.[53] The LECs based on complexes containing **dm-2-piq** ligand exhibit better EQEs than the LECs based on complexes containing **1-piq** ligands. These results are consistent with higher PLQYs of the thin films of complexes containing **dm-2-piq** ligand blended with 20 wt.% BMIM[PF_6] (*Table 4.3*). It can be attributed to the photophysical data revealing a larger degree of ^{3}MLCT character for the excited state of complexes bearing the **dm-2-piq** ligands. The optimized LECs based on complex **6** and **7** show peak EQE as high as 1.73 and 2.05%, respectively. Notably, such device efficiencies are among the highest reported values for the LECs based on multiple-nuclear metal complexes in the literature.[55] To further increase the device efficiency of LECs, the host-guest strategy has been shown to be effective since the self-quenching effect of the emissive molecules can be reduced.[54] In this work, relatively more efficient complexes **6**, and **7** were chosen as guest complexes doped in the host complex **B** (see *Figure ES4.25* in the Experimental Section) to fabricate host-guest LECs. The higher energy gap complex **B**, known to display blue emission, exhibits superior carrier balance and thus it is suitable for serving as the host complex.[55] Constant-current mode was employed to optimize the device efficiency of LEC based on complex **B**.[56] The measured

EL properties of the host-guest LECs based on complex **B** doped with complex **6** and **7** (5 wt.%) are summarized in *Table 4.7* and the EL spectra of the host-guest LECs doped with **6** and **7** are shown in *Figure 4.17a* and *4.17b*, respectively. Compared to the neat-film LECs based on complexes **6** and **7,** the EL spectra of host-guest LECs possessing distinct optical structure and shifted emission zone position are significantly different due to altered microcavity effect. In addition, different EL spectra can be observed when adjusting the constant device current. It indicates that the emission zone position moves when the device current changes. In spite of altered EL spectra, the host-guest LECs still exhibit red EL and the color saturation is better than the EL spectra from neat-film LECs.

Table 4.7 Summary of the device EL characteristics of the host-guest LECs based on emissive layers of host complex **B** doped with guest complex **6** or **7** (5 wt.%).

Guest complex	Current (μA)	EL_{max} (nm)[a]	B_{max} (cd m^{-2})[b]	$\eta_{ext, max}$ (%)[c]	$\eta_{c, max}$ (cd A^{-1})[d]	$\eta_{P, max}$ (lm W^{-1})[e]
6	0.1	648	0.25	4.54	2.48	2.54
	0.15	660	0.46	4.23	3.08	3.15
7	0.1	641	0.80	6.03	8.05	8.09
	0.15	613	1.53	5.92	10.18	10.16

a EL peak wavelength of EL spectrum. b Maximal brightness. c Maximal external quantum efficiency. d Maximal current efficiency. e Maximal power efficiency.

The time-dependent voltages of the host-guest LECs based on the host complex **B** doped with 5 wt.% guest complexes **6** and **7** are shown in *Figure 4.18a* and *4.19a*, respectively. Low operating currents employed in LECs are used to achieve better device efficiency. Under constant-current operation, the time-dependent voltages of both host-guest LECs show a similar decreasing trend. Initially, the electrochemically doped layers are not well formed, and large carrier injection barriers result in higher voltages to reach the required current. During the formation of the electrochemically doped layers, the device voltages decrease rapidly due to significantly reduced carrier injection barriers. Finally, after the electrochemically doped layers are well formed, the device voltages reach steady states (*ca.* 3.1 V).

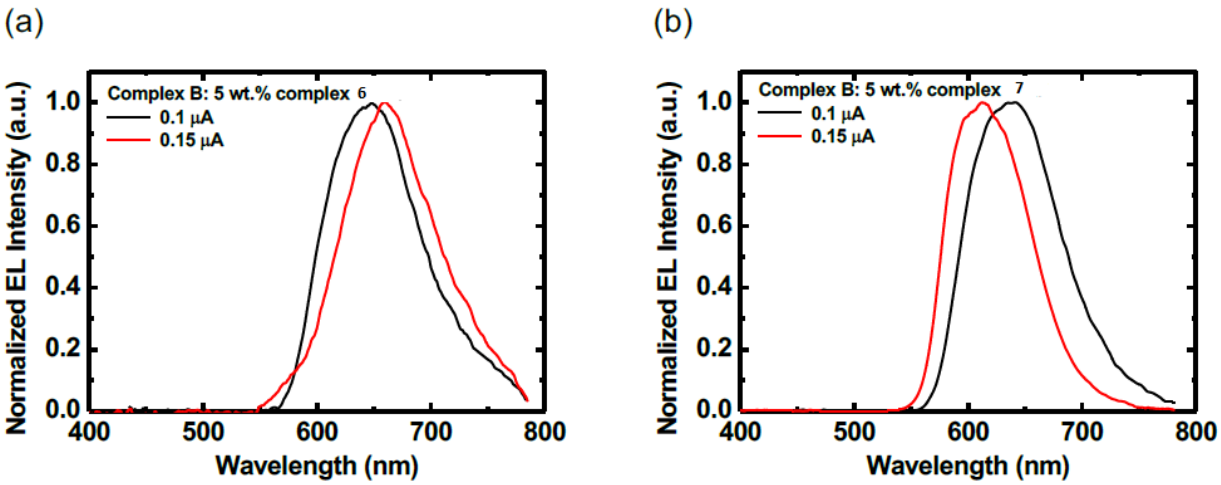

Figure 4.17 EL spectra of the host-guest LECs based on host complex **B** doped with 5 wt.% guest complex (a) **6** and (b) **7** under constant currents of 0.1 (black trace) and 0.15 μA (red trace).

The time-dependent brightness and EQEs of the host-guest LECs based on the host complex **B** doped with 5 wt.% guest complexes **6** and **7** are shown in *Figure 4.18b-c* and *4.19b-c*, respectively. When the growing electrochemically doped layers reduce the carrier injection barriers gradually, the balance of carrier injection improves and thus the brightness rapidly increases with time under a constant device current. After reaching the maximum brightness, the brightness gradually decreases, which is attributed to emissive material degradation and exciton quenching caused by the extending electrochemically doped layers. Since both host-guest LECs are operated in constant currents, the time-dependent EQE follows a similar trend as the brightness. As expected, both host-guest LECs show significantly enhanced EQEs (>2.6-fold) due to reduced exciton quenching of the guest complex and improved carrier balance in the host complex **B**. The optimized host-guest LECs based on the host complex **B** doped with 5 wt.% guest complexes **6** and **7** show the peak EQE of *ca.* 4.5 and 6%, respectively. Such device efficiencies are the highest ever reported for bi and/or multimetallic emitters and amongst the highest for red phosphors, confirming that the proposed heterobimetallic complexes are potential candidates for use in efficient LECs.

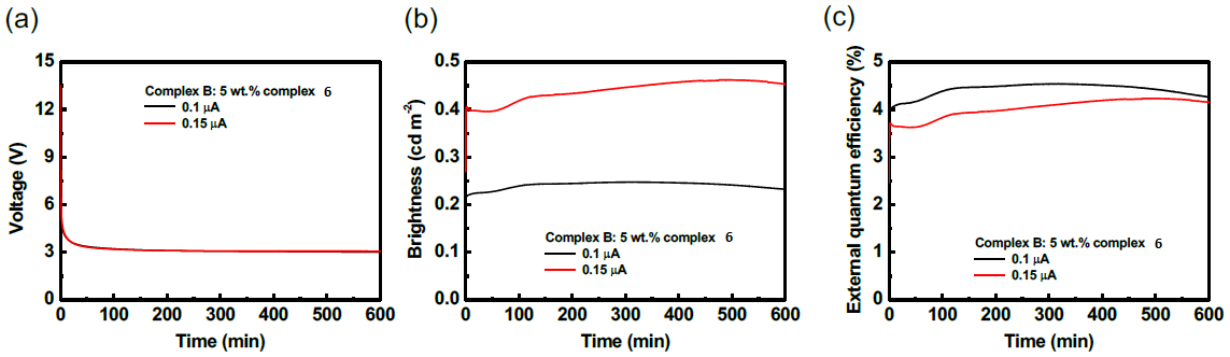

Figure 4.18 Time-dependent (a) current density, (b) brightness, and (c) EQE of the host-guest LECs based on host complex **B** doped with 5 wt.% guest complex **6** under constant current of 0.1 (black trace) and 0.15 μA (red trace).

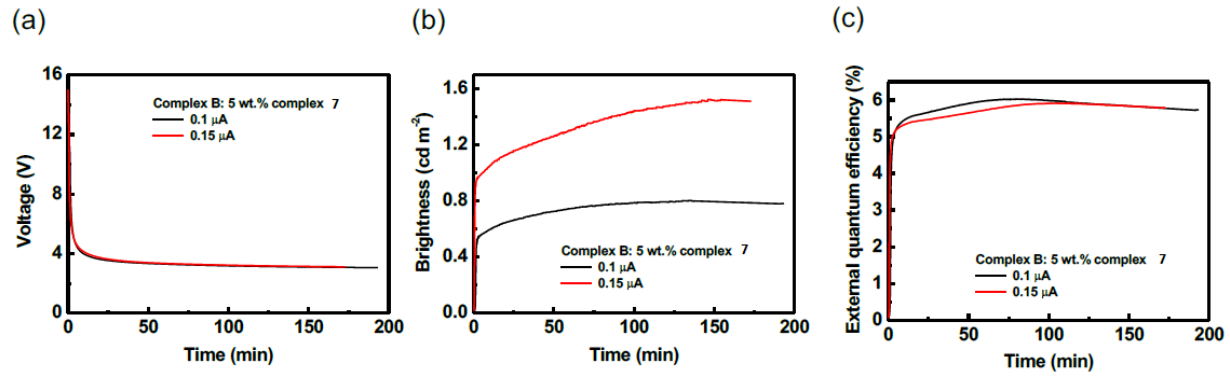

Figure 4.19 Time-dependent (a) current density, (b) brightness, and (c) EQE of the host-guest LECs based on host complex B doped with 5 wt.% guest complex **7** under constant currents (0.1 and 0.15 μA).

4.4 Conclusion

Four novel cationic heterobimetallic Ir^{III}/M^{I} complexes, have been presented. The monometallic $[Ir^{III}(C^N)_2(IMesAcacH)]PF_6$ parental species, where C^N=2-phenyl-pyridine (ppy), 2-phenyl-benzotiazole (2-pbt), and 1-phenylisoquinoline (1-piq), display photoluminescence that is partially quenched by the presence of a close-lying quenching state involving the IMesAcacH ancillary ligand in its pro-carbenic form. Negligible electronic coupling between the two metal centers is observed in the bimetallic species at their electronic ground state when compared to the monometallic parental complexes, yet the

former display reversible electrochemical processes. Nonetheless, the presence of the M^{I} metal ion onto the metalloligand (IPr)M(IMesAcac) sizeably modifies the electronic properties of the "acac" motif, which increases its donating ability. The bimetallic species bearing the 1-piq ligand, **4** and **5,** display bright red photoluminescence arising from a long-lived excited state ^{3}IL/^{1}MLCT involving the "Ir(1-piq)" fragment. the increased ^{1}MLCT character of the emitting state with admixed ^{3}IL/^{1}MLCT nature yields a two-fold increase of the PLQY and *k*r for the bimetallic complexes when compared to the benchmark mononuclear parental complexes. The lesser geometrical distortion of the excited states in **6** and **7,** causes an increase of the luminescence in both solutions and thin films. The remarkable emission properties of these compounds as well as their suitable redox properties prompted their use as efficient electroactive compounds in solution-processed LECs. Notably, devices based on host-guest architectures with improved charge carrier transport properties displayed outstanding performances reaching the highest EQE values for bi-metallic complexes and amongst the highest for red LECs reported to date.

4.5 Experimental section

4.5.1 General considerations

All procedures involving iridium complexes were carried out under an argon atmosphere using standard Schlenk techniques. The ligand 1-phenyl isoquinoline,[47,57] dm-2-pic,[57,58] IMesAcacH,[41] and the chloro-bridged iridium dimers[39] were synthetized accordingly to previously reported methods.

4.5.2 Synthesis

$[Ir(C^N)_2Cl]_2$ (1.0 equiv.) was dissolved in 5 mL of methanol and $AgPF_6$ (2.1 equiv) was added. The solution was stirred for 5 hours under argon atmosphere at room temperature. The silver chloride was filtered off and IMesAcacH ligand (2.0 equiv.) was added to the reaction mixture, which was refluxed overnight. After cooling at room temperature, an aqueous solution of KPF_6 was added and a precipitate was formed. The solid was filtered off and washed carefully with water and diethyl ether.

[Ir(ppy)$_2$(κ^2O,O-IMesAcacH)]PF$_6$ (1). Yield: 44%. ^{1}H NMR (500 MHz, 298 K, d6-acetone) δ: 8.94 (s, 1H), 8.68 (d, J=5.0 Hz, 1H), 8.63 (d, J=5.7 Hz, 1H), 8.20 (d, J=7.6 Hz, 2H), 8.10–8.02 (m, 2H), 7.73 (d, J=7.8 Hz, 1H), 7.67 (d, J=7.8 Hz, 1H), 7.42 (dd, J=17.4, 10.9 Hz, 2H), 7.27 (s, 1H), 7.23 (s, 1H), 7.03 (s, 1H), 6.89 (s, 1H), 6.84 (t, J= 8.1 Hz, 1H), 6.75 (t, J=8.0 Hz, 1H), 6.67 (t, J=7.5 Hz, 1H), 6.56 (t, J=7.5 Hz, 1H), 6.26 (d, J=7.7 Hz, 1H), 6.02 (d, J=8.5 Hz, 1H), 2.39 (d, J=2.6 Hz, 5H), 2.32 (d, J=1.8 Hz, 5H), 2.21 (s, 3H), 1.64 (s, 2H), 1.53 (s, 2H). ^{13}C NMR (125.77 MHz, 298 K, d6-acetone) δ: 185.1, 168.1, 168.0, 155.7, 148.9, 148.2, 145.3, 144.7, 142.0, 141.4, 141.2, 140.96, 138.8, 138.8, 136.5, 135.6, 135.5, 135.4, 135.2, 133.5, 132.9, 131.4, 130.0, 129.97, 129.5, 129.2, 128.9, 128.8, 127.4, 124.1, 124.0, 122.6, 122.5, 121.7, 121.5, 119.2, 113.4, 28.9, 26.5, 20.2, 20.0, 17.1, 16.6, 15.8. HR-ESI-MS: 863.2959 ([M]+), 863.2934 [$C_{45}H_{42}IrN_4O_2$]+; elemental analysis calcd for $C_{45}H_{42}F_6IrN_4O_2P\cdot 2H_2O$: C 51.77, H 4.14, N 5.37; found: C 51.76, H 4.13, N 5.30.

Ir(2-pbt)$_2$(κ^2O,O-IMesAcacH)]PF$_6$ (2). Yield: 62%. ^{1}H NMR (500 MHz, 298 K, d6-acetone) δ: 8.89 (s, 1H), 8.34 (d, J=7.9 Hz, 1H), 8.30 (d, J=8.0 Hz, 1H), 8.03 (d, J=8.2 Hz, 1H), 7.84–7.78 (m, 2H), 7.74 (d, J=7.7 Hz, 2H), 7.69–7.59 (m, 3H), 7.53 (t, J=7.6 Hz, 1H), 7.20 (s, 1H), 7.16 (s, 1H), 7.10 (s, 1H), 6.95 (s, 2H), 6.85 (t, J=7.4 Hz, 1H), 6.72 (t, J=7.4 Hz, 1H), 6.60 (t, J=7.5 Hz, 1H), 6.46 (d, J=7.6 Hz, 1H), 6.23 (d, J=7.7 Hz, 1H), 2.43 (s, 3H), 2.35 (s, 3H), 2.24 (s, 4H), 2.08 (s, 5H), 2.02 (s, 5H), 1.66 (s, 3H), 1.38 (s, 3H). ^{13}C NMR (125.77 MHz, 298 K, d6-acetone) δ: 186.5, 181.2, 181.1, 156.0, 150.3, 150.0, 142.1, 141.7, 141.5, 141.3, 141.2, 141.2, 136.7, 135.7, 135.3, 135.1, 134.7, 134.5, 131.8, 131.5, 131.1, 130.6, 130.4, 129.98, 129.9, 129.7, 129.4, 128.46, 127.7, 127.1, 126.1, 126.0, 123.9, 123.8, 122.4, 122.4, 118.6, 118.5, 113.6, 28.9, 26.3, 20.2, 20.1, 17.1, 16.4, 16.4, 15.5. HR-ESI-MS: 975.2385 ([M]+), 975.2373 [$C_{49}H_{42}IrN_4O_2S_2$]$^+$; elemental analysis calcd for $C_{49}H_{42}F_6IrN_4O_2PS_2\cdot H_2O$: C 51.71 H 3.90 N 4.92; found: C 48.45 H 3.62 N 4.60.

Ir(1-piq)$_2$(κ^2O,O-IMesAcacH)]PF$_6$ (3). Yield: 87%. ^{1}H NMR (500 MHz, 298 K, d6-acetone) δ: 9.17–9.14 (m, 2H), 9.08–9.04 (m, 2H), 8.87 (s, 1H), 8.54 (dd, J=12.5, 6.3 Hz, 2H), 8.37 (d, J=8.0 Hz, 1H), 8.24 (d, J=8.0 Hz, 1H), 8.20 (t, J=7.7 Hz, 2H), 7.94 (t, J=9.3 Hz, 5H), 7.87– 7.81 (m, 3H), 7.26 (s, 1H), 7.19 (s, 1H), 7.01 (s, 1H), 6.97 (d, J= 8.1 Hz, 1H), 6.86 (t, J=8.1 Hz, 1H), 6.73 (s, 1H), 6.70 (t, J=6.9 Hz, 1H), 6.59–6.52 (m, 3H), 6.14 (d, J=6.9 Hz, 1H), 2.36 (d, J=6.8 Hz, 7H), 2.31 (s, 4H), 2.27 (s, 3H), 2.18 (s, 3H), 1.62 (s, 3H), 1.03 (s, 3H). ^{13}C NMR (125.77 MHz, 298 K, d6-acetone) δ: 205.2, 185.3, 168.7, 168.5, 155.8, 146.6, 146.1, 146.0, 145.1, 142.0, 140.97, 140.6, 139.97, 137.8, 137.7, 136.4, 135.4, 135.4, 135.3,

135.3, 134.4, 133.5, 131.8, 131.3, 129.99, 129.8, 129.5, 129.1, 128.9, 128.8, 127.8, 127.7, 127.3, 126.5, 126.4, 126.2, 126.2, 121.5, 121.4, 120.9, 120.8, 113.3, 28.9, 26.5, 20.2, 20.0, 17.1, 16.7, 16.6, 15.3. HR-ESI-MS: 963.3258 ([M]+), 963.3248 $[C_{53}H_{46}IrN_4O_2]^+$; elemental analysis calcd for $C_{53}H_{46}F_6IrN_4O_2P \cdot H_2O$: C 55.92 H 4.11 N 4.86; found: C 56.53 H 4.30 N 4.98.

{[Ir(1-piq)$_2$][Cu(IPr)](μ-1κ^2O,O:2κ^1C-IMesAcac)}PF_6 (4). Yield: 71%. ^{1}H NMR (500 MHz, 298 K, CD_2Cl_2) δ: 8.98 (d, J=8.7 Hz, 1H), 8.88 (d, J=7.9 Hz, 1H), 8.26–8.19 (m, 2H), 8.11 (d, J=6.3 Hz, 2H), 7.97 (t, J=8.9 Hz, 2H), 7.87–7.80 (m, 2H), 7.81–7.74 (m, 2H), 7.54 (t, J= 7.7 Hz, 2H), 7.43 (d, J=6.0 Hz, 2H), 7.20 (d, J=7.6 Hz, 2H), 7.15 (d, J=7.6 Hz, 2H), 7.04 (s, 2H), 6.95 (t, J=7.4 Hz, 1H), 6.88 (t, J=7.4 Hz, 1H), 6.78 (s, 1H), 6.71 (d, J=14.6 Hz, 1H), 6.66 (t, J=7.3 Hz, 3H), 6.56 (t, J=7.3 Hz, 1H), 6.46 (d, J=7.6 Hz, 1H), 6.37 (s, 1H), 6.08 (d, J=7.5 Hz, 1H), 2.28 (s, 7H), 1.71 (d, J=10.7 Hz, 9H), 1.26 (s, 3H), 1.04 (dd, J=6.6, 3.3 Hz, 12H), 0.83 (d, J=6.9 Hz, 6H), 0.72 (d, J=6.9 Hz, 6H).0.48 (s, 3H); 13C NMR (125.77 MHz, 298 K, CD_2Cl_2) δ: 181.4, 176.9, 169.9, 168.8, 168.4, 147.3, 144.8, 139.7, 137.4, 135.1, 134.8, 134.6, 134.3, 134.1, 133.3, 131.3, 130.5, 130.3, 130.2, 129.95, 129.9, 129.7, 129.4, 129.1, 128.8, 128.3, 127.4, 127.2, 126.6, 126.5, 124.2, 124.2, 123.96, 53.4, 30.6, 29.7, 28.6, 28.5, 25.9, 24.2, 23.9, 23.2, 23.1, 21.0, 17.6, 17.0, 16.9, 15.3. HR-ESI-MS: 1413.5345 ([M]+), 1413.5345 $[C_{80}H_{81}CuIrN_6O_2]^+$; elemental analysis calcd for $C_{80}H_{81}CuF_6IrN_6O_2P$: C 61.62 H 5.24 N 5.39; found: C 60.15 H 5.17 N 5.26.

{[Ir(2-pbt)$_2$][Au(IPr)](μ-1κ^2O,O:2κ^1C-IMesAcac)}PF_6 (5). Yield: 49%.^{1}H NMR (500 MHz, 298 K CD_2Cl_2) δ: 9.01–8.97 (m, 1H), 8.88 (d, J=7.8 Hz, 1H), 8.23 (dd, J=11.0, 7.2 Hz, 2H), 8.12 (d, J=6.3 Hz, 2H), 7.97 (t, J=7.5 Hz, 2H), 7.88–7.80 (m, 2H), 7.80–7.74 (m, 2H), 7.53 (t, J=7.7 Hz, 2H), 7.44 (dd, J=6.1, 3.3 Hz, 2H), 7.17 (d, J= 7.5 Hz, 2H), 7.13 (d, J=7.7 Hz, 2H), 7.11 (s, 2H), 6.96 (t, J=7.3 Hz, 1H), 6.88 (t, J=7.3 Hz, 1H), 6.78 (s, 1H), 6.72 (s, 1H), 6.70 (s, 1H), 6.67 (t, J=7.4 Hz, 1H), 6.57 (t, J=7.1 Hz, 1H), 6.47 (d, J=7.4 Hz, 1H), 6.37 (s, 1H), 6.09 (d, J=7.4 Hz, 1H), 2.37 (s, 3H), 2.28 (s, J= 82.2 Hz, 6H), 1.76 (s, J=17.4 Hz, 3H), 1.72 (d, J=3.9 Hz, 6H),1.26 (s, 2H) 1.07 (d, J=5.2 Hz, 13H), 0.88 (d, J=6.9 Hz, 7H), 0.78 (d, J= 6.9 Hz, 6H)., 0.50 (s, 3H). 13C NMR (125.77 MHz, 298 K, CD_2Cl_2) δ: 186.4, 183.96, 181.9, 169.2, 168.8, 158.3, 147.6, 146.9, 146.6, 146.4, 145.4, 145.4, 140.3, 140.1, 139.5, 137.9, 137.7, 135.5, 135.1, 135.1, 134.9, 134.7, 134.6, 133.9, 133.7, 131.8, 131.7, 131.0, 130.5, 130.5, 130.3, 130.2, 129.7, 129.5, 129.2, 128.8, 128.8, 127.8, 127.6, 126.97, 126.9, 126.8, 126.6, 124.4, 124.4, 124.4, 121.7, 121.7, 120.8, 120.4, 114.2, 53.8, 28.9, 26.5, 24.2,

24.1, 23.9, 23.8, 21.6, 21.5, 17.98, 17.4, 17.2, 15.7, 1.2. HR-ESI-MS: 1547.5656 ([M]+), 1547.5724 $[C_{80}H_{81}AuIrN_6O_2]^+$; elemental analysis calcd for $C_{80}H_{81}AuF_6IrN_6O_2P\cdot 3CH_2Cl_2$: C 51.19 H 4.32 N 4.50; found: C 50.77 H 4.35 N 4.50.

{[Ir(dm-2-piq)$_2$][Cu(IPr)](μ-1κ^2O,O:2κ^1C-IMesAcac)}PF_6 (6): Yield: 75%. ^{1}H NMR (500 MHz, 298 K, CD_2Cl_2) δ 8.13 (t, *J* = 9.1 Hz, 1H), 7.99 (dd, *J* = 12.3, 8.9 Hz, 1H), 7.75 (d, *J* = 7.9 Hz, 1H), 7.71 (d, *J* = 6.9 Hz, 1H), 7.56 (s, 1H), 7.54–7.44 (m, 2H), 7.41 (t, *J* = 6.2 Hz, 1H), 7.38 – 7.34 (m, 1H), 7.30 – 7.24 (m, 1H), 7.16–7.10 (m, 2H), 7.08–7.03 (m, 1H), 6.98 (s, 1H), 6.70 (d, *J* = 20.5 Hz, 1H), 6.51 (d, *J* = 12.4 Hz, 1H), 6.44 (s, 1H), 2.40 (s, 1H), 2.31 (s, 2H), 2.25 (s, 1H), 2.20 (td, *J* = 13.7, 6.9 Hz, 2H), 1.19 (s, 2H), 1.05 (s, 1H), 1.00 (d, *J* = 6.6 Hz, 6H), 0.80 (s, 1H), 0.74–0.68 (m, 3H), 0.64 (d, *J* = 6.9 Hz, 2H), 0.08 (s, 1H). ^{13}C NMR (126 MHz, 298 K, CD_2Cl_2) δ 180.7, 178.7, 176.5, 170.0, 169.3, 158.1, 148.7, 148.3, 148.0, 147.5, 147.0, 146.4, 144.7, 139.3, 138.6, 137.7, 135.1, 135.0, 134.6, 134.4, 134.2, 134.1, 131.2, 131.1, 130.9, 130.4, 130.3, 130.2, 129.8, 129.7, 129.6, 129.3, 128.1, 127.8, 126.1, 126.0, 125.5, 124.8, 124.6, 124.2, 124.1, 123.7, 117.7, 117.3, 112.1, 67.8, 28.5, 28.4, 25.6, 25.1, 24.0, 23.8, 23.2, 23.1, 22.3, 21.8, 21.2, 20.9, 20.6, 20.5, 18.6, 17.2, 16.5, 15.5. MS: 1469.59 ($[M+H]^+$), 1469.60 $[C_{84}H_{89}CuIrN_6O_2]^+$; Anal. calcd for $C_{84}H_{89}CuF_6IrN_6O_2P\cdot 2CH_2Cl_2\cdot H_2O$: C 57.28 H 5.31 N 4.66; found: C 56.87 H 5.76 N 5.17.

{[Ir(dm-2-piq)$_2$][Au(IPr)](μ-1κ^2O,O:2κ^1C-IMesAcac)}PF_6 (7): Yield: 80%. ^{1}H NMR (500 MHz, 298 K, CD_2Cl_2) δ 8.17 (dd, *J* = 8.6, 6.0 Hz, 1H), 8.03 (dd, *J* = 15.3, 8.9 Hz, 1H), 7.77 (dd, *J* = 16.4, 7.5 Hz, 1H), 7.60 (s, 1H), 7.58–7.49 (m, 2H), 7.48 – 7.43 (m, 1H), 7.43–7.39 (m, 1H), 7.33–7.27 (m, 1H), 7.15 (d, *J* = 7.8 Hz, 2H), 7.11–7.07 (m, 1H), 6.74 (d, *J* = 10.2 Hz, 1H), 6.55 (d, *J* = 8.2 Hz, 1H), 6.48 (s, 1H), 2.45 (s, 2H), 2.35 (s, 2H), 2.32–2.18 (m, 3H), 1.47 (s, 1H), 1.34–1.20 (m, 5H), 1.06 (dd, *J* = 19.6, 11.1 Hz, 8H), 0.89 (s, 1H), 0.80 (d, *J* = 6.9 Hz, 2H), 0.75 (d, *J* = 6.9 Hz, 3H), 0.12 (s, 1H). ^{13}C NMR (126 MHz, CD_2Cl_2) δ 186.1, 183.0, 181.0, 157.9, 149.5, 148.6, 148.3, 147.6, 147.5, 144.9, 144.9, 139.3, 138.8, 137.8, 135.0, 134.8, 134.6, 134.5, 133.8, 133.4, 131.0, 130.5, 130.3, 129.9, 129.7, 129.6, 129.6, 129.3, 128.2, 127.8, 126.1, 125.6, 124.7, 124.5, 123.9, 117.7, 117.3, 28.4, 25.3, 23.6, 23.4, 23.3, 21.3, 21.0, 18.5, 17.1, 16.5, 15.5, 0.7. MS: 1603.64 ($[M+H]^+$), 1603.63 $[C_{84}H_{89}AuIrN_6O_2]^+$; Anal. calcd for $C_{84}H_{89}AuF_6IrN_6O_2P\cdot H_2O$: C 57.10 H 5.19 N 4.76; found: C 56.87 H 5.17 N 4.70.

Synthesis of the [Gd(IMesAcacH)(NO_3)$_3$] complex. $Gd(NO_3)_3 \cdot 6H_2O$ (1 equiv) was dissolved in 3 mL of methanol, IMesAcacH (1 equiv) was added, then the mixture was stirred for 24 hours at room temperature. The precipitate obtained was recrystallized in CH_2Cl_2 that was collected as a white powder (yield 66%). Elemental analysis calcd for $C_{23}H_{26}GdN_5O_{11}$: C, 39.14 H, 3.71 N, 9.92; found C 38.53 H 4.22 N, 9.08.

Supplementary data

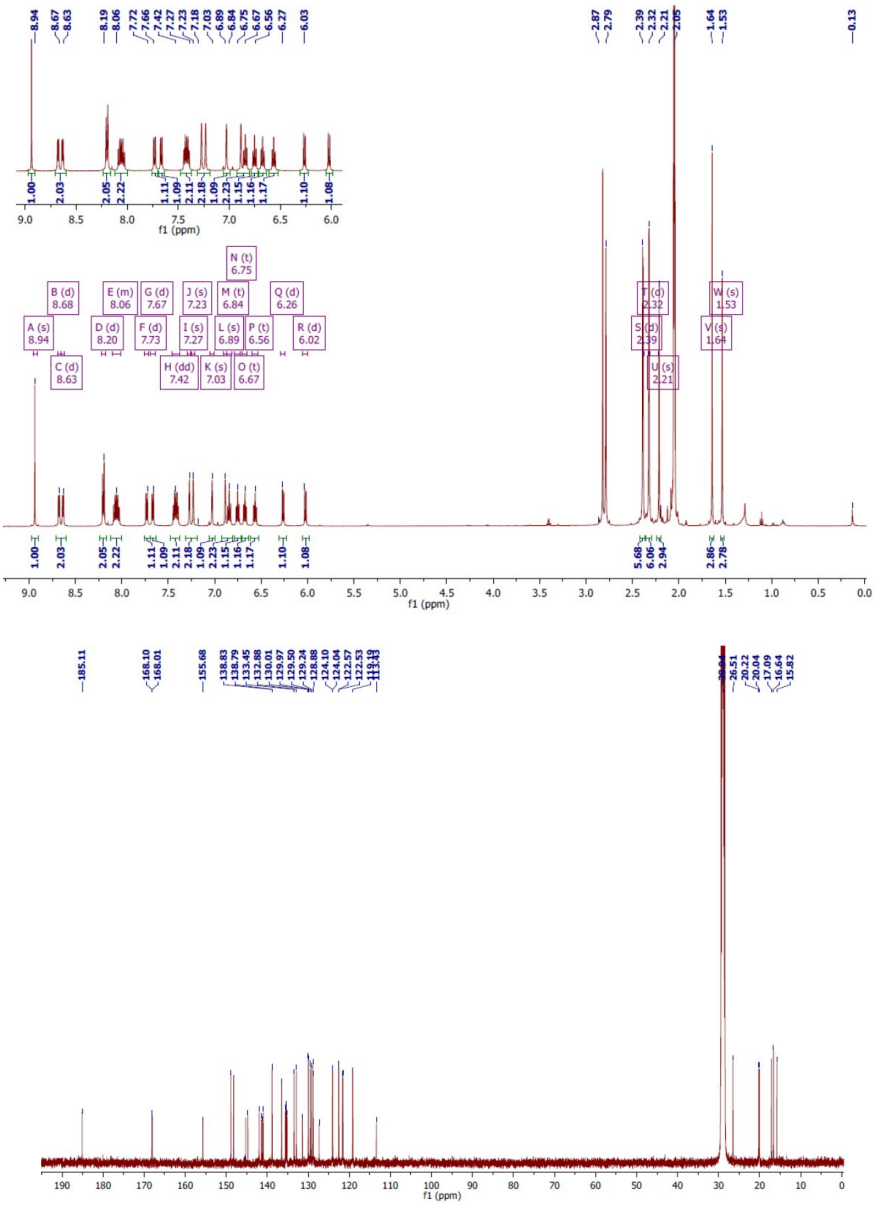

Figure ES4.1 ^{1}H (500 MHz, *top*) and ^{13}C NMR (125 MHz, *bottom*) spectra recorded for complex **1** in acetone-*d*6 at 298 K.

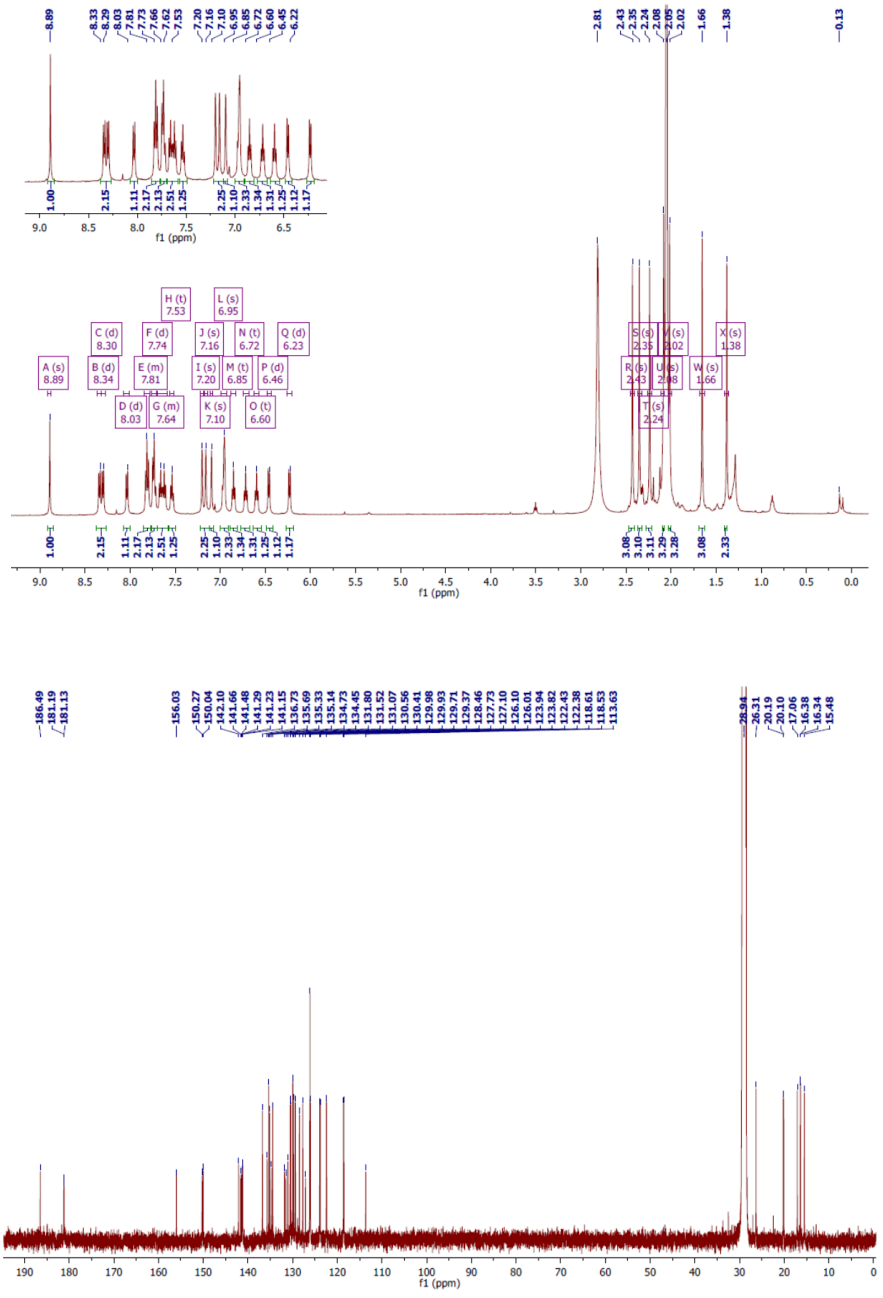

Figure ES4.2 ^{1}H (500 MHz, *top*) and ^{13}C NMR (125 MHz, *bottom*) spectra recorded for complex **2** in acetone-*d*6 at 298 K.

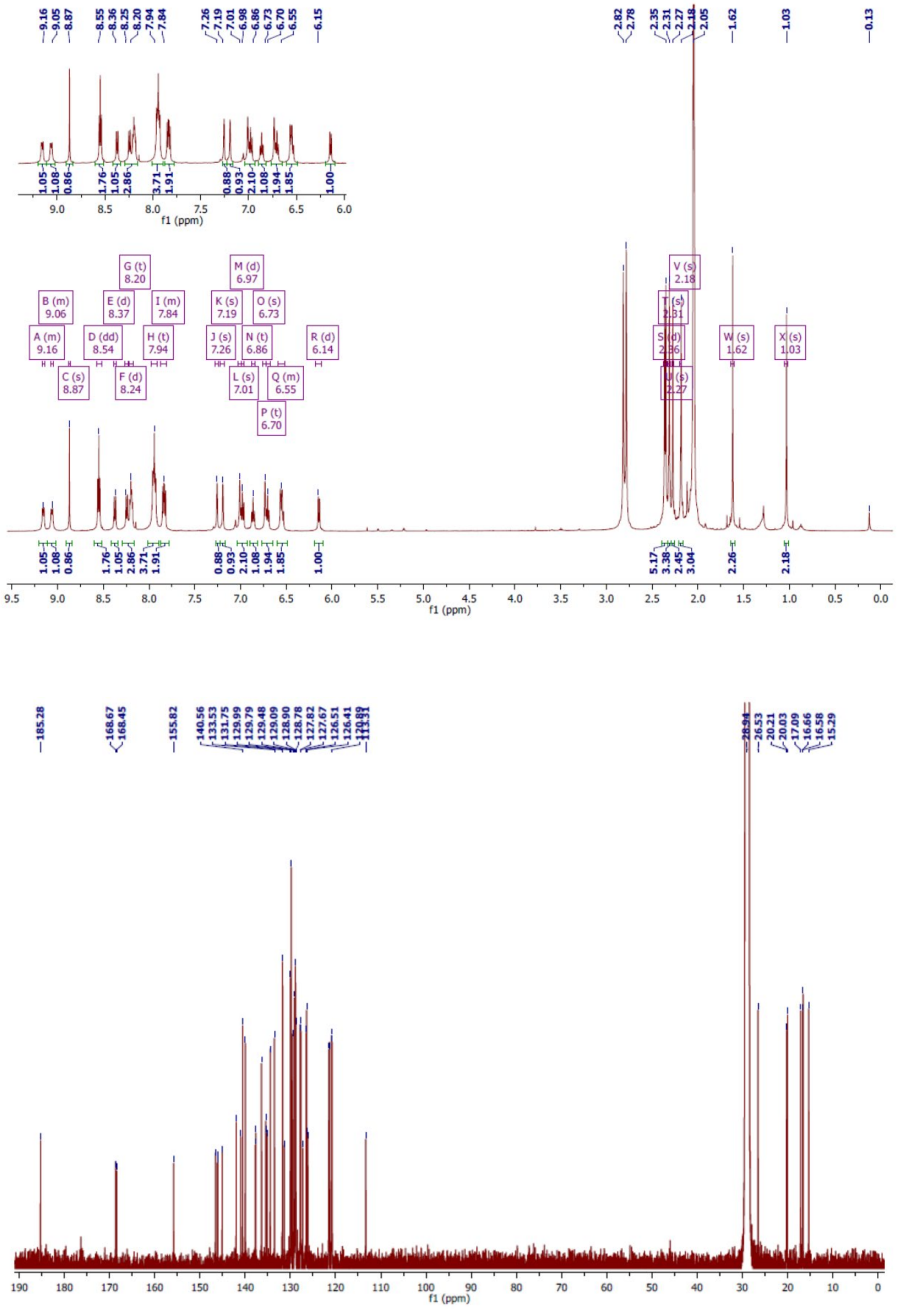

Figure ES4.3 ^{1}H (500 MHz, *top*) and ^{13}C NMR (125 MHz, *bottom*) spectra recorded for complex **3** in acetone-*d*6 at 298 K.

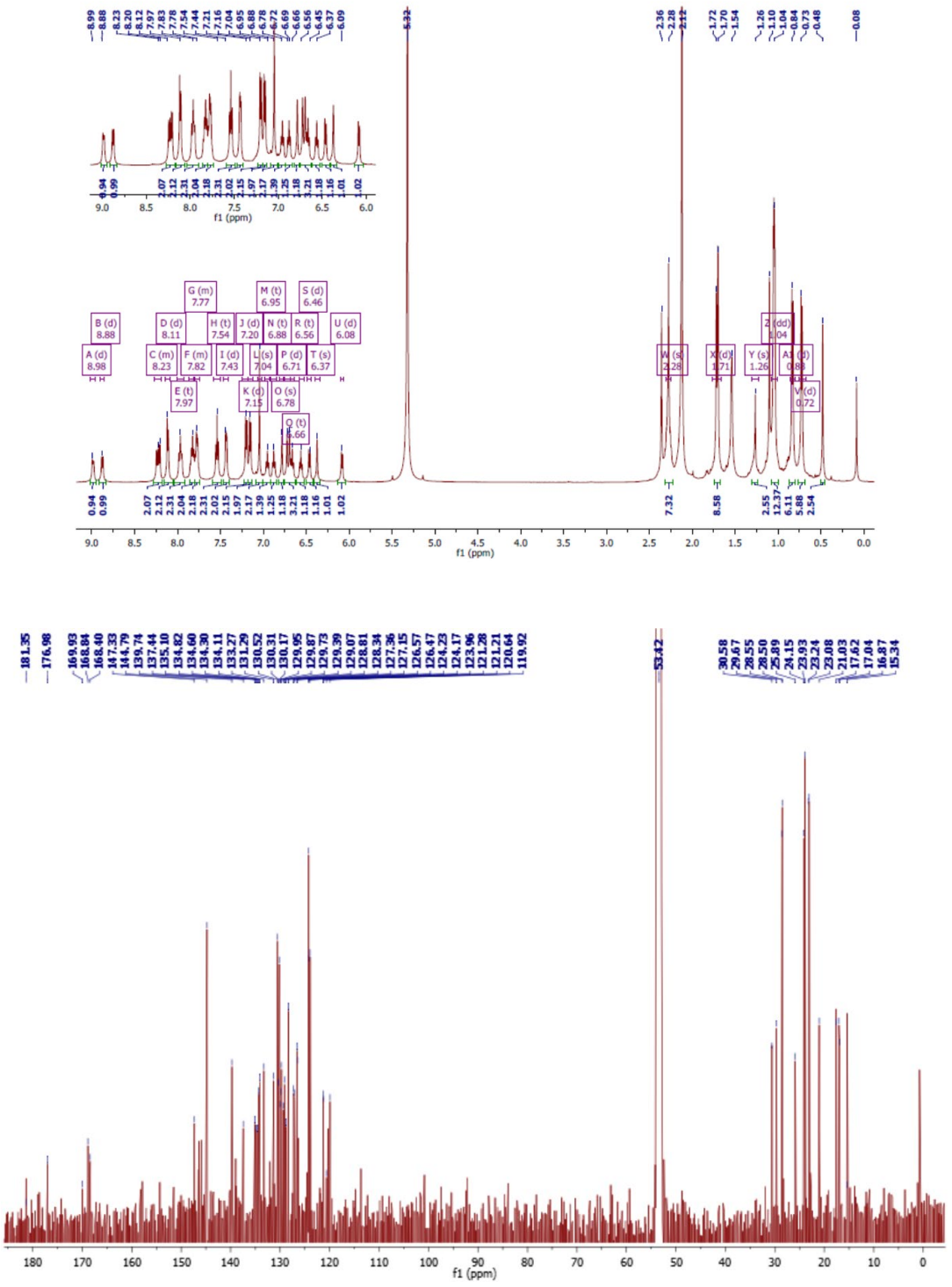

Figure ES4.4 ^{1}H (500 MHz, *top*) and ^{13}C NMR (125 MHz, *bottom*) spectra recorded for complex **4** in CD_2Cl_2 at 298 K.

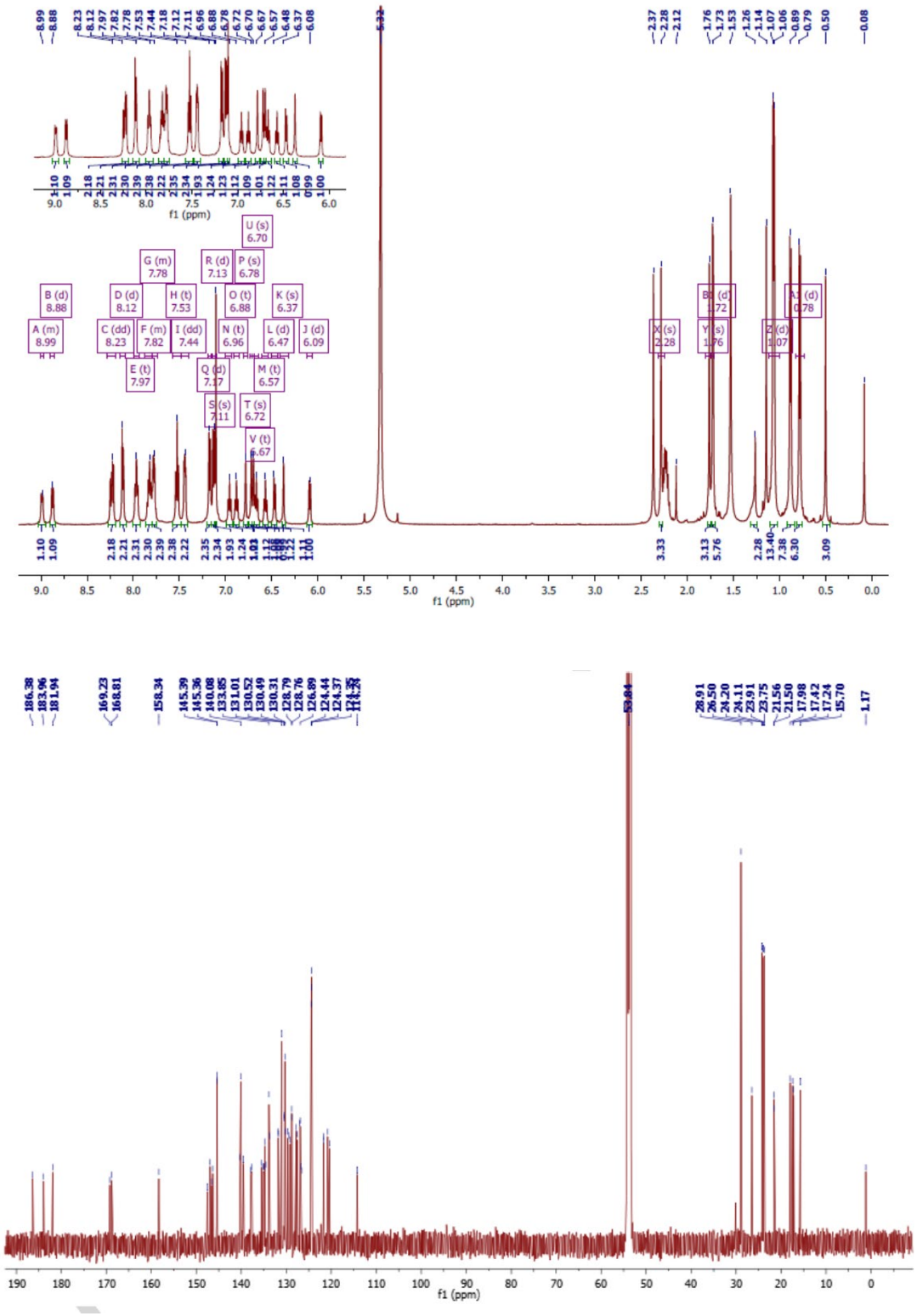

Figure ES4.5 ^{1}H (500 MHz, *top*) and ^{13}C NMR (125 MHz, *bottom*) spectra recorded for complex **5** in CD_2Cl_2 at 298 K.

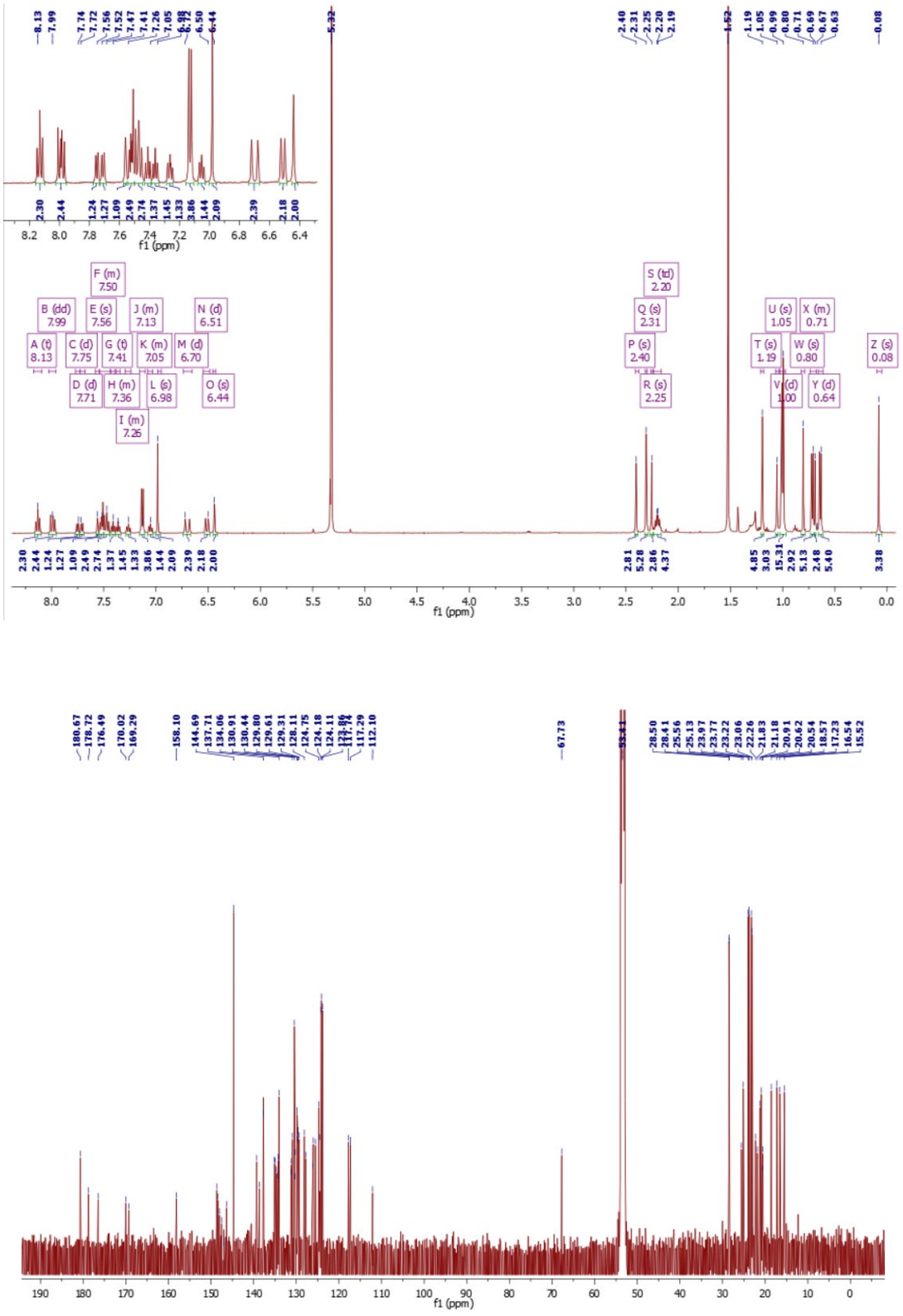

Figure ES4.6. ^{1}H (500 MHz, *top*) and ^{13}C NMR (126 MHz, *bottom*) spectra recorded for complex **6** in CD_2Cl_2 at 298 K.

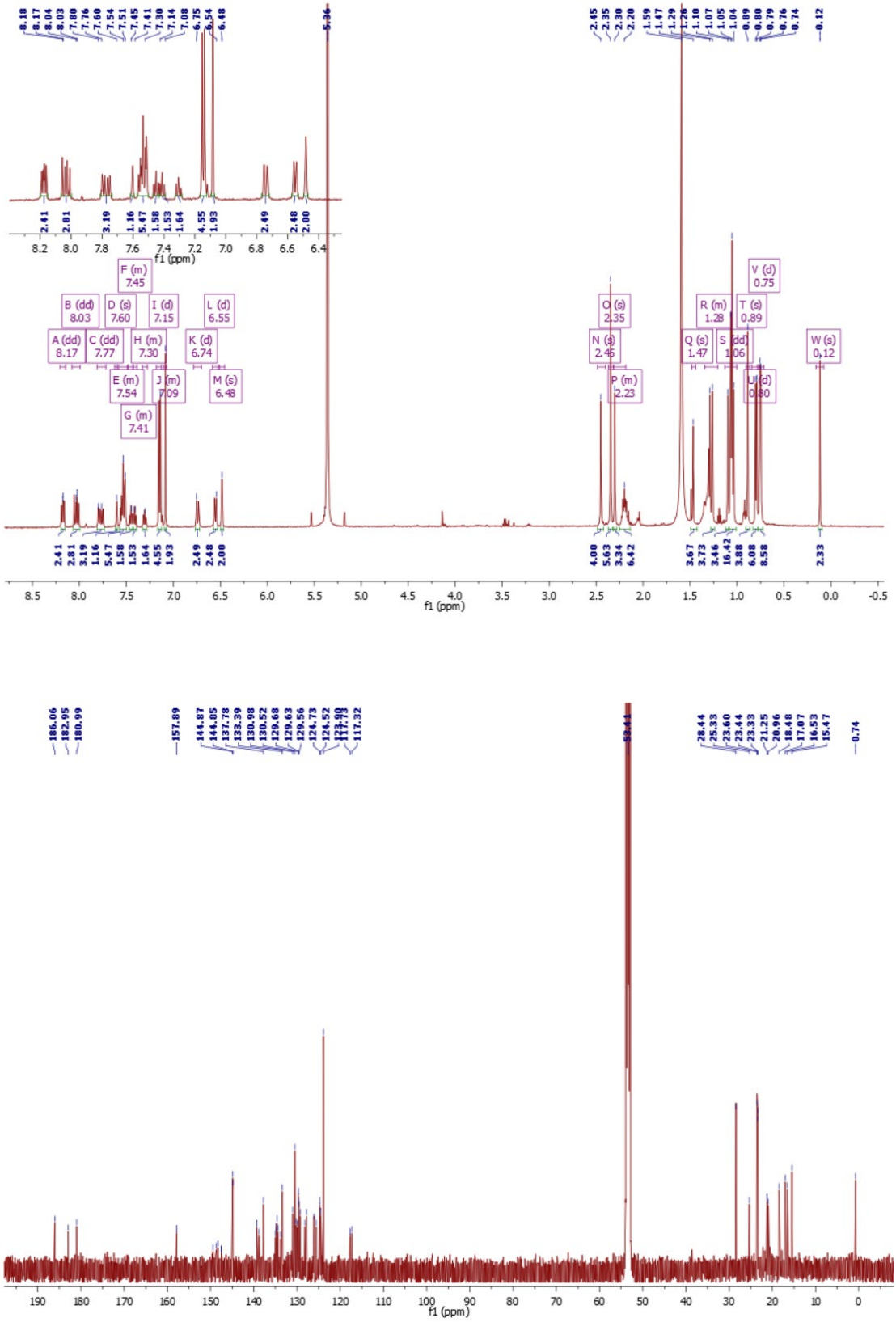

Figure ES4.7. ^{1}H (500 MHz, *top*) and ^{13}C NMR (125 MHz, *bottom*) spectra recorded for complex **7** in CD_2Cl_2 at 298 K.

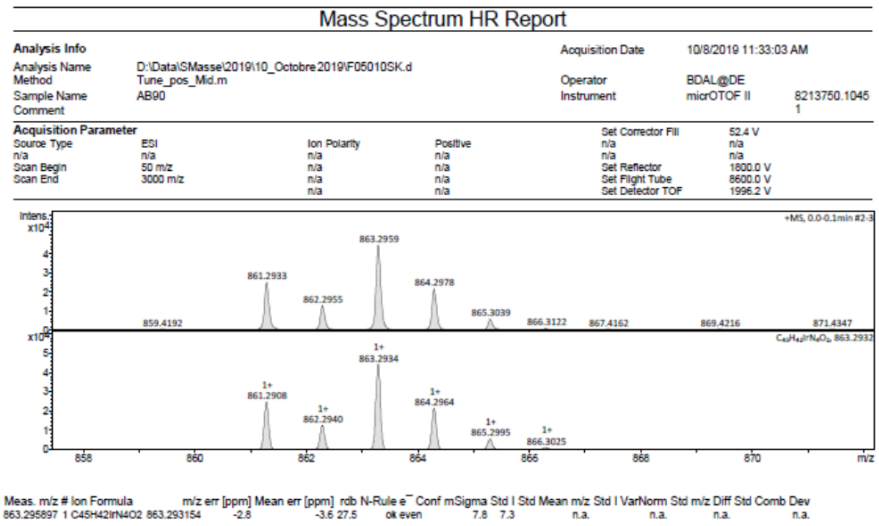

Figure ES4.8. High-resolution ESI-MS spectrum of compound **1**.

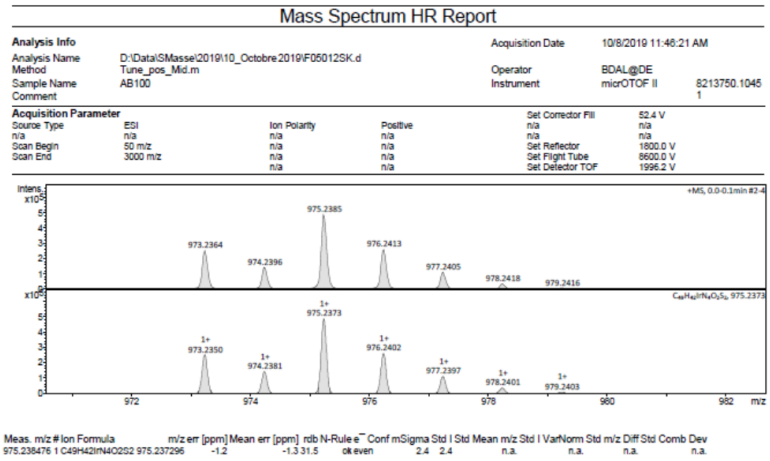

Figure ES4.9. High-resolution ESI-MS spectrum of compound **2**.

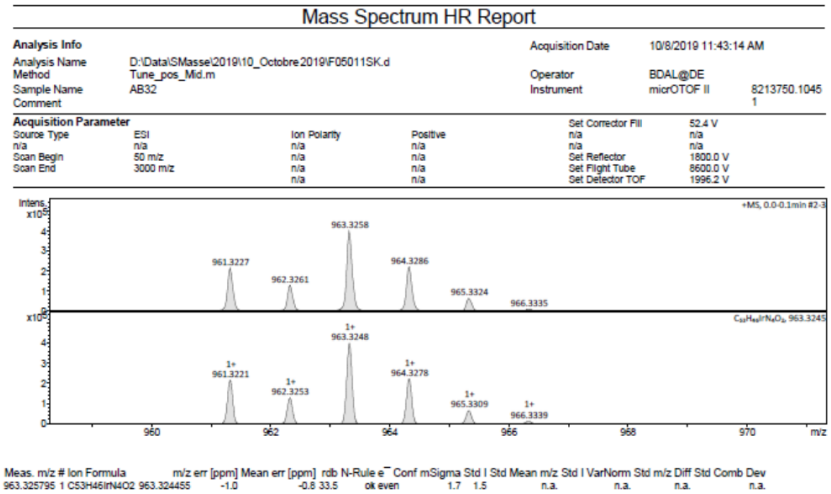

Figure ES4.10. High-resolution ESI-MS spectrum of compound **3**.

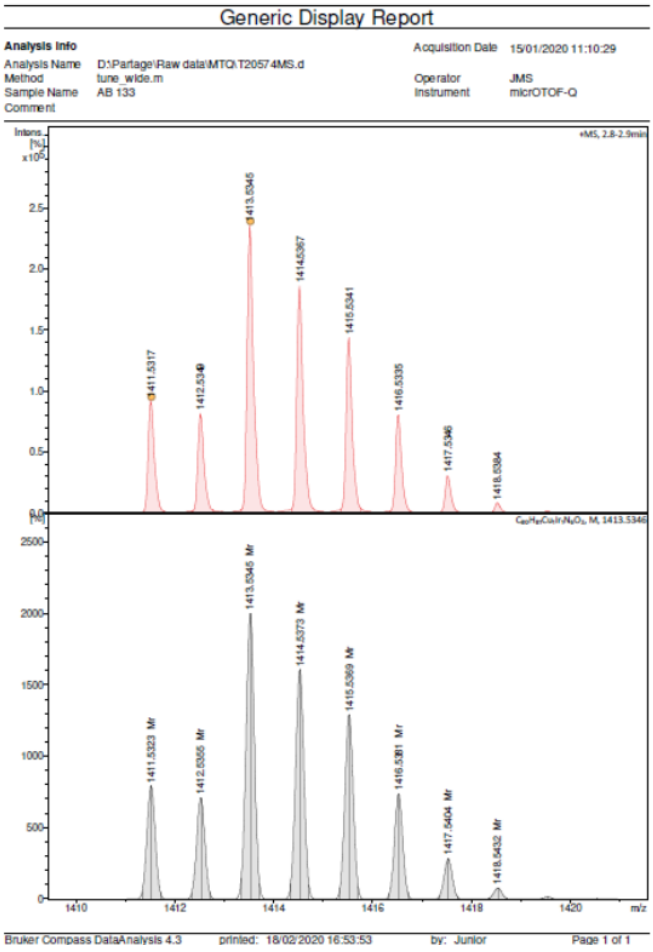

Figure ES4.11. High-resolution ESI-MS spectrum of compound **4**.

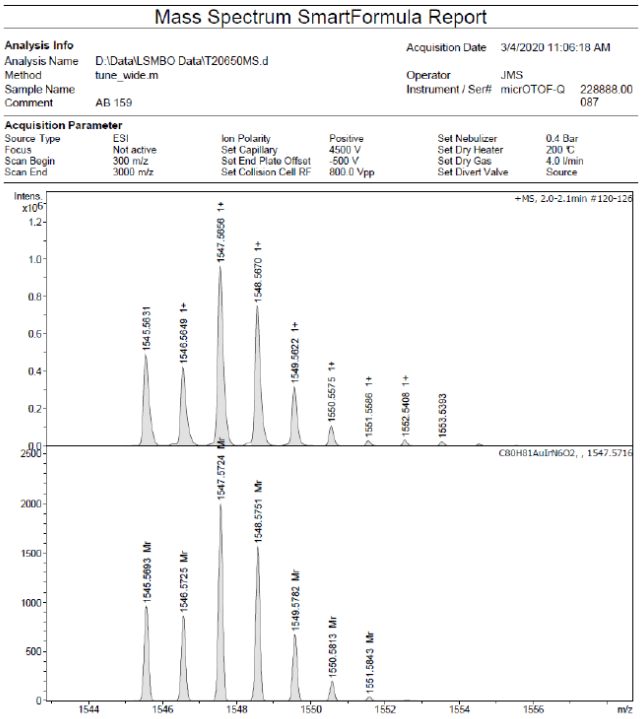

Figure ES4.12. High-resolution ESI-MS spectrum of compound **5**.

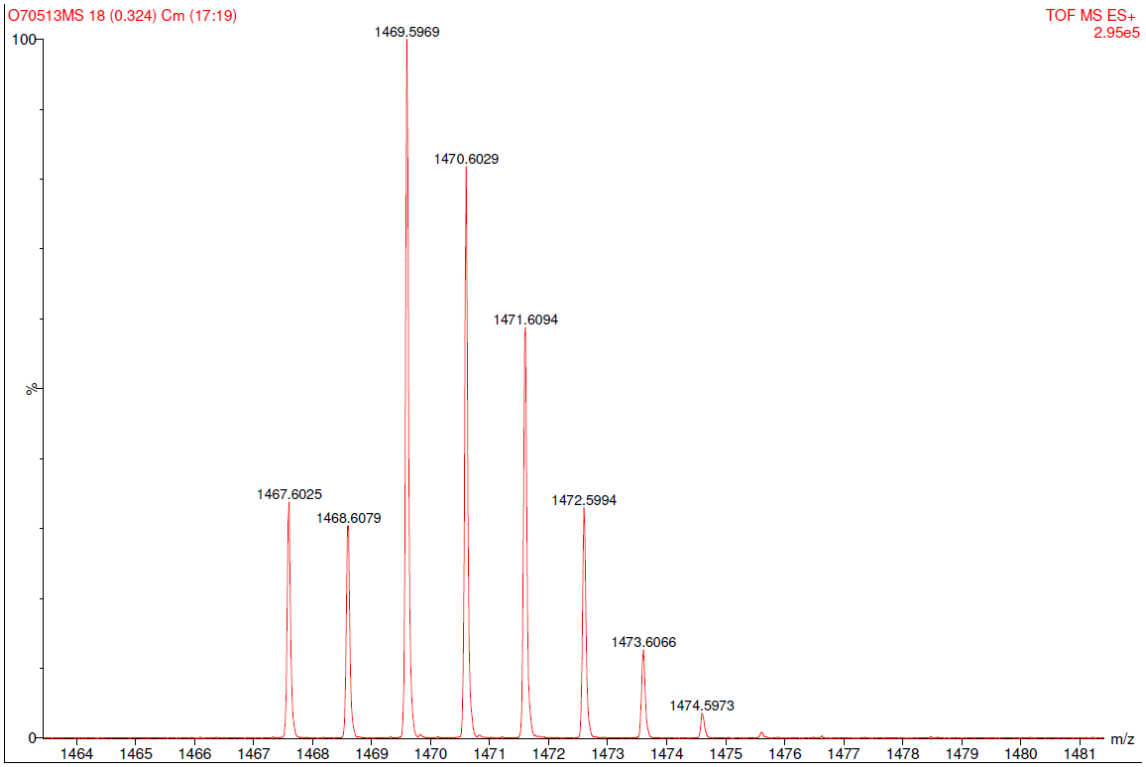

Figure ES4.13 High-resolution HR-ESI-MS spectrum of compound **6.**

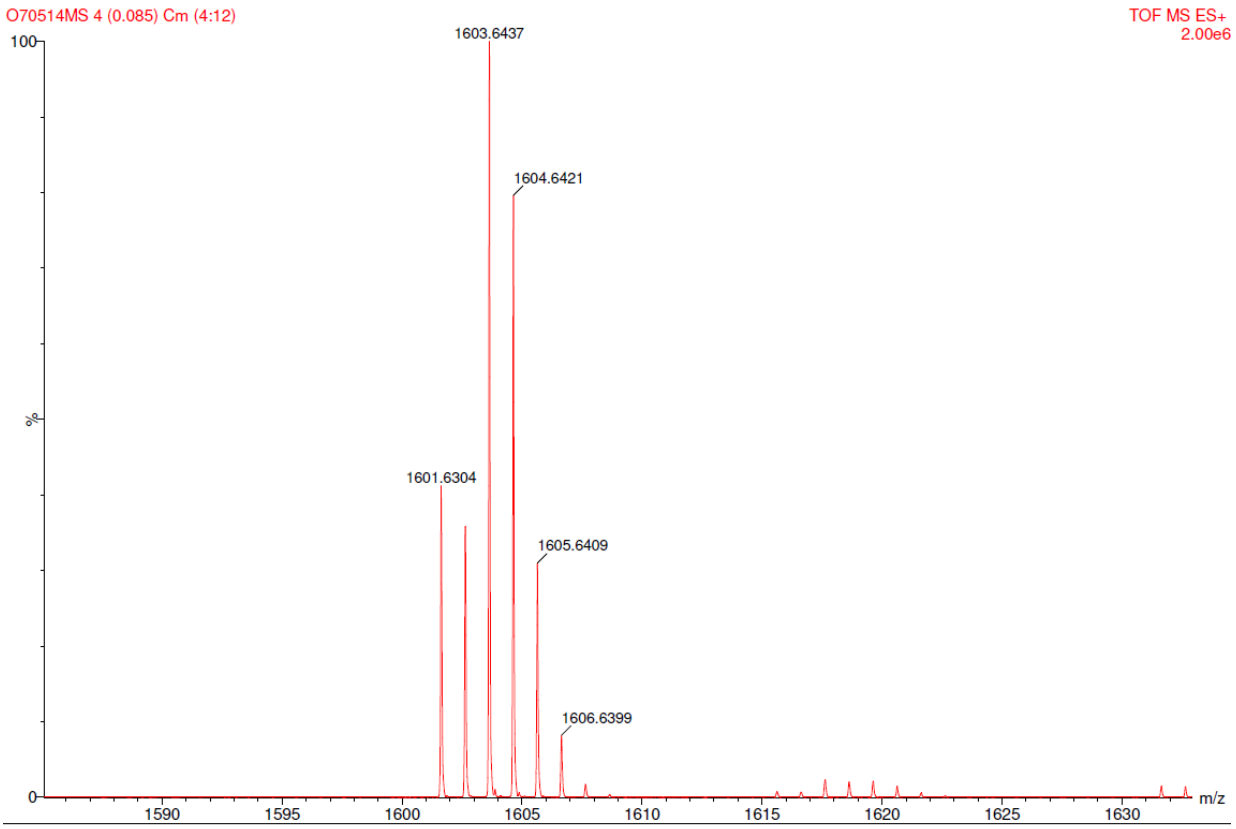

Figure ES4.14 High-resolution HR-ESI-MS spectrum of compound **7**.

4.5.3 Stability test

0.137 mL of TBACl (5 mg, 0.018 mmol, 0.036 M) in acetone-d6 was added to compound **1** (5 mg, $4.96X10^{-3}$ mmol) in 0.5 mL of acetone-d6. The resulting solution was recorded at 300 MHz at different times (see Figure 4.3)

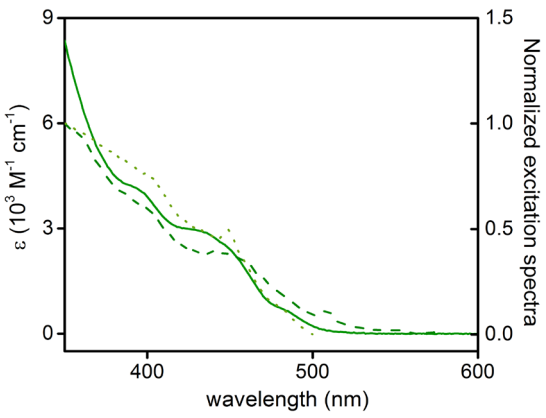

Figure ES4.15 UV-Vis (solid traces) and excitation spectra for **1** recorded at λ_{em} = 520 nm (dotted trace) and 600 nm (dashed trace) in acetone at concentration of 3.0×10^{-5} M in degassed condition.

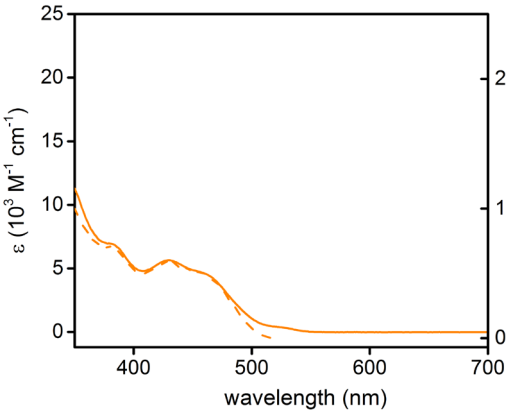

Figure ES4.16. UV-Vis (solid trace) and excitation spectrum (dashed trace) for **2** recorded at λ_{em} = 540 nm in acetone at concentration of 3.0×10^{-5} M in degassed condition.

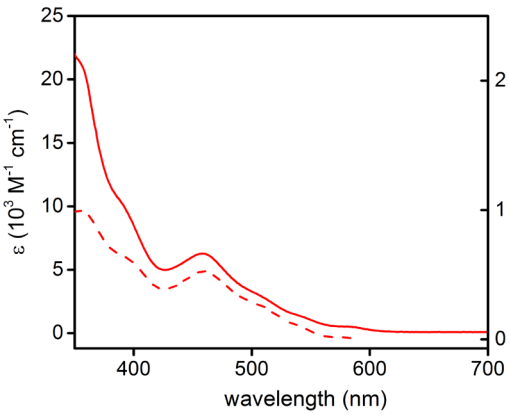

Figure ES4.17. UV-Vis (solid trace) and excitation spectrum (dashed trace) for **3** recorded at λ_{em} = 610 nm in acetone at concentration of 3.0×10^{-5} M in degassed condition.

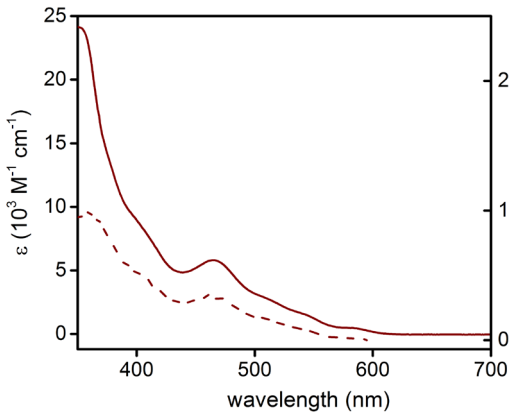

Figure ES4.18. UV-Vis (solid trace) and excitation spectrum (dashed trace) for **4** recorded at λ_{em} = 615 nm in acetone at concentration of 3.0×10^{-5} M in degassed condition.

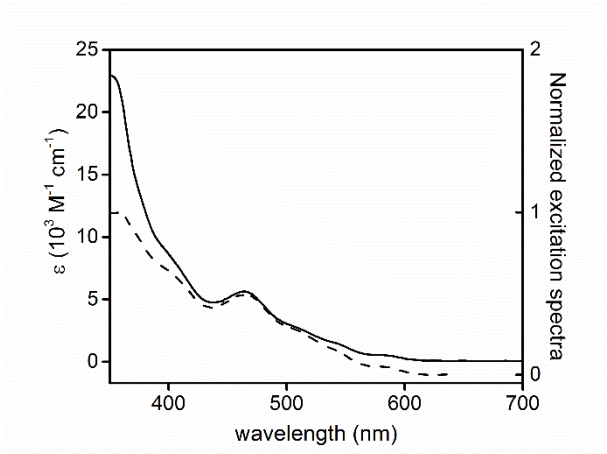

Figure ES4.19. UV-Vis (solid trace) and excitation spectrum (dashed trace) for **5** recorded at λ_{em} = 615 nm in acetone at concentration of 3.0×10^{-5} M in degassed condition.

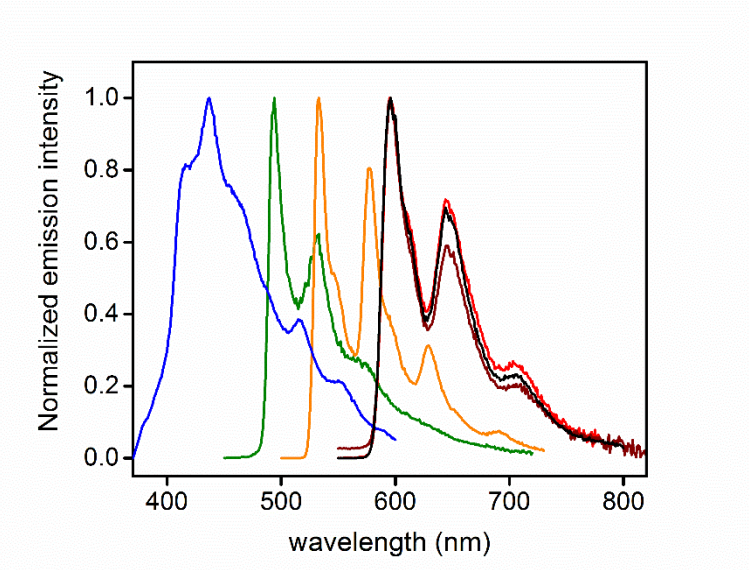

Figure ES4.20. Emission spectrum of the complex GdIII-IMesAcac (blue trace) in in 2Me-THF glassy matrix at 77 K upon excitation at λexc = 350 nm. Comparison is also made with compounds **1** (green trace), **2** (orange trace), **3** (red trace) and **4** (dark red trace) and **5** (black trace) in 2Me-THF glassy matrix at 77 K. Samples were excited at λexc = 400, for **1**–**2**, 420, 450 and 460 nm, for **3**, **4** and **5**, respectively.

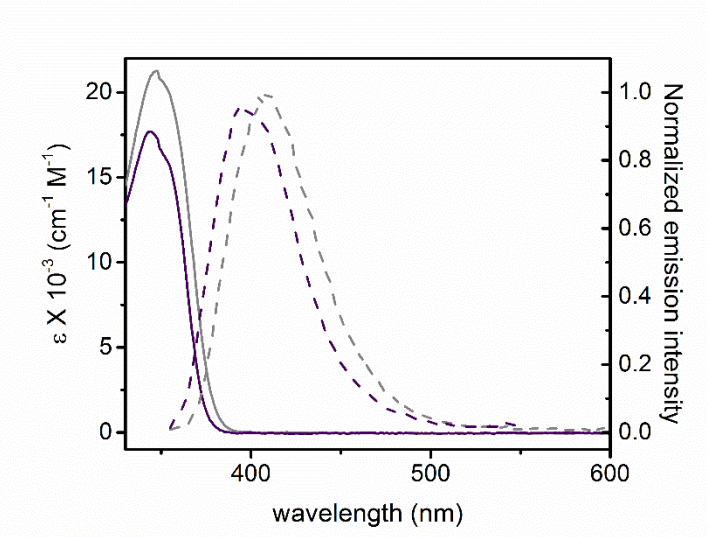

Figure ES4.21. Electronic absorption (solid traces) and emission spectra (dashed traces) for the parental complexes **[(IPr)CuI(IMesAcac)]** (violet traces) **and [(IPr)AuI(IMesAcac)]** (gray traces) in acetone at concentration of 3.0×10-5 M in degassed condition. Samples

were excited at λexc = 340 nm for **[(IPr)CuI(IMesAcac)]** and λexc = 335 nm for **[(IPr)AuI(IMesAcac)]**

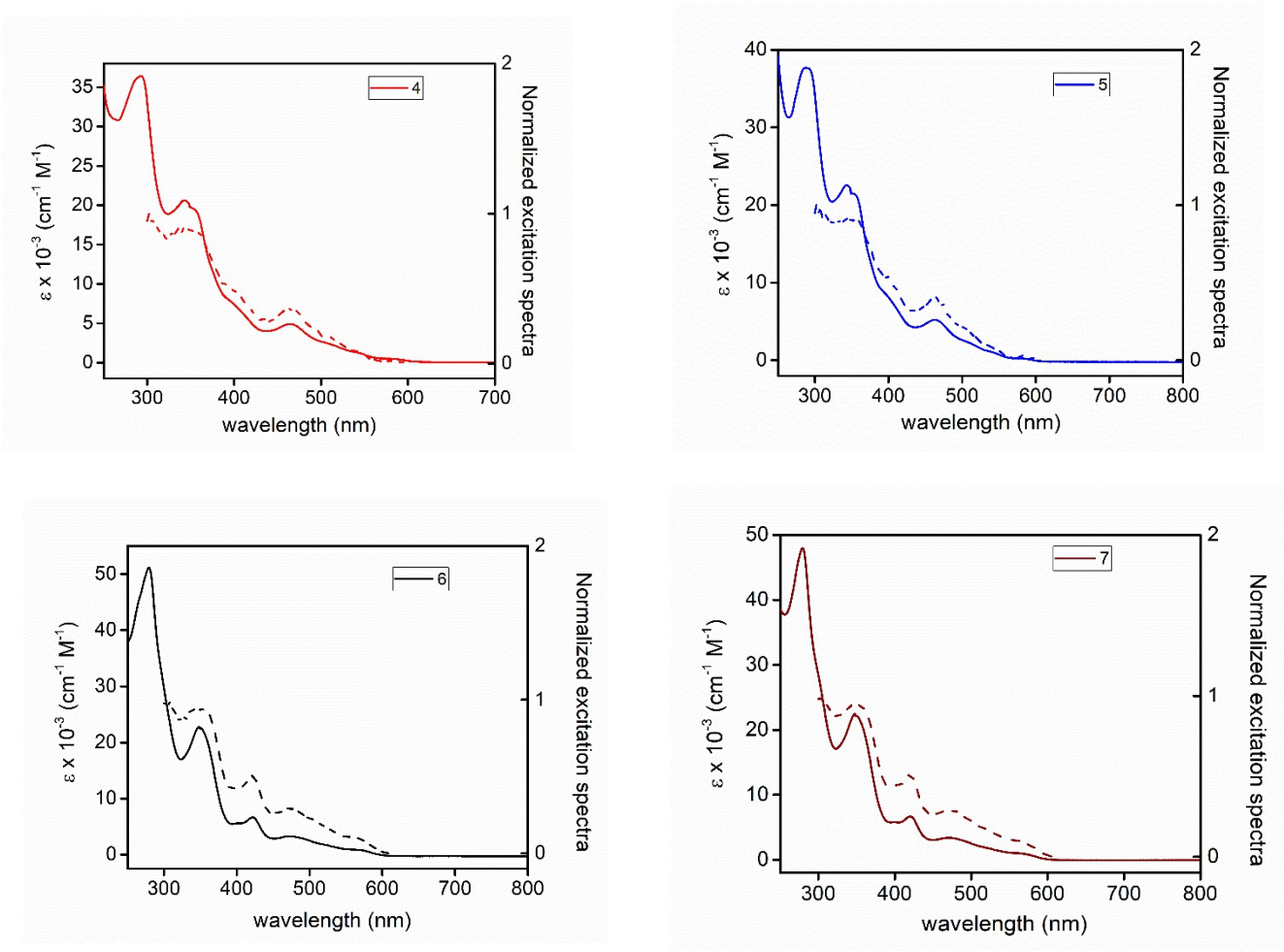

Figure ES4.22. UV-Vis (solid traces) and excitation spectra (dashed trace) recorded at λ_{em} = 610 nm for **4** (red trace) and **5** (blue trace), respectively, and λ_{em} = 630 nm for for **6** (black trace) and **7** (dark red trace), respectively. Spectra were recorded in dichloromethane at concentration of 3.0×10^{-5} M in degassed condition.

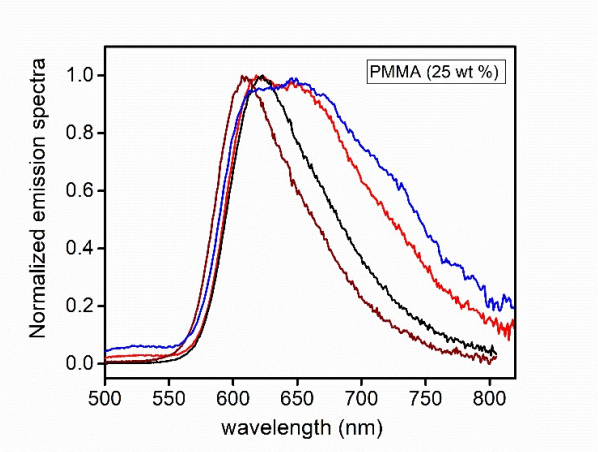

Figure ES4.23 Emission spectra of spin-coated thin film at 25 wt % doping level in PMMA for samples of **4** (red trace), **5** (blue trace), **6** (black trace) and **7** (dark red trace) upon λ_{exc} = 450 nm.

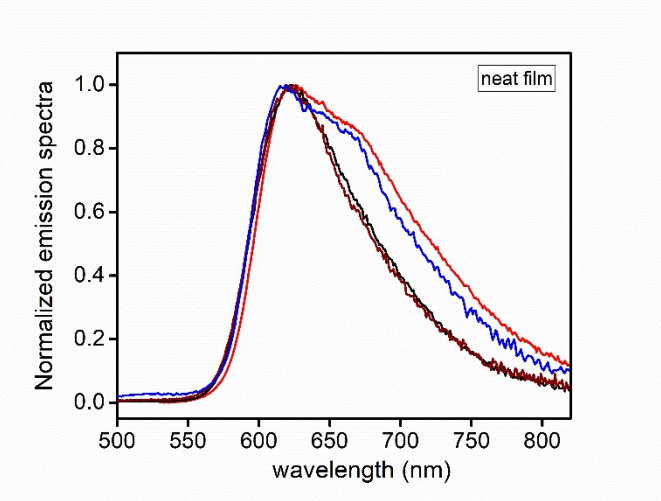

Figure ES4.24 Emission spectra of spin-coated neat thin films for samples of **4** (red trace), **5** (blue trace), **6** (black trace) and **7** (dark red trace) upon λ_{exc} = 450 nm.

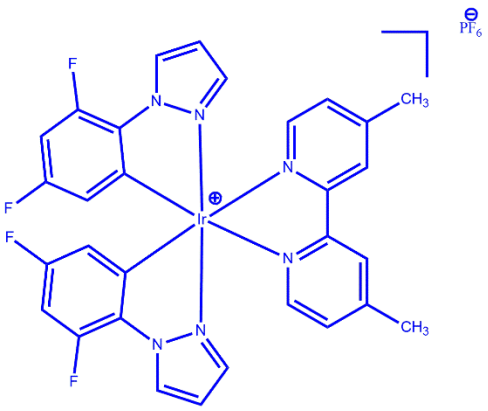

Figure ES4.25 Chemical structure of complex **B.**

Table ES4.1 Crystal data and structure refinement for compound **2.**

Identification code CCDC 1983127

Empirical formula C52 H48 F6 Ir N4 O3 P S2

Formula weight 1178.23

Temperature 120(2) K

Wavelength 0.71073 Å

Crystal system, space group Trigonal, R -3 :H

Unit cell dimensions:

a = 24.8875(8) Å α = 90 deg.

b = 24.8875(8) Å β = 90 deg.

c = 49.001(3) Å γ = 120 deg.

Volume 26284(2) $Å^3$

Z, Calculated density 18, 1.340 Mg/m^3

Absorption coefficient 2.444 mm^{-1}

F(000) 10620

Crystal size 0.200×0.160×0.120 mm

θ range for data collection 1.912 to 30.016 deg.

Limiting indices -34<=h<=35, -35<=k<=34, -68<=l<=68

Reflections collected / unique 142570 / 17078 [R(int) = 0.0347]

Completeness to θ = 25.242 99.9 %

Absorption correction Semi-empirical from equivalents

Max. and min. transmission 0.7460 and 0.6200

Refinement method Full-matrix least-squares on F^2

Data / restraints / parameters 17078 / 2 / 647

Goodness-of-fit on F^2 1.041

Final R indices [I > 2σ(I)] R1 = 0.0337, wR2 = 0.0926

R indices (all data) R1 = 0.0415, wR2 = 0.0978

Extinction coefficient n/a

Largest diff. peak and hole 1.965 and -1.154 e $Å^{-3}$

Table ES4.2 Crystal data and structure refinement parameters for **4**.

Identification code mmab210209

Empirical formula C80 H81 Cu F6 Ir N6 O2 P

Formula weight 1559.21 g/mol

Temperature 120(2) K

Wavelength 0.71073 Å

Crystal system, space group triclinic, P -1

Unit cell dimensions:

a = 16.086(3) Å α = 73.990(4)°

b = 22.446(4) Å β = 74.532(4)°

c = 24.507(4) Å γ = 82.235(5)°

Volume 8179.(2) Å3

Z, Calculated density 4, 1.266 g/cm^3

Absorption coefficient 1.964 mm^{-1}

F(000) 3176

Crystal size 0.100×0.120×13.000 mm

Theta range for data collection 1.86 to 28.19°

Index ranges -21<=h<=21, -29<=k<=29, -32<=l<=32

Reflections collected 544155

Independent reflections 39582 [R(int) = 0.2731]

Max. and min. transmission 0.8280 and 0.0150

Structure solution technique direct methods

Structure solution program SHELXT 2014/5 (Sheldrick, 2014)

Refinement method Full-matrix least-squares on F^2

Refinement program SHELXL-2018/3 (Sheldrick, 2018)

Function minimized Σ w(Fo2 - Fc2)2

Data / restraints / parameters 39582 / 44 / 1622

Goodness-of-fit on F^2 1.410

Δ/σmax 5.572

Final R indices 24030 data; I>2σ(I) R1 = 0.1393, wR2 = 0.3504

all data R1 = 0.2078, wR2 = 0.4061

Weighting scheme w = 1/[σ2(Fo2)+(0.2000P)2]

where P = (Fo2+2Fc2)/3

Largest diff. peak and hole 5.818 and -3.175 $eÅ^{-3}$

R.M.S. deviation from mean 0.277 $eÅ^{-3}$

Table ES4.3 Crystal data and structure refinement parameters for **7**.

Identification code mmab210204

Empirical formula C84 H89 Au F6 Ir N6 O2 P

Formula weight 1748.74 g/mol

Temperature 173(2) K

Wavelength 0.71073 Å

Crystal system, space group monoclinic, P 1 21/n 1

Unit cell dimensions:

a = 11.7615(4) Å α = 90°

b = 48.5624(19) Å β = 94.218(2) °

c = 29.5972(11) Å γ = 90 °

Volume 16859.1(11) $Å^3$

Z, Calculated density 8, 1.378 g/cm^3

Absorption coefficient 3.394 mm^{-1}

F(000) 7008

Theta range for data collection 1.93 to 27.95°

Index ranges -15<=h<=15, -56<=k<=64, -38<=l<=38

Reflections collected 183935

Independent reflections 39979 [R(int) = 0.1269]

Structure solution technique direct methods

Structure solution program SHELXT 2014/5 (Sheldrick, 2014)

Refinement method Full-matrix least-squares on F^2

Refinement program SHELXL-2018/3 (Sheldrick, 2018)

Function minimized Σ w(Fo2 - Fc2)2

Data / restraints / parameters 39979 / 89 / 1788

Goodness-of-fit on F^2 0.993

Δ/σmax 9.770

Final R indices 18521 data; I>2σ(I) R1 = 0.0762, wR2 = 0.1796

all data R1 = 0.1768, wR2 = 0.2203

Weighting scheme w=1/[σ2(Fo2)+(0.0987P)2]

where P = (Fo2+2Fc2)/3

Largest diff. peak and hole 1.423 and -1.700 eÅ^{-3}

R.M.S. deviation from mean 0.166 eÅ^{-3}

4.5.4 Computational analysis

The structures of the complexes **1–4** in the electronic ground state have been fully optimized at the DFT/ B3LYP[59] level of theory using essentially double-z basis sets including scalar relativistic effects for all atoms.[60] The use of triple-z basis sets does not modify drastically the results obtained for the smallest system, namely complex 1 (systematic ~10 nm red-shift of the singlet transitions). This justifies the use of double-z basis sets for the large systems,

which could not be handled otherwise. The calculations have been performed in acetone within the COSMO (conductor-like-screening model) model.[61] The absorption spectra have been computed at the TD-DFT level (80 roots for complexes **1–3** and 60 roots for complex 4) including spin-orbit effects at the perturbation level of theory within the zero-order relativistic approximation (ZORA).[62] The structures of the low-lying triplet excited states Tn (n=1–4) have been optimized at the same level of theory using the Tamm-Dancoff approximation (TDA) in order to avoid triplet instability problems.[63] The calculations have been performed with the ADF 2019 package (ADF, SCM, Theoretical Chemistry, Vrije Universiteit, Amsterdam, The Netherlands https:// www.scm.com/doc/ADF/index.html) and the analysis with Theodore http://theodore-qc.sourceforge.net/.

The structures of **4-7** complexes in the electronic ground state have been fully optimized at the DFT/B3LYP[59] level of theory using double-ζ basis sets including scalar relativistic effects for all atoms.[60] The calculations have been performed in CH_2Cl_2 within the COSMO (conductor-like-screening model) model.[61] The absorption spectra have been computed at the TD-DFT level (50 roots) including spin-orbit effects at the perturbation level of theory within the zero-order relativistic approximation (ZORA). The structures of the lowest T1 triplet states have been optimized at the same level of theory using the Tamm- Dancoff approximation (TDA) in order to avoid triplet instability problems.[62] The calculations have been performed with the ADF 2019 package (ADF, SCM, Theoretical Chemistry, Vrije Universiteit, Amsterdam, The Netherlands https://www.scm.com/doc/ADF/index.html).

4.6 Authors contributions

Lenka Pallova, Quentin Marchand, Vincent César (Université de Toulouse) and Stéphane Bellemin-Laponnaz (Université de Strasbourg) contributed to the synthesis of the IMesAcacH and [(IPr)M^{I}(IMesAcac)]. Federico Polo (University of Venice) and Chantal Daniel and Christophe Gourlaouen (Université de Strasbourg) provided the electrochemical analysis and the computational investigation.
Yun-Xin Wang, Chin-Wei Lu (Providence University) and Pei-Wan Hsiao, Yin Chen, Hai-Ching Su (National Yang Ming Chiao Tung University) are warmly acknowledged for the hard work doing for electrochemiluminescence, devices fabrication and performances.
All the collaborators are kindly acknowledged for their fundamental contribution to the work.

4.7 References

1. [a] *Iridium(III) in optoelectronic and photonics applications (Ed.: E. Zysman-Colman),* **2017**, Wiley, New York; [b] N. Armaroli, H. J. Bolink, *Photoluminescent materials and electroluminescent devices in Topics in Current Chemistry*, Springer, Heidelberg, **2016**; [c] H. Yersin, *Highly Efficient OLEDs with Phosphorescent Materials*, **2008** Wiley-VCH, Weinheim.
2. [a] A. J. Howarth, R. Patia, D. L. Davies, F. Lelj, M. O. Wolf, K. Singh, Eur. J. *Inorg. Chem.* **2014**, 3657; [b] C. Latouche, D. Skouteris, F. Palazzetti, V. Barone, *J. Chem. Theory Comput.* **2015**, *11*, 3281; [c] D. Han, L. Zhao, X. Han, *Photochem. Photobiol. Sci.* **2019**, *18*, 2766; [d] B. J. Powell, *Coord. Chem. Rev.* **2015**, *295*, 46; [e] H. Brahim, C. Daniel, *Comput. Theor. Chem.* **2014**, *219*, 1040; [f] H. Brahim, B. Haddad, M. Boukabene, S. Brahim, B. Ariche, *Comput. Theor. Chem.* **2017**, *8*, 1101; [g] H. Brahim, B. Haddad, S. Brahim, A. Guendouzi, *J. Mol. Model.* **2017**, *23*, 344; [h] D. Hadji, H. Brahim, *Theor. Chem. Acc*. **2018**, 137.
3. [a] G. Denti, S. Campagna, S. Serroni, M. Ciano, V. Balzani, *J. Am. Chem. Soc.* **1992**, *114*, 2944; [b] S. Serroni, A. Juris, S. Campagna, M. Venturi, G. Denti, V. Balzani, *J. Am. Chem. Soc.* **1994**, *116*, 9086; [c] V. Balzani, A. Juris, M. Venturi, S. Campagna, S. Serroni, *Chem. Rev.* **1996**, *96*, 759; [d] L. De Cola, P. Belser, *Coord. Chem. Rev.* **1998**, *177*, 301; [e] S. Welter, N. Salluce, P. Belser, M. Groeneveld, L. De Cola, *Coord. Chem. Rev*. **2005**, *249*, 1360; [f] M. Gagliardo, G. Rodr&guez, H. H. Dam, M. Lutz, A. L. Spek, R. W. A. Havenith, P. Coppo, L. De Cola, F. Hartl, G. P. M. van Klink, G. van Koten, *Inorg. Chem*. **2006**, *45*, 2143; [g] A. Barbieri, B. Ventura, R. Ziessel, *Coord. Chem. Rev.* **2012**, *256*, 1732; [h] K. J. Arma, J. A. G. Williams, *Dalton Trans.* **2006**, 2172; [i] C. Sabatini, A. Barbieri, F. Barigelletti, K. J. Armb, J. A. G. Williams, *Photochem. Photobiol. Sci.* **2007**, *6*, 397.
4. J. H. Van Diemen, R. Hage, J. G. Haasnoot, H. E. B. Lempers, J. Reedijk, J. G. Vos, L. De Cola, F. Barigelletti, V. Balzani, *Inorg. Chem.* **1992**, *31*, 3518.
5. [a] M. Cavazzini, P. Pastorelli, S. Quici, F. Loiseau, S. Campagna, *Chem. Commun.* **2005**, 5266; [b] E. A. Plummer, J. W. Hofstraat, L. De Cola, *Dalton Trans.* **2003**, 2080; [c] F. Lafolet, S. Welter, Z. Popovic, L. De Cola, *J. Mater. Chem.* **2005**, *15*, 2820; [d] V. L. Whittle, J. A. G. Williams, *Inorg. Chem.* **2008**, *47*, 6596; [e] V. L. Whittle, J. A. G. Williams, *Dalton Trans.* **2009**, 3929; [f] A. Auffrant, A. Barbieri, F. Barigelletti, J.-P. Collin, L. Flamigni, C. Sabatini, J.-P. Sauvage, *Inorg. Chem.* **2006**, *45*, 10990.
6. R. D. Costa, G. Fernandez, L. Sanchez, N. Martin, E. Ortì, H. J. Bolink, *Chem. Eur. J.* **2010**, *16*, 9855.
7. F. Neve, A. Crispini, S. Serroni, F. Loiseau, S. Campagna, *Inorg. Chem.* **2001**, *40*, 1093.
8. A.M. Soliman, D. Fortin, P. D. Harvey, E. Zysman-Colman, *Dalton Trans.* **2012**, *41*, 9382.
9. [a] G. Li, D. G. Congrave, D. Zhu, Z. Su, M. R. Bryce, *Polyhedron* **2018**,*140*,146; [b] G. Li, D. Zhu, X. Wang, Z. Su, M. R. Bryce, *Chem. Soc. Rev.* **2020**, *49*, 765.

10. [a] S. Bettington, M. Tavasli, M. R. Bryce, A. S. Batsanov, A. L. Thompson, H. A. Al Attar, F. B. Dias, A. P. Monkman, *J. Mater. Chem.* **2006**, *16*, 1046; [b] A. M'hamedi, A. S. Batsanov, M. A. Fox, M. R. Bryce, K. Abdullah, H. A. Al-Attar, A. P. Monkman, *J. Mater. Chem.* **2012**, *22*, 13529.
11. Y. Zheng, A. S. Batsanov, M. A. Fox, H. A. Al-Attar, K. Abdullah, V. Jankus, M. R. Bryce, A. P. Monkman, *Angew. Chem. Int. Ed*. **2014**, *53*, 11616; *Angew. Chem.* **2014**, *126*, 11800.
12. D. G. Congrave, Y.-T. Hsu, A. S. Batsanov, A. Beeby, M. R. Bryce, *Dalton Trans.* **2018**, *47*, 2086.
13. D. G. Congrave, A. S. Batsanov, M. R. Bryce, *Dalton Trans.* **2018**, *47*,16524.
14. B A.M'hamedi, M. A. Fox, A. S. Batsanov, H. A. Al-Attar, A. P. Monkman, M. R. Bryce, *J. Mater. Chem. C* **2017**, *5*, 6777.
15. Y-B. Gong, P. Zhang, Y-R. Gu, J.-Q. Wang, M.-M. Han, C. Chen, X.-J. Zhan, Z.-L. Xie, B. Zou, Q. Peng, Z.-G. Chi, Z. Li, *Adv. Opt. Mater.* **2018**, *6*, 1800198.
16. [a] R. E. Daniels, S. Culham, M. Hunter, M. C. Durrant, M. R. Probert, W. Clegg, J. A. G. Williams, V. N. Kozhevnikov, *Dalton Trans.* **2016**, *45*, 6949; [b] M. Z. Shafikov, R. Daniels, V. N. Kozhevnikov, *J. Phys. Chem. Lett.* **2019**,*10*, 7015.
17. [a] P.-H. Lano[, C. M. Tong, R. W. Harrington, M. R. Probert, W. Clegg, J. A. G. Williams, V. N. Kozhevnikov, *Chem. Commun.* **2014**, *50*, 6831; [b] V. N. Kozhevnikov, *ECS J. Solid State Sci. Technol.* **2019**, *8*, R84.
18. [a] X. Yang, X. Xu, J.-S. Dang, G. Zhou, C.-L. Ho, W.-Y. Wong, *Inorg. Chem.* **2016**, *55*, 1720; [b] X. Yang, Z. Feng, J. Zhao, J.-S. Dang, B. Liu, K. Zhang, G. Zhou, *ACS Appl. Mater. Interfaces* **2016**, *8*, 33874.
19. V. N. Kozhevnikov, M. C. Durrant, J. A. G. Williams, *Inorg. Chem.* **2011**, *50*, 6304.
20. G. Turnbull, J. A. G. Williams, V. N. Kozhevnikov, *Chem. Commun.* **2017**, *53*, 2729.
21. M. Z. Shafikov, S. Tang, C. Larsen, M. Bodensteiner, V. N. Kozhevnikov, L. Edman, J. *Mater. Chem. C* **2019**, *7*, 10672.
22. R. MuÇoz-Rodrìguez, E. BuÇuel, N. Fuentes, J. A. G. Williams, D. J. Cardenas, *Dalton Trans*. **2015**, *44*, 8394.
23. [a] D. Bourissou, O. Guerret, F. P. Gabbaı¨, G. Bertrand, *Chem. Rev*. **2000**, *100*, 39; [b] M. N. Hopkinson, C. Richter, M. Schedler, F. Glorius, *Nature* **2014**, *510*, 485; [c] S. P. Nolan, *N-Heterocyclic Carbenes in Synthesis*, Wiley- VCH, Weinheim **2006**; [d] *N-Heterocyclic Carbenes: From Laboratory Curiosities to Efficient Synthetic Tools*, 2nd ed., (Ed.: S. Diez-Gonzalez), RSC, London, **2016**.
24. L. Mercs, A. Neels, H. Stoeckli-Evans, M. Albrecht, *Inorg. Chem.* **2011**, *50*, 8188;
25. J. A. Mata, F. E. Hahn, E. Peris, *Chem. Sci.* **2014**, *5*, 1723. E. Peris, *Chem. Rev.* **2018**, *118*, 9988;
26. L. Mercs, M. Albrecht, *Chem. Soc. Rev.* **2010**, *39*, 1903. [a] C. A. Smith, M. R. Narouz, P. A. Lummis, I. Singh, A. Nazemi, C-H. Li, C. M. Crudden, *Chem. Rev.* **2019**, *119*, 4986; [b] M. Nussbaum, O. Schuster, M. Albrecht, *Chem. Eur. J.* **2013**, *19*, 17517.
27. A.G. Tennyson, E. L. Rosen, M. S. Collins, V. M. Lynch, C. W. Bielawski, *Inorg. Chem*. **2009**, *48*, 6924.
28. S. Gonell, M. Poyatos, E. Peris, *Chem. Eur. J.* **2014**, *20*, 9716.
29. S. Ibanez, A. Guerrero, M. Poyatos, E. Peris, *Chem. Eur. J.* **2015**, *21*, 10566.

30. [a] R. D. Costa (Ed.), in *Light-emitting Electrochemical Cells: Concepts, Advances and Challenges*, Springer, **2017**; [b] E. Fresta, R. D. Costa, *J. Mater. Chem. C*, **2017**, *5*, 5643.
31. [a] Q. Pei, G. Yu, C. Zhang, Y. Yang, A. J. Heeger, *Science*, **1995**, *269*, 1086; [c]Q. Pei, A. J. Heeger, *Nature Mater.*, **2008**, *7*, 167; [d] J. D. Slinker, J. A. DeFranco, M. J. Jaquith, W. R. Silveira, Y.-W. Zhong, J. M. Moran-Mirabal, H. G. Craighead, H. D. Abruña, J. A. Marohn, G. G. Malliaras, *Nature Mater.*, **2007**, *6*, 894
32. R. D. Costa, E. Ort., H. J. Bolink, F. Monti, G. Accorsi, N. Armaroli, *Angew. Chem. Int. Ed.* **2012**, *51*, 8178.
33. [a] R. Englman and J. Jortner, *Mol. Phys.*, **1970**, *18*, 145; [b] J. V. Caspar and T. J. Meyer, *Inorg. Chem.*, **1983**, *22*, 2444;[c] J. V. Caspar and T. J. Meyer, *J. Phys. Chem.*, **1983**, *87*, 952; [d] E. M. Kober, J. V. Caspar, R. S. Lumpkin and T. J. Meyer, *J. Phys. Chem.*, **1986**, *90*, 3722.
34. [a] E. V. Puttock, M. T. Walden, J. A. G. Williams, *Coord. Chem. Rev.*, **2018**, *367*,127; [b] Q.-C. Zhang, H. Xiao, Z. Zhang, L.-J. Xu and Z.-N. Chen, *Coord. Chem. Rev.*, **2019**, *378*, 121; 42; [c] G. Li, D. Zhu, Z.Wang,Z. Su, M. R. Bryce, *Chem. Soc. Rev.*, **2020**, *49*, 765;d) G. Li, D. G. Congrave, D. Zhu, Z. Su, M. R. Bryce, *Polyhedron*, **2018**, *140*, 146; e) M. Mauro, *Chem. Comm.* **2021**, *57*, 5857.
35. [a] M. Z. Shafikov, A. V. Zaytsev and V. N. Kozhevnikov, *Inorg. Chem.*, **2021**, *60*, 642; [b] M. Z. Shafikov, R. Daniels and V. N. Kozhevnikov, *J. Phys. Chem. Lett.*, **2019**, *10*, 7015; [c] X. Yang, Z. Feng, J. Zhao, J.-S. Dang, B. Liu, K. Zhang and G. Zhou, *ACS Appl. Mater. Interfaces*, **2016**, *8*, 33874; [d] R. E. Daniels, S. Culham, M. Hunter, M. C. Durrant, M. R. Probert, W. Clegg, J. A. G. Williams and V. N. Kozhevnikov, *Dalton Trans.*, **2016**, *45*, 6949; [e] M. Z. Shafikov, S. Tang, C. Larsen, M. Bodensteiner, V. N. Kozhevnikov and L. Edman, *J. Mater. Chem. C*, **2019**, *7*, 10672; [f] M. Z. Shafikov, P. Pander, A. V. Zaytsev, R. Daniels, R. Martinscroft, F. B. Dias, J.A. G. Williams and V. N. Kozhevnikov, *J. Mater. Chem. C*, **2021**, *9*, 127; [g] Z. Hao, K. Zhang, K. Chen, P. Wang, Z. Lu, W. Zhu and Y. Liu, *Dalton Trans.*, **2020**, *49*, 8722; [h] M. Z. Shafikov, R. Daniels, P. Pander, F. B. Dias, J. A. G. Williams and V. N. Kozhevnikov, *ACS Appl. Mater. Interfaces*, **2019**, *11*, 8182
36. [a] Y. Zheng, A. S. Batsanov, M. A. Fox, H. A. Al-Attar, K. Abdullah, V. Jankus, M. R.Bryce and A. P. Monkman, *Angew. Chem., Int. Ed.*, **2014**, *53*, 11616; [b] A. M'hamedi, M. A. Fox, A. S. Batsanov, H. A. Al-Attar, A. P. Monkman and M. R. Bryce, *J. Mater. Chem. C*, **2017**, *5*, 6777.
37. M. Z. Shafikov, S. Tang, C. Larsen, M. Bodensteiner, V. N. Kozhevnikov and L.Edman, J. Mater. Chem. C, 2019, 7, 10672;. R. D. Costa, G. Fernandez, L. Sanchez, N. Martin, E. Ortí, H. J. Bolink, *Chem. Eur. J.*, **2010**, *16*, 9855; M.-G. La-Placa, A. M. Igual-Munõz, J. Romero, R. E. Daniels, V. N. Kozhevnikov, M. Sessolo, H. J. Bolink, *ECS Solid State Sci. Tech.*, **2019**, *8*, R84.
38. V. César, V. Mallardo, A. Nano, G. Dahm, N. Lugan, G. Lavigne, S. Bellemin-Laponnaz, *Chem. Commun.* **2015**, *51*, 5371.
39. M. Nonoyama, *Bull. Chem. Soc. Jpn.* **1974**, *47*, 767.
40. P. Coppo, E. A. Plummer, L. De Cola, *Chem. Commun.* **2004**, 1774.

41. V. César, V. Mallardo, A. Nano, S. F. DePeter, S. Bastin, A. Sournia-Saquet, A. Maisse-François, N. Lugan, S. Bellemin-Laponnaz, *ACS Omega* **2018**, *3*, 15582.
42. J. Dai, K. Zhou, M. Li, H. Sun, Y. Chen, S. Su, X. Pu, Y. Huang, Z. Lu, *Dalton Trans.* **2013**, *42*, 10559.
43. [a] J. V. Caspar, T. J. Meyer, *J. Phys. Chem.* **1983**, *87*, 952; [b] E. M. Kober, J. V. Caspar, R. S. Lumpkin, T. J. Meyer, *J. Phys. Chem*. **1986**, *90*, 3722.
44. H. Yersin, A. F. Rausch, R. Czerwieniec, T. Hofbeck, T. Fischer, *Coord. Chem. Rev.*, **2011**, *255*, 2622,
45. [a] S. Lamansky, P. Djurovich, D. Murphy, F. Abdel-Razzaq, H.-E. Lee, C. Adachi, P. E. Burrows, S. R. Forrest, M. E. Thompson, *J. Am. Chem. Soc.* **2001**, *123*, 4304;[b] S. Lamansky, P. Djurovich, D. Murphy, F. Abdel-Razzaq, R. Kwong, I. Tsyba, M. Bortz, B. Mui, R. Bau, M. E. Thompson, *Inorg. Chem.* **2001**, *40*, 1704.
46. [a] H. Yersin, A. F. Rausch, R. Czerwieniec, T. Hofbeck, T. Fischer, *Coord. Chem. Rev*. **2011**, *255*, 2622; [b] A. F. Rausch, H. H. H. Homeier, P. I. Djurovich, Mark E. Thompson, H. Yersin, Proc. SPIE 6655, *Organic Light Emitting Materials and Devices XI*, 66550F, **2007**.
47. Y.-J. Su, H.-L. Huang, C.-L. Li, C.-H. Chien, Y.-T. Tao, P.-T. Chou, S. Datta, R.-S. Liu, *Adv. Mater.* **2003**, *15*, 884
48. R. Visbal, M. Concepcion Gimeno, *Chem. Soc. Rev.* **2014**, *43*, 3551.
49. J. Li, P. I. Djurovich, B. D. Alleyne, M. Yousufuddin, N. N. Ho, J. C. Thomas, J. C. Peters, R.Bau, M. E. Thompson, *Inorg. Chem.* **2005**, *44*, 1713.
50. A.Kapturkiewicz, J. Nowacki, P. Borowicz, *Electrochim. Acta* **2005**, *50*, 3395.
51. A.J. Bard, L. R. Faulkner in *Electrochemical Methods: Fundamentals and Applications*, 2nd Ed., Wiley, **2000**
52. [a] G.-R. Lin, H.-F. Chen, H.-C. Shih, J.-H. Hsu, Y. Chang, C.-H. Chiu, C.-Y. Cheng, Y.- S. Yeh, H.-C. Su, K.-T. Wong, *Phys. Chem. Chem. Phys.* **2015**, *17*, 6956; [b] J.-H. Hsu, H.-C. Su, *Phys. Chem. Chem. Phys.* **2016**, *18*, 5034; [c] H.-C. Su, *ChemPlusChem* **2018**, *83*, 197; d) Z.-P. Yang, H.-C. Su, *Adv. Funct. Mater.* **2020**, *30*, 1906788.
53. C.-L. Lee, C.-Y. Cheng, H.-C. Su, *Org. Electron.* **2014**, *15*, 711. 44;
54. [a]R. D. Costa, G. Fernandez, L. Sanchez, N. Martin, E. Ortí, H. J. Bolink, *Chem. Eur. J.,***2010**, *16*, 9855; [b] M.-G. La-Placa, A. M. Igual-Munõz, J. Romero, R. E. Daniels, V. N. Kozhevnikov, M. Sessolo, H. J. Bolink, *ECS Solid State Sci. Tech.,* **2019**, *8*, R84.
55. [a] A. R. Hosseini, C. Y. Koh, J. D. Slinker, S. Flores-Torres, H. D. Abruña, G. G. Malliaras, *Chem. Mater.* **2005**, *17*, 6114;[b] B. Chen, Y. Li, Y. Chu, A. Zheng, J. Feng, Z. Liu, H. Wu, W. Yang, *Org. Electron.* **2013**, *14*, 744; [c] A. Pertegás, N. M. Shavaleev, D. Tordera, E. Ortí, M. K. Nazeeruddin, H. J. Bolink, *J. Mater. Chem. C* **2014**, *2*, 1605; [d] M. D. Moore, M. H. Bowler, J. E. Reynolds, V. M. Lynch, Y. Shen, J. D. Slinker, J. L. Sessler, *ACS Appl. Mater. Interfaces* **2018**, *10*, 24699; [e] G.-Y. Chen, B.-R. Chang, T.-A. Shih, C.-H. Lin, C.-L. Lo, Y.-Z. Chen, Y.-X. Liu, Y.- R. Li, J.-T. Guo, C.-W. Lu, Z.-P. Yang, H.-C. Su, *Chem. Eur. J.* **2019**, *25*, 5489; [f] G.-X. Yu, C.-H. Lin, Y.-X. Liu, R.-H. Yi, G.-Y. Chen, C.-W. Lu, H.-C. Su, *Chem. Eur. J.* **2019**, *25*, 13748.
56. Y.-Z. Chen, D. Luo, C.-H. Hsiang, R.-H. Yi, C.-H. Lin, C.-W. Lu, S.-W. Liu, C.-H. Chang, H.-C. Su, *Org. Electron.* **2020**, *77*, 105515.

57. N. Miyaura, A. Suzuki, *J. Chem. Soc. Chem. Commun.* **1979**, 866
58. B. Alleyne, R. Kwong, W. Yeager, C.Xia, *PCT Int. Appl*. (**2010**), WO 2010033550 A1
59. P. J. Stephens, F. J. Devlin, C. F. Chabalowski, M. J. Frisch, *J. Phys. Chem*. **1994**, *98*, 11623.
60. E. Van Lenthe, E. J. Baerends, *J. Comput. Chem*. **2002**, *23*, 1142.
61. A.Klamt, *J. Phys. Chem.* **1995**, *99*, 2224.
62. [a] E. van Lenthe, R. van Leeuwen, E. J. Baerends, J. G. Snijders, *Int. J. Quantum Chem*. **1996**, *57*, 281; [b] F. Wang, T. Ziegler, *J. Chem. Phys*. **2005**, *123*, 154102; [c] F. Wang, T. Ziegler, E. van Lenthe, S. van Gisbergen, E. J. Baerends, *J. Chem. Phys.* **2005**, *122*, 204103.
63. M. J. G. Peach, D. J. Tozer, *J. Phys. Chem. A* **2012**, *116*, 9783

5. Bright blue-emitting heteroleptic *bis*-tridentate Ir(III) complexes bearing a 1,2,4-triazolate scaffold

ABSTRACT

In this chapter a series of three phosphorescent *bis*-tridentate Ir(III) complexes is described, namely **TR1–TR3**. All complexes bear a 1,2,4-triazolate-based scaffold as chromophoric tridentate ligand and a *bis*-N-heterocyclic carbene ligand. The stepwise synthesis starts with the deprotonation of carbene from the $[fpbmiH_2][PF_6]_2$ and $[bpbmiH_2][PF_6]_2$ following by the addition of the triazolyl derivative at high temperature. The photophysical characterization shows a vibronic emission profile with high PLQY (51.7-81.8%) in the sky-blue region with a long-lived excited state lifetime (3.1-6.2 μs) in degassed dichloromethane solution. The retention of the high quantum yield in PMMA thin film (63%) makes **TR1** the most suitable compound as robust dopant emitters for OLED devices.

5.1 State-of-art and introduction

Cyclometalated iridium(III) complexes are currently under intense investigation owing to their unique optical and redox properties. This outstanding class of photoactive compounds finds appealing applications as luminescent bio-imaging probes[1], photocatalytic systems[2] and especially as efficient and robust emitters in light-emitting devices, such as OLED and LEC[3].

The heavy atom induces high spin-orbit coupling (SOC) leading to an efficient population of lower-lying triplet manifolds via intersystem crossing (ISC) processes, enabling fast radiative deactivation channels from the lowest-lying excited state with mixed ^{1}MLCT/^{3}LC character. As a consequence, high photoluminescence quantum yield and relatively short excited-state lifetime, falling within hundreds of nanoseconds to few microseconds range may be achieved.[4]

Nowadays, green and orange-red Ir(III) emitters have found use in real-market technology. Yet, design of robust and stable (deep-)blue phosphors is still a challenge.[5] Since the pioneering work of Thompson and Forrest with the first blue emitting iridium complex for OLED, iridium(III)bis[4,6-di-fluorophenyl]-pyridinato-N,C$^{2'}$picolinate, named FIrpic [6], several strategies have been explored aiming at improving long-term robustness, color purity (deep-)blue region while keeping high photo- and electro-luminescence efficiency. A fundamental requirement for (deep-)blue emission is a large energy gap between the emissive T_1 and the ground state. However, such energetic requirement is accompanied by a decrease of energy barrier between the T_1 and the close-lying quenching ^{3}MC states. As such barrier decreases, ^{3}MC states become thermally accessible, opening up for more efficient and detrimental non-radiative channels.[7]

Alternatives solutions to FIrpic were reported by Thompson and co-workers in 2003. The proposed Ir(C^N)$_3$ complexes, where C^N is a phenylpyridine-type of ligands, showed an emission maximum at 450 nm for *fac*-4,6dfppy (4,6dfppy = 4,6-difluorophenyl pyridine), and stronger luminescence (PLQY = 43%) compared to the analogue with phenylpyrazolate ligand, named Ir(46dfppz)$_3$ (PLQY = 0.1%).[8] A further investigation on the latter revealed that the poor emissive properties in solution come from the thermally accessible non-radiative states localized on the ppz-type of ligand.

In this regard, the success of NHCs carbenes as ligand scaffold in luminescent organometallic compounds lies in the improvement of the ligand field, which in turn helps to rise further up in energy quenching MC states and design compounds with improved photophysical features.[9,6b]

A first work on the use of NHC ligands in the preparation of luminescent iridium(III) complexes was reported by Thompson and co-workers, which investigated two homoleptic neutral derivatives with general formula *fac*-[Ir(C^C:)$_3$], where C^C: is a bidentate monoanionic ligand, such as 1-phenyl-3-methylimidazolin-2-ylidene (pmi) and 1-phenyl-3-methylbenzimidazolin-2-ylidene (pmb). In spite of the high-energy emission (λ_{em} = 380 nm) both derivatives displayed poor to moderate PLQY at room temperature (0.2 and 5%).[10]

The same group has more recently proposed a fused pyridine NHC carbene to replace the more classical C^N phenyl-pyridine-based ligand scaffolds. The new structure of NHC Ir(III) complex is tris-(N-phenyl,N-methyl-pyridoimidazol-2-yl)iridium(III), named Ir(pmp)$_3$. The *fac*- and *mer*- complexes reached an emission maximum of 380 nm, keeping a ϕ_{PL}= 76 and 78% for *fac*-Ir(pmp)$_3$ and *mer*-Ir(pmp)$_3$, respectively.[11] Zysman-Colman introduced 3-methyl-1-(3/4-(trifluoromethyl)phenyl)-1H-3λ4-imidazole as pre-carbenic ligands demonstrating that the introduction of electron-withdrawing CF_3 group onto phenyl ring, yielding complexes *para/meta*-Ir(CF_3pmi)$_3$,[12] with much improved photo- and electro-luminescence efficiencies compared to parental complexes *fac*-[Ir(pmi)$_3$].

Other examples bearing the imidazo[1,5-a]pyridine-3-ylidene scaffold as ligand where reported by the group of Mashima[13] . The compounds have general formula Ir(C^C)$_3$ where the pro-ligand C^C is (pyridyl[1,2-a]{2-phenylimidazol}-3-ylidene chloride), named [pypiH_2][Cl] and (pyridyl[1,2-a-{2-(p-methoxy)phenylimidazol}-3-ylidene chloride) named [pympiH_2][Cl]. However, these derivatives showed photoluminescence in frozen glassy matrix at 77K only. All these compounds are displayed in *Figure 5.1*.

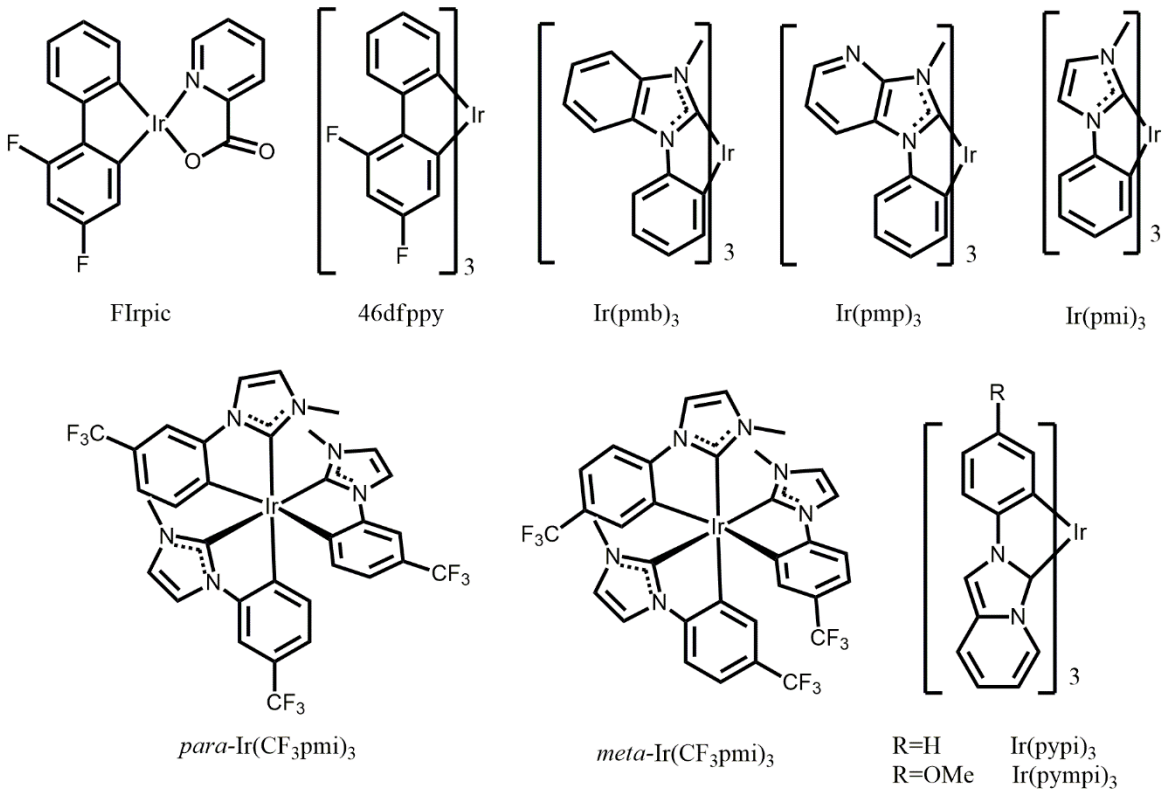

Figure 5.1 Chemical structure of selected *tris*-cyclometalated iridium(III) emitters with either [Ir(C^N)$_3$] or [Ir(C^C:)$_3$] type of formula.

Although the huge success of the homoleptic iridium complexes for OLED, the structural instability, owing to the meridional to facial isomerization upon thermal and photo-excitation[8], and possible ligand-loss degradation pathways[14], encourages the research to find an alternative structure to *tris*-bidentate compounds.

As reported in the introduction about pincer-bis carbene ligand, bidentate ligands bind through two donor sites, causing the chelating effect around the metal. This effect is the enhanced affinity of a chelating ligand for a metal ion compared to its monodentate ligand counterpart(s). The result is a more stable and robust ligand-metal bond.[15]

As firstly reported by Campagna[16], Scandola[17] and Williams[18], cyclometalated iridium complexes containing two tridentate ligands display structural and photophysical advantages. In sharp contrast to *tris*-bidentate compounds, the *bis*-tridentate counterparts exist as achiral mixture, avoiding the issue given by geometrical isomers. Moreover, the usage of a tridentate chelating ligand improves the photo- and thermal stability, due to multiple metal-chelate coordination bonding that provides higher molecular rigidity.[19]

Following the success of this strategy, other groups[20] have pursued to study new ligand combination in order to improve the photoluminescence efficiency as well as shifting the emission towards the blue region.

Metal complexes bearing at least one NHC carbene in a tridentate ligand have long been explored with ruthenium[21], rhodium[22] and other metals. The first NHC pincer ligand complexed to an early transition metal appeared in 2003, when Kawaguchi reported the synthesis of an imidazolium-linked bis(phenol) proligand and its titanium(IV) complexes.[23] Since then, the employment of carbene pincer chelates has attracted much attention organometallic chemistry. The first examples with iridium was reported in 2008 by Braustein *et al.*, but the photophysical properties of the described compounds were not investigated.[24] In a following investigation of Braunstein, De Cola and coworkers, a series of homoleptic bis-tridentante complexes of general formula $[Ir^{nBu}(C_{NHC}{}^{Me}CC_{NHC})_2]X$, where $^{nBu}(C_{NHC}{}^{Me}CC_{NHC})$ is (4,6-dimethyl-1,3-phenylene-κC^2)bis(1-butylimidazol-2-ylidene) and X is I^- or PF_6^-. These compounds revealed near-UV emission (lem = 380 nm) with relatively high PLQY and good performance as dopants in LEC devices.[20c] Since then, cyclometalating tridentate *bis*-NHC ligands largely replaced the common N^C^N-coordinating scaffold, thus becoming the main ligand for Ir(III) tridentate complexes.

If on one hand the dicarbene ligand improves the ligand field strength, enhancing the ^{3}MC states in energy and leading to a smaller k_{nr}, on the other hand a phenyl triazolyl pyridine derivative allows to tune the emission wavelength.[19,25] Recently, Chou and coworkers reported an interesting series of compounds bearing an azolate moiety onto the dianionic chelate ligand.[26] These latter compounds exhibit improved stability which provides more resistance against cleavage of metal-ligand bonds.[27]

Another example reported by Chi and coworkers was the synthesis of six new iridium compounds bearing a monoanionic tridentate chelate 4-(tert-butyl)-2-(2,4-difluorophenyl)-6-(3-isopropylimidazol-2-ylidene)pyridine, named (phpyim-H2)PF_6 and a dianionic tridentate chelates derived from functional 2-pyrazol-3-yl-6-phenylpyridine chelates (see *Figure 5.2*). The compounds reveal a wide range of emission wavelengths from 473 to 608 nm with a quantum yield close to the unity, except for those complexes where the central pyridine was replaced by the isoquinolinyl group.[28] Despite the use of a tridentate chelating ligand, these results are worse than those reported by Chou *et al.*[26b] A new class of Ir(III) phosphors bearing bis(imidazolylidene) benzenes and functional 2-pyrazolyl-6-phenyl pyridine (or

isoquinoline) chelates was investigated for OLED application. The compounds showed a blue shift in a range of 467 to 595 nm with a quantum yield higher than 98%.

Despite the wide usage of pyrazolate moiety, 1,2,4-triazolate possesses comparable σ-donating ability but stronger π-accepting character given by an additional endocyclic N-atom. This would result in a deeper HOMO of the metal complex.[29,25] The strategy to exploit these kind of ligands lies on the expected interaction between the ligand π and the metal d_{π} orbitals, lowering the HOMO level that would be helpful for targeting (deep-)blue emission.[30,26b]

Aiming at efficient and robust blue-emitting iridium(III) complexes as potential dopants for OLEDs, hereafter it will be described a novel series of neutral heteroleptic *bis*-tridentate iridium(III) derivatives bearing either a 2-(2,4-difluorophenyl)-6-(5-(trifluoromethyl)-4H-1,2,4-triazol-3-yl)pyridine, named $L1H_2$ or a 2-(5-(trifluoromethyl)-4H-1,2,4-triazol-3-yl)-6-(4-(trifluoromethyl)phenyl)pyridine, named $L2H_2$, as chromophoric ligand. The synthesis and photophysical investigation of the three complexes is herein described and the chemical structures are displayed in *Figure 5.4*. In agreement with related systems previously reported[25], complexes **TR1-TR3** display ^{1}MLCT/^{3}LC low-lying excited state with a strong vibronic emission profile in the blue region arising from the 2-phenyl-6-(4H-1,2,4-triazol-3-yl)pyridine ligand.

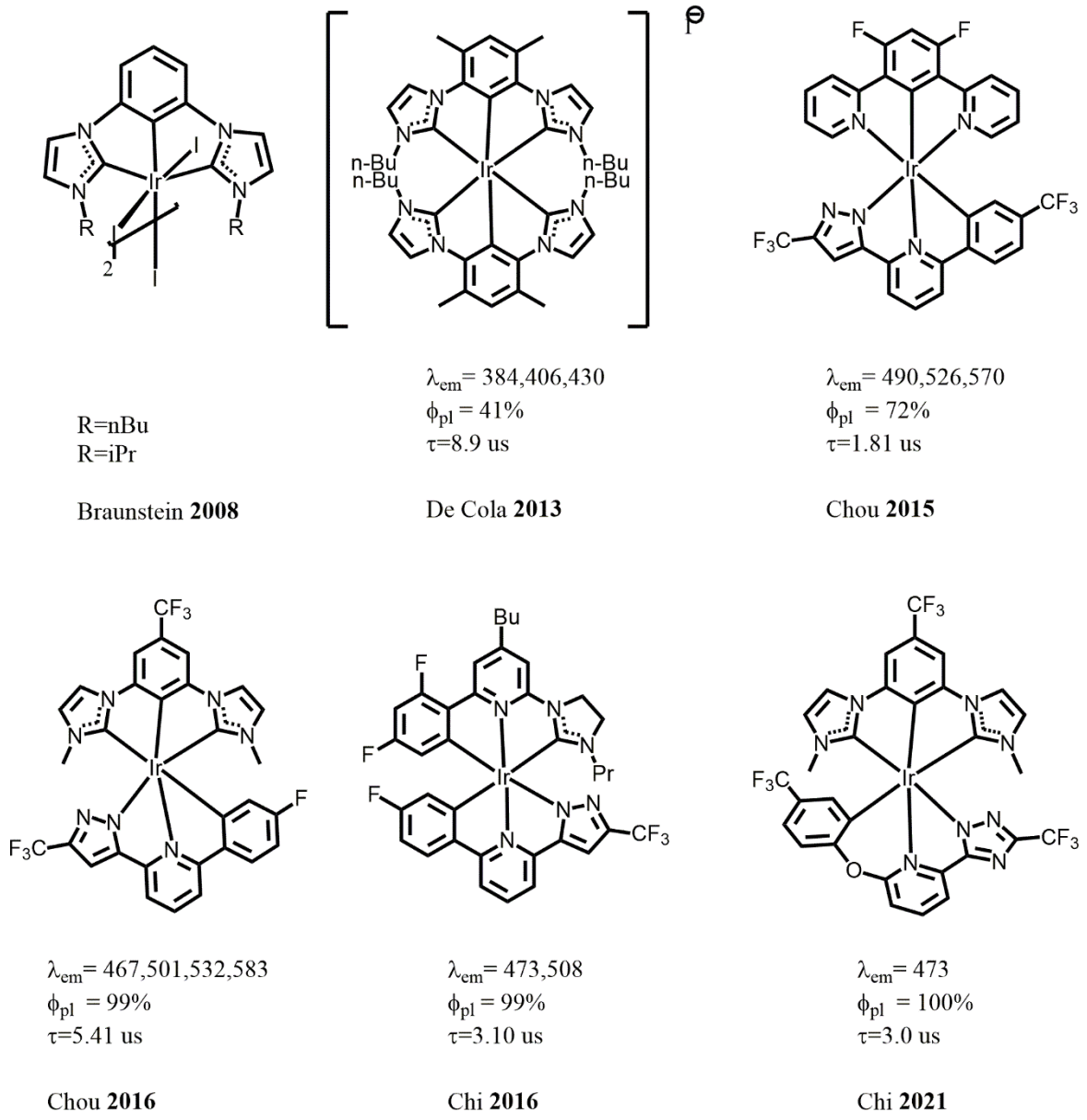

Figure 5.2 Chemical structure of selected Ir^{III} complexes bearing tridentate *bis*-carbene pincer chelates.

5.2 Results and discussion

5.2.1 Synthesis

In order to modulate the optical properties of the final complexes, two tridentate proligands based on the phenyl-*bis*-imidazolium scaffolds were firstly targeted, namely [**fpbmiH$_2$**][**PF$_6$**]$_2$ and [**bpbmiH$_2$**][**PF$_6$**]$_2$ bearing an electron-withdrawing CF_3 and a moderate electron-donating *tert*-butyl group, respectively, in position 5 of the phenyl group (see *Figure*

5.3). It should be noticed that introduction of a bulky substituent in this position is also important to promote coordination in a tridentate fashion by avoiding roll-over of the imidazole moiety and unwanted bidendate chelation.[31,26b]

For the synthesis of the both *bis*-carbene pincers, the starting material 2,6-dibromophenyl was converted to the corresponding 1,3-di(1H-imidazol-1-yl)benzene, followed by methylation at the 3-position of the imidazole to give the final *bis*-3-methyl-imidazolium hexafluorophosphate, accordingly to previous reports (*Scheme 5.1*).[32]

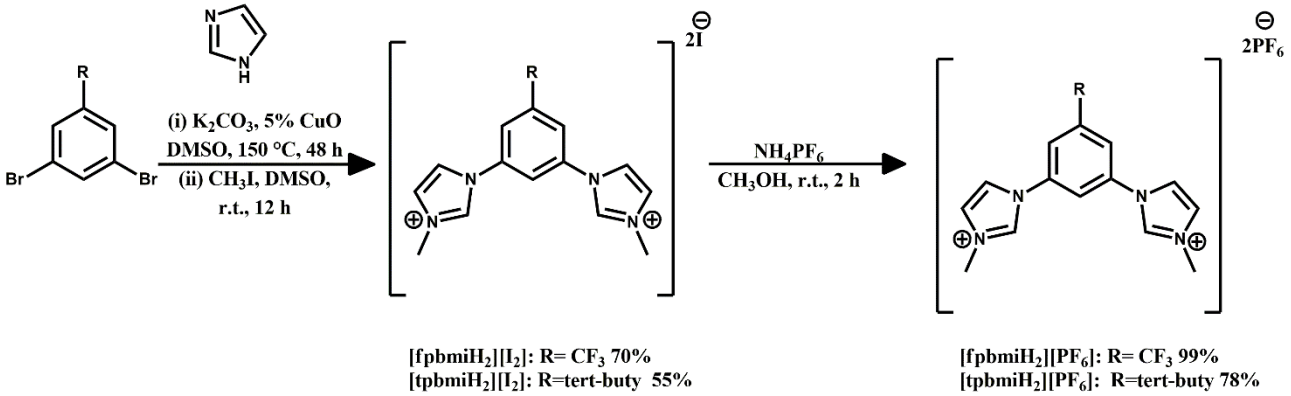

Scheme 5.1 Synthetic general procedure for pincer bis-carbene.

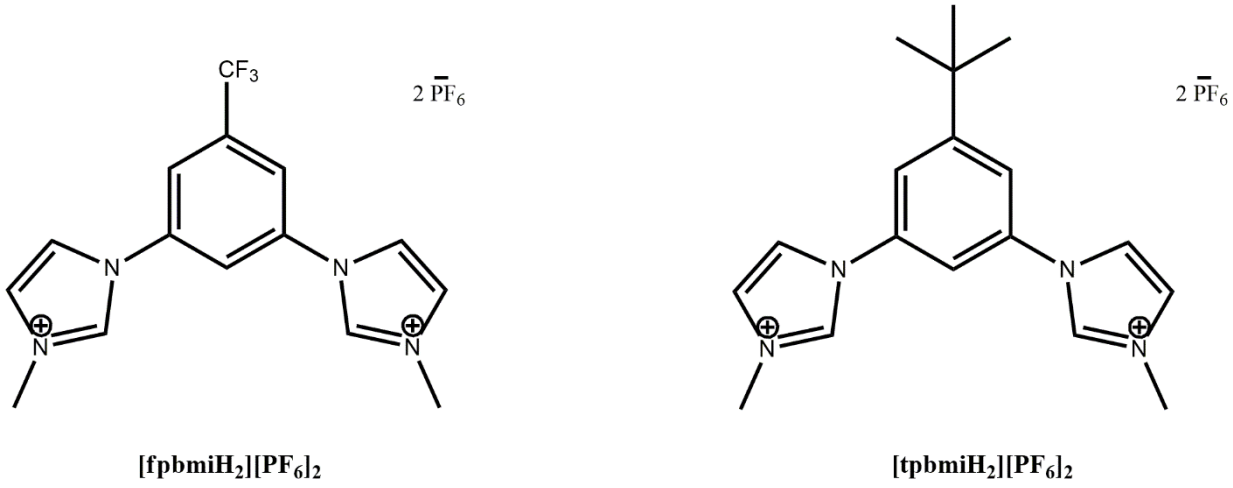

Figure 5.3 Chemical structure of the *bis*-carbenic proligand [**fpbmiH$_2$**][**PF$_6$**]$_2$ and [**tpbmiH$_2$**][**PF$_6$**]$_2$.

The synthetic pathway employed for the synthesis of [**fpbmiH$_2$**][**PF$_6$**]$_2$ and [**tpbmiH$_2$**][**PF$_6$**]$_2$ is a Cu(I) catalyzed Ullmann-type coupling reaction between the 1,3-

dibromo-benzene and 1H-imidazole. The diimidazolium cations were obtained using methyl iodide by methylation at N(3) position. The target *bis*(hexafluorophosphate) salts were obtained straightforwardly by anion metathesis from the iodine salts.

The target 1,2,4-triazolyl derivatives were prepared by a stepwise reaction (see *Scheme 5.2*). The Suzuki coupling between the difluoro-phenyl boronic acid and the 6-bromo-2-cyano pyridine is followed by the introduction of the triazole ring by treatment with hydrazine monohydrate and trifluoroacetic anhydride (for $L1H_2$ and $L2H_2$), or acylation with trimethylacetyl chloride (for $L3H_2$) in agreement with modified procedures already reported.[33]

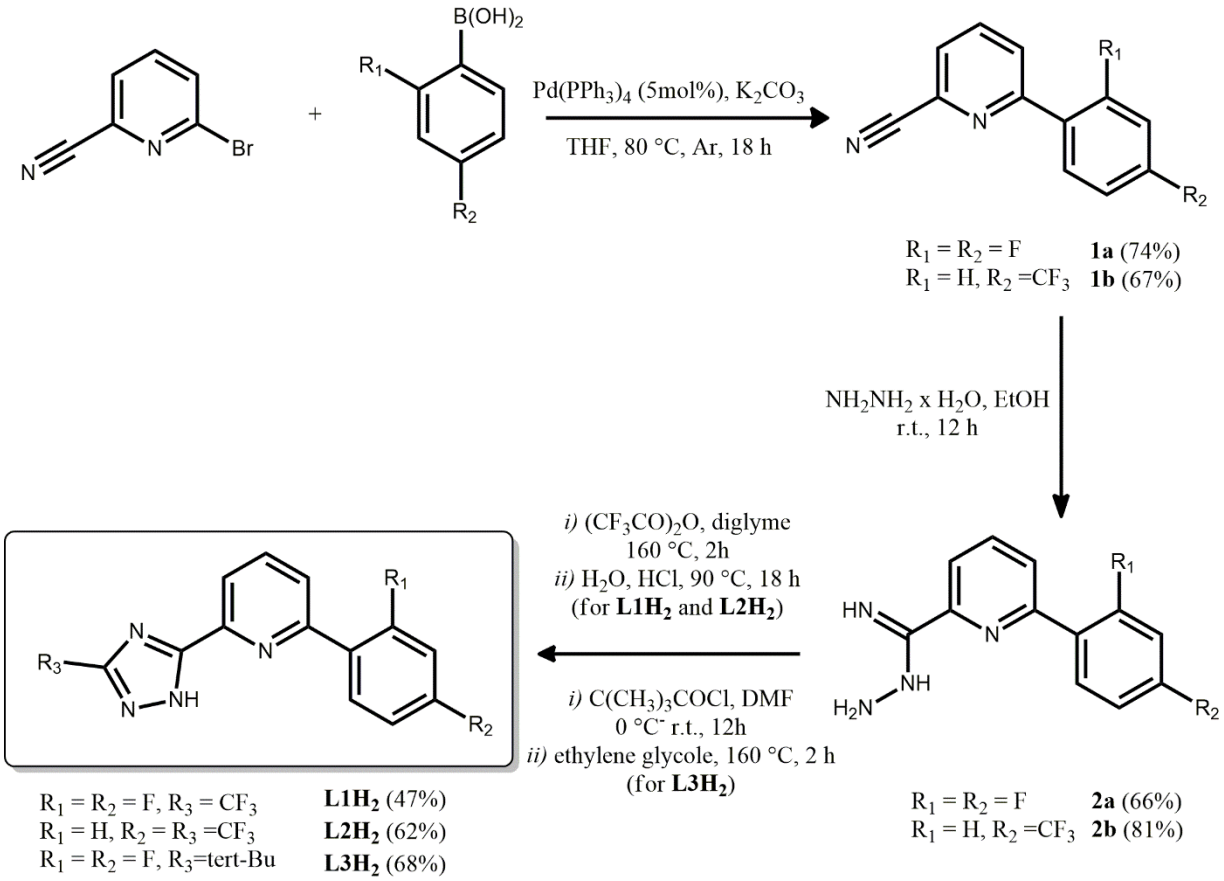

Scheme 5.2 Synthetic procedure for the triazolyl derivative ligands **$L1H_2$**, **$L2H_2$** and **$L3H_2$**.

The target Ir(III) metal complexes were synthesized following the same method reported elsewhere (*Scheme 5.3*). First, the *bis*(imidazolium) proligand reacted with $[Ir(1,5\text{-cod})Cl]_2$ in a ratio of 2:1 equiv., and an excess (10 equiv.) of NaOAc in refluxing dry acetonitrile. As reported previously,[34,26b] solvent molecules coordinates two sites of the

metal, leaving the last site to hydride ligand. The formation of the intermediate [Ir(CH_3CN)$_2$(H)(tpbmi)] is evident by the presence at the negative region (-23.0 ppm) of the ^{1}H NMR peak (see *Figure ES5.5*). However, the intermediate was not purified and isolated, and the NMR was done on the crude of the reaction. The second step was followed by the addiction of the triazolyl derivatives in refluxing decalin, along with a further excess of NaOAc. Upon purification by column chromatography, the desired complexes **TR1-TR3** were obtained as yellow powders ranging from 5% to 16% yield. All compounds were fully characterized by ^{1}H, ^{13}C and ^{19}F NMR, high resolution mass spectrometry and elemental analysis (see *Figure ES5.6-5.12*). The successful formation of the target complexes was confirmed by the predicted number of signals. Moreover, the retention of the bis-carbene peaks, due to the symmetric plan lying on this ligand and the lack of the imidazolium proton (N-C*H*-N) at δ *ca.* 9.10 ppm, assessed the coordination of the *bis*(imidazolium) proligand around the metal center. On the other hand, the triazolyl derivatives maintains the asymmetric arrangement of the signals.

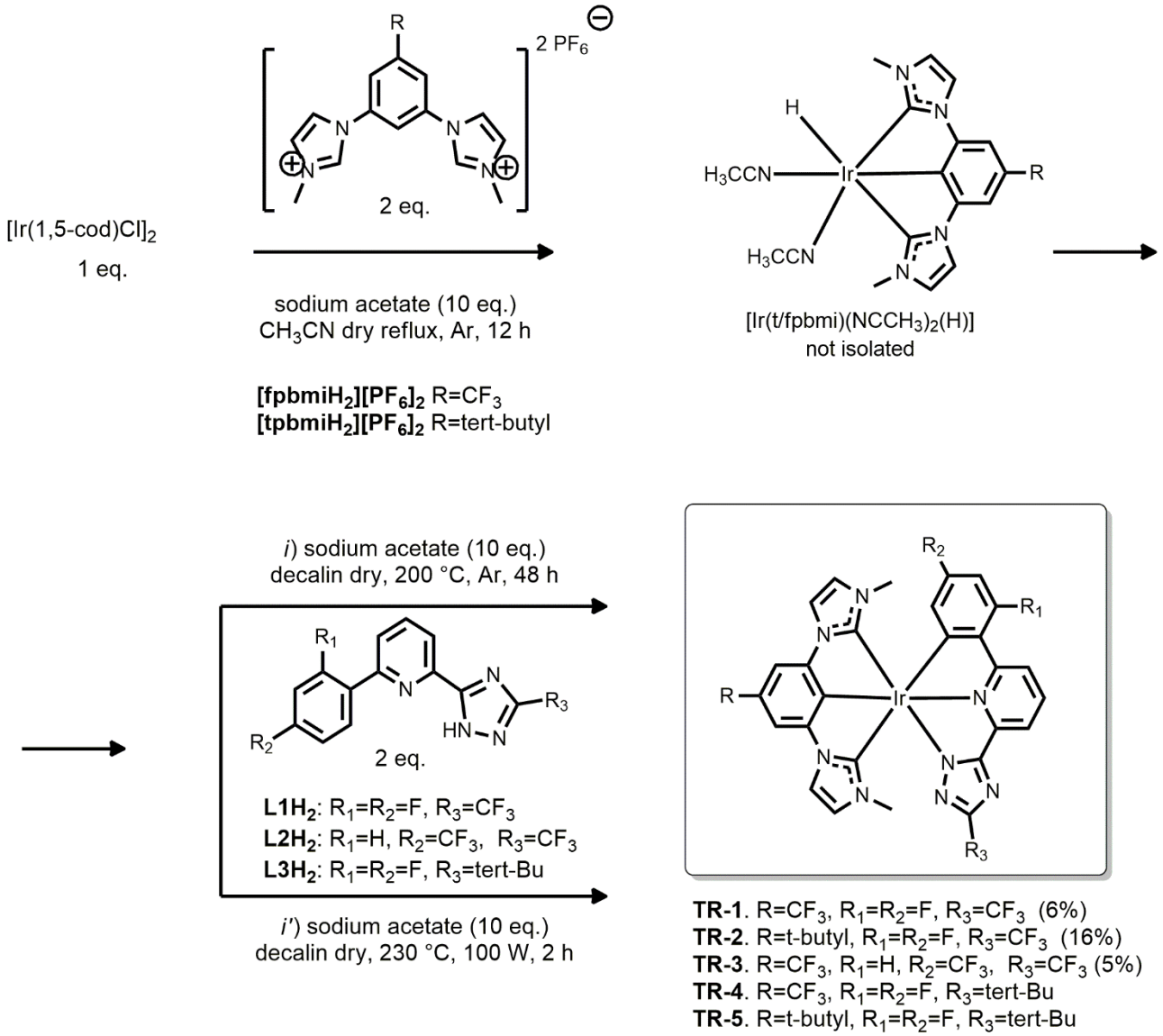

Scheme 5.3. Synthetic procedure for the Ir(III) metal complexes **TR1-TR5**.

The same reactions were performed under microwave (MW) irradiation. Although the first step was the same in both of the procedures, the cyclization from the second step was tried by heating at 230°C for 2 h under MW (100). The compounds **TR1** and **TR3** were synthesized according to this procedure. All complexes were tested by the two synthetic paths but, in both cases, the reactions were not well reproducible, so it was not possible to compare them in terms of yield and purity. For most experiments, either a very low quantity of the compound was isolated (1-2 mg starting from 200 mg) along with a large amount of impurities, or just the not coordinated triazolyl derivative was detected by NMR. A future improvement of the reaction conditions should ensure the efficiency of the two methods.

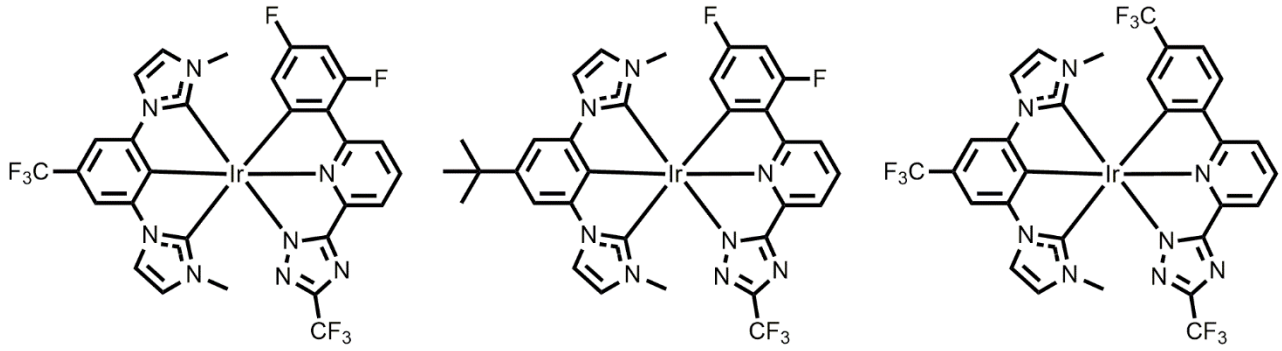

TR1 **TR2** **TR3**

6% **16%** **5%**

Figure 5.4 Chemical structure of the investigated blue-emitting *bis*-tridentate complexes **TR1**–**TR3**.

Unfortunately, two out of five planned complexes were not successfully isolated and characterized, namely **TR4** and **TR5**, but detected by mass spectroscopy only (see *Figure 5.5* and *Figures ES5.13-14*). The difficult is supposed due to the very low yield (probably <5%) and the presence of a lot of impurities.

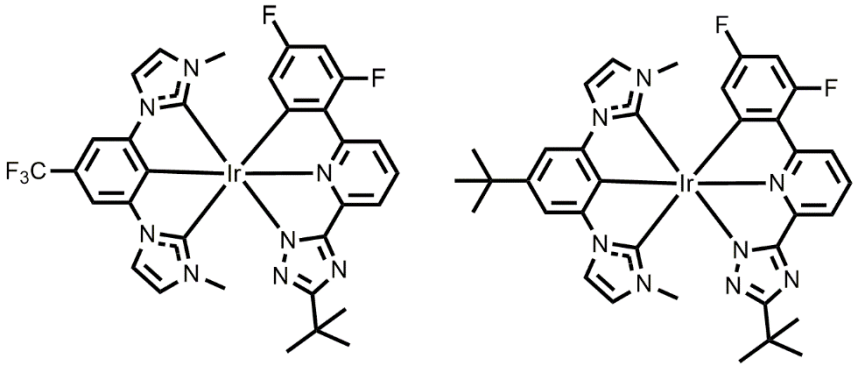

TR4 **TR5**

Figure 5.5 Chemical structure of the two not isolated complexes.

It is also known that if the final cyclization of the phenyl ring from the triazolyl ligand does not occur, a tridentate-bidentate Ir(III) complex might be formed instead. A proof, confirming the undesired compound, was done on the analogue complex **TR2** starting from the iodium salt of the biscarbene, $[tpbmiH_2][I]_2$. Regrettably, the foreseen cyclization in

decalin at 200 °C did not take place and the compound was not detected. ^{1}H NMR and MS spectra confirmed the alternative product given by the former step in xylene at 150 °C (see *Scheme 5.4* and *Figure ES.5.9* and *ES5.15*). As reported previously in literature,[26b] the pendant phenyl ring of 2-phenyl-6-(4H-1,2,4-triazol-3-yl)pyridine ligand remains un-coordinated as demonstrated by the presence of the proton resonance at d = 8.25 ppm.

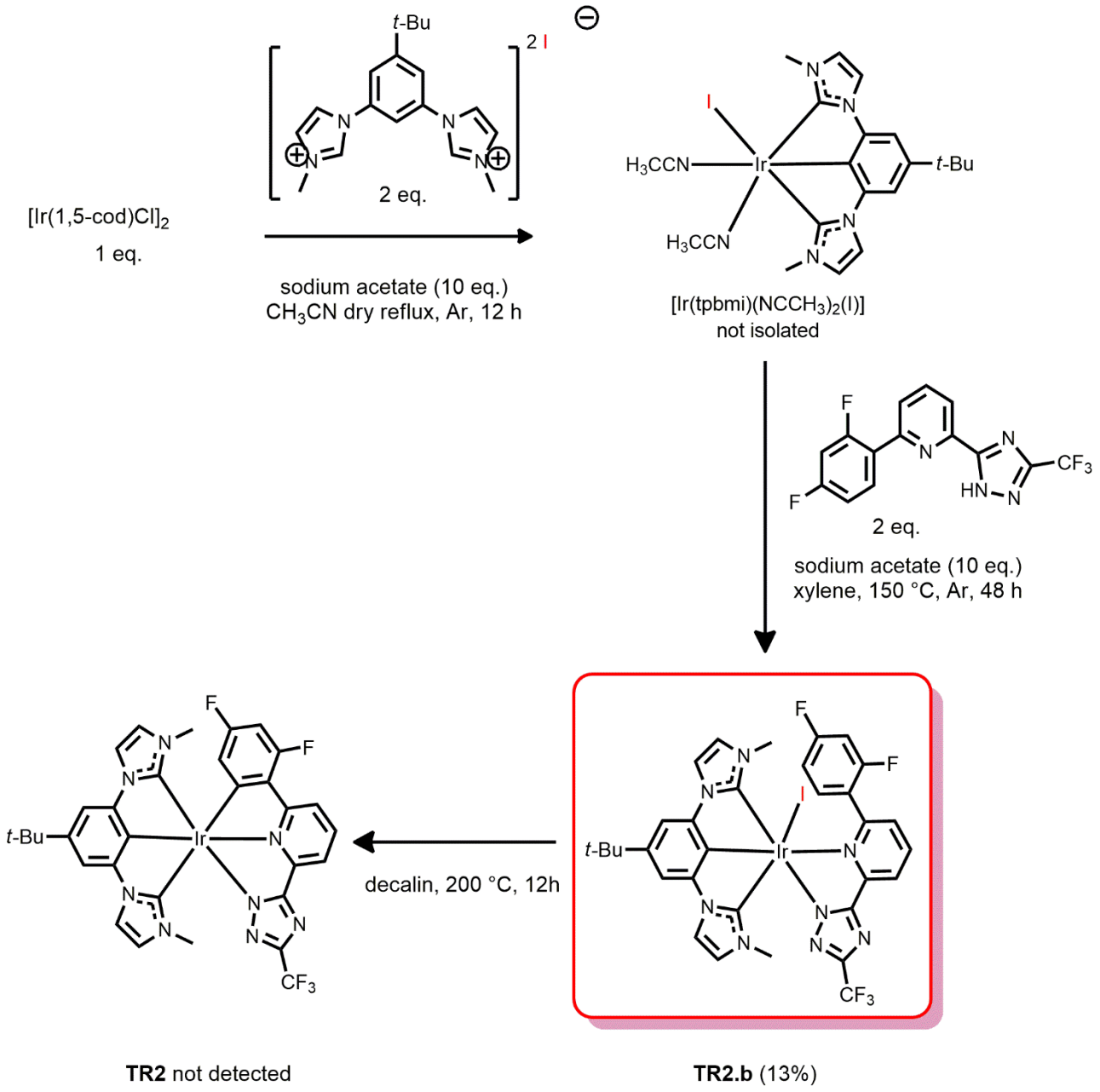

Scheme 5.4 Synthetic scheme for tridentate-bidentate Ir(III) complexes, **TR2.b**.

Single crystal X-ray diffraction studies on **TR2** confirmed the proposed structure. The crystals were obtained by slow diffusion of n-hexane into a dichloromethane solution of the compound. As shown in *Figure 5.6*, the two NHC carbenes of the *bis*(imidazolium) chelate take the *trans-C,C* configuration with an average Ir–C(15)/ Ir-C(26) distance of 2.032 Å. The two peripheral carbene units were measured with a bite angle of 154.3°, displaying a slightly geometrical distortion of the octahedron. The central phenyl group exhibits the shortest Ir-C distance (1.981 Å) among all Ir-C bonds detected. On the other side, the triazolyl derivative displays the longest Ir-N distance for N(1) with 2.112 Å along with a bite angle N-Ir-C of 157.22°, similar to the angle reported for the bis-carbene. In conclusion, the distance Ir-N from the pyridine ring shows similar length to the Ir-C(15) with 2.060 Å.

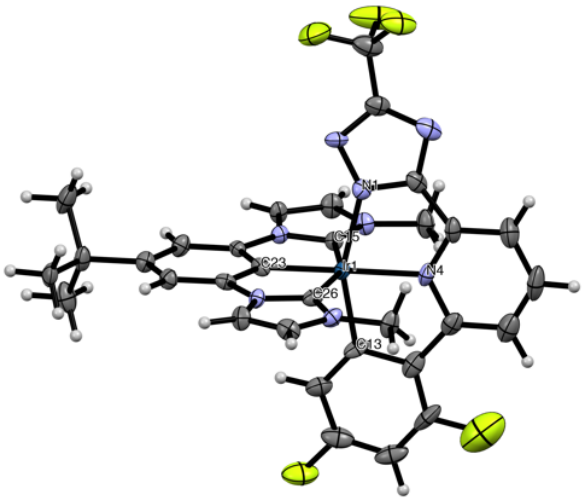

Figure 5.6 ORTEP diagram of compound **TR2** with thermal ellipsoids shown at 50% probability level obtained by single-crystal X-ray diffractometric analysis. Solvate molecules is omitted for clarity. Selected bond lengths (Å) and angles (°): Ir(1)–C(13)= 2.016; Ir(1)–N(4) = 2.060; Ir(1)–N(1) = 2.112; Ir(1)–C(15) = 2.059; Ir(1)–C(23) = 1.981; Ir(1)–C(26) = 2.058. N(1)–Ir(1)–N(4) = 77.24; Ir(1)–N(4)–C(13) = 49.14.

5.2.2 Photophysical characterization

Firstly, the photophysical properties of the investigated Ir(III)-complexes **TR1-TR3** were studied in dilute CH_2Cl_2 solution in both air-equilibrated and degassed condition at room temperature at concentration 3×10^{-5} M and in a glassy matrix of 2Me-THF. The data are listed in *Table 5.1* and the electronic absorption and emission spectra in air-equilibrated conditions are depicted in *Figure 5.7.*

In the UV-vis spectra, the intense absorption band at λ_{abs} = *ca.* 325 nm with ε = 12.8, 19.6 and 12.3 $\times$ 10^3 M for **TR1**, **TR2** and **TR3**, is ascribed to the ^{1}LC ($^1\pi$-π^*) ligand centered involving triazolyl-based terdentate ligand L1H2 and L2H2. This assignment is made by comparison with the corresponding absorption spectra of free ligand $L1H_2$ and $L2H_2$ (see *Figure 5.8* and *Table 5.2*). At longer wavelengths, in the region λ_{abs} = 370–400 nm the band can be confidentially ascribed to a single metal-to-ligand charge-transfer (^{1}MLCT) electronic transition from metal and metalated *bis*-NHC moiety towards the phenylpyridine portion of the terdendate triazolyl-containing ligand.

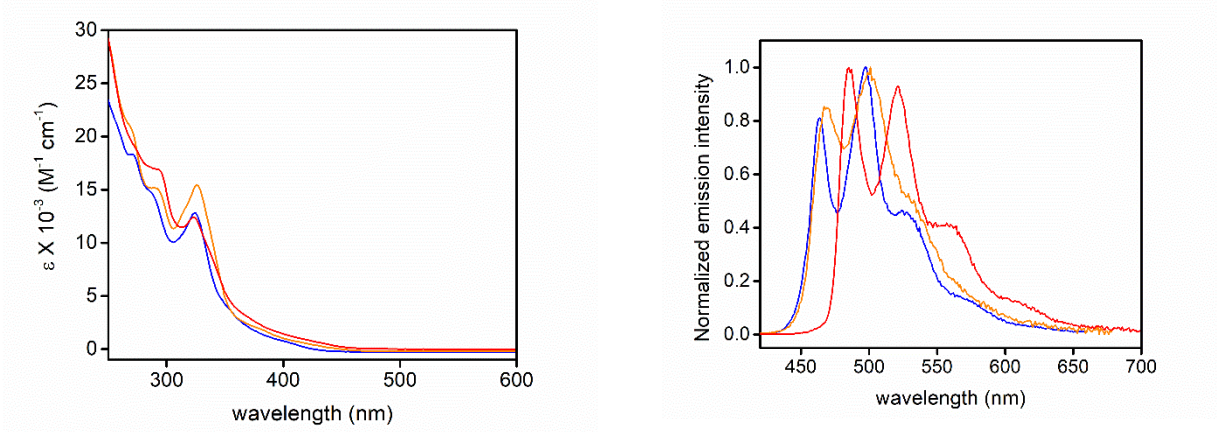

Figure 5.7 Electronic absorption (*left*) and emission (*right*) spectra for **TR1-3** complexes in dichloromethane at concentration of 3.0×10^{-5} M in degassed condition. Samples were excited at λ_{exc} = 355 nm for **TR1** (blue trace), 400 nm for **TR2** (orange trace), and 380 nm for **TR3** (red trace)**.**

The photoluminescence (PL) properties reveal similar behavior for all compounds upon irradiation at λ_{exc} = 355–400 nm. The samples display emission spectra within the sky-blue region with vibronic profile with the highest-energy maxima at λ_{em} = 463, 468 and 485 nm, for **TR1**, **TR2** and **TR3**, respectively. Expectantly, degassed samples undergo a

sizeable increase of the emission intensity with PLQY of 51.7-81.8% accompanied by prolongation of the excited-state lifetime (τ = 3.1–6.2 μs) confirming the triplet nature of the emissive excited state. Therefore, it is proposed that the emissive excited state is a mixing of ^{3}MLCT and ^{3}LC character, with a larger contribution of the ^{3}LC for complexes **TR1** and **TR3**. On the contrary, complex **TR2** reveals a slightly more ^{3}MLCT character. This picture is supported by the shorter lifetime (τ = 3.1 μs) and the higher $k_r = 26.4\times10^4$ s^{-1} recorded for **TR2** compared to **TR1** and **TR3**, which in turns give higher PLQY (81.8% for compound **TR2**).

Table 5.1 Photophysical properties of complexes **TR1-3** in air-equilibrated and degassed CH_2Cl_2 solution at a concentration of 3.0×10^{-5} M at room temperature and 77 K in 2-MeTHF glassy matrix.

Cmpd	$\lambda_{max,abs}$ (ε) [nm, (10^3 M^{-1} cm^{-1})]	λ_{em} [nm]	PLQY (%)		τ_{obs}		k_r [10^4 s^{-1}]	k_{nr} [10^4 s^{-1}]	λ_{em} [nm]	τ_{obs} [μs]
			air-equilibrated	*degassed*	*air-equilibrated*	*degassed*			*77 K*	
TR1	271 (18.3), 285 (14.9), 324 (12.8), 398 (0.8)	463,497, 525 (sh)	1.5	61.6	128 ns	6.2 μs	9.94	6.19	460, 493, 522	7.1
TR2	270 (26), 289 (19.5), 325 (19.6), 382 (2.94)	468, 500, 530 (sh)	2.4	81.8	83 ns	3.1 μs	26.4	5.87	463, 496, 530	3.7
TR3	292 (16.9), 324 (12.3), 367 (3.2), 402 (1.3)	485,521, 561 (sh)	2.9	51.7	217 ns	4.5 μs	11.5	10.7	481, 518, 557	5.9

sh denotes a shoulder; k_r = PLQY/τ; k_{nr} = (1 – PLQY)/τ.

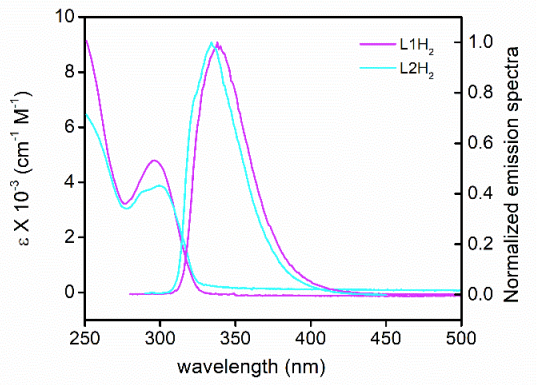

Figure 5.8 Electronic absorption and emission spectra of ligands **L1H$_2$-L2H$_2$** in air equilibrated conditions at $3\cdot10^{-5}$ M in DCM. The samples have been excited at λ_{exc} = 270 nm.

Table 5.2 Photophysical properties of **L1H$_2$-L2H$_2$** in CH_2Cl_2 in air equilibrated conditions at room temperature.

	$\lambda_{max,abs}$ (ε) [nm, (10^3 M^{-1} cm^{-1})]	λ_{em} [nm]
L1H$_2$	296 (4.79)	337
L2H$_2$	296 (3.81)	333

Moreover, further analysis of complex **TR2** in solvents with different polarities shows only a minor change of the band shape and emission wavelength, being the bathochomic shift from λ_{em} = 468 to 473 nm when going from toluene to DMF (see *Figure 5.9* and *Table 5.3*). This result supports the overall mainly ^{3}LC nature of the emissive excited state.

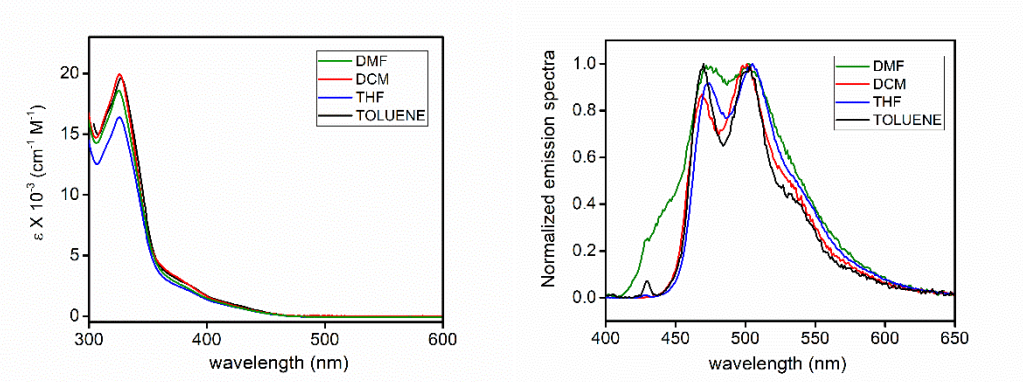

Figure 5.9 Electronic absorption (*left*) and emission spectra (*right*) of **TR2** in air equilibrated conditions at $3 \cdot 10^{-5}$ M recorded in solvents with different polarities. **DMF**, **CH_2Cl_2**, **THF** and **toluene**. The samples have been excited at λ_{exc} = 270 nm.

Table 5.3 Photophysical properties of **TR2** in DMF, CH_2Cl_2, THF and toluene in air equilibrated conditions at room temperature.

Solvent	$\lambda_{max,abs}$ (ε) [nm, (10^3 M^{-1} cm^{-1})]	λ_{em} [nm]
Toluene	326 (19.6), 388 (2.4), 430 (0.9)	469,503
CH_2Cl_2	326 (19.9), 388 (2.4), 430 (0.7)	468, 501
THF	325 (16.3), 388 (2.0), 430 (0.6)	472,504
DMF	325 (19.4), 388 (1.8), 430 (0.6)	473, 501

Low temperature experiments in frozen 2Me-THF glassy matrix at 77 K were carried out to gain deeper insights onto the nature of the emissive excited state. Upon excitation at λ_{exc} = 380 nm, for all three samples emission spectra display only a minor hypsochromic shift compared to the room temperature photoluminescence (shift 141 cm^{-1}). In addition, time-resolved decay analysis reveals that **TR1** and **TR3** maintain a longer lifetime (τ = 7.1 and 5.9 µs, respectively), while sample of complex **TR2** displays the shortest one (τ = 3.7 µs) among the investigated series, in accordance with photoluminescence data recorded at room temperature. All complexes display three main emission peaks moving from 460 to 481 nm with an average spacing of *ca.* 1400 cm^{-1} attributable to the intraligand vibrational modes as C=C and C=N stretching (see *Figure 5.10*).

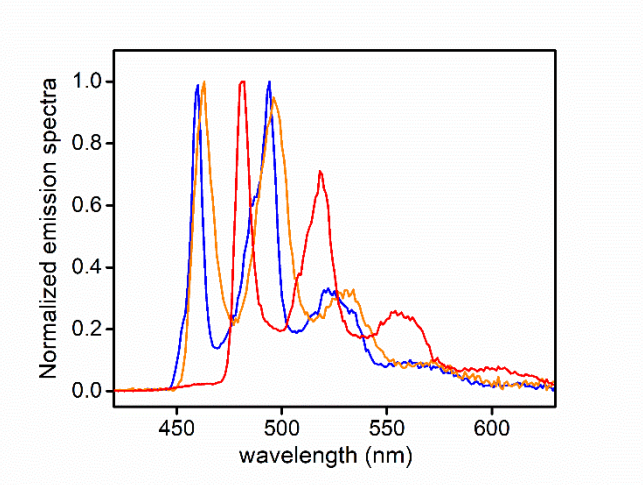

Figure 5.10 Emission spectra for **TR1-3** complexes in in 2-MeTHF at 77 K. Samples were excited at λexc = 380 nm. (**TR1**, blue trace; **TR2**, orange trace; **TR3** red trace).

The emission spectra of **TR1-3** in PMMA thin films at 5 wt.% doping level are showed in *Figure 5.11* and data are summarized in *Table 5.4*. The corresponding excitation spectra are displayed in *Figure ES5.17*. The thin films were obtained by the spin-coating technique using Suprasil quartz slabs. As far as complex **TR1** is concerned, its emission profile maintains similar shape to that recorded in solution (*Figure 5.7*), with also no shift of the maxima (λ_{em} = 463, 497 and 524 nm). Expectantly, lifetime decay becomes biexponential with the appearance of two component, namely a shorter one of τ = 2.5 µs (32%) and a longer one with τ = 5.9 µs (68%). This latter recalls the lifetime value found in solution (τ = 6.2 µs). Moreover, the PLQY is similar as well with value of 63.0% in thin film *vs* 61.6% in

degassed conditions. Overall, these finding indicate that at such low doping concentration **TR1** sample display a no intermolecular interactions amongst emissive complexes and negligible triplet-triplet annihilation phenomena.

Complex **TR2** displays a different emission profile in doped PMMA when compared to the sample in CH_2Cl_2 solution. In particular, emission profile in thin-film appears broader and featureless with a maximum centered at λ_{em} = 470 nm. This emission is characterized by an excited state decay kinetics (when measured at λ_{em} = 470) that can be fitted with a bi-exponential model, being τ_1 = 487 ns (84%) and τ_2 = 1.6 µs (16%), along with highly quenched emission (PLQY = 7.3%). Overall, these finding support the idea that compound **TR2** in PMMA thin-film display a much more pronounced tendency towards intermolecular aggregation and triplet-triplet quenching processes. It should be pointed out that a vibronically-structured band is also visible at shorter wavelength (λ_{em} = 417 and 439 nm). At the current stage this band is tentatively assigned to the presence of an impurity in the sample. A series of additional experiments are required to clearly elucidate the origin of such band. Unfortunately, they could have not been done so far due to the lack of additional sample.

As for complex **TR3**, photoluminescence spectrum in PMMA display a vibronic progression with similar wavelength maxima than those observed in solution but with different intensity ratio. Bi-exponential lifetime is recoded as well, with τ_1 = 498 ns (80%) and τ_2 = 1.6 µs (20%) along with a PLQY of 9.0%, indicative of quenching process occurring to a larger extent if compared to the CH_2Cl_2 solution sample.

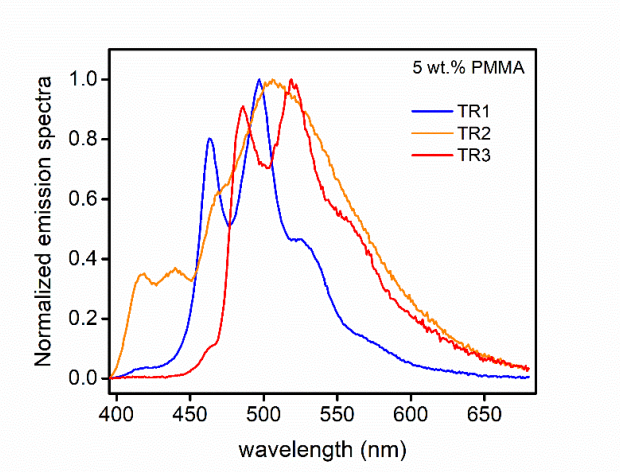

Figure 5.11 Emission spectra for **TR1-TR3** 5 wt.% in PMMA thin films. λ_{exc} = 380 nm

Table 5.4 Photophysical properties of complexes **TR1-3** 5 wt.% in PMMA thin films.

Cmpd	λ_{em} [nm]	PLQY (%)	τ_{obs}
TR1	463,497,524 (*sh*)	63.0	5.9 μs (67.9%) 2.5 μs (32.0%)
TR2	417,439,470 (*sh*), 506	7.3	1.6 μs (16.3%) 487.1 ns (83.6%)
TR3	486,518,557 (*sh*)	9.0	1.6 μs (19.1%) 498.3 ns (80.8%)

5.3 Conclusion

In this chapter, it has been described the synthesis and characterization of three novel phosphorescent tridentate Ir(III) complexes bearing a triazolyl derivative ligand as chromophoric ligand and a bis-N-heterocylic carbene to provide the stability of the molecule. For complex **TR2** the atoms connectivity was confirmed by the single X-ray structure. All complexes investigated herein display a stable and long lived vibronic sky-blue phosphorescence. The assignments of the nature of the electronic transitions involved were based on experimental findings.

Compounds **TR1-TR3** display an emission spectrum that are comparable to related derivatives reported by Chi *et al.*.[25,28] On the other hand, the slightly decrease of the PLQY in **TR1-TR3** may be attributed to the non-optimal bite angle of the coordinated [fpbmi] and [tpbmi] ligands. The introduction of a nitrogen atom between the two fluorine on the phenyl ring of the chromophoric ligand can stabilize better the HOMO level, enlarging the HOMO-LUMO gap and may provide more hyspochromically shifted emisison spectra.[19] Investigation in this respect are currently ongoing in the research group where I have carried out my thesis. To conclude, further investigation about dopants emitters for OLED devices should be carried out on **TR1**, which reveals the better photophysical behavior in PMMA thin films.

5.4 Experimental section

5.4.1 Synthesis of [fpbmiH2][PF$_6$] and [tpbmiH2][PF$_6$]

1H-imidazole (3 equiv.), K_2CO_3 (3.3 g, 23.9 mmol or 3.1 g, 23.0 mmol) and CuO (5 mol.%) were added to a solution of 1,3-dibromo-5-tertbutyl-benzene (2.0 g, 6.84 mmol) or 1,3-dibromo-5-(trifluoromethyl)benzene (2.0 g, 6.58 mmol) in DMSO (20 mL) and stirred for 48 h at 150 °C. The solvent was evaporated, and the crude was dissolved in dichloromethane and the yellow solution was filtered on celite. After evaporation of the solvent, the compound is obtained as an oil, then that was μsed for the next step without further purification. CH_3I (1.5 mL, 3.5 eq.) was added to the solution of the crude in DMSO (5 mL) and stirred for 12 h at room temperature. Dichloromethane (40 mL) was added to the solution under stirring and a solid precipitated. Then, it was filtered, washed with DCM and dried under vacuum. Yield of **[fpbmiH$_2$][PF$_6$]$_2$** 70% (2.5 g, 4.58 mmol). Yield of **[tpbmiH$_2$][PF$_6$]$_2$** 55% (2.2 g, 3.77 mmol).

[fpbmiH$_2$][PF$_6$]$_2$ or **[tpbmiH$_2$][PF$_6$]$_2$** was dissolved in methanol (5 mL) and NH_4PF_6 (2.5 eq) was added. The solution stirred for 2 h at room temperature. A white solid precipitated and then filtered, giving the final compound. Yield of **[fpbmiH$_2$][PF$_6$]$_2$** 99% (2.26 g, 3.77 mmol). Yield of **[tpbmiH$_2$][PF$_6$]$_2$** 78% (506 mg, 0.86 mmol).

[fpbmiH$_2$][PF$_6$]$_2$ ^{1}H NMR (500 MHz, CD_3CN) δ: 9.14 (s, 1H), 8.19 (d, *J* = 3.0 Hz, 1H), 7.94 (t, *J* = 1.9 Hz, 1H), 7.65 (t, *J* = 1.8 Hz, 1H), 4.02 (s, 2H). $^{13}C\{^1H\}$ NMR (126 MHz, CD_3CN) δ: 135.8, 124.6, 121.7, 121.4, 114.2. ESI-MS calcd *m/z* 154.06 for $C_{18}H_{24}N_4^{2+}$: Found for (m/z): 154.06. Anal. calcd for $C_{15}H_{15}F_{15}N_4P_2$: C 30.12 H 2.73 N 9.37. Found C 28.44 H 2.67 N 9.48.

[tpbmiH$_2$][PF$_6$]$_2$ ^{1}H NMR (500 MHz, CD_3CN) δ: 9.08 (s, 1H), 7.89 (t, *J* = 1.8 Hz, 1H), 7.83 (d, *J* = 2.0 Hz, 1H), 7.74 (t, *J* = 2.0 Hz, 1H), 7.62 (t, *J* = 1.7 Hz, 1H), 4.00 (s, 1H), 1.46 (s, 4H). $^{13}C\{^1H\}$ NMR (126 MHz, CD_3CN) δ : 136.6, 136.0, 125.0, 121.8, 121.4, 121.0, 117.3, 36.4. ESI-MS calcd *m/z* 148.10 for $C_{18}H_{24}N_4^{2+}$: Found for *m/z* 148.10. Anal. calcd for $C_{18}H_{24}F_{12}N_4P_2$: C 36.87 H 4.13 N 9.56. Found C 35.43 H 4.14 N 9.59.

Supplementary data

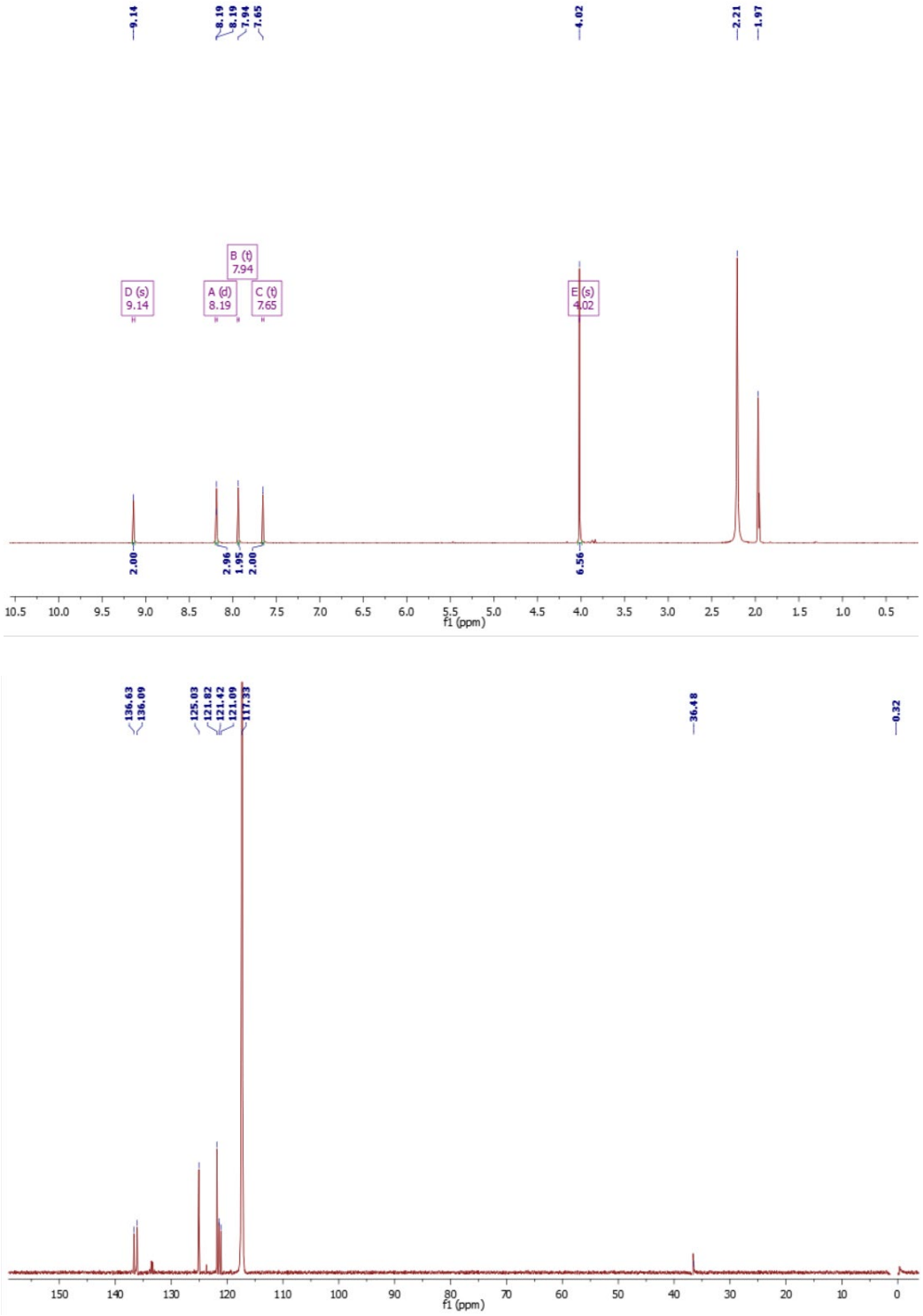

Figure ES5.1 ^{1}H NMR (up) and ^{13}C{^{1}H} NMR (bottom) recorded at 500 MHz in CD_3CN at 298 K for ligand **[fpbmiH_2][PF_6].**

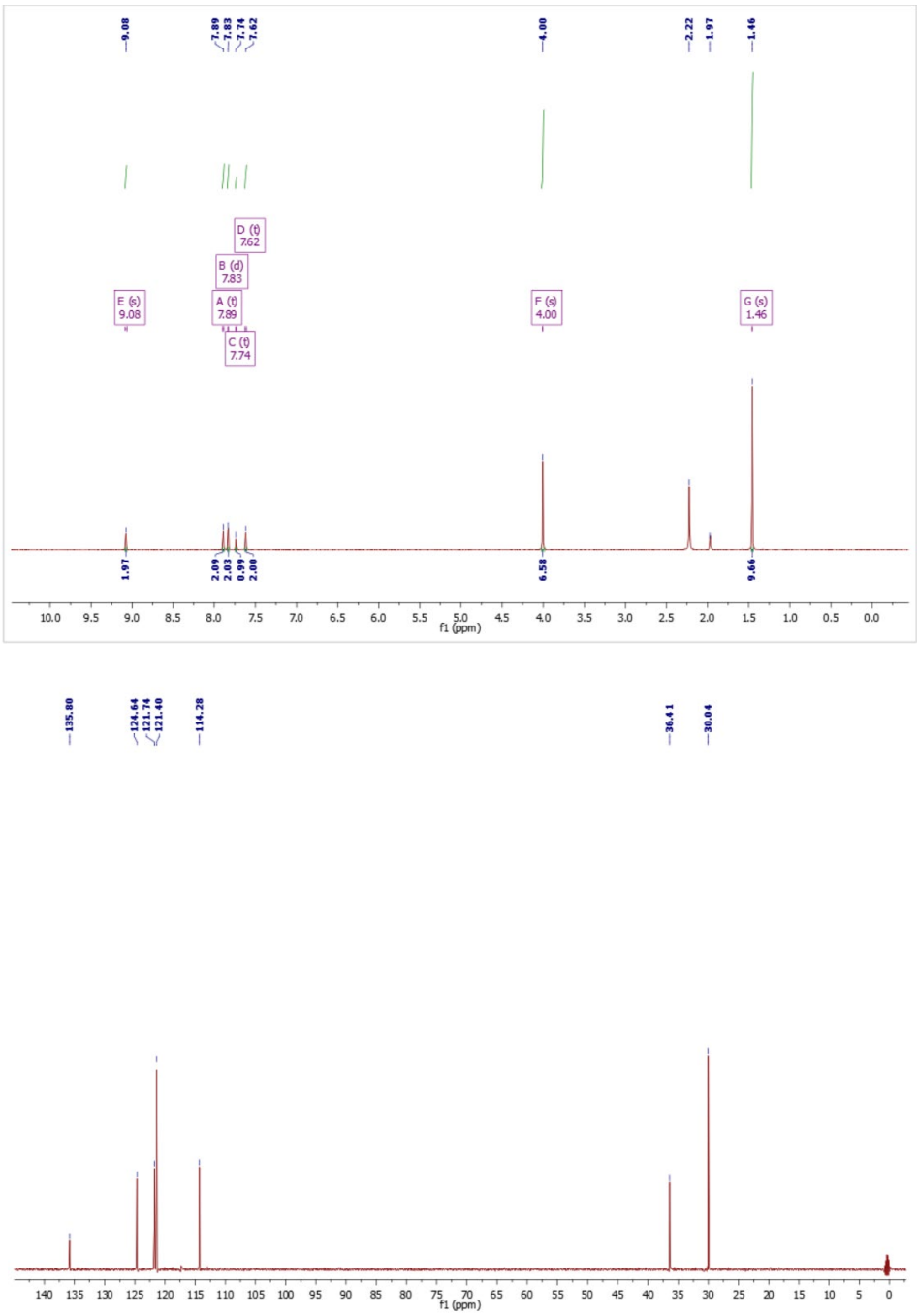

Figure ES5.2 ^{1}H NMR (up) and $^{13}C\{^{1}H\}$ NMR (bottom) recorded at 500 MHz in CD_3CN at 298 K for ligand **[tpbmiH_2][PF_6]**.

5.4.2 Synthesis of $L1H_2$ and $L2H_2$

Synthesis of 1a

A two neck bottom flask was charged with 2-bromo-6-cyano-pyridine (2.0 g, 11.0 mmol), 2,4-difluorophenyl boronic acid (2.1 g, 13.2 mmol) and $Pd(PPh_3)_4$ (0.5 mol.%) then degassed and filled 3 times with argon. In a second two neck bottom flask, K_2CO_3 (4.4 g, 31.9 mmol) was dissolved in a solution of 40 mL of THF:H_2O (v/v 3:1) and bubbled for 15 minute with argon. This solution was added to the solid under argon and the mixture was refluxed at 80 °C for 48 h. After cooling to room temperature, the solution was extracted with ethyl acetate and water, the organic phase was dried with Na_2SO_4 and the solvent removed under vacuum. The product was purified by chromatographic column on SiO_2 μsing a mixture of hexane/ethyl acetate (80:20) by gradient to collect the white solid (Yield 74%, 1.76 g, 8.14 mmol). ^{1}H NMR (300 MHz, $CDCl_3$) δ : 8.18 – 8.07 (m, 1H), 8.04 – 7.99 (m, 1H), 7.90 (td, J = 7.9, 3.0 Hz, 1H), 7.66 (dd, J = 7.1, 2.9 Hz, 1H), 7.26 – 7.00 (m, 1H), 6.94 (ddd, J = 11.3, 8.6, 2.5 Hz, 1H). The chemical characterization is in agreement with the data already reported elsewhere for this compound.[33]

Synthesis of 1b

A two neck bottom flask was charged with 2-bromo-6-cyano-pyridine (1.0 g, 5.5 mmol), (4-(trifluoromethyl)phenyl)boronic acid (1.3 g, 7.1 mmol) and $Pd(PPh_3)_4$ (0.5 mol %) then degassed and filled 3 times with argon. In a second two neck bottom flask, K_2CO_3 (1.5 g, 11.0 mmol) was dissolved in a solution of 40 mL of THF:H_2O (v/v 3:1) and bubbled for 15 minutes with argon. This solution was added to the solid under argon and the mixture was refluxed at 80 °C for 48 h. After cooling to room temperature, the solution was extracted with ethyl acetate and water, the organic phase was dried with Na_2SO_4 and the solvent removed under vacuum. The product was purified by chromatographic column on SiO_2 μsing a mixture of hexane/ethyl acetate (90:10) by gradient to collect the white solid (Yield 67%, 1.2 g, 4.82 mmol).

^{1}H NMR (500 MHz, CD_2Cl_2) δ : 8.22 (dd, *J* = 8.8, 0.7 Hz, 1H), 8.07 (dd, *J* = 8.2, 1.0 Hz, 1H), 8.03 – 7.98 (m, 1H), 7.82 (dd, *J* = 8.8, 0.6 Hz, 1H), 7.76 (dd, *J* = 7.5, 1.0 Hz, 1H). ^{13}C{^{1}H} NMR (126 MHz, CD_2Cl_2) δ : 157.1, 140.6, 138.2, 133.9, 131.6, 131.4, 127.6, 127.4, 125.9, 125.8, 125.1, 123.9, 123.0, 117.2, 53.4. ^{19}F NMR (471 MHz, CD_2Cl_2) δ -63.09. ESI-MS calcd 248.06 for $C_{13}H_7F_3N_2$: found 249.06 ($[M+H]^+$): Anal. Calc for $C_{13}H_7F_3N_2$: C 62.91 H 2.84 N 11.29. Found C 62.91 H 2.85 N 11.62.

Synthesis of 2a

6-(2,4-difluorophenyl)picolinonitrile (2.0 mg, 9.69 mmol) was dissolved in ethanol (60 mL) and N_2H_4 H_2O (5 mL, 96.9 mmol) was added. The solution stirred at room temperature for 18 h. The precipitate formed overnight was filtered and washed with cold ethanol, then dried over filter. (Yield 66%, 1.6 g, 6.44 mmol).

^{1}H NMR (500 MHz, DMSO) δ: 8.25 (dd, *J* = 15.9, 9.0 Hz, 1H), 7.91 (d, *J* = 8.0 Hz, 1H), 7.85 (t, *J* = 7.8 Hz, 1H), 7.71 (d, *J* = 8.9 Hz, 1H), 7.40 (t, *J* = 9.3 Hz, 1H), 7.24 (t, *J* = 8.5 Hz, 1H), 5.85 (s, 2H), 5.44 (s, 2H). ^{13}C{^{1}H} NMR (126 MHz, DMSO) δ : 166.3, 164.0, 163.9, 162.0, 161.9, 161.6, 161.5, 159.6, 159.5, 152.3, 150.0, 143.4, 137.5, 123.7, 123.7, 123.2, 123.2, 112.6, 112.4, 105.2, 105.0, 104.8. ^{19}F{^{1}H} NMR (471 MHz, DMSO) δ : -109.30, -112.25. ESI-MS calcd 248,09 for $C_{12}H_{10}F_2N_4$: Found for 249.09 ([M+H]$^+$): Anal. Calc for $C_{12}H_{10}F_2N_4$: C 58.06 H 4.06 N 22.57. Found C 58.34 H 4.06 N 21.00.

Synthesis of 2b

6-(4-(trifluoromethyl)phenyl) picolinonitrile (1.9 mg, 7.93 mmol) was dissolved in ethanol (60 mL) and N_2H_4 H_2O (4 mL, 79.3 mmol) was added. The solution stirred at room temperature for 18 h. The solvent was evaporated and the white solid was washed and filtered with water. (Yield 81%, 2.7 g, 9.7 mmol).

^{1}H NMR (500 MHz, DMSO) δ : 8.42 (d, *J* = 6.6 Hz, 1H), 7.99 (d, *J* = 7.3 Hz, 1H), 7.91 (dt, *J* = 15.3, 7.8 Hz, 1H), 7.85 (d, *J* = 8.2 Hz, 1H), 5.96 (s, 1H). ^{13}C{^{1}H} NMR (126 MHz, DMSO) δ : 153.0, 152.0, 142.5, 138.1, 127.8, 126.1, 120.5, 119.3, 39.7. ^{19}F{^{1}H} NMR (471 MHz, DMSO) δ: -61.02. ESI-MS calcd 280,09 for $C_{13}H_{11}F_3N_4$: Found for 281.10 ([M + H]+): Anal. Calc for $C_{13}H_{11}F_3N_4$: C 55.71 H 3.96 N 19.99. Found C 55.58 H 4.21 N 19.33.

General procedure for $L1H_2$ and $L2H_2$

A two neck round bottom flask was loaded with **1a** or **2a** (3.5 g, 14.11 mmol for **$L1H_2$**; 2.7 g, 9.77 mmol for **$L2H_2$**) and suspended in diethylene glycol dimethyl ether (30 mL for **$L1H_2$**; 20 mL for **$L2H_2$**). Trifluoroacetic anhydride (4.3 mL, 31.04 mmol for **$L1H_2$**; 3 mL, 21.49 mmol for **$L2H_2$**) was slowly added to the mixture at room temperature. The solution was stirred for ten minutes at room temperature then heated at 160 °C for 2 h. After cooling to room temperature, distillated water (84 mL for **$L1H_2$**; 58 mL for **$L2H_2$**) was added, followed by HCl (2.4 mL for **$L1H_2$**; 1.6 mL for **$L2H_2$**) and the mixture stirred at 90 °C overnight. The solution

was then cooled down to room temperature and stirred for 1 hour. The white precipitate was filtered and washed with water and petroleum ether.

$L1H_2$. Yield 47% (2.16 g, 6.65 mmol). ^{1}H NMR (500 MHz, CD_3CN) δ: 8.37 (td, J = 9.0, 6.7 Hz, 1H), 8.13 (dd, J = 7.7, 1.1 Hz, 1H), 8.08 (t, J = 7.8 Hz, 1H), 8.01 (ddd, J = 7.9, 2.1, 1.2 Hz, 1H), 7.22 (dddd, J = 8.9, 8.2, 2.5, 0.9 Hz, 1H), 7.16 (ddd, J = 11.7, 9.1, 2.5 Hz, 1H). $^{13}C\{^{1}H\}$ NMR (126 MHz, CD3CN) δ: 155.9, 152.3, 145.2, 138.7, 132.8, 126.0, 125.9, 120.3, 117.3, 117.3, 112.0, 111.8, 104.4. $^{19}F\{^{1}H\}$ NMR (471 MHz, CD_3CN) δ -65.94, -109.97, -113.20. ESI-MS calcd 326.06 for $C_{14}H_7F_5N_4$: Found 327.06 for ($[M + H]^+$): Anal. calcd for $C_{14}H_7F_5N_4$: C 51.54 H 2.16 N 17.17. Found C 50.46 H 2.24 N 16.85.

$L2H_2$. Yield 62% (2.18 g, 6.08 mmol). ^{1}H NMR (500 MHz, CD_2Cl_2) δ 8.26–8.22 (m, 1H), 8.09 (t, *J* = 7.8 Hz, 1H), 8.00 (dd, *J* = 8.0, 1.0 Hz, 1H), 7.83 (d, *J* = 8.2 Hz, 1H). $^{13}C\{^{1}H\}$ NMR (126 MHz, CD_2Cl_2) δ: 164.7, 164.6, 162.7, 162.6, 161.8, 161.7, 159.8, 159.7, 155.7, 155.1, 154.7, 152.8, 152.7, 144.7, 138.4, 132.1, 132.1, 132.1, 132.0, 126.3, 126.2, 122.7, 122.6, 120.3, 118.2, 112.0, 112.0, 111.9, 111.8, 104.7, 104.5, 104.3. $^{19}F\{^{1}H\}$ NMR (471 MHz, CD_2Cl_2) δ: -63.01, -65.75. ESI-MS calcd 358.07 for $C_{15}H_8F_6N_4$: Found 359.07 for ($[M + H]^+$): Anal. Calcd for $C_{15}H_8F_6N_4$: C 50.29 H 2.25 N 15.64. Found C 50.28 H 2.54 N 15.13.

$L3H_2$. Yield 68% (3.01 g, 9.06 mmol). ^{1}H NMR (500 MHz, CD_2Cl_2) δ: 8.10 (d, J = 6.9 Hz, 1H), 8.06 (td, J = 8.9, 6.7 Hz, 1H), 7.91 (t, J = 7.8 Hz, 1H), 7.81 (dd, J = 8.3, 1.7 Hz, 1H), 7.04 (td, J = 8.3, 2.8 Hz, 1H), 6.97 (ddd, J = 11.4, 8.9, 2.5 Hz, 1H), 1.43 (s, 9H). $^{19}F\{^{1}H\}$ NMR (471 MHz, CD_2Cl_2) δ: -109.39, -112.80. The chemical characterization is in agreement with the data already reported elsewhere for this compound.[33]

Supplementary data

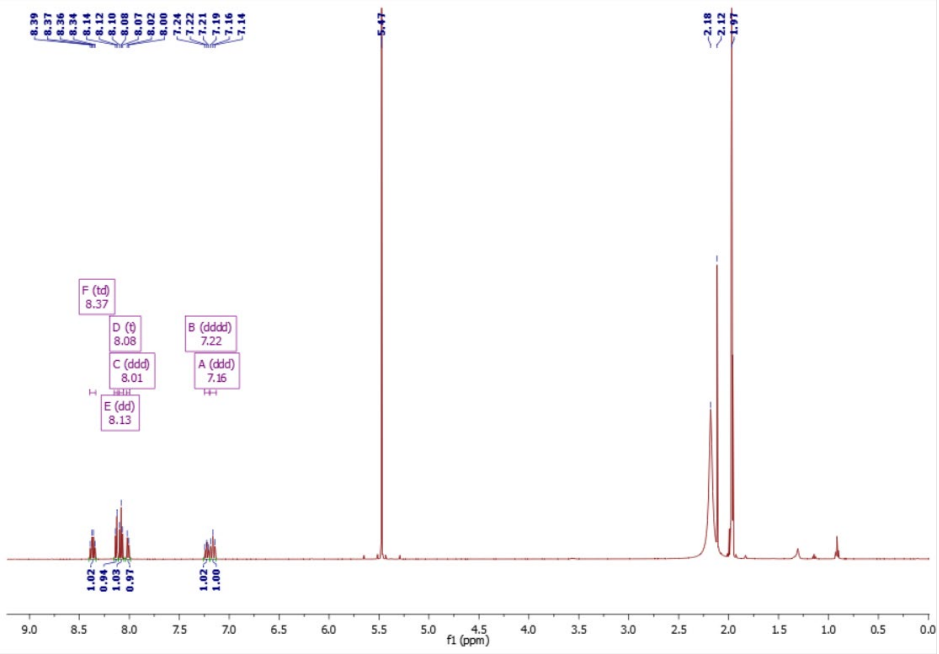

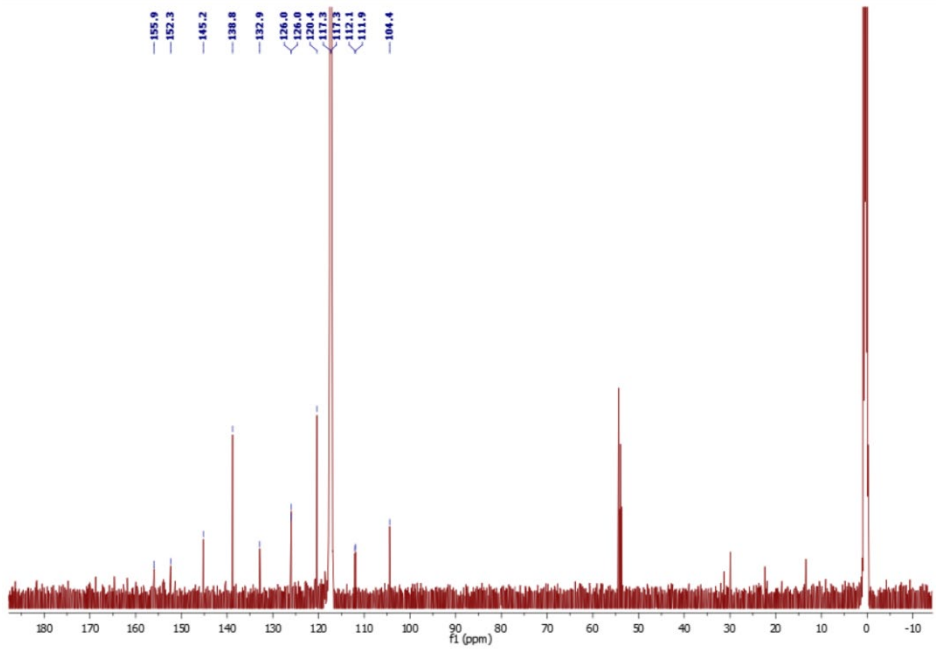

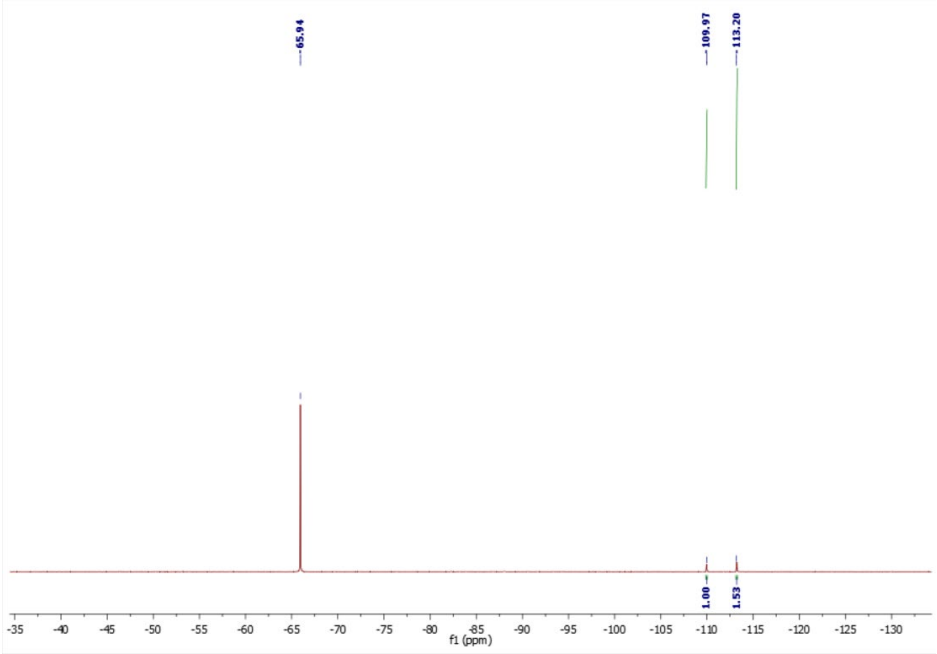

Figure ES5.3 ^{1}H NMR (up), $^{13}C\{^{1}H\}$ NMR (middle) and $^{19}F\{^{1}H\}$ NMR (bottom) recorded at 500 MHz in CD_3CN at 298 K for ligand **L1H$_2$**.

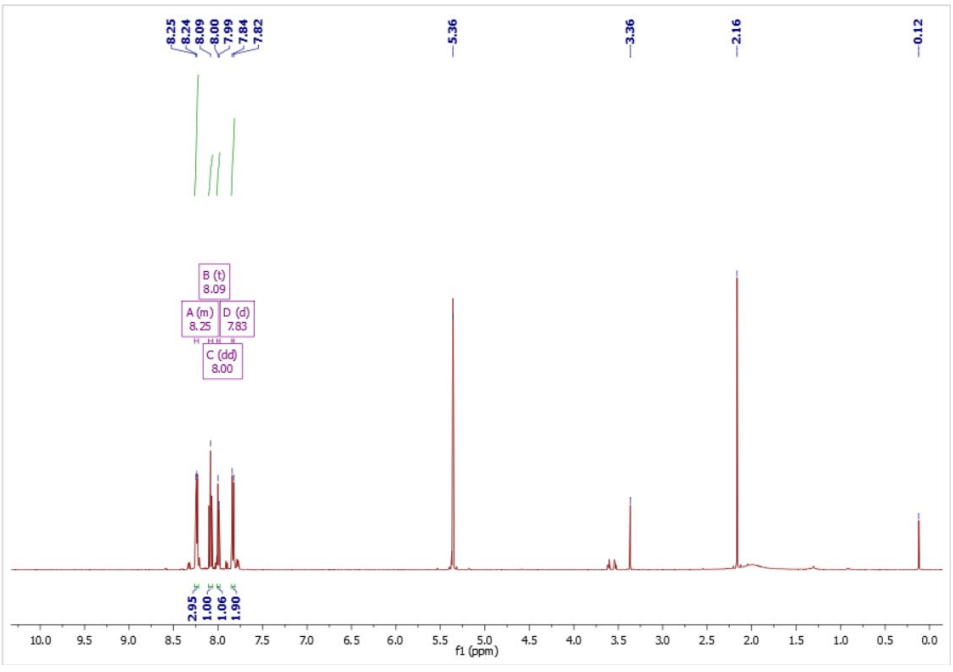

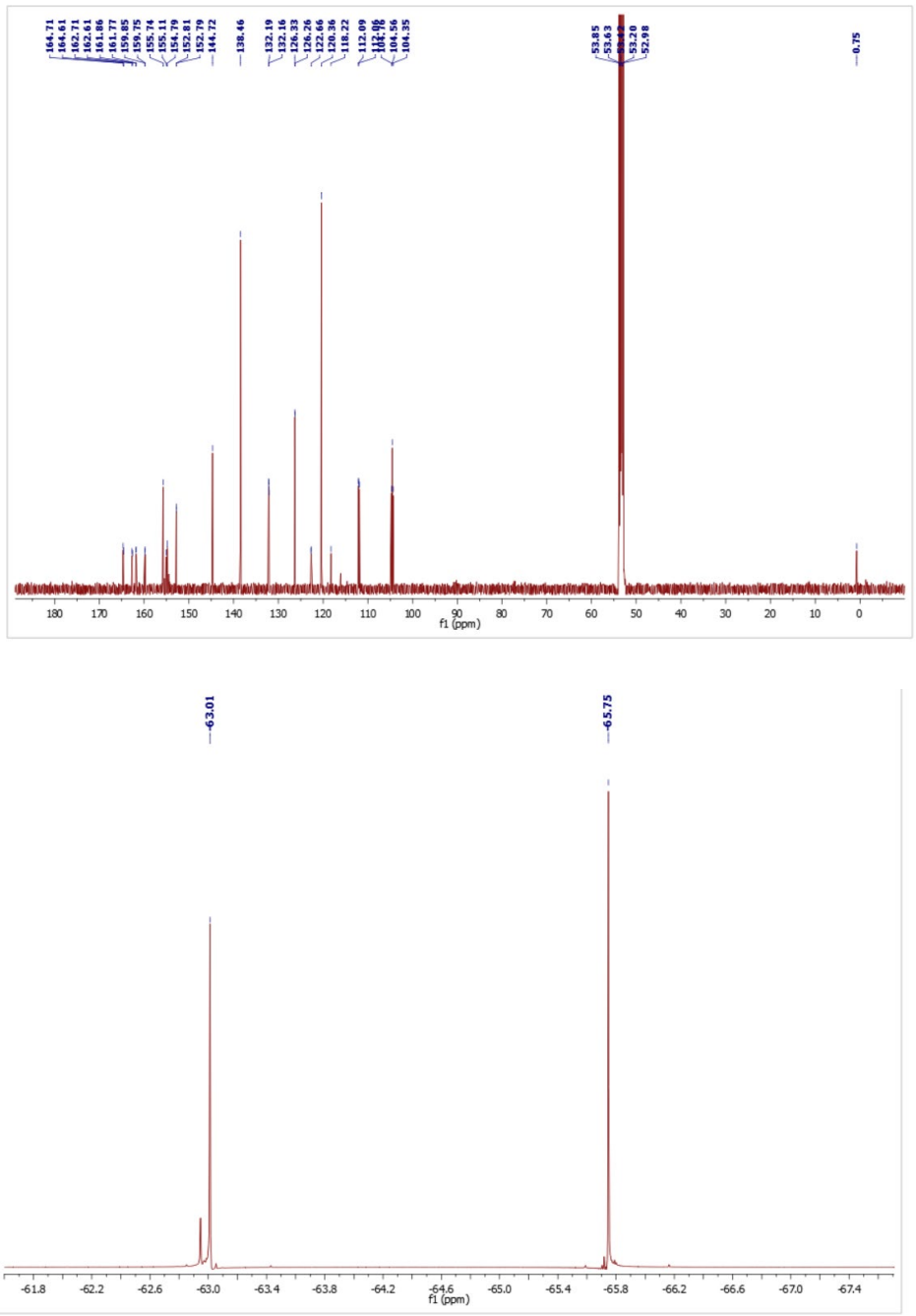

Figure ES5.4 ^{1}H NMR (up), $^{13}C\{^{1}H\}$ NMR (middle) and $^{19}F\{^{1}H\}$ NMR (bottom) recorded at 500 MHz in CD_2CL_2 at 298 K for ligand **L2H$_2$**.

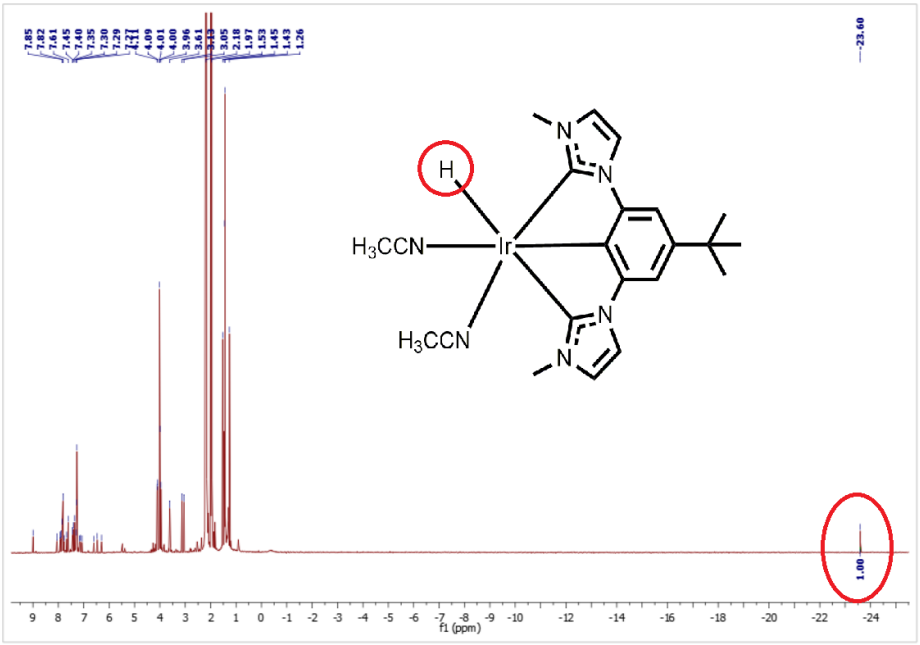

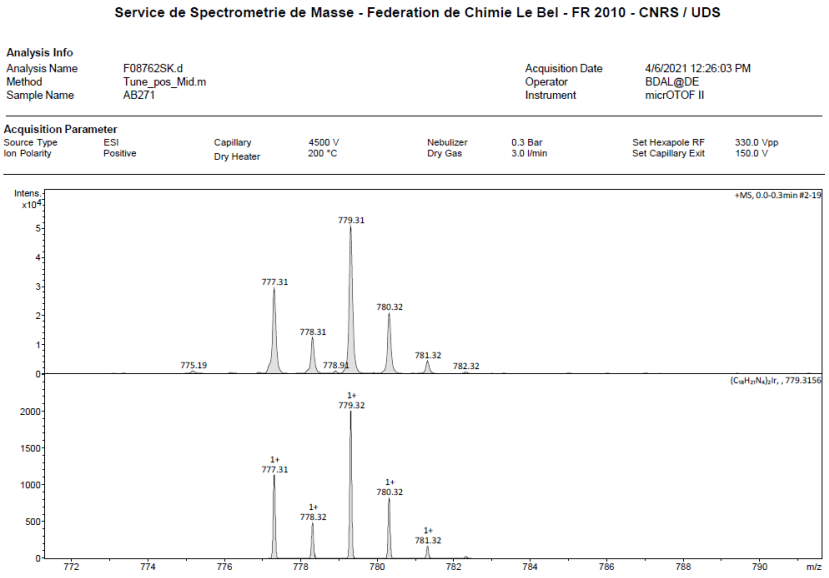

Figure ES5.5 ^{1}H NMR (*top*) recorded at 500 MHz in CD_3CN and HR-MS spectra (*bottom*) for the intermediate $[Ir(CH_3CN)_2(H)(tpbmi)]$.

5.4.3 General procedure for the synthesis of the target Ir(III) complexes

A mixture of **[fpbmiH$_2$][PF$_6$]$_2$** or **[tpbmiH$_2$][PF$_6$]$_2$** (1 equiv.), [Ir(COD)(μ-Cl)]$_2$ (0.5 equiv.), and NaOAc (10 equiv.) was first heated in anhydrous acetonitrile (15 mL) under inert atmosphere for 12 h and then evaporated to dryness. Decalin (15 mL) and triazolyl ligand **L1H$_2$** or **L2H$_2$** (1 equiv.) were added and the mixture was heated at 200°C for 48 h for **TR2** and at 230°C for 2 hours at 100 W for **TR1** and **TR3**. After cooling down, decalin was removed under vacuum and the crude of the reaction was dissolved in dichloromethane and then filtered over celite. The solvent was evaporated, and the compound was purified on chromatographic column on SiO_2 using DCM/n-hexane (80:20) for **TR1** and **TR2** and DCM/ethyl acetate (50:50) for **TR3**.

TR1: Yield 6% (15 mg, 0.018 mmol). ^{1}H NMR (500 MHz, CD_2Cl_2) δ: 8.12 (d, J = 6.9 Hz, 1H), 8.02 (t, J = 7.9 Hz, 1H), 7.93 (d, J = 7.4 Hz, 1H), 7.74 (d, J = 14.2 Hz, 2H), 7.63 (d, J = 19.7 Hz, 4H), 6.75 (d, J = 2.0 Hz, 2H), 5.52 (s, 1H), 2.85 (s, 7H).^{13}C{^{1}H} NMR (126 MHz, CD_2Cl_2) δ: 165.4, 162.7, 148.9, 144.8, 140.2, 137.8, 126.3, 126.2, 122.1, 121.6, 121.6, 121.0, 120.9, 116.1, 116.0, 115.9, 115.7, 115.6, 108.2, 108.1, 104.8.^{13}C NMR (DEPT, 126 MHz, CD_2Cl_2) δ 165.4, 164.3, 162.7, 162.3, 155.5, 148.9, 146.4, 146.3, 144.8, 138.2, 137.8, 126.3, 126.2, 123.7, 122.1, 121.6, 121.6, 121.0, 120.9, 116.4, 116.0, 116.0, 115.9, 115.7, 115.6, 108.2, 108.1, 104.8, 104.4. ^{19}F{^{1}H} NMR (471 MHz, CD_2Cl_2) δ: -60.56, -63.97, -109.07, -110.47. ESI-MS calcd 822.11 for $C_{29}H_{17}F_8IrN_8$: Found 823.11 for (M+H): Anal. calcd for $C_{29}H_{17}F_8IrN_8 \cdot H_2O$: C 41.48; H 2.28; N 13.34. Found C 41.95; H 2.50; N 12.38.

TR2: Yield 16% (25 mg, 0.03 mmol). ^{1}H NMR (500 MHz, acetone-d$_6$) δ: 8.32 (dd, *J* = 8.2, 1.0 Hz, 1H), 8.18 (t, *J* = 7.9 Hz, 1H), 8.12 (dd, *J* = 7.8, 1.0 Hz, 1H), 8.06 (d, *J* = 2.0 Hz, 2H), 7.67 (s, 2H), 7.01 (d, *J* = 2.0 Hz, 2H), 6.46 (ddd, *J* = 12.7, 9.3, 2.5 Hz, 1H), 5.45 (dd, *J* = 8.8, 2.5 Hz, 1H), 2.88 (s, 7H), 1.55 (s, 7H). ^{13}C{^{1}H} NMR (126 MHz, CD_2Cl_2) δ: 165.4, 165.2, 164.7, 160.6, 149.6, 149.0, 146.4, 144.4, 144.2, 137.6, 137.2, 120.91, 120.8, 120.1, 119.9, 116.7, 116.6, 116.2, 115.8, 115.7, 115.4, 115.3, 105.2, 105.1, 96.4, 96.2, 96.0. ^{13}C NMR (DEPT, 126 MHz, CD_2Cl_2) δ 165.4, 165.2, 164.7, 164.1, 164.0, 162.7, 162.0, 160.6, 149.6, 149.5, 149.0, 146.4, 146.1, 144.4, 144.2, 137.6, 137.2, 126.1, 126.0, 120.9, 120.9, 120.8, 120.1, 119.9, 116.7, 116.7, 116.6, 116.6, 116.2, 115.8, 115.7, 115.4, 115.3, 107.7, 107.6, 105.2, 105.1, 104.8, 96.4, 96.2, 96.0. ^{19}F{^{1}H} NMR (471 MHz, acetone-d$_6$) δ -63.84, -110.51,

-111.71. ESI-MS calcd 310.18 for $C_{32}H_{26}F_5IrN_8$: Found 811.18 for (M+H): Anal. calcd for $C_{32}H_{26}F_5IrN_8 \cdot 2H_2O$: C 45.44; H 3.57; N 13.25. Found C 45.62; H 3.37; N 13.02.

TR3: Yield 5% (15 mg, 0.017 mmol). ^{1}H NMR (500 MHz, acetone-d_6) δ: 8.39 (dd, *J* = 8.1, 0.9 Hz, 1H), 8.29 (d, *J* = 2.1 Hz, 1H), 8.25 (t, *J* = 7.9 Hz, 1H), 8.17 (d, *J* = 2.1 Hz, 2H), 8.07 (d, *J* = 8.1 Hz, 1H), 7.88 (s, 2H), 7.14 (d, *J* = 2.2 Hz, 2H), 7.05 (d, *J* = 2.1 Hz, 2H), 2.89 (s, 5H). ^{13}C{^{1}H} NMR (126 MHz, CD_2Cl_2) δ: 138.0, 131.1, 124.3, 122.1, 121.6, 118.0, 117.2, 116.9, 115.9, 115.7, 104.9, 104.7. ^{13}C NMR (DEPT, 126 MHz, CD_2Cl_2) δ: 165.0, 162.4, 159.2, 155.0, 149.2, 147.4, 145.4, 144.7, 143.3, 137.9, 131.1, 131.1, 130.4, 130.2, 124.3, 124.1, 123.9, 122.1, 121.6, 118.0, 118.0, 117.2, 116.9, 115.9, 115.7, 104.9, 104.9, 104.9, 104.7, 104.7,^{19}F{^{1}H} NMR (471 MHz, acetone-d_6) δ: -60.42, -63.21, -63.91. ESI-MS calcd 854.11 for $C_{30}H_{18}F_9IrN_8$: Found 855.11 for (M+H): Anal. calcd for $C_{30}H_{18}F_9IrN_8 \cdot C_4H_8O_2$: C 43.36; H 2.78; N 11.90. Found C 42.81; H 2.64; N 11.97.

TR2.b: Yield 13% (23 mg, 0.02 mmol). ^{1}H NMR (500 MHz, CD_2Cl_2) δ: 8.25 (dd, J = 7.9, 1.7 Hz, 1H), 7.74 (t, J = 7.7 Hz, 1H), 7.49 (dd, J = 18.8, 2.0 Hz, 2H), 7.04 (s, 1H), 6.95 (s, 1H), 6.88 (t, J = 1.5 Hz, 2H), 6.69 (dd, J = 7.5, 1.6 Hz, 1H), 6.37 (td, J = 9.0, 3.1 Hz, 1H), 6.22 (td, J = 9.3, 2.4 Hz, 1H), 6.01 (td, J = 8.3, 6.4 Hz, 1H). ^{19}F{^{1}H} NMR (471 MHz, CD_2Cl_2) δ -63.32, -107.73, -112.03. ESI-MS calcd 838.10 for $C_{32}H_{27}F_5IIrN_8$: Found 839.11 for (M+H).

Supplementary data

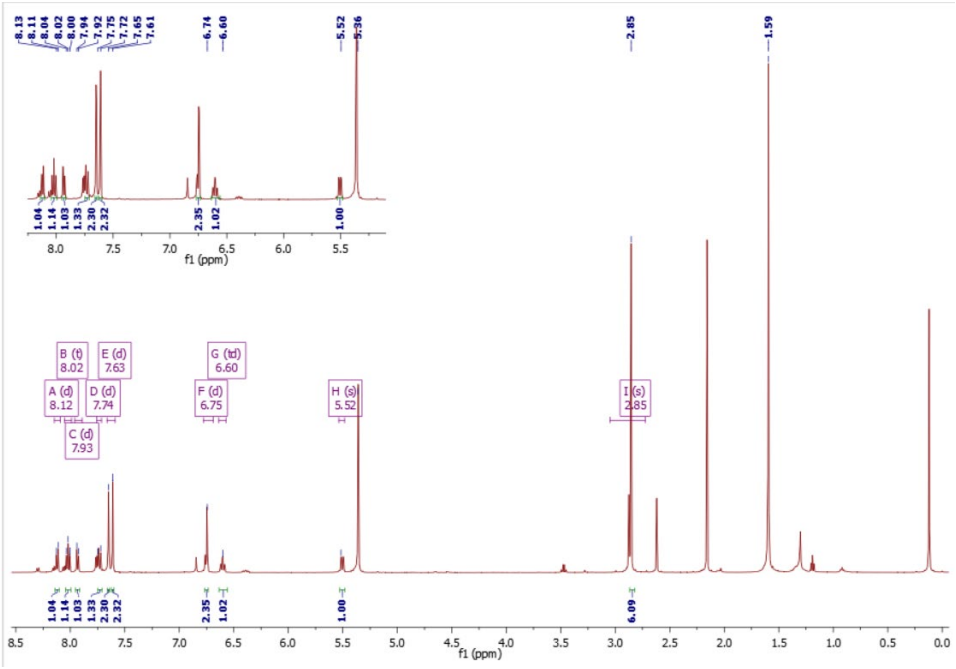

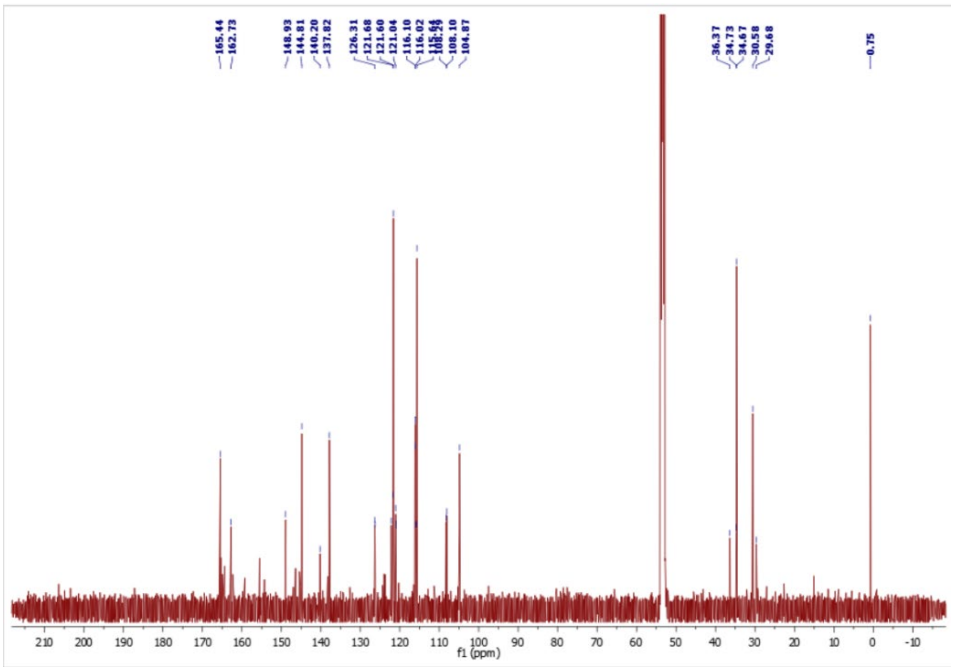

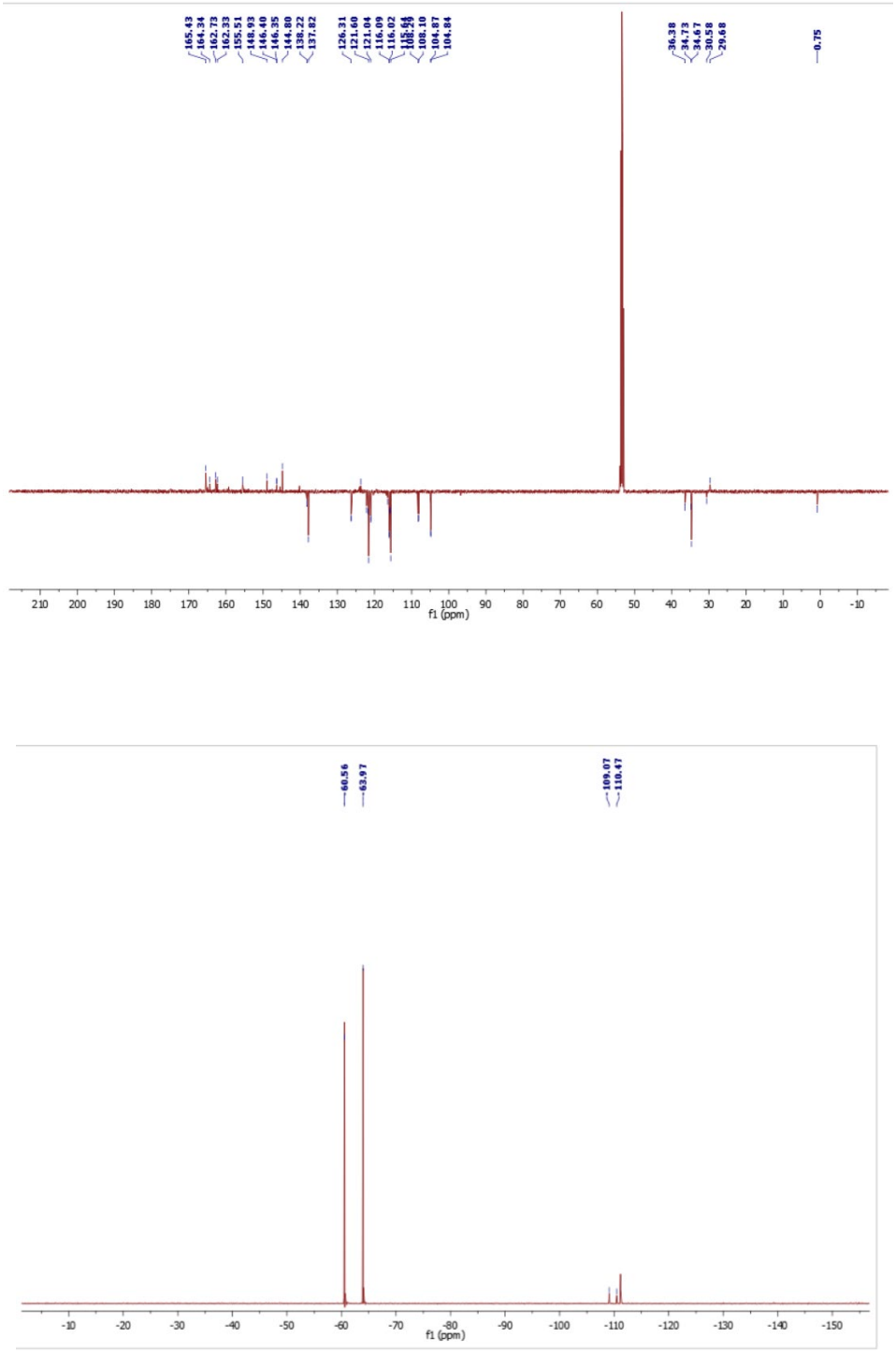

Figure ES5.6 ^{1}H NMR (up), $^{13}C\{^{1}H\}$ NMR and ^{13}C-DEPT NMR (middle) and $^{19}F\{^{1}H\}$ NMR (bottom) recorded at 500 MHz in CD_2Cl_2 at 298 K for compound **TR1**.

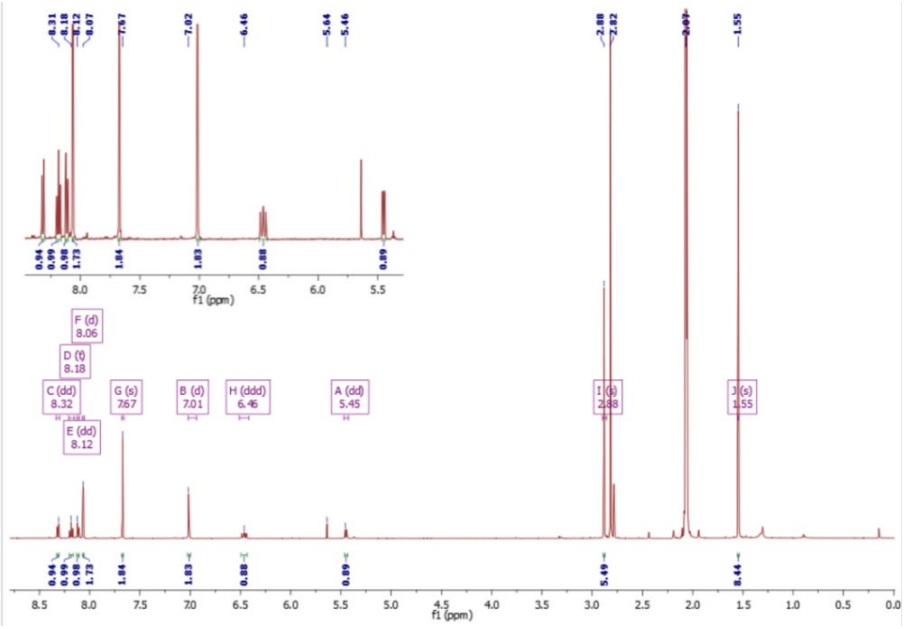
F (d) 8.06
D (t) 8.18
C (dd) 8.32
E (dd) 8.12
G (s) 7.67
B (d) 7.01
H (ddd) 6.46
A (dd) 5.45
I (s) 2.88
J (s) 1.55
f1 (ppm)

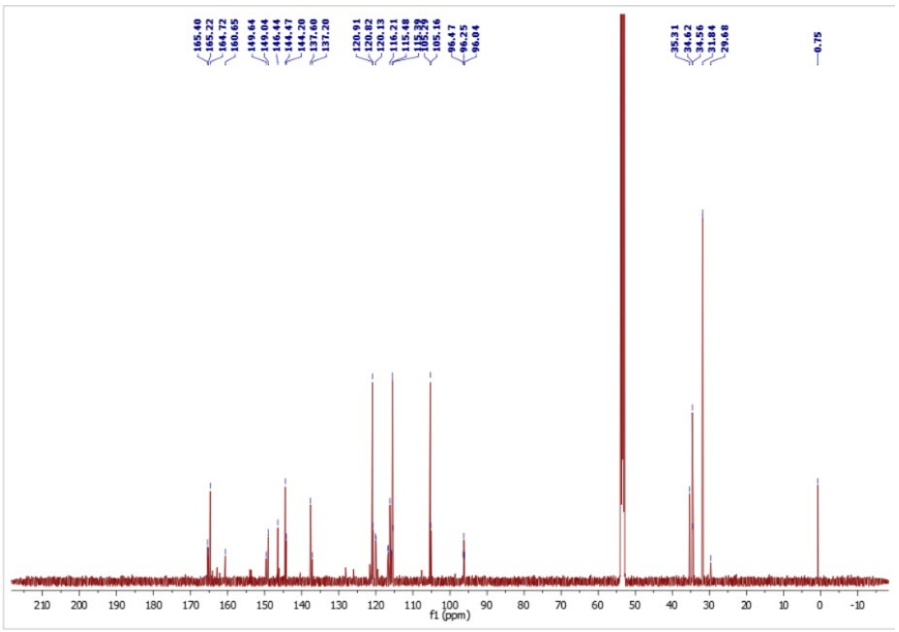
f1 (ppm)

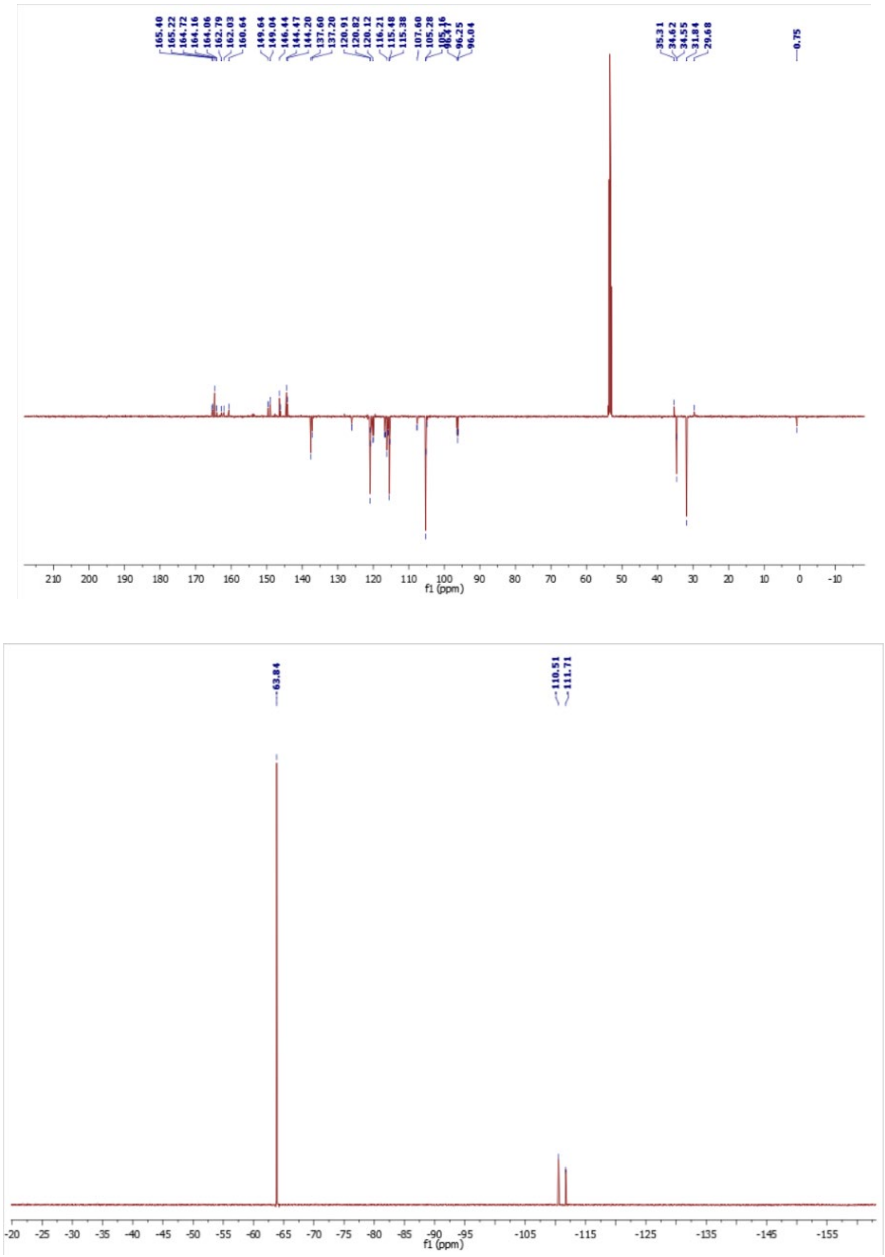

Figure ES5.7 ^{1}H NMR (up), $^{13}C\{^{1}H\}$ NMR and ^{13}C-DEPT NMR (middle) and $^{19}F\{^{1}H\}$ NMR (bottom) recorded at 500 MHz in d_6-acetone for ^{1}H and ^{19}F and CD_2Cl_2 for $^{13}C\{^{1}H\}$ and ^{13}C-DEPT at 298 K for compound **TR2**.

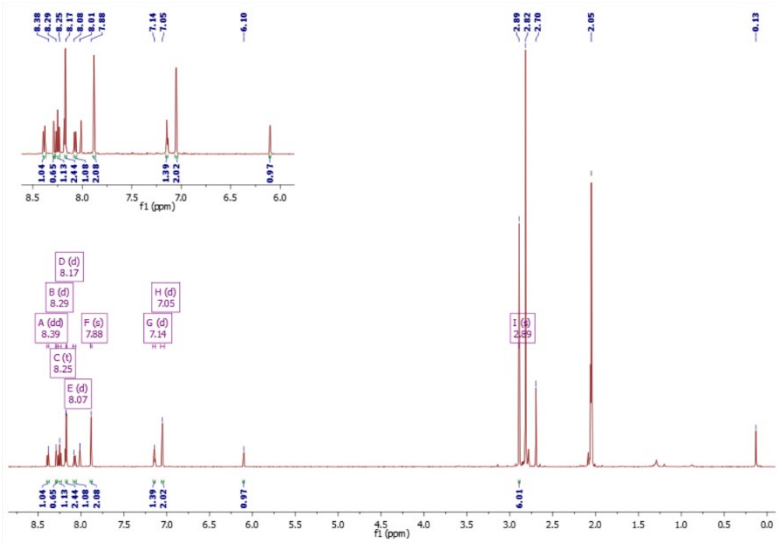
D (d) 8.17
B (d) 8.29
A (dd) 8.39
F (s) 7.88
H (d) 7.05
G (d) 7.14
I (s) 2.89
C (t) 8.25
E (d) 8.07
f1 (ppm)

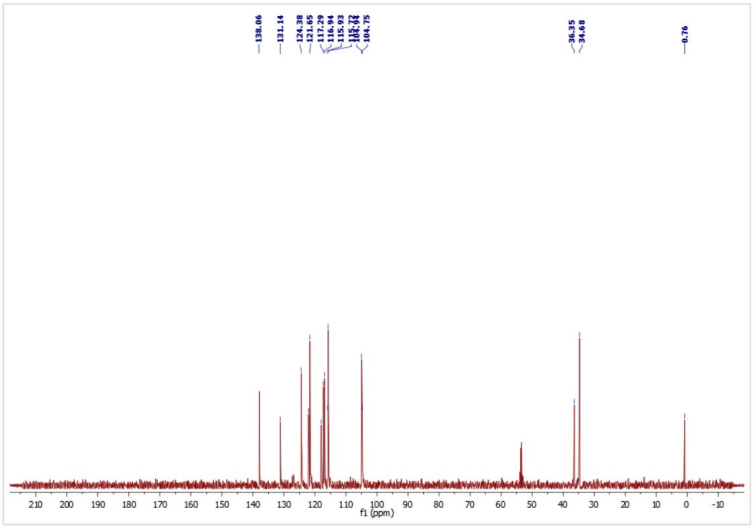
f1 (ppm)

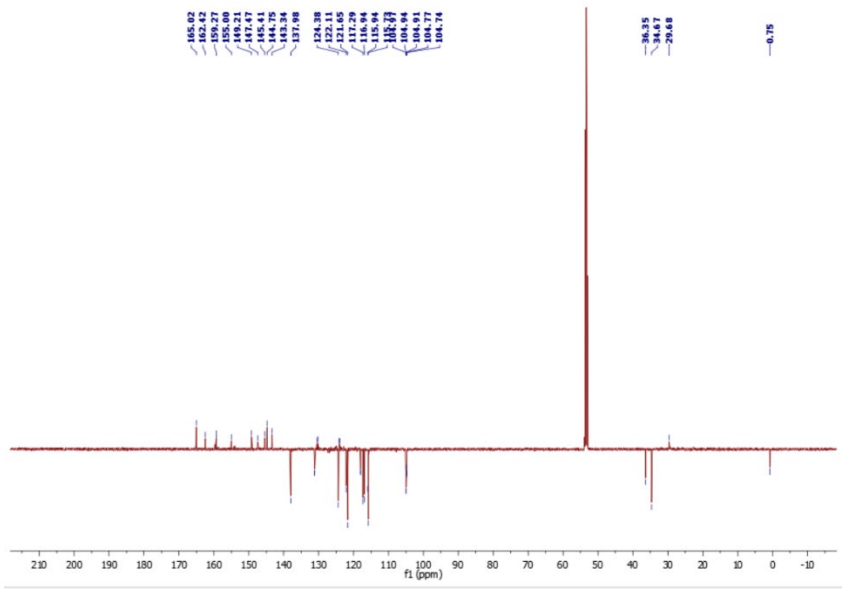
f1 (ppm)

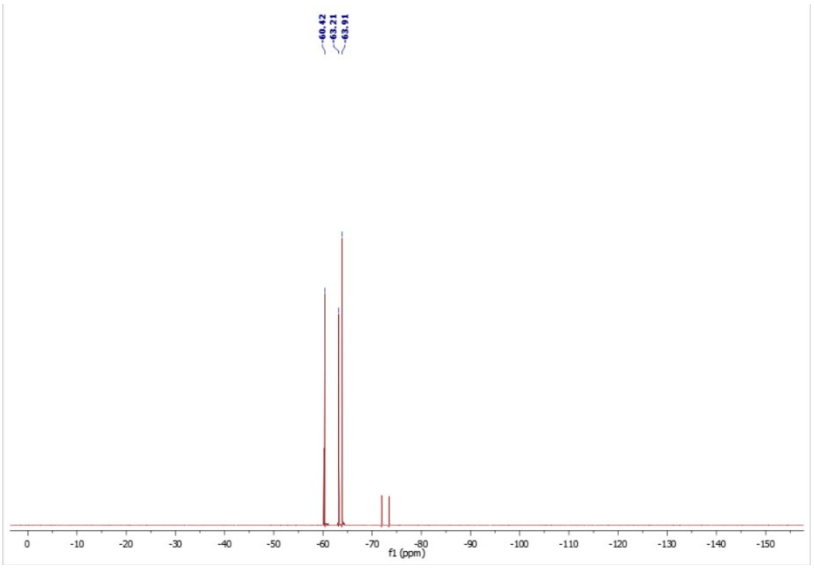

Figure ES5.8 ^{1}H NMR (up), $^{13}C\{^{1}H\}$ NMR and ^{13}C-DEPT NMR (middle) and $^{19}F\{^{1}H\}$ NMR (bottom) recorded at 500 MHz in d_6-acetone for ^{1}H and ^{19}F and CD_2Cl_2 for $^{13}C\{^{1}H\}$ and ^{13}C-DEPT at 298 K for compound **TR3**.

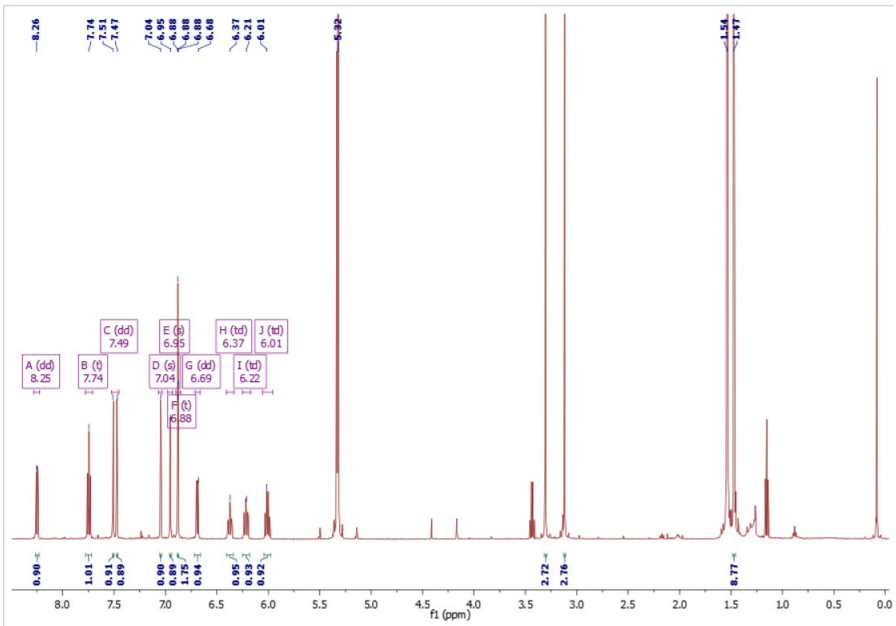

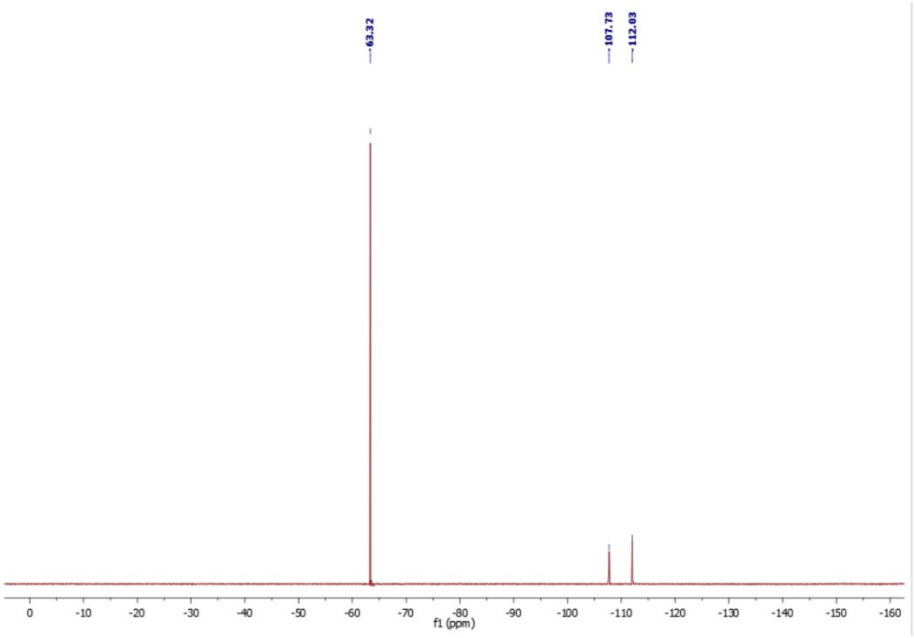

Figure ES5.9 ^{1}H (*up*) and $^{19}F\{^{1}H\}$ (*bottom*) NMR recorded at 500 MHz in CD_2Cl_2 at 298 K for compound **TR2.b.**

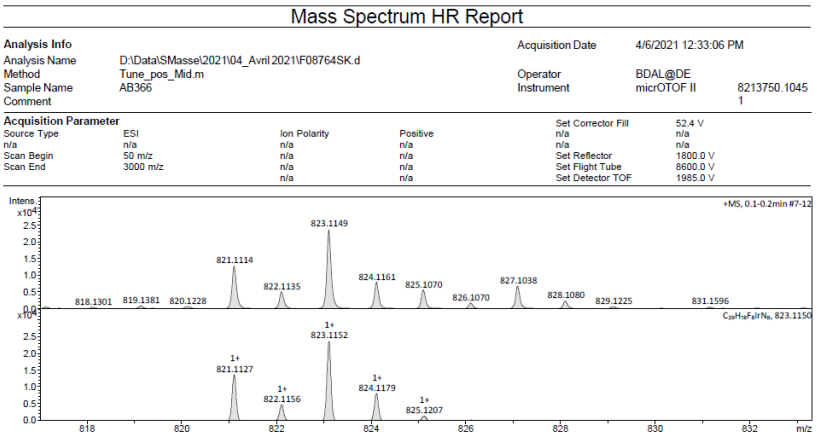

Figure ES5.10 HR-MS spectra for compound **TR1**.

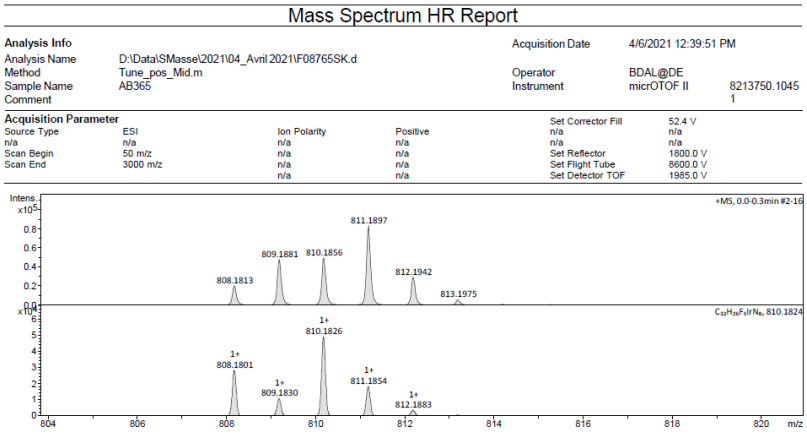

Figure ES5.11 HR-MS spectra for compound **TR2**.

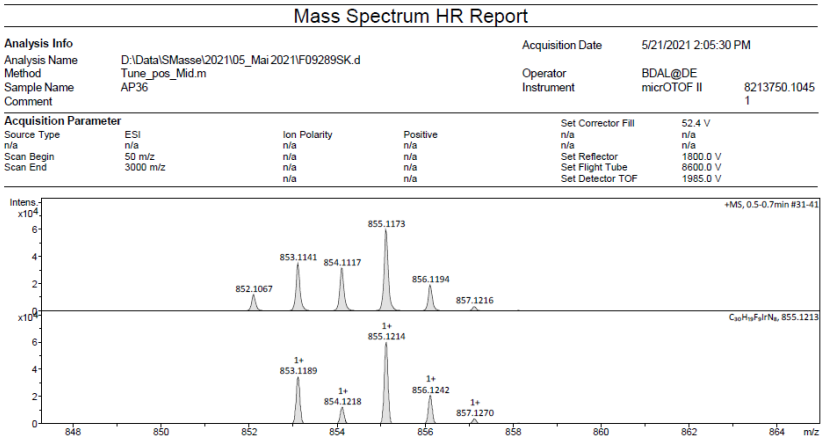

Figure ES5.12 HR-MS spectra for compound **TR3**.

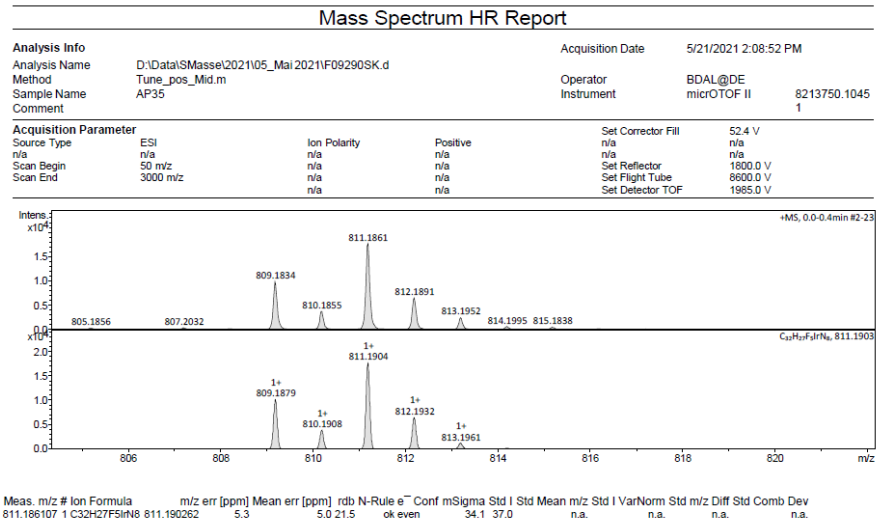

Figure ES5.13 HR-MS spectra for compound **TR4**.

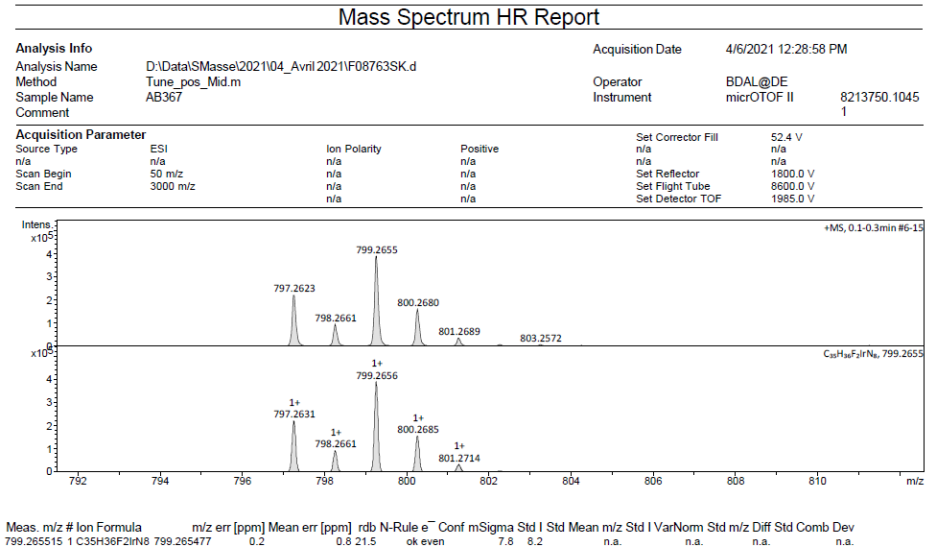

Figure ES5.14 HR-MS spectra for compound **TR5**.

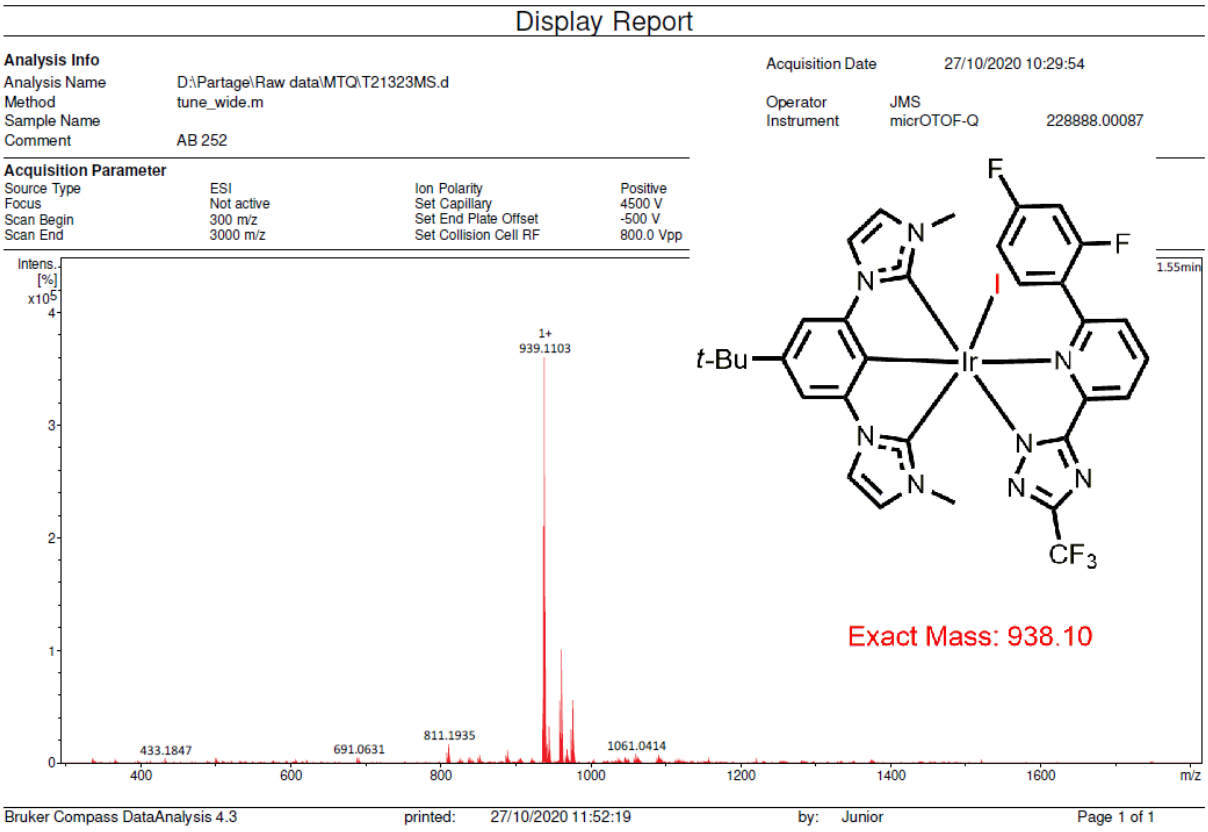

Figure ES5.15 HR-MS spectra for compound **TR2.b**.

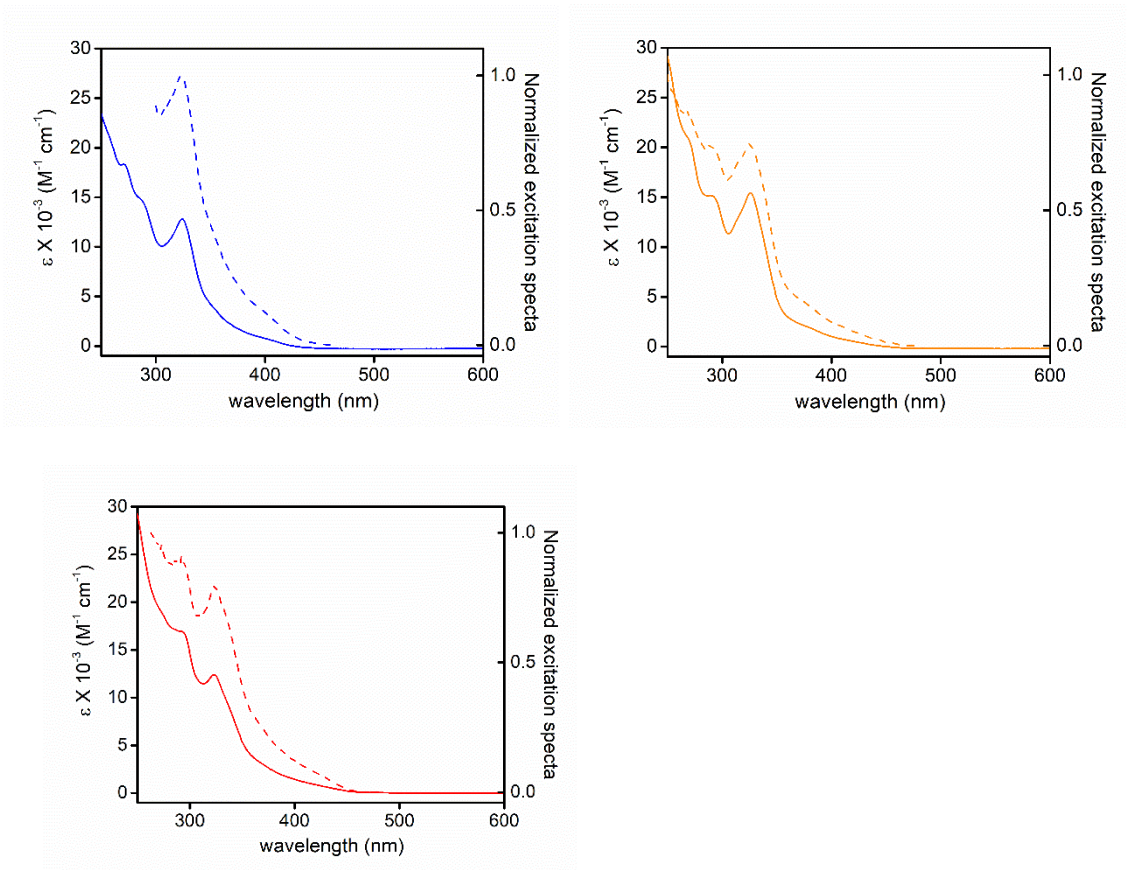

Figure ES5.16 Absorption (*solid line*) and normalized excitation spectra (*dashed line*) for complexes **TR1** (blue trace), **TR2** (orange trace) and **TR3** (red trace).

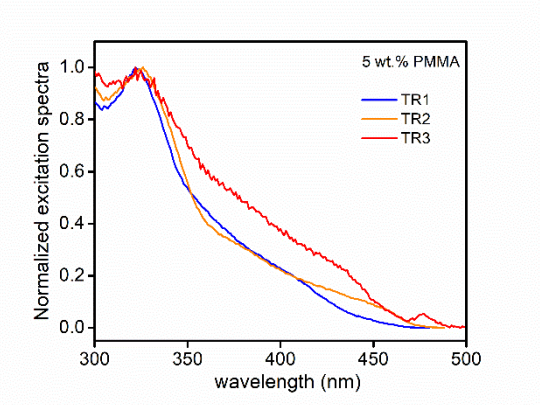

Figure ES5.17 Normalized excitation spectra of **TR1-TR3** 5wt.% in PMMA thin film.

Table ES5.1 Crystal data and structure refinement for complex **TR2.**

Identification code mmab210615

Empirical formula C33 H28 Cl2 F5 Ir N8

Formula weight 894.73

Temperature 120(2) K

Wavelength 0.71073 A

Crystal system, space group Monoclinic, P 21

Unit cell dimensions a = 8.6946(3) A alpha = 90 deg.

b = 21.4073(7) A beta = 105.8490(10) deg.

c = 9.3899(3) A gamma = 90 deg.

Volume 1681.28(10) A^3

Z, Calculated density 2, 1.767 Mg/m^3

Absorption coefficient 4.195 mm^{-1}

F(000) 876

Crystal size 0.100 x 0.080 x 0.050 mm

Theta range for data collection 2.255 to 28.040 deg.

Limiting indices -11<=h<=11, -27<=k<=28, -12<=l<=12

Reflections collected / unique 47412 / 8019 [R(int) = 0.0840]

Completeness to theta = 25.242 100.0 %

Absorption correction Semi-empirical from equivalents

Max. and min. transmission 0.7325 and 0.6916

Refinement method Full-matrix least-squares on F^2

Data / restraints / parameters 8019 / 1 / 447

Goodness-of-fit on F^2 1.067

Final R indices [I>2sigma(I)] R1 = 0.0342, wR2 = 0.0591

R indices (all data) R1 = 0.0445, wR2 = 0.0641

Absolute structure parameter 0.006(5)

Extinction coefficient n/a

5.5 Authors contributions

Ariitea Peu (M1 student) and Emilie Voirin (DMO, IPCMS, Université de Strasbourg & CNRS) are kindly acknowledged for their help with the synthesis of the bis-carbene and the triazolyl proligands. Corinne Bailly is acknowledged for performing X-ray diffrattometric analysis.

5.6 References

1. [a] K. Y. Zhang, P. Gao, G. Sun, T. Zhang, X. Li, S. Liu, Q. Zhao, K. Kam-Wing Lo, W. Huang, *J. Am. Chem. Soc.* **2018**, 140, 25, 7827; [b] D-L. Ma, S. Lin, W. Wang, C. Yang, C-H. Leung, *Chem. Sci.*, **2017**, *8*, 878; [c] K. Y. Zhang, T. Zhang, H. Wei, Q. Wu, S. Liu, Q. Zhao, W. Huang, *Chem. Sci.*, **2018**, *9*, 7236; [d] K. K-W. Lo, K. Y. Zhang, *RSC Adv.*, **2012**, *2*, 12069; [e] W. Liu, R. Gust *Chem. Soc. Rev.,* **2013**,*42*, 755.
2. [a] J. D. Nguyen, E. M. D'Amato, J. M. R. Narayanam, C. R. J. Stephenson, *Nat. Chem.*, **2012**, *4*, 854. [b] D. M. Schultz, T. P. Yoon, *Science*, **2014**, *343*, 1239176.
3. [a] H. Yersin (Ed.) in *Highly Efficient OLEDs with Phosphorescent Materials*, Wiley-VCH, Weinheim, **2008**; [b] Y. Chi, T.-K. Chang, P. Ganesan, P. Rajakannu, *Coord. Chem. Rev.* **2017**, *346*, 91; [c] E. Zysman-Colman Iridium(III) in *Optoelectronic and Photonics Applications*, **2017.**
4. H. Yersin, A. F. Raµsch, R. Czerwieniec, T. Hofbeck, T. Fischer, *Coord Chem Rev.*, **2011**, *255*, 2622.
5. [a] Y. Chi, T.-K. Chang, P. Ganesan and P. Rajakannu, *Coord. Chem. Rev.*, **2017**, *346*, 91; [b] W. Song and J. Y. Lee, *Adv. Opt. Mater.*, **2017**, *5*, 1600901.
6. [a] Adachi, C.; Kwong, R. C.; Djurovich, P.; Adamovich, V.; Baldo, M. A.; Thompson, M. E.; Forrest, S. R. *Appl. Phys. Lett.* **2001**, *79*, 13, 2082, [b] S. Lamansky, P. Djurovich, D. A. Murphy, L.Feras, A. Hae-Eun, B. Chihaya, E. Paul, S. R. Forrest, M. E. Thompson, *J. Am. Chem. Soc.* **2001**, *123*, 4304.
7. A.F. Henwood and E. Zysman-Colman, *Chem. Commun.*, **2017**, *53*, 807.
8. A.B. Tamayo, B. D. Alleyne, P. I. Djurovich, S. Lamansky, I. Tsyba, N. N. Ho, R.Bau, M. E. Thompson, *J.Am.Chem.Soc.*, **2003**, *125*, 7796.
9. A.A. Danopoulos, T. Simler, P. Braunstein, Chem. Rev. 2019, 119,3730, M. N. Hopkinson, C. Richter, M. Schedler, F. Glorius, *Nature*, **2014**, *510*, 485.

10. T. Sajoto, P.I. Djurovich, A. Tamayo, M. Yousufuddin, R. Bau, M. E. Thompson, R.J. Holmes, S. R. Forrest, *Inorg. Chem.* **2005**, *44*, 22, 7992.
11. J. Lee, H-F. Chen, T. Batagoda, C. Coburn, P. I. Djurovich, M. E. Thompson, S. R. Forrest, *Nature Mater.*, **2016**, *15*, 92.
12. A.K. Pal, S. Krotkµs, M. Fontani, C. F. R. Mackenzie, D. B. Cordes, A. M. Z. Slawin, I. D. W. Samuel, E. Zysman-Colman, *Adv. Mater.* **2018**, *30*, 1804231.
13. C.-H. Chien, S. Fujita, S. Yamoto, T. Hara, T. Yamagata, M. Watanabe, K. Mashima, *Dalton Trans.* **2008**, 916.
14. M. J. Jurow, A. Bossi, P. I. Djurovich, M. E. Thompson, *Chem. Mater.* **2014**, *26*, 22, 6578.
15. F.P. Dwyer, D.P. Mellor, *Chelating agents and metal chelates. Elsevier,* **2012***.*
16. A.Mamo, I. Stefio, M. F. Parisi, A. Credi, M. Venturi, C. Di Pietro, S. Campagna, *Inorg. Chem.* **1997**, *36*, 5947.
17. [a] M. Polson, S. Fracasso, V. Bertolasi, M. Ravaglia, F. Scandola, *Inorg. Chem.* **2004**, *43*, 1950. [b] Polson, M.; Ravaglia, M.; Fracasso, S.; Garavelli, M.; Scandola, F. *Inorg. Chem.* **2005**, *44*, 1282.
18. A.J. Wilkinson, A.E. Goeta, C.E. Foster, J.A.G. Williams, *Inorg. Chem.* **2004**, *43*, 6513
19. Z-L. Zhu, W-C- Chen, S-F. Ni, J. Yan, S. F. Wang, L-W. Fu, H-Y. Tsai, Y. Chi, C-S. Lee *J. Mater. Chem. C*, **2021**, *9*, 1318.
20. [a] Y. Chi, T.-K. Chang, P. Ganesan, P. Rajakannu, *Coord. Chem. Rev.* **2017**, *346*, 91; [b] T. Yutaka, S. Obara, S. Ogawa, K. Nozaki, N. Ikeda, T. Ohno, Y. Ishii, K. Sakai, M. Haga, Inorg. Chem. **2005**, 44, 4737; [c] N. Darmawan, C.-H. Yang, M. Mauro, M. Raynal, S. Heun, J. Pan, H. Buchholz, P. Braunstein, L. De Cola, *Inorg. Chem.* **2013**, *52*, 10756. [d] M.A. Esteruelas, D. Gomez-Bautista, A.M. Lopez, E. Onate, J.-Y. Tsai, C. Xia, *Chem. Eur. J.* **2017**, *23*, 15729.
21. M. Scholl, S. Ding, C.W. Lee, R.H. Grubbs, *Org. Lett.* **1999**, *1*, 953.
22. N. Matsumura, J. Kawano, N. Fukunishi, H. Inoue, *J. Am. Chem. Soc.* **1995**, *117*, 3623.
23. [a] D. Pugh, A. A. Danopoulos, *Coord Chem Rev.* **2007**, 251, 610; [b] A. Hidenori, T. Matsuo and H. Kawaguchi, *Chem. Commun.*, **2003**, *17,* 2204.
24. M. Raynal, C.S.J. Cazin, C. Vallée, H. Olivier-Bourbigou, P. Braunstein, *Chem Commun.* **2008**, 3983.
25. Z.-L. Zhu, L.-Y. Hsu, W.-S. Tai, S.-F. Ni, C.-S. Lee, Y. Chi, *Mater. Today Energy* **2021**, *20*, 100636.
26. [a] B. Tong, H. Y. Ku, J.I. Chen, Y.Chi, H.-C Kao, C.-C. Yeh, C.-H. Chang, S.-H. Liu, G.-H Lee, P.-T. Chou, *J. Mater. Chem. C* **2015**, *3*, 3460. [b] C.-Y. Kuei, W.-L. Tsai, B. Tong, M. Jiao, W.-K Lee, Y. Chi, C.-C. Wu, S.-H. Liu, G.-H. Lee, P.-T. Chou, *Adv. Mater.* **2016**, *28*, 2795.
27. J. Lin, N-Y. Chau, J-L. Liao, W-Y. Wong, C-Y. Lu, Z-T. Sie, C-H. Chang, M. A. Fox, P. J. Low, G-H. Lee, Y. Chi, *Organometallics.* **2016**, *35*, 1813
28. J. Lin, N-Y. Chau, J-L. Liao, W-Y. Wong, C-Yu Lu, Z-T Sie, C-H. Chang, Mark A. Fox, Paul J. Low, G-H. Lee, Y. Chi, *Organometallics.* **2016**, *35*, 1813.
29. W.R. Browne, R. Hage, J.G. Vos, Coord. Chem. Rev. **2006**, *250*, 1653; G. Aromí, L.A. Barrios, O. Roubeau, P. Gamez, *Coord. Chem. Rev.* **2011**, *255*, 485

30. J. Li, P. I. Djurovich, B.D. Alleyne, M. Yousufuddin, N. N. Ho, J. C. Thomas, J. C. Peters, R. Bau, M.E. Thompson, *Inorg. Chem.* **2005**, *44*,1713.
31. [a] M. Raynal , R. Pattacini , C. S. J. Cazin , C. Vallée , H. Olivier-Bourbigou , P. Braunstein , *Organometallics.* **2009**, *28*, 4028.
32. [a] V. C. Vargas, R. J. Rubio, T. K. Hollis, M.E. Salcido, *Org. Lett.* **2003**, *5*, 4847; [b] V. Charra, P. De Fremont, P-A. R. Breuil, H. Olivier-Bourbigou, P. Braunstein, *J. Organometallics. Chem.,* **2015**, *795*, 25.
33. J. Sanning, L. Stegemann, P. R. Ewen, C. Schwermann, C. G. Daniliuc, D. Zhang, N. Lin, L. Duan, D. Wegner, N. L. Doltsinis, C. A. Strassert, *J. Mater. Chem. C*, **2016**,*4*, 2560.
34. A. R. Chianese, A. Mo, N. L. Lampland, R. L. Swartz, P. T. Bremer, *Organometallics*, **2010**, *29*, 13.

6. Experimental techniques

ABSTRACT

In this last chapter, the main experimental methods used for the characterization of the metal complexes herein reported are described. The conditions for the basic chemical characterization as NMR, mass, infrared, thermogravimetric and elemental analysis are briefly reported. Spectrophotometry, spectrofluorimetry, time-resolved emission and photoluminescence quantum yield measurement techniques are explained and illustrated by an experimental and theoretical point of view.

6.1 Chemical characterization

Nuclear magnetic resonance spectra were recorded using a Bruker Avance III HD 300 and 500 spectrometer equipped with a N_2 cryo-probe CPPBBO Prodigy at 298 K. ^{1}H, ^{13}C and ^{19}F NMR spectra were calibrated to residual solvent signals. Infrared spectra were recorded using a Fourier-transformed attenuated total reflectance infrared (FT-ATR-IR) spectrometer from Perkin Elmer. Elemental analyses were obtained at the AMS Fédération de Chimie Le Bel, University of Strasbourg on a Flash 2000 ThermoFischer Scientific apparatus. Thermogravimetric analysis was performed on a Q50 apparatus of TA Instruments, at a scanning rate of 5 °C min^{-1} and with nitrogen as purge gas. HR-ESI-MS spectra were recorded on a MicroToF Bruker equipped with an electrospray ionization source.

6.2 Spectrophotometry

In an electronic absorption spectrum, the value of the extinction coefficient gives information about the probability of an electronic transition to occur. This is experimentally measured by means of measuring the absorbance, A, of a sample. Absorbance is defined as

$$A = \log (I_0 / I) \qquad Eqn.\ 6.1$$

where I_0 is the light intensity irradiate before crossing the sample and I is the light intensity after crossing the sample. Its value is related to the concentration of the chromophore by the Lambert-Beer relationship as by equation 6.2:

$$A(\lambda) = \varepsilon(\lambda) \cdot c \cdot l \qquad Eqn.\ 6.2$$

where c is the concentration of the sample (in mol L^{-1}), l is the optical path of the light-matter interaction (in cm) and ε (λ) is the molar extinction coefficient. The value of this latter is indicative of the degree of permittivity of an absorption process at a given wavelength λ, and it can span from smaller value (1-10^2 M^{-1} cm^{-1}) to larger values (10^2-10^6 M^{-1} cm^{-1}). The larger the value the more allowed is the transition. [1]

For all the samples investigated in this thesis, the steady state absorption was measured with a Varian Cary 100 double-beam UV–VIS spectrophotometer and baseline corrected. The general scheme of a double-beam spectrometer is showed in *Figure 6.1*. The light from lamp (deuterium arc lamp for 180-250 nm and tungsten filament lamp for 250-900 nm) crosses the monochromator and then it is split into two beams with a beam splitter and directed to the sample and reference cuvette with the help of mirrors. One beam irradiates the solvent as reference and the other one irradiates the sample. Two absorbance values are measured, namely A_s and A_r, and the true absorbance of the chromophore, that is defined as $A = As - Ar = \log(I_s/I_r)$, is thus recorded automatically.[2]

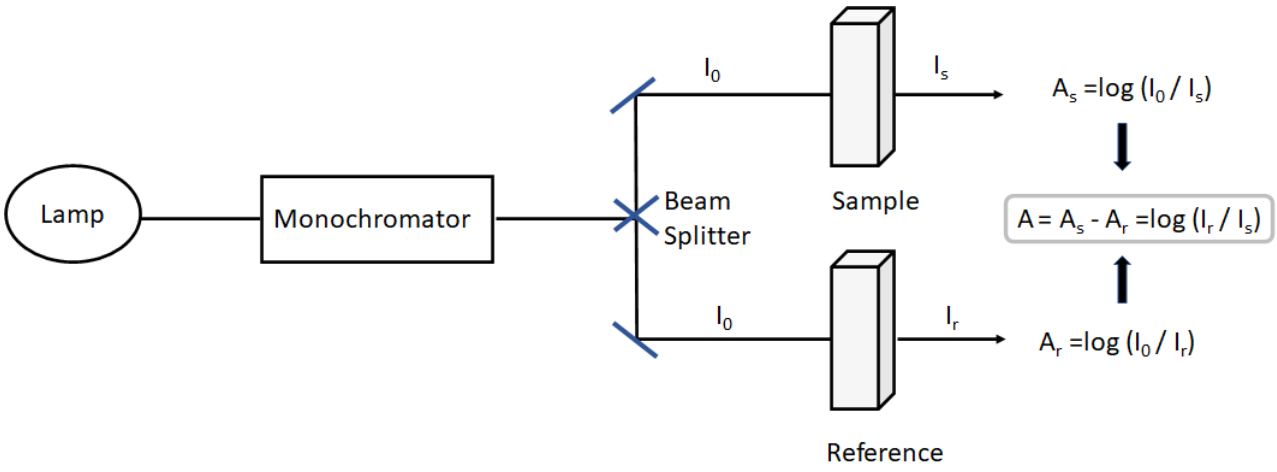

Figure 6.1 Schematic representation of a double-beam spectrophotometer.

6.3 Spectrofluorimetry

Steady-state emission spectra were recorded on a Horiba Jobin−Yvon IBH FL-322 Fluorolog 3 spectrometer equipped with a 450 W xenon arc lamp, double-grating excitation, and emission monochromators (2.1 nm mm^{-1} of dispersion; 1200 grooves mm^{-1}) and a Hamamatsu R13456 red sensitive Peltier-cooled photomultiplier (PMT) detector. The light generated by the xenon lamp (I_{ex} 100-1100 nm) passes through the monochromator M1, which selects the excitation wavelength that will be used to excite the sample. The luminescence of the sample is collected at 90° respect to the incident light (λex) as to minimize the excitation and diffused light linearly propagated through the sample. The monochromator M2 selects the emission wavelength that will be collected by the detector.[2] A schematic representation is given in *Figure 6.2*.

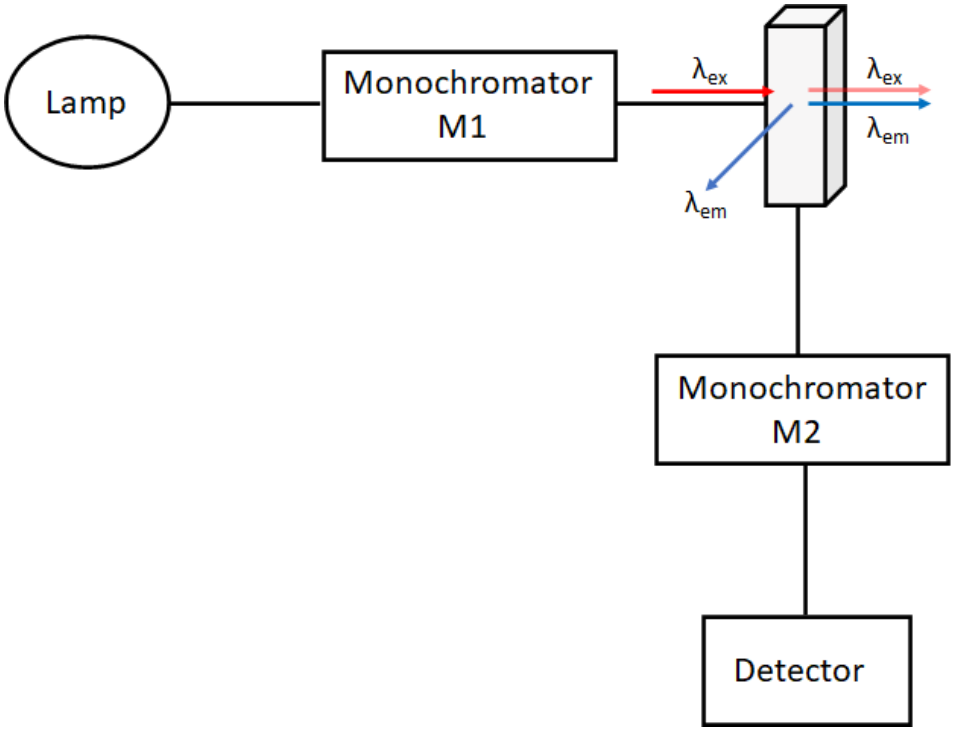

Figure 6.2 Schematic diagram of a spectrofluometer.

Emission and excitation spectra were corrected for source intensity (lamp and grating) and emission spectral response (detector and grating) by standard correction curves. For emission measurements, the monochromator of excitation (M1) is fixed at a certain wavelength, while the monochromator of emission (M2) tests different wavelength; vice-versa for excitation measurements, M1 scans different wavelengths and M2 is fixed at one wavelength.

6.4 Time-resolved emission

Time-resolved measurements were performed using either the time-correlated single-photon counting (TCSPC) or the Multi-Channel Scaling (MCS) electronics option. TCSPC is a technique based on the ability to detect and count individual photons to measure the luminescence decay of a sample. The decay profile is given by the time difference between the sample excitation and the detection of emitted photons. The source is a pulsed, low intensity, high repetitive (1-100 KHz) light-emitting diode (LED) lamp or laser. When the sample is excited, an electrical pulse is directed to the “START” input of the time-to-

amplitude (TAC) converter. When the sample emits light, the electrical response generated by the first detected photon is used as the "STOP" signal for the TAC. The START pulse initiates the charging of a capacitor while the STOP pulse stopped it. The time between the two pulses, which is proportional to the final voltage, is then calculated. Several repetitions of this measurements result in the creation of a histogram of events that corresponds to the luminescent decay curve (*Figure 6.3 and Figure 6.4a*). [2] The x- axis is the time difference and the y-axis the number of photons detected for this time difference. When much less than 1 photon is detected per excitation pulse, the histogram represents the waveform of the decay (*Figure 6.4b*). If the count rate is higher the histogram is biased to shorter times. This is because with TCSPC only the first photon can be observed. Multiple photons per pulse can be measured for decay times near a microsecond or longer.[3]

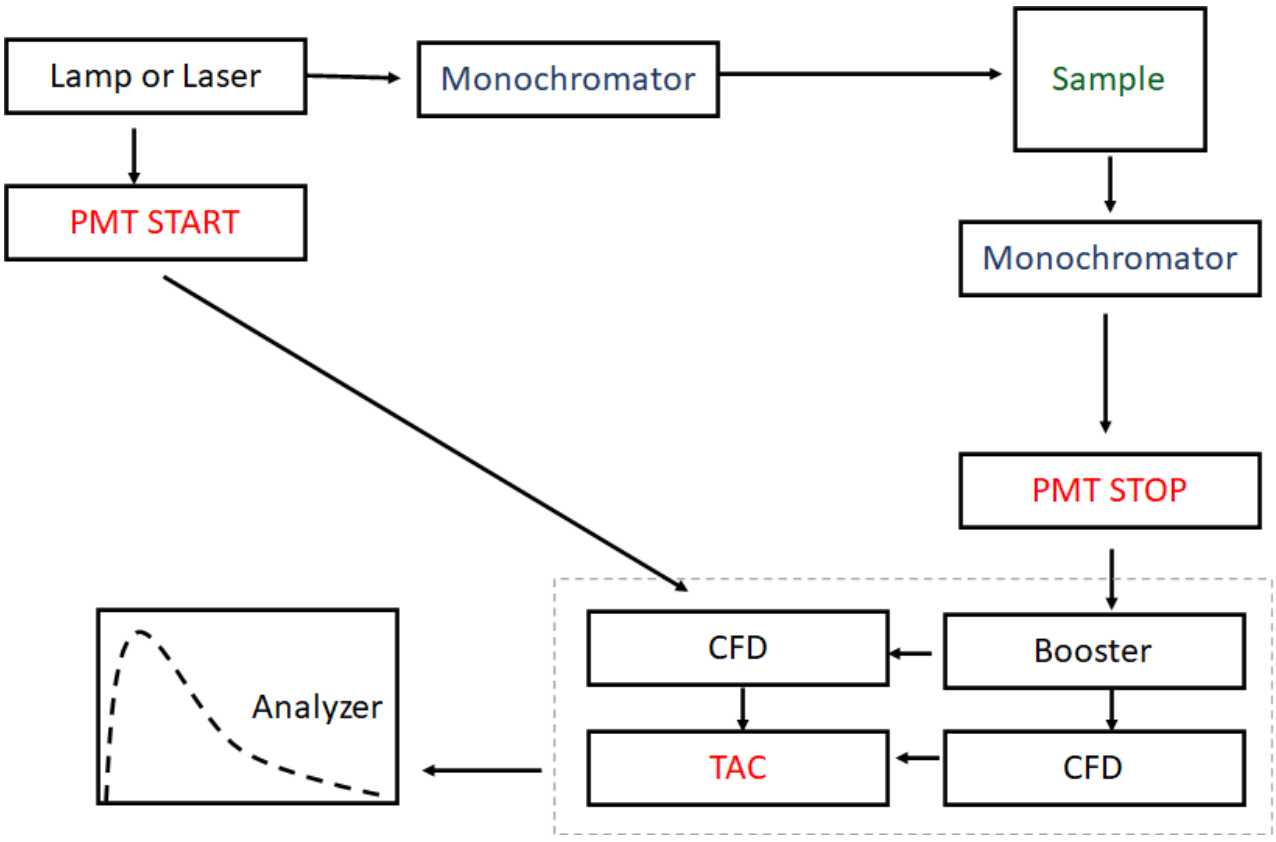

Figure 6.3 Schematic diagram of the working principle of Time-Correlated Single Photon Counting (TCSPC) technique.

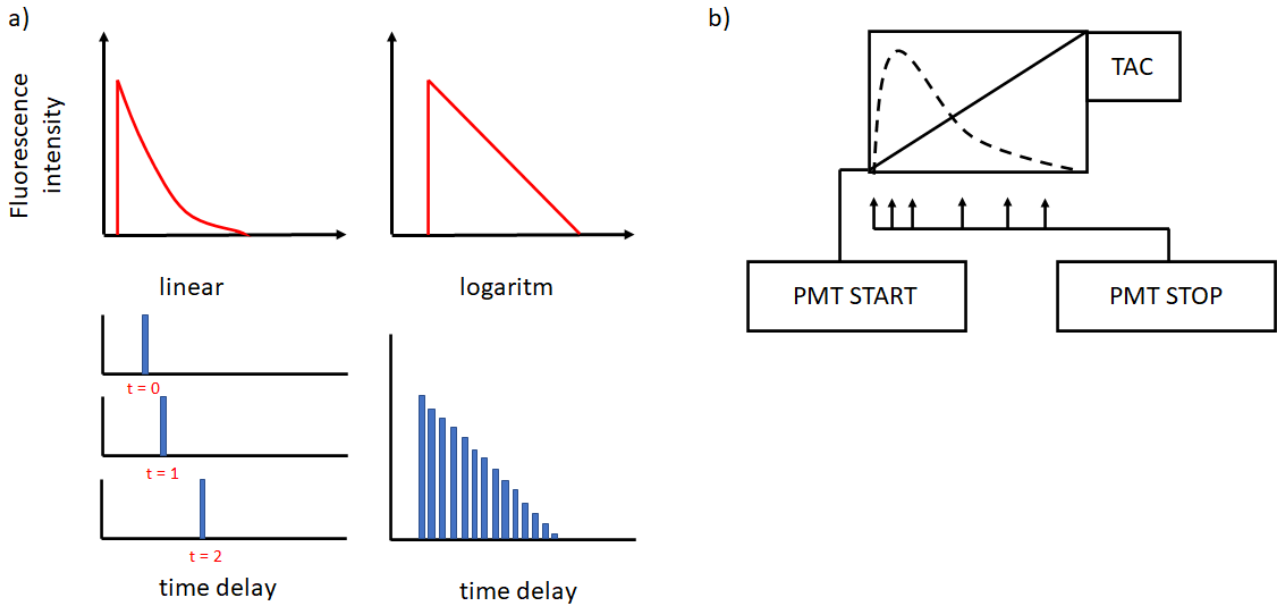

Figure 6.4 General scheme of working principle of exponential and logarithmic decay

The analysis were performed by a TimeHarp 260 board installed on a PicoQuant FluoTime 300 fluorimeter (PicoQuant GmbH, Germany), equipped with a PDL 820 laser pulse driver. A pulsed laser diode LDH-P-C-375 (I_{exc} = 375 nm, pulse full width at half maximum FWHM <50 ps, repetition rate 200 kHz–40 MHz) was used to excite the sample and mounted directly on the sample chamber at 90°. The photons were collected by a PMA Hybrid-07 single photon counting detector. The data were acquired by using the commercially available software EasyTau II (PicoQuant GmbH, Germany), while data analysis was performed using the built-in software FluoFit (PicoQuant GmbH, Germany).

Data fitting of the recorded decay curves was performed by employing the maximum likelihood estimation (MLE) method. The quality of the fit was assessed by inspection of the reduced χ^2 function and of the weighted residuals. For multi-exponential decays, the intensity, namely *I*(t), has been assumed to decay as the sum of individual single exponential decays (Equation 6.3):

$$I(t) = \sum_{i=1}^{n} \alpha_i exp\left(-\frac{t}{\tau_i}\right) \qquad Eqn. 6.3$$

where τ_i are the decay times and α_i are the amplitude of the component at *t* = 0. In the tables, the percentages to the pre-exponential factors, α_i are listed upon normalization.

Intensity average lifetimes were calculated by using the following Equation (6.4):[3]

$$\bar{\tau} = \frac{a_1\tau_1^2 + a_2\tau_2^2}{a_1\tau_1 + a_2\tau_2} \qquad Eqn.\,6.4$$

To rule out the possible origin of the bi-exponential decays as due to any trace impurities, crystalline samples were used to prepare the solutions for spectroscopical investigation.

6.5 Photoluminescence quantum yield

6.5.1 Relative method for diluted solution samples

Luminescence quantum yields were measured in optically dilute solutions (optical density <0.1 at the excitation wavelength) and compared to reference emitter by following the method of Demas and Crosby (Equation 6.5): [4]

$$\phi = \phi_{ref} \times \left(\frac{I_s}{I_{ref}}\right) \times \left(\frac{Abs_{ref}}{Abs_s}\right) \times \left(\frac{\eta_s}{\eta_{ref}}\right)^2 \qquad Eqn.\,6.5$$

Where ref and s refer to the standard and the sample, respectively; ϕ_{ref} is the photoluminescence quantum yield of the standard, I is the intensity, Abs is the absorption and η is the refractive index of the solvent used.

All the solvents were spectrophotometric grade. Deaerated samples were prepared by the freeze-pump-thaw technique by using a homemade quartz cuvette equipped with a Rotaflo stopcock (see *Figure 6.5*).

Figure 6.5 Homemade quartz cuvette equipped with a Rotaflo stopcock (*left*) and then attached to the freeze-pump-thaw (*right*).

6.5.2 Absolute method for solid-state samples

Photoluminescence quantum yield can be described as the ratio between the number of emitted photons and the number of absorbed photons, that is the definition of integrated quantum yield. Since the number of emitted photons is proportional to the fluorescence intensity I_f and the number of absorbed photons is proportional to the absorbed light intensity I_a, so the PLQY is described by the following equation (6.6):[6]

$$\phi = \frac{I_f}{I_a} \qquad Eqn\ 6.6$$

The integrating sphere is a hollow sphere with a perfectly diffusing inner surface that allows total reflection of light. The slit through which light radiation passes is to all intents and purposes a black body, which totally absorbs the incident radiation, without reflecting it. A xenon arc lamp provides the light that passes through a monochromator, then collimated with a mirror toward the center of the integrating sphere. Here, the light moves to the sample and then to the detector (*Figure 6.6*).[5]

All the PLQYs on spin-coated thin-film samples were recorded at a fixed excitation wavelength by using a Hamamatsu Photonics absolute PLQY measurements system Quantaurus QY equipped with continuous wave (CW) xenon light source (150 W),

monochromator, integrating sphere, C7473 photonics multi-channel analyzer and employing the commercially available U6039-05 PLQY measurement software (Hamamatsu Photonics Ltd., Shizuoka, Japan).

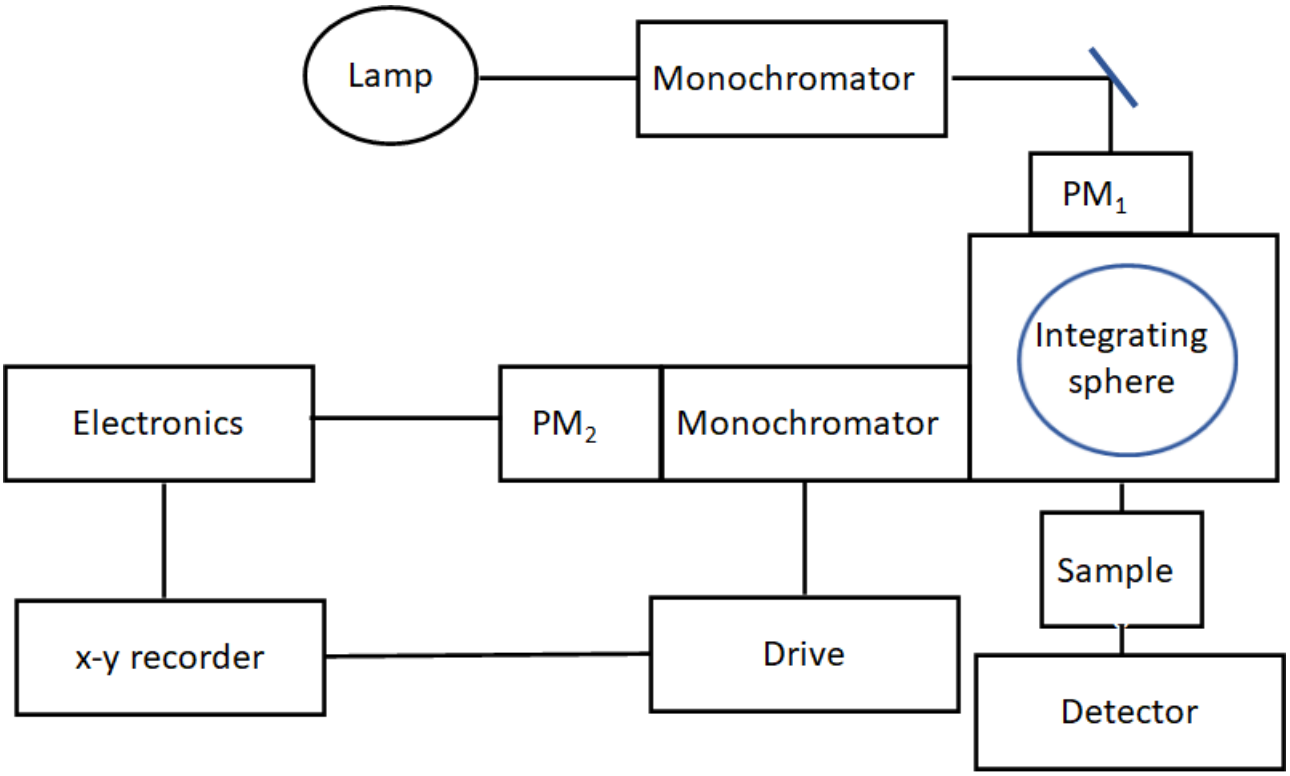

Figure 6.6 Schematic diagram of the working principle of an integrating sphere.

6.6 References

1. J. P. Fackler, *Modern Inorganic Chemistry*, Texas A&M University, **2017**
2. L. Moggi, A. Juris, M. T. Gandolfi, *Manuale del fotochimico*, Bononia University Press, **2006**
3. J. R. Lakowicz*, Principles of Fluorescence Spectroscopy,* Springer, third edition.
4. [a] G. A. Crosby, J. N. C. Demas, *J. Am. Chem. Soc.* **1970**, *92*, 7262; [b] H. Ishida, J.-C. Bünzli, A. Beeby, *Pure Appl. Chem.* **2016**, *88*, 701; [c] C. Würth, M. Grabolle, J. Pauli, M. Spieles, U. Resch-Genger, *Nat. Prot.* **2013**, *8*, 1515.
5. W.R. Ware,W. Rothman, *Chem. Phys. Lett.,***1976**, *39*,3,449
6. I. Baraldi, *La Luminescenza*, Bonomia University Press, **2007**

Acknowledgements

This last section of my thesis is dedicated to all those people who have accompanied me during my PhD journey and how they influenced my professional and personal path, making me grow as scientist and as person.

On top of the list, my professor, supervisor and mentor Dr. Matteo Mauro. He gave me the possibility to join him at the University of Strasbourg as PhD student, after a lot of slammed doors. It meant a lot for me and I will be grateful to him forever, because I had the possibility to change my professional future. I wanted to do research and I could do what I desired. I could learn a lot more. Nothing was easy, I worked hard and I nailed it, at the end. Thanks to my advisor, I discovered a new chemistry that I liked so much (luminescent complexes) and especially those with iridium, the metal that will always be in my heart. He transmitted to me the passion for this kind of chemistry and especially the curiosity to know more and more. All scientific discussions we had, had a strong impact on my will to pursue the way of research. Thanks to the experience gained with him at IPCMS labs, I recognized my skills and how to improve them.

My experience was exceptional also because of the people I met, starting from my PhD colleagues Julien, Yannick and Damien who helped me a lot to get settled with the new work-place, labs, facilities and the “complicated” French bureaucratic system. I’m also grateful to Sophie and Flavien for the laughter and talks during the work-time, that made everything less serious; Nico for his companionship in the office, and Dr. Thierry Achard for his advices, funny and varied discussions about family, academy and daily life topics.

A special gratitude goes to all the students I had in lab with me (Olivier, Sinan, Zhengang) and especially those I had the pleasure to supervise (Zakaria, Mohammed and Ariitea). Thanks to the students, I developed my teaching and mentoring skills. Their experimental problems and questions drove me to search and study more, looking at the same issue from a different point of view, trying to explain something complicated using simple words.

A more general thanks goes to all people from DMO, my host department where I could carry out my research. Emilie V. and C., Emeric, Benoit and Nicholas deserve a special mention for their help with instruments and lab troubles. Then, all collaborators, already

mentioned one by one in each chapter, who helped me make my job a complete “chemical romance” are warmly acknowledged for their fundamental contribution during these years.

Hoping to not have forgotten anyone early, I wish to acknowledge those people who support me more as a person than as a scientist. First of all, my family, so my dad, mum and my “little” brother who never made me miss their encouragement and emotional support despite the distance. They always believed in me, in my skills and in my strength, even when I didn’t. Nonetheless we went through hard times who forced us to stay far away from each other, they have always been there for me, sharing feelings, worries and struggles.

Lastly, I let my big final gratitude to the person who have lived with me every day, knowing every fear of mine, every doubt, and every thought about everything along these years, my boyfriend Francesco. I have always believed that this experience in Strasbourg might be good if I have been alone, but actually it was great because of him. He was my support, my firm point, my rock, and someone who I could always rely on.

“Everyone we meet comes into our lives for a reason”: some of them help us to improve as workers, some of them to make us better people, others do both.

In these three years, I have met all those people and I’m very grateful to one of them for who I am now.

Thanks.

Anna BONFIGLIO

Novel phosphorescent N-heterocyclic carbene-based complexes: from photocatalysis and biomedicine applications to optoelectronic devices

Résumé

Différentes classes de ligands à base de carbène N-hétérocyclique (NHC) ont été explorées pour la préparation et l'étude de nouvelles familles d'émetteurs, basées sur des complexes métalliques Ir(III) et Re(I). Quatre nouveaux complexes tricarbonyles de rhénium(I), où **Re1** et **Re2** sont neutres et **Re3** et **Re4** sont cationiques, ont été étudiés comme système photocatalytique pour les monomères de PEG-diacrylate. Les cinq nouveaux complexes hétéroleptiques d'iridium (III) **Ir1-Ir5** ont montré une combinaison de propriétés optiques et d'activité de destruction de cellules tumorales, ce qui en fait une nouvelle classe d'agents theragnostiques puissants. Une nouvelle famille de complexes hétérodinucléaires (**4-7**) a montré de meilleures propriétés optiques que les congénères mononucléaires parentaux (**1-3**). Parmi les complexes dinucléaires, les complexes **6** et **7** affichent les meilleures performances dans les dispositifs LEC. Trois nouveaux complexes tridentés bleus d'iridium(III) **TR1-TR3** ont révélé une application future possible comme émetteurs dopants dans les OLEDs.

Mot clés : Carbènes N-hétérocycliques - rhénium - iridium – photocatalyseur – métallo médicament – LEC-OLED

Résumé en anglaise

Different classes of N-heterocyclic carbene (NHC)-based ligands were explored for the preparation and investigation of novel families of emitters, based on Ir(III) and Re(I) metal complexes. Four novel tricarbonyl rhenium(I) complexes, where **Re1** and **Re2** are neutral and **Re3** and **Re4** are cationic, were explored as photocatalytic system for PEG-diacrylate monomers. New five heteroleptic iridium (III) complexes **Ir1**-**Ir5** displayed a combination of optical proprieties and tumor cell killing activity, making them a new class of potent theragnostic agents. A novel family of hetero-dinuclear (**4-7**) complexes showed better optical properties than the parental mononuclear congeners (**1-3**). Among dinuclear complexes, **6** and **7** display the best performances in LEC devices. Three new blue tridentate iridium(III) complexes **TR1-TR3** revealed a possible future application as dopant emitters in OLEDs.

Key words : N-heterocyclic carbenes - rhenium - iridium– photocatalyst – metallodrug – LEC- OLED